GEOLOGICAL SURVEY OF CANADA
COMMISSION GÉOLOGIQUE DU CANADA

CURRENT RESEARCH 1998-E

RECHERCHES EN COURS 1998-E

Natural Resources Canada
Ressources naturelles Canada

Canada

NOTICE TO LIBRARIANS AND INDEXERS

The Geological Survey's Current Research series contains many reports comparable in scope and subject matter to those appearing in scientific journals and other serials. Most contributions to Current Research include an abstract and bibliographic citation. It is hoped that these will assist you in cataloguing and indexing these reports and that this will result in a still wider dissemination of the results of the Geological Survey's research activities.

AVIS AUX BIBLIOTHÉCAIRES ET PRÉPARATEURS D'INDEX

La série Recherches en cours de la Commission géologique contient plusieurs rapports dont la portée et la nature sont comparables à celles des rapports qui paraissent dans les revues scientifiques et autres périodiques. La plupart des articles publiés dans Recherches en cours sont accompagnés d'un résumé et d'une bibliographie, ce qui vous permettra, on l'espère, de cataloguer et d'indexer ces rapports, d'où une meilleure diffusion des résultats de recherche de la Commission géologique.

GEOLOGICAL SURVEY OF CANADA
COMMISSION GÉOLOGIQUE DU CANADA

CURRENT RESEARCH 1998-E

RECHERCHES EN COURS 1998-E

1998

Includes/comprend:

Cordillera and Pacific Margin
Cordillère et marge du Pacifique

Interior Plains and Arctic Canada
Plaines intérieures et région arctique du Canada

Canadian Shield
Bouclier canadien

Eastern Canada and National and General Programs
Est du Canada et programmes nationaux et généraux

Catalogue No. M44-1998/5E
ISBN 0-660-17595-9

Available in Canada from
Geological Survey of Canada offices:

601 Booth Street
Ottawa, Ontario K1A 0E8

3303-33rd Street N.W.
Calgary, Alberta T2L 2A7

101-605 Robson Street
Vancouver, B.C. V6B 5J3

A deposit copy of this publication is also available for reference
in selected public libraries across Canada

Price subject to change without notice

Cover illustration

Mafic mylonite in the Hemlo shear zone, Hemlo, Ontario. See paper by S. Lin, this volume. Photograph by S. Lin. GSC 1998-044

Photo en page couverture

Mylonite mafique dans la zone de cisaillement de Hemlo, Hemlo (Ontario). Cette photographie se rapporte à l'étude de S. Lin dans le présent volume. Photo : S. Lin, GSC 1998-044

Separates

A limited number of separates of the papers that appear in this volume are available by direct request to the individual authors. The addresses of the Geological Survey of Canada offices follow:

Geological Survey of Canada
601 Booth Street
Ottawa, Ontario
K1A 0E8
(FAX: 613-996-9990)

Geological Survey of Canada (Calgary)
3303-33rd Street N.W.
Calgary, Alberta
T2L 2A7
(FAX: 403-292-5377)

Geological Survey of Canada (Pacific)
101-605 Robson Street
Vancouver, British Columbia
V6B 5J3
(FAX: 604-666-1124)

Geological Survey of Canada (Pacific)
P.O. Box 6000
9860 Saanich Road
Sidney, British Columbia
V8L 4B2
(FAX: 604-363-6565)

Geological Survey of Canada (Atlantic)
Bedford Institute of Oceanography
P.O. Box 1006
Dartmouth, Nova Scotia
B2Y 4A2
(FAX: 902-426-2256)

Geological Survey of Canada (Quebec)
Quebec Geoscience Centre
2535, boulevard Laurier
C.P. 7500
Sainte-Foy (Québec)
G1V 4C7
(FAX: 418-654-2615)

Tirés à part

On peut obtenir un nombre limité de «tirés à part» des articles qui paraissent dans cette publication en s'adressant directement à chaque auteur. Les adresses des différents bureaux de la Commission géologique du Canada sont les suivantes :

Commission géologique du Canada
601, rue Booth
Ottawa (Ontario)
K1A 0E8
(Télécopieur : 613-996-9990)

Commission géologique du Canada (Calgary)
3303-33rd Street N.W.,
Calgary, Alberta
T2L 2A7
(Télécopieur : 403-292-5377)

Commission géologique du Canada (Pacifique)
101-605 Robson Street
Vancouver, British Columbia
V6B 5J3
(Télécopieur : 604-666-1124)

Commission géologique du Canada (Pacifique)
P.O. Box 6000
9860 Saanich Road
Sidney, British Columbia
V8L 4B2
(Télécopieur : 604-363-6565)

Commission géologique du Canada (Atlantique)
Institut océanographique Bedford
P.O. Box 1006
Dartmouth, Nova Scotia
B2Y 4A2
(Télécopieur : 902-426-2256)

Commission géologique du Canada (Québec)
Centre géoscientifique de Québec
2535, boulevard Laurier
C.P. 7500
Sainte-Foy (Québec)
G1V 4C7
(Télécopieur : 418-654-2615)

CONTENTS

CORDILLERA AND PACIFIC MARGIN
CORDILLÈRE ET MARGE DU PACIFIQUE

INTERIOR PLAINS AND ARCTIC CANADA
PLAINES INTÉRIEURES ET RÉGION ARCTIQUE DU CANADA

CANADIAN SHIELD
BOUCLIER CANADIEN

EASTERN CANADA AND NATIONAL AND GENERAL PROGRAMS
EST DU CANADA ET PROGRAMMES NATIONAUX ET GÉNÉRAUX

Cordillera and Pacific Margin

Cordillère et marge du Pacifique

Stratigraphy, structural stacking, and paleoenvironment of the Cache Creek Group, central British Columbia[1]

L.C. Struik, F. Cordey[2], M.J. Orchard, and H. Sano[3]
GSC Pacific, Vancouver

Struik, L.C., Cordey, F., Orchard, M.J., and Sano, H., 1998: Stratigraphy, structural stacking, and paleoenvironment of the Cache Creek Group, central British Columbia; in *Current Research 1998-E; Geological Survey of Canada, p. 1–10.*

Abstract: Oceanic rocks of the Cache Creek Group near Fort St. James (NTS 93 K) form a thrust imbricate stack cut by steeply dipping strike-slip faults including the Pinchi Fault. The thrust stack consists of upper Paleozoic and Mesozoic rock suites. Paleontologically dated upper Paleozoic rocks include bioclastic limestone and ribbon chert. Mesozoic rocks include greywacke, siltstone, argillite, ribbon chert, limestone, and basalt tuff. Trembleur ultramafic unit of the Cache Creek Group in part forms klippe thrust onto early Mesozoic sedimentary rocks. The sedimentological character of the upper Paleozoic limestone and the new chemistry of the upper Paleozoic basalt indicate development of these rocks on an oceanic plateau.

Résumé : Les roches océaniques du Groupe de Cache Creek qui se trouvent à proximité de Fort St. James (SNRC 93 K) forment un empilement chevauchant en écailles que recoupent des décrochements à fort pendage, dont la faille de Pinchi. Cet empilement est formé d'un cortège de roches du Paléozoïque supérieur et du Mésozoïque. Les roches que la datation paléontologique situe au Paléozoïque supérieur renferment des calcaires bioclastiques et des cherts rubanés. Les roches mésozoïques comprennent des grauwackes, des siltstones, des argilites, des cherts rubanés, du calcaire et des tufs basaltiques. Une partie de l'unité ultramafique de Trembleur du Groupe de Cache Creek forme une klippe qui repose sur des roches sédimentaires du Mésozoïque précoce. Le caractère sédimentologique du calcaire du Paléozoïque supérieur et la nouvelle composition chimique des basaltes également du Paléozoïque supérieur indiquent que ces roches se sont développées sur un plateau océanique.

---

[1] Contribution to the Nechako NATMAP project; a joint mapping project of the Geological Survey of Canada and British Columbia Geological Survey Branch

[2] Université Claude Bernard Lyon I, 27-43 Bd. du 11 Novembre, 69622 Villeurbanne cedex, France

[3] Department of Earth and Planetary Sciences, Kyushu University, 812-81 Japan

INTRODUCTION

George Mercer Dawson thought the limestone at Mount Pope near Fort St. James looked just like the limestone of the Marble Canyon near Cache Creek in southern British Columbia (Dawson, 1878). His assignment of these rocks to the Cache Creek Group still stands, although the correlation of the limestones may be over simplified. Since Dawson's time, rocks of the Cache Creek Group have been described as a unique oceanic assemblage of an allochthonous terrane and has been used to characterize a large part of the Mesozoic collision and amalgamation history of the Canadian Cordillera (Monger and Ross, 1971; Monger et al., 1972; Paterson, 1973; Silberling and Jones, 1984).

New bedrock geological mapping was begun in the Fort Fraser and Manson River map areas in central British Columbia as part of the Nechako NATMAP Project (1995–2000) (NTS 93 K, 93 N, Fig. 1; Struik and McMillan, 1996; Struik and MacIntyre, 1997, 1998; MacIntyre and Struik, 1997, 1998). The area was first regionally mapped by Armstrong (1942, 1949), and subsequently has had a thorough remapping of its surficial deposits (Plouffe, 1994). Previous detailed bedrock mapping was done in several places by the British Columbia Geological Survey Branch, university graduate students, and the mineral exploration industry (Bellefontaine et al., 1995).

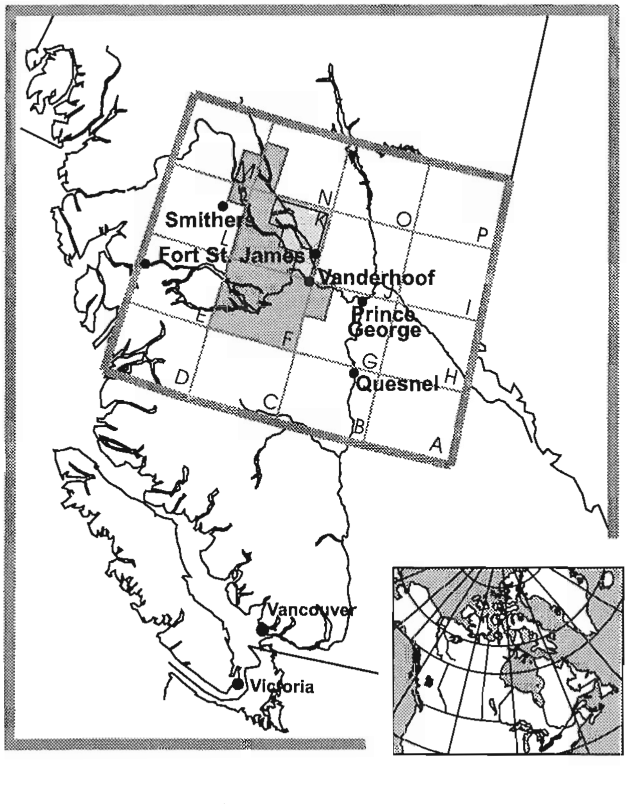

__Figure 1.__ Location of the study area in relation to surrounding NTS maps of the Parsnip River (93) 1:1 000 000 scale map.

The Cache Creek Group includes the remains of an oceanic plate caught in the suture between exotic and pericratonic terranes along the Triassic margin of western North America (Gabrielse and Yorath, 1991). The exotic paleontology of the Cache Creek Group itself with respect to the North American cratonal rocks has been key to the argument that it now occupies the place where the ancient edge of the craton used to be (Monger and Ross, 1971). Much has happened to these rocks since amalgamation to the western edge of North America. This paper introduces new ideas on the age range, paleoenvironment, and structural style of the Cache Creek Group rocks in central British Columbia and their role in constraining the history of the Pinchi Fault. These ideas are partly developed, as field mapping and laboratory work continues.

GEOLOGY

The Cache Creek Group of Cache Creek Terrane in central British Columbia is flanked to the east by the Triassic and Early Jurassic Takla Group of Quesnel Terrane, and to the west by various units of the upper Paleozoic to Early Jurassic

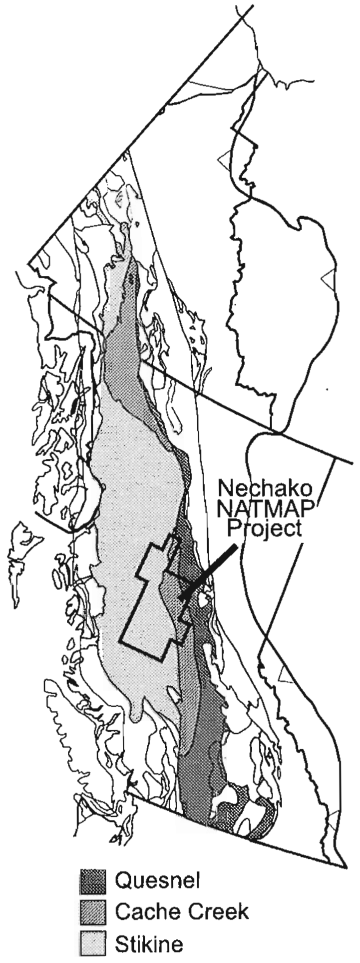

__Figure 2.__ Terrane map of the Cordillera emphasizing the terranes of the Nechako Project area.

Stikine Terrane (Fig. 2). These terranes outcrop along the length of the Cordillera (Wheeler and McFeely, 1991), and represent oceanic and island arc suites obducted onto the North American margin during the Mesozoic (Monger et al., 1972; Paterson, 1973; Gabrielse and Yorath, 1991).

Cache Creek Group rocks consist of limestone, basalt (flows, breccias, tuffs), ribbon chert, ultramafite, serpentinite, greywacke, siltstone, and slate. Feldspar porphyry dacite and diorite intrude these rocks as dykes and plutons. This work builds on the regional mapping of Armstrong (1949) and the detailed mapping of Paterson (1973) and Ash et al. (1993). Those works should be referred to for more complete descriptions and distributions of some of the rocks units described here.

Struik et al. (1996) introduced informal names for several units of the Cache Creek Group and some of those will be used here. They also supported the idea of Bellefontaine et al. (1995) that sedimentary and volcanic rocks mapped by Armstrong (1949) and (Paterson, 1973) as Takla Group near Pinchi Lake should be included in the Cache Creek Group. That notion is fundamental to some of the tectonic interpretations suggested here for the history of obduction of the Cache Creek Group and Pinchi Fault.

Units of the Cache Creek Group near Fort St. James include: Pope succession, undifferentiated basalts, Trembleur ultramafic, Railway complex, Sowchea succession, and Tezzeron succession (called Pinchi succession by Struik et al., 1996; Cordey and Struik, 1996; Fig. 3, 4).

Unit descriptions

Upper Paleozoic to Triassic

Trembleur ultramafic (uCTRCCu)

Trembleur ultramafic is a formal unit used by Armstrong (1942, 1949) and Paterson (1973) to include primarily harzburgite, dunite, peridotite, and other ultramafite near Stuart and Trembleur lakes. Locally the ultramafite is a layered cumulate, and invariably has been partly or wholly altered to serpentinite. Trembleur ultramafic occurs as fault-bounded blocks surrounded by other units of the Cache Creek Group.

This analysis examined five exposures of the Trembleur ultramafic in the Fort St. James area: Mount Murray, Pinchi Mountain, northeast of Mount Pope, Mount Nielsp, and Shass Mountain. Of these sites, ultramafite at Mount Nielsp forms a klippe resting on Triassic sedimentary rocks of the Cache Creek Group. That model of thrust overlap is used to explain the distribution of the other ultramafic rocks.

Similar ultramafic rocks are found at each of the five sites, and in various states of alteration and deformation. The ultramafic rocks are characteristically dun weathering and green to black on fresh surface. They consist of variably serpentinized pyroxenes and olivine. On Mount Murray, interlayered harzburgite and dunite contain layer-parallel bands of chromite. On Mount Nielsp, between areas of harzburgite are zones with lenses of partly to wholly serpentinized harzburgite and pyroxenite encased in a serpentine matrix. Near the base of the unit the rock is mostly talc and serpentine. At Shass Mountain talc veins (0.5–10 cm) are common and occur in local concentrations of parallel to subparallel planar sets, and the ultramafic rocks are locally crosscut by dykes of metabasalt.

Railway complex (uCTRCCr)

Gabbro and basalt of the Railway complex underlie a narrow belt along the south side of Pinchi Lake and possibly parts of Shass Mountain. The gabbro is intimately mixed with basalt and microgabbro, and these rocks are crosscut by numerous veins and veinlets of plagioclase and cryptocrystalline quartz. The best exposures are found on the ridge just south of the B.C. Rail line, south of Pinchi Lake and east of Pinchi Creek. These rocks were mapped as "Basic rocks south of Pinchi Lake" by Paterson (1973), who suggested the complex was unconformably overlain by Upper Triassic limestone and volcaniclastics to the north, and possibly underlain by ultramafic rocks to the south.

The gabbro and basalt locally crosscut each other although some exposures in the area exhibit a complete spectrum of textural variation between the gabbro and basalt. The gabbro is dark green and has medium to fine crystals of nearly equal proportions of plagioclase and hornblende (0.5–2 mm). The hornblende is an alteration product of augite, and epidote and chlorite are locally abundant. Some of the rock is very magnetic.

The basalt is dark olive and weathers rusty brown, and generally aphanitic to felted with submillimetre-size plagioclase. In most places it is massive, and in the northeasternmost exposures near the railway line it is a breccia (5–25 mm clasts). In places the basalt is highly altered having cavity fillings and veins rich in chlorite and epidote.

Underlying much of the core of Shass Mountain is a unit of gabbro and amphibolite. These rocks are best exposed west of the peak. The amphibolite unit contains dismembered lenses of the gneissic gabbro. The hornblende gabbro occurs as small bodies and 0.1 to 3 m lenses within the amphibolite. It is grey- to brown-weathering and has speckled fresh surfaces. The gabbro is mostly fine grained and locally medium grained, and composed of plagioclase (65–75%) and hornblende (25–35%) with minor accessories. The hornblende defines a weak to strong foliation, more prominent in the mafic-rich portions.

The amphibolite is fine grained, weathers medium brown, and is green-black to black on fresh surfaces. It consists of hornblende (70–85%) and calcic plagioclase (15–30%), and is interlayered (20–100 cm) with the gabbro. Well developed amphibole foliation flows around weakly to nonfoliated gabbro blocks. The thickness of the amphibolite surrounding the diorite blocks is generally 2–10 cm.

Quartz and epidote veins (1–5 cm thick) intrude throughout both the amphibolite and gabbro. Some of the veins are planar, and others show deformational structures.

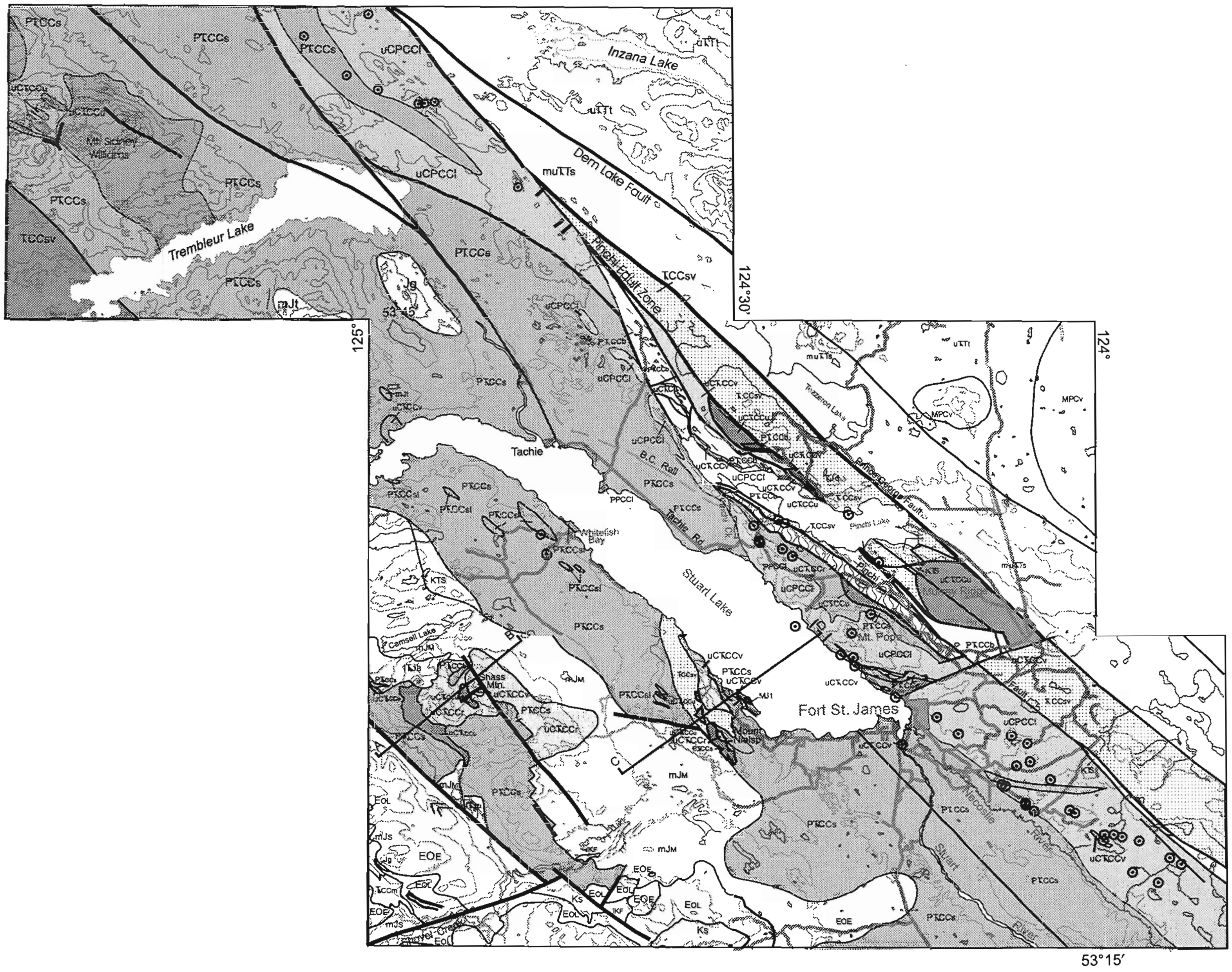

Figure 3. *Geological reference map of the area near Fort St. James modified from Bellefontaine et al. (1995) to include some of the geological interpretations from this project. Solid thin lines are approximate and assumed bedrock geological contacts, and thick lines are approximate and assumed faults. For legend see Figure 4.*

Miocene and Pliocene

MPCv	Chilcotin Group: olivine basalt

Eocene

EOE	Endako Group: basalt, andesite
EOL	Ootsa Lake Group: rhyolite, dacite, andesite

Cretaceous and Tertiary

KTS	Sifton Formation: conglomerate, sandstone, siltstone, shale, coal

Cretaceous

KS	Andesite plagioclase porphyry
IKF	Fraser phase: granodiorite, K-feldspar megacrystic

Jurassic

Jg	Granodiorite
mJt	Tonalite, diorite
mJs	Surgarloaf phase: granodiorite, subporphyritic
mJM	McKnab Lake: biotite hornblende, quartz diorite and tonalite

Triassic and Jurassic

ITRJB	Boer phase: diorite, gabbro
TRJd	Diorite

Triassic

Takla Group (uTRTt, muTRTs)

uTRTt	Tuff, cherty tuff, siliceous argillite
muTRTs	Argillite, greywacke, siltstone, shale, minor, limestone, tuff, basalt

upper Carboniferous to Triassic

Cache Creek Group (TRCCsv - PTRCCb)

TRCCsv	Tezzeron succession: greywacke,siltstone, slate, basalt tuff, minor, limestone, siliceous argillite
	Sowchea succession (PTRCCs-PTRCCsl)
PTRCCs	Argillite, chert, siltstone, phyllite, sandstone, limestone, basalt
PTRCCsl	Limestone, greenstone, chert
uCPCCl	Pope succession: limestone, greenstone, chert
uCTRCCv	Basalt, minor limestone, argillite, chert
uCTRCCr	Railway complex: grabbro, diorite, diorite, peridotite, hornblendite, pyroxenite
uCTRCCu	Trembleur Ultramafic: serpentinite, harzburgite, dunite, peridotite, carbonatized equivalents
PTRCCb	Blueschist (chert, schist, greywacke, metabasalt, limestone)

Pennsylvanian to Jurassic

TRccm	Hornblende diorite, biotite-hornblende quartz diorite, biotite granodiorite, minor amphibolite

⊙ Conodont sample locations

Figure 4. *Legend to the geological map of Figure 3.*

Pope succession (uCPCCl)

Pope succession consists mainly of light grey-weathering, light brown-grey and grey micrite, clastic and bioclastic limestone (*see also* Sano and Struik, 1997; and Sano, 1998). Interlayered with the limestone in a few places are thin basalt breccia and ribbon chert units. It is well exposed at Mount Pope where a nearly continuous section can be mapped from the shore of Stuart Lake to the top of the mountain, between Stuart and Pinchi lakes, and between Necoslie River and Spad Lake (Fig. 3, 4). Locally the limestone shows bedding generally defined by accumulations of limestone fragments and bioclasts (crinoids and fusulinids). Mostly the limestone appears massive although detailed examination or partial silicification will reveal thin- to medium-sized bedding (Sano and Struik, 1997; Sano, 1998). The unit is greater than 800 m thick.

Sano (1998) describes one section of upper Pope limestone as:

> "A 220 m thick sequence of resedimented limestone and basaltic volcaniclastic rocks of the Pope formation are exposed in a quarry east of Fort St. James. The rocks are informally designated the Spad Lake member. Fragmented and abraded fusuline debris from the limestone are preliminarily assessed an upper Asselian age. The base of the Spad Lake member is basalt breccia. The lower to middle part has disorganized, completely unsorted limestone breccia (debris flows) and crudely graded granule-pebble limestone conglomerate (basal Bouma sequence) of shallow-marine affinity. The bedded thick upper part has graded, densely-packed granule-pebble limestone conglomerate, crudely laminated limestone sandstone, and stylonodular-bedded siliceous lime-mudstone with chert nodules, and is interpreted as turbidites resedimented by high-density turbidity currents. Spad Lake member was probably formed on an upper flank of a shallow-marine buildup resting upon a basaltic substratum probably of a plateau, or seamount. Pope formation limestone may be from the platform-top."

A layer of basalt breccia (10–40 m thick) is interlayered with limestone near the base of the Pope succession on the southwest side of Mount Pope. Some of the breccia fragments are tinged with maroon and the matrix can be olive or maroon. In places the basalts are altered by hydrothermal influxes of carbonate. Small crystals in the matrix include plagioclase and some pyroxene. Locally thin beds of basalt tuff are interlayered with the limestone low in the Pope succession.

The age of the limestone has been determined from fusulinids, conodonts, and radiolaria to be mostly Late Carboniferous to Permian (Dawson, 1878; Armstrong, 1942, 1949; Thompson, 1965; Paterson, 1973; Orchard and Struik, 1996; Orchard et al., 1997, 1998). Locally, limestone conglomerates and finer grained clastic limestones host a mixed assemblage of Triassic, Permian, and Late Carboniferous age. These rocks have been interpreted in part as localized cave-fill deposits (Sano, 1998), and probably cannot be clearly differentiated from the Pope succession.

Undifferentiated basalt (uCTRCCv)

Cache Creek Group basalt near Fort St. James is mainly olive, aphanitic to finely crystalline, massive to breccia. At the old bridge over the Stuart River, on Highway 27, basalt is interlayered with thin limestone beds rich in crinoidal debris. An easily accessible exposure of typical massive aphanitic basalt underlies the observation platform at the golf course west of Fort St. James. Pillowed basalt and basalt breccia are found in a single locality just south of Kluskus Creek. Several exposures of metabasalt are scattered through the area of blueschist metamorphism on the north shore of Pinchi Lake, and in greenschist metamorphism underlying the peak of Shass Mountain.

New chemical analyses of the various basalts reveal an ocean platform signature (H. LaPierre, pers. comm., 1997). The basalts are Upper Carboniferous, Permian, and Triassic, from association with enclosed or bordering fossiliferous limestone or ribbon chert.

Permian to Mesozoic (mainly Middle and Upper Triassic)

Sowchea succession (PTRCCs and PTRCCsl)

This unit underlies a large area mainly to the southwest of Stuart Lake. The rocks consist of siltstone, slate, chert, limestone, and lesser amounts of greywacke, and are grey to dark grey, thinly bedded, and commonly disrupted by bedding-parallel and nearly bedding-parallel slip. Locally these rocks are interbedded with intraformational conglomerates and breccias. Most of the fine-grained sedimentary rocks are very siliceous, ranging from cherty argillites and slates to muddy cherts. Typical of these rocks are the easily accessible outcrops at the west end of the Sowchea Bay Provincial Park and the limestones of western Whitefish Bay, each on southwestern Stuart Lake.

Near Shass Mountain, the metasiltstone weathers brown and is generally grey and dark grey. It has a schistose texture defined by finely crystalline muscovite. Local mineral growths include plagioclase, hornblende, quartz, and biotite. The metasiltstone is interbedded with recrystallized ribbon chert and locally appears as lenses in quartzite (Letwin, 1997; Letwin and Struik, 1997).

Ribbon cherts form lenses within the mainly fine-grained clastic units, and in most places south of Stuart Lake are recrystallized to fine sugary quartzite with thin slate interbeds. Better preserved, yet highly disrupted beds of ribbon chert are exposed along the shore of Stuart Lake and roadcuts just to the northwest of Fort St. James. At the Stuart Lake Sailing Club they are interbedded with siltstone and intraformational siltstone conglomerates (Cordey and Struik, 1996). A roadcut on the road along the north shore of Stuart Lake leading from Fort St. James to the Stuart Lake Lodge exposes highly disrupted cherts in fault contact to the west with Pope succession limestone.

Near Whitefish Bay the unit contains limestone and limestone conglomerate beds. Flattened pebble- and granule-size clasts in the limestone matrix consist of slate and cherty slate. The limestone and conglomerate are interbedded with 1–4 m beds of siltstone and intraformational conglomerate.

Marble is exposed at one place south of the west end of Camsell Lake. It forms a 7 m cliff and consists of mostly pure calcite (1–3 mm) with individual crystals showing strain striations. Some iron stain occurs at the base of the outcrop.

The age of the Sowchea succession is in part Late Permian, and Middle and Upper Triassic as determined from radiolaria (Cordey and Struik, 1996) and conodonts (Orchard and Struik, 1996).

Tezzeron succession (TRCCsv)

Tezzeron succession is an informal division of greywacke and basalt tuff underlying the region southwest of the Prince George Fault to the southern shores of Pinchi Lake and at Mount Nielsp west of southern Stuart Lake (Fig. 3). It consists of greywacke, chert sandstone, siltstone, slate, basalt tuff, and minor limestone. Good exposures of this succession are found at and in the vicinity of Tsilcoh River falls, on the shores of southeastern Pinchi Lake, and south of Tezzeron Lake north of the Pinchi mine (Fig. 3). This succession was mapped by Armstrong (1949) and Paterson (1973) as Takla Group, and by Bellefontaine et al. (1995) and Struik et al. (1996) as Cache Creek Group. Paterson interpreted the unit to unconformably overlie the Railway complex at Pinchi Lake.

The greywacke is composed of plagioclase, augite, chert, and rounded volcanic rock fragments (0.2–2 mm) and is gradational with the chert sandstone. Beds are generally thin (0.2–7 cm), evenly layered, and locally graded where finer grained. Characteristic of these rocks are ripup clasts of siltstone, local accumulations of carbonized wood fragments (mainly small twigs), and local mud cracks. Pebble conglomerate of rounded and oblate chert and basalt clasts generally are thicker bedded (20–200 cm) and separated by siltstone and greywacke. Good examples of the conglomerate are exposed just south of the mouth of the Tsilcoh River.

The basalt tuff is brown weathering, dark olive, and consists of finely crystalline plagioclase and augite (1–2.5 mm), and at the top of the succession is an augite porphyry agglomerate. The tuff contains some rounded chert and minor granitic clasts of sand and granule size, and rare wood twig fragments. The chert granules have visible radiolaria.

The limestone is light grey weathering, grey and dark grey, occurs as thin units commonly gradational with the greywacke, and locally contains colonial corals, crinoid fragments, and pelecypods (Paterson, 1973). In places it weathers brown where it forms thin interbeds with greywacke and limestone matrix conglomerate. The limy conglomerate contains fragments of basalt. Paterson lists a point count of the fragments from this conglomerate as basalt (50%), chert (45%), and gabbro (5%).

A succession of greywacke and limestone underlying ultramafic rocks at Mount Nielsp is included in Tezzeron succession because of its lithological similarity to Tezzeron succession greywacke and limestone near Pinchi and Tezzeron lakes. Generally the greywacke has a sandy texture and consists of quartz, chert, and mafic volcanic clasts.

Tezzeron succession rocks are very similar to clastic assemblages of the upper part of the Cache Creek Group in Yukon Territory (Cache Creek Group assemblage 3 of Gordey and Stevens, 1994) and in southern British Columbia (Shannon, 1982; Monger, 1985), and somewhat like parts of Triassic Sitlika clastic assemblage near Takla Lake (Schiarizza et al., 1998). Paterson (1973) described chromite grains in Tezzeron succession greywacke, and those grains may have been derived from the ultramafite of the Cache Creek Group. These correlations, the absence of chert clast-bearing volcaniclastics in the Takla Group, and the presence of ultramafic components is why we include these rocks with the Cache Creek Group.

The age of the Tezzeron succession is determined from *Monotis* and coral fossils indicative of an Upper Triassic age and an ammonite indicative of Early Jurassic age (Armstrong, 1949; Paterson, 1973). Tezzeron succession is time correlative with the youngest parts of the Sowchea succession.

STRUCTURE

Cache Creek Group rocks near Stuart Lake and Fort St. James are locally folded, cleaved, sheared, and brittlely faulted. In the vicinity of Shass Mountain these structures are in part overprinted by hornfels presumably induced by intrusion of the McKnab Lake phase and Boer suite plutons.

Folds are upright to overturned tight to open, and are best displayed in Sowchea greywacke, siltstone, and chert succession. In places well formed axial planar cleavage occupies the limbs of folds — mostly the cleavage is layer-parallel and defined by disruptions in the laminations and thin beds. Folds in the Sowchea succession are asymmetric to the northeast. Disruption of bedding by irregular boudinage and dismembering of folds is common in interbedded successions of ribbon chert and muddy and silty clastics. Where successions of chert are preserved they show chevron to tight concentric folds, with well developed cleavage in the slate interbeds.

The Pope Limestone forms broad open folds and is in shallow thrust fault contact with underlying younger ribbon cherts (Struik et al., 1996). The Trembleur ultramafic at Mount Nielsp and the Pope succession in most places are thrust onto Triassic and Upper Permian sedimentary rocks of the Sowchea succession or the Triassic Tezzeron succession.

The base of the ultramafic rocks at Mount Nielsp consists of fish of serpentinite surrounded by talcose sheaths. Upsection from the basal contact the material changes to fish of partly altered harzburgite and some pyroxenite surrounded by serpentinite sheaths and bands. These rocks overlie relatively undeformed fine-grained greywackes and sandstones correlated with the Tezzeron succession and thought to be latest Triassic or Early Jurassic.

Harzburgite and variously serpentinized equivalents at Pinchi Mountain are interpreted to be underlain by the Tezzeron succession that is exposed in the surrounding lowlands (Fig. 5). Similarly the ultramafic rocks of Mount Murray may be a klippe overlying Tezzeron succession rocks that underlie the area to the north, east, and southeast of the mountain. Ultramafic rocks at Shass Mountain may form folded thrust sheets or a westerly dipping thrust panel (Fig. 5).

Pope succession limestone almost everywhere overlies or is surrounded by younger sedimentary rocks, and therefore the basalt contacts have been interpreted to be thrust faults. These thrust imbricate sequences are generally caught between steeply dipping faults. In places it is unclear whether the contacts between the Cache Creek Group units are steep faults or thrust faults.

The Pinchi fault zone is defined by a dense set of steeply dipping faults, some of which have had dextral strike-slip motion and locally deform Upper Cretaceous conglomerate and sandstone (Struik, 1994). The fault regionally appears to form the eastern boundary to the Cache Creek Group. From mapping in 1997, the Pinchi Fault is considered a coincidental boundary to the Cache Creek Group and that the suture between Cache Creek and Quesnel terranes actually lies primarily hidden by overburden and has been down-dropped on the east side of the Pinchi Fault. The Prince George Fault forms the local eastern boundary to the Cache Creek Group in the region of Fort St. James.

At Pinchi Lake the imbricate thrust stack of the Cache Creek Group, represented by klippe of Trembleur ultramafic overlying Tezzeron succession sedimentary rocks is bisected by the Pinchi Fault. Within the Pinchi fault zone at this locality lies a blueschist suite consisting of metabasalt, greywacke, dolostone, ribbon chert, and limestone. Paterson and Harakal (1974) dated these rocks as 211–218 Ma based on K-Ar dating of phengitic muscovite within the blueschist.

Considering that the Pinchi Fault is known to have Cretaceous or younger motion on it and that it is known to be associated with Eocene mercury mineralization and deforms Eocene sedimentary rocks to the north (Paterson, 1973), and that the fault is bound by Cache Creek Group rocks on either side, it is suggested that the blueschist suite represents a structural and metamorphic panel that is unrelated to the regional Pinchi Fault. Instead the blueschist is interpreted to be a another of the thrust panels in the imbricated Cache Creek succession.

PALEOENVIRONMENT

The nature of the Cache Creek Group units, the characteristics of the Pope limestone, and the chemical signature of the mafic rocks in sum can be interpreted to indicate that Cache Creek Group rocks of central British Columbia formed in an ocean platform environment. However the units are distinct enough in time and remain unlinked in space, so they may represent several distinct oceanic environments forced to cohabit a Mesozoic collision zone.

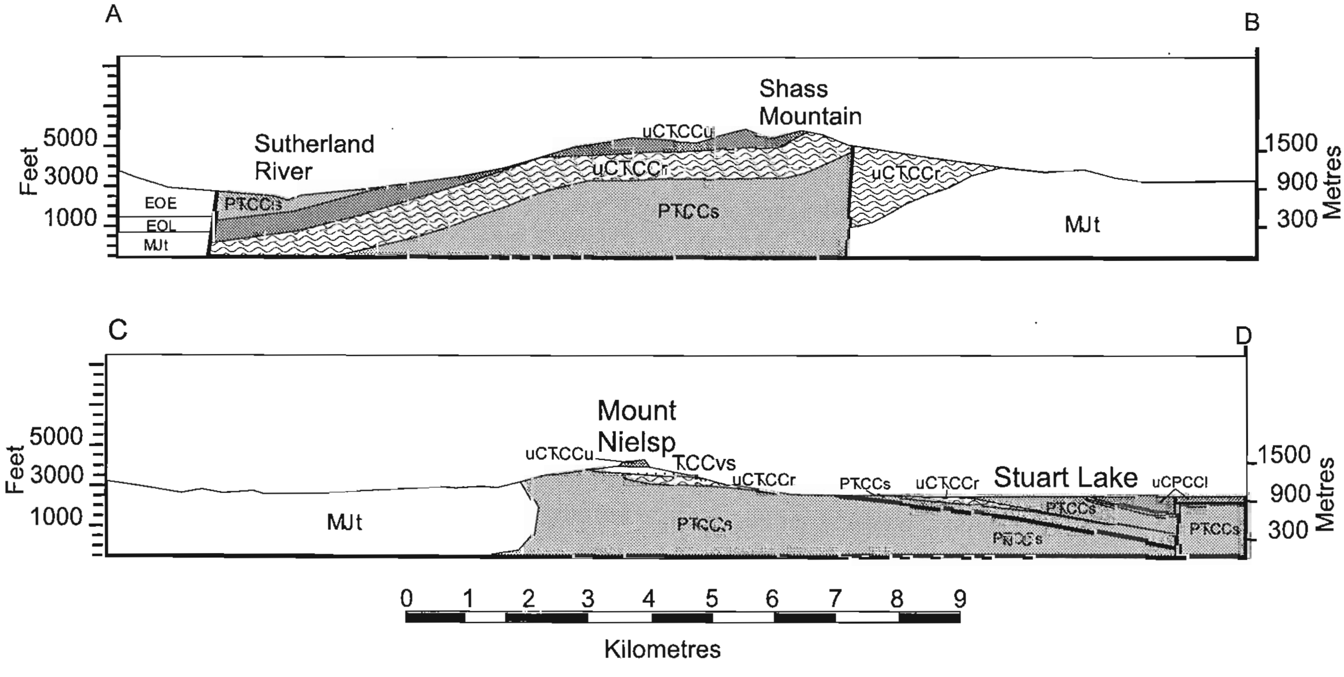

__Figure 5.__ Interpretative structural cross-sections in the Stuart Lake area. See Figure 3 for location of the sections.

Nowhere near Stuart Lake in central British Columbia does the Cache Creek Group retain intact remnants of a classical ophiolite sequence — a rift-generated ocean crust. In particular sheeted dyke complexes are not exposed, nor is there a section where ultramafic rocks, gabbros, mafic dykes, pillowed basalt, and pelagic sedimentary rocks can be found in succession. The rock units themselves appear to be distinct suites in time and environment (Fig. 6). The ultramafic rocks are now highest in the sections as thrust klippe. The Pope limestone near Stuart Lake and Fort St. James mostly represents the Upper Carboniferous and Late early Permian, whereas the expansive Sowchea sedimentary rocks are mostly Upper Permian and Middle and Upper Triassic. Northwest of Tezzeron Lake, Upper Permian and Early Triassic limestone and basalt tuff sequences occupy the position which to the southeast is taken by the older Pope succession (Kloch Lake succession of Orchard et al., 1998). These successions and complexes appear to be bound by thrusts or strike-slip faults and as such probably do not represent a single oceanic environment in time or space.

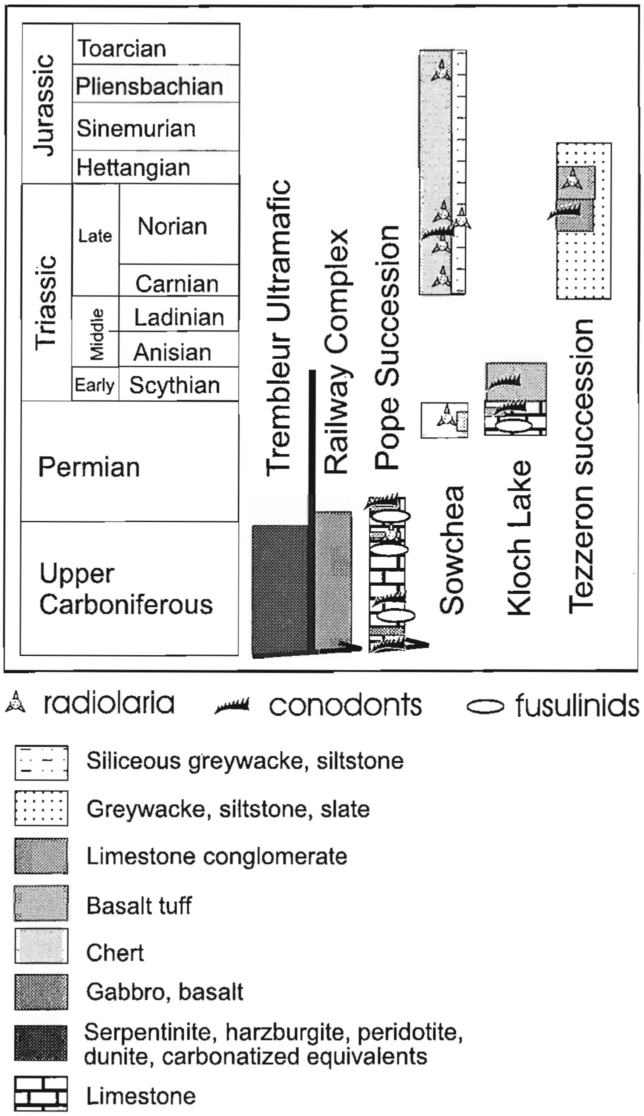

Figure 6. The structural and stratigraphy units of the Cache Creek Group near Fort St. James, with their paleontological ages and dominant lithologies.

The sedimentological character of the Pope limestone can be best explained by deposition as fragmental debris shed from a shallow water bank built on an oceanic atoll or platform consisting of mafic volcanics or intrusives (Struik et al., 1996; Sano, 1998). Sano (1998) and Sano and Struik (1997) described these limestones as local debris flows and turbidites in the Early Permian and early Upper Carboniferous.

CONCLUSIONS

The Cache Creek Group near Fort St. James can be divided into late Paleozoic and early Mesozoic units. Most of the clastic sedimentary rocks of the area appear to be of latest Permian and Triassic age whereas the Pope limestone, and some of the basalt are Late Carboniferous and Early Permian. The ribbon chert successions may be either Paleozoic or Mesozoic, and the Trembleur ultramafic and Railway complex ages are unknown. The Pope succession limestone and the Trembleur ultramafic are probably most everywhere thrust onto young sequences of the Cache Creek Group. The Pinchi Fault appears to be a young strike-slip fault that cuts the imbricated Cache Creek Group in the vicinity of Pinchi Lake.

ACKNOWLEDGMENTS

Claire Floriet, Janice Letwin, Robert L'Heureux, Jennifer Hobday, Chris Anderson, Stephen Wetherup, Mike Hrudey, Andy Blair, Crystal Huscroft, Angie Justason, and Samara Lewis each contributed to the mapping of Cache Creek Group during the Nechako Project to date. Discussions with Jim Monger, Ian Paterson, Wayne Bamber, Phillipe Erdmer, and Steve Gordey have been very useful in guiding the Cache Creek Group research. Hillary Taylor and Peter Krauss have each contributed to the extraction and preparation of the microfossils and the paleontological database upon which this work relies. Jim Roddick generously provided a critical review of the manuscript on short notice.

REFERENCES

Armstrong, J.E.
1942: The Pinchi Mercury Belt; Geological Survey of Canada, Paper 42-11, p. 1-18.
1949: Fort St. James map-area, Cassiar and Coast Districts, British Columbia; Geological Survey of Canada, Memoir 252, 210 p.

Ash, C., MacDonald, R.W.J., and Paterson, I.A.
1993: Geology of the Stuart and Pinchi Lakes area, central British Columbia (93K); British Columbia Ministry of Energy, Mines, and Petroleum Resources, Open File 1993-9.

Bellefontaine, K.A., Legun, A., Massey, N., and Desjardins, P.
1995: Digital geological compilation of northeast B.C. – southern half (NTS 83D, E, 93F, G, H, I, J, K, N, O, P); British Columbia Ministry of Energy, Mines, and Petroleum Resources, Open File 1995-24.

Cordey, F. and Struik, L.C.
1996: Radiolarian biostratigraphy and implications, Cache Creek Group of Fort Fraser and Prince George map areas, central British Columbia; *in* Current Research 1996-E; Geological Survey of Canada, p. 7-18.

Dawson, G.M.
1878: Report on explorations in British Columbia, chiefly in the basins of the Blackwater, Salmon, and Nechako Rivers, and on Francois Lake; Geological Survey of Canada, Report of Progress 1876-1877, pt. III, p. 17-54.

Gabrielse, H. and Yorath, C.J.
1991: Tectonic synthesis, Chapter 18; *in* Geology of the Cordilleran Orogen in Canada, (ed.) H. Gabrielse and C.J. Yorath; Geological Survey of Canada, Geology of Canada, no. 4, p. 677-705 (*also* Geological Society of America, The Geology of North America, v. G-2).

Gordey, S.P. and Stevens, R.A.
1994: Tectonic framework of the Teslin region, southern Yukon Territory; *in* Current Research 1994-A; Geological Survey of Canada, p. 11-18.

Letwin, J.M.
1997: The geology of Shass Mountain, central British Columbia; B.Sc. thesis, University of Alberta, Edmonton, Alberta, 46 p.

Letwin, J.M. and Struik, L.C.
1997: Geology of Shass Mountain, central British Columbia; *in* Current Research 1997-A; Geological Survey of Canada, p. 103-106.

MacIntyre, D.G. and Struik, L.C.
1997: Nechako NATMAP Project, 1996 Overview; *in* Geological Fieldwork 1996: a Summary of Field Activities and Current Research, (ed.) D.V. Lefebure, W.J. McMillan, and J.G. McArthur; British Columbia Ministry of Employment and Investment, Geological Survey Paper 1997-1, p. 39-45.
1998: Nechako NATMAP Project, 1997 Overview; *in* Geological Fieldwork 1997; British Columbia Ministry of Employment and Investment, Paper 1998-1, p. 1-1 to 1-8.

Monger, J.W.H.
1985: Structural evolution of the southwestern Intermontane Belt, Ashcroft and Hope map areas, British Columbia; *in* Current Research, Part A; Geological Survey of Canada, Paper 85-1A, p. 349-358.

Monger, J.W.H. and Ross, C.A.
1971: Distribution of fusulinaceans in the western Canadian Cordillera; Canadian Journal of Earth Sciences, v. 8, p. 259-278.

Monger, J.W.H., Gabrielse, H., and Souther, J.A.
1972: Evolution of the Canadian Cordillera: a plate tectonic model; American Journal of Science, v. 272, p. 577-602.

Orchard, M.J. and Struik, L.C.
1996: Conodont biostratigraphy, lithostratigraphy, and correlation of the Cache Creek Group near Fort St. James, British Columbia; *in* Current Research 1996-A; Geological Survey of Canada, p. 77-82.

Orchard, M.J., Struik, L.C., and Taylor, H.
1997: Conodont biostratigraphy and correlation, Cache Creek Group, Fort St. James, British Columbia; *in* Current Research 1997-A; Geological Survey of Canada, p. 95-102.
1998: New conodont data from the Cache Creek Group, central British Columbia; *in* Current Research 1998-A; Geological Survey of Canada, p. 99-105.

Paterson, I.A.
1973: The geology of the Pinchi Lake area, central British Columbia; Ph.D. thesis, University of British Columbia, Vancouver, British Columbia, 263 p.

Paterson, I.A. and Harakal, J.E.
1974: Potassium-argon dating of blueschists from Pinchi Lake, central British Columbia; Canadian Journal of Earth Sciences, v. 7, p. 1007-1011.

Plouffe, A.
1994: Surficial geology of the Tezzeron Lake; Geological Survey of Canada, Open File 2846, scale 1:100 000.

Sano, H.
1998: Preliminary report on resedimented carbonates associated with basaltic rocks of Cache Creek Group near Spad Lake, east of Fort St. James, central British Columbia; *in* Current Research 1998-A; Geological Survey of Canada, p. 89-97.

Sano, H. and Struik, L.C.
1997: Field properties of Pennsylvanian-Lower Permian limestones of Cache Creek Group, northwest of Fort St. James, central British Columbia; *in* Current Research 1997-A; Geological Survey of Canada, p. 85-93.

Schiarizza, P., Massey, N., and MacIntyre, D.G.
1998: Geology of the Sitlika Assemblage in the Takla Lake area (93N/3, 4, 5, 6, 12), central British Columbia; *in* Geological Fieldwork 1997; British Columbia Ministry of Employment and Investment, Paper 1998-1, p. 4-1 to 4-20.

Shannon, K.R.
1982: Cache Creek Group and contiguous rocks, near Cache Creek, British Columbia; M.Sc. thesis, University of British Columbia, Vancouver, British Columbia, 72 p.

Silberling, N.J. and Jones, D.L. (ed.)
1984: Lithotectonic terrane maps of the North American Cordillera; United States Geological Survey, Open File Report 84-523, scale 1:2 500 000.

Struik, L.C.
1994: Geology of the McLeod Lake map area, central British Columbia; Geological Survey of Canada, Open File 2439, 18 p., and map, scale 1:250 000.

Struik, L.C. and MacIntyre, D.G.
1997: Nechako Project Overview, central British Columbia, year two; *in* Current Research 1997-A; Geological Survey of Canada, p. 57-64.
1998: Nechako Project Overview, central British Columbia, year three; *in* Current Research 1998-A; Geological Survey of Canada, p. 79-87.

Struik, L.C. and McMillan, W.J.
1996: Nechako Project Overview, central British Columbia; *in* Current Research 1996-A; Geological Survey of Canada, p. 57-62.

Struik, L.C., Floriet, C., and Cordey, F.
1996: Geology near Fort St. James, central British Columbia; *in* Current Research 1996-A; Geological Survey of Canada, p. 71-76.

Thompson, M.L.
1965: Pennsylvanian and Early Permian fusulinids from Fort St. James area, British Columbia, Canada; Journal of Paleontology, v. 39, p. 224-234.

Wheeler, J.O. and McFeely, P.
1991: Tectonic assemblage map of the Canadian Cordillera and adjacent parts of the United States of America; Geological Survey of Canada, Map 1712A, scale 1:2 000 000.

Geological Survey of Canada Project 950036

Quaternary geology and terrain inventory, Eastern Cordillera NATMAP Project. Report 5: stratigraphic correlations of glacial deposits in the Beaver Mines map area, southwestern Alberta[1]

Philip J. Holme[2], Stephen R. Hicock[2], and Lionel E. Jackson, Jr.
Terrain Sciences Division, Vancouver

Holme, P.J., Hicock, S.R., and Jackson, L.E., Jr., 1998: Quaternary geology and terrain inventory, Eastern Cordillera NATMAP Project. Report 5: stratigraphic correlations of glacial deposits in the Beaver Mines map area, southwestern Alberta; in *Current Research 1998-E; Geological Survey of Canada, p. 11–17.*

Abstract: A stratigraphic cross-section of glacial deposits was constructed from the investigation of sediments in 10 cliff-bank exposures along the Castle River valley and its tributaries in southwest Alberta. The presence of two montane tills at seven sections is suggested as evidence for retreat of montane ice from the maximum of the late Wisconsinan glaciation and a subsequent minor readvance. Continental till is not found in the Castle River valley upstream of Hunting Eagle section, although it occurs at higher elevations immediately adjacent to the valley. A single clast of Canadian Shield lithology was found in montane till at one exposure, Washout section. A reconstruction of glacial history compatible with these findings excludes continental ice from the Castle River valley by still-stands of montane ice retreating from readvance positions.

Résumé : Une coupe stratigraphique de dépôts glaciaires a été constituée à partir d'une étude effectuée sur des sédiments prélevés dans dix affleurements de berge et de falaise le long de la vallée de la rivière Castle et de ses affluents dans le sud-ouest de l'Alberta. La présence de deux tills subalpins dans sept coupes témoignerait du retrait des glaces subalpines du pléniglaciaire du Wisconsinien supérieur et d'une réavancée mineure subséquente. Le till continental est absent dans la vallée de la rivière Castle en amont de la coupe de Hunting Eagle, même si on en a observé dans des terrains plus élevés jouxtant la vallée. Un seul claste de la lithologie du Bouclier canadien a été repéré dans un till subalpin, soit dans la coupe de Washout. Selon une reconstitution de l'histoire glaciaire qui tient compte de ces observations, l'arrêt des glaces subalpines en retrait par rapport aux positions de réavancée aurait empêché les glaces continentales en progression d'envahir la vallée de la rivière Castle.

---

[1] Contribution to Eastern Cordillera NATMAP Project

[2] Department of Earth Sciences, University of Western Ontario, London, Ontario N6A 5B7

INTRODUCTION

Quaternary stratigraphy at four cliff-bank exposures in the Beaver Mines (82 G/8) map area was described and sampled during the 1997 summer field season (Fig. 1). This was the final field season of the Eastern Cordillera NATMAP Project in southwestern Alberta. These findings supplement similar data gathered from six cliff exposures visited during the 1995 and 1996 seasons and provide a representative succession of subsurface glacial deposits in the Castle River valley. This work contributes to the surficial geology component of the Eastern Cordillera NATMAP Project and forms the basis of the first author's M.Sc. thesis in the Department of Earth Sciences at the University of Western Ontario (London, Ontario).

PREVIOUS WORK AND THE PRESENT STUDY

Investigations of Quaternary stratigraphy in southwestern Alberta have been conducted by numerous authors and have produced two contradictory reconstructions of glacial history. The initial and, until recently, widely accepted reconstruction viewed the stratigraphy as representing up to four glaciations (Alley, 1973; Stalker and Harrison, 1977; Jackson, 1980, 1994; Jackson et al., 1989). The second interpretation, proposed originally by Horberg (1954) and further developed by Wagner (1966) and Bayrock (1969), asserts that the deposits support only a single late Wisconsinan glaciation. Investigations during the Eastern Cordillera NATMAP Project have led to rejection of the multiple glaciation model in favour of the single late Wisconsinan glaciation model (Leboe, 1995; Little, 1995; Jackson et al., 1996; Holme, 1997). Stratigraphic studies in central Alberta by Liverman et al. (1989) and Young et al. (1994) are also in agreement with the single glaciation hypothesis.

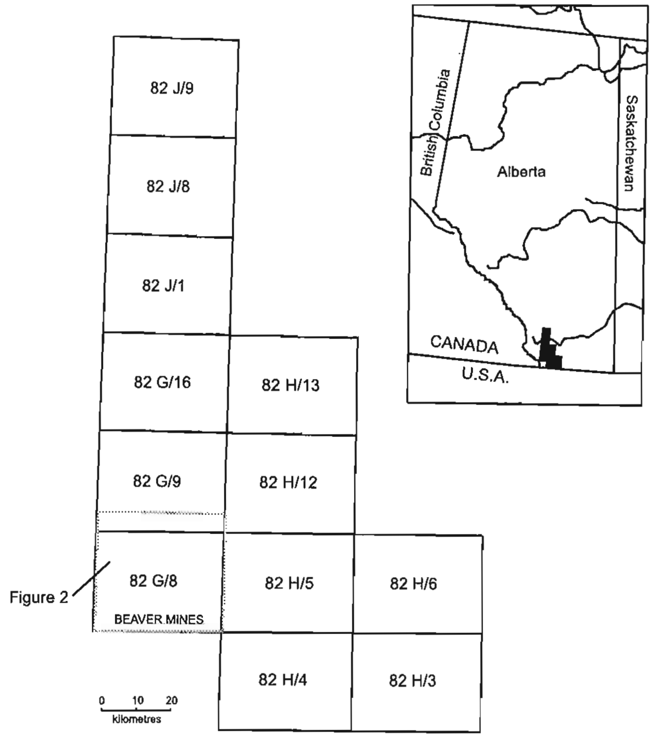

Figure 1. Location of the southeastern Cordillera NATMAP and Beaver Mines map area within the National Topographic System of Canada.

FIELD METHODS

Cliff-bank sections providing significant exposures of glacial deposits were selected for description and then cleared of colluvial cover to allow description and sampling of in situ sediments. Sediment sampling was restricted to till units. Samples for textural, carbonate, and geochemical analyses were taken to establish general till characteristics while samples for Atterberg limits were taken from select units to classify them according to the Universal Soil Classification scheme. Pebble samples were collected for lithological study to determine ice provenance while till fabric and glaciotectonic measurements were made in till units to obtain ice-flow direction data. Statistical analysis and plotting of measurements were done using the StereoNet for Windows (1.41) software developed by Per Ivar Steinsund (Varden 94, N-9018 Tromsø, Norway). These data are represented here by their S1 and S3 values where S1 is the normalized eigenvalue associated with the strongest eigenvector and S3 is associated with the weakest (May et al., 1980). The ratio S3/S1 is an isotropic index indicating the degree of similarity of a fabric to one which is randomly oriented (uniform) (Benn, 1994). The resultant plots were then analyzed to determine ice-flow direction and till genesis. Interpretations of fabric plot modalities are based on the interpretive approach advocated by Hicock et al. (1996).

QUATERNARY STRATIGRAPHY

The four cliff sections described during the 1997 field season are presented on a west-to-east transect along Castle River valley and its tributaries (Fig. 2, 3). Stratigraphy is described from the base of the sections upward. For descriptions of the 1995–1996 sections see Holme (1997).

Screwdriver Creek section

This exposure is located in the north-central part of the map sheet on the north bank of Screwdriver Creek about 3 km north of the hamlet of Beaver Mines. The section is a 13 m high cut-bank exposure incised into a lake plain with bedrock exposed at its base. A brief description follows.

Unit 1 is a highly consolidated, fissile, structureless, stony diamicton. The upper 50 cm is less stony and less consolidated with orange-brown mottles.

Unit 2 is alternating beds of sand and silt 2–5 cm thick. Occasional clasts occur in the sand beds. They become stonier in lower 90 cm of unit. The upper contact is abrupt and irregular; the lower contact is abrupt and regular.

Unit 3 is a stony, slightly consolidated diamicton becoming more consolidated and indurated with depth. Its matrix becomes less sandy with depth except near the base where sand content increases. Clasts range from granules to 20 cm cobbles. The lower contact is abrupt and irregular.

The lower diamicton (unit 1) is interpreted as a deformed lodgement till (Fig. 3). Lodgement is suggested by the high degree of consolidation and the presence of clearly lodged clasts. The till fabric plot is bimodal with S1=0.524 and S3/S1=0.221, suggesting deformation. The lower half of the upper diamicton (unit 3) is interpreted as a deformation till. This is suggested by the bimodal to multimodal fabric plot with S1=0.520 and S3/S1=0.313. The upper half of the unit is thought to be a meltout till due to its lesser consolidation, but no fabric data was gathered to support this interpretation.

McRae section

This section is located at the downstream end of a 350 m long bedrock cliff along the south bank of Castle River about 1.5 km upstream from the river's confluence with Mill Creek. Quaternary cover in the cliff section thins rapidly upstream and disappears about 200 m from the described section. Slumping obscures the sediment-bedrock contact.

Unit 1 is a consolidated, cohesive diamicton with a sandy silt loam matrix. A large block of vertically dipping, unsorted cobble gravel, present in the upper 2 m, was likely incorporated into the unit as a frozen block and then rotated. The diamicton becomes highly consolidated and less stony in the lower 8 m of the unit. At this depth the matrix is a mottled and banded silty loam. Numerous sand pockets with sand stringers sheared out of them are present throughout most of unit. Occasional sand lenses are present within the diamicton.

Unit 2 is a very stony diamicton with clasts ranging from granules to cobbles. Its sandy matrix is cohesive and quite consolidated. It has an abrupt and irregular upper contact. Its lower contact is irregular and includes incorporated blocks of the underlying unit.

Unit 3 is a cohesive fine sand and silt (upper half). A coarse-grained sand lens is present in the upper 12 cm of the unit. The lower half of unit consists of chaotically interbedded silt and strongly crossbedded medium sand.

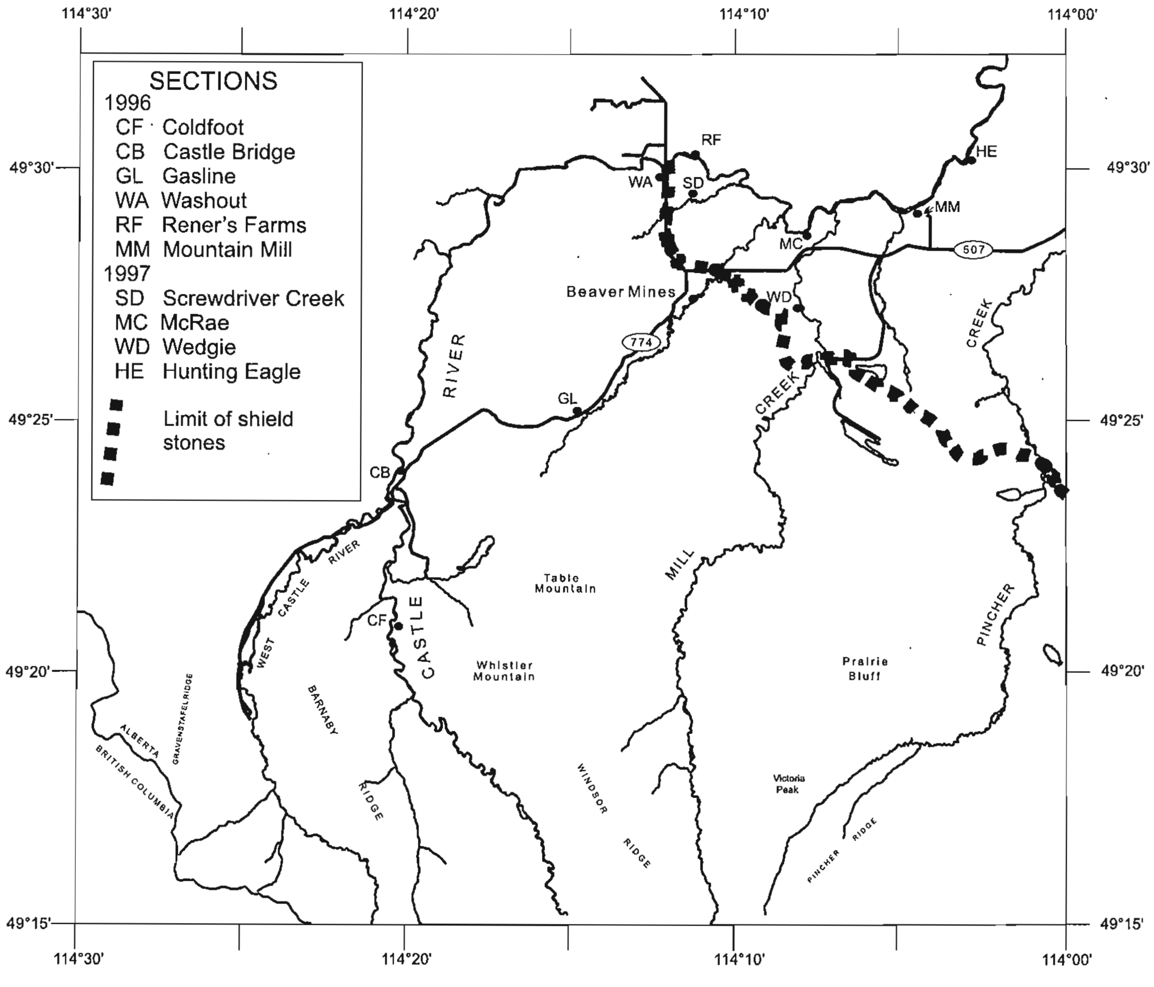

Figure 2. Locations of described sections and local western Canadian Shield erratics found on the surface.

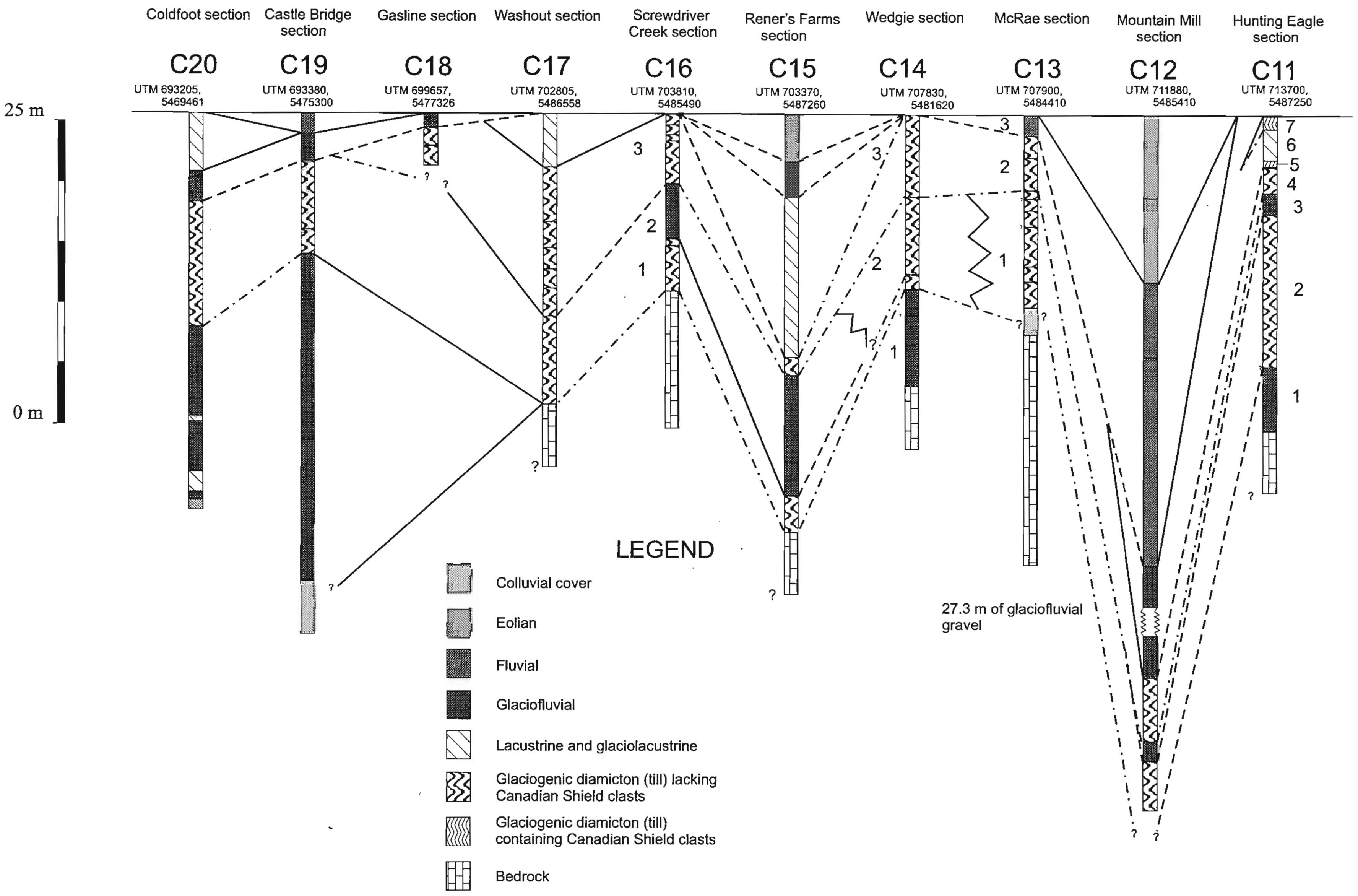

Figure 3. *Generalized stratigraphy of sections along the Castle River valley and its tributaries. Numbers refer to unit numbers in text. Tentative correlations are denoted by lines linking sections. See Holme (1997) for discussion of 1995– 1996 sections. Solid lines indicate depositional contacts; dashed lines, erosional; dot- dash, glacially sheared contacts.*

The diamicton comprising the lowermost unit in the section (unit 1) is interpreted as a basal till. Two fabrics were measured within the unit, both in the upper third. The lower fabric was quite strong with S1=0.615 and S3/S1=0.138 while the upper was considerably weaker with S1=0.503 and S3/S1=0.235. The lower fabric is bimodal and suggests deformed lodgement whereas the upper fabric is multimodal, indicating a deformation till.

Wedgie section

This section is located on the north bank of Mill Creek about 5 km above the creek's confluence with Castle River. The section is 20 m high by about 20 m across with bedrock exposed at the base.

Unit 1 is unsorted cobble and boulder gravel. Clasts are subangular to rounded and the matrix coarsens downward from granules to pebbles. A few lenses of granules and pebbles are present in the lower two-thirds of the unit. A layer of calcrete 15 cm thick is present at the bedrock contact.

Unit 2 is a fissile, consolidated and cohesive diamicton with a greyish-dark brown sand and silt matrix. Clasts range from granules to 60 cm boulders. Sand and gravel content increases toward the base. The upper contact is abrupt and undulating.

Unit 3 (lower half) is diamicton interbedded with matrix-rich, unsorted, pebble gravel. Gravel units are moderately consolidated and contain pockets of the diamicton. Diamicton and gravel beds become more mixed at depth resulting in a sandier, less stony matrix. The upper half of unit 3 is consolidated diamicton with an isolated boulder concentration in the upper third of this interval. In the lower half of this interval, it contains sand which was incorporated through shearing of the uppermost gravel bed in lower half of unit 3.

The lower diamicton (unit 2) is interpreted as a strongly deformed lodgement till based on its bimodal fabric (S1=0.480 and S3/S1=0.348). The lower half of unit 3 (consisting of interbedded diamicton and gravel) is interpreted as an ice-marginal deposit. The upper half of unit 3 (consisting of the consolidated diamicton) is interpreted as a deformation till based on its multimodal fabric with S1=0.480 and S3/S1=0.410.

Hunting Eagle section

The section is located on the east bank of the Castle River immediately northeast of the map area in NTS 82 G/9, about 6 km west of the town of Pincher Creek. The section is exposed in a large slump scar approximately 35 m high by 150 m long with bedrock exposed at the base. The summary presented here is a composite of two separate exposures (sections A and B) at the section. Section A was about 26 m in height, located at the downstream end of the exposure whereas section B was about 20 m high and located at the upstream end of the exposure.

Unit 1 is a consolidated, unsorted gravel containing clasts from granules to boulders.

Unit 2 is a highly consolidated, stony diamicton. It has an abrupt and irregular upper contact and there are numerous fractures throughout it. Shearing is evident in the lower two-thirds of the unit where numerous sand stringers are sheared up from chaotically bedded sand pockets.

Unit 3 is a chaotic mix of coarse-grained sand beds with diamicton pockets. Sand beds are strongly crossbedded, faulted, and folded. Facies change across the section to extremely stony diamicton overlying medium sand with gravel lenses which in turn overlies fissile diamicton. The upper contact of the unit at the northern end of the exposure is transitional over 25 cm whereas it is abrupt and irregular at southern end of the exposures.

Unit 4 is diamicton with silty sand matrix. It is consolidated and fissile and slightly cohesive. Its upper contact is gradational over 10 cm. It is moderately stony with clasts from granules to 10 cm cobbles. Sand stringers are present, especially near base.

Unit 5 is highly sheared silt overlying highly sheared diamicton. Its upper contact is irregular. It becomes more diamicton-rich with depth.

Unit 6 is extremely fissile silt. It is stoneless at northern end of section but it becomes moderately stony at the southern end of the section in lower part of unit.

Unit 7 is consolidated, moderately stony diamicton. It has a medium brown clayey silt matrix with orange mottles. It is highly fractured; many fractures are filled with gypsum crystals. Clasts from granules to cobbles. Four clasts from the Canadian Shield were found within this unit.

The lowermost diamicton (unit 2) is interpreted as a locally deformed lodgement till. Three till fabrics were measured in unit 2, two at section A and a third at section B. The upper fabric at section A is multimodal (S1=0.504 and S3/S1=0.310) whereas the lower fabric is bimodal (S1=0.445 and S3/S1=0.382). Despite the low eigenvalues of the lower fabric, it is stronger than the upper fabric as is evident from its bimodality. Both fabrics suggest a deformation till. The fabric done in the upper part of unit 2 at section B is a unimodal plot with S1=0.654 and S3/S1=0.226 suggesting a lodgement till.

The unit of heavily sheared silt and diamicton (unit 5) which overlies unit 4 is interpreted as a deformation till based on the degree of shearing evident within the sediment. The uppermost till (unit 7) is interpreted as a deformation till based on the multimodal nature of its fabric (S1=0.516 and S3/S1=0.240).

PROPOSED INTERPRETATIONS OF GLACIAL HISTORY

Montane ice advances

Holme (1997) established a minimum extent for the retreat of montane ice from the Maximum Glaciation (informal term of Jackson et al. (1996) and here referred to as the M1 advance) as lying upstream from Rener's Farms section in the Castle

River valley. Evidence at the Rener's Farms section was based on the presence of M1 till and till correlated to the subsequent montane readvance (here referred to informally as the M2 advance) separated by a fluvial unit. Two new sections, Screwdriver Creek and Hunting Eagle, have similar stratigraphy and exposed bedrock, but their locations are down-ice from the proposed retreat limit of M1 glacial ice. Sedimentological characteristics and stratigraphic relations of deposits at Wedgie and McRae sections suggests that till correlated to the M2 advance directly overlies till correlated to the M1 advance and further defines the retreat limit.

Holme (1997) cited the presence of a clast from the Canadian Shield as evidence for two tills (units 2 and 3) at the Washout section, with the location of the clast defining the intertill contact. Re-evaluation of the interstratified sediment complex overlying unit 2 (units 3, 4, and 5), however, suggests an ice-contact depositional environment related to glacial ice retreating from the M2 advance and forces re-evaluation of unit 2 at Washout. Three interpretations are possible to explain the shield clast and all depend on the extent of retreat of M1 ice. If M1 glacial retreat did not reach upstream of the Washout section, but to a point between it and Rener's Farms section, then unit 2 correlates to both M1 and M2. If M1 ice did retreat upstream of Washout section then two possibilities arise; either 1) the subglacial till underlying the ice-contact unit consists of both M2 till and M1 till whose upper part was reworked during the M2 readvance, or 2) M1 till at the site was completely reworked and removed by ice from the M2 readvance.

Laurentide ice advances

Laurentide erratics from the late Wisconsinan Maximum Glaciation are present in the northeast corner of the Beaver Mines map area at elevations up to 1340 m, yet no Laurentide till is present within the Castle River valley from 1143 m to 1215 m elevation, upstream of Hunting Eagle section (Holme, 1997). Two preliminary hypotheses were proposed which account for this pattern, 1) continental ice advanced westward into the Castle River valley as montane ice retreated from the M2 advance but the Laurentide deposits were subsequently eroded by montane glaciofluvial activity, or 2) continental ice advanced between the M1 and M2 advances with the deposits being eroded by M2 readvance (Holme, 1997). Continued study and the addition of new data from the 1997 field season has spurred re-evaluation of these hypotheses.

With the reinterpretation of Washout units 3, 4, and 5 as ice-contact sediments from retreating M2 glacial ice, hypothesis 1 no longer explains the shield clast in unit 2 because the deposit antedates incursion of continental ice. Hypothesis 2 is able to account for the presence of a shield clast at Washout section and the absence of Laurentide till within the Castle River valley, but suggests that shield clasts should also be present within M2 till as reworked glacial debris. The lack of shield clasts from all sediments coeval with, or older than, the M2 advance casts doubt on the validity of this model also. A third hypothesis is suggested to explain the situation.

Hypothesis 3: Montane ice retreating from the M2 advance position experienced a still-stand in the Castle River valley between Mountain Mill section and Hunting Eagle section while Laurentide ice advanced into the area. Continental ice was prevented from advancing westward up the Castle River valley by the Castle Valley Glacier, but was able to continue unimpeded immediately north and south of the valley. This resulted in the deposition of Laurentide till and erratics at elevations above the Castle River valley from Washout section to Mountain Mill section. After retreat of the Laurentide Ice Sheet, the Castle Valley Glacier retreated to near the Washout section where it again experienced a still-stand and deposited the ice-contact unit. The thick sequence of glaciofluvial gravels with shield clasts at Mountain Mill section is further evidence of the still-stand of the M2 glacier margin in this area (*see* Stalker (1969) for description).

A consequence of this model is the potential for Canadian Shield clasts to have been deposited upstream by continental ice and then reworked during the M2 readvance.

CONCLUSIONS

Data gathered from four cliff-bank exposures were combined with results from six previously visited sections to reconstruct a succession of glacial deposits and events along the Castle River valley and its tributaries in southwest Alberta. All glacial deposits in Castle River valley date from the late Wisconsinan Glaciation. Stratigraphic correlation and sedimentological interpretation of eight sections suggest evidence for two advances of montane glacial ice interrupted by retreat up-ice of the Rener's Farms and Gasline sections. A single shield clast was found within till correlated to the montane readvance (M2) at Washout section. Shield-stone-bearing continental till was found at only one exposure, Hunting Eagle section, although it is also present at higher elevations flanking the Castle River valley. A sequence of events is proposed to account for these findings: the advancing Laurentide Ice Sheet was prevented from pressing up Castle River valley by a still-stand of M2 ice. The Laurentide Ice Sheet was deflected north and south where it continued westward unimpeded. The coalescence of montane and continental glaciers is further supported by the thick glaciofluvial gravel containing Canadian Shield clasts at Mountain Mill section.

ACKNOWLEDGMENTS

The authors gratefully acknowledge field assistance by Crystal Huscroft and the hospitality of Bruce Mowat.

REFERENCES

Alley, N.F.
1973: Glacial stratigraphy and the limits of the Rocky Mountain and Laurentide ice sheets in southwestern Alberta, Canada; Bulletin of Canadian Petroleum Geology, v. 21, p. 153-177.

Bayrock, L.A.
1969: Incomplete continental glacial record of Alberta, Canada; Quaternary Geology and Climate, Publication 1701, National Academy of Sciences, Washington, D.C., p. 99-103.

Benn, D.I.
1994: Fabric shape and the interpretation of sedimentary fabric data; Journal of Sedimentary Research, v. A64, No. 4, October, p. 910-915.

Hicock, S.R., Goff, J.R., Lian, O.B., and Little, E.C.
1996: On the interpretation of subglacial till fabric; Journal of Sedimentary Research, v. 66, no. 5, September, p. 928-934.

Holme, P.J.
1997: Quaternary geology and terrain inventory, Eastern Cordillera NATMAP Project. Report 4: investigations of continental and montane advances in the Beaver Mines map area, southwestern Alberta; *in* Current Research 1997-A; Geological Survey of Canada, p. 177-182.

Horberg, L.
1954: Rocky Mountain and continental Pleistocene deposits in the Waterton region, Alberta, Canada; Bulletin of the Geological Society of America, v. 66, p. 1093-1150.

Jackson, L.E., Jr.
1980: Glacial stratigraphy and history of the Alberta portion of the Kananaskis Lakes map area; Canadian Journal of Earth Sciences, v. 17, p. 459-477.
1994: Quaternary geology and terrain inventory, Foothills and adjacent plains, southwestern Alberta: some new insights into the last two glaciations; *in* Current Research 1994-A; Geological Survey of Canada, p. 237-242.

Jackson, L.E., Jr., Little, E.C., Leboe, E.R., and Holme, P.J.
1996: A re-evaluation of the paleoglaciology of the maximum continental and montane advances, southwestern Alberta; *in* Current Research 1996-A; Geological Survey of Canada, p. 165-175.

Jackson, L.E., Jr., Rutter, N.W., Hughes, O.L., and Clague, J.J.
1989: Glaciated fringe; *in* Chapter 1 of Quaternary Geology of Canada and Greenland, (ed.) R.J. Fulton; Geological Survey of Canada, Geology of Canada, no.1 (*also* Geological Society of America, The Geology of North America, v. K-1).

Leboe, E.R.
1995: Quaternary geology and terrain inventory, Eastern Cordillera NATMAP Project. Report 2: surficial geology and Quaternary stratigraphy, Pincher Creek and Brocket map areas, Alberta; *in* Current Research 1995-A; Geological Survey of Canada, p. 167-175.

Little, E.C.
1995: Quaternary geology and terrain inventory, Eastern Cordillera NATMAP Project. Report 3: two continental glacial advances in Waterton and Cardston map areas, Alberta; *in* Current Research 1995-A; Geological Survey of Canada, p. 177-182.

Liverman, D.G.E., Catto, N.R., and Rutter, N.W.
1989: Laurentide glaciation in west-central Alberta: a single (Late Wisconsinan) event; Canadian Journal of Earth Sciences, v. 26, p. 266-274.

May, R.W., Dreimanis, A., and Stankowski, W.
1980: Quantitative evaluation of clast fabrics within the Catfish Creek Till, Bradtville, Ontario; Canadian Journal of Earth Sciences, v. 17, p. 1064-1074.

Stalker, A. MacS.
1969: A probable late Pinedale terminal moraine in Castle River Valley, Alberta; Geological Society of America, Bulletin, v. 80, p. 2115-2122.

Stalker, A. MacS. and Harrison, J.E.
1977: Quaternary glaciation of Waterton-Castle River region; Bulletin of Canadian Petroleum Geology, v. 25, p. 882-906.

Wagner, W.P.
1966: Correlation of Rocky Mountain and Laurentide glacial chronologies in southwestern Alberta, Canada; Ph.D. thesis, Department of Geology, University of Michigan, Ann Arbor, Michigan, 141 p.

Young, R.R., Burns, J.A., Smith, D.G., Arnold, L., and Rains, R.B.
1994: A single late Wisconsin, Laurentide glaciation, Edmonton area and southwestern Alberta; Geology, v. 22, p. 683-686.

Geological Survey of Canada Project 930043

INTERIOR PLAINS AND ARCTIC CANADA

PLAINES INTÉRIEURES ET RÉGION ARCTIQUE DU CANADA

New observations on the geology of eastern Ellesmere Island, Canadian Arctic, part I: structure and stratigraphy in the vicinity of Franklin Pierce and Allman bays

T. de Freitas[1] and A. Sweet
GSC Calgary, Calgary

de Freitas, T. and Sweet, A., 1998: New observations on the geology of eastern Ellesmere Island, Canadian Arctic, part I: structure and stratigraphy in the vicinity of Franklin Pierce and Allman bays; in *Current Research 1998-E; Geological Survey of Canada, p. 21–30.*

Abstract: New map data have resolved the controversial Lower Cretaceous age for the conglomerates in the footwall of the Scoresby Bay Thrust. Most known Cretaceous deposits are interpreted as structural slivers associated with several extensive, flat thrusts. Erosional remnants of the thrust sheets are represented by several conspicuous klippen. In one of these klippen, the Cretaceous Kanguk Formation and Tertiary Cape Lawrence Formation are in structural contact with flat-lying Cape Lawrence Formation conglomerate. Many other klippen are composed of Ordovician or Silurian carbonates, and these are in thrust contact with Cretaceous Isachsen Formation or Tertiary Cape Lawrence Formation. These structural relationships are confirmed by new paleontological age determinations. Leaf impressions from sandstone interbeds in the thick, syntectonic conglomerates of the Cape Lawrence Formation indicate a Tertiary age.

Résumé : De nouvelles données cartographiques ont permis de régler la controverse sur la datation des conglomérats du Crétacé inférieur observés dans le mur du chevauchement de Scoresby Bay. La plupart des gisements connus du Crétacé sont interprétés comme des fragments structuraux associés à plusieurs chevauchements subhorizontaux de grande amplitude. Des résidus d'érosion des nappes de charriage sont représentés par plusieurs klippes bien visibles. Dans une de ces klippes, la Formation de Kanguk du Crétacé et la Formation de Cape Lawrence du Tertiaire sont en contact structural avec les conglomérats horizontaux de la Formation de Cape Lawrence. De nombreuses autres klippes sont formées de roches carbonatées ordoviciennes ou siluriennes et elles chevauchent par contact la Formation d'Isachsen du Crétacé ou la Formation de Cape Lawrence du Tertiaire. Ces contacts structuraux sont confirmés par de nouvelles datations paléontologiques. Les empreintes de feuille observées dans des grès interstratifiés dans les conglomérats syntectoniques de forte épaisseur de la Formation de Cape Lawrence révèlent un âge tertiaire.

---

[1] Imperial Oil Resources Limited, Research Centre, 3535 Research Road NW, Calgary, Alberta T2L 2K8

INTRODUCTION

Aspects of the Cretaceous and Tertiary outliers of eastern Ellesmere Island (Fig. 1) were described previously by de Freitas et al. (1997). In their paper, a Cretaceous age for the conglomerates in the footwall of the Scoresby Bay Thrust was suggested, based on paleontological age determinations from several isolated outcrops. This age was indicated by the authors as highly controversial, because coarse, Lower Cretaceous syntectonic deposits are unknown in the Arctic Archipelago. In addition, genetically related conglomeratic outliers farther north (Fig. 1, 2) have yielded Tertiary macrofossils.

As part of the continuing effort by the Geological Survey of Canada to map this region (Fig. 1), additional bedrock data were collected by T. de Freitas in July of 1997. Two main findings are reported. First, complex map relationships of lower Paleozoic, Cretaceous, and Tertiary deposits in the footwall of the Parrish Glacier Thrust are resolved. Second, Tertiary macro- and microfossils have been discovered in beds that are clearly part of the syntectonic conglomerate succession.

LITHOLOGY

Work is in progress on many aspects of the lower Paleozoic succession on eastern Ellesmere Island. In this report, formations shown in Figure 3 are described only briefly. These lithological descriptions will be important to future field geologists in mapping areas not completely mapped during this work. Additional bedrock information can be found in a companion paper (de Freitas, 1998b; *see also* de Freitas, 1991; de Freitas et al., 1997; de Freitas and Nowlan, in press).

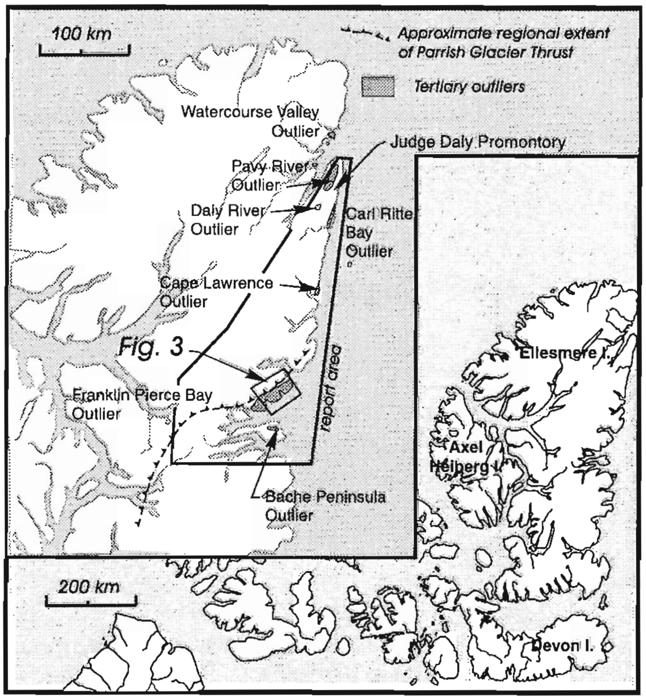

Figure 1. *Location of study area (and Fig. 3, smallest polygon) in the Canadian Arctic Islands.*

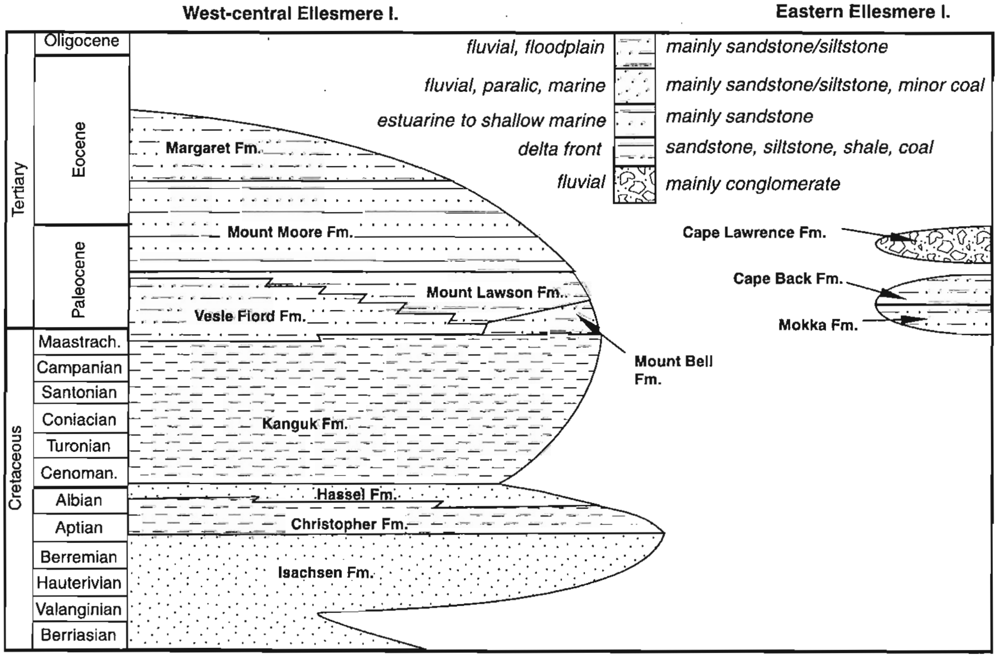

Figure 2. *Summary stratigraphic correlation of upper Mesozoic–lower Cenozoic strata, central and eastern Ellesmere Island. Modified from Miall (1991) and Embry (1991). For alternative stratigraphic nomenclature, see Ricketts (1994).*

Cambrian and Ordovician formations

The oldest rock units in the hanging wall of the Parrish Glacier Thrust are Cambrian in age and assigned to the Ella Bay Formation (Ꞓeb, about 160 m thick). This formation is generally a coarsely crystalline dolostone that forms a conspicuous red- and orange-weathering band marking the trace of the regional Parrish Glacier Thrust. It should be noted, however, that the Parrish Glacier Thrust cuts down- and upsection to the west and east of Figure 3, respectively. Above the Ella Bay Formation, there is a thick sequence of coarse, locally conglomeratic sandstone, assigned to the Dallas Bugt Formation (Ꞓdb, about 500 m thick). The formation is divisible into two informal members, a lower purple-weathering sandstone and conglomerate member and an upper member containing abundant, thick-bedded, very light yellow-grey-weathering, cross-stratified sandstone, with locally common *Skolithos* burrows. Kerr (1973) assigned this formation to an undivided Precambrian sequence, and Long (1989) assigned it to the Ellesmere Group. Our usage of the name Dallas Bugt Formation is based on two criteria. First, the formation lacks the many thick, interbedded mudrock units that characterize the Ellesmere Group farther north (Trettin, 1994). Second, it is characterized by abundant, cross-stratified sandstone and *Skolithos* burrows, which are distinguishing features of the Dallas Bugt Formation on Bache Peninsula and North Greenland (Peel et al., 1982; *see also* de Freitas, 1998a).

The Kane Basin Formation (Ꞓkb, about 90 m thick) forms a readily mappable unit in the report area. It is a shallow-marine, bioturbated siltstone and sandstone, which forms a recessive, dark-weathering band above the light yellow-, red- and brown-weathering Dallas Bugt Formation and below the cliff-forming Scoresby Bay Formation.

The Scoresby Bay Formation (Ꞓsb, about 340 m thick) consists of resistant, medium grey- and pale yellowish orange-weathering limestone and dolostone, with locally abundant trilobites in the lower part. The overlying Parrish Glacier Formation (Ꞓpg) is more recessive than the Scoresby Bay Formation. It consists of continuous, medium-bedded, yellow- and grey-weathering limestone and dolostone, deposited primarily under shallow-marine and intertidal depositional environments. Red-weathering dolostone, silty dolostone, and mudrock are locally conspicuous features of the formation.

The overlying Cass Fjord Formation (ꞒOcf, about 380 m thick) is broadly similar lithologically to the Parrish Glacier Formation, except that it does not weather red, and it commonly contains a basal 10–20 m thick resistant limestone unit. On aerial photographs, the Cass Fjord Formation is a slightly lighter grey than the underlying Parrish Glacier Formation. Of all the lower Paleozoic formations in the report area, the Cass Fjord–Parrish Glacier contact tends to be one of the most difficult to recognize.

Two members of the Cass Fjord Formation are recognized in the report area. These correspond to members described from central Ellesmere Island (de Freitas and Fritz, 1995). Each member features a lower, open-marine limestone succession and upper, restricted-marine dolostone and limestone succession. The lower limestone parts tend to be slightly more resistant and darker weathering than the upper parts. An important local development of the upper member is abundant sandstone, which occur a few metres beneath the overlying Cape Clay Formation. This interval is undoubtedly a correlative of the Kap Coppinger Member (Cass Fjord Formation) and to the Permin Land Formation of North Greenland (Higgins et al., 1991).

Ordovician formations above the Cass Fjord Formation feature lithologies remarkably similar to those described from other parts of Ellesmere Island (e.g. Trettin, 1994). The Cape Clay Formation (Occ, about 100 m thick) is a resistant, dolomitic limestone with common thrombolites and intraclast conglomerate beds in the lower part. The Christian Elv Formation (Oce, about 400 m thick) is a more recessive, lighter grey-weathering unit that contains numerous, 3–10 m thick, shallowing-upward sequences consisting of platy and thick-bedded dolostone and limestone. The formation has a distinctive, resistant, locally mappable, thrombolitic limestone upper member. The Baumann Fiord Formation (Ob, about 400 m thick) contains three members, a lower gypsum member, a middle microbialite-rich dolomitic limestone member, and an upper, restricted-marine, platy limestone and dolostone member. The Eleanor River Formation is a resistant, open-marine dolomitic limestone unit that forms high cliffs in many areas. The middle and upper part of the formation contains interbeds of restricted-marine, platy limestone and dolostone. The overlying recessive Bay Fiord Formation (Ocb, about 350 m thick) has two mappable members, a lower member consisting of platy limestone, dolostone, and minor gypsum, and an upper member containing platy dolostone and limestone. The base of the upper member features a resistant, open-marine, cliff-forming unit that is an obvious feature on aerial photographs and in cliff exposures. Elsewhere, this limestone unit is a separate member and the Bay Fiord is divisible into three members. The overlying Thumb Mountain Formation (Oct, about 300 m thick), like the Eleanor River Formation (Oe, about 300 m thick), is a cliff-forming unit of burrow-mottled dolomitic limestone. The thin Irene Bay Formation (Oci, about 20 m thick) is a green, rubbly weathering, argillaceous limestone with common, well preserved macrofossils. The lower Allen Bay Formation (OSa, about 100 m thick) is much like the Thumb Mountain Formation and contains rare, large fossils in a burrow-mottled dolomitic limestone.

Silurian formations

The Allen Bay Formation (OSa) is very similar lithologically to the Allen Bay Formation of central and southern Ellesmere Island (de Freitas, 1991). The lower member is Ordovician and consists of mottled dolomitic limestone, as stated above. The bulk of the formation, represented by the middle member, consists of thick-bedded, coarsely crystalline dolostone, overlain by a limestone member (OSal), consisting of very resistant, shallow-marine, finely crystalline limestone that forms local, precipitous cliffs. The contact with the overlying Cape Storm Formation is sharp and marked by a distinct

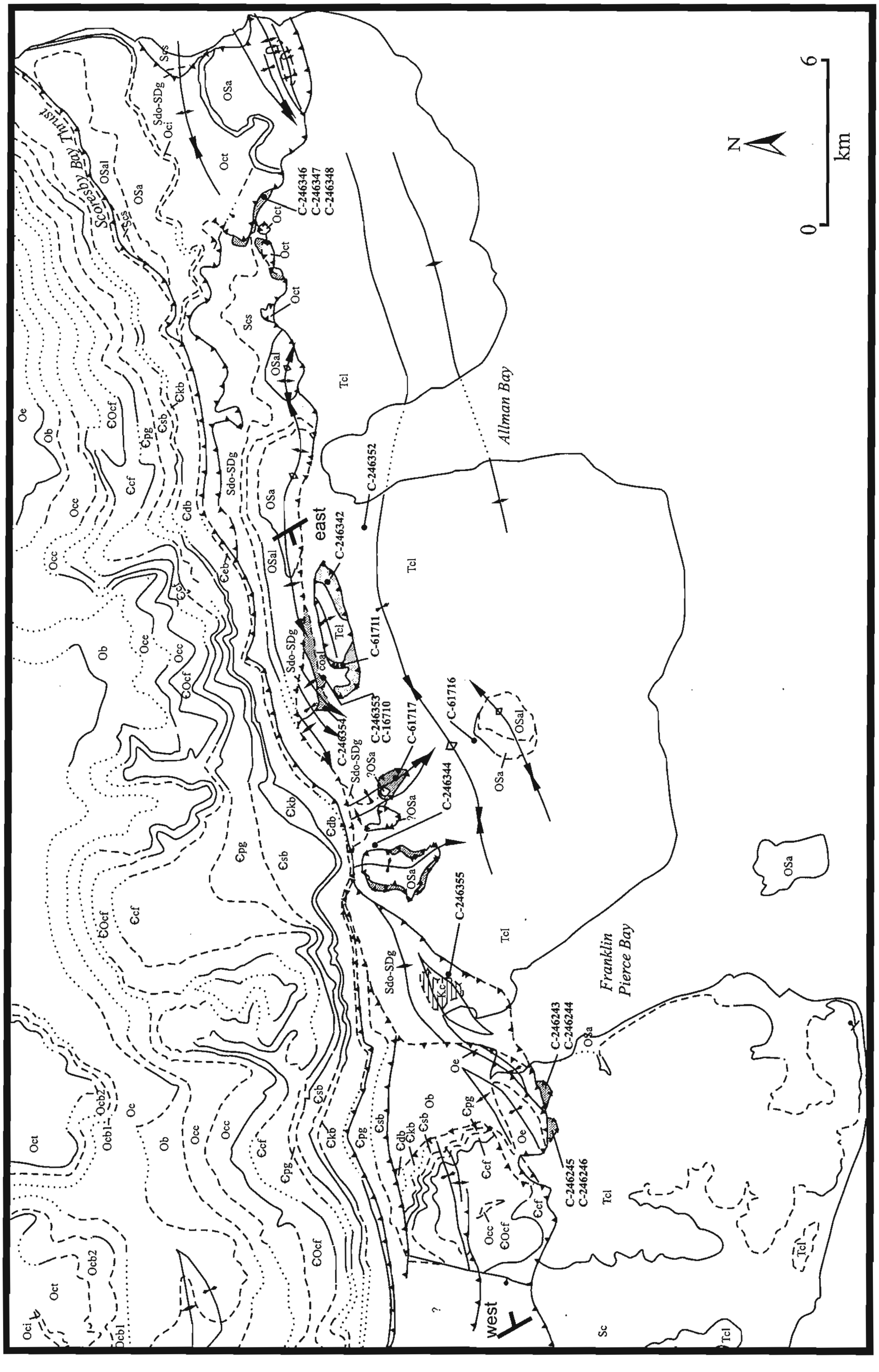
Scoresby Bay Thrust
Allman Bay
Franklin Pierce Bay
east
west
N
0
6
km
Tcl
OSa
OSal
Oct
Oci
Scs
Sdo-SDg
Sc
Oe
Ob
Occ
Oc
Ocb1
Ocb2
€Ocf
€cf
€pg
€sb
€kb
€db
€eb
coal
C-246346
C-246347
C-246348
C-246352
C-246342
C-61711
C-61716
C-61717
C-246353
C-16710
C-246354
C-246344
C-246355
C-246243
C-246244
C-246245
C-246246

TERTIARY

Tcl *CAPE LAWRENCE FORMATION: brown to reddish brown; granule to boulder grade; thick-bedded; carbonate lithoclasts featuring lithologies of lower Paleozoic succession in hanging wall of the Parrish Glacier Thrust, common clast imbrication; <10% interbedded fine- to medium-grained sandstone*

CRETACEOUS

▒ *KANGUK FORMATION: Mudrock: grey-weathering, poorly consolidated.*

☰ *CHRISTOPHER FORMATION: Mudrock, black, poorly consolidated*

▓ *ISACHSEN FORMATION: Sandstone and coal (interbedded). Sandstone: white-weathering; poorly consolidated; cross-stratified.*

SILURIAN

Sc *UNDIVIDED SILURIAN CARBONATES: includes Allen Bay, Cape Storm, and Douro formations, as described below.*

Sdo-SDg *UNIDIVIDED DOURO AND GOOSE FIORD FORMATIONS: Limestone and sandstone. Limestone: dolomitic, sandy and silty, greyish yellow-green, medium- and thin-bedded, finely crystalline, bioturbated, highly fossiliferous. Sandstone: calcareous and dolomitic, greyish yellow-green, fine-grained, massive, bioturbated, fossiliferous*

Scs *CAPE STORM FORMATION: Dolostone and sandstone. Dolostone: calcareous, sandy and silty, greyish yellow-green and greyish yellow, medium- and thin-bedded, finely crystalline, laminated, stromatolitic. Sandstone: calcareous and dolomitic, greyish yellow-green, fine-grained, well sorted, massive, bioturbated*

SILURIAN AND UPPER ORDOVICIAN

OSal *Limestone member: Limestone: dolomitic, greyish yellow, thick-bedded, finely crystalline; resistant, locally laminated and stromatolitic.*

OSa *ALLEN BAY FORMATION: Limestone and dolostone. Limestone (in lower and upper part): dolomitic, greyish yellow, medium- and thick-bedded, finely crystalline, burrow-mottled in lower part; laminated, stromatolitic, conglomeratic in upper part; rare fossils including gastropods, stromatoporoids, brachiopods. Dolostone: light grey and greyish yellow, finely to medium crystalline, laminated, massive, <5% vuggy porosity*

UPPER ORDOVICIAN

Cornwallis Group

Oci *IRENE BAY FORMATION: Limestone: dolomitic, argillaceous; greyish yellow green, medium-bedded, rubbly weathering; finely crystalline, burrow-mottled, abundant fossil fragments, Arctic-Ordovician fossil fauna*

Oct *THUMB MOUNTAIN FORMATION: Limestone: dolomitic, argillaceous intervals in upper part; yellowish grey, greenish in argillaceous upper part; thick-bedded, resistant, finely crystalline, abundantly burrow-mottled, Arctic-Ordovician fossil fauna in upper part*

Ocb2 *BAY FIORD FORMATION (upper member): limestone and dolostone; yellowish grey and medium grey, thin- and medium-bedded, finely crystalline, laminated, mudcracks; contains a basal 10-15 m thick, resistant, burrow-mottled dolomitic limestone*

Ocb1 *lower member: limestone, dolostone, minor gypsum. Limestone and dolostone: yellowish grey and medium grey, thin- and medium-bedded, finely crystalline, laminated, mudcracks; gypsum: calcareous, white, laminated*

▲▲▲ *Thrust fault (defined approximate, assumed or projected through overburden or ice; teeth indicate upthrust side)*

MIDDLE ORDOVICIAN

Oe *ELEANOR RIVER FORMATION: limestone and minor dolostone: yellowish grey and pale yellowish brown; thick-bedded, resistant; finely crystalline, abundant burrow mottles, minor chert*

Ob *BAUMANN FIORD FORMATION: gypsum, limestone, and dolostone. Gypsum: (mostly in lower 66% of formation) white, thin-bedded, recessive, laminated, calcareous, common intraclast conglomerate. Limestone and dolostone: (mostly in upper 33%) gypsiferous; yellowish grey, medium- and thin-bedded; finely crystalline, intraclast conglomerates , laminated, ocally abundant thrombolites*

Oce *CHRISTIAN ELV FORMATION: limestone and dolostone: yellowish grey, medium- and thick-bedded; finely crystalline, intraclast conglomerates , laminated, locally abundant thrombolites in upper part; bedding planes feature numerous trace fossils*

LOWER ORDOVICIAN AND UPPER CAMBRIAN

Occ *CAPE CLAY FORMATION: limestone and dolostone: yellowish grey, medium- and thick-bedded; finely crystalline, resistant, intraclast conglomerates; laminated, locally abundant thrombolites in upper part*

UPPER CAMBRIAN

ЄOcf *CASS FJORD FORMATION (upper member): limestone and dolostone: sandy in upper part, yellowish grey and light grey, medium- and thick-bedded; finely crystalline, intraclast conglomerates, laminated, thrombolites in lower part*

Єcf *lower member: limestone and dolostone: sandy in lower part, yellowish grey and light grey, local red-weathering, medium- and thick-bedded; finely crystalline, intraclast conglomerates, laminated, mud cracks*

MIDDLE CAMBRIAN

Єpg *PARRISH GLACIER FORMATION (upper member): limestone and dolostone: sandy; yellowish grey, locally red-weathering; medium- and thick-bedded; finely crystalline, intraclast conglomerates, burrow mottles; laminated, rare thrombolites*

LOWER CAMBRIAN

Єsb *SCORESBY BAY FORMATION: dolostone: calcareous and some limestone in lower part; yellowish grey, pale yellowish brown, and bright yellowish orange, thick-bedded, resistant; medium and locally coarsely crystalline, bioturbated, trilobites*

Єkb *KANE BASIN FORMATION: Sandstone, siltstone, and mudrock: yellowish grey and dark grey; thin-bedded recessive, laminated; some Skolithos burrows in lower part*

Єdb *DALLAS BUGT: Sandstone and conglomerate: yellowish grey, moderate red, pale yellowish orange; thick-bedded; medium-grained, conglomeratic (pebble grade) in middle part; abundant trough cross-stratified*

Єeb *ELLA BAY FORMATION: Dolostone: bright yellowish orange and greyish yellow; thick-bedded, coarsely crystalline; resistant, massive*

east *Line of section shown in Figure 5*

Geological boundary (defined, approximate, projected through ice or overburden)

Normal fault (defined, approximate)

Anticline, syncline (arrow indicates plunge)

***Figure 3.** Bedrock geology map, southeastern part of the Dobbin Bay map area, eastern Ellesmere Island. For location see Figure 1. GSC fossil sample locations are shown.*

break in slope. The Cape Storm Formation (Scs) is composed of silty limestone, sandstone, and argillaceous limestone, which feature sedimentary structures of restricted-marine and tidal flat aspect. The overlying undivided Goose Fiord and Douro formations (Sdo–SDg) constitute a fossiliferous limestone succession with few sandstone interbeds. These strata are locally rubbly weathering, and many fossils weather out in the felsenmeer-covered uplands. The conspicuous reef-bearing Silurian units in the hanging wall in the northern part of the area represented in Figure 3 (*see also* de Freitas and Nowlan, in press) are not apparent in the Silurian footwall succession.

Cretaceous formations

These units (Fig. 2–5) are areally restricted and generally poorly exposed. They are, however, distinctive outcrops and appear as vegetation-covered, brown- and black-weathering exposures that contrast with the lighter coloured, surrounding bedrock.

Isachsen Formation

The Isachsen Formation consists of white- and brown-weathering, poorly consolidated, coaly sandstone and coal. Near sample C-246353 (Fig. 3), coal is abundant, accounting for up to 50 per cent of the known streambank exposures. The formation is poorly exposed in most areas and generally outcrops as dark-weathering, soupy mud overlain by sparse or, more usually, plentiful vegetation. Where streams dissect these deposits, large coal chunks are obvious lithoclasts in the recent stream gravels. Near sample C-246354, an unconformable contact between the Isachsen and overlying Cape Lawrence Formation is exposed. Coal analyses of samples C-246243 to C-246246 are described in de Freitas et al. (1997).

Table 1 lists the more abundant palynomorphs found in the six Early Cretaceous age samples. The taxa listed are not particularly age diagnostic beyond inferring a probable age within the Early Cretaceous. There are also occurrences of species having a more restricted age range. *Clavatipollenites* and a possible specimen of *Liliacidites* sp., the ranges of which start in the Barremian, occur in sample C-246347; *Penetetrapites mollis* Hedlund and Norris, and *Impardicaspora trireticulosus*, with Aptian and younger ages, occur in sample C-246348; *Tigrisporites reticulatus,* with most usually a Aptian to Albian age range, occur in sample C-246353; *Clavatipollenites,* in sample C-246354, is known to range from Barremian to present. In sum, the palynological assemblage indicates a probable Aptian age for these coal/sandstone/mudstone exposures. Therefore, these ages and lithofacies, and especially the presence of coal, allies these outcrops to the Isachsen Formation.

Christopher Formation

Sample C-246353 was collected from the top of a low plateau underlain by gently folded Silurian carbonates. Observed from aircraft, this plateau is dark weathering and supports abundant vegetation, and thus has similar characteristics to Cretaceous outliers farther east and west of this locality. A brief stop on this plateau in July of 1997 confirmed that the plateau vegetation is rooted in a thin, mud unit resting on deformed Silurian carbonates. Microfossils from this unit include *Tricolpites micromunus* (Groot & Penny) Singh, sample C-246355, which has an age range that starts in the Middle Albian. Two explanations for the mud unit are possible: 1) it may represent a thin exposure of Christopher Formation, or 2) it may be Holocene in age and represent deposition in a glaciomarine environment. In the second case, deposition from glaciofluvial or glaciomarine processes would likely produce a poorly sorted deposit containing many lower Paleozoic lithoclasts, as is typical of the Quaternary sediments in adjacent regions. However, the fine-grained muds do not contain lower Paleozoic clasts. Further, if the Albian fossils are allochthonous, they would have travelled more than 100 km from the west, from exposed Albian deposits, and through an uplifted, resistant lower Paleozoic sequence of rock. Thus, an Albian age is suggested for these deposits, and the palynomorphs are in situ components. In support of an assignment to the Christopher Formation, Embry (1991) indicates that the basal contact of this Christopher Formation forms an overlap relationship with many older units in the Sverdrup and Franklinian basins, particularly on Melville Island, west and south of this report area. The presence of dinoflagellates in most of these samples indicates a paralic to marine depositional environment.

Kanguk Formation

The only known outcrop of the Kanguk Formation occurs within the largest klippe (yielding samples C-61711 and C-246342; Fig. 2). These exposures were visited briefly in 1997, and poorly exposed and vegetation-covered mudrock was sampled for palynomorphs. Assignment of these rocks to the Kanguk Formation is based mainly on the presence of abundant dinoflagellates and miospores that indicate a marine depositional environment and most probably a Turonian age. The palynological assemblage recovered from sample C-246342 included the dinoflagellates *Chatangiella granulifera* (Manum) Lentin and Williams, *Hystrichospheridium, Isebelidinium, Odontochitina, Palambages,* and *Trithyrodinium suspectum* (Manum and Cookson) Davey; and the miospores *Foveotetradites fistulosus* (Dettmann) Singh and *Tigrisporites verrucatus* Singh. The combined presence of *Chatangiella granulifera* and *Foveotetradites fistulosus* is evidence for a Turonian age (Sweet and McIntyre, 1988; Núñez-Betelu, 1994). This implies an age extension for *Tigrisporites verrucatus,* which has previously been found in Cenomanian strata (Singh, 1983). The unit contrasts with the Isachsen Formation because of a conspicuous absence of coal.

Tertiary (Cape Lawrence Formation)

The Cape Lawrence Formation (Tcl) consists mainly of boulder, cobble, and pebble conglomerates. These are generally well cemented and form precipitous cliffs. High plateaus are dissected by streams that have formed deep, inaccessible

Table 1. Palynomorph identifications.

A=abundant, C=common, S=scarce, R=rare	C-246246 (traverse NW of Cape Hawks); coal	C-246247 (traverse NW of Cape Hawks); siderite concertions	C-246248 (traverse NW of Cape Hawks); sand and coal	C-246253 (traverse of Allman and Franklin Pierce bays); coal/sandstone	C-246253 (traverse of Allman and Franklin Pierce bays); coal	C-246255 (traverse of Allman and Franklin Pierce bays); mud on Goose Fiord
MIOSPORES						
Alisporites & other bisaccates	A	A	A	A	A	A
Acanthotriletes varispinosus						
Cerebropollenites meszoicus	A	C	C	C	C	C
Cicatricosiporites spp.	R	R	R		R	S
Classopollis sp.	R		R		R	
Concavissimisporites spp.					R	
Cycadopites sp.				R	R	R
Densoisporites cf. *D. crassus*	R		S	R	R	
Deltoidospora sp.		C	S		S	S
Eucommiidites troedssonii		R	R			
Foraminisporis asymmetricus					R	S
Gleicheniidites senonicus	C	C	C	C	C	A
Lycopodiumsporites austroclavatidites	S	S	R		S	R
Neoraistrickia cf. *N robusta*	C	C		R		R
Osmundacidites wellmanii	R	R		R	C	A
Perinopollenites elatoides	R	S		R		
Pilosisporites trichopapillosus						
Podocarpidites sp.	S				R	
Sestrosporites pseudoalveolatus						
Stereisporites antiquasporites	C	C	C		A	A
Taxodiaceae/Cupressaceae/Taxaceae	A	A	A	A	A	A
Trilobosporites sp.			R			
Vitreisporites pallidus			R			R
Dinoflagellates	C	S	A		C	C
Canningia sp.			A			
Hystrichospheridium spp.	R				C	C
Odontichitina sp.	R	R	R		R	R
Gonyaulacysta sp.			S		C	R

canyons. Orthoclast conglomerates predominate, although paraconglomeratic fabric occurs locally. These deposits were interpreted previously as the result of deposition in braided streams that were sourced in uplifted lower Paleozoic strata in the thrust sheets to the north (de Freitas et al., 1997).

Very minor sandstone and siltstone interbeds were investigated for possible macrofossil occurrences, but only a single locality, C-246344, yielded poorly preserved leaf impressions. E. McIver and J. Basinger (University of Saskatchewan) examined these samples and reported that they are cf. *Ushia* sp. cf. *U. kolakovskii*, which is a common taxon in lower Paleocene beds of the Expedition, Strand Bay, Iceberg Bay, and Buchanan Lake formations in the Canadian Arctic Islands. Assignment to the genus indicates a Tertiary age, but if species assignment is correct, then the leaves are Paleocene or Eocene. Two siltstone samples, C-246344, associated with the leaf impressions, and C-246352, were processed for palynology. The most productive, C-246352, yielded rare specimens of *Liliaciidtes* sp., tricolpate pollen, the fungi *Phragmothyrites* sp., and a species of *Dicellaesporites* that together support a Tertiary age (R.M. Kalgutkar, pers. comm., 1998).

STRUCTURE

Fieldwork during the 1997 field season yielded many surprises regarding the geometric relationships of the coal- and conglomerate-bearing rock units in the footwall of the Parrish

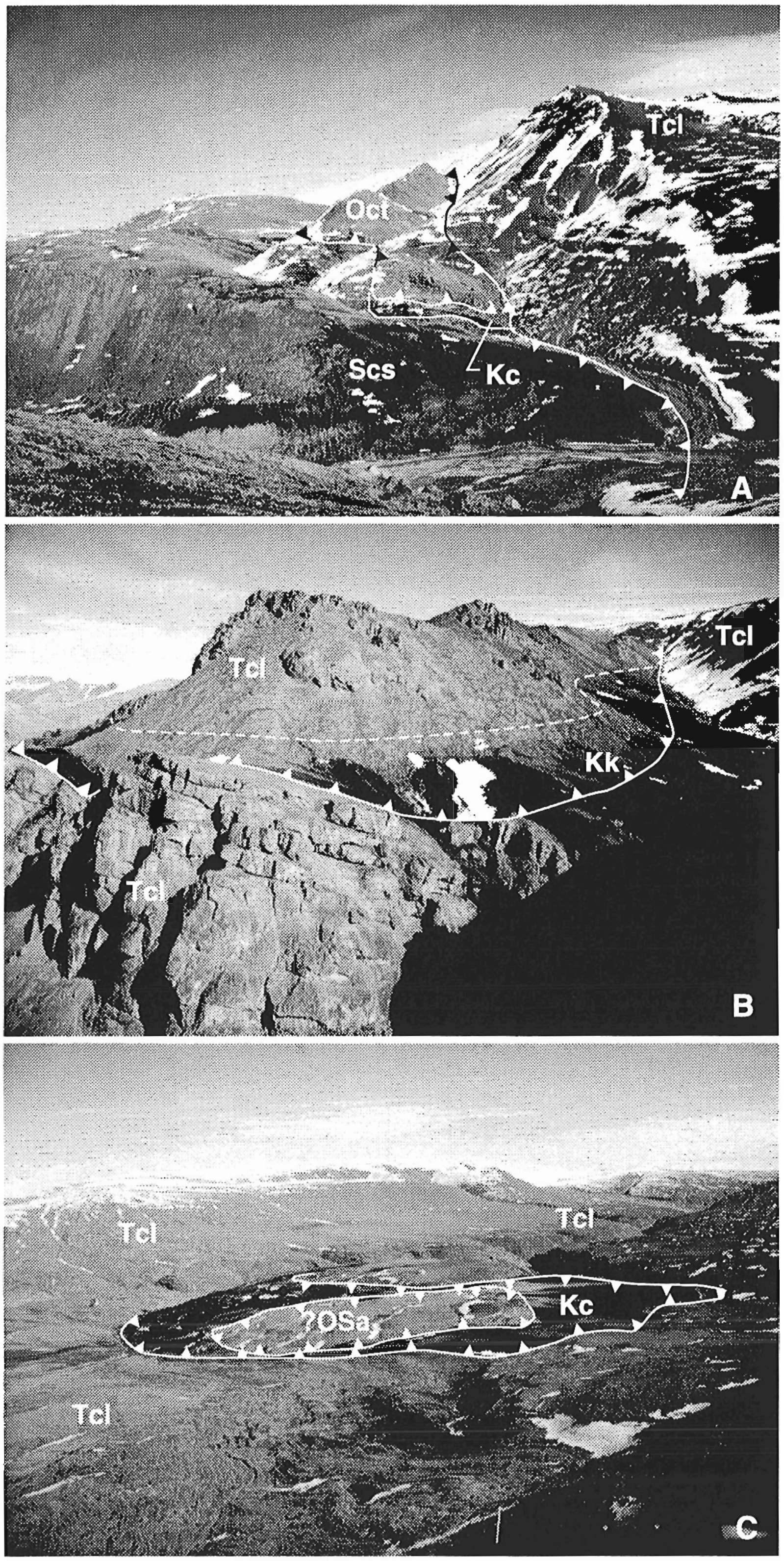

Figure 4.

Photographs of three klippen as mapped in Figure 2. For symbols see Figure 3 legend. ***A)*** *View to east of large klippe east of Allman Bay. This is the second klippe east of Allamn Bay on Figure 3. Note that the topographically highest strata to right are conglomerates of the Cape Lawrence Formation. West-east length of klippe is about 2 km. Kc = Christopher Formation.* ***B)*** *View to southeast of large klippe between Allman and Franklin Pierce bays. This is the only klippe in the region involving Cape Lawrence Formation conglomerates. Structural relationships are confirmed by age dating. Barren sample C-61711 was collected in the dark band just above the thrust on left of photograph. Sample C-246342 behind and to the east of hill was collected from the same dark band; this sample yielded palynomorphs indicating assignment to the Kanguk Formation. Height of cliff in foreground is about 30 m. Kk=Kanguk Formation.* ***C)*** *Large, poorly exposed klippe with dark weathering Isachsen Formation overlain by a thin ?Allen Bay Formation. Sample C-61717 was collected from this klippe. Width of klippe is about 1 km. Kc=Christopher Formation.*

Glacier Thrust. The Parrish Glacier Thrust is by far the most regionally continuous structure in the map area. Its trace is approximately west-east and it carries about 3 km of Cambrian through Lower Devonian carbonates and clastics. To the east, the thrust rests progressively on younger formations, but to the west (west of the area represented in Fig. 3), in the adjacent Sawyer Bay map area, the thrust involves the oldest known exposures of the Franklinian succession, the Kennedy Channel Formation.

The footwall structure of the Parrish Glacier Thrust is complex. Several large thrust sheets involving Devonian and Cambrian carbonates were identified. These flat thrusts are sinuous and their hanging walls have complex minor, upright, or overturned folds. Flat thrust geometries are particularly apparent in the northeast-facing cliffs in the eastern extremity of the area represented in Figure 3. There, the folded thrust contact of the Silurian and Ordovician carbonate formations is discontinuously exposed. Good exposures of the thrust are also available northwest of Allman Bay, where Silurian carbonates have been thrusted on Tertiary carbonates, and the apparent dip of the thrust is about 15°.

The Parrish Glacier footwall contains at least four klippen, located between Franklin Pierce and Allman bays and a further three to the east of Allman Bay (Fig. 3–5). The most western klippe in the report area was first recognized by Ray Thorsteinsson of the GSC in 1984. It is composed of gently folded, Allen Bay Formation limestone in structural contact with a discontinuous layer of coal-bearing Cretaceous Isachsen Formation. East of this, a second klippe occurs. It consists of Allen Bay Formation resting directly on the Cape Lawrence Formation (Fig. 3).

The third klippe, which yielded Cretaceous microfossils (C-61717), is a conspicuous feature in the region. Although poorly exposed, the coal-bearing sandstone and mudrock are extensively vegetated and appear as a dark, semicircular patch. The northern end of this dark outcrop contains small mounds of more resistant Allen Bay Formation that are likely the erosional remnants of a once more extensive klippe (Fig. 4C).

The eastern klippe in this region (yielding Cretaceous fossils from C-246342 and C-61711) is the largest of all, but unusual in that it involves Tertiary Cape Lawrence Formation conglomerate beds and coal-bearing Cretaceous Isachsen Formation in thrust contact with Cape Lawrence Formation (Fig. 4B, 5). The vertical succession in this area involves lower, autochthonous, gently folded Douro and Goose Fiord formations unconformably overlain by Isachsen Formation coaly sandstone; a second unconformable contact is followed by resistant, cliff-forming Tertiary Cape Lawrence Formation conglomerates. This unit is overlain by a thrust fault carrying Cretaceous, poorly consolidated mudrock of the Kanguk Formation, which is unconformably overlain by about 20 m of gently folded Cape Lawrence Formation conglomerate (Fig. 5).

East of Allman Bay, three small klippen of Ordovician Thumb Mountain Formation occur (Fig. 4A). In all cases, these klippen rest on deformed, although poorly exposed, Cretaceous coal-bearing siliciclastics. However, these siliciclastics are thin and, in some cases, too small to be shown at the present map scale. The central klippe is best exposed, and Ordovician strata at its base are represented by a cataclasite.

DISCUSSION AND FUTURE WORK

Based on the information presented here, controversial aspects about the age and stratigraphic setting of coal-bearing strata in the footwall of the Parrish Glacier Thrust are put to rest. It seems now that the Cretaceous strata were structurally emplaced during Tertiary convergent tectonics. Before regional shortening, Cretaceous units were likely deposited on flat-lying Silurian and Ordovician formations. Cretaceous strata were then moved to a structurally elevated position during Tertiary thrusting. Preservation as klippen in the footwall, near to the southern exposed limit of south-vergent thrusting is undoubtedly related to the ramp flat thrust geometry of the regional Parrish Glacier Thrust. The conglomerates of the Cape Lawrence Formation are the sedimentary record of this regional shortening and uplift event. The syntectonic deposits were also involved in convergent tectonics, and, in

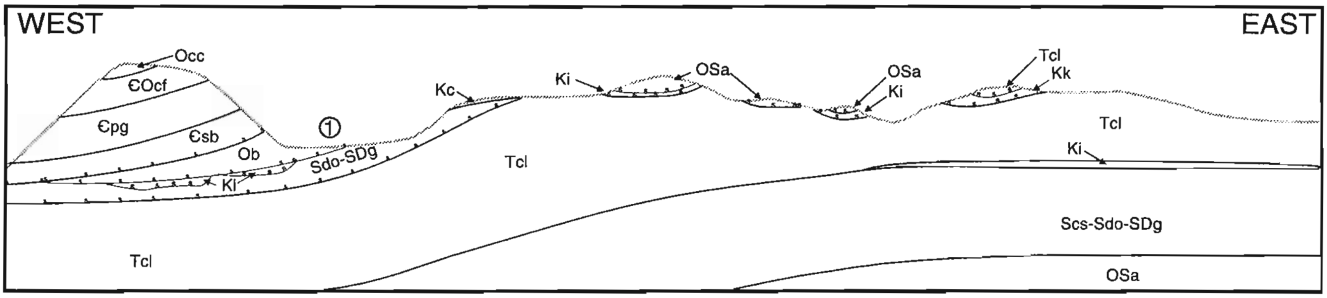

Figure 5. Schematic cross-section showing main structural features south of the Parrish Glacier Thrust near Franklin Pierce and Allman bays. For approximate location of the cross-section and lithologies see Figure 3. Not to scale. Number on left side of the cross-section is the valley at the head of Franklin Pierce Bay. Ki=Isachsen Formation; Kc=Christopher Formation; Kk=Kanguk Formation.

one case, their structural involvement is evident in a large klippe preserved between Allman and Franklin Pierce bays (Fig. 3).

Future work should focus on regions west of Franklin Pierce Bay. An emphasis in this work should be to resolve map relationships in the complex footwall of the Parrish Glacier Thrust. This is particularly apparent in the Cambrian strata to the north of Cretaceous samples C-246243 to C-C245246. Several dark patches are visible on aerial photographs and from reconnaissance aerial observations of that region. These hint at further structural complexities not apparent in the present summary map (Fig. 3).

CONCLUSIONS

Cretaceous deposits are more widespread in the report area than once thought. These strata occur primarily as thin thrust slivers or as structurally emplaced lenses beneath klippen containing lower Paleozoic carbonates. In most cases, thrusting has entrained Lower Cretaceous Isachsen Formation, but in one area, the Kanguk Formation is preserved in the basal part of a klippe. The Cape Lawrence Formation syntectonic conglomerates are Tertiary in age, based on several leaf impressions and microfossils.

ACKNOWLEDGMENTS

Discussions with Larry Lane and Ulrich Mayr improved the content of the manuscript. Dave Beedell provided cheerful and dependable field assistance. The age ranges stated for selected species are based on references retrieved from the PALYLIT database, available at GSC Calgary.

REFERENCES

de Freitas, T.
1991: Stratigraphy, mud build-ups, and carbonate platform development of the Upper Ordovician to Lower Devonian sequence, Ellesmere, Hans, and Devon islands, Arctic Canada; Ph.D. thesis, University of Ottawa, Ottawa, Ontario, 431 p.

de Freitas, T.
1998a: New observations on the geology of eastern Ellesmere Island, Canadian Arctic, part II: Cambro-Ordovician stratigraphy of the Parrish Glacier region; *in* Current Research 1998-E; Geological Survey of Canada.
1998b: New observations on the geology of eastern Ellesmere Island, Canadian Arctic, part III: Cambro-Ordovician stratigraphy of the Dobbin Bay, Scoresby Bay, and Franklin Pierce Bay areas; *in* Current Research 1998-E; Geological Survey of Canada.

de Freitas, T. and Fritz, W.H.
1995: Age and stratigraphy of the Cass Fjord Formation, Arctic Canada; *in* Current Research 1995-E; Geological Survey of Canada, p. 97-104.

de Freitas, T. and Nowlan, G.S.
in press: A new, major Silurian reef tract and overview of regional Silurian reef development, Canadian Arctic and North Greenland; Bulletin of Canadian Petroleum Geology.

de Freitas, T., Sweet, A.R., and Thorsteinsson, R.
1997: A problematic Early Cretaceous age for the conglomerates that have been assigned to the Eureka Sound Group, east-central Ellesmere Island, Arctic Archipelago; *in* Current Research 1997-E; Geological Survey of Canada, p. 21-32.

Embry, A.F.
1991: Mesozoic history of the Arctic Islands; Chapter 14; *in* Geology of the Innuitian Orogen and Arctic Platform of Canada and Greenland, H.P. Trettin (ed.); Geological Survey of Canada, Geology of Canada, no. 3, p. 370-433 (*also* Geological Society of America, The Geology of North America, v. E).

Higgins, A.K., Ineson, J.R., Peel, J.S., Surlyk, F., and Sønderholm, M.
1991: Lower Paleozoic Franklinian Basin of North Greenland; Grønlands Geologiske Undersøgelse, Bulletin 160, p. 71-139.

Kerr, J.W.
1973: Geology, Kennedy Channel and Lady Franklin Bay, District of Franklin; Geological Survey of Canada, Map 1359A, scale 1:25 000.

Long, D.G.F.
1989: Kennedy Channel Formation: key to the early history of the Franklinian continental margin, central eastern Ellesmere Island, Arctic Canada; Canadian Journal of Earth Sciences, v. 26, p. 1147-1159.

Miall, A.D.
1991: Late Cretaceous and Tertiary basin development and sedimentation, Arctic Islands; Chapter 15; *in* Geology of the Innuitian Orogen and Arctic Platform of Canada and Greenland, (ed.) H.P. Trettin; Geological Survey of Canada, Geology of Canada, no. 3, p. 437-458 (*also* Geological Society of America, The Geology of North America, v. E).

Núñez-Betelu, L.
1994: Sequence stratigraphy of a coastal to offshore transition, Upper Cretaceous Kanguk Formation: a palynological, sedimentological, and rock-eval characterization of a depositional sequence, northeastern Sverdrup Basin, Canadian Arctic; University of Calgary, Ph.D. dissertation, Calgary, Alberta, 569 p.

Peel, J.S., Dawes, P.R., Collinson, J.D., and Christie, R.L.
1982: Proterozoic-basal Cambrian stratigraphy across Nares Strait: correlation between Inglefield Land and Bache Peninsula; *in* Nares Strait and the Drift of Greenland: a Conflict in Plate Tectonics, (ed.) P.R. Dawes and J.W. Kerr; Meddelesser om Grønland, Geoscience 8, p. 105-115.

Ricketts, B.
1994: Basin Analysis, Eureka Sound Group, Axel Heiberg and Ellesmere islands, Canadian Arctic Archipelago; Geological Survey of Canada, Memoir 439, 119 p.

Singh, C.
1983: Cenomanian microfloras of the Peace River area, northwestern Alberta; Research Council of Alberta, Bulletin 44, 322 p.

Sweet, A.R. and McIntyre, D.J.
1988: Late Turonian marine and nonmarine palynomorphs from the Cardium Formation, north-central Alberta foothills, Canada; *in* Sequences, Stratigraphy, Sedimentology: Surface and Subsurface, (ed.) D.P. James and D.A. Leckie; Canadian Society of Petroleum Geologists, Memoir 15, p. 499-516.

Trettin, H.P.
1994: Pre-Carboniferous geology of the northern part of the Arctic Islands: Part 1, Hazen Fold Belt adjacent parts of central Ellesmere Fold Belt, Ellesmere Island; Geological Survey of Canada, Bulletin 430, 248 p.

Geological Survey of Canada Project 860006

New observations on the geology of eastern Ellesmere Island, Canadian Arctic, part II: Cambro-Ordovician stratigraphy of the Parrish Glacier region

T. de Freitas[1]
GSC Calgary, Calgary

de Freitas, T., 1998: New observations on the geology of eastern Ellesmere Island, Canadian Arctic, part II: Cambro-Ordovician stratigraphy of the Parrish Glacier region; in *Current Research 1998-E; Geological Survey of Canada, p. 31–40.*

Abstract: The type sections of the Copes Bay and Parrish Glacier formations, and bounding formations, at the snout of Parrish Glacier were examined as part of a larger regional Geological Survey of Canada mapping project. The Ella Bay and Kennedy Channel formations were the oldest units encountered. These units contain rock types already described, and no stratigraphic revision is necessary. However, the overlying, dominantly clastic units, assigned previously to the Ellesmere Group, are lithologically similar, and more appropriately assigned, to the Dallas Bugt Formation. The overlying Scoresby Bay Formation is a resistant dolostone and minor limestone succession containing trilobites of the *Bonnia–Olenellus* Zone. The overlying Parrish Glacier Formation is generally more recessive and contains Middle Cambrian trilobites, together with striking red-weathering mudrock and dolostone. The highest Cambrian unit, the Copes Bay Formation, is abandoned, because regionally mappable formations spanning this interval were described much earlier and so have priority.

Résumé : Les stratotypes des formations de Copes Bay et de Parrish Glacier et les formations limitrophes situés au front du glacier Parrish ont été étudiés dans le cadre d'un projet de cartographie régionale de plus grande envergure réalisée par la Commission géologique du Canada. Les unités les plus anciennes rencontrées sont les formations d'Ella Bay et de Kennedy Channel. Elles renferment des lithotypes qui ont déjà fait l'objet d'une description. Par conséquent, une mise à jour de la stratigraphie se révèle superflue. Toutefois, les unités essentiellement clastiques sus-jacentes, attribuées antérieurement au Groupe d'Ellesmere, ont une lithologie similaire et sont attribuées plus pertinemment à la Formation de Dallas Bugt. La Formation de Scoresby Bay sus-jacente est une succession de dolomie résistante et de quantités mineures de calcaire contenant des trilobites de la Zone à *Bonnia–Olenellus.* La Formation de Parrish Glacier sus-jacente est généralement plus récessive et renferme des trilobites du Cambrien moyen, ainsi que des mudrocks et des dolomies de couleur d'altération rouge frappant. L'unité supérieure du Cambrien, la Formation de Copes Bay, est abandonnée, parce que les formations susceptibles d'être cartographiées à l'échelle régionale qui couvrent cet intervalle ont déjà été décrites et sont donc prioritaires.

---

[1] Imperial Oil Resources Limited, Research Centre, 3535 Research Road NW, Calgary, Alberta T2L 2K8

INTRODUCTION

Thorsteinsson (1963, p. 390–393) named the Parrish Glacier and Copes Bay formations more than 30 years ago, from exposures at the terminus of Parrish Glacier, east-central Ellesmere Island (Fig. 1). Kerr (1973a, b, c) later mapped the region currently under review by the Geological Survey of Canada (Fig. 1) and he recognized the Parrish Glacier, Copes Bay, and many other formations throughout the structurally complex and rugged, glaciated region (Fig. 2). In addition to these reconnaissance maps (Kerr, 1973a, b, c), Kerr (1967) published descriptions of the map units that have since formed the standard reference on the bedrock geology of eastern Ellesmere Island (Fig. 1). More recent publications include a study on Judge Daly Promontory by Trettin (1994). Trettin mapped part of this region, but he did not recognize the Parrish Glacier and Copes Bay formations. Long (1989a, b) examined the Ellesmere Group, Kennedy Channel, and Ella Bay formations near Parrish Glacier and regions farther north and west, but he did not examine any of the younger Cambrian to Silurian formations. T. de Freitas examined the Silurian and Upper Ordovician units as part of a doctoral thesis at the University of Ottawa (de Freitas, 1991). This work was carried out in March through June, 1988, from a mobile camp using cross-country skis, nansen sledge, and a snow machine.

Another notable study in an adjacent area is that by Christie (1967), who examined exposures on the rugged coasts of Bache Peninsula, using dog teams handled by residents of Grise Fiord, a hamlet on southern Ellesmere Island. He made excellent observations of the stratigraphy and structure of that region. Frisch (1988) much later examined the Precambrian bedrock geology of Bache Peninsula and regions south and prepared several 1:250 000 scale map sheets.

As part of a Geological Survey of Canada effort to map the region lying between 79°N and northern Judge Daly Promontory, and east of the drainage divide (Fig. 1), the type sections of the Copes Bay and Parrish Glacier formations were visited

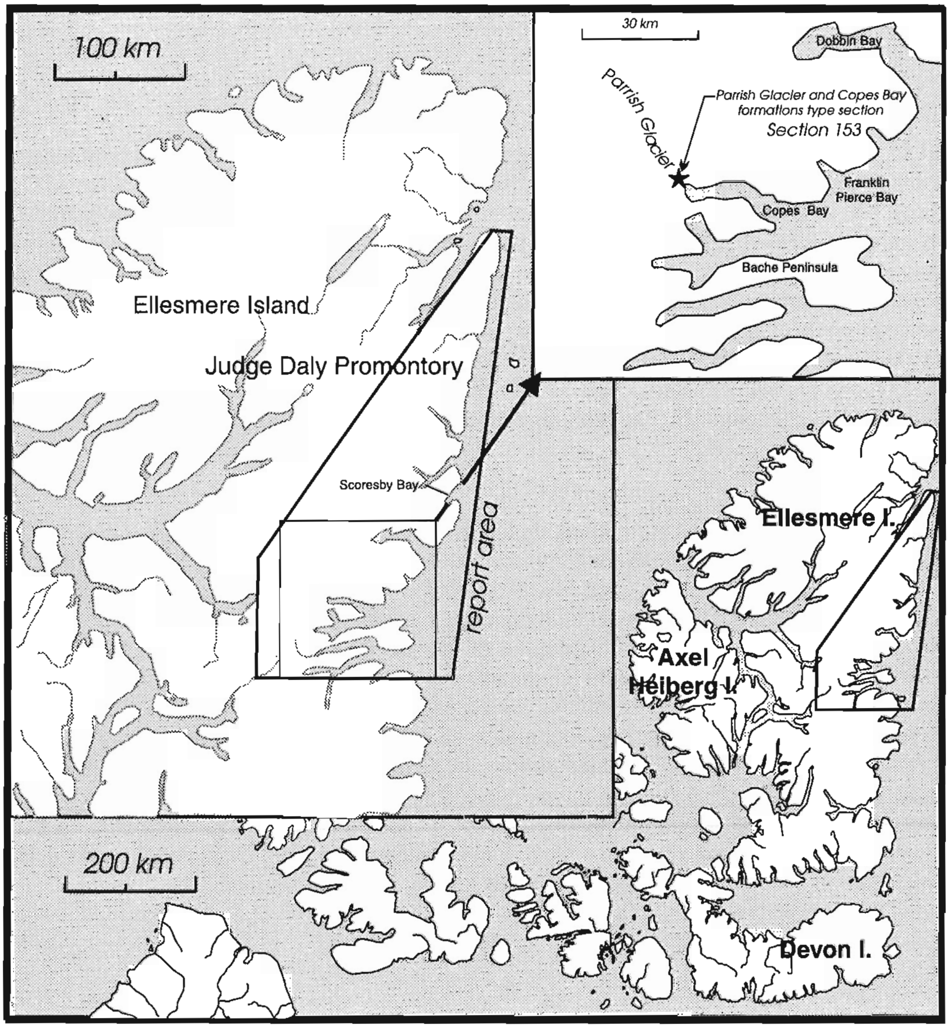

Figure 1. *Location of the Parrish Glacier section in the Canadian Arctic Islands. Polygon in upper left inset represents map area currently under review by the Geological Survey of Canada.*

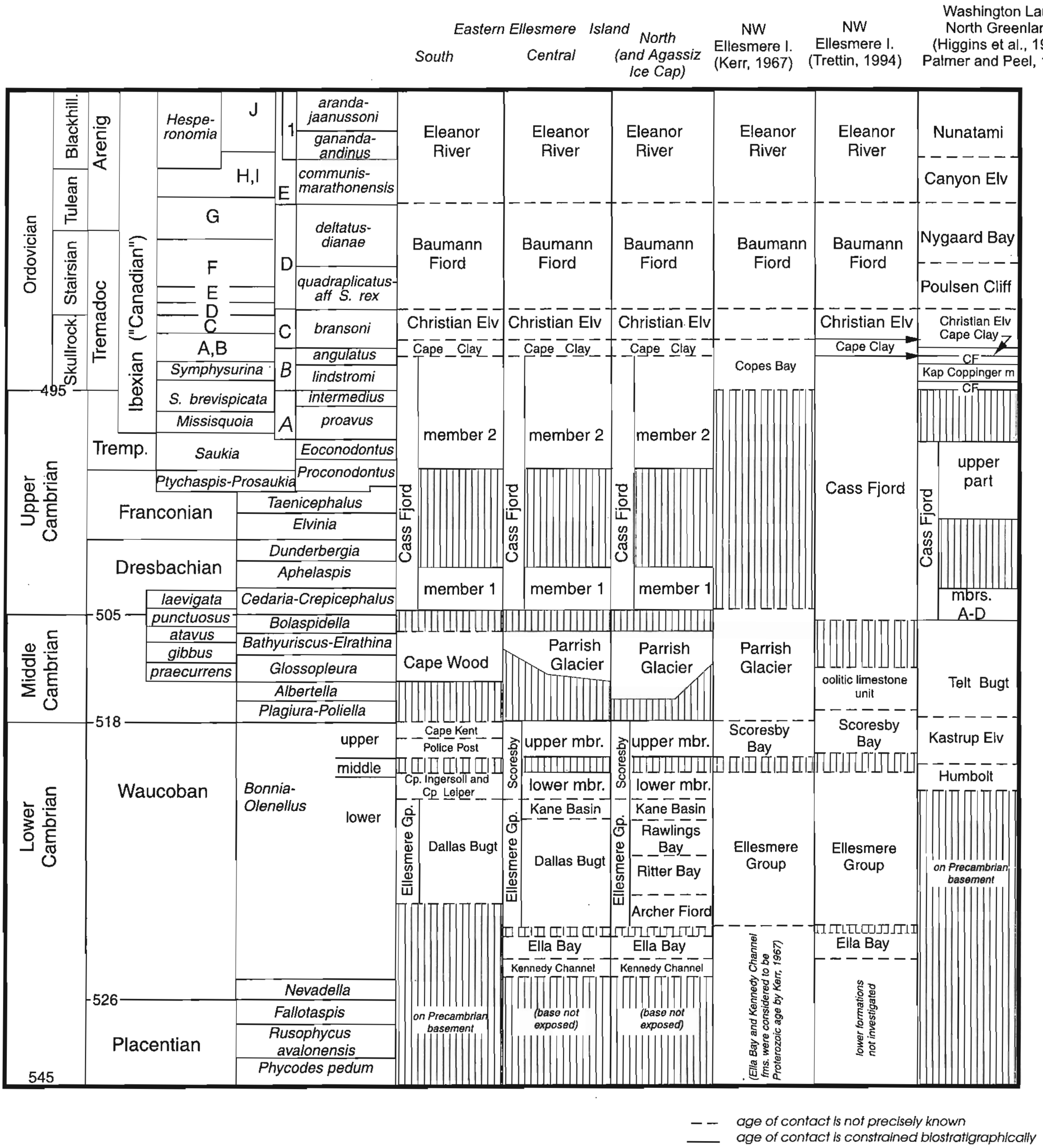

Figure 2. Correlation chart of some Ordovician and Cambrian strata, Canadian Arctic and North Greenland. From de Freitas and Fritz (1995); de Freitas et al. (1997). On west-central Ellesmere Island, the base of the Cape Clay Formation is disconformable. The same contact on Bache Peninsula is very sharp: it may be disconformable as well, but there is yet no supporting physical or paleontological evidence.

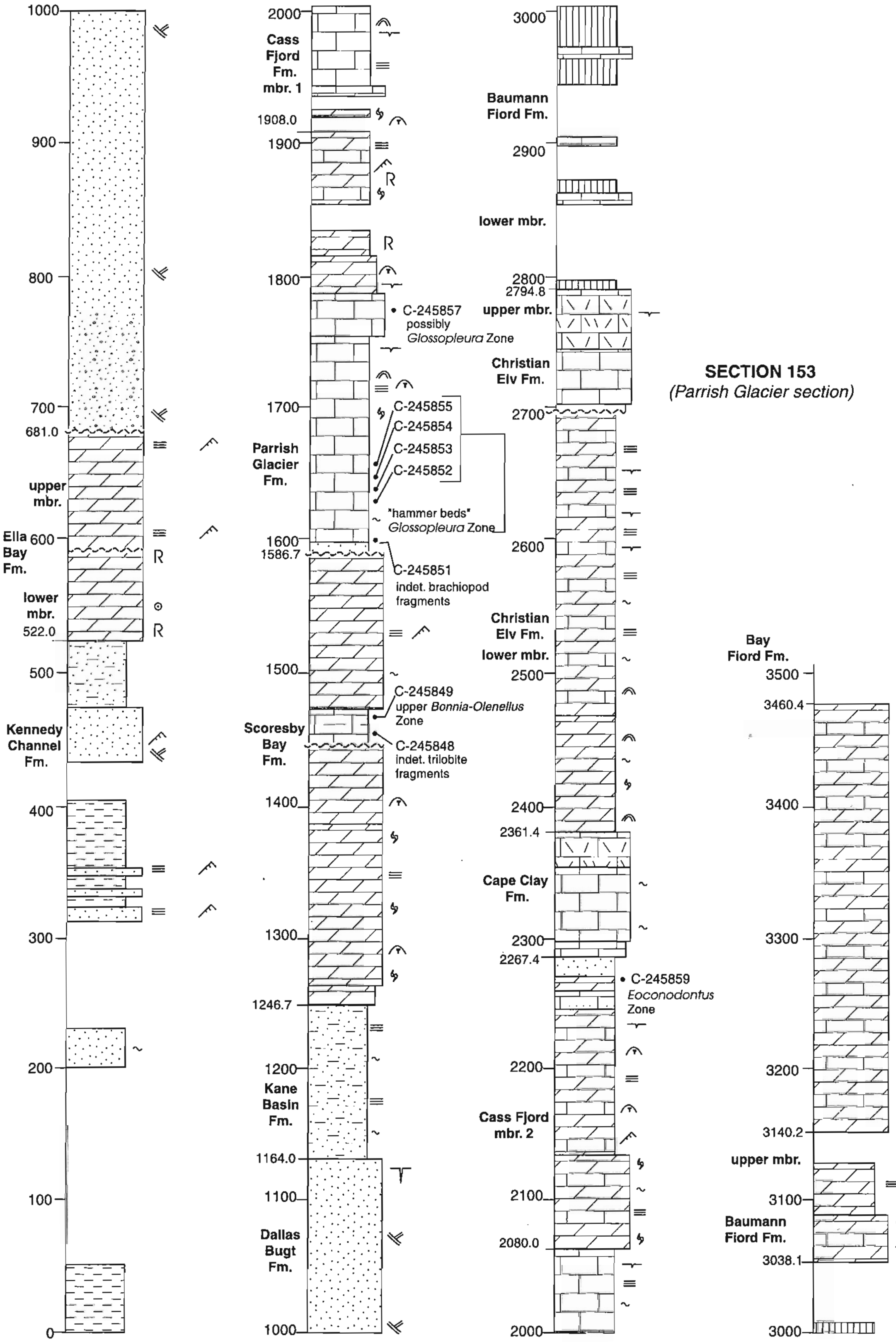

__Figure 3.__ Graphic section logs of the type section of the Parrish Glacier and the abandoned Copes Bay Formation. 'Hammer beds' in the basal part of the Parrish Glacier Formation are the same beds that yielded Middle Cambrian trilobites and are reported by Thorsteinsson (1963). The term 'hammer beds' refers to the hammer broken and left there by Bill Kerr 43 years ago, found during the 1995 fieldwork.

over a period of about 12 days, during early June of 1995. Two campsites were established next to Parrish Glacier. Data from the northern camp are reported in de Freitas and Nowlan (in press); data from the southern camp, at the snout of Parrish Glacier, are reported in this paper.

KENNEDY CHANNEL FORMATION

The Kennedy Channel Formation was named by Kerr (1967) for a sequence of mudrock and sandstone. This is the oldest known unit in the Franklinian succession, but its base is not exposed in the Canadian Arctic or in North Greenland, where the correlative of the Kennedy Channel Formation is known as the Skagen Group (Higgins et al., 1991). More than 522 m of this formation are exposed near Parrish Glacier (Fig. 3). It is the lowest unit in the hanging wall panel of the Parrish Glacier Thrust. The lowest unit in the formation is a dark grey to black, micaceous, sulphurous mudrock with rare *Zoophycus* and ?*Chrondrites* traces. The mudrock is interbedded with fine-grained, well-sorted, tabular and trough cross-stratified sandstone. Cross-stratification contains reactivation surfaces and bundled forsets. Rare quartzite granules are concentrated along the forsets. Some beds are graded with Bouma A-B sequences.

Kerr (1967) considered it to be Precambrian. Trilobites collected later by Long (1989a) indicated a late Early Cambrian age for the formation. More recently, more complete fossils of the *Bonnia-Olenellus* Zone have been recovered from the upper part of this formation on central Judge Daly Promontory (B. Pratt, pers. comm., 1997).

The sedimentological evidence indicates that the Kennedy Channel Formation was deposited on a storm-influenced medial to outer shelf. Cross-stratified sandstone was possibly deposited under much shallower conditions, perhaps in tidally influenced, nearshore settings.

ELLA BAY FORMATION

Kerr (1967) applied the name Ella Bay Formation to a thick sequence of dolostone, breccia, mudrock, and limestone on central Judge Daly Promontory. At Parrish Glacier (Fig. 3, 4), the Ella Bay Formation is 159 m thick and divisible into two informal members. The lower member is about 80 m thick and consists of pale red-weathering, laminated dolostone, featuring abundant wavy, parallel laminae, polygonal mudcracks, laminar and wavy microbialites, and abundant intraclast conglomerates. The lowest 10.0 m of this unit consist of ooid grainstone. The lower member is overlain disconformably

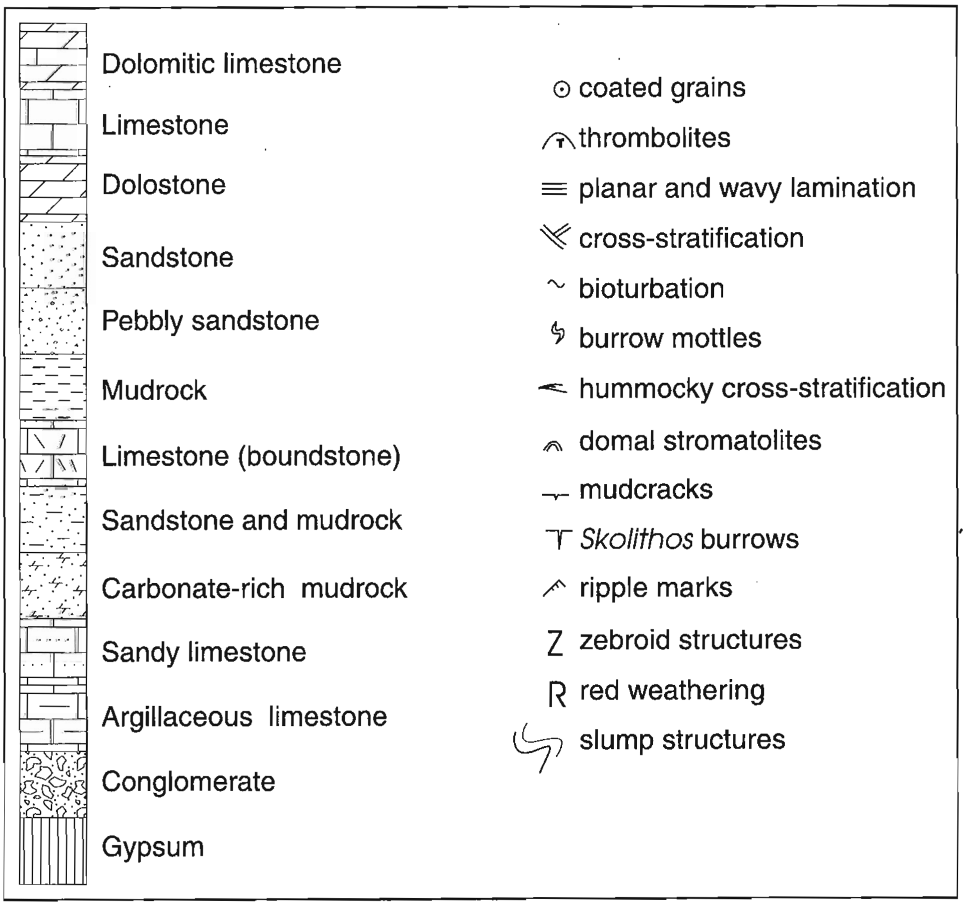

Figure 3. *Legend*

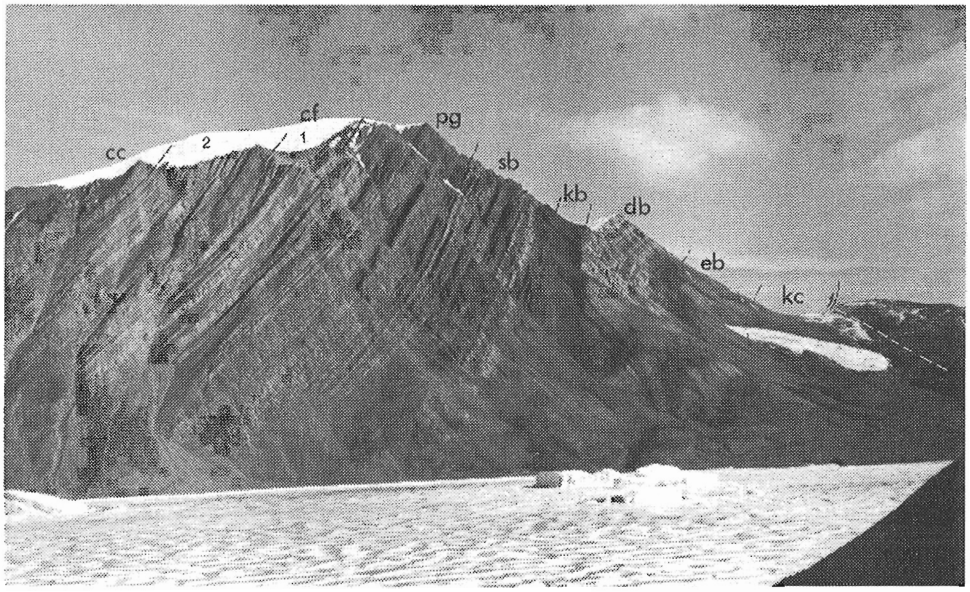

Figure 4. *Cliff exposures containing the Kennedy Channel (kc), Ella Bay (eb), Dallas Bugt (db), Kane Basin (kb), Scoresby Bay (sb), Parrish Glacier (pg), Cass Fjord (lower and upper members, cf1, cf2), and Cape Clay (cc) formations. This cliff is about 1.5 km east of the measured section shown in Figure 2. The Kennedy Channel Formations rests on the Parrish Glacier Thrust. Height of cliff is about 800 m.*

by pale yellowish-orange-weathering, thick-bedded, massive, medium crystalline dolostone. The lower contact with the Kennedy Channel Formation is covered.

These rock characteristics suggest that the Ella Bay Formation was deposited under shallow and intertidal, depositional settings. The lower ooid grainstone indicates agitated, shallow-marine conditions.

DALLAS BUGT FORMATION

The term, Dallas Bugt Formation, was first used by Peel et al. (1982) for a series of sandstone and conglomerate exposed on Bache Peninsula and adjacent North Greenland. However, these beds were described much earlier by Christie (1967), who had assigned them to the Sverdrup Member of the Precambrian Rensselaer Bay Formation. At Parrish Glacier, the Dallas Bugt Formation was investigated by Long (1989b), who assigned these beds to the Ellesmere Group. He based this assignment on a regional correlation of the type Ellesmere Group beds, exposed on north-central Judge Daly Promontory. However, the Ellesmere Group is more than 3 km thick locally, and contains thick, interbedded mudrock and sandstone units that in some cases form regionally mappable formations (e.g. Rawlings Bay and Ritter Bay formations). It contrasts with the purple-, red-, and white-weathering sandstone and minor conglomerates exposed near Parrish Glacier on nearby Bache Peninsula. Lack of the mudstone facies and a lithological similarity to the Dallas Bugt Formation on Bache Peninsula indicates assignment to the Dallas Bugt, instead of to the combined Rawlings Bay–Archer Fiord formations, as suggested earlier by Long (1989b).

The Dallas Bugt Formation is exposed throughout a large area of southern and central Ellesmere Island (Thompson and Pratt, 1995). The name is also applied to the lowest Paleozoic sandstone on adjacent North Greenland and to strata on Bache Peninsula, as stated above. The formation is mappable between Parrish Glacier and Scoresby Bay; however, to the north of Scoresby Bay and to the west of Dobbin Bay, mudrock interbeds form a significant, mappable part of the clastic sequence, and the nomenclature of Long (1989b) and Kerr (1967) can be applied to these beds.

At Parrish Glacier, about 483 m of this formation is exposed (Fig. 3, 4). The lower 100 m is a coarse- to medium-grained sandstone with common conglomerate interbeds, containing well rounded, granule- and pebble-sized, quartzite lithoclasts. In one of these beds a granite pebble was noted. Conglomerate beds are red- and purple-weathering, while finer grained siliciclastics, in the upper part of the formation, tend to weather shades of orange and grey. It should be noted, however, that these colours and conglomerate interbeds occur at stratigraphically different levels in different areas, and the abundance of conglomerate-bearing intervals lessens to the north and west. Distinguishing features of the formation are common trough- and tabular cross-stratification and *Skolithos* burrows. The latter trace fossil occurs exclusively in the upper part of the formation.

Conglomerate beds in the lower and middle parts of the formation were likely deposited in a high-energy foreshore setting and in braided fluvial or fluvial distributary settings. Upper *Skolithos*-bearing beds were likely deposited in a high-energy shelf setting.

KANE BASIN FORMATION

The Kane Basin Formation was originally named by Kerr (1967) from a type section in Judge Daly Promontory. The unit is a regional marker and everywhere forms a recessive dark-weathering and readily mappable unit (Fig. 3). It is absent on Bache Peninsula. On central Ellesmere Island, this unit is a probable correlative of the upper, green-weathering argillaceous sandstone, as described by Thompson and Pratt (1995). The formation is 82.7 m thick and consists of interbedded micaceous mudrock, siltstone, and sandstone, containing wave ripples, current ripples, and tempestites. Some beds contain well preserved *Zoophycus*. The lower contact with the underlying Dallas Bugt Formation is sharp and conformable. The Formation was probably deposited on a distal, storm-influenced shelf setting.

SCORESBY BAY FORMATION

The Scoresby Bay Formation was named by Kerr (1967) from a type section approximately 10 km north of Scoresby Bay. Near Parrish Glacier, the formation is 340 m thick and consists of resistant, coarsely crystalline, grey-, brown-, and orange-weathering dolostone. From a distance, the formation forms rugged cliffs and is significantly more resistant than the underlying Kane Basin Formation or overlying Parrish Glacier Formation. The formation is characterized by several bright yellow- and orange-weathering dolostone beds. These beds are a distinguishing feature throughout most of the report area. At Parrish Glacier and elsewhere, these beds contain abundant zebroid fabrics and saddle dolomite, which, in some areas, are associated with massive, colliform pyrite. A minor disconformity occurs in the middle part of the formation, and a thin, trilobitic limestone unit occurs above this disconformity (Fig. 3). Fossils from this lower interval are assigned to the *Bonnia–Olenellus* Zone. The hiatus associated with the medial Scoresby Bay unconformity is minor, because upper Kane Basin Formation beds have also yielded *Bonnia–Olenellus* Zone trilobites (de Freitas, 1998a). The lower contact with the Kane Basin Formation is gradational.

The Scoresby Bay Formation was deposited in restricted- and, rarely, open-marine shelf.

PARRISH GLACIER FORMATION

Thorsteinsson (1963) named the Parrish Glacier Formation for a 265 m thick succession of alternating limestone, shale, and minor argillaceous siltstone and argillaceous limestone from a type section on the west side of Copes Bay (Fig. 1, 3). Kerr (1967) later mapped the unit through most of central, southern, and northeastern Ellesmere Island. He indicated that a distinguishing feature of the formation through most of this large area was its recessive nature, abundance of limestone, and colour banding; the latter feature, in particular, includes conspicuous, 2–20 m thick, red-weathering, argillaceous dolostone and mudrock intervals.

The Parrish Glacier has been revised in many areas since Kerr's reconnaissance mapping. Beds in an unnamed structural culmination east of Trold Fiord were assigned to the Parrish Glacier Formation, although they lacked the distinctive red-weathering beds as seen in the type section. They have since yielded Late Cambrian trilobites and are assigned to the Cass Fjord Formation (de Freitas and Fritz, 1995). Other recent work has shown that the top of the Parrish Glacier Formation is correlated with an interval within the Cass Fjord Formation (Mayr, 1978; Thorsteinsson and Mayr, 1987, p. 39).

Confusion about the age and assignment of the Parrish Glacier Formation is perhaps due to two things. First, the age of the Parrish Glacier Formation has been established in only one area, the type section, but the contact with the overlying Copes Bay Formation and correlation to well known Cambrian stratigraphy in central and southern Ellesmere Island were not firmly established during Kerr's (1967) field investigations. Secondly, the most conspicuous lithological feature of the formation, red-weathering carbonates and siliciclastics, have a large age range and are characteristic of both the Parrish Glacier and Cass Fjord formations.

The Parrish Glacier is the same age as the Cape Wood Formation (Christie, 1967; Thompson and Pratt, 1995), which is well exposed on Bache Peninsula. Like the Parrish Glacier Formation, this unit contains red-weathering siliciclastics and carbonate. However, the Cape Wood Formation is much thinner and contains a greater proportion of dolostone and sandstone than the Parrish Glacier Formation, which contains thick limestone intervals and only a few sandstone and dolostone interbeds. Moreover, in central and northern parts of the report area, north of Dobbin Bay, the Parrish Glacier Formation contains distinct mappable members and rock types very unlike those of the type Cape Wood Formation (de Freitas, 1998b).

The base of the Parrish Glacier Formation is disconformable. The lower 10 cm of the formation is a sandy dolostone, which is overlain by a thick succession of limestone and lesser dolostone, sandstone, siltstone, and mudrock. The limestone is medium to thick bedded, locally burrow mottled, finely crystalline, and contains intraclast conglomerate, ripple marks, polygonal mudcracks, symmetrical ripple marks, low-angle cross-stratification, planar- and wavy-parallel laminae, and molar tooth structures. Sandstone is rare, accounting for less than 3 per cent of the measured section. Dolostone and mudrock occur primarily in the middle and upper parts of the formation. The dolostone is silty, or sandy and yellow- and orange-weathering. Interbedded mudrock is dolomitic, pale red weathering, and locally sandy, and it contains molar tooth structures, polygonal mudcracks, and ripple marks. Together these sedimentary structures indicate shallow restricted-marine and intertidal conditions. Redbeds indicate sedimentation in a continental setting, perhaps in an alluvial floodplain.

Several trilobite samples were collected from the Parrish Glacier Formation. The cluster shown at about 1650 m above the base of the section (Fig. 2, 3, C-245852–245855) were the same beds that yielded *Clavaspidella* more than 40 years ago (Thorsteinsson, 1963). While collecting fossils from these beds, Ray Thorsteinsson's assistant (W. Kerr) broke his geological hammer. The hammer handle was discovered in 1995, in the course of this fieldwork, and the beds were again collected. Bill Fritz identified the samples and indicated a Middle Cambrian age or *Glossopleura* Zone.

CASS FJORD FORMATION

Beds here assigned to the Cass Fjord Formation were originally included in the Copes Bay Formation by Thorsteinsson (1963) and Kerr (1967, 1973a, b, c). However regional mapping in many areas of the Arctic has shown that there are three formations within the Copes Bay Formation (Cass Fiord, Cape Clay, and Christian Elv formations). The Cass Fjord and Cape Clay formations were named previously by Poulsen (1927). Because two of these names have priority and because the formations can be mapped through most of the Arctic Islands, the Copes Bay Formation is abandoned. The ages of the two mappable members of the Cass Fjord Formation are described in de Freitas and Fritz (1995).

The Cass Fjord Formation is 359.4 m thick. On aerial photographs, this contact occurs below a less resistant sequence of rock that weathers to lighter shades of grey (on monochrome photographs) than the underlying Parrish Glacier Formation. In outcrop, the base of the Cass Fjord Formation contains a thin, resistant, rarely thrombolitic limestone, which may or may not be recognizable on aerial photographs. The basal contact in many cases is subtle, and of all the formation contacts in east-central Ellesmere Island, this contact is the most difficult to recognize. In felsenmeer-covered uplands, the contact usually must be checked on the ground.

As in west-central Ellesmere Island (de Freitas and Fritz, 1995), two unconformity bounded, mappable members are recognized. Trilobites were not recovered from the lower reaches of Parrish Glacier, but elsewhere, these fossils indicate a early Late Cambrian and late Late Cambrian age for members 1 and 2, respectively.

Member 1 of the Cass Fjord Formation is 172 m thick and consists of a basal, thin, resistant, thrombolitic limestone, overlain by uniform succession of interbedded limestone and lesser dolostone. The lithologies are very similar to those of member 2. The strata contain sedimentary structures indicative of restricted-marine or intertidal conditions, including polygonal mudcracks, molar tooth structures, intraclast conglomerates, and planar-parallel lamination. The lower contact is not exposed in the measured section, but elsewhere, it is sharp but apparently unconformable (de Freitas and Fritz, 1995).

Member 2 of the Cass Fjord Formation (187.4 m thick) contains a lower, resistant succession of interbedded brown- and grey-weathering dolomitic limestone and less common, light grey, recessive dolostone. The upper part of the member is more recessive and lighter grey weathering, reflecting an increase in the proportion of light grey dolostone. The member contains abundant sedimentary structures indicative of restricted- or intertidal-marine conditions: these include mudcracks, planar-parallel lamination, intraclast conglomerates, laterally linked hemispherical stromatolites, and molar tooth structures.

A noteworthy development in the upper Cass Fjord Formation is trough, tabular and herringbone cross-stratified sandstone, which is recognized in many parts of the Canadian Arctic Islands and North Greenland. In the latter region, these sandstones have been assigned to the Kap Coppinger Member. They are significant, because they represent the first stratigraphic-sedimentological link with tectonism on eastern North Greenland that culminated in Caledonian orogenesis in Silurian and Devonian time. These sandstones are recognized in most sections of the Cass Fjord Formation, but are too thin to show at the present map scale.

CAPE CLAY FORMATION

This cliff-forming, 94 m thick unit consists of light grey- and brown-weathering, mottled, dolomitic lime mudstone. It was first identified by Koch (*in* Poulsen, 1927). The upper part, as on nearby Bache Peninsula, consists of thrombolite boundstone. Microbialites are of the "Hawker Bay" type (de Freitas and Mayr, 1995). These microbialites are cerebroform, about 1 to 3 m in maximum diameter, and contain a clotted interior and laminated, stromatolitic exterior. These mounds occur regionally in the Cape Clay Formation, and also in the correlative Johansen Land Formation on North Greenland. The lower contact with the Cass Fjord Formation is gradational. Elsewhere, the contact is disconformable or there is a disconformity metres below the lower contact (Bryant and Smith, 1990; de Freitas and Fritz, 1995).

CHRISTIAN ELV FORMATION

The Christian Elv Formation was first described by Henriksen and Peel (1976), from North Greenland. In the report area, two members are recognized: a lower member, consisting of interbedded limestone and dolostone, and an upper, more resistant member, consisting of thick-bedded limestone. The lower member contains interbedded limestone, dolomitic limestone, and dolostone with common planar-parallel laminae, bioturbation structures, and burrow mottles. Less common sedimentary structures include polygonal mudcracks, wavy and domal stromatolites, and brown chert nodules. Rare columnar stromatolite and thrombolite mounds, sandstone, and 1.0–3.0 m thick gypsum beds also occur. The upper member is about 120 m thick and at least half this member consists of thrombolite mounds. The basal contact of the Christian Elv Formation is gradational and drawn below the first, significant, light grey-weathering unit above the more resistant Cape Clay Formation.

The lower member was deposited under restricted-marine and locally supratidal conditions, whereas the upper part was deposited under open-marine conditions, suitable for benthic microbe growth. A sharp, possibly disconformable contact exists between the lower and upper members.

BAUMANN FIORD FORMATION

The Baumann Fiord Formation is poorly exposed along Parrish Glacier. Three informal members are recognized, but these are too thin to show at the present map scale. The lower member is about 243.3 m thick and is generally covered. Exposures consist mostly of gypsum, interbedded with gypsiferous, thin-bedded limestone, and rare thrombolite mounds. Some of these mounds are up to 3.0 m thick and are rarely associated with intraclast conglomerates. The middle member is about 42 m thick and cliff forming. It consists of burrow mottled, locally laminated dolomitic limestone with rare fossil fragments. The upper member is 60.1 m thick and consists of gypsiferous dolomitic limestone and dolostone with abundant planar-parallel laminae, rare intraclast conglomerates, and polygonal mudcracks.

The basal contact of the formation is well exposed and appears to be gradational: carbonates of the upper Christian Elv Formation appear to be interbedded with gypsum, and are replaced upsection by Baumann Fiord Formation gypsum. Bedding plane slip attributed to folding has caused strong deformation of some of the lower, ductile gypsum beds. The Baumann Fiord Formation was deposited on an open- and restricted-marine shelf. Member lithology reflects relative sea-level change. The presence of gypsiferous carbonates and gypsum indicate restricted-marine and supratidal settings. More open-marine conditions are inferred for deposition of the cliff forming middle member.

ELEANOR RIVER FORMATION

The Eleanor River Formation is a cliff-forming, 320.2 m thick sequence of dolomitic limestone. The lower 10–20 m of the formation contains interbedded dolomitic limestone and dolostone with planar-parallel lamination and rare burrow mottles. Black chert nodules occur rarely in the lower part of the formation, which is overlain by a thick succession of burrow-mottled dolomitic limestone. In about the middle of the formation, several, metre-scale shallowing-upward sequences occur. These contain a lower burrow mottled limestone and an upper dolomitic limestone with planar-parallel laminae and rare polygonal mudcracks. The lower contact with the Baumann Fiord Formation is not exposed at Parrish Glacier.

The Eleanor River Formation was deposited in an open-marine, shallow-shelf setting. Intertidal conditions occurred periodically as is evident by mudcrack-bearing dolomitic limestone intervals.

CONCLUSIONS AND RECOMMENDATIONS

The Parrish Glacier Formation is a regionally mappable unit in eastern Ellesmere Island. It is recognized by a characteristic red banding associated with light yellow- and grey-weathering dolostone and limestone. The formation has yielded fossils that corroborate the Middle Cambrian age established much earlier by Thorsteinsson (1963). This formation is overlain by the Cass Fjord, Cape Clay, and Christian Elv formations. Based on Kerr's original air photo sketches and on the original descriptions of the formations by Thorsteinsson (1963), it is recommended that the Copes Bay Formation be abandoned and replaced by names coined many years before and mapped in most of central and southern Ellesmere Island (the Cass Fjord and Cape Clay formations). The sandstone beds beneath these were assigned previously to the Ellesmere Group, but these beds more closely resemble the Dallas Bugt Formation of Bache Peninsula and are thus assigned to this formation.

Future fieldwork should focus on obtaining fossils from the Ella Bay and Kennedy Channel formations. The Lower Cambrian trilobite biostratigraphy has evolved recently and the *Bonnia–Olenellus* Zone is subdivided into several zones. These may be useful for better correlation of the Kennedy Channel and Ella Bay formations.

ACKNOWLEDGMENTS

Bill Fritz provided the much needed biostratigraphic information, which forms a crucial tool for regional correlation. Godfrey Nowlan identified conodonts from the top of the Cass Fjord Formation.

REFERENCES

Bryant, I.D. and Smith, M.P.
1990: A composite tectonic-eustatic origin for shelf sandstones at the Cambrian-Ordovician boundary in North Greenland; Journal of the Geological Society of London, v. 147, p. 795-809.

Christie, R.L.
1967: Bache Peninsula, Ellesmere Island, Arctic Archipelago; Geological Survey of Canada, Memoir 347, 63 p.

de Freitas, T.
1991: Stratigraphy, mud build-ups, and carbonate platform development of the Upper Ordovician to Lower Devonian sequence, Ellesmere, Hans, and Devon islands, Arctic Canada; Ph.D. thesis, University of Ottawa, Ottawa, Ontario, 431p.
1998a: New observations on the geology of eastern Ellesmere Island, Canadian Arctic, part III: Cambro-Ordovician stratigraphy of the Dobbin Bay, Scoresby Bay, and Franklin Pierce Bay areas; *in* Current Research 1998-E; Geological Survey of Canada.
1998b: New observations on the geology of eastern Ellesmere Island, Canadian Arctic, part IV: Cambro-Ordovician stratigraphy of the Rawlings Bay area and nunataks of the Agassiz Ice Cap; *in* Current Research 1998-E; Geological Survey of Canada.

de Freitas, T. and Fritz, W.H.
1995: Age and stratigraphy of the Cass Fjord Formation, Arctic Canada; *in* Current Research, 1995-E, Geological Survey of Canada, p. 97-104.

de Freitas, T. and Mayr, U.
1995: Kilometre-scale microbial buildups in a rimmed carbonate platform, arctic Canada: new insights on Lower Ordovician reef facies; Bulletin of Canadian Petroleum Geology, v. 43, p. 407-432.

de Freitas, T. and Nowlan, G.S.
in press: A new, major Silurian reef tract and overview of regional Silurian reef development, Canadian Arctic and North Greenland; Bulletin of Canadian Petroleum Geology.

de Freitas, T., Harrison, J.C., and Mayr, U.
1997: Mineral showings and sequence stratigraphic correlation charts of the Canadian Arctic Islands and parts of North Greenland; Geological Survey of Canada, Open File 3410, 3 charts.

Frisch, T.
1988: Reconnaissance geology of the Precambrian Shield of Ellesmere, Devon, and Coburg islands, Canadian Arctic Archipelago; Geological Survey of Canada, Memoir 409, 102 p.

Henricksen, N. and Peel, J.S.
1976: Cambrian-Early Ordovician stratigraphy in south-western Washington Land, western Greenland; Grønlands Geologiske Undersølgelse Rapport 80, p. 17-23.

Higgins, A.K., Ineson, J.R., Peel, J.S., Surlyk, F., and Sønderholm, M.
1991: Lower Paleozoic Franklinian Basin of North Greenland; Grønlands Geologiske Undersøgelse, Bulletin 160, p. 71-139.

Kerr, J.W.
1967: Stratigraphy of central and eastern Ellesmere Island; Geological Survey of Canada, Paper 67-27, 63 p.
1973a: Geology, Kennedy Channel and Lady Franklin Bay, District of Franklin; Geological Survey of Canada, Map 1359A (scale 1:25,000).
1973b: Geology, Sawyer Bay, District of Franklin; Geological Survey of Canada, Map 1357A, scale 1:25 000.
1973c: Geology, Dobbin Bay, District of Franklin; Geological Survey of Canada, Map 1358A, scale 1:25 000.

Long, D.G.F.
1989a: Kennedy Channel Formation: key to the early history of the Franklinian continental margin, central eastern Ellesmere Island, Arctic Canada; Canadian Journal of Earth Sciences, v. 26, p. 1147-1159.
1989b: Ella Bay Formation: Early Cambrian shelf differentiation in the Franklinian basin, central and eastern Ellesmere Island, Arctic Canada; Canadian Journal of Earth Sciences, v. 26, p. 2621-2635.

Mayr, U.
1978: Stratigraphy and correlation of lower Paleozoic formations, subsurface of Cornwallis, Devon, Somerset, and Russel islands, Canadian Arctic Archipelago; Geological Survey of Canada, Bulletin 276, 55 p.

Palmer, A. and Peel, J.S.
1981: Dresbachian trilobites and stratigraphy of the Cass Fjord Formation, western North Greenland; Grønlands Geologiske Undersøgelse, Bulletin 141, 46 p.

Peel, J.S., Dawes, P.R., Collinson, J.D., and Christie, R.L.
1982: Proterozoic-basal Cambrian stratigraphy across Nares Strait: correlation between Inglefield Land and Bache Peninsula; *in* Nares Strait and the drift of Greenland: a conflict in plate tectonics, (ed.) P.R. Dawes and J.W. Kerr; Meddelesser om Grønland, Geoscience 8, p. 105-115.

Poulsen, C.
1927: The Cambrian, Ozarkian and Canadian faunas of northwest Greenland; Meddelelser om Grønland, Bd. 70, no. 2.

Thomspon, C. and Pratt, B.R.
1995: Preliminary stratigraphy of Lower and Middle Cambrian rocks, east-central Ellesmere Island, Canadian Arctic Islands; *in* Current Research, 1995-E, Geological Survey of Canada, p. 165-168.

Thorsteinsson, R.
1963: Copes Bay; *in* Geology of North-central Part of the Arctic Archipelago, Northwest Territories; Y.O. Fortier et al.; Geological Survey of Canada, Memoir 320, p. 386-395.

Thorsteinsson, R. and Mayr, U.
1987: The sedimentary rocks of Devon Island, Canadian Arctic Archipelago; Geological Survey of Canada, Memoir 411, 182 p.

Trettin, H.P.
1994: Pre-Carboniferous geology of the northern part of the Arctic Islands: Part 1, Hazen Fold Belt adjacent parts of central Ellesmere Fold Belt, Ellesmere Island; Geological Survey of Canada, Bulletin 430, 248 p.

Geological Survey of Canada Project 860006

New observations on the geology of eastern Ellesmere Island, Canadian Arctic, part III: Cambro-Ordovician stratigraphy of the Dobbin Bay, Scoresby Bay, and Franklin Pierce Bay areas

T. de Freitas[1]
GSC Calgary, Calgary

de Freitas, T., 1998: New observations on the geology of eastern Ellesmere Island, Canadian Arctic, part III: Cambro-Ordovician stratigraphy of the Dobbin Bay, Scoresby Bay, and Franklin Pierce Bay areas; in *Current Research 1998-E; Geological Survey of Canada, p. 41–50.*

Abstract: Fieldwork in east-central Ellesmere Island has confirmed the regional extent of many lower Paleozoic formations, including the Kennedy Channel, Ella Bay, Dallas Bugt, Kane Basin, Scoresby Bay, Parrish Glacier, and Cass Fjord formations. Two regionally extensive, unconformity-bounded members are recognized within the Scoresby Bay Formation. The lower member is within the lower *Bonnia–Olenellus* Zone and the upper member is within the upper part of the same zone. Other newly documented age data include the occurrence of *Ehmaniella* Zone trilobites in the basal part of the Parrish Glacier Formation, indicating an age slightly younger than that in the type section. The base of the Cass Fjord Formation is within the *Cedaria–Crepicephalus* Zone, which is the same age as that established from east-central Ellesmere Island. The base of member two of the Cass Fjord Formation is slightly older than established elsewhere and rests within the *Taenicephalus* Zone.

Résumé : Les travaux effectués dans le centre est de l'île d'Ellesmere ont confirmé l'extension régionale de nombreuses formations du Paléozoïque inférieur, dont les formations de Kennedy Channel, d'Ella Bay, de Dallas Bugt, de Kane Basin, de Scoresby Bay, de Parrish Glacier et de Cass Fjord. Deux membres limités par une discordance, d'extension régionale, ont été identifiés dans la Formation de Scoresby Bay. Le membre inférieur se trouve dans la partie inférieure de la Zone à *Bonnia–Olenellus* et le membre supérieur, dans la partie supérieure de la même zone. D'autres données nouvellement documentées sur les âges comprennent la présence de trilobites de la Zone à *Ehmaniella* dans la partie basale de la Formation de Parrish Glacier, ce qui indique un âge légèrement plus récent que celui du stratotype. La base de la Formation de Cass Fjord est située dans la Zone à *Cedaria–Crepicephalus*, dont l'âge est équivalent à celui déterminé dans le centre est de l'île d'Ellesmere. La base du deuxième membre de la Formation de Cass Fjord, située dans la Zone à *Taenicephalus*, est légèrement plus ancienne que l'âge déterminé ailleurs.

---

[1] Imperial Oil Resources Limited, Research Centre, 3535 Research Road NW, Calgary, Alberta T2L 2K8

INTRODUCTION

This paper is the third in a series reviewing the new bedrock geological data collected from east-central Ellesmere Island. The first companion paper is a review of the structure and stratigraphy of the Franklin Pierce Bay region, and the second contains lithological and paleontological data on Cambro-Ordovician strata from the Parrish Glacier region. This paper contains similar information, but from a different region. Length restriction on papers in this volume necessitate publication of an abridged series of papers. Information on the regional geology and structure are available in de Freitas and Sweet (1998) and de Freitas (1998a, b) and only new information is presented here.

As part of a Geological Survey of Canada effort to map the region lying between 79°N and northern Judge Daly Promontory, and east of the drainage divide (Fig. 1), the three stratigraphic sections, including the type section of the Scoresby Bay Formation, were visited for about one month, during parts of June and July of 1996 and 1997. Several campsites were established in the region. These were supplied by a helicopter stationed in Eureka, some 1.5 h one-way flying time away. Many of the camp moves were accomplished by backpacking or, more rarely, on cross-country skis.

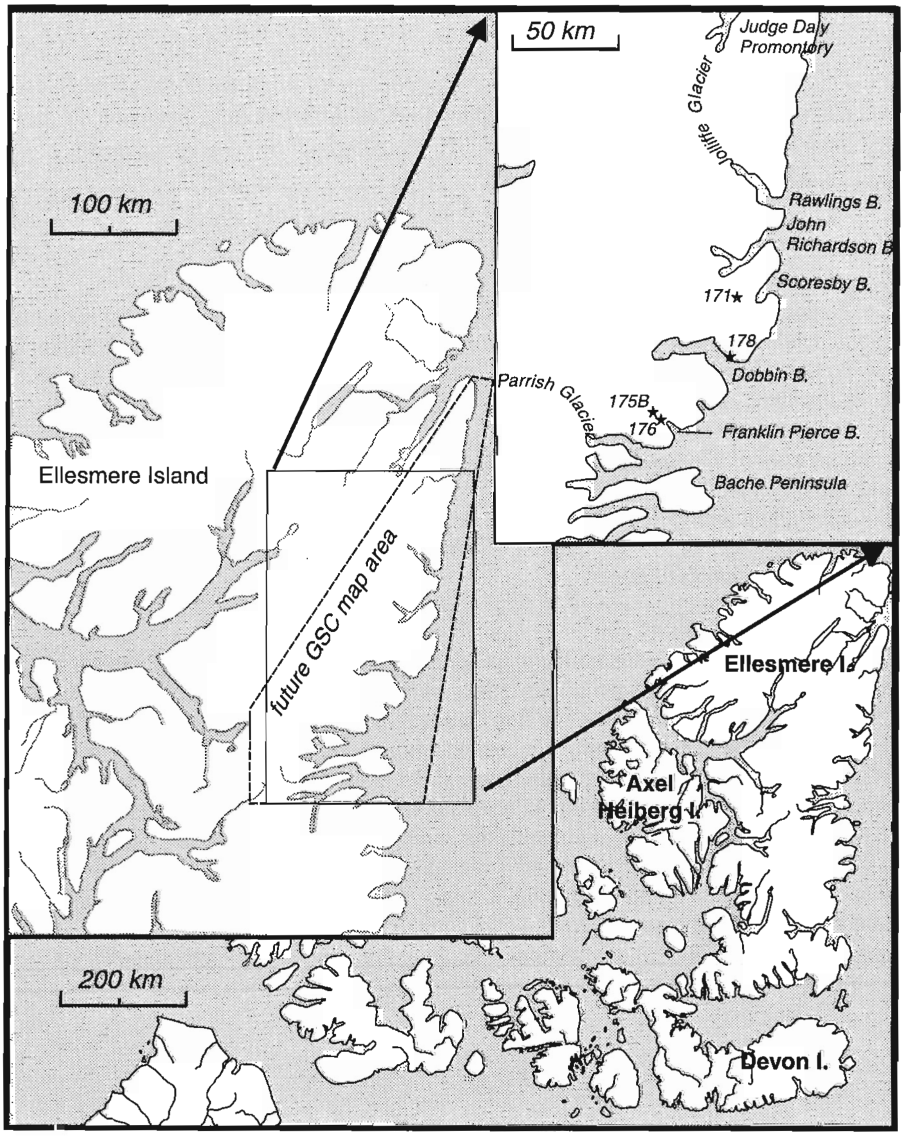

Figure 1. Location of study area in the Canadian Arctic Islands. Polygon in upper left map inset represents map area currently under review by the Geological Survey of Canada.

LITHOLOGY

The formations described below range from Lower Cambrian (Kennedy Channel Formation) to the Lower Ordovician Cape Clay Formation. Correlation of these formations is shown in Figure 2.

Kennedy Channel Formation

The upper 667 m of the Kennedy Channel Formation is exposed in the basal part of section 171 (Fig. 3). The formation at this locality is generally poorly exposed. It consists of limestone, sandstone, siltstone, and dolostone. These rock types weather to various shades of yellow and grey. The

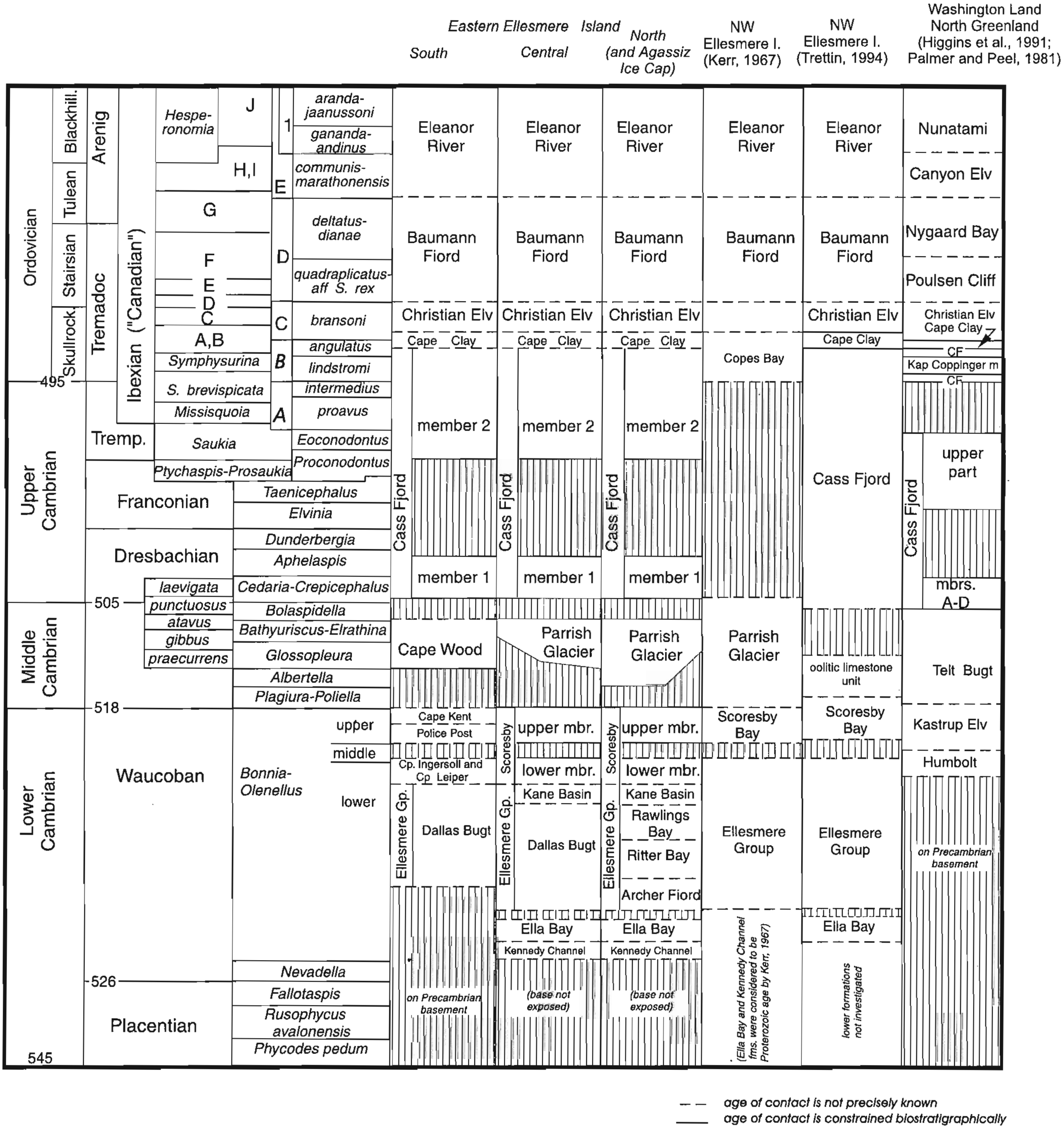

Figure 2. Correlation chart of some Ordovician and Cambrian strata, Canadian Arctic and North Greenland. The Ehmaniella Zone mentioned in the text and graphic section logs is approximately equivalent to the Bathyriscus–Elrathina *Zone.*

sandstone, located mostly in the basal part of the formation, is well sorted, fine- to medium-grained, yellowish grey, and contains ripple marks, wavy-parallel lamination, bioturbation structures, molar tooth structures, and rare, hummocky cross-stratification. Overlying carbonate beds (limestone, dolostone, and dolomitic limestone) weather light grey and yellowish grey and are typically silty or sandy. The carbonate strata are heavily bioturbated locally and contain laterally linked hemispherical stromatolites, planar-parallel lamination, and rare intraclast conglomerates. In places, the dolostone contains saddle dolomite and ankerite. These data indicate that the Kennedy Channel Formation was deposited in a range of outer to inner shelf depositional environments. Very shallow water and perhaps intertidal conditions occasionally prevailed during deposition of the upper part of the formation.

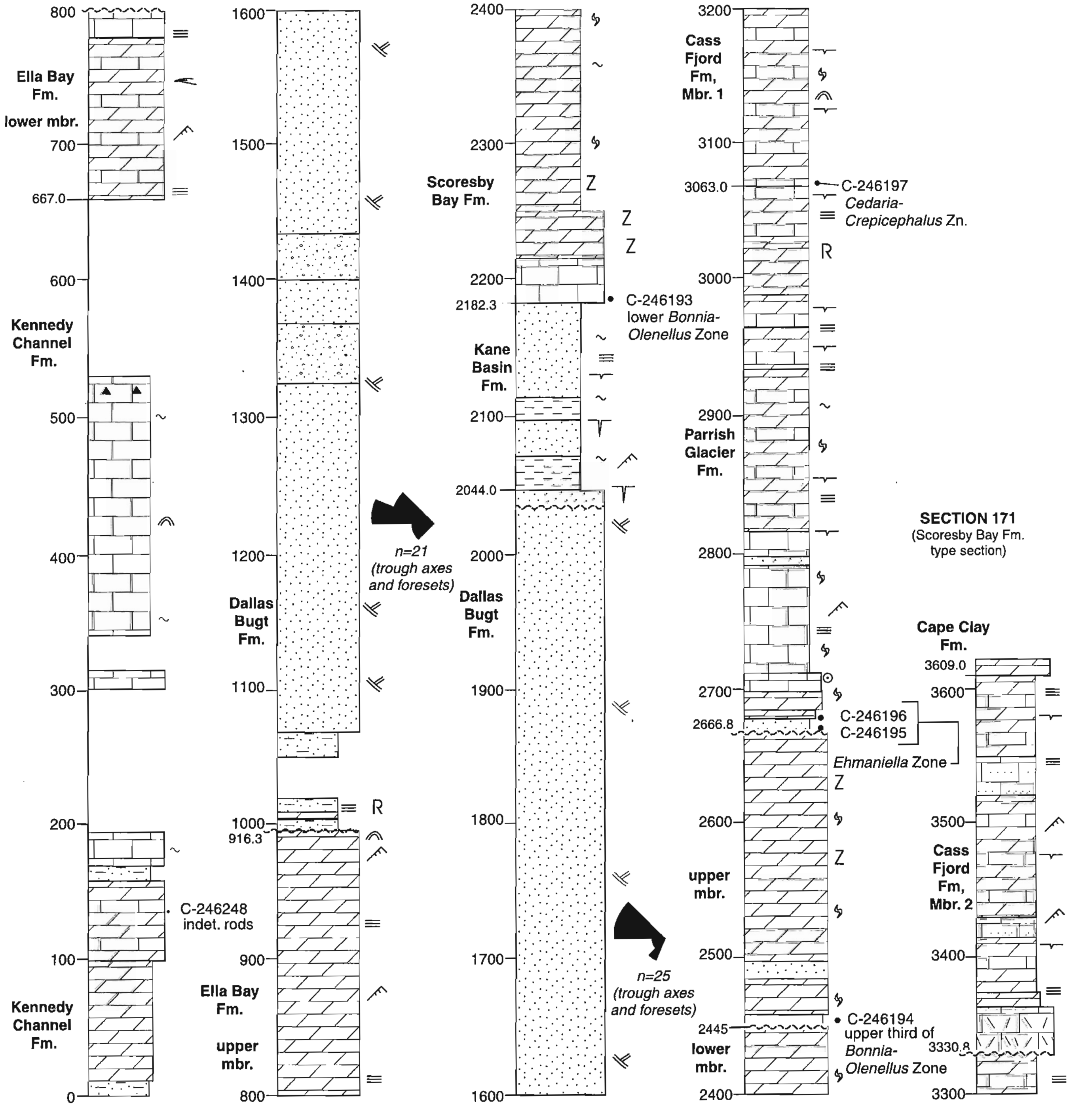

Figure 3. Graphic section log of the type section of the Scoresby Bay Formation and associated Cambrian-Ordovician formations (section 171, about 15 km north of Scoresby Bay). See Figure 4 for legend.

Few fossils have been recovered. *Teichichnus* and *Zoophycus* have been identified in a few beds. Rod-like fossils were collected from about 150 m above the base of the formation (Fig. 4, C-246248), but these were found to be not diagnostic of a particular age (B. Fritz, pers. comm., 1997). The occurrence of *Teichichnus* indicates a probable Cambrian age, but better age control is reported by Long (1989) who collected fragmentary trilobites indicating a Waucoban age. However, more precise dating is indicated by B. Pratt (pers. comm., 1997), who found complete trilobites of the *Bonnia-Olenellus* Zone.

Ella Bay Formation

The Ella Bay Formation was examined in two sections (171 and 178, Fig. 3, 5). At section 171 (Fig. 3), the formation is about 249 m thick and contains two informal members. These members are also found in the Ella Bay Formation in the vicinity of Parrish Glacier (de Freitas, 1998a).

The lower member consists mostly of greyish green-weathering, finely crystalline limestone and dolomitic limestone. Sedimentary structures in these strata include bioturbation, wavy- and planar-parallel laminae, and rare mudcracks. Gypsum pseudomorphs occur a few metres below the upper contact. The upper member consists mostly of thick-bedded, moderate yellowish orange-, pale yellowish orange-, and locally, moderate red-weathering dolostone, containing wavy microbialites, intraclast conglomerates, wavy-parallel laminae, ripple marks, and rare, laterally linked hemispherical stromatolites. At section 178 (Fig. 5), only the upper 140 m of the member are present. These strata consist of silty, yellow-, grey- and dusky yellow-weathering dolostone and red-weathering mudrock with ripple marks, hummocky cross-stratification, intraclast conglomerates, and zebroid structures. No age-diagnostic fossils were recovered from the Ella Bay Formation. The lower contact with the Kennedy Channel Formation is not exposed, but elsewhere this contact is described as gradational and conformable (Long, 1989).

The above evidence indicates that the Ella Bay Formation was deposited under restricted, shallow-marine and locally intertidal to supratidal conditions.

Dallas Bugt Formation

The Dallas Bugt Formation is about 1128 m thick at section 171 and 493 m thick at section 178. The formation was not encountered at sections 175B and 176 (Fig. 4).

At section 171, the lower 100 m of this formation contains a poorly exposed succession of red- and green-weathering mudrock interbedded with rare, medium- to fine-grained sandstone. Above this is a lithologically homogeneous succession of medium- to coarse-grained, trough cross-stratified sandstone. At about 320 m above the lower contact, the lowest conglomerate beds are encountered. These contain pebble- to local cobble-grade quartzite lithoclasts interstratified with coarse-grained sandstone. Well- to very well-rounded and imbricated lithoclasts commonly weather out from the conglomerates, and clasts feature very polished surfaces. The upper 400 m of the formation is, again, a homogeneous, well sorted, medium-grained sandstone with abundant trough cross-stratification with northwestward flow indicators. The upper contact contains a minor disconformity, above which is a finer grained sandstone with abundant *Skolithos* burrows. The lower contact with the Ella Bay Formation is a very significant unconformity. No conglomerates are exposed there, but at Parrish Glacier, the lower contact is overlain by a pebbly sandstone (de Freitas, 1998a).

At section 178, two members are recognized. The lower member, about 100 m thick, is mostly covered. It is similar lithologically to the basal beds in section 171, described above. In this 100 m thick recessive interval, green- and red-weathering mudrock is locally interbedded with sandy dolostone and sandstone. Some of the dislodged blocks contain laterally linked hemispherical stromatolites and wavy microbialites. The contact with the upper member of the Dallas Bugt Formation is not exposed, but is assumed to be gradational, since interbedded red-weathering mudrock and sandstone occur in a 30 to 60 m interval above the recessive unit. The bulk of the formation at this locality (upper member, section 178, Fig. 5) consists of sandstone and conglomerate. The conglomerate occurs sporadically throughout the middle and upper parts of the formation. Conglomerates contain granule-size and, less commonly, pebble-size lithoclasts of well rounded quartzite. Some of the clasts are imbricated, and sandstone and pebbly sandstone is extensively trough cross-stratified and well sorted. Many trough foresets contain quartzite granules and northwestward flow indicators. Most conglomerate beds are red stained and give the Dallas Bugt Formation a banded red and yellow appearance when viewed from a distance of a few kilometres. As in section 171, abundant *Skolithos* burrows are confined to the upper part of the formation.

The sedimentological evidence suggests that the bulk of the Dallas Bugt Formation was deposited in a braided fluvial environment. The lower red-weathering unit was probably a product of sedimentation in an arid alluvial floodplain. Unidirectional flow indicators presumably reflect transport of sediment toward the basin, from a cratonic source area. *Skolithos* in the upper part of the formation indicates a marine influence, but *Skolithos* is known to occur in fluvial environments as well. Sandstone and conglomerate beds feature flat, parallel bedding suggesting few channellized sandstone bodies. On the other hand, thick Lower Cambrian sandstone packages in various parts of North America, similar lithologically to the Dallas Bugt Formation, have been interpreted as products of a high energy shelf.

Kane Basin Formation

The Kane Basin Formation was measured and described in three sections. In section 171 (Fig. 3) it is 138.3 m thick, in section 175B (Fig. 4) it is more than 55.5 m thick, and in section 178 (Fig. 5) it is 117 m thick.

The formation forms a distinctive dark, recessive-weathering band above the resistant yellow weathering sandstone of the Dallas Bugt Formation and below resistant carbonates of the Scoresby Bay Formation. The Kane Basin Formation consists mainly of interbedded mudrock, siltstone,

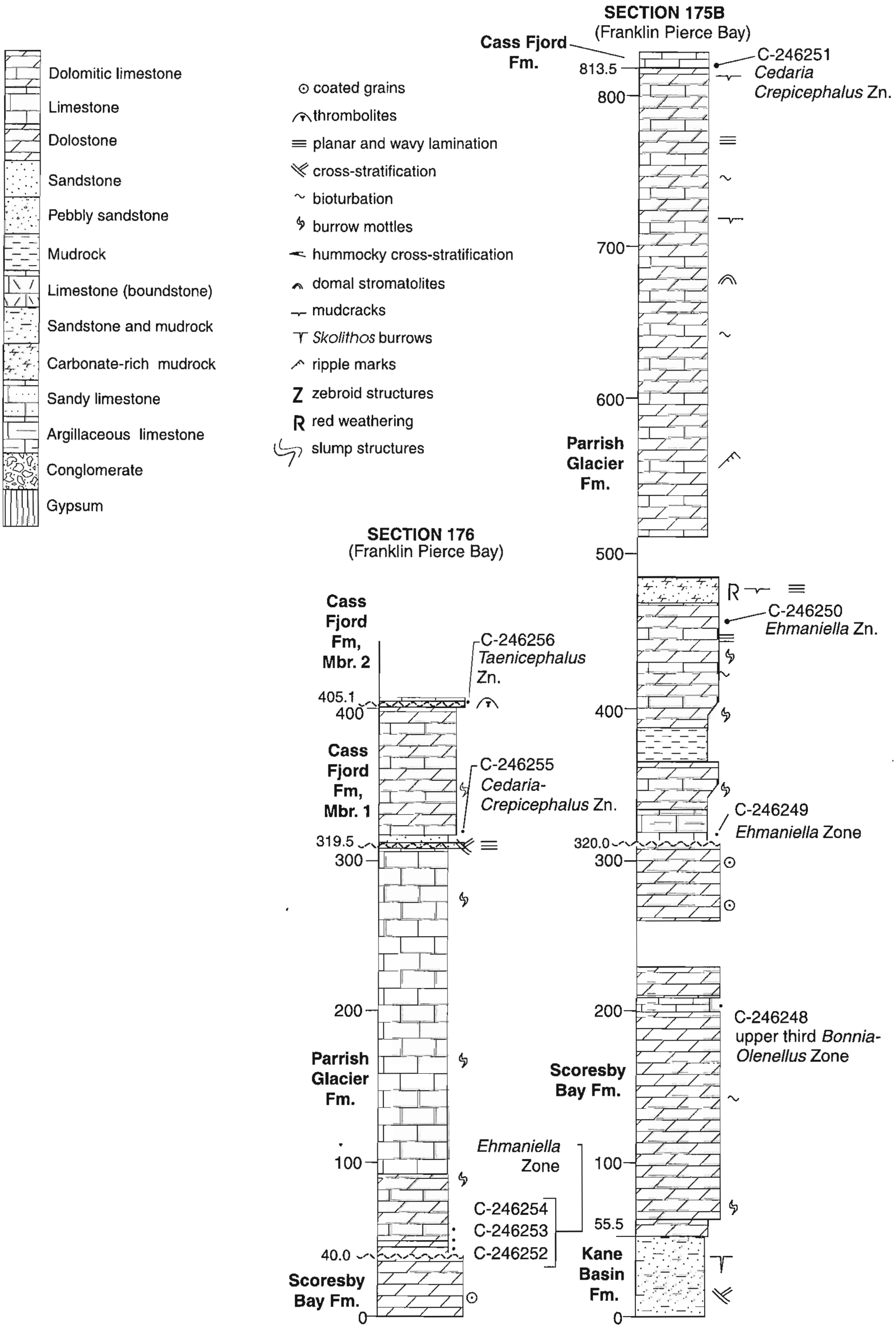

Figure 4. Two graphic section logs of the Kane Basin, Scoresby Bay, Cass Fjord, and Parrish Glacier formations, both located about 8 km north of the head of Franklin Pierce Bay. Legend applies to Figures 3 and 5.

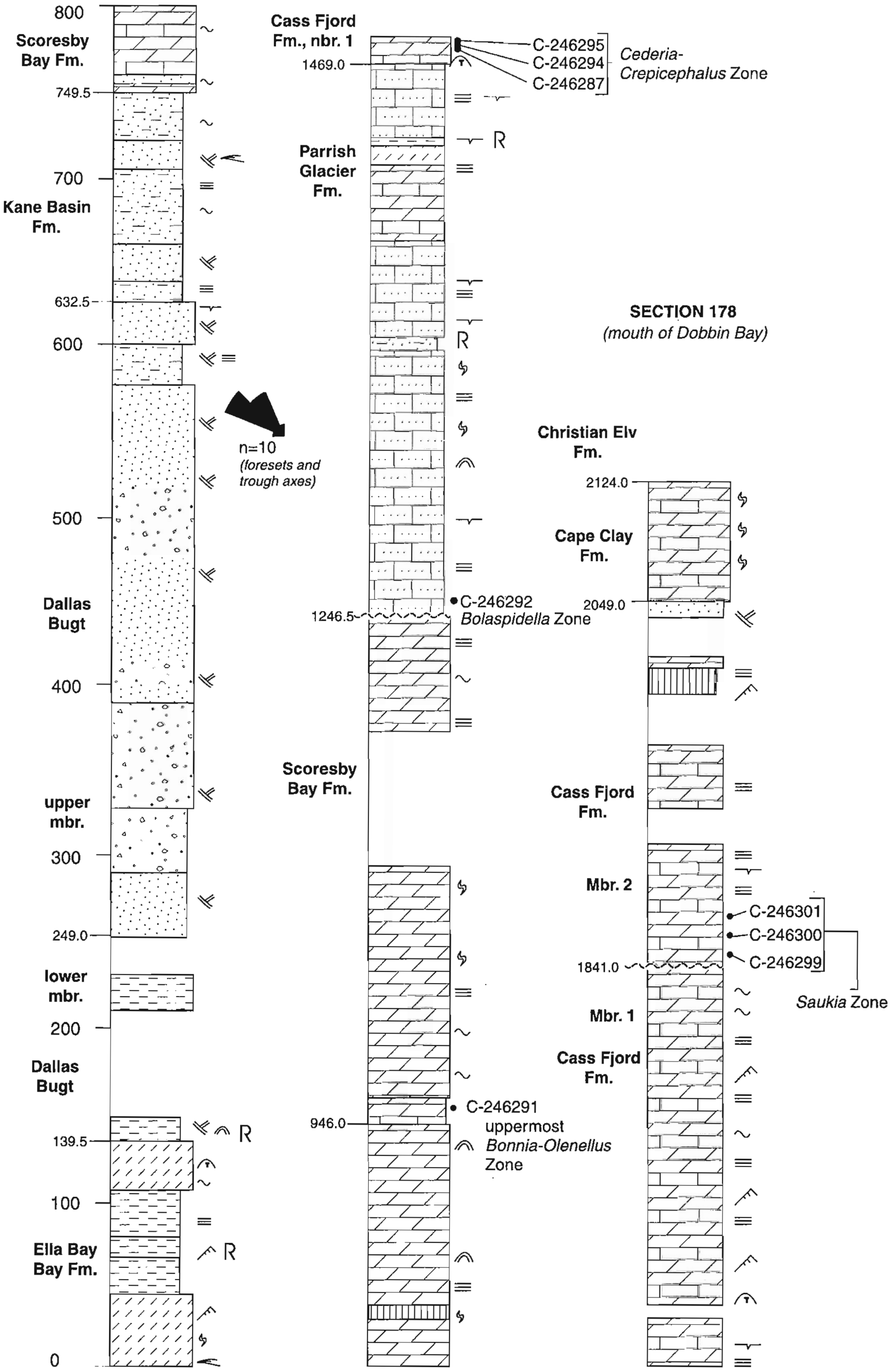

Figure 5. Graphic section log of the type section of the Scoresby Bay Formation (section 178, mouth of Dobbin Bay). See Figure 4 for legend.

and lesser sandstone. The sandstone is micaceous, dusky yellow weathering, well sorted, and fine- to medium-grained with common *Skolithos, Teichichnus,* and *Zoophycus* burrows and swaly and hummocky cross-stratification. Bedding surfaces of both the sandstone and siltstone contain parting lineations, gutter casts, tool marks, molar tooth structures, and polygonal mudcracks. The lower contact with the Dallas Bugt Formation is gradational.

The above evidence indicates that the Kane Basin Formation was deposited in a range of depositional environments. The presence of *Zoophycus* and swaly and hummocky cross-stratification suggests an open-marine, storm-influenced shelf depositional setting. More restricted and perhaps intertidal environments are indicated by the occurrence of mudcracks, *Teichichnus* traces, and molar tooth structures. Higher energy storm-induced combined flows likely produced gutter casts, flute and tool marks, and parting lineations.

Scoresby Bay Formation

The Scoresby Bay Formation was encountered in all measured sections (Fig. 3, 4, 5). It is 265 m thick at section 175B, more than 40 m thick at section 176, 301 m thick at section 178, and 485 m thick at section 171. The latter occurrence is the type section of the formation. Two locally mappable members are recognized.

The Scoresby Bay Formation is a cliff-forming unit throughout the anticipated map area. Seen from a distance, the formation contains orange and grey colour bands, which are in contrast to the overlying, less resistant Parrish Glacier Formation and underlying, darker weathering, recessive Kane Basin Formation. Two members are recognized, but they are lithologically similar.

Both members of the Scoresby Bay Formation contain numerous shallowing-upward cycles, a few metres to more than 60 m thick. Most of these cannot be correlated regionally, except for one, as discussed below. The lower parts of these cycles contain medium to coarsely crystalline, petroliferous dolostone, which is abundantly burrow mottled. Minor occurrences of fenestrae, burrow mottles, ooid grainstone, and wavy-parallel laminae also occur in the lower parts of cycles. The upper parts of the cycles typically consist of dark and pale yellowish orange-weathering, coarsely crystalline dolostone with laterally linked hemispherical stromatolites, wavy microbialites, burrow mottles, and up to 5 per cent vuggy porosity. Some of these burrow mottles are replaced with saddle dolomite. One of these cycles in the middle part of the formation contains a limestone unit up to 30 m thick. This limestone unit forms the base of the upper member. The member contact is sharp and may represent a minor disconformity.

Zebroid dolostone is abundant in much of the Scoresby Bay Formation at section 171 (Fig. 3). As shown in de Freitas (1998b), zebroid dolostone is characteristic of the formation throughout a large region of eastern Ellesmere Island, north of Scoresby Bay. The zebroid structures are associated with abundant saddle dolomite and minor breccia.

Although most of the formation consists of thick bedded dolostone, an unusual occurrence of a 2.0 m thick interval of bedded gypsum is noted in section 178 (Fig. 5). No other gypsum occurrences are observed in the Scoresby Bay Formation in eastern Ellesmere Island (*see also* de Freitas and Sweet, 1998; and de Freitas 1998a, b).

The lower contact with the Kane Basin Formation is everywhere gradational and conformable, in contrast to descriptions by Kerr (1967) and Trettin (1994). These workers interpreted the contact as a distinct, regional unconformity. The conformable, gradational contact is exemplified in section 178, where the basal 20 m of the Scoresby Bay Formation consists of interbedded dolomitic limestone and dusky yellow-weathering, trough cross-stratified sandstone, which is similar lithologically to Kane Basin Formation.

In all the measured sections of the Scoresby Bay Formation, a thin limestone unit occurs in about the middle part of the formation, as described above. In some cases this unit is only a few metres thick; in others it is 20 to 30 m thick. In section 178, the limestone unit yielded *Bonnia* n. sp., *Olenellus* sp., ?*Nephrolenellus* sp., and *Proliostracus* sp. indicating the uppermost *Bonnia–Olenellus* Zone (C-246291, L. Bohach, written report, 1998). At section 175B, the correlative limestone unit contains *Bolbolenellus* sp., *Bonnima* sp., *Illtydaspis quartetensis*?, *Olenellus (Mesonacis)* sp., *O. (Paedeumias)*, and *Zacanthopsis expansa* from the upper third of the *Bonnia–Olenellus* Zone (C-246248, W. Fritz, pers. comm., 1997). At section 171, the limestone unit yielded cf. *Bolbolenellus euryparia, Eotychoparia* sp., *Hyolithes* sp., *Olenellus clarki*?, and *Wimanella*? sp. (C-246194, W. Fritz, pers. comm., 1997) from the upper third of the *Bonnia–Olenellus* Zone. In addition to these trilobites, upper *Bonnia–Olenellus* Zone fauna were collected at Parrish Glacier (section 153, de Freitas, 1998a). At section 171, trilobites (C-246193) of the lower *Bonnia–Olenellus* Zone were collected and include "*Cassinneria*" sp. and aff. *Olenellus truemani.*

The Scoresby Bay Formation was deposited under shallow subtidal and locally supratidal depositional environments. It is overall shallowing upward, with deposition of the basal part of the formation interpreted as having occurred under more open-marine conditions. The Kane Basin Formation is in the lowest part of this shallowing-upward sequence. A maximum flooding surface may occur within the basal part of this formation (de Freitas et al., 1997).

Parrish Glacier Formation

The Parrish Glacier Formation was investigated in all four sections (Fig. 3, 4, 5). In section 176, it is 280 m thick; in section 178, it is 223 m thick; in section 175B, it is 494 m thick; and in section 171, it is 396 m thick.

The Parrish Glacier Formation is a well bedded succession of interbedded light grey, yellow, and red limestone and lesser dolostone and sandstone. It contrasts with the underlying, more resistant and more uniformly coloured Scoresby Bay Formation. The formation contains numerous rock types, but silty, dolomitic limestone clearly predominates. The limestone is commonly burrow-mottled, laminated, and contains common intraclast conglomerates, trace fossils, and rare mudcracks. The upper part of the formation contains more abundant dolostone and conspicuous red-weathering mudrock interbeds. These strata exhibit common polygonal mudcracks, planar-parallel lamination, ripple marks, flaser lamination, flute marks, and gutter casts. A few greyish yellow-, red-, and dusky yellow-weathering, bioturbated sandstone beds occur sporadically throughout the formation.

In section 175B, the lower part of the formation contains at least two shallowing-upward cycles. Each cycle contains a lower, recessive, argillaceous limestone or mudrock that grades upward into more resistant carbonate units, occasionally associated with red-weathering sandstone and mudrock. These cycles have not been observed in the three other measured sections, including section 176 only 2 km away. However, sections 175B and 176 are separated by the Parrish Glacier Thrust, which likely has a large amount of horizontal displacement associated with it.

The lower contact of the Parrish Glacier Formation is sharp and unconformable. In section 171, this contact is overlain by a 2.0 m thick, bioturbated, dolomitic, medium-grained sandstone.

Fritz identified trilobites from the lowest beds of the formation at section 171 (C-246195, C-246196) and recognized *Glypaspis* sp., *Olenoides* sp., *Spencella* sp., *Stenothecoides* sp., *Ehmaniella*? sp., *Helcionella* sp., and *Kootenia* sp., which together indicate the *Ehmaniella* Zone. In section 175B (C-246249, C-246250), aff. *Parkaspis endecamera,* cf. *Spencella* sp., *Ehmania*? sp., and *Ehmaniella* sp. occur in the basal part of the formation and also indicate the *Ehmaniella* Zone. In section 176 (C-246252, C-246253, C-246254), the *Ehmaniella* Zone is indicated by the presence of *Glypaspis* sp., *Dorypyge* sp., *Kootenia* sp., *Scenella* sp., *Bathyocos* sp., and *Ehmaniella* sp. In section 178 (C-246292), *Bolaspidella* Zone trilobites were identified. These are much younger than the other collections. There are two possible explanations. First, these trilobites were collected from a scree slope and could have been transported from a higher stratigraphic level; or second, the contact was chosen incorrectly. The latter is considered less likely, because of the regional distinctiveness of the lower contact of the Parrish Glacier Formation.

Cass Fjord Formation

In de Freitas and Sweet (1998), the Copes Bay Formation (Thorsteinsson, 1963) was discussed and it was concluded that the name is redundant. The formation is now replaced by the Christian Elv, Cape Clay, and Cass Fjord formations. The Cass Fjord Formation is the lowest formation in the abandoned Copes Bay Formation. On eastern Ellesmere Island, its basal contact is drawn on aerial photographs below the sequence of rock that features a slightly lighter shade of grey than the underlying Parrish Glacier Formation. In outcrop, the Parrish Glacier Formation contains distinct, interbedded red-, yellow-, and grey-weathering carbonates and so is distinct from the pale-weathering carbonates of the Cass Fjord Formation.

Two regionally mappable members are recognized. Member 1 in section 175B (Fig. 4) is about 86 m thick. The basal 7.0 m of the member contains a yellowish grey, trough cross-stratified sandstone. This is overlain by a uniform sequence of dolomitic limestone, containing planar-parallel laminae, polygonal mudcracks, wavy microbial laminites, columnar stromatolites, laterally linked hemispherical stromatolites, and thrombolites. The lower contact with the Parrish Glacier Formation is sharp and unconformable. In sections 171 and 178 (Fig. 3, 5), member 1 (268 m thick and 380 m thick, respectively) is similar lithologically to member 1 in section 175B. In addition to these rock types, the basal part of the formation in section 178 contains a basal, 3.0 m thick thrombolite boundstone.

Member 2 occurs in sections 171 and 178 (Fig. 3, 5). In section 171, member 2 is about 279 m thick. The lower 23 m consist of a cliff-forming dolomitic limestone containing thrombolites in the base and middle and laterally linked stromatolites at the top. This resistant unit is overlain by a thick, uniform interval of thin- to thick-bedded dolomitic limestone containing polygonal mudcracks and wavy microbial and planar-parallel laminae. In section 178, member 2 (208 m thick) contains a lower, trilobitic limestone, about 45 m thick. This is overlain by dolomitic limestone, containing polygonal mudcracks, planar-parallel lamination, and ripple marks. In the upper part of the member, sandstone, and particularly bedded gypsum, is observed. The gypsum-bearing interval is about 12 m thick and forms a light band on aerial photographs. This is the southernmost occurrence of gypsum in the Cass Fjord Formation. It occurs as far north as Rawlings Bay, but it was not noted to the west of Dobbin Bay, in the Agassiz Ice Cap nunataks.

Beds adjacent to member contacts were searched extensively for fossils. Trilobites were found to be exceedingly rare, and many hours were spent recovering just a few fragmentary specimens. Particularly important fossil collections were obtained from sections 176 and 178 (Fig. 4, 5). In section 176 (C-246255), the basal part of the lower member yielded *Bonneterrina*? sp. and is thus within the *Cedaria-Crepicephalus* Zone. Another collection from this same biozone was obtained from section 171 (C-246197, *Welleraspis* sp.). The basal beds in section 175B (C-246251) yielded *Geneviella*? sp. and *Welleraspis*? sp., also of the *Cedaria-Crepicephalus* Zone. Similar trilobites of the *Cedaria-Crepicephalus* Zone were collected from section 178 (C-246287, C-246294, C-246295). The upper member in section 176 (C-246256) yielded *Conaspis* sp. *Parabolinoides* sp., *Ptychaspis*? sp., and *Taenicephalus*? sp. indicating assignment to the *Taenicephalus* Zone. In eastern Ellesmere Island, the basal contact of member 2 is slightly younger and falls within the *Saukia* Zone (de Freitas and Fritz, 1995).

Cape Clay Formation

A single complete section of the Cape Clay Formation was measured. At section 178, it is about 75 m thick and consists of pale yellowish brown-weathering, finely crystalline, burrow-mottled, dolomitic limestone containing abundant intraclast conglomerate beds. It does not contain thrombolitic boundstone as observed at Parrish Glacier (*see* de Freitas, 1998a). Although several conodont fossils were collected, none were processed for this report. Elsewhere, the formation is lower Tremadoc (Fig. 2; *see also* de Freitas, 1998a).

The above, limited data indicate that the Cape Clay Formation was deposited under open-marine conditions. It is a regional marker unit representing transgression in North Greenland and most of Arctic Canada (de Freitas et al., 1997).

CONCLUSIONS AND RECOMMENDATIONS

Map units in the Franklin Pierce Bay and Dobbin Bay regions are firmly established and most are now age constrained with numerous trilobite collections. The base of the Parrish Glacier Formation is firmly dated as Middle Cambrian, within the *Ehmaniella* Zone, which is slightly younger than the age established at the Parrish Glacier type section (*Glossopleura* Zone, *see* de Freitas, 1998a). The type section of the Scoresby Bay Formation is described and shown to be a readily mappable unit in the report area. Its base falls within the lower *Bonnia-Olenellus* Zone. Two regionally extensive members are described and the contact between them is disconformable. Basal beds of the upper member have yielded upper *Bonnia-Olenellus* Zone fossils from numerous localities.

Trilobites in the underlying Kane Basin and Dallas Bugt formations were not recovered, but trace fossils indicate that these formations are no older than Cambrian. Elsewhere, *Bonnia–Olenellus* Zone trilobites from the underlying Kennedy Channel Formation indicate that the Kane Basin Formation and also the Dallas Bugt Formation are the same age as the lower Scoresby Bay Formation. The contact between the Kane Basin and Scoresby Bay formations has been interpreted previously as disconformable (Kerr, 1967; Trettin, 1994), but evidence reported herein clearly indicates a conformable contact, and the two formations form part of a thick regressive succession of strata.

Two members of the Cass Fjord Formation occur on northeastern Ellesmere Island. In most cases an unconformity is identified and is associated with a number of missing trilobite biozones. The unconformity is also recognized on adjacent North Greenland. These data indicate that two new formations should be named and the Cass Fjord Formation should be raised to group status. The age of the basal contact of the Cass Fjord Formation is firmly established as *Cedaria–Crepicephalus* Zone. The basal contact of member 2 of the Cass Fjord Formation is within the *Taenicephalus* Zone, which is slightly older than on west-central Ellesmere Island, where it occurs within the *Saukia* Zone (de Freitas and Fritz, 1995).

Future work should focus on the nature of the lower contact of the Cass Fjord Formation. This contact is not obvious on aerial photographs, and even on foot traverses, it is difficult to recognize. This is in contrast to the same contact on west-central Ellesmere Island, where the base of the Cass Fjord Formation is an obvious unconformity (de Freitas and Fritz, 1995). This contact was not investigated in detail on the Agassiz Ice Cap, and further work here is required.

ACKNOWLEDGMENTS

Bill Fritz and Lisa Bohach provided the biostratigraphic information. Without these data, regional correlations through the complex and heavily glaciated fold and thrust belt would be unreliable. Many thanks to Paul Crowley and Dave Beedell for their tireless and cheerful field assistance.

REFERENCES

de Freitas, T.
1998a: New observations on the geology of eastern Ellesmere Island, Canadian Arctic, part II: Cambro-Ordovician stratigraphy of the Parrish Glacier region; *in* Current Research 1998-E; Geological Survey of Canada.
1998b: New observations on the geology of eastern Ellesmere Island, Canadian Arctic, part IV: Cambro-Ordovician stratigraphy of the Rawlings Bay area and nunatäks of the Agassiz Ice Cap; *in* Current Research 1998-E; Geological Survey of Canada.
de Freitas, T. and Fritz, W.H.
1995: Age and stratigraphy of the Cass Fjord Formation, Arctic Canada; *in* Current Research 1995-E; Geological Survey of Canada, p. 97-104.
de Freitas, T. and Sweet, A.
1998c: New observations on the geology of eastern Ellesmere Island, Canadian Arctic, part I: structure and stratigraphy in the vicinity of Franklin Pierce and Allman bays; *in* Current Research, 1998-E; Geological Survey of Canada.
de Freitas, T., Harrison, J.C., and Mayr, U.
1997: Mineral showings and sequence stratigraphic correlation charts of the Canadian Arctic Islands and parts of North Greenland; Geological Survey of Canada, Open File 3410, 3 charts.
Higgins, A.K., Ineson, J.R., Peel, J.S., Surlyk, F., and Sønderholm, M.
1991: Lower Paleozoic Franklinian Basin of North Greenland; Grønlands Geologiske Undersøgelse, Bulletin 160, p. 71-139.
Kerr, J.W.
1967: Stratigraphy of central and eastern Ellesmere Island; Geological Survey of Canada, Paper 67-27, 63 p.
Long, D.G.F.
1989: Kennedy Channel Formation: key to the early history of the Franklinian continental margin, central eastern Ellesmere Island, Arctic Canada; Canadian Journal of Earth Sciences, v. 26, p. 1147-1159.
Palmer, A. and Peel, J.S.
1981: Dresbachian trilobites and stratigraphy of the Cass Fjord Formation, western North Greenland; Grønlands Geologiske Undersøgelse, Bulletin 141, 46 p.
Trettin, H.P.
1994: Pre-Carboniferous geology of the northern part of the Arctic Islands: Part 1, Hazen Fold Belt and adjacent parts of central Ellesmere Fold Belt, Ellesmere Island; Geological Survey of Canada, Bulletin 430, 248 p.
Thorsteinsson, R.
1963: Copes Bay; *in* Geology of North-central Part of the Arctic Archipelago, Northwest Territories; Y.O. Fortier, et al., Geological Survey of Canada, Memoir 320, p. 386-395.

Geological Survey of Canada Project 860006

New observations on the geology of eastern Ellesmere Island, Canadian Arctic, part IV: Cambro-Ordovician stratigraphy of the Rawlings Bay area and nunataks of the Agassiz Ice Cap

T. de Freitas[1]
GSC Calgary, Calgary

de Freitas, T., 1998: New observations on the geology of eastern Ellesmere Island, Canadian Arctic, Part IV: Cambro-Ordovician stratigraphy of the Rawlings Bay area and nunataks of the Agassiz Ice Cap; in *Current Research 1998-E; Geological Survey of Canada, p. 51–61.*

Abstract: The Scoresby Bay Formation is the same age as established at the type section and adjacent areas. The formation is divisible into two parts: the upper part contains a lower limestone interval yielding upper *Olenellus* Zone trilobites. Zebroid structures are a characteristic feature of the formation throughout most of east-central Ellesmere Island. Some zebroid fractures contain isopachous and massive pyrite and abundant hydrothermal dolomite.

Four distinct members of the Parrish Glacier Formation are recognized. Member 1, at the base, is an open-marine limestone with common, trilobite-bearing grainstone. Member 2 is a slope and basinal facies calcareous siltstone. Member 3 is a variegated unit consisting of slope facies olistostromes and shelf-margin oolitic grainstone and thrombolite boundstone. Member 4 consists of restricted-shelf limestone and dolostone and a few continental redbeds. These four members have yielded trilobites ranging from the *Glossopleura* or *Albertella* Zone to *Bolaspidella* Zone.

Résumé : L'âge de la Formation de Scoresby Bay est identique à celui qui a été déterminé au stratotype et dans les régions environnantes. La formation se devise en deux parties : la partie supérieure renferme un intervalle inférieur de calcaire contenant des trilobites de la partie supérieure de la Zone à *Olenellus*. Les structures zébrées sont caractéristiques de la formation dans presque tout le centre est de l'île d'Ellesmere. Certaines fractures zébrées renferment de la pyrite isopaque et massive et de la dolomite hydrothermale en abondance.

Quatre membres distincts de la Formation de Parrish Glacier sont reconnus. Le membre 1, situé à la base de la formation, est un calcaire de milieu marin ouvert contenant du grainstone à trilobites. Le membre 2 est formé d'un siltstone calcaire à faciès de talus et de bassin. Le membre 3 est une unité bariolée composée d'olistostromes à faciès de talus et de grainstone oolithique et boundstone à thrombolites de bordure de plate-forme continentale. Le membre 4 comprend des calcaires et des dolomies de plate-forme continentale à circulation restreinte et quelques couches rouges continentales. Ces quatre membres ont livré des trilobites de la Zone à *Glossopleura* ou à *Albertella* à la Zone à *Bolaspidella.*

---

[1] Imperial Oil Resources Limited, Research Centre, 3535 Research Road NW, Calgary, Alberta T2L 2K8

INTRODUCTION

This paper is the fourth in a series reviewing the new data on bedrock geology collected from east-central Ellesmere Island (Fig. 1). In this paper, lithological and paleontological data are reported from Radmore Harbour and from nunataks and valley walls on the Agassiz Ice Cap. Information on previous works and aspects of the structure and stratigraphy can be found in the three companion papers (de Freitas, and Sweet, 1998; de Freitas 1998a, b).

As part of a Geological Survey of Canada effort to map the region lying between 79°N and northern Judge Daly Promontory, and east of the drainage divide (Fig. 1), various, key Cambro-Ordovician exposures were visited during the summers of 1996 and 1997.

LITHOLOGY

The following descriptions pertain only to the sections indicated in this report. Additional bedrock information and a brief discussion of previous work can be found in the companion papers (de Freitas, and Sweet, 1998; de Freitas 1998a, b).

Kennedy Channel

The Kennedy Channel Formation was described and measured at section 180 only (Fig. 2, 4), where more than 200 m are exposed. The formation at this locality is characterized by dark grey- and red-weathering mudrock, siltstone, and minor sandstone. Graded Bouma A-B sequences and current ripples commonly occur, suggesting deposition on a submarine slope. The lower contact is not exposed.

Ella Bay Formation

The Ella Bay Formation is present in sections 172-173, 179, and 180 (Fig. 3, 4, 5). The southwesternmost facies of the Ella Bay Formation of this report occurs in section 180 (Fig. 4). Here it is 651 m thick and consists of interbedded dolostone, limestone, siltstone, and mudrock. The dolostone is yellowish grey weathering, medium crystalline, and contains planar-parallel laminae, intraclast conglomerates, abundant fenestrae, and laterally linked hemispherical stromatolites. Oolite occurs sporadically in the middle and upper parts of the formation. At the base of the formation, there is the unusual occurrence of a 2.0 m thick-bedded gypsum unit, which is associated with silty, mudcrack-bearing dolostone. A distinct, approximately 45 m thick mudrock unit occurs 295 m above the base of the section. The lower contact with the Kennedy Channel Formation at this locality is gradational and conformable.

At section 172-173 (Fig. 3), more than 500 m of the Ella Bay Formation are exposed, and consist of interbedded dolostone and mudrock. The yellowish grey- to light grey-weathering, medium to coarsely crystalline dolostone in this formation contains abundant ripple marks and wavy-parallel lamination. At 130.5 m above the base of the section, the lower dolostone is abruptly overlain by a conspicuous, very dark grey- to black-weathering mudrock unit. This may be a correlative of the mudrock unit at about 300 m above the base of the formation in section 180, mentioned above. It has a gradational contact with massive, coarsely crystalline dolostone exhibiting synsedimentary slump structures and intraclast conglomerates. At about 400 m above the base of the section, dolostone is associated with quartzite-lithoclast-bearing, granule-grade conglomerate beds. Above these strata, the Ella Bay Formation contains interbedded mudrock, granule conglomerate, and local oolitic and laminated dolostone.

At section 179 (Fig. 5), the Ella Bay Formation is more than 585 m thick. The lower part of the formation consists of interbedded mudrock and yellow-weathering, thick-bedded, coarsely crystalline dolostone. Several olistostromes occur in the basal portion of the section, and a 20 m thick mudrock interval about 80 m above the base of the section contains gossans. These were sampled for base and precious metals, but the results were discouraging. Above 200 m, the formation is arranged into at least three shallowing-upward sequences of limestone and dolostone. Cycles contain sedimentary structures such as thrombolite boundstone, grainstone, planar-parallel laminae, fenestrae, trough cross-stratification, laterally linked hemispherical stromatolites, and mudcracks. The highest shallowing-upward cycle is marked at its base by a phosphatic hardground, overlain by a dark grey-weathering mudrock, then by a thick-bedded, laminated dolostone. The latter unit is disconformably overlain by the Archer Fiord Formation.

The above evidence indicates that the Ella Bay Formation was deposited in a range of depositional settings, primarily on a shallow subtidal carbonate shelf. Several shallowing-upward cycles were formed by base level fluctuations. One of the most significant of these was a carbonate platform drowning event, now preserved as a very dark mudrock-dolostone contact. The regional extent of this drowning event, however, is not presently known.

Ellesmere Group

The Ellesmere Group was first named by Kerr (1967, p. 18) for a 368 to 1412 m thick sequence of clastics and minor carbonates exposed throughout most of eastern Ellesmere Island north of, and including, Bache Peninsula (Fig. 1). In de Freitas (1998a), it was recommended that the Dallas Bugt Formation be assigned to the Ellesmere Group as originally intended by Kerr (1967) for the *Skolithos*-bearing beds on Bache Peninsula. Thus, the Dallas Bugt Formation (and Ellesmere Group) is exposed in a region bounded to the north by John Richardson Bay, to the west by the head of the Dobbin Bay, and to the south by Parrish Glacier. North and west of Dobbin Bay, however, the Ellesmere Group contains several thick mudrock interbeds, and thus it is practical to map three separate formations in this region (Kerr, 1967). They are the Rawlings Bay, Ritter Bay, and Archer Fiord formations.

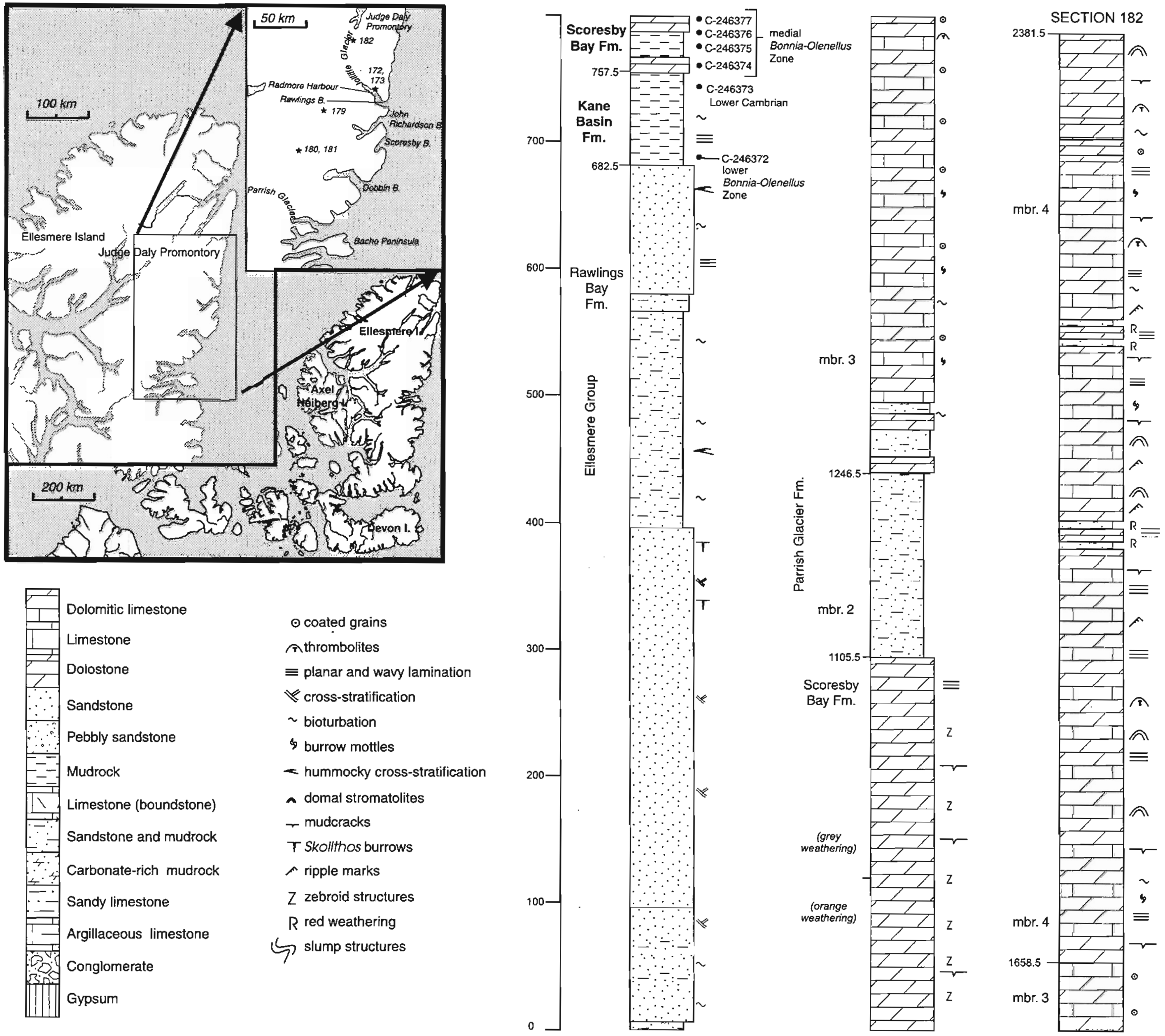

Figure 1. Location of study area in the Canadian Arctic Islands, legend, and graphic log of section 182. Vertical scale is in metres. Legend applies to all graphic section logs in this report.

There are many other locally mappable units within the group, such as the carbonates within the Archer Fiord Formation (see below) and mudrock beds in the Rawlings Bay Formation, but because of extensive ice cover and scale of regional mapping, it is impractical to map these units. In addition, some of these units are demonstrably laterally discontinuous. This is exemplified on the high-relief cliff faces at Radmore Harbour. In these exposures, mudrock units, some up to an estimated 80 m thick, are laterally discontinuous and cannot be correlated across the bay or between the limbs of the broad anticline, which is oriented at a high angle to the harbour.

Archer Fiord Formation

In an attempt to unravel the regional lithological variability in the basal part of the Archer Fiord Formation and upper Ella Bay Formation, Long (1989) interpreted an upper lagoonal mudrock facies in the Ella Bay Formation. By doing this, he had the Ella Bay–Ellesmere Group contact as conformable and unconformable on his regional cross-section. On the other hand, Kerr (1967) interpreted the contact as an important regional, and local, angular unconformity. In North Greenland, it is associated with an extensive olistostrome bed containing blocks greater than 100 m in diameter (Higgins et al., 1991).

In all of the measured sections of this report, the basal contact is unconformable, and Long's (1989) lagoonal facies, visited by the author, are placed within the basal Archer Fiord Formation. The definition of the latter formation is thus extended to include strata containing quartzite, lithoclast-bearing conglomerates, and slope- and shelf-facies sandstone, siltstone, mudrock, and carbonates. The Archer Fiord is everywhere overlain by the mudrock-bearing Ritter Bay Formation.

At Radmore Harbour (section 172-173, Fig. 3), the Archer Fiord Formation is about 320 m thick and consists mainly of interbedded sandstone, siltstone, mudrock, and dolostone. Sedimentary structures in the micaceous sandstone include planar-parallel laminae, hummocky cross-stratification, and climbing ripples, associated with very rare, thin, granule- or pebble-grade conglomerates. Rare dolostone

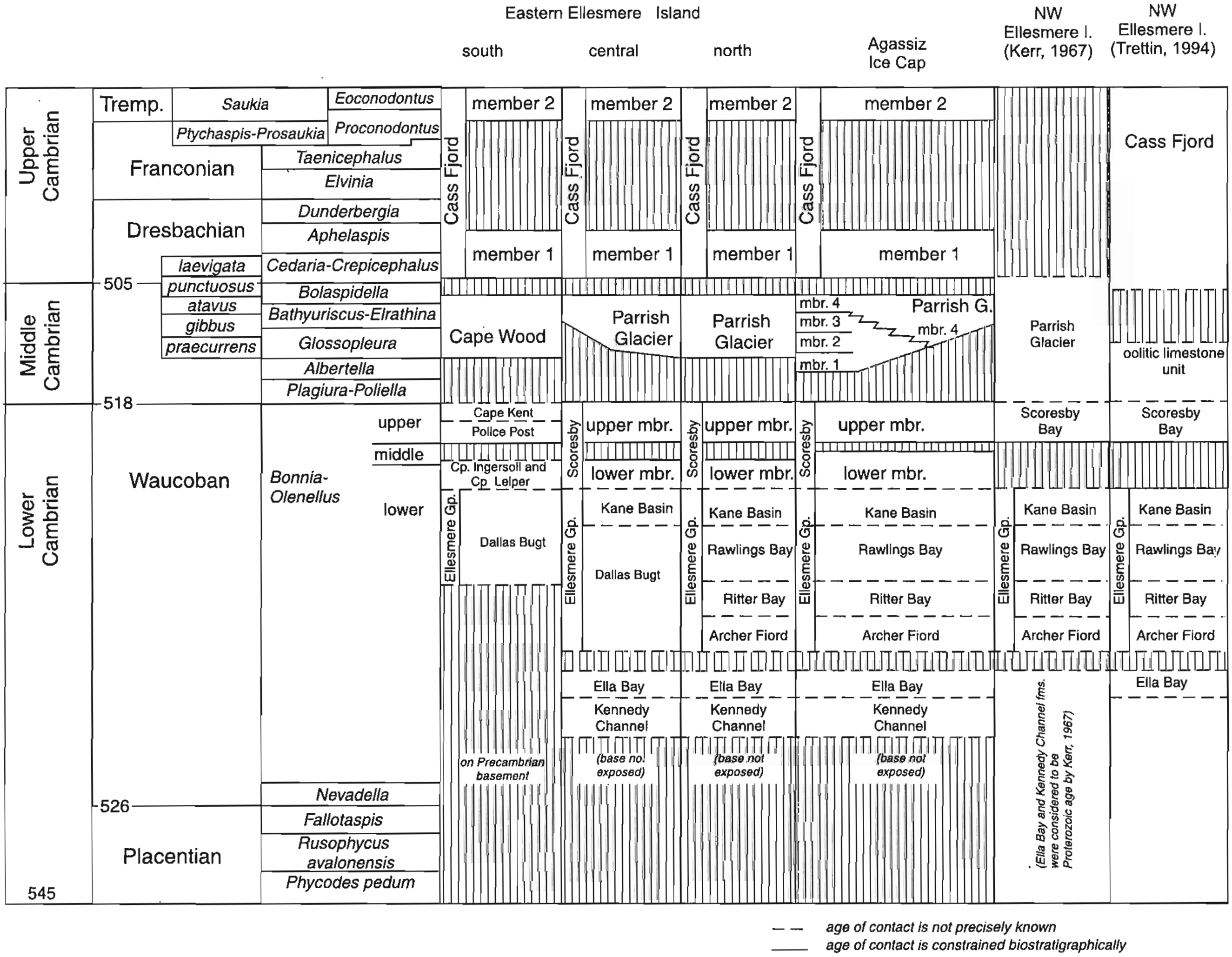

Figure 2. Stratigraphic correlation chart. Biozones in left hand column are from de Freitas et al. (1997).

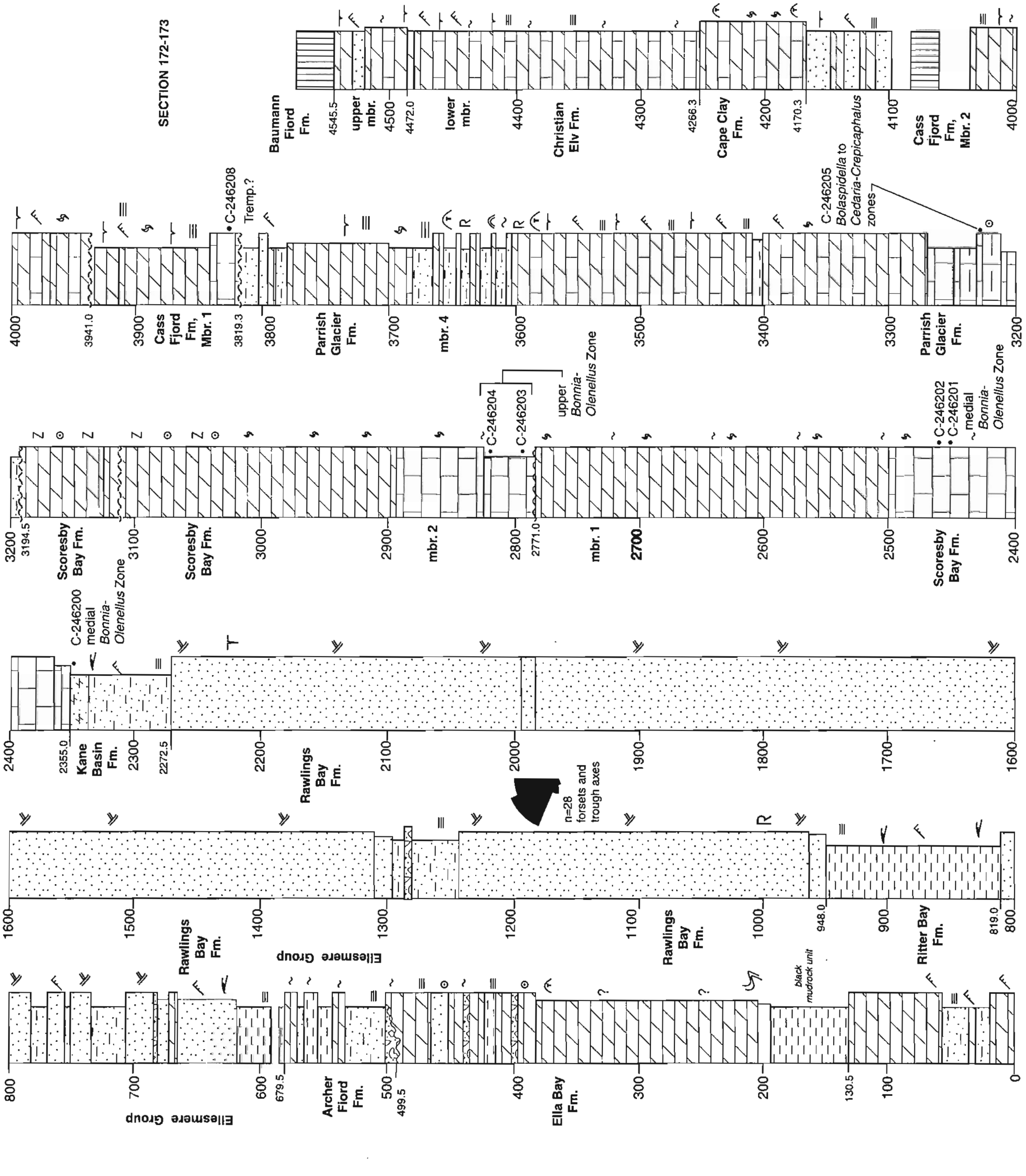

Figure 3. Graphic logs of sections 172-173, Radmore Harbour. For legend, see Figure 1.

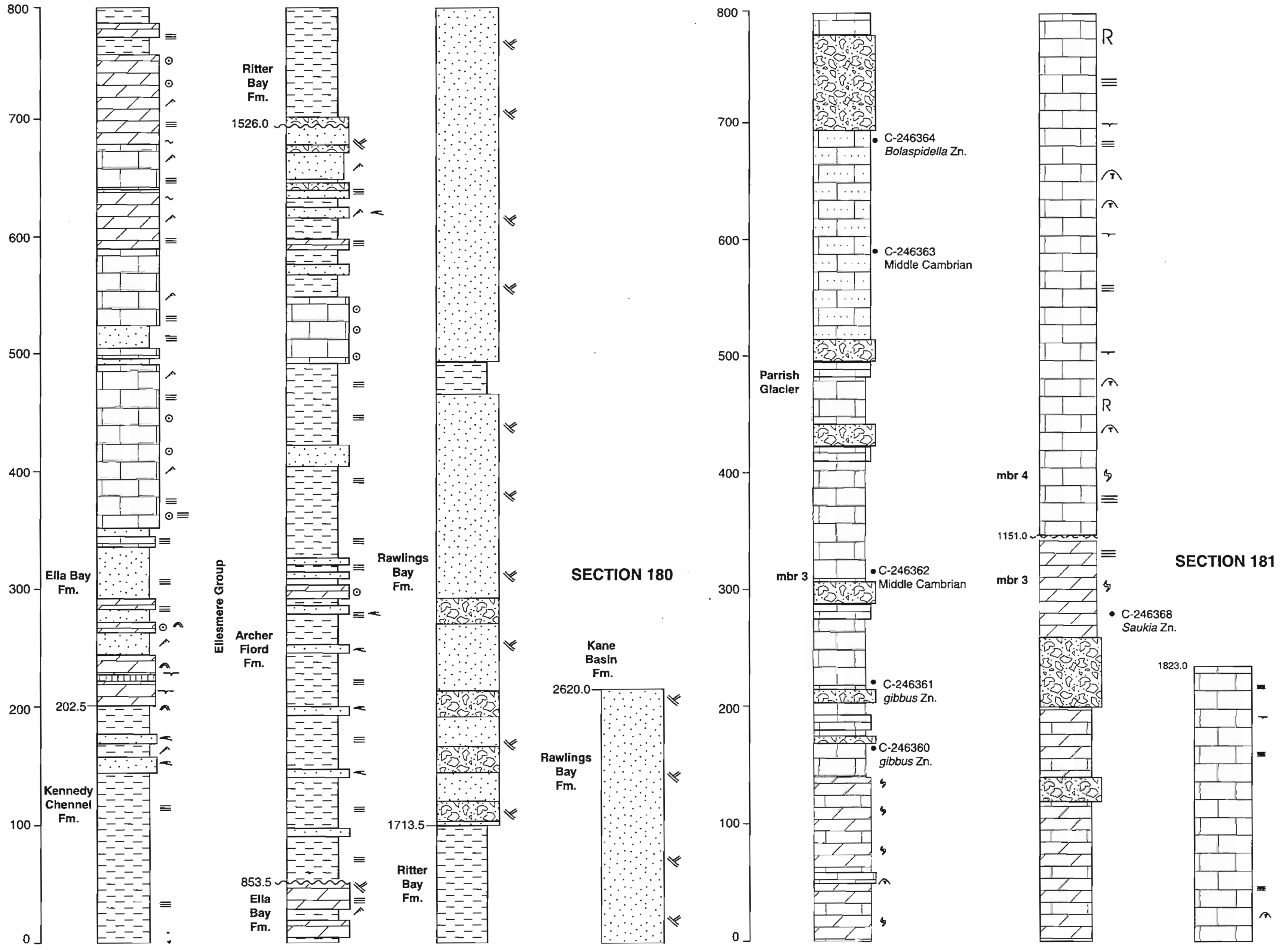

Figure 4. *Graphic logs of sections 180 and 181, Agassiz Ice Cap. The two sections are separated by a large glacier that presumably covers the Scoresby Bay and Kane Basin formations. For legend, see Figure 1.*

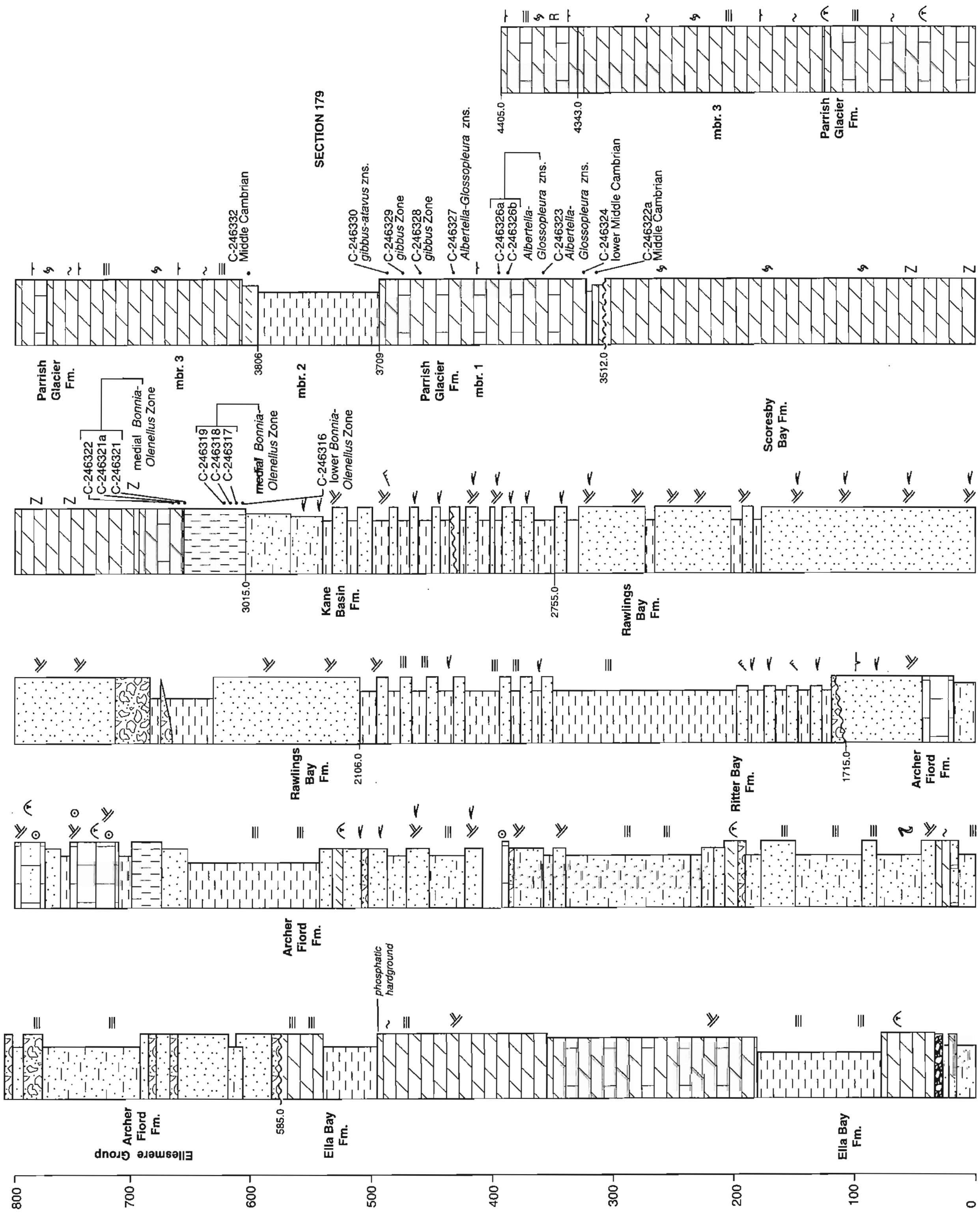

Figure 5. Graphic logs of section 179, Agassiz Ice Cap. For legend, see Figure 1.

interbeds in the basal part of the formation contain planar-parallel lamination and fenestrae. The formation, however, lacks common carbonate beds in the upper part of the formation as documented in sections 180 and 179. The lower contact of the Archer Fiord Formation at this locality is disconformable and is overlain by a laterally discontinuous granule- and pebble-grade quartzite conglomerate.

At section 179 (Fig. 5), the Archer Fiord Formation is about 1130 m thick. It is overall coarsening upward and consists of irregularly interbedded sandstone, conglomerate, mudrock, limestone, and dolostone. The rare conglomerate beds contain granule-size quartzite lithoclasts. The sandstone weathers to various shades of brown, yellow, and dark red; it is fine to coarse grained and is rarely associated with graded beds and slump structures. Carbonate beds are common at the top of the formation. Two carbonate rock types are observed: 1) boundstone units (consisting of columnar stromatolite boundstone and thrombolite boundstone) and 2) well sorted oolitic grainstone. Some of the grainstone beds feature obvious trough cross-stratification and are interbedded with sandstone and siltstone. Columnar stromatolites in some beds are at a low angle to regional bedding and thus may represent olistoliths. The lower contact with the Ella Bay Formation is sharp and disconformable and is overlain by a coarse grained, pebbly sandstone.

At section 180-181 (Fig. 4), the Archer Fiord Formation is about 673 m thick. Most of the formation consists of fine- and medium-grained, well sorted sandstone and lesser interbedded siltstone, mudrock, and carbonate. Predominant sedimentary structures included planar-parallel lamination, ripple marks, rare slump structures, and hummocky cross-stratification. Common oolite beds in the upper part of the formation are locally crossbedded.

The Archer Fiord Formation represents deposition on a submarine slope. Slope instability is suggested by synsedimentary folding and common conglomerate beds. Transported components in the formation suggest that the contiguous shelf was composed of a mixed carbonate-clastic system. Well rounded quartzite lithoclasts are likely multicyclic and had an origin in a high-energy, nearshore or fluvial depositional environment. Ooids and stromatolite mounds may have been transported downslope from the contiguous shelf margin. The basal unconformity above the Ella Bay Formation is an important regional unconformity in Arctic Canada and in North Greenland.

Ritter Bay Formation

At section 180 (Fig. 4), the Ritter Bay Formation is 188 m thick and consists of a uniform succession of laminated mudrock and siltstone. The lower 7.5 m of the formation contain a lenticular, polymicitic, ortho- and paraconglomerate bed with large phyllite and smaller, well rounded quartzite lithoclasts.

At section 172-173 (Fig. 3), the Ritter Bay Formation is 129 m thick and consists of a coarsening-upward succession of interbedded dark grey mudrock, siltstone, and sandstone. Planar-parallel lamination is the predominant sedimentary structure; hummocky cross-stratification and ripple marks are less common. The lower contact with the underlying Archer Fiord Formation is sharp.

At section 179 (Fig. 5), the Ritter Bay Formation is 391 m thick. The lower disconformable contact is overlain by a 3.0 m thick, lenticular (channellized) conglomerate composed of well rounded and locally imbricated quartzite pebbles. These likely represent the fill of a incised valley that was eroded into mudcracked and cross-stratified sandstone of the upper Archer Fiord Formation. The bulk of the formation at this locality consists of interbedded mudrock and lesser fine- and medium-grained sandstone. Sedimentary structures in this unit include abundant hummocky cross-stratification, planar-parallel lamination, and ripple marks. *Skolithos* burrows occur rarely in the top of the formation.

The above evidence indicates that the Ritter Bay Formation was deposited on a distal, storm-influenced shelf. The lower part of the formation contains local incised valley-fill units of fluvial origin.

Rawlings Bay Formation

At section 172-173 (Fig. 3), the Rawlings Bay Formation is about 1325 m thick and consists of a uniform succession of trough cross-stratified, medium- to coarse-grained sandstone. Granule grade conglomerate accounts for less than 1 per cent of the unit. The top 20.0 m contains numerous *Skolithos* burrows. The lower contact with the Ritter Bay Formation is gradational.

At section 180 (Fig. 4), the formation is about 907 m thick. Granule-grade conglomerates account for about 30 to 40 per cent of the interval. These strata are overlain by mudrock and medium- to coarse-grained sandstone containing abundant trough cross-stratification, and rare *Skolithos* burrows. The lower contact with the Ritter Bay Formation is gradational and conformable.

At section 182 (Fig. 1), the formation is more than 683 m thick and consists mostly of well sorted, medium- and fine-grained sandstone and interbedded siltstone. Sedimentary structures include trough and hummocky cross-stratification and planar-parallel lamination. The Rawlings Bay Formation at this locality features the finest grained clastic facies observed within the report area.

At section 179 (Fig. 5), the Rawlings Bay Formation is 649 m. The lower part of the formation contains a 16.5 m thick channellized orthoconglomerate and paraconglomerate with granule-grade quartzite lithoclasts and large phyllite intraclasts. This is overlain by a thick succession of medium-grained, well sorted, abundantly trough cross-stratified sandstone containing less than 2 or 3 per cent granules. *Skolithos* occurs rarely in the middle and upper parts of the formation.

The above evidence indicates that the Rawlings Bay Formation was deposited on a storm-influenced shelf.

Kane Basin Formation

In section 172-173 (Fig. 3), the formation is 83 m thick and consist of interbedded sandstone and siltstone with abundant sedimentary structures, including hummocky cross-stratification, tool marks, ripple marks, trough cross-stratification, and graded beds. A single sedimentary dyke, with a northeasterly orientation, occurs in the section. Some of the hummocky cross-stratified beds appear to have convex-down geometries, suggesting erosion prior to deposition of the storm bed.

The Kane Basin Formation is 75 m thick in section 182 (Fig. 1) and 260 m thick in section 179 (Fig. 5). In these sections the formation consists predominantly of sandstone and siltstone with ripple marks, hummocky cross-stratification, planar-parallel laminae, and rare *Zoophycus, Teichichnus,* and *Thallasinoides.*

In all exposures of the Kane Basin Formation the lower contact with the Rawlings Bay Formation is gradational.

Trilobites collected from the uppermost beds in the Kane Basin Formation in section 172-173 (C-246200) yielded *Oblella* sp. and *Olenellus laxoculus*? indicating medial *Bonnia–Olenellus* Zone. Trilobites from section 182 include *Mesolenellus* sp. and olenellinids (C-246372 and C-246373) of the lower *Bonnia–Olenellus* Zone.

The above indicates that the Kane Basin Formation was deposited on a shallow, storm-influenced shelf.

Scoresby Bay Formation

The Scoresby Bay Formation is 348 m thick in section 182 (Fig. 1) and about 497 m thick in section 179 (Fig. 5). The lower part of the formation at both localities consists of fossiliferous, thick-bedded limestone gradationally overlain by orange-weathering dolostone with distinctive and abundant zebroid structures, planar-parallel laminae, and mudcracks. Zebroid textures are particularly well developed in section 179.

In section 172-173 (Fig. 3), the formation is 839 m thick and contains facies resembling that in section 182, but two members are recognized. The lower member (416 m thick) and upper member (423.5 m thick) are lithologically similar. The lower part of the lower member contains a lower, trilobitic grainstone unit that yielded many well preserved fossils. This interval is overlain by a thick succession of resistant dolostone (members 1 and 2) containing several 20–60 m thick, shallowing-upward cycles. Dolostone in the basal part of the cycles is medium grey- and yellowish grey-weathering, burrow mottled, and massive. The upper parts of these cycles consist of pale yellowish orange-weathering dolostone with planar-parallel laminae and local oncolite rudstone. In the middle of the formation, the basal contact of one of these cycles is disconformable and is overlain by a thin limestone unit that marks the base of the upper member. These members occur also in the Dobbin Bay region (*see* de Freitas, 1998b).

Massive pyrite occurs in the basal part of the Scoresby Bay Formation at the head of Radmore Harbour. Sulphide minerals were quantified, but economic concentrations of industrial minerals were not found. The massive pyrite occurs as isopachous crusts in zebroid fractures and is associated with hydrothermal dolomite.

In all exposures of the Scoresby Bay Formation, the lower contact with the Kane Basin Formation is gradational.

Numerous trilobite samples were collected from the base of the upper member. Samples C-246374, C-246375, C-247376, and C-246377 from the lower part of section 182 yielded *Wanneria logani*, and *Wanneria* sp. indicating the medial *Bonnia–Olenellus* Zone. In section 179, sample C-246316 contained *Wannerellus* cf. *W. tricarinatus*, indicating the lower *Bonnia–Olenellus* Zone. Samples C-246317, C-246318, C-246319, C-246321, C-246321a, C-246322 from section 179 yielded *Bonnia* sp., *Ekwipagetia marginata, Olenellus* cf. *O. transitans, Salterella* sp., and *Wanneria* sp., of the medial *Bonnia–Olenellus* Zone. In section 172-173 samples C-246200, C-246201, C-246202 yielded *Hyolithellus* sp., *Kutorgina* sp., *Oblella* sp., *Olenellus laxoculus*?, *O.* sp. 1., *O.* sp. 2, and aff. *Wanneria mediocris*?, indicating medial *Bonnia–Olenellus* Zone. Samples from the middle limestone unit in section 172-173 (C-246203 and C-246304) yielded *Bonnia semidiscoidea, Eoptychoparia*? sp., *Illtydaspis*? sp., *Nisusia* sp., *Olenellus (Paedeumias)* sp., *O.* sp., *Onchocephalus* sp., *Paterina* sp., *Syspacephalus* sp., and *Zacanthopsis* sp., indicating the upper *Bonnia–Olenellus* Zone.

The above evidence indicates that the Scoresby Bay Formation was deposited on a shallow-water shelf. The formation is overall upward shallowing, with the oldest, trilobite-bearing strata representing fully open-marine conditions. Zebroid dolostone is a shallow-burial, diagenetic feature, possibly related to the flux of hot subsurface brines. These brines are significant from an economic standpoint, because in other areas, they have a link with economic mineral emplacement.

Parrish Glacier Formation

At section 179 (Fig. 5), the Parrish Glacier Formation is more than 893 m thick, and four members are recognized. The lowest member (197 m thick) is an extremely fossilferous limestone. Almost every bed encountered in this section contained well preserved but fragmentary trilobites. Tempestites and hummocky cross-stratification are observed where beds are not extensively bioturbated. Member 2 is a thin-bedded calcareous siltstone unit featuring planar-parallel lamination, and ripple marks. Member 3 (about 537 m thick) is a lithologically uniform succession of limestone and dolostone which is massive or contains faint burrow mottles, planar-parallel lamination, thrombolites, and mudcracks. Only the basal part of member 4 is exposed at this locality. It is at least 62 m thick and consists of yellowish grey, finely crystalline dolostone with planar-parallel laminae, burrow mottles, mudcracks, and common red-weathering, silty limestone.

All member contacts are gradational. The lower contact with the Scoresby Bay Formation is sharp and disconformable.

At section 182 (Fig. 1), the Parrish Glacier is 1276.0 m thick and contains three members (2, 3, and 4). Member 1 (as in section 179) was not recognized. However, the upper Scoresby Bay Formation at this site was not accessable and member 1 may be presently included within the upper Scoresby Bay Formation. Member 2 (141 m thick) is a thin-bedded, calcareous siltstone with abundant starved ripples and planar-parallel lamination. This is overlain gradationally by a thick succession (member 3, 412 m thick) of dolomitic limestone containing abundant oolites and oncoidal rudstone, rarely interbedded with thrombolite boundstone and limestone containing mudcracks, burrow mottles, and flaser laminae. Member 4 (723 m thick) has a sharp lower contact with member 3 and is more recessive and lighter weathering. It also contains distinct, red- and orange-weathering siltstone and carbonate beds in the middle part of the formation, which are typical of the Parrish Glacier Formation in the type section. Other carbonate beds feature a variety of shallow-water and intertidal sedimentary structures, such as mudcracks, planar-parallel lamination, laterally linked hemispherical stromatolites, and thrombolites.

In section 172-173 (Fig. 3), the Parrish Glacier Formation is 625 m thick and consists of interbedded siltstone, dolostone, and limestone. The entire section is assigned to member 4. The limestone is finely crystalline, thick bedded, and contains burrow mottles, planar-parallel laminae, and intraclast conglomerate. Carbonate beds interbedded with red-weathering siltstone tend to be more dolomite rich and contain a greater proportion of sand and silt. Mudcracks are common throughout the formation. Sporadically occurring thrombolites, in the middle part of the formation, are associated with redbeds and herringbone cross-stratified sandstone. The lower contact is sharp and unconformable and is overlain by a 3.0 m thick siltstone unit with several, thin carbonate-chert pebble beds.

In section 181 (Fig. 4), the Parrish Glacier is more than 1823 m thick and is dominated by slope-facies argillaceous carbonate and thick olistostromes. Rock units are arranged into coarsening-upward sequences, typically capped by one or more olistostromes. The thicknesses of the cycles and capping olistostrome increase upsection. Transported clasts range from several centimetres to more than 30 m in diameter. A random check on clast lithology indicates that many of the clasts are composed of oolite and thrombolite boundstone. This unit is assumed to be a slope facies of member 3 (section 182). Conglomerate beds form distinct, apparent northwest-facing clinoforms in outcrop, and the equivalent upslope, in situ shelf-margin facies are presently ice covered.

At about 1151 m above the base of section 181, there is an abrupt and perhaps disconformable contact overlain by a thick succession of limestone assigned to member 4. It contains many shallow-water indictors such as mudcracks, planar-parallel lamination, and thrombolites. As in section 172-173, thrombolites occur in association with red-weathering carbonates.

Many trilobites were collected from all members of the Parrish Glacier Formation. A poorly preserved trilobite was collected from the basal part of member 4 in section 172-173 (C-246205). It is *Modocia* sp., which ranges from the *Bolaspidella* to *Cedaria–Crepicephalus* zones. This age assignment is much younger than expected, because elsewhere, the lowest beds of the Parrish Glacier Formation typically yield middle Middle Cambrian trilobites.

There are more trilobites visible in exposures of member 1, section 179, than in any other lower Paleozoic formation in the Arctic Islands. Most of the member beds contain many well preserved, although fragmentary, trilobites. The highest sample in the member (C-246330) yielded *Peronopsis fallax* and *Bathyuriscus* sp., indicating *Ptychagnostus gibbus* to *Ptychagnostus atavus* zones. Sample C-246329 contained *Peronopsis fallax, P. montis, Ptychagnostus gibbus, Mexicella* sp., and *Pegetia* sp., which are assigned to the *Ptychagnostus gibbus* Zone. Sample C-246328 yielded *Peronopsis fallax, P. montis, Ptychagnostus* sp., *Elrathina* sp., *Tonkinella* sp., and *Oryctocephalus* sp. indicating the *Ptychagnostus gibbus* Zone. Samples C-246323, C-246327, C-246326b, and C-146326a contained *Elrathina* sp., *Kochaspis*? sp., *Kootenia dawsoni, Litagnostus* sp., *Ogygopsis klotzi, O. typicalis, Oryctocephalus* sp. aff. *O. matthewi, O.* sp., *Pagetia* sp., *Pagetides* sp., *Peronopsis brighamensis, P. bonnerensis, Wenkchemnia* sp., and *Zacanthoides* sp., indicating *Albertella* to *Glossopleura* zones. Sample C-246324 contained ?*Alokistocare* sp., *Poliella* sp. 1, and *Elrathina* sp. indicating lower Middle Cambrian. Sample C-246322a contained *Elrathina* sp. and *Peronopsis* sp. of Middle Cambrian age. The lower part of member 3 at section 179 (C-246332) yielded *Elrathina* sp. of Middle Cambrian age.

In section 181 (Fig. 4), samples C-246360 and C-246361 yielded *Ogygopsis klotzi*?, *Peronopsis fallax, P. montis, Tonkinella* sp., and *Elrathina* sp. of the *Ptychagnostus gibbus* Zone. Samples C-246362 and C-246363 contained only ?*Ptychagnostus* of Middle Cambrian age, and sample C-246364 yielded trilobites of the *Bolaspidella* Zone. Highest samples in the member (C-246368) were questionably placed in the *Saukia* Zone. These are poorly preserved and considerably younger than would be expected, and so the zone assignment is in doubt.

The above evidence indicates that the Parrish Glacier Formation was deposited in a range of depositional environments, including shallow-restricted shelf (member 4), slope and shelf margin (members 1 and 3, section 181), and basinal (member 2). Local continental sedimentation occurred during deposition of the redbeds.

Cass Fjord Formation

The Cass Fiord Formation is 351 m thick in section 173-173 (Fig. 3) and contains two regionally mappable members (de Freitas, 1998a, b). Rock types in the formation are remarkably similar to those in the vicinity of Dobbin Bay. The lower 20 m of the formation features a cliff-forming dolomitic limestone with thrombolites, intraclast beds, and many burrow mottles. The lower part of member 2 is slightly more resistant and consists of thick-bedded dolomitic limestone with planar-parallel lamination, burrow mottles, and ripple marks. The upper portion of member 2 contains a significant thickness of gypsum. Gypsum beds are overlain by a thick interval of well sorted, trough cross-stratified and herringbone cross-stratified sandstone equivalent to the Kap Coppinger Member of the Cass Fjord Formation on North Greenland. Many trilobites of the *Cedaria–Crepicephalus* Zone were collected from more southern localities. A single fragmentary and very poorly preserved trilobite (C-246208) from the base of member 1 was speculatively assigned to the Trempeleauean stage, but this is much younger than expected; thus, the age assignment is considered suspect. The lower contact with the Parrish Glacier Formation is sharp and likely disconformable.

The Cass Fjord Formation was deposited under a range of shallow subtidal, intertidal, and supratidal conditions.

Cape Clay Formation

The Cape Clay Formation was investigated in a single section only (172-173, Fig. 3), where it is 96 m thick. It contains many burrow mottles and thrombolites of the "Hawker Bay" type (de Freitas and Mayr, 1995). These facies are characteristic of an open-marine depositional setting. Conodont samples were collected from the formation but were not processed for this work.

Christian Elv Formation

The Christian Elv Formation was examined only in section 172-173 (Fig. 3), where it is 179 m thick. It is divided into two members. The lower member consists of dolomitic limestone with common planar-parallel laminae, trace fossils (*Thallasinoides* and *Teichichnus*), and mudcracks. These strata are overlain abruptly by a more resistant upper member, consisting of interbedded sandstone and limestone. The sandstone is cross-stratified and fine grained. The limestone beds are dolomitic and burrow mottled. The lower contact with the Cape Clay Formation is gradational.

The limited available evidence indicates that the Christian Elv Formation was deposited on a shallow-water restricted shelf. More open-marine conditions likely existed during deposition of the upper member.

CONCLUSIONS

The formations originally assigned to the Ellesmere Group (Kerr, 1967) are shown to be regionally mappable. However, minor modification of the Archer Fiord Formation, exposed in nunataks of the Agassiz Ice Cap, is necessary to include the lithologically variable assemblage of sandstone, limestone, and siltstone above the Ella Bay Formation. This revision also eliminates the need to interpret a lagoonal facies in the upper Ella Bay Formation, as suggested earlier by Long (1989).

The Scoresby Bay Formation in this area is similar lithologically to that in the type section. In this region, however, zebroid structures are much more abundant, and in at least one outcrop, the hydrothermal-dolomite-filled zebroid fractures are partly occluded by massive pyrite. Assays of these samples, however, yielded uneconomical concentrations of industrial minerals.

Four members of the Parrish Glacier Formation are recognized. These include rocks deposited in basinal slope, shelf margin, restricted shelf, and continental depositional settings. Regional relationships imply a diachronous lower contact for member 4.

ACKNOWLEDGMENTS

Bill Fritz (GSC) and Lisa Bohach (University of Victoria) provided the biostratigraphic information. Without these data, regional correlations through the complex, and heavily glaciated fold and thrust belt would not be reliable. I extend many thanks to Paul Crowley and Dave Beedell for their tireless and cheerful field assistance.

REFERENCES

de Freitas, T.
1998a: New observations on the geology of eastern Ellesmere Island, Canadian Arctic, part II: Cambro-Ordovician stratigraphy of the Parrish Glacier region; *in* Current Research 1998-E; Geological Survey of Canada.

de Freitas, T.
1998b: New observations on the geology of eastern Ellesmere Island, Canadian Arctic, part III: Cambro-Ordovician stratigraphy of the Dobbin Bay, Scoresby Bay, and Franklin Pierce Bay areas; *in* Current Research 1998-E; Geological Survey of Canada.

de Freitas, T. and Mayr, U.
1995: Kilometre-scale microbial buildups in a rimmed carbonate platform, arctic Canada: new insights on Lower Ordovician reef facies; Bulletin of Canadian Petroleum Geology, v. 43, p. 407-432.

de Freitas, T. and Sweet, A.
1998: New observations on the geology of eastern Ellesmere Island, Canadian Arctic, part I: structure and stratigraphy in the vicinity of Franklin Pierce and Allman bays; *in* Current Research 1998-E; Geological Survey of Canada.

de Freitas, T., Harrison, J.C., and Mayr, U.
1997: Mineral showings and sequence stratigraphic correlation charts of the Canadian Arctic Islands and parts of North Greenland; Geological Survey of Canada, Open File 3410, 3 charts.

Higgins, A.K., Ineson, J.R., Peel, J.S., Surlyk, F., and Sønderholm, M.
1991: Lower Paleozoic Franklinian Basin of North Greenland; Grønlands Geologiske Undersøgelse, Bulletin 160, p. 71-139.

Kerr, J.W.
1967: Stratigraphy of central and eastern Ellesmere Island; Geological Survey of Canada, Paper 67-27, 63 p.

Long, D.G.F.
1989: Ella Bay Formation: Early Cambrian shelf differentiation in the Franklinian Basin, central eastern Ellesmere Isand, Arctic Canada; Canadian Journal of Earth Sciences, v. 26, p. 2621-2635.

Trettin, H.P.
1994: Pre-Carboniferous geology of the northern part of the Arctic Islands: part 1, Hazen Fold Belt and adjacent parts of the central Ellesmere Fold Belt, Ellesmere Island; Geological Survey of Canada, Bulletin 430, 248 p.

Geological Survey of Canada Project 860006

Porosity characteristics of shale formations from the Western Canada Sedimentary Basin[1]

T.J. Katsube, W.C. Cox[2], and D.R. Issler[3]
Mineral Resources Division, Ottawa

Katsube, T.J., Cox, W.C., and Issler, D.R., 1998: Porosity characteristics of shale formations from the Western Canada Sedimentary Basin; in *Current Research 1998-E; Geological Survey of Canada, p. 63–74.*

Abstract: Fifty-seven shale samples from several Cretaceous stratigraphic units (Viking Formation of Colorado Group to Belly River Group) in the southern section of the Western Canada Sedimentary Basin were obtained for porosity analysis by helium and mercury porosimetry. This is part of a joint study between PanCanadian Petroleum Limited and the Geological Survey of Canada to investigate the source of subhydrostatic pressures within the basin.

Results indicate that these samples have petrophysical characteristics of extremely tight and well compacted shales, suggesting that most samples have experienced maximum paleoburial depths of more than 2.5–3.0 km. Given current sample depths of 0.5–2.8 km, this implies up to 2 km of erosion over the study area. These shales are generally at an early stage of diagenetic alteration. There is a general east to west decrease in pore-surface area, suggesting either an increase in degree of cementation or grain size or both, with some exceptions in the deeper formations.

Résumé : Cinquante-sept échantillons de shale ont été prélevés dans plusieurs unités stratigraphiques du Crétacé, soit de la Formation de Viking du Groupe de Colorado au Groupe de Belly River, dans la partie sud du Basin sédimentaire de l'Ouest du Canada, afin d'analyser leur porosité à l'aide du porosimètre à l'hélium et au mercure. Cette étude a été réalisée conjointement par PanCanadian Petroleum Limited et la Commission géologique du Canada dans le but d'étudier la source des pressions subhydrostatiques du bassin.

Les résultats révèlent que les caractéristiques pétrophysiques de ces échantillons sont celles de shales très peu perméables et très compacts. Par conséquent, la plupart des échantillons ont fort probablement été enfouis à une profondeur maximale de plus de 2,5 à 3,0 km. La profondeur actuelle des échantillons étant de 0,5 à 2,8 km, on peut conclure que la région étudiée a été affectée par une érosion allant jusqu'à 2 km de profondeur. Les shales en sont généralement à un stade initial d'altération diagénétique. On observe une diminution est-ouest générale de la surface des pores, ce qui traduirait un accroissement du degré de cimentation ou de la granulométrie ou des deux, sauf quelques exceptions dans les formations plus profondes.

---

[1] Research completed under the Industrial Partners Program (IPP) of the Geological Survey of Canada in collaboration with PanCanadian Petroleum Limited

[2] PanCanadian Petroleum Ltd., 150-9th Ave. S.W., Calgary, Alberta T2P 2S5

[3] GSC Calgary, Calgary

INTRODUCTION

Fifty-seven shale samples from various Cretaceous stratigraphic units (Colorado to Belly River groups) in the southern section of the Western Canada Sedimentary Basin (Fig. 1, Table 1), were obtained for porosity determination and analysis by helium and mercury porosimetry. This is part of a joint study between PanCanadian Petroleum Limited (PanCanadian) and the Geological Survey of Canada to investigate the possibility of shale physical property changes, in response to unloading by erosion of overburden, contributing to the development of subhydrostatic pressures within the Cretaceous succession of the Western Canada Sedimentary Basin. Grain density (δ_{GD}), helium porosity (ϕ_{He}), dry bulk density (δ_{BD}), skeletal density (δ_{SD}), mercury porosities (ϕ_{Hg1}, ϕ_{Hg2}), pore surface area (A), residual or storage porosity (ϕ_s), residual porosity ratio (ϕ_{rr}), and pore-size distribution mode (d_m) have been determined for all samples. In addition, PanCanadian Petroleum Limited has provided pressure gradient data for the Viking Formation. The purpose of this paper is to document the methods of investigation and the results of the data analysis.

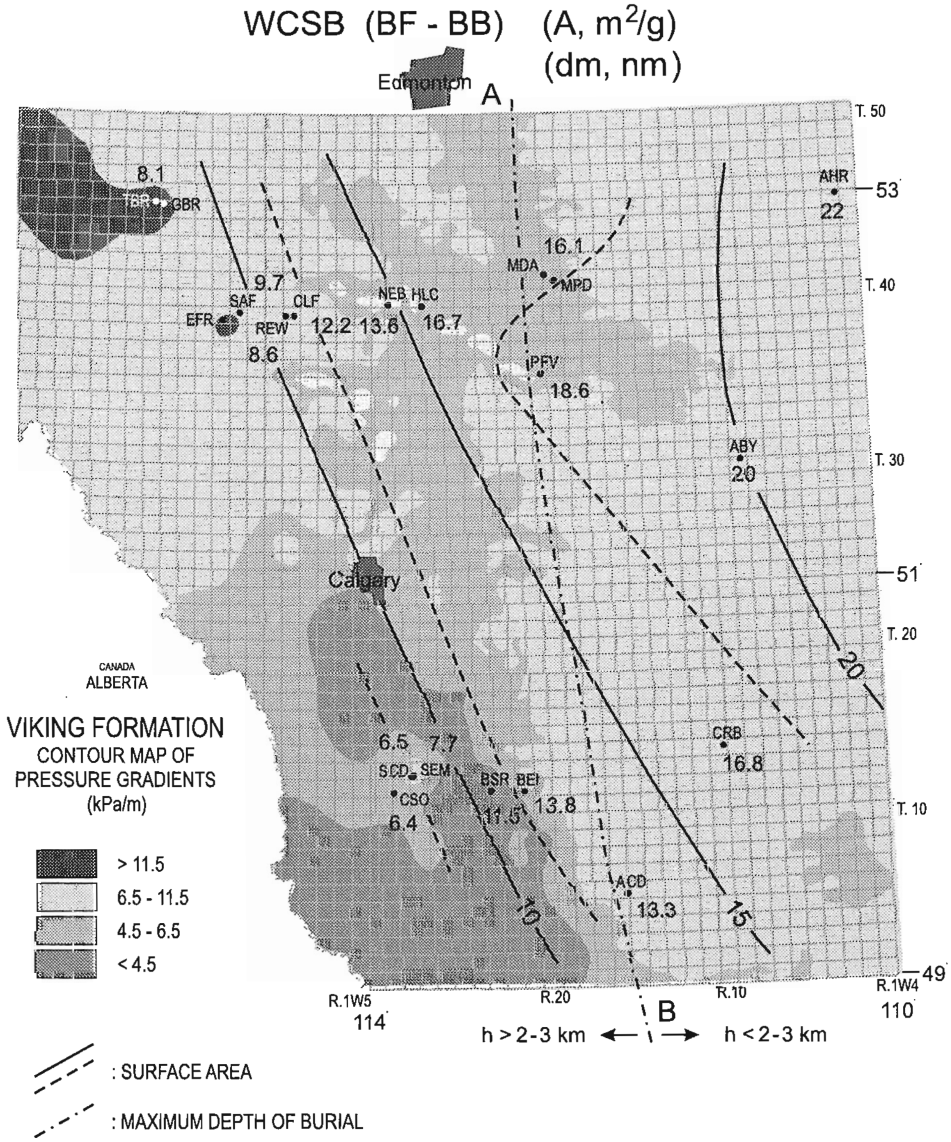

Figure 1. *Map of pore surface area (A) distribution for Western Canada Sedimentary Basin (WCSB) shales (Belle Fourche Formation, BF to Belly River Group, BB) above the Westgate Formation. The units of A are m²/g. Samples from west of line A-B are interpreted to have reached maximum paleoburial depths of ≥2.5 km; samples to the east reached maximum paleoburial depths of <2.5 km. The background is a simplified contour map of Viking Formation pressure gradients.*

Table 1a. Shale sample information and identification for the southern part of the study area (southern section of the Western Canada Sedimentary Basin).

Sample (No.)	Depth (km)	Well (I.D.)	Fm.	P_G (kPa/m)
SEM-01	1.580	Sinclair E. Matthews #1 4-8-13-27W4	UC	6.5-7.0
SEM-02	1.605		UC	
SEM-03	1.644		UC	
SEM-04	1.663		UC	
SEM-05	1.677		UC	
SEM-06	1.688		UC	
CSO-05	2.576	Rising (Canadian Superior) Oxley 6-7-12-28W4	SWS	5.0-5.5
CSO-10	2.581		SWS	
CSO-15	2.586		SWS	
CSO-20	2.591		BF	
CSO-25	2.596		BF	
CSO-30	2.601		BF	
CSO-35	2.606		BF	
CRB-01	0.565	CPOG Rainbow 6-23-14-10W	UC	9.0-9.5
CRB-02	0.574		SWS	
CRB-03	0.580		BF	
BEI-01	0.582	Banner et al Ironsup 7-9-12-21W4	UC	4.5-5.0
BEI-02	0.591		UC	
ACD-01	0.550	Amoco A-1 Conrad 11-12-6-16W4	SWS	7.0-7.5
ACD-03R	0.560		SWS	
ACD-04R	0.564		bnt	
ACD-07R	0.579		BF	
ACD-010R	0.594		BF	
ACD-013R	0.609		BF	
ACD-015	0.619		FS	
ACD-017	0.630		WG	
SCD-01	1.687	Sinclair C & E Dahl 2A 3-7-13-27W4	UC	6.5-7.0
SCD-02	2.095		BF	
SCD-03	2.103		WG	
BSR-04	1.244	Barons Superior #1 16-10-12-23W4	BF	3.5-4.0
BSR-09	1.254		FS	
BSR-12	1.260		WG	

P_G = Pressure gradient in the Viking Formation for each perspective well
UC = Upper Colorado Group (Colorado Group)
SWS = Second White Specks Formation
BF = Belle Fourche Formation
bnt = Bentonite
FS = Fish Scales Formation
WG = Westgate Formation

SHALE PORE STRUCTURE AND PARAMETERS

Basic pore structure parameters

A summary published previously (Katsube and Williamson, 1994, in press) on pore structure parameters used to characterize shales is repeated in part here. Among these parameters are effective porosity, ϕ_E, partial porosity, ϕ_a, residual porosity ratio, ϕ_{rr}, and pore surface area, A. The ϕ_E represents the pore space in all interconnected pores, and is expressed by

Table 1b. Shale sample information and identification for the northern part of the study area (southern section of the Western Canada Sedimentary Basin).

Sample (No.)	Depth (km)	Well (I.D.)	Fm.	P_G (kPa/m)
ABY-02	0.698	Amoco B-1 Youngstown Ev 6-34-30-8W4	SWS	7.5-8.0
ABY-07	0.723		SWS	
ABY-16	0.775		WG	
ABY-21	0.800		WG	
AHR-23R	0.487	Anderson Husky Roros 10-35-45-2W4	WG	9.5-10
AHR-25R	0.498		WG	
MDA-01	0.908	Merland Donalda 11-30-41-18W4	SWS	5.5-6.0
MDA-02	0.911		SWS	
MPD-01	1.000	Mobil Penzl 1B Donalda 11-15-41-18W4	WG	6.0-6.5
MPD-02	1.000		WG	
MPD-03	1.003		WG	
MPD-04	1.005		WG	
PFV-01	0.621	Paz Fennbv 9-3-36-19W4	BBR	5.5-6.0
HLC-01	1.447	Husky et al Lacombe 8-6-40-25W4	SWS	3.5-4.0
NEB-01	1.019	Nugate Blackfalds 13-5-40-27W4	BR BR	4.5-5.0
NEB-02	1.028			
CLF-01	1.797	CPOG Leaf 16-15-39-5W5	UC	9.5-10.0
REW-01	2.067	Resman et al Willgr 16-18-39-5W5	SWS	9.0-9.5
REW-02	2.203		VG	
SAF-01	2.214	SPC ATL Ferrier 14-22-39-8W5	UC	10.5-11.0
SAF-02	2.511		WG	
GBR-01	2.537	Gulf et al Brazr 16-30-45-12W5	WG	12.0-12.5
GBR-02	2.546		VG	
EFR-01	2.768	Esso Ferrier 6-10-39-9W5	WG	11.0-11.5
TBR-01	2.284	Trilogy et al Brazr 12-35-45-13W5	BS	12.0-12.5

P_G = Pressure gradient in the Viking Formation for each perspective well.
BR = Belly River Group
BBR = Basal Belly River Group
UC = Upper Colorado Group (Colorado Group)
SWS = Second White Specks Formation
BS = Blackstone Formation
WG = Westgate Formation
VG = Viking Formation

$$\phi_E = \phi_s + \phi_c \qquad (1)$$

where ϕ_s and ϕ_c are the porosities of the storage and connecting pores, respectively. The display format used for the pore-size distribution, d (Fig. 2), has each decade of the logarithmic pore-size scale (x-axis) subdivided into five ranges with equal physical spacing (Katsube and Issler, 1993). The porosity contained in each pore-size range is represented by ϕ_a. In principle, the sum of ϕ_a for all pore sizes is equal to ϕ_E. The ϕ_{rr} is represented by

$$\phi_{rr} = \phi_s/\phi_E. \qquad (2)$$

Pore surface area (A), in this case, is the sum of the pore surface area of all pore sizes represented by cylindrical tubes of varied diameters and length, and can be expressed by

$$A = \Sigma[4\phi_{ai}/(d_{ai}\ \delta_{BD})],\ (i=1 \text{ to } n) \qquad (3)$$

where ϕ_{ai} and d_{ai} are the partial porosity and geometric mean pore size for the i-th pore-size range and d_{BD} is the bulk density (Katsube et al., 1997).

Parameter determination

Helium and mercury-injection porosimetry methods were used to determine ϕ_E (Katsube et al., 1992a; Katsube and Issler, 1993; Issler and Katsube, 1994). Porosities determined by helium porosimetry are represented by ϕ_{He}, and those determined by mercury porosimetry are represented by ϕ_{Hg1} and ϕ_{Hg2}. The parameters, ϕ_{Hg1} and ϕ_{Hg2} represent the sum of the partial porosity values for the pore-sizes ranges of 0.003-10 µm and 0.003-250 µm, respectively (Katsube and Issler, 1993). Different laboratories may use different drying temperatures (25-116°C) that sometimes result in different values for the same sample (Katsube et al., 1992a). The ϕ_{rr} is determined by taking the ratio of the total mercury residual volume following extrusion over the total mercury intrusion volume using mercury porosimetry (Katsube et al., 1997). This is based on the assumption that mercury is trapped in the storage pores on depressurization. Grain density (δ_{GD}) has been determined by helium porosimetry, and dry bulk density (δ_{BD}) and skeletal density (δ_{SD}) have been determined by mercury porosimetry. In principle, δ_{GD} and δ_{SD} are identical.

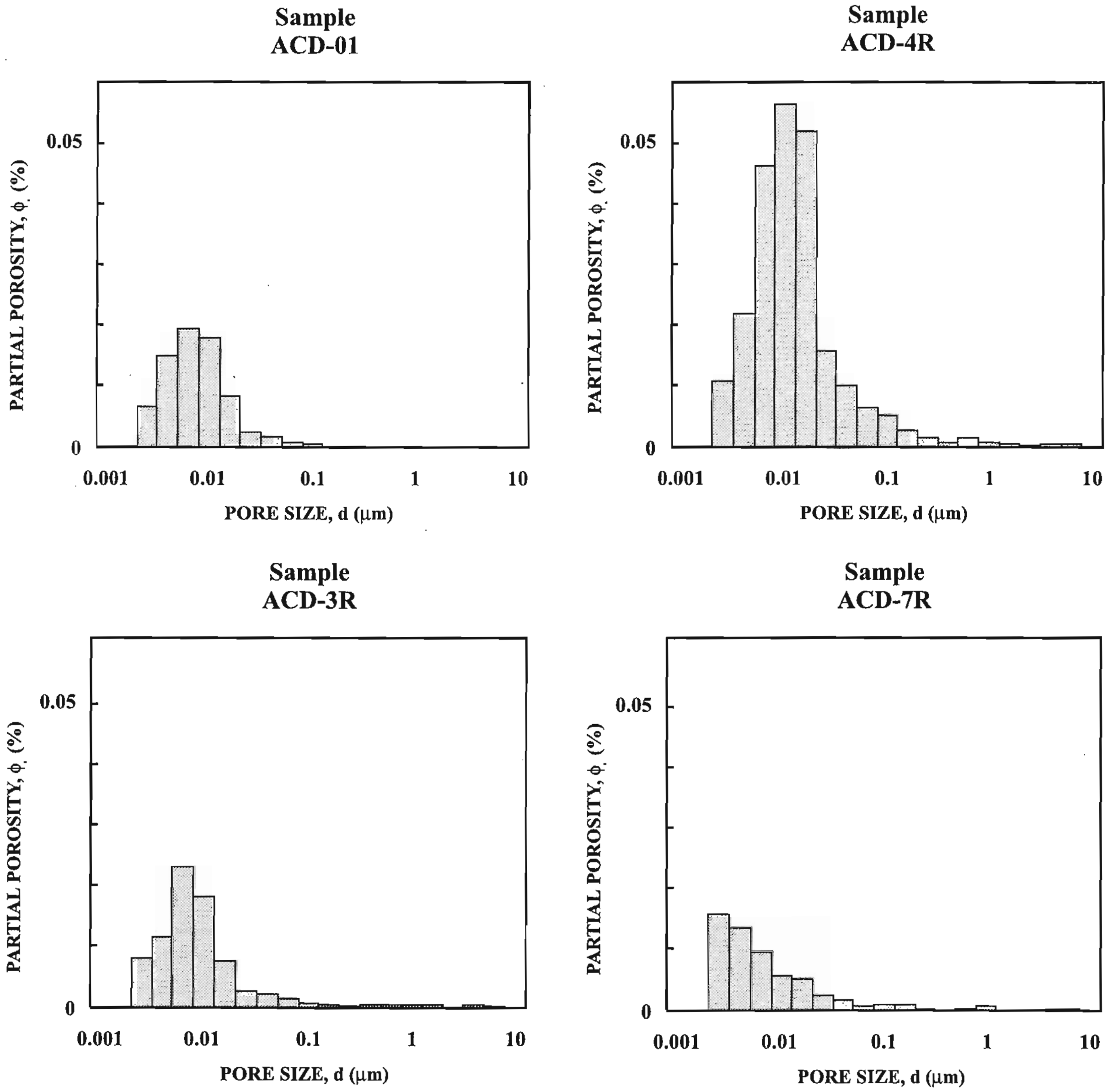

Figure 2. Histograms representing typical unimodal pore-size distributions of the Western Canada Sedimentary Basin (WCSB) shale samples that were investigated.

METHOD OF INVESTIGATION

Samples and sample preparation

Shale samples were collected from drill core obtained from petroleum exploration wells along two transects across southern Alberta (Fig. 1). They were selected on the basis of core availability and their distribution with respect to Viking Formation pressure gradients, which are 3.5-12.5 kPa/m for the sampled locations. The samples are mainly from shales of the late Albian-earliest Campanian Colorado Group (Viking, Westgate, Fish Scales, Belle Fourche, and Second White Specks formations and the undifferentiated upper Colorado Group). Three samples from the Campanian age Belly River Group are included also (*see* Bloch et al., 1993, for stratigraphic nomenclature). Sample depths range from approximately 500 m in the easternmost portions of the basin to 2800 m in the deep basin to the west. Table 1 lists information on sample numbers, depths, well names, stratigraphic units, and Viking Formation pressure gradients.

The samples comprise a range of rock types from bioturbated to laminated siltstones, mudstones, and claystones with a broad variation in mineralogical composition and organic matter content. Detailed geochemical, mineralogical, and petrological analyses have been undertaken for these samples and the results will be reported elsewhere. As part of the petrophysical investigations, at least two fragments (2-6 g) were taken from each of the original 57 samples for helium and mercury porosity determination. Additional fragment specimens were collected for 23 of the samples for repeat analyses to check on the accuracy and reliability of the measurements.

Method of formation pressure gradient (P_G) determination

A regional Viking Formation pressure gradient map for the study area was constructed, using drillstem test data available from the digital Canadian Institute of Formation Evaluation drillstem test database. Maximum formation pressures for each test were obtained from either a stabilized shut-in pressure or a Horner extrapolation of continuously building shut-in pressures, in order to determine the true reservoir pressure. Only the highest quality pressure data were selected to compute the formation pressures (P_f), and the pressure gradient (P_G) was determined by dividing P_f by the depth of the recorder used to obtain that data. Anomalous formation pressure lows resulting from hydrocarbon production pressure depletion were screened out by use of data such as pressure versus elevation plots. The resulting pressure gradient map (Fig. 1 and 5) shows low P_G values in the southwest part of the study area, extending to the north and cutting across topographic variations as well as geological variations within the Viking Formation. The lower P_G values in the southeast portion of the study area are clearly associated with local topographic highs — the Cypress Hills.

Helium porosity measurements

Samples used for helium porosimetry were oven dried for 24 h at 105°C (220°F), while under vacuum. This was followed by cooling, in a desiccator, prior to the helium porosity measurements. The helium porosities (ϕ_{He}) were determined by first using a Boyle's Law double-celled helium porosimeter to obtain grain volume. Then the bulk volume of the samples was obtained using the mercury immersion (Archimedes principle) technique. Pore volumes were computed from the difference between the bulk and grain volumes. These measurements and procedures generally follow the recommended practices of the American Petroleum Institute (American Petroleum Institute, 1960). Further details of the procedures and equipment used in this study have been described in the literature (Loman et al., 1993).

Mercury porosimetry measurements

Specimens of the shale samples used for mercury intrusion porosimetry were initially oven dried for 24 h at 105°C (220°F), while under vacuum. This was followed by cooling, in a desiccator, prior to the measurement. The pore-size distribution of the samples was then determined by mercury intrusion porosimetry, following the procedures described in previous publications (e.g. Katsube and Walsh, 1987; Katsube and Issler, 1993), using an equilibration time of 45 s for each of the high pressure steps, and 10 s for the low pressure (<0.7 MPa) steps. This technique was first suggested by Washburn (1921). In principle, the mercury porosimeter can generate pressures high enough to force mercury into all accessible pores and measure the volume of mercury taken up by them (Rootare, 1970). Assuming cylindrical pore shapes, the Washburn equation (Rootare, 1970) relates the amount of pressure, p, required to force mercury into pores with pore-size diameter, d, greater than or equal to

$$d = -4\gamma\cos(\theta)/p, \qquad (4)$$

where γ is the surface tension of mercury, and θ is the contact angle. Values of θ=140° and γ=0.48 N/m were used in this study. These measurements were made by using a Micromeritics Autopore 9200 mercury porosimeter with an available pressure range of 0.14-420 MPa and an equivalent pore-size range of 250-0.003 μm.

Determination of pore-size distribution

The mercury injection pressure was incrementally increased from 0.14 MPa to 420 MPa in 56 pressure steps, and the volume of mercury intruded for each step measured. The pressure steps, more or less, equally divide the entire pressure range on a logarithmic scale. As each pressure step represents a certain pore size, the volume of mercury intruded for each step can be converted into the porosity of that pore size (e.g. Katsube and Issler, 1993). The pore-size distributions are plotted in a standard format (*see* Fig. 2) by grouping the data into different size classes (*see* Katsube and Issler, 1993; Katsube and Williamson, 1994).

Table 2a. Helium and mercury porosity data for the shale samples from the southern part of the study area (southern section of the Western Canada Sedimentary Basin).

Sample	Fm	h	δ_{GD}	δ_{BD}	δ_{SD}	ϕ_{He}	ϕ_{Hg1}	ϕ_{Hg2}	A	ϕ_s	ϕ_{rr}	ϕ_{cc}	d_m
SEM-01	UC	1.58	2.71	2.59	2.73	5.4	4.7	4.9	8.1	2.8	0.59	1.9	7.9
SEM-02		1.61	2.68	2.61	2.75	7.1	4.7	5.2	10.7	1.4	0.30	3.3	5.0
SEM-03		1.64	2.66	2.62	2.70	3.7	2.6	2.9	5.7	0.91	0.35	1.7	5.0
SEM-04		1.66	2.65	2.61	2.73	6.6	4.2	4.5	9.6	1.2	0.28	3.0	5.0
SEM-05		1.68	2.65	2.59	2.69	3.2	2.9	3.5	6.1	1.5	0.51	1.4	5.0
SEM-06		1.69	2.71	2.58	2.70	5.4	4.0	4.4	9.0	1.8	0.46	2.2	5.0
CSO-05	SWS	2.58	2.58	2.55	2.65	2.4	3.3	3.8	8.1	1.3	0.39	2.0	3.2
CSO-10		2.58	2.64	2.57	2.69	7.1	4.1	4.4	10.0	0.90	0.22	3.2	3.2
CSO-15		2.59	2.56	2.53	2.62	1.6	2.7	3.2	6.5	1.1	0.40	1.6	3.2
CSO-20	BF	2.59	2.62	2.57	2.65	4.1	2.8	3.1	5.9	1.2	0.43	1.2	5.0
CSO-25		2.60	2.71	2.63	2.72	2.8	2.9	3.3	5.6	1.5	0.53	1.4	5.0
CSO-30		2.60	2.69	2.62	2.71	1.8	2.9	3.6	5.2	1.7	0.58	1.2	5.0
CSO-35		2.61	2.65	2.64	2.75	1.5	3.6	4.0	7.0	1.8	0.49	1.8	5.0
CRB-01	UC	0.57	2.65	2.27	2.64	15.8	13.5	14.3	15.6	7.7	0.57	5.8	20
CRB-02	SWS	0.57	2.59	2.26	2.59	19.4	12.4	12.7	18.8	7.9	0.64	4.5	13
CRB-03	BF	0.58	2.65	2.22	2.52	19.8	9.3	11.9	16.1	9.0	0.97	0.3	5.0
BEI-01	UC	0.58	2.73	2.49	2.64	8.4	5.6	5.9	13.1	3.2	0.58	2.4	5.0
BEI-02		0.59	2.68	2.48	2.68	8.3	7.0	7.3	14.6	4.1	0.59	2.9	7.9
ACD-01	SWS	0.55	2.69	2.45	2.65	8.4	7.3	7.5	13.2	4.3	0.59	3.0	7.9
ACD-03R		0.56	2.73	2.46	2.68	8.1	7.8	8.3	13.3	4.6	0.59	3.2	7.9
ACD-04R	bnt	0.56	2.70	2.04	2.69	26.6	23.4	24.3	35.9	17.3	0.74	6.1	13
ACD-07R	BF	0.58	2.63	2.51	2.68	2.4	5.7	6.3	13.1	3.2	0.56	2.5	3.2
ACD-010R		0.59	2.63	2.51	2.67	2.3	5.1	5.6	13.5	2.3	0.46	2.8.	5.0
ACD-013R		0.61	2.65	2.38	2.65	9.6	9.6	10.3	13.4	6.0	0.63	3.6	5/1
ACD-015	FS	0.62	2.55	2.33	2.53	8.1	7.5	7.7	20.2	4.4	0.59	3.1	30
ACD-017	WG	0.63	2.74	2.33	2.66	13.6	11.3	12.5	14.8	7.6	0.67	3.3	5.0
													20
SCD-01	UC	1.69	2.67	2.58	2.67	3.7	3.0	3.4	6.74	2.0	0.65	1.1	
SCD-02	BF	2.10	2.64	2.61	2.70	8.1	3.3	3.7	6.33	1.7	0.51	1.6	3.2
SCD-03	WG	2.10	2.74	2.53	2.73	15.1	6.9	7.3	11.5	4.4	0.64	2.5	7.9
													7.9
BSR-04	BF	1.24	2.52	1.87	1.95	1.4	4.0	4.5	13.5	2.4	0.61	1.6	
BSR-09	FS	1.25	2.59	2.52	2.63	2.3	3.9	4.2	9.5	1.8	0.45	2.2	5.0
BSR-12	WG	1.26	2.74	2.48	2.66	6.9	6.5	6.9	9.7	3.8	0.58	2.7	5.0
													7.9

h = Depth (km) from which the sample was obtained
δ_{GD} = Grain density (g/mL) determined by helium porosimetry
δ_{BD} = Dry bulk density (g/mL) determined by mercury porosimetry
δ_{SD} = Skeletal density (g/mL) determined by mercury porosimetry
ϕ_{He} = Total porosity determined by helium porosimetry (%)
ϕ_{Hg1} = Total porosity determined by mercury porosimetry for pore sizes up to 10 µm (%)
ϕ_{Hg2} = Total porosity determined by mercury porosimetry for pore sizes up to 250 µm (%)
A = Pore surface area (m²/g)
ϕ_s = Residual or storage porosity (%)
ϕ_{rr} = ϕ_s/ϕ_{Hg1}
ϕ_{cc} = Connecting porosity (ϕ_{Hg1}-ϕ_s)
d_m = Mode of nano-pore distribution (nm)
UC = Upper Colorado Group (Colorado Group)
SWS = Second White Specks Formation
BF = Belle Fourche Formation
bnt = Bentonite
FS = Fish Scales Formation
WG = Westgate Formation

Table 2b. Helium and mercury porosity data for the shale samples from the northern part of the study area (southern section of the WCSB).

Sample	Fm	h	δ_{GD}	δ_{BD}	δ_{SD}	ϕ_{He}	ϕ_{Hg1}	ϕ_{Hg2}	A	ϕ_s	ϕ_{rr}	ϕ_{cc}	d_m
ABY-02	SWS	0.70	2.52	2.19	2.53	17.5	12.8	13.3	19.7	8.1	0.63	4.7	20
ABY-07		0.72	2.62	2.14	2.57	26.5	15.4	16.5	20.3	9.2	0.60	6.2	20
ABY-16	WG	0.78	2.72	2.24	2.66	16.2	15.3	15.6	21.7	9.5	0.62	5.2	13
ABY-21		0.80	2.87	2.25	2.75	13.5	16.6	18.4	22.5	10.3	0.62	6.3	20
AHR-23R	WG	0.49	2.63	2.17	2.71	20.7	18.1	19.6	23.5	11.4	0.63	6.7	20
AHR-25R		0.50	2.72	2.14	2.61	20.7	16.9	18.0	20.4	10.5	0.62	6.4	20
MDA-01	SWS	0.91	2.61	2.37	2.62	9.3	8.8	9.4	15.5	5.2	0.59	3.6	7.9
MDA-02		0.91	2.58	2.30	2.56	8.2	9.6	10.2	16.6	5.6	0.58	4.0	13
MPD-01	WG	1.00	3.48	3.18	3.34	4.6	4.6	4.8	4.6	2.9	0.62	1.8	20
MPD-02		1.00		2.42	2.72		10.6	11.1	14.5	6.2	0.59	4.4	20
MPD-03		1.00		2.33	2.70		10.4	13.8	12.4	9.0	0.87	7.9	20
MPD-04		1.00		2.32	2.68		12.6	13.8	17.8	7.6	0.61	5.0	13
PFV-01	BBR	0.62	2.70	2.19	2.62	17.7	16.2	16.8	18.6	9.7	0.60	6.5	32
HLC-01	SWS	1.45	2.72	2.49	2.69	7.7	6.8	7.5	16.7	3.5	0.51	3.3	5
NEB-01	BR	1.02	2.71	2.43	2.70	11.9	9.9	10.3	13.0	5.7	0.58	4.2	20
NEB-02		1.03	2.61	2.33	2.60	13.5	9.9	10.4	14.2	5.5	0.56	4.4	20
CLF-01	UC	1.80	2.76	2.53	2.69	7.1	5.8	6.3	12.2	3.2	0.56	2.6	5.0
REW-01	SWS	2.07	2.57	2.51	2.62	1.0	3.9	4.4	8.6	2.0	0.51	1.9	5.0
REW-02	VG	2.20	2.65	2.51	2.66	4.6	5.3	5.7	7.3	3.1	0.58	2.2	13
SAF-01	UC	2.21	2.77	2.55	2.69	7.6	4.7	5.1	9.7	2.4	0.50	2.4	5.0
SAF-02	WG	2.51	2.71	2.99	3.19	9.0	6.1	6.6	9.4	3.6	0.59	2.5	7.9
GBR-01	WG	2.54	2.63	2.55	2.74	3.0	6.4	6.8	12.1	3.4	0.53	3.0	7.9
GBR-02	VG	2.55	2.64	2.53	2.69	3.8	5.4	5.9	12.2	3.4	0.63	2.0	5.0
EFR-01	WG	2.77	2.63	2.58	2.70	1.9	4.0	4.8	9.2	2.6	0.64	1.4	3.2
TBR-01	BS	2.28	2.65	2.56	2.67	3.3	3.8	4.1	8.1	2.2	0.57	1.6	5.0

h = Depth (km) from which the sample was obtained
δ_{GD} = Grain density (g/mL) determined by helium porosimetry
δ_{BD} = Dry bulk density (g/mL) determined by mercury porosimetry
δ_{SD} = Skeletal density (g/mL) determined by mercury porosimetry
ϕ_{He} = Total porosity determined by helium porosimetry (%)
ϕ_{Hg1} = Total porosity determined by mercury porosimetry for pore sizes up to 10 μm (%)
ϕ_{Hg2} = Total porosity determined by mercury porosimetry for pore sizes up to 250 μm (%)
A = Pore surface area (m^2/g)
ϕ_s = Residual or storage porosity (%)
ϕ_{rr} = ϕ_s/ϕ_{Hg1}
ϕ_{cc} = Connecting porosity (ϕ_{Hg1}-ϕ_s)
d_m = Mode of nano-pore distribution (nm)
BR = Belly River Group
BBR = Basal Belly River Group
UC = Upper Colorado Group (Colorado Group)
SWS = Second White Specks Formation
BS = Blackstone Formation
WG = Westgate Formation
VG = Viking Formation

ANALYTICAL RESULTS

Results of the grain density (δ_{GD}) and porosity (ϕ_{He}) determinations by helium porosimetry are presented in Table 2a for the shale samples from the southern part of the study area, and in Table 2b for the northern part. Typical examples of the pore-size distribution determined by mercury porosimetry are presented in Table 3 and in Figure 2. Data for partial porosity, ϕ_a, which is the porosity contributed by each pore-size range, are listed in the columns of Table 3 for each sample. The parameter, d_a (first column), is the geometric mean for each pore-size range (nm). The data derived from the pore-size distribution are listed in the lower section of Table 3. These are dry bulk density (δ_{BD}), skeletal density (δ_{SD}), mercury porosities (ϕ_{Hg1}, ϕ_{Hg2}), pore surface area (A), residual or storage porosity (ϕ_s), residual porosity ratio (ϕ_{rr}), and mode of pore-size distribution (d_m). Previous studies (Katsube et al., 1992b) suggest that d_m represents the pore size of the main fluid-flow paths through the rock. These data for all 57 samples are listed in Tables 2a and 2b.

In principle, ϕ_{Hg1}, ϕ_{Hg2}, and ϕ_{He} represent the effective porosity, f_E (Katsube and Williamson, 1994). However, differences in experimental technique and measurement procedures lead to systematic variations among these parameters. For the mercury porosimetry method, it is more certain that f_{Hg1} is accurate for its limited pore-size range (0.003-10 µm), because ϕ_{Hg2} which encompasses a broader pore-size range (0.003-250 mm), may include measurement errors such as those originating from the space between the specimen and sample container (Katsube and Issler, 1993). On the other hand, ϕ_{He} is generally larger than either ϕ_{Hg1} or ϕ_{Hg2} (Table 2) because it includes the porosity of pores smaller than 3 nm (Katsube and Williamson, 1994), the lower limit for the pore-sizes measured by the mercury porosimetry method that was used. Although analysis of the porosity measurement procedures are beyond the scope of this paper, it should be noted that most porosity values less than 5%, produce f_{He} values systematically smaller than both the ϕ_{Hg1} and ϕ_{Hg2} values (Table 2). This is contrary to theory, suggesting that measurement procedural errors may be suspected.

Table 3. Typical examples of pore-size distribution data for different pore-size ranges, d, obtained by mercury porosimetry for 8 shale samples from the southern part of the study area (southern section of the Western Canada Sedimentary Basin).

Sample #	ACD-01	ACD-3R	ACD-4R	ACD-7R	ACD-10	ACD-13	ACD-15	ACD-17
d_a(nm)	ϕ_a (%)							
3.2	0.66	0.79	1.08	1.55	1.58	1.14	2.03	0.67
5.0	1.50	1.13	2.18	1.33	1.63	1.19	2.29	0.98
7.9	1.94	2.29	4.63	0.93	0.80	1.14	1.45	1.68
12.6	1.79	1.79	5.63	0.55	0.40	0.88	0.63	2.02
20.0	0.83	0.76	5.18	0.50	0.25	1.09	0.40	3.42
31.6	0.25	0.27	1.57	0.23	0.15	0.86	0.21	1.16
50.1	0.17	0.22	1.02	0.18	0.13	0.88	0.16	0.49
79.4	0.07	0.15	0.65	0.08	0.05	0.74	0.12	0.19
126	0.05	0.07	0.51	0.10	0.08	0.90	0.02	0.12
200	0.00	0.05	0.27	0.10	0.00	0.45	0.07	0.02
316	0.00	0.02	0.14	0.03	0.03	0.29	0.00	0.05
501	0.00	0.05	0.08	0.00	0.00	0.00	0.12	0.07
794	0.00	0.05	0.14	0.03	0.00	0.02	0.00	0.07
1259	0.00	0.05	0.08	0.08	0.00	0.00	0.00	0.09
1995	0.00	0.05	0.06	0.00	0.00	0.00	0.00	0.09
3162	0.00	0.00	0.02	0.00	0.00	0.00	0.00	0.05
5012	0.00	0.05	0.04	0.03	0.00	0.00	0.00	0.12
7943	0.00	0.02	0.04	0.03	0.00	0.00	0.00	0.05
ϕ_{Hg1}	7.3	7.8	23.4	5.7	5.1	9.6	7.5	11.3
ϕ_{Hg2}	7.5	8.3	24.3	6.3	5.6	10.3	7.7	12.5
δ_{BD}	2.45	2.46	2.04	2.51	2.51	2.38	2.33	2.33
δ_{SD}	2.65	2.68	2.69	2.68	2.67	2.65	2.53	2.66
A	13.2	13.3	35.9	13.1	13.5	13.4	20.2	14.8
ϕ_{rr}	0.59	0.59	0.74	0.56	0.46	0.63	0.59	0.67
ϕ_s	4.3	4.6	17.3	3.2	2.3	6.0	4.4	7.6
d_m	7.9	7.9	13	3.2	5.0	5/130	5.0	20
h	550	560	564	579	594	609	619	630

δ_a = Geometric mean pore-sizes for the different pore-size ranges, d (nm)
ϕ_a = Partial porosity (%)
ϕ_{Hg1} = Total porosity measured by mercury porosimetry for pore sizes up to 10 µm (%)
ϕ_{Hg2} = Total porosity measured by mercury porosimetry for pore sizes up to 250 µm (%)
δ_{BD} = Dry bulk density (g/mL)
δ_{SD} = Skeletal density (g/mL)
A = Pore surface area (m²/g)
ϕ_{rr} = ϕ_s/ϕ_{Hg1}
ϕ_s = Residual or storage porosity (%)
d_m = Mode of pore-size distribution (nm)
h = Depth (m) from which the sample was obtained

The pore-size distribution patterns of shales are generally characterized by unimodal distributions (Katsube and Williamson, 1994). This is regardless of the magnitudes of their porosities or the depths from which these shales are obtained. This is in contrast with other rocks, such as igneous rocks (e.g. granites), where bimodal and trimodal distributions are common (Agterberg et al., 1984; Katsube and Hume, 1987). This unimodal pore-size distribution can be characterized by the following four parameters (Katsube and Williamson, in press): effective porosity (ϕ_E), mode of pore-size distribution (d_m), surface area (A), and residual porosity ratio (ϕ_{rr}). These data are included in Tables 2a and 2b.

DISCUSSION

Values for grain (δ_{GD}), dry bulk (δ_{BD}), and skeletal densities (δ_{SD}) of these shales are in the ranges of 2.52–2.87, 2.04–2.64, and 2.52–2.75 g/mL, respectively, with the exception of samples MPD-01 (δ_{GD}=3.48 g/mL, δ_{BD}=3.18 g/mL, δ_{SD}=3.34 g/mL) and SAF-02 (δ_{SD}=3.19 g/mL), which have higher values and sample BSR-04 (δ_{BD}=1.87 g/mL, δ_{SD}=1.95 g/mL), which has lower values. These δ_{BD} values are similar to those previously reported for shales (δ_{BD}=1.73–2.61 g/mL, Issler and Katsube, 1994; Katsube and Williamson, 1994). The δ_{SD} (including δ_{BD}) value for sample BSR-04 may be erroneously low, given the large discrepancy between the corresponding δ_{GD} (2.52 g/mL) value. The porosity values (ϕ_{He},ϕ_{hg1}, and ϕ_{Hg2}) for these shales are in the range of 1.0–26.6%, which is comparable to previous values reported for shales (1.4–39.3%; Issler and Katsube, 1994; Katsube and Williamson, 1994).

The histograms in Figure 2 are representative of the generally unimodal pore-size distributions of these shales which display small d_m values, and are typical of tight shales (Katsube and Issler, 1993; Katsube and Williamson, 1994; Katsube et al., 1995). Most of the d_m values are equal to or smaller than 7.9 nm, except for those from the eastern part of our study area (Fig. 1). These characteristics are typical of well compacted shales having extremely small pore throats and highly tortuous flow paths which results in very low permeabilities (Katsube and Williamson, 1994, 1995). The bentonite sample (ACD-4R, Fig. 2) is anomalous with respect to the other shales: it has unusually high porosity values (23–27%) for its depth and an atypically low d_m (13 nm) value for shales with such high porosities (Katsube and Issler, 1993; Katsube and Williamson, 1994). Based on previous work (Katsube and Issler, 1993; Katsube et al., 1995; Katsube and Williamson, 1995), these small d_m characteristics suggest that the majority of these shale samples have experienced burial depths greater than the critical depths of burial (CDB, Katsube and Williamson, 1994, 1995), which is 2.5–3.0 km. The one-dotted broken line, A-B, in Figure 1 represents the division between samples showing d_m<7.9 nm to the west and d_m>7.9 nm to the east. Based on this pore-size criterion, it is interpreted that the shale samples west of the A-B line have experienced maximum paleoburial depths of at least 2.5 km. This implies that shallow samples immediately west of the A-B line provide minimum erosion estimates of 1.0–2.0 km for this area.

A histogram or frequency distribution for the pore surface area (A) values of the Western Canada Sedimentary Basin shales is displayed in Figure 3, and is compared to those of three other basins. The A values for the Oak Ridge National Reservation and Venture Gas Field (Sable Basin) are generally below 10 m^2/g, and represent shales that are well cemented or have experienced significant diagenetic alteration (Katsube and Williamson, 1994; Dorsch et al., 1996). Shales from the Beaufort-Mackenzie Basin are relatively unaltered and have experienced little or no diagenetic cementation (Bloch and Issler, 1996). High A values imply fine-grained and poorly cemented or uncemented shales. Low A values imply well cemented fine- or coarse-grained shales, or

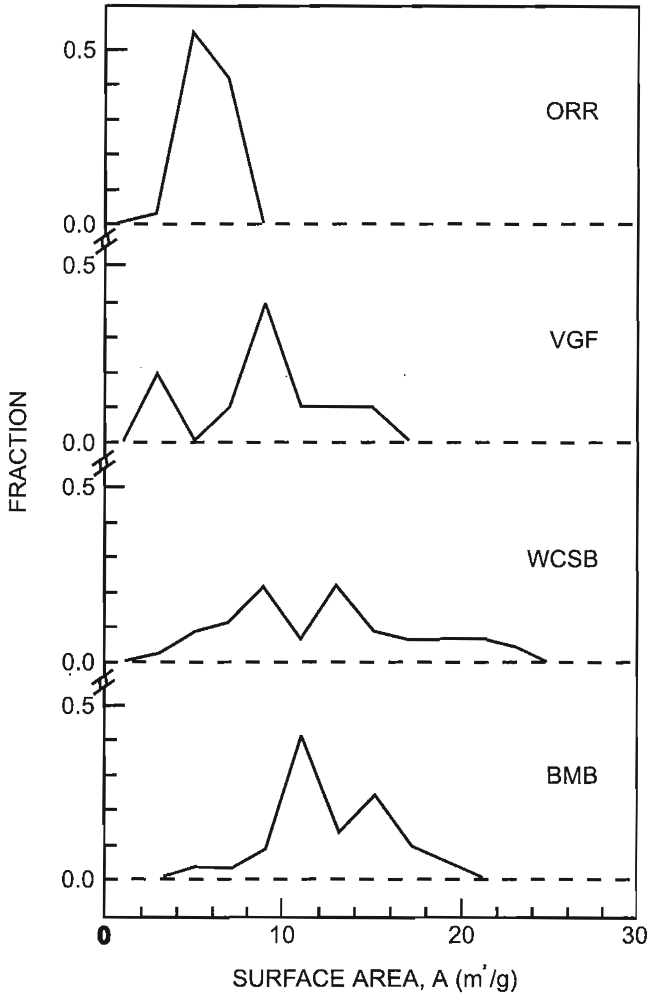

Figure 3. Histograms displaying shale pore surface area (A) distributions in four basins: the ORR (Oak Ridge National Reservation, Tennessee, U.S.A.), the VGF (Venture Gas Field, offshore Nova Scotia), the WCSB (Western Canada Sedimentary Basin, Western Canada), and the BMB (Beaufort-Mackenzie Basin, northern Canada).

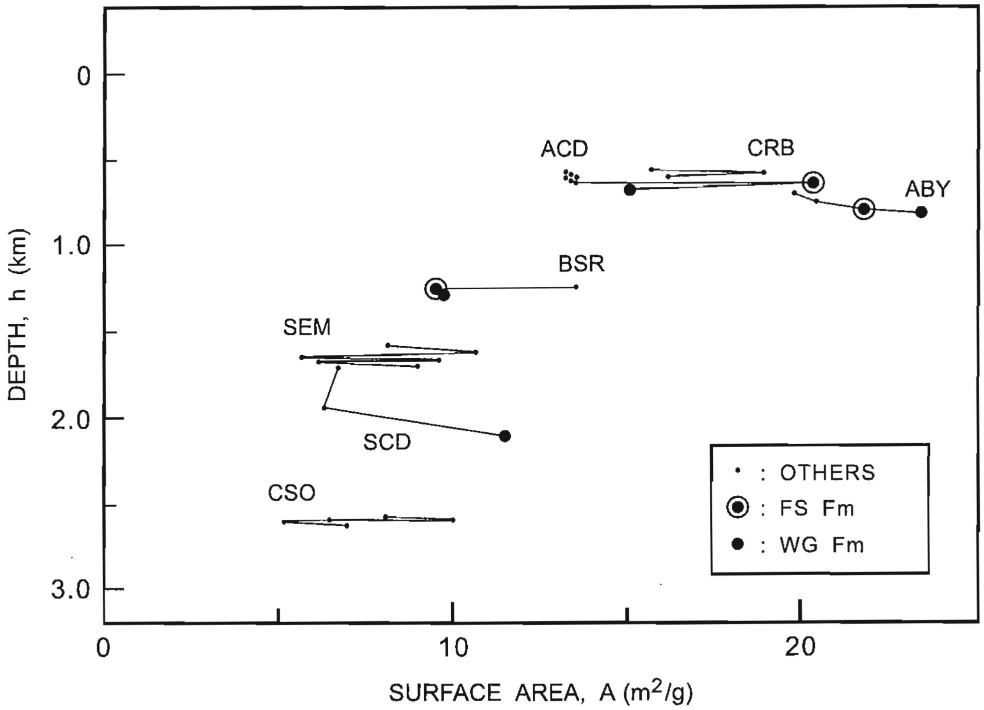

Figure 4.

Down-hole pore surface area (A) distributions for wells, in the Western Canada Sedimentary Basin , from which three or more shale samples were analyzed (see Table 1 for well codes: e.g. ACD, CRB; FS: Fish Scales, WG: Westgate).

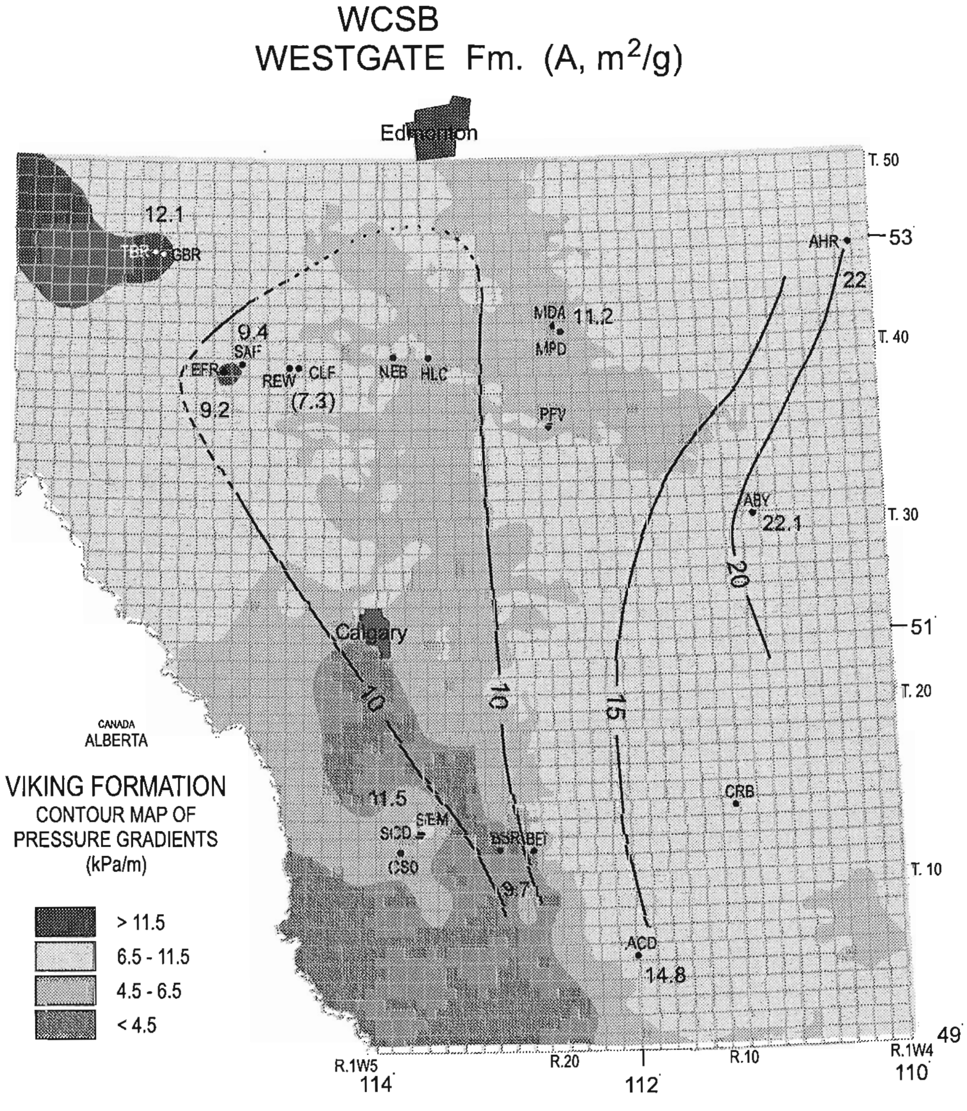

Figure 5.

Map of pore surface area (A) distribution for the Westgate Formation in the Western Canada Sedimentary Basin (WCSB). The units of A are m²/g. The background is a simplified contour map of Viking Formation pressure gradients.

uncemented coarse-grained shales (Katsube et al., 1998). Western Canada Sedimentary Basin shales show the widest range of values of these four basins, but display characteristics that more closely resemble those of the Beaufort-Mackenzie Basin than the Oak Ridge National Reserve or Venture Gas Field. This suggests that the Western Canada Sedimentary Basin shales are either poorly cemented with a wide range of grain sizes, or contain a section with some cemented shales.

The down-hole distribution of A for wells from which three or more samples were analyzed are displayed in Figure 4. Each well shows a wide range of A values, but the variation between wells is larger than the variation within individual wells. Average A values for each well were determined and plotted in Figure 1. The A values for the Fish Scales and Westgate formations were eliminated from these determinations, since most values for these formations differ considerably from those of the other formations (Tables 2a, b; Fig. 4). The A distribution for the formations above the Fish Scales Formation displays a general decrease from east to west (Fig. 1). This suggests that there is either an increased degree of cementation or coarsening in grain size, or both, towards the west in these formations. A similar plot for the Westgate Formation is displayed in Figure 5. In this case, a zone of low A extending in the north-south direction about the central section of the study area is seen. No plot was produced for the Fish Scales Formation, due to an insufficient number of samples.

The ϕ_{rr} is plotted against A in Figure 6, for the three of the Western Canada Sedimentary Basin Cretaceous formations: Westgate, Belle Fourche, and Second White Specks. Although, the correlation between the two parameters is rather poor, the correlation factor (r) being 0.38–0.73 for the three formations, a clear variation in slope (a_1) of the linear relationships is seen. This linear relationship is represented by the reduced major axis (RMA, Davis, 1986; Katsube and Agterberg, 1990). The slope of the ϕ_{rr}-A relationship is 0.009–0.026 g/m^2, with Second White Specks Formation displaying the largest value and the Westgate Formation the smallest (Fig. 6). These a_1 values are positive but are smaller than those (a_1=0.4–0.6; Katsube et al., 1997) of the Jurassic shales from the Venture Gas Field (Sable Basin; Katsube and Williamson, 1994), which are characterized by an advanced stage of diagenetic cementation. However, they are considerably larger than those of the Late Cretaceous to Tertiary shales from the Beaufort-Mackenzie Basin, which are characterized by little diagenetic cementation (Bloch and Issler, 1996).

CONCLUSIONS

Results of analyzing the porosity and pore-size distribution data for the 57 shale samples from several formations (Viking Formation to Belly River Group) in the southern part of the Western Canada Sedimentary Basin, indicate the following:

1. These shales display pore-size distribution characteristics of tight and well compacted, very low permeability shales. In addition, most of these samples have experienced burial depths greater than 2.5–3.0 km, implying on the order of 2 km of overburden removal for at least the western section of the study area.
2. The pore surface area (A) characteristics suggest that these shales consist of a wide range of grain sizes, and that their degree of diagenetic cementation is generally low.
3. There is an east to west decrease in pore surface area (A) values within the Colorado Group shales (Second White Specks Formation-Belly River Group) for this study area. This suggests that there is either an increase in the degree of diagenetic cementation or coarsening of grain size, or both, towards the west. The shale pore surface area (A) distribution in the Westgate Formation differs somewhat from the other Colorado Group shales, with a zone of low A values extending in the north-south direction about the central section of the study area.
4. The residual porosity ratio versus pore surface area relationship (ϕ_{rr}-A) suggests that these shales have characteristics somewhere between well cemented and poorly cemented shales, with the possibility of the Second White Specs shales being on the higher end of the degree of cementation. This is somewhat contradictory to (2), and requires further investigation.

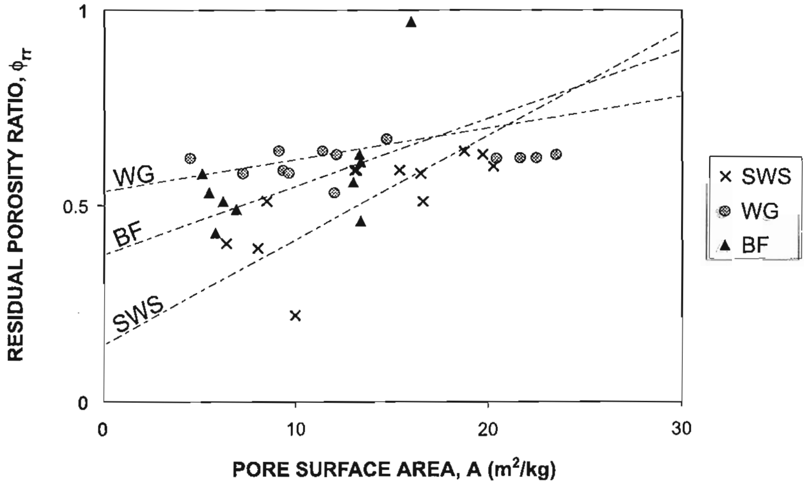

Figure 6.

Residual porosity ratio (ϕ_{rr}) as a function of pore surface area (A) for three formations in the Western Canada Sedimentary Basin : WG (Westgate), BF (Belle Fourche) and SWS (Second White Specks). The equations for the reduced major axis (RMA, Davis, 1986; Katsube and Agterberg, 1990) and the correlation factor (r) for the three formations are

RMA: $\phi_{rr} = a_0 + a_1A$ (r),
SWS: $\phi_{rr} = 0.15 + 0.026A$ (r = 0.73),
BF: $\phi_{rr} = 0.37 + 0.017A$ (r = 0.40),
WG: $\phi_{rr} = 0.53 + 0.009A$ (r = 0.38).

ACKNOWLEDGMENTS

The data used in this study were obtained as a result of a joint study between PanCanadian Petroleum Limited and the Geological Survey of Canada. The core samples used in this study were obtained from the Alberta Energy and Utility Board Core Research Center. The mercury porosimetry was carried out at ORTECH International (Toronto, Ontario) under the supervision of B. Smith, and the helium porosimetry was performed at K&A Energy Consultants Inc. (Tulsa, Oklahoma) under the supervision of J.M. Loman. The authors thank J.B. Percival (GSC, Ottawa) for critically reviewing this paper. They have benefited considerably from her very useful and constructive comments. The authors also thank S. Connell (GSC, Ottawa) for her comments.

REFERENCES

Agterberg, F.P., Katsube, T.J., and Lew, S.N.
1984: Statistical analysis of granite pore size distribution data, Lac du Bonnet batholith, Eastern Manitoba; *in* Current Research, Part A; Geological Survey of Canada, Paper 84-1A, p. 29-37.

American Petroleum Institute (API)
1960: Recommended practices for core-analysis procedure; API Recommended Practice 40 (RP 40) First Edition, American Petroleum Institute, Washington, D.C., 55 p.

Bloch, J. and Issler, D.R.
1996: Petrographic and geochemical analyses of Beaufort-Mackenzie Basin shales; Geological Survey of Canada, Open File 3220, 95 p.

Bloch, J., Schröder-Adams, C., Leckie, D.A., McIntyre, D.J., Craig, J., and Staniland, M.
1993: Revised stratigraphy of the lower Colorado Group (Albian to Turonian), Western Canada; Bulletin of Canadian Petroleum Geology, v. 41, no. 3, p. 325-348.

Davis, J.C.
1986: Statistics and Data Analysis in Geology; John Wiley & Sons, p. 200-204.

Dorsch, J., Katsube, T.J., Sanford, W.E., Dugan, B.E., and Tourkow, L.M.
1996: Effective porosity and pore-throat sizes of Conasauga group mudrock: application, test and evaluation of petrophysical techniques; Oak Ridge National Laboratory (U.S. Department of Energy), ORNL/GWPO-021, p. 113.

Issler, D.R. and Katsube, T.J.
1994: Effective porosity of shale samples from the Beaufort-Mackenzie Basin, northern Canada; *in* Current Research 1994-B; Geological Survey of Canada, p. 19-26.

Katsube, T.J. and Agterberg, F.P.
1990: Use of statistical methods to extract significant information from scattered data in petrophysics; *in* Statistical Applications in the Earth Sciences, (ed.) F.P. Agterberg and G.F. Bonham-Carter; Geological Survey of Canada, Paper 89-9, p. 263-270.

Katsube, T.J. and Hume, J.P.
1987: Pore structure characteristics of granitic rock samples from Whiteshell Research Area; *in* Geotechnical Studies at Whiteshell Research Area (RA-3); CANMET, Report MRL 87-52, p. 111-158.

Katsube, T.J. and Issler, D.R.
1993: Pore-size distribution of shales from the Beaufort-Mackenzie Basin, northern Canada; *in* Current Research, Part E; Geological Survey of Canada, Paper 93-1E, p. 123-132.

Katsube, T.J. and Walsh, J.B.
1987: Effective aperture for fluid flow in microcracks; International Journal of Rock Mechanics and Mining Sciences and Geomechanics Abstracts, v. 24, p. 175-183.

Katsube, T.J. and Williamson, M.A.
1994: Effects of diagenesis on shale nano-pore structure and implications for sealing capacity; Clay Minerals, v. 29, p. 451-461.
1995: Critical depth of burial of subsiding shales and its effect on abnormal pressure development; Proceedings of the Oil and Gas Forum '95, Energy from Sediments, Geological Survey of Canada, Open File 3058, p. 283-286.
in press: Shale petrophysical characteristics: Permeability history of subsiding shales; *in* Proceedings on Shale Research, GSA Annual Meeting - New Orleans, Louisiana, November 6-9, 1995, p. 363-385.

Katsube, T.J., Bloch, J., and Cox, W.C.
1998: The effect of diagenetic alteration on shale pore-structure and its implications for abnormal pressures and geophysical signatures; *in* Overpressures in Petroleum Exploration, the Proceedings of the Overpressures in Petroleum Exploration Workshop (organizers: A. Mitchell, D. Swarbrick, J. Dainelli), April 7-8, 1998, Pau, France.

Katsube, T.J., Bloch, J., and Issler, D.R.
1995: Shale pore structure evolution under variable sedimentation rates in the Beaufort-MacKenzie Basin; *in* Proceedings of the Oil and Gas Forum' 95 ("Energy from Sediments"), Geological Survey of Canada, Open File 3058, p. 211-215.

Katsube, T.J., Dorsch, J., and Connell, S.
1997: Pore surface area characteristics of the Nolichucky Shale within the Oak Ridge Reservation (Tennessee, U.S.A.): implication for fluid expulsion efficiency; *in* Geological Survey of Canada, Current Research 1997-E; p. 117-124.

Katsube, T.J., Scromeda, N., and Williamson, M.
1992a: Effective porosity of tight shales from the Venture Gas Field, offshore Nova Scotia; *in* Current Research, Part D; Geological Survey of Canada, Paper 92-1D, p. 111-119.

Katsube, T.J., Williamson, M., and Best, M.E.
1992b: Shale pore structure evolution and its effect on permeability; *in* Symposium Volume III of the Thirty-Third Annual Symposium of the Society of Professional Well Log Analysts (SPWLA), The Society of Core Analysts Preprints, Oklahoma City, Oklahoma, June 15-17, 1992, Paper SCA-9214, p. 1-22.

Loman, J.M., Katsube, T.J., Correia, J.M., and Williamson, M.A.
1993: Effect of compaction on porosity and formation factor for tight shales from the Scotian Shelf; *in* Current Research, Part E; Geological Survey of Canada, Paper 93-1E, p. 331-335.

Rootare, H.M.
1970: A review of mercury porosimetry; Perspectives of Powder Metallurgy, v. 5, p. 225-252.

Washburn, E.W.
1921: Note on a method of determining the distribution of pore sizes in a porous material; Proceedings of the National Academy of Science, v. 5, p. 115-116.

Geological Survey of Canada Project 870057

CANADIAN SHIELD

BOUCLIER CANADIEN

Structural setting of the Hemlo gold deposit, Ontario[1]

Shoufa Lin[2]
Continental Geoscience Division, Ottawa

Lin, S., 1998: Structural setting of the Hemlo gold deposit, Ontario; in *Current Research 1998-E; Geological Survey of Canada, p. 77–88.*

Abstract: Four generations (G_1 to G_4) of ductile structures are recognized in the Hemlo area. G_2 deformation is the strongest and is responsible for the dominant fabric in most outcrops. The ore body is folded by F_2 (at the outcrop, the ore body, and possibly the camp scale), and the main gold mineralization occurred either early during G_2 or before G_2 and before peak metamorphism. The two ore zones at Hemlo spatially coincide with the two limbs of a camp-scale F_2 fold. They occur at the stratigraphically lower contact of a volcanic feldspar-quartz porphyry with a metasedimentary unit. A fragmental rock (metaconglomerate) and a barite horizon also occur at the contact and are closely associated with the ore. The contact and the (permeable) fragmental rock are considered to be mechanical traps and the barite is considered to be a chemical trap.

Résumé : Quatre générations (G_1 à G_4) de structures ductiles ont été individualisées dans la région de Hemlo. La déformation G_2, la plus intense, est responsable de la fabrique qui prédomine dans la plupart des affleurements. Le corps minéralisé est plissé par la phase F_2 à l'échelle de l'affleurement, du corps minéralisé et probablement du camp. La principale minéralisation aurifère s'est formée soit au début de la phase G_2, soit antérieurement à cette phase et avant le métamorphisme maximal. À Hemlo, les deux zones minéralisées coïncident dans l'espace avec les deux flancs d'un pli F_2 à l'échelle du camp. Ces zones se situent au contact stratigraphique inférieur d'un porphyre quartzo-feldspathique volcanique accompagné d'une unité métasédimentaire où l'on a observé des roches clastiques (métaconglomérats) et un niveau de barytine étroitement associés au minerai. Le contact et les roches clastiques perméables sont considérés comme des pièges mécaniques et l'horizon de barytine, comme un piège chimique.

---

[1] Research completed under the Industrial Partners Program (IPP) of the Geological Survey of Canada in collaboration with the Canadian Mining Industry Research Organization (CAMIRO).

[2] Manitoba Energy and Mines, 59 Elizabeth Drive, Thompson, Manitoba R8N 1X4

INTRODUCTION

The origin of the Hemlo gold deposit, site of the largest producing gold mines in Canada, is very controversial. Genetic models that have been proposed include epithermal/syngenetic models (Goldie, 1985; Valliant and Bradbrook, 1986), porphyry models (Kuhns, 1988; Kuhns et al., 1994; Johnston et al., 1995), shear zone models (e.g. Hugon, 1986), and a late calc-silicate replacement model (Pan and Fleet, 1995). To better understand the geological setting and genesis of the deposit, an important factor in developing an efficient exploration strategy for finding other Hemlo-type deposits, the Canadian Mining Industry Research Organization (CAMIRO) (formerly the Mining Industry Technology Council of Canada, or MITEC) initiated a three year (1995–1997) multidisciplinary research project, sponsored by 14 major mining/exploration companies from Canada, the United States, and Australia. Major components and main researchers of the project include 1) Hemlo Atlas (R.H. Sutcliffe, consultant), 2) structural geology (S. Lin, GSC), 3) alteration, geochemistry, and metamorphism (A.E. Williams-Jones and

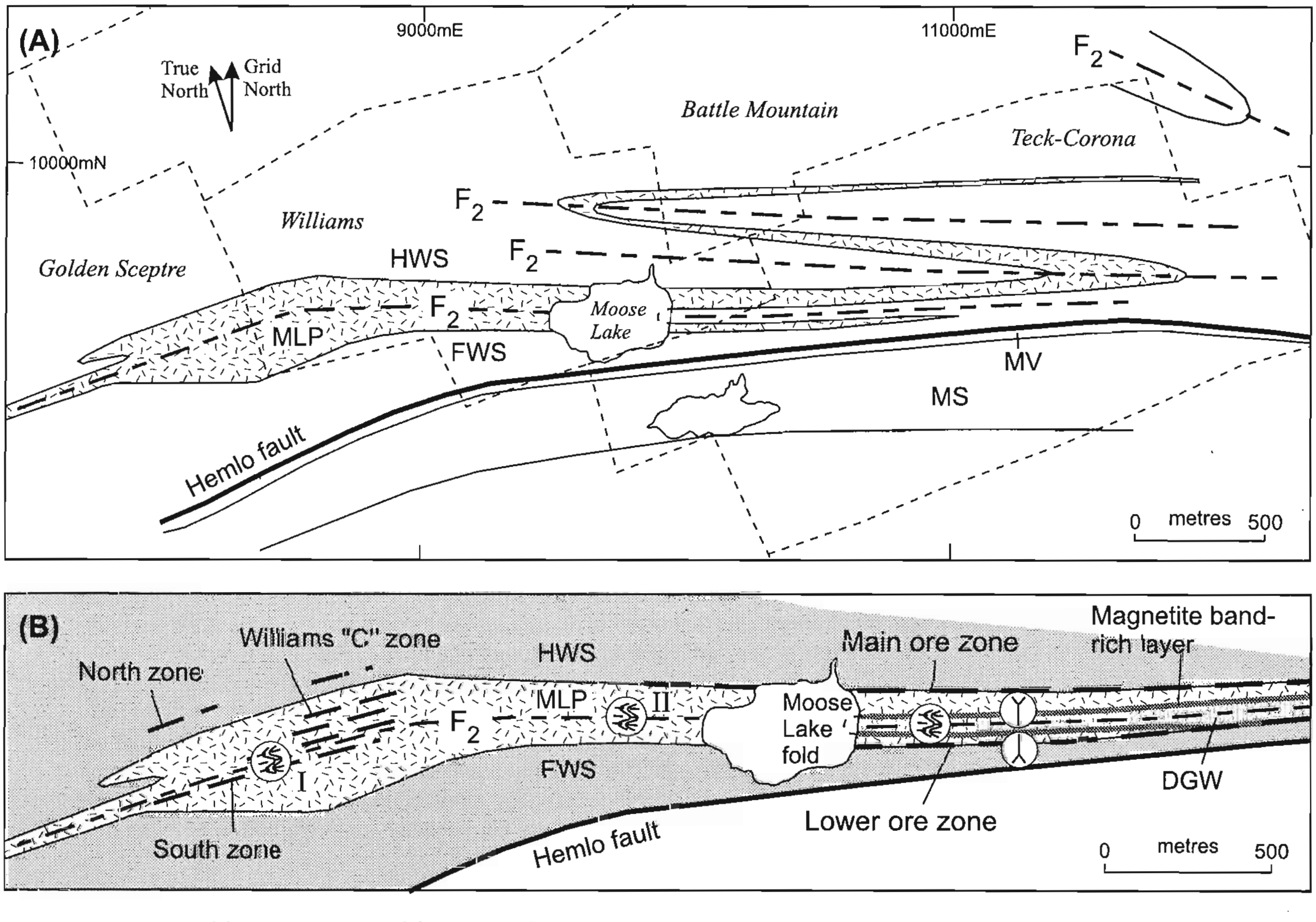

Figure 1. A) Simplified geological map showing the major structures of the Hemlo camp (modified and simplified from Kusins et al., 1991 and Muir, 1993). The patterned unit is the Moose Lake porphyry. F_2: axial surface trace of F_2 folds. ***B)*** *Simplified geological map showing structures associated with the Moose Lake fold and the distribution of ore zones. The location of the main and lower ore zones as shown are mainly surface projections. Note that these two zones coincide with the two limbs of the Moose Lake fold. Major lines of evidence for the Moose Lake fold include: 1) repetition of major lithological units (the hanging wall/footwall sediments, the barite horizon (spatially coincident with the two ore zones), the Moose Lake porphyry, and the magnetite band-rich wacke at the base of the dark grey wacke); 2) younging direction reversal; and 3) high-angle relationship between S_0/S_1 and S_2 along the axial surface trace, in contrast to subparallelism between them along the limbs of the fold. Symbol I corresponds to features shown in Figure 2A of this report, and II to Plate 1d of Muir (1993). DGW: dark grey wacke; FWS: footwall sediments; HWS: hanging wall sediments; MLP: Moose Lake porphyry; MV/MS: mafic metavolcanic rocks/metasedimentary rocks south of the Hemlo fault.*

others, McGill University), 4) geochronology (D.W. Davis, Royal Ontario Museum), and 5) geophysics (W.A. Morris and others, McMaster University; L.E. Reed, consultant). The CAMIRO project, which is focused on an area of about 10 km by 6 km around the deposit, is supported by regional geological mapping by geologists of the Ontario Geological Survey (S. Jackson, G. Beakhouse, and T. Muir) in the Heron Bay-Hemlo greenstone belt. This report is only concerned with the structural geology component of the CAMIRO project, which was jointly funded by CAMIRO and GSC through GSC's Industrial Partners Program (IPP).

Previous structural work has demonstrated that rocks in the Hemlo deposit area, including the ore body, are strongly deformed by multiple generations of structures, (e.g. Patterson, 1983; Hugon, 1986; Kuhns et al., 1986, 1994; Muir and Elliott, 1987; Muir, 1993; Michibayashi, 1995). The deformation obscured critical primary geological relationships, and significantly modified the geometry of both the ore body and the host rocks. It therefore has hampered the understanding of the processes responsible for the formation of the Hemlo deposit.

The purpose of the current structural study was to carry out a systematic structural analysis of the Hemlo deposit area through detailed surface and underground mapping and compilation of available data, including the unpublished data collected by geologists of the three mines at Hemlo (the Williams mine, the Golden Giant mine, and the David Bell mine). This work is primarily intended to elucidate the structural history and three-dimensional geometry of the area. An understanding of the geometry and kinematics of individual generations of structures can help us to 'undeform' the rocks and to gain insight in the predeformational geometry. Such a restoration can be used as a test to the various models that have been proposed for the deposit.

Due to a confidentiality requirement, only preliminary results of the first year's work (1995) are summarized in this report. The ideas presented here have been substantiated by later work in 1996–1997. The final report of the study was submitted to CAMIRO in April, 1998.

GEOLOGICAL SETTING

The Hemlo gold deposit is hosted in the Heron Bay-Hemlo greenstone belt of the Wawa Subprovince of the Superior Province. The greenstone belt mainly consists of a sequence of Archean metasedimentary and felsic, intermediate, and mafic metavolcanic rocks of possibly ≥2720 Ma to ca. 2688 Ma. It is intruded by granodioritic-tonalitic plutons and related dykes of ca. 2719 Ma, ca. 2688–2684 Ma, and ca. 2678 Ma (all ages based on Corfu and Muir, 1989).

Major lithological units in the mine area are the 'hanging wall (meta)sediments', the 'footwall (meta)sediments' and an intervening feldspar-quartz porphyry (the Moose Lake porphyry) (Fig. 1). A fragmental rock and barite (not shown in Fig. 1) occur between the porphyry and the metasediments. These rocks were metamorphosed to middle amphibolite grade (Muir, 1982; Kuhns et al., 1994).

The vast majority of the ore at Hemlo occurs in two zones, referred to as the main and lower ore zones in this report (Fig. 1B). The main ore zone occurs at the contact between the Moose Lake porphyry and the hanging wall sediments. It includes the 'A' and 'B' zones of the Williams mine, the main zone of the Golden Giant mine, and the 'A' zone of the David Bell mine. The lower ore zone occurs at the contact between the Moose Lake porphyry and the footwall sediments. It includes the lower zone of the Golden Giant mine and the 'C' zone of the David Bell mine. Additional ore lenses occur in the Moose Lake porphyry and in the adjacent hanging wall sediments. They include those at the 'C' zone of the Williams mine, and the adjacent North zone (pit) and South zone in the Golden Sceptre property (Fig. 1B).

The hanging wall and footwall sediments appear identical, as has been noted by many previous workers (e.g. Kusins et al., 1991), and geologists at the Williams mine have mapped them as the same unit. The present study demonstrates that they are stratigraphically the same unit and the two contacts along which the main and lower ore zones occur are connected by folding (Fig. 1; *see* below).

LITHOLOGY

The hanging wall and footwall sediments are dominated by feldspar+quartz+biotite±amphibole schist (metawacke). Primary structures, mainly bedding, are recognizable in many outcrops. Near their contact with the porphyry or the ore, they are rich in bedding-parallel calc-silicate bands and locally contain kyanite, staurolite, and garnet. These calc-silicate bands are generally very regular and concordant to bedding, and the calc-silicate band-bearing metasedimentary rocks can be traced from near the ore zones, where there is extensive hydrothermal alteration, laterally into areas of no significant alteration. These are consistent with an interpretation that the calc-silicate bands are metamorphosed marly beds in the sedimentary protolith (Burk et al., 1986), but inconsistent with a suggestion that they are a result of alteration (Pan and Fleet, 1995; Johnston, 1996). The hanging wall and footwall sediments are altered near the ore and have generally gradational contact with the ore. It is therefore possible that they form part of the host rock of the ore.

The Moose Lake porphyry is felsic and consists of abundant quartz phenocrysts in a fine-grained matrix. Near its contact with the ore, it is sericitized (and metamorphosed) to form the 'quartz-eye sericite schist'. The contact between the ore and the (altered) porphyry is generally very sharp.

Although the Moose Lake porphyry appears massive at many outcrops, it is very heterogeneous in other outcrops and a primary layering is preserved locally (Fig. 2A). It is closely associated with a volcaniclastic rock containing clasts identical to the porphyry (Fig. 2B). It does not cut across the stratigraphy; after unfolding, it is bounded on one side by the hanging wall/footwall sediments with the fragmental rock and barite at the contact, and on the other side by a dark grey wacke (described below). These observations are most consistent with a volcanic origin for the porphyry. Although some of the

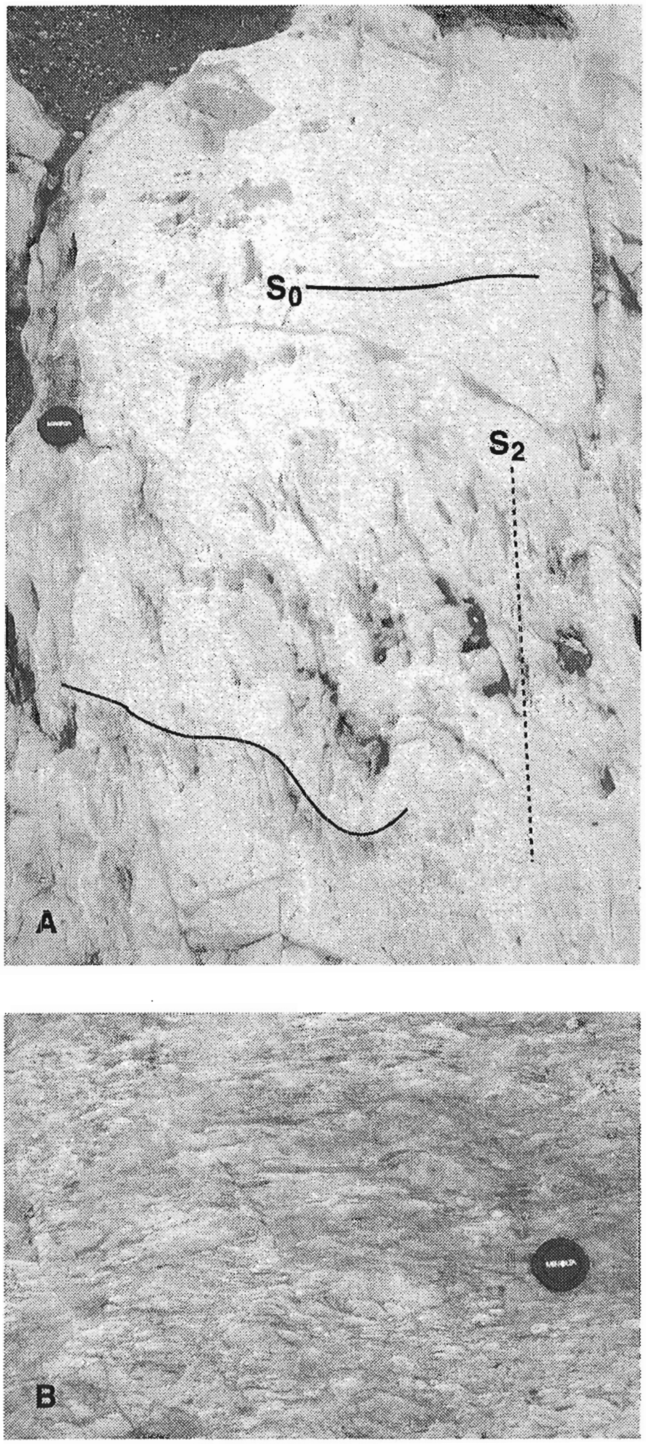

***Figure 2. A)** Moose Lake porphyry. Note the heterogeneous nature and a pre-F_2 layering (S_0) that is folded by F_2. The high angle relationship between S_2 and S_0 or the enveloping surface of F_2 folds is consistent with that the outcrop is close to the closure of the Moose Lake fold. **B)** Volcaniclastic rocks spatially closely associated with, and containing clasts identical to, the Moose Lake porphyry. Both from the Golden Sceptre South zone. Location 1 in Figure 1B.*

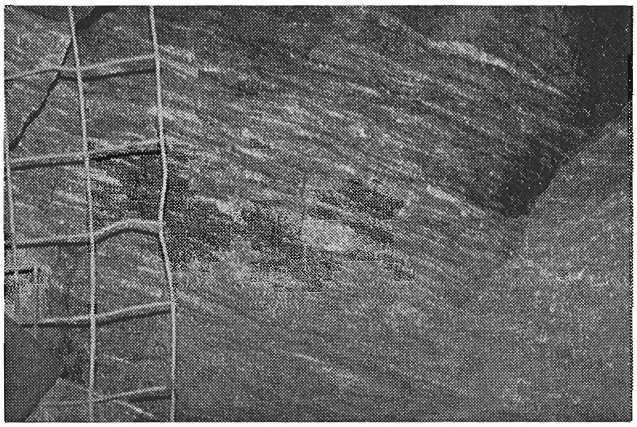

***Figure 3.** Mafic fragmental rock with felsic clasts in a biotite-rich matrix; underground, Golden Giant mine. Longer edge = about 1 m.*

observations are not incompatible with a subvolcanic intrusive environment, intrusive rocks, if present, are not a major component of the unit. Most previous mappers have also mapped the porphyry as a metavolcanic unit (e.g. Muir, 1982; Burk et al., 1986; Valliant and Bradbrook, 1986).

The dark grey wacke is exposed between two limbs of the folded Moose Lake porphyry beneath (underground) and east of Moose Lake (Fig. 1B). On fresh surfaces, the rock appears dark coloured and massive, and some workers (Johnston et al., 1995) have suggested that it is a metadiorite. However, on weathered surfaces, bedding, including well preserved graded bedding at one outcrop, is locally clearly recognizable, indicating that the rock is sedimentary in origin, as has been mapped by most previous workers. The rock contains magnetite-rich layers, locally iron-formation, especially near the contact with the porphyry (Fig. 1B).

The fragmental rock consists of mainly felsic heterolithic clasts in a biotite-rich matrix (Fig. 3) and is referred to as the 'mafic fragmental' by the mine geologists. It has been interpreted as a metaconglomerate (Burk et al., 1986). It is generally strongly deformed. It is spatially closely associated with the ore, generally mineralized to sub-ore grade, and has gradational contacts with the ore. Remnant fragmental features are recognized in the ore. These observations indicate that the host rock of the ore is at least partly the fragmental rock. The observation that the thickness of the fragmental unit is antithetic to the thickness of the ore (e.g. Burk et al., 1986; Kusins et al., 1991) can be readily explained by the interpretation that the main host rock of the ore is the fragmental rock.

The barite is spatially associated with both the main and lower ore zones and forms part of the baritic ore. It is banded and has isotope signatures similar to sedimentary barite exposed west of Hemlo (Cameron and Hattori, 1985; Thode et al., 1991). It is most probably the protolith of the baritic ore.

Both the main and lower ore zones consist of feldspathic ore, sericitic ore, and several minor types (Kuhns, 1986). The feldspathic ore is a massive to banded to fragmental rock that consists of microcline (40–55%, locally up to 90%), quartz

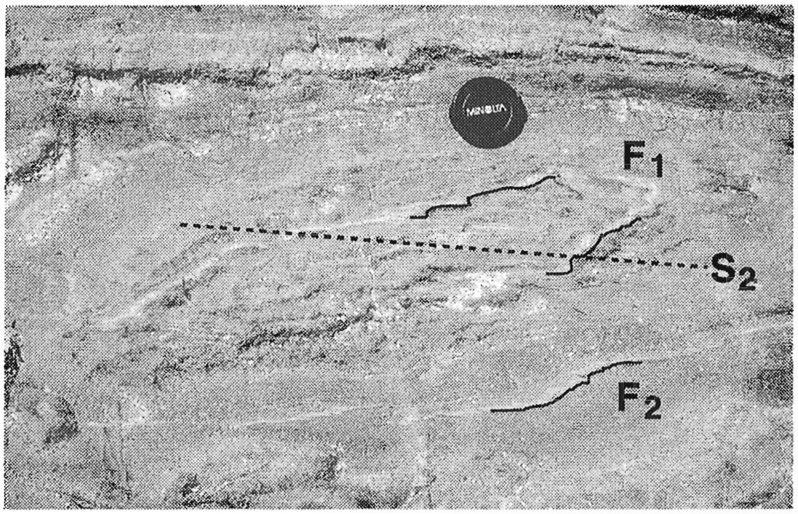

Figure 4.

A doubly-plunging F_1 fold (possible sheath fold) overprinted by F_2; Back 40s outcrop, Williams property. The F_2 folds have "S" asymmetry.

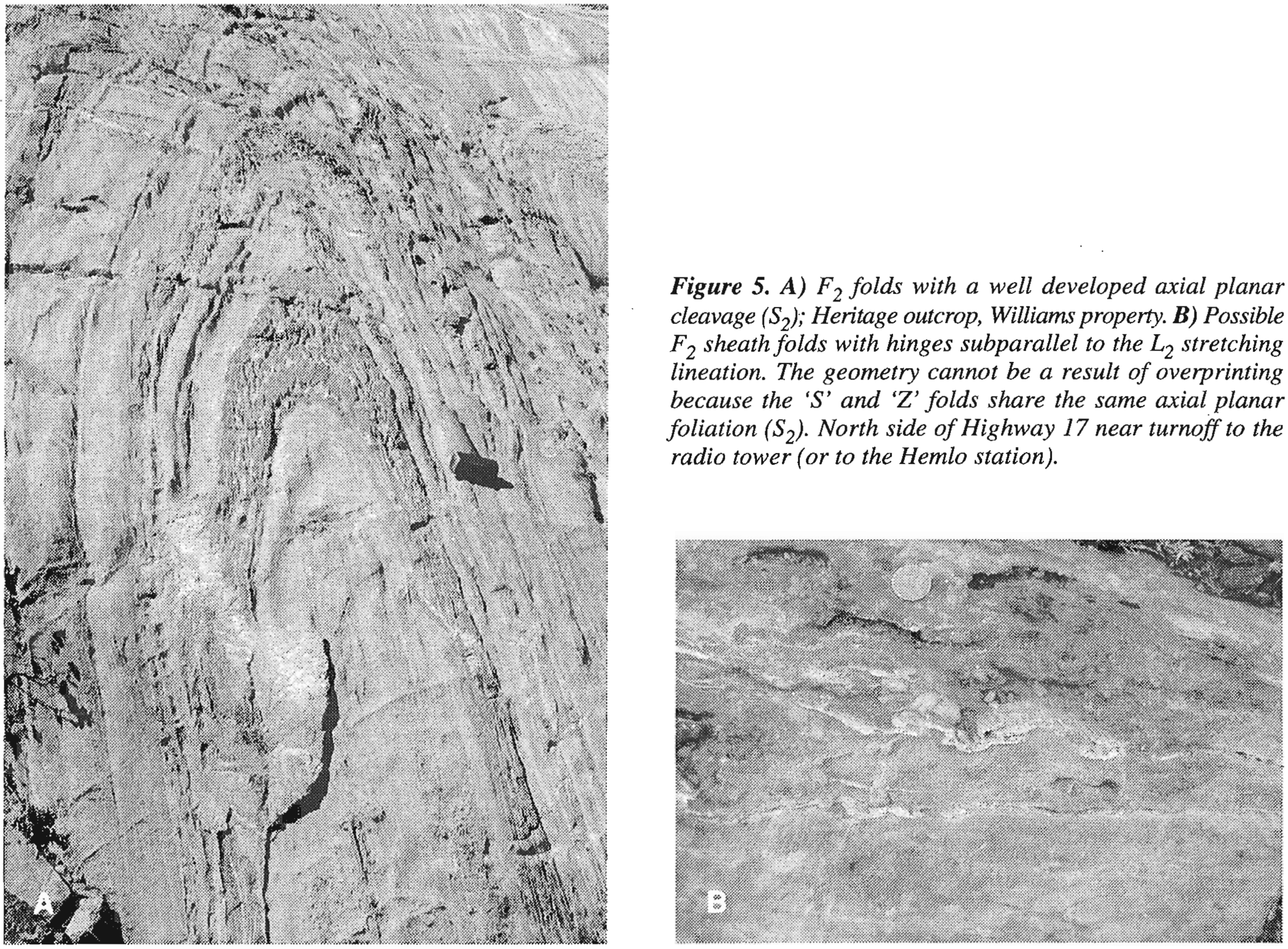

Figure 5. A) *F_2 folds with a well developed axial planar cleavage (S_2); Heritage outcrop, Williams property.* ***B)*** *Possible F_2 sheath folds with hinges subparallel to the L_2 stretching lineation. The geometry cannot be a result of overprinting because the 'S' and 'Z' folds share the same axial planar foliation (S_2). North side of Highway 17 near turnoff to the radio tower (or to the Hemlo station).*

(10–40%), muscovite, green (vanadium-rich) mica, and minor biotite (Kuhns, 1986). It normally contains 3–35% pyrite and molybdenite. The sericitic ore is strongly foliated. It is composed of quartz (40–60%), muscovite (15–30%, locally up to 60%), feldspar, biotite, and green mica (Kuhns, 1986). It contains up to 15% pyrite and traces of molybdenite. Gold is disseminated in the ore.

All the rocks described above, including the ore, are intruded by abundant feldspar porphyry dykes.

MESOSCOPIC STRUCTURES

Four generations (G_1 to G_4) of ductile structures are recognized in the Hemlo area. They are broadly consistent with those of Muir and Elliot (1987).

G_1 deformation is indicated by a locally preserved foliation (S_1) and folds (F_1) that are overprinted by F_2 folds and S_2 foliation. Figure 4 shows a doubly-plunging F_1 fold (possibly a sheath fold) overprinted by F_2 'S' folds.

The S_2 foliation is the dominant foliation in the Hemlo area. It is axial planar to tight to isoclinal F_2 folds (Fig. 5A). The L_2 lineations, defined by elongate clasts and mineral alignment, are well developed and most intense in the Hemlo fault zone, where mylonites and straight gneisses are widespread. They are moderately to steeply plunging in the mine area and in the Hemlo fault zone. The F_2 fold hinges are generally subparallel to the L_2, and F_2 sheath folds were observed at one outcrop (Fig. 5B).

G_1 structures described above are only present locally. They are spatially closely associated with, and have a style very similar to that of, G_2 structures. No macroscopic G_1 structures have been recognized. It is very likely that both G_1 and G_2 structures are related to a single deformation event (episode). Recent advances in structural geology show that a single deformation episode can, and often does, produce more than one generations of structures.

F_3 folds overprint the G_2 structures. They are generally open with a locally developed axial planar crenulation cleavage (Fig. 6). F_3 folds have a consistent 'Z' asymmetry. This asymmetry, together with S-C structures and asymmetrical boudinage, indicate that F_3 was associated with regional dextral shearing. The F_3 fold hinges are generally steep in the mine area.

F_4 folds are open kinks, generally having 'S' asymmetry.

Structures in the ore

The ore body is affected by G_2 and later generations of deformation. Both G_2 and G_3 structures are widespread in the ore. An example of F_2 folds that affect the ore is shown in Figure 7. In the example, a molybdenite seam in a feldspathic ore is deformed by an isoclinal F_2 fold which has well developed S_2 as axial planar foliation.

Both the feldspathic and sericitic ore have generally well developed S_2 foliation. The foliation is defined by white mica and by compositional layering. F_3 folds overprint the S_2 foliation. They are widespread in the ore body.

Timing of intrusion of feldspar porphyry dykes

The feldspar porphyry dykes are subparallel to S_2, including in the hinge areas of F_2 folds (e.g. Plate 10a of Muir, 1993). They were boudinaged during G_2 and bear a weak S_2 foliation (Fig. 8). They are generally folded by F_3 (Fig. 6), but have not been observed to have been folded by F_2. Based on these, it is interpreted that the dykes intruded late during G_2.

METAMORPHISM

Rocks at the Hemlo camp are generally metamorphosed to amphibolite facies (Burk et al. 1986; Kuhns et al., 1994; Muir, 1993). Metamorphic mineral assemblages are garnet+staurolite+kyanite±sillimanite for pelite and hornblende±garnet for metabasite. Preliminary results indicate that peak metamorphism

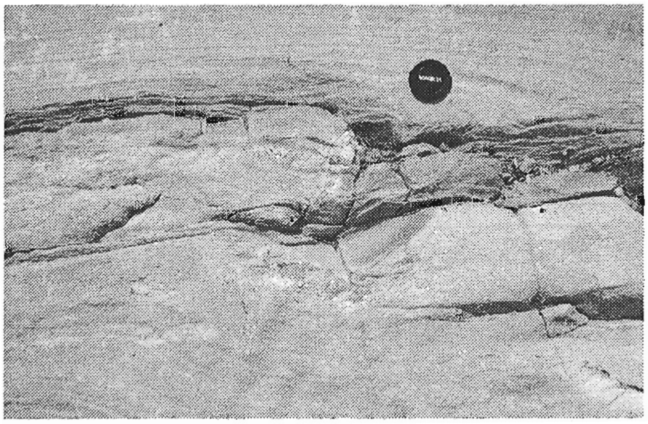

Figure 6. *An F_3 fold deforms a feldspar porphyry dyke, near the west shore of Moose Lake within the Williams property. A weak crenulation cleavage is developed parallel to the axial plane.*

Figure 7. *Deformed ore, underground, Golden Giant mine. Note the isoclinally-folded molybdenite seam to the left of the pencil. The two limbs of the fold are indicated by the arrows.*

occurred very late during G_2 to after G_2, before G_3. For example, microscopic observations in garnet-hornblende metabasite show that inclusion trails in both garnet and hornblende porphyroblasts are straight to slightly curved and are continuous with S_2 in the matrix (Fig. 9), indicating that these minerals grew very late during G_2 to after G_2.

MACROSCOPIC STRUCTURE OF THE MAIN ORE ZONE

During ten years of mining, geologists of the three operating companies have collected vast amount of data, in the forms of level plans, sections, drill cores and core logs, etc. Major efforts were made in this study to compile the data. Preliminary results based on compilation of the data from the Williams and the Golden Giant mines show that the main ore zone (or the 'B' zone of the Williams mine) is thickened by as much as four times by folding. The folds are strongly noncylindrical and have a geometry of proto-sheath folds (Fig. 10). They are F_2 folds with the S_2 as the axial planar foliation.

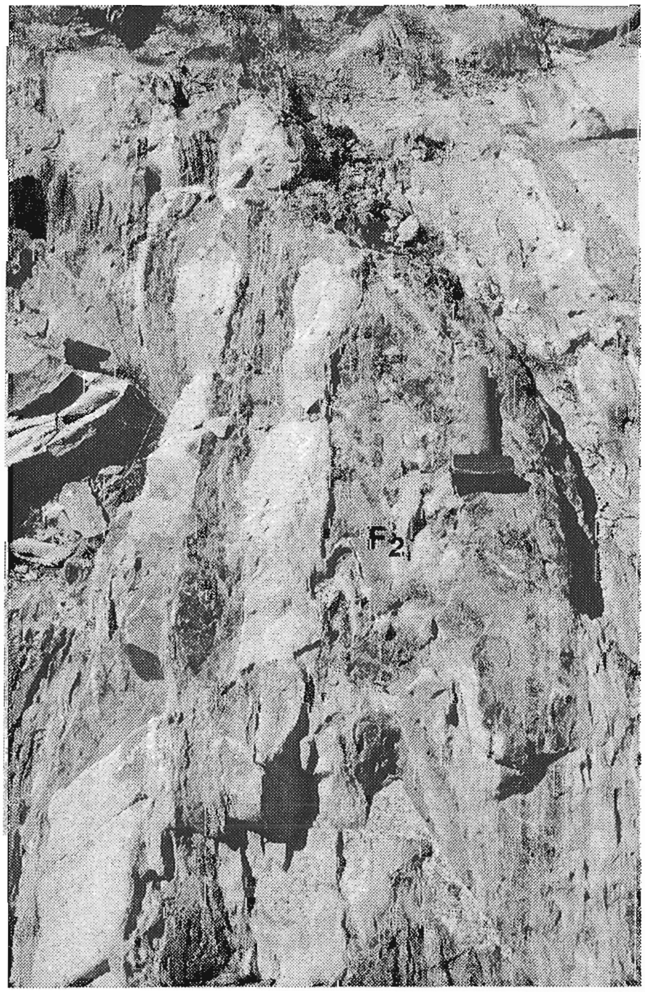

Figure 8. *Feldspar porphyry dykes subparallel to S_2, boudinaged during G_2 and bearing a weak S_2 foliation, Heritage outcrop, Williams property. Note that they are not folded by the F_2 fold near the centre of the photograph.*

MACROSCOPIC STRUCTURE AT THE CAMP SCALE

Several large-scale folds have been mapped in the Hemlo area (Fig. 1A). The folding results in repetition of lithological units and reversal of younging directions. Field relationships indicate that they are F_2 folds.

Figure 9. *Photomicrograph of a garnet (Gt)-hornblende (Hb) metabasite. The garnet and hornblende porphyroblasts contain inclusion trails that are continuous with the S_2 foliation in the matrix. The inclusion trails in the two garnet porphyroblasts at the lower edge of the photograph are straight in the middle and slightly curved towards the upper and lower margins. The inclusion trails in the hornblende porphyroblasts near upper edge of the photograph are straight. Both the geometries of inclusion trails are present in both garnet and hornblende porphyroblasts in the same thin section. These geometries indicate that the porphyroblasts grew late syn-G_2 to post-G_2. Plain light. Shorter edge = about 7 mm. Sample from near the east shore of Botham Lake.*

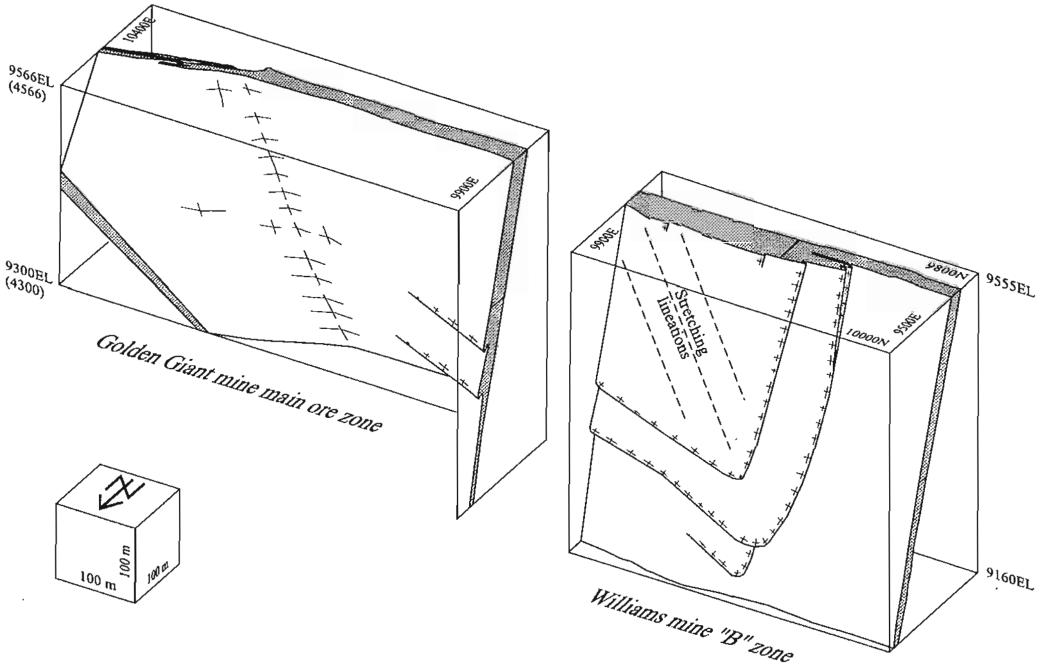

Figure 10. Orthographic projection of the Hemlo main ore zone based on compilation of level plans and sections from the Golden Giant mine and the Williams mine. Looking down to the southeast.

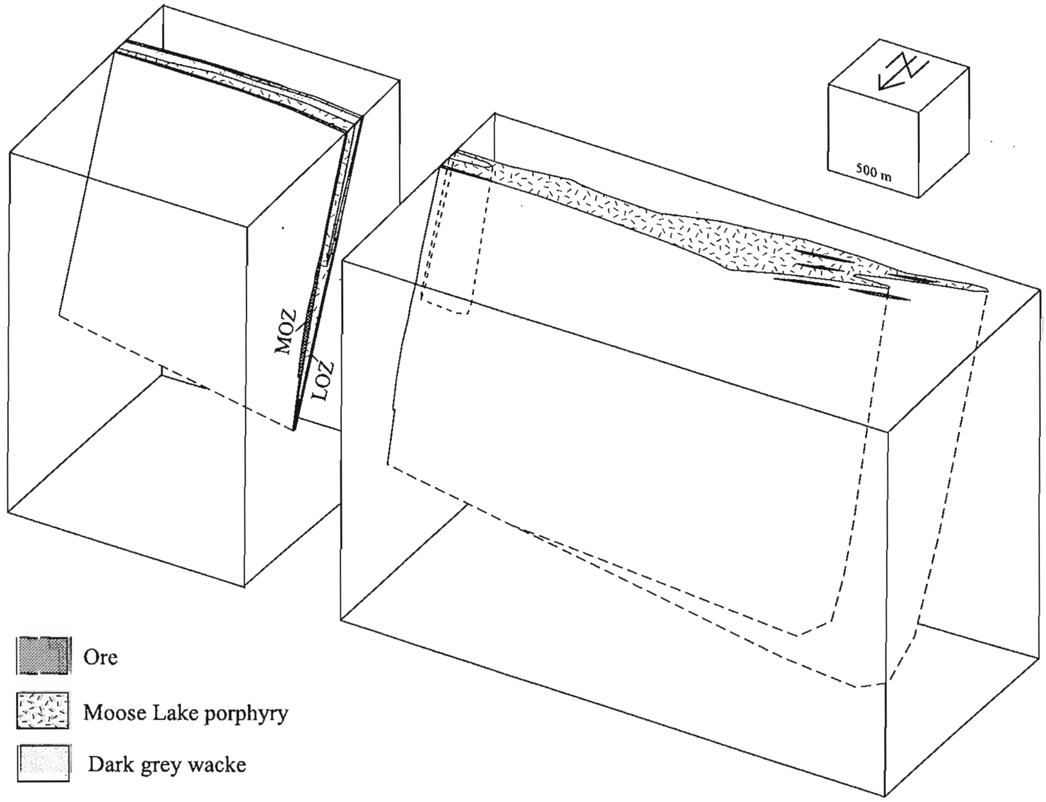

Figure 11. Schematic block diagram showing a possible geometrical interpretation of the Hemlo camp. MOZ: main ore zone; LOZ: lower ore zone. Note that the two ore zones are spatially associated with the folded contact between the Moose Lake porphyry and the hanging wall/footwall sediments (not shown; compare with Figure 1B). Looking down towards southeast.

As described above, mineralization at Hemlo is concentrated in two zones, the main and lower ore zones. The general geometry of the area, repetition of lithological units and younging direction reversal indicate that the two ore zones are located at two limbs of a large-scale F_2 fold, the Moose Lake fold (Fig. 1B). Lithological units that are repeated by the fold include the hanging wall/footwall sediments, the Moose Lake porphyry, the barite horizon (coincident with the two ore zones), and the magnetite band-rich layer at the base of the dark grey wacke. Along the interpreted axial surface trace the angle between S_2 and the enveloping surface of F_2 folds is high (Fig. 1B) and along the interpreted fold limbs S_2 is subparallel to bedding. The Moose Lake fold is also noncylindrical and has the geometry of a proto-sheath fold (Fig. 11).

TIMING OF MINERALIZATION AND ALTERATION

The following observations and interpretations suggest that alteration and mineralization occurred before G_2 or early during G_2:

a) Felspar porphyry dykes cut the ore and are not mineralized. They intruded late during F_2 and are folded by F_3. Therefore, the mineralization must have occurred prior to late F_2 and F_3.

b) The ore is in general strongly deformed, especially in the main and lower ore zones. It is folded by F_2 (at the outcrop, the ore-body, and possibly the camp scale), and bears a generally strong S_2 foliation.

c) Feldspathic ore is in general less deformed than the sericitic ore, indicating that the alteration mineral assemblage controlled the intensity and localization of deformation.

d) In the hinge area of the Moose Lake fold (F_2) (e.g. the 'C' zone of the Williams mine), numerous ore lenses are subparallel to the axial plane (S_2) (Fig. 1B, 11). They either formed along S_2 during F_2 folding or they represent a transposed pre-F_2 ore body.

Considering that peak metamorphism occurred very late during G_2 to after G_2, the alteration and mineralization, which occurred before G_2 or early during G_2, must have taken place before peak metamorphism.

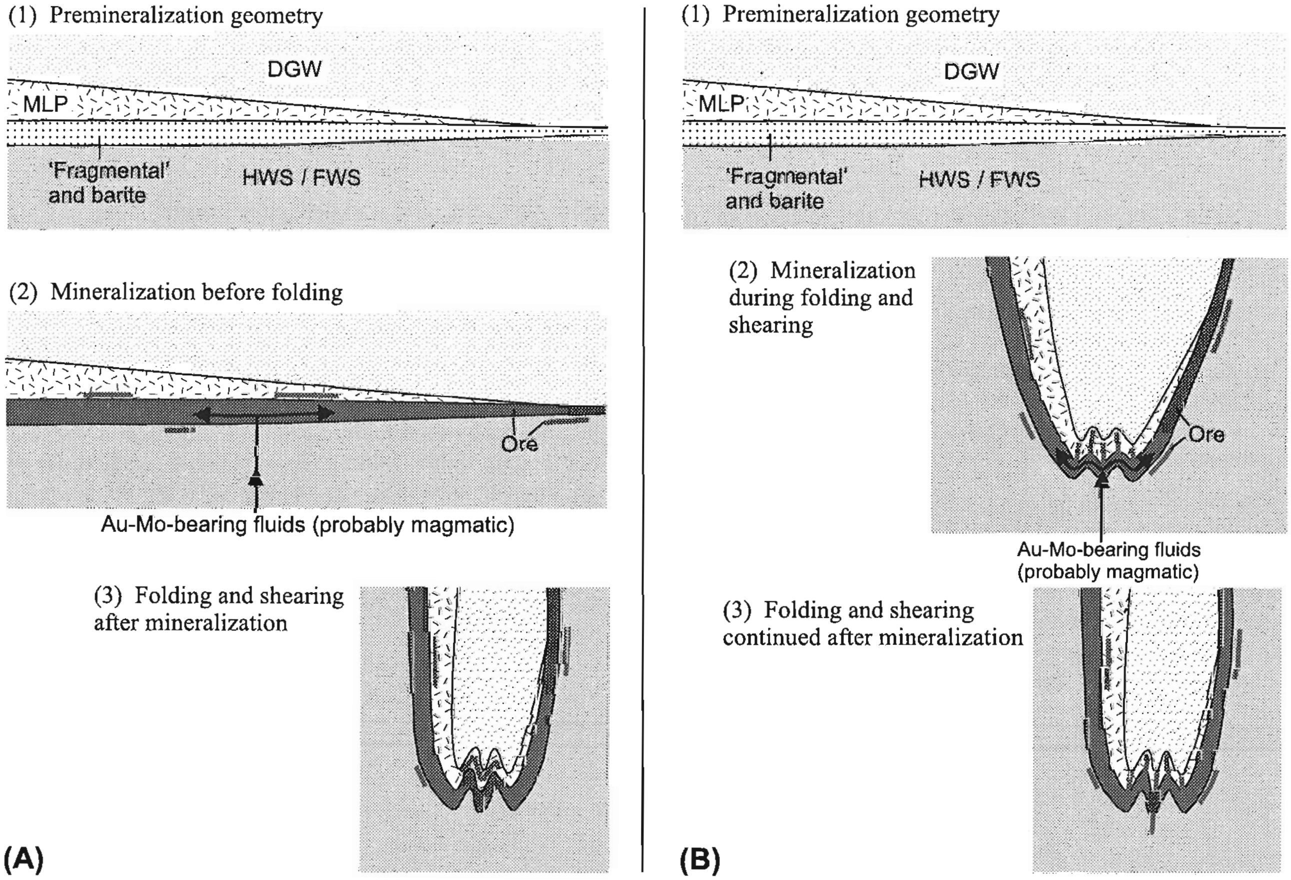

__Figure 12.__ Schematic diagrams showing two possible scenarios for the geological evolution of the Hemlo camp, with mineralization taking place previous to folding (__A__) and early syn-folding (__B__), respectively. In both scenarios, the fragmental unit, as a permeable layer, is interpreted to be a mechanical trap and the barite horizon a chemical trap. DGW: dark grey wacke; FWS: footwall sediments; HWS: hanging wall sediments; MLP: Moose Lake porphyry.

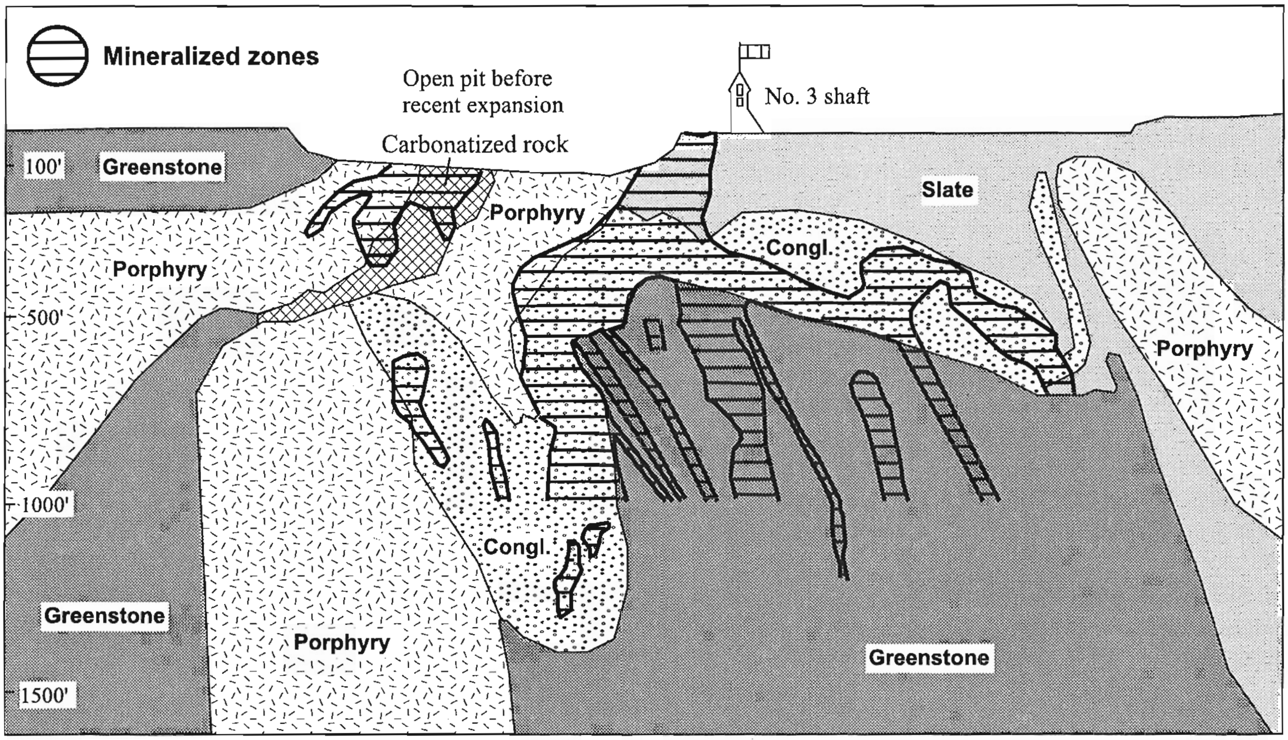

Figure 13. A section (looking east) of the Dome mine, Timmins, Ontario (redrawn from a diagram in a field trip handout supplied by, and published with permission of the Dome mine). See text for discussion. Congl.: conglomerate.

IMPLICATIONS FOR ORE GENESIS MODELS

The mineralization occurred prior to late F_2, and therefore could not have been related to the dextral shearing associated with F_3. The interpretation that the mineralization occurred during dextral transcurrent shearing (e.g. Hugon, 1986) and the suggestion that the mineralization took place during post-F_3 late calc-silicate alteration (e.g. Pan and Fleet, 1995) is therefore inconsistent with the results of the present study.

The two ore zones coincide with two limbs of the Moose Lake fold (Fig. 1). Based on well preserved younging indicators, e.g. graded bedding in the hanging wall and footwall sediments and in the dark grey wacke, the ore zones are located at the stratigraphically lower contact of the Moose Lake porphyry which is a metavolcanic rock (Fig. 11). This is inconsistent with an interpretation that the Hemlo gold deposit is a porphyry deposit associated with the Moose Lake porphyry (e.g. Johnston et al., 1995). It should be noted that this does not exclude the possibility that the deposit is porphyry-related; the alteration mineral assemblages (potassic and sericitic alteration; Kuhns, 1988) and metal abundances (enrichment in Au, Mo, As, Sb, Hg, and Tl) indicate that the mineralization fluids had a magmatic source (e.g. Burk, 1987; Kuhns, 1988).

The alteration and mineralization at Hemlo occurred before deformation or early in the deformation history and before peak metamorphism, and the location of mineralization mainly coincides with, and was probably controlled by, the contact between the Moose Lake porphyry and the hanging wall/footwall sediments where the fragmental unit and the barite horizon is located. These two points should be considered in any genetic modelling of the deposit.

Two possible scenarios for the geological evolution of the Hemlo camp that are consistent with the available data are schematically shown in Figure 12. In scenario A, mineralization occurs before folding; in scenario B, early during folding. In both scenarios, the contact between the Moose Lake porphyry and the hanging wall/footwall sediments and the (permeable) fragmental rock (metaconglomerate) at the contact, below the less permeable massive part of the porphyry, are considered as mechanical traps, and the barite horizon at the contact as a chemical trap (Burk, 1987; Thode et al., 1991). In scenario B, mineralization also occurred in zones parallel to the axial plane near the hinge of the Moose Lake fold.

Comparison with the structural setting of the Dome mine

The Dome mine, Timmins, Ontario, is located near the Dome Fault which is a branch of the Destor–Porcupine Fault, a major fault in the Abitibi greenstone belt. At the mine, a sequence of metavolcanic rocks ('greenstones') are overlain by a metaconglomerate and slate (Rogers, 1982). Quartz porphyries of ca. 2691 Ma (Corfu et al., 1989) are also present.

The sequence is deformed by a northeasterly plunging anticline which is outlined by the geometry of the metaconglomerate (Fig. 13). The location of mineralization is apparently controlled by the (permeable) conglomerate and the geometry of the fold. The mineralization mainly occurs near the crest of the anticline, in stockworks in the conglomerate and in zones (ankerite and quartz veins) parallel to the axial plane of the fold in the greenstone (Fig. 13). This interpretation, which needs to be tested by further work, is very similar to scenario B above for the Hemlo gold deposit in that the mineralization at both deposits is localized in a permeable horizon (metaconglomerate) under less permeable rocks (massive porphyry and/or slate) and in zones parallel to the axial plane of the folds, although the styles of mineralization at the two deposits are quite different. Both deposits are spatially associated with large scale fault zones and the mineralization occurs after the emplacement of the quartz porphyries.

ACKNOWLEDGMENTS

The work was jointly funded by CAMIRO and GSC through GSC's Industrial Partners Program (IPP) and both organizations are thanked for their support. The following are sincerely thanked for their support, discussions, and field trips which have contributed significantly to the work: the sponsors of the CAMIRO Hemlo research project, CAMIRO research co-ordinators, geologists at the three mining companies at Hemlo (especially Rob Baldwin, Paul DeGagne, Pierre Desautels, Cliff Duke, Al Guthrie, Bob Kusins, Hugh Lockwood, Doug MacIlveen, Colin Mackenzie, and Gord Skrecky), my colleagues at the GSC (especially François Robert, Benoit Dubé, and Howard Poulsen), geologists from the Ontario Geological Survey (Tom Muir, Steve Jackson, and Gary Beakhouse), and the co-researchers of the project. Steve Price of the Dome mine is thanked for discussion of the geology of the mine. Howard Poulsen and Cees van Staal are thanked for critically reading earlier versions of the report. The report is published with permission of the CAMIRO.

REFERENCES

Burk, K.L.
1987: Geological setting of the Tech-Corona gold-molybdenum deposit, Hemlo, Ontario; M.Sc. thesis, Queen's University, Kingston, Ontario, 241 p.

Burk, R., Hodgson, C.J., and Quartermain, R.A.
1986: The geological setting of the Teck-Corona Au-Mo-Ba deposit, Hemlo, Ontario, Canada; *in* Proceedings of Gold'86, An International Symposium on the Geology of Gold, Toronto, Ontario, 1986, p. 311-326.

Cameron, E.M. and Hattori, K.
1985: The Hemlo gold deposit, Ontario: a geochemical and isotopic study; Geochimica et Cosmochimica Acta, v. 49, p. 2041-2050.

Corfu, F. and Muir, T.L.
1989: The Hemlo-Heron Bay greenstone belt and Hemlo Au-Mo deposit, Superior Province, Canada, 1. Sequence of igneous activity determined by zircon U-Pb geochronology; Chemical Geology (Isotope Geoscience Section), v. 79, p. 183-200.

Corfu, F., Krogh, T.E., Kwok, Y.Y., and Jensen, L.S.
1989: U-Pb zircon geochronology in the southern Abitibi greenstone belt, Superior Province; Canadian Journal of Earth Sciences, v. 26, p. 1747-1763.

Goldie, R.
1985: The sinters of the Ohaki and Champagne pools, New Zealand: possible modern analogues of the Hemlo gold deposit, Northern Ontario; Geoscience Canada, v. 12, p. 60-64.

Hugon, H.
1986: The Hemlo gold deposit, Ontario, Canada: a central portion of a large-scale, wide zone of heterogeneous ductile shear; *in* Proceedings of Gold'86, An International Symposium on the Geology of Gold, Toronto, Ontario, 1986, p. 379-387.

Johnston, P.
1996: Geological setting of the Hemlo gold deposit, Ontario, Canada; Ph.D. thesis, Queen's University, Kingston, Ontario, 297 p.

Johnston, P., Kusins, R., and Mason, R.
1995: Complex magmatic hydrothermal alteration associated with high level porphyritic intrusions at Hemlo, Ontario; Geological Association of Canada-Mineralogical Association of Canada, Program with Abstracts, v. 20, p. A50.

Kuhns, R.J.
1986: Alteration styles and trace element dispersion associated with the Golden Giant deposit, Hemlo, Ontario, Canada; *in* Proceedings of Gold'86, An International Symposium on the Geology of Gold, Toronto, Ontario, 1986, p. 340-353.
1988: The Golden Giant deposit, Hemlo, Ontario: geologic and geochemical relationships between mineralization, alteration, metamorphism, magmatism and tectonism; Ph.D. thesis, University of Minnesota, Minnespolis, Minnesota, 458 p.

Kuhns, R.J., Kennedy, P., Cooper, P., Brown, P., Mackie, B., Kusins, R., and Frieson, R.
1986: Geology and mineralization associated with Golden Giant deposit, Ontario, Canada; *in* Proceedings of Gold'86, An International Symposium on the Geology of Gold, Toronto, Ontario, 1986, p. 327-339.

Kuhns, R.J., Sawkins, F.J., and Ho, E.
1994: Magmatism, metamorphism, and deformation at Hemlo, Ontario, and the timing of Au-Mo mineralization in the Golden Giant mine; Economic Geology, v. 89, p. 720-756.

Kusins, R., Chong, A., Johnston, P., McIlveen, D., and McNena, K.
1991: Geology of the Golden Giant Mine and Golden Sceptre Orebody; *in* Geology and gold deposit of the Hemlo area, (comp., ed.), T.L. Muir, B.R. Schnieders, and M.C. Smyk; Geological Association of Canada-Mineralogical Association of Canada-Society of Economic Geologists, Joint Annual Meeting, Toronto'91, Field Trip A1 Guidebook, p. 16-33.

Michibayachi, K.
1995: Two phase syntectonic gold mineralization and barite remobilization within the main ore body of the Golden Giant mine, Hemlo, Ontario, Canada; Ore Geology Review, v. 10, p. 31-50.

Muir, T.L.
1982: Geology of the Hemlo area, District of Thunder Bay; Ontario Geological Survey, Report 217.
1993: The geology of the Hemlo gold deposit area; Ontario Geological Survey, Open File Repot 5877, 264 p.

Muir, T.L. and Elliott, C.G.
1987: Summary of Field Work and Other Activities 1987; Ontario Geological Survey, Miscellaneous Paper 137, p. 117-129.

Pan, Y. and Fleet, M.E.
1995: The late Archean Hemlo gold deposit, Ontario, Canada: a review and synthesis; Ore Geology Reviews, v. 9, p. 455-488.

Patterson, G.C.
1983: Exploration history in the Hemlo; *in* The Geology of Gold in Ontario; Ontario Geological Survey, Miscellaneous Paper 110, p. 227-229.

Rogers, D.S.
1982: The geology and ore deposits of the No. 8 shaft area, Dome Mine; *in* Proceedings of the CIM Gold Symposium (September, 1980), Geology Division of Canadian Institute of Mining and Metallurgy Special Publication 24, p. 161-168.

Thode, H.G., Ding, T., and Crocket, J.H.
1991: Sulphur isotope and elemental geochemistry studies of the Hemlo gold mineralization, Ontario: sources of sulphur and implications for the mineralization process; Canadian Journal of Earth Sciences, v. 28, p. 13-25.

Valliant, R.I. and Bradbrook, C.J.
1986: Relationship between stratigraphy, faults and gold deposits, Page-Williams Mine, Ontario, Canada; *in* Proceedings of Gold'86, An International Symposium on the Geology of Gold, Toronto, Ontario, 1986, p. 355-361.

Geological Survey of Canada Project 850014

Standardization and assessment of geological descriptions from water well records, Greater Toronto and Oak Ridges Moraine areas, southern Ontario[1]

H.A.J. Russell, T.A. Brennand[2], C. Logan, and D.R. Sharpe
Terrain Sciences Division, Ottawa

Russell, H.A.J., Brennand, T.A., Logan, C., and Sharpe, D.R., 1998: Standardization and assessment of geological descriptions from water well records, Greater Toronto and Oak Ridges Moraine areas, southern Ontario; in *Current Research 1998-E; Geological Survey of Canada, p. 89–102.*

Abstract: Archival drilling records from water wells, geotechnical, mineral exploration, and hydrogeological studies provide subsurface information for regional geological and hydrogeological investigations. This paper evaluates methods by which water well material descriptions may be standardized. In Ontario, material descriptions are reported in three attribute fields using 82 terms, thus theoretically permitting over 500 000 permutations. Materials descriptions are rationalized to ten classes then reclassified according to two methods, 1) first-attribute method (FAM), and 2) rule-based method (RBM). The first-attribute method is presently applied by hydrogeologists in southern Ontario and uses only the first attribute field; it is a simple, effective method able to broadly delimit aquifers and nonaquifers. The rule-based method applies conditional rules developed from regional geological models. This method is more geologically accurate, and is recommended where water well data are to be integrated into geological and hydrogeological investigations. Successful applications are summarized and general recommendations made.

Résumé : Des données provenant de forage de puits d'eau et d'études géotechniques, hydrogéologiques et de prospection minière, renseignent sur les conditions souterraines nécessaires aux études géologiques et hydrogéologiques régionales. Le présent article évalue les méthodes permettant de normaliser les descriptions des matériaux des puits d'eau. En Ontario, les descriptions de matériaux sont consignées dans trois champs d'attributs à l'aide de 82 termes, ce qui, théoriquement, permet de faire plus de 500 000 permutations. La rationalisation des descriptions de matériaux a permis de distinguer dix classes qui ont par la suite été reclassées selon deux méthodes : (1) la méthode des premiers attributs et (2) la méthode basée sur des règles. La méthode des premiers attributs, actuellement appliquée par les hydrogéologistes dans le sud de l'Ontario, utilise uniquement le premier champ d'attributs. Il s'agit d'une méthode simple et efficace pouvant délimiter grossièrement les formations aquifères et non aquifères. La méthode basée sur des règles applique des règles conditionnelles élaborées à partir de modèles géologiques régionaux. D'un point de vue géologique, cette méthode est plus précise. Il est recommandé de l'appliquer là où les données sur les puits d'eau doivent être intégrées aux études géologiques et hydrogéologiques. Les applications réussies sont présentées brièvement dans le présent article, lequel contient également des recommandations d'ordre général.

---

[1] Contribution of the Oak Ridges Moraine NATMAP Project

[2] Department of Geography, Simon Fraser University, Burnaby, British Columbia V5A 1S6

INTRODUCTION

Bedrock lithology and sediment texture (materials) are important to geological, geotechnical, and hydrogeological subsurface investigations as both allow inference of depositional environments and both are important controls on geotechnical and hydrogeological parameters. These data are commonly attained by expensive drilling programs, with large quantities of subsurface information archived in hard copy and digital formats (e.g. Belanger, 1975; McCleneghan and Dilabio, 1995). The availability and quantity of such data varies by region, related to the nature of natural resource exploitation (agriculture, mineral, forestry), the degree of infrastructure development (highways, railroads, bridges), the population density, and the timing of development. In glaciated terrain the most extensive archival data sets are geotechnical reports and water well records (e.g. Belanger and Harrison, 1980). Appropriate utilization of these data in regional geological (e.g. Russell et al., 1996b) and hydrogeological investigations (e.g. Anonymous, 1994; Holysh, 1995; LeGrand and Rosen, 1998) can significantly reduce project costs.

THE PROBLEM

Public concern regarding sustainable water resources and water quality have resulted in renewed interest in aquifer delineation (Kehew et al., 1998) and classification (Kreye et al., 1994; Fagan et al., 1997). These objectives are best achieved through basin analysis methodologies (e.g. Miall, 1984; Eyles et al., 1985; Sharpe et al., 1992). The Oak Ridges Moraine NATMAP–Hydrogeology Project (e.g. Sharpe et al., 1996) in the Greater Toronto and Oak Ridges Moraine areas is an example of such a project (Fig. 1). This project is focusing attention on the need for a more accurate model of the regional three-dimensional geology and hydrostratigraphy of this glaciated terrain (e.g. Sharpe et al., 1997). To delineate stratigraphic units, local site investigations often entail drilling numerous, continuously cored drillholes through the thick overburden (up to 160 m, Fenco-MacLaren, 1994). This methodology is economically prohibitive for regional investigations. Rather, interpretations from expensive, strategically placed and continuously-cored drillholes (high-quality data) must be extended regionally by integration with existing, spatially extensive, archival data. To this end, a multicomponent database composed of a relational database, a GIS database, and flat file data assemblage, has been developed (Russell et al., 1996b; Brennand et al., 1997b; Brennand, 1998). A MOE water well data set, with about 33 000 water well records, is the largest single data contributor to the relational database. This paper explores the task of extracting meaningful and standardized geological descriptions from this data set.

THE DATA: BACKGROUND TO THE MOE WATER WELL DATABASE

Legislation requiring well contractors to submit water well reports to the Ontario Department of Mines was passed in 1946 (Watt, 1952). In that year less than 500 reports were submitted from across the Province, but this number rapidly increased in succeeding decades. The management of these reports passed to the Ontario Water Resources Commission (OWRC) in 1956, and they have since published periodic summaries (e.g. Watt, 1961). A computerized database, the Water Well Information System (WWIS), was instituted by MOE in 1972 to aid input and retrieval of records (Mantha, 1988). This database (complete to 1992) contains information, on up to 212 parameters, for over 325 000 water wells across Ontario. In this paper only water wells records that fall within the study area and are accurately located (Kenny et al., 1997) (~33 000 wells with >142 000 geological units; Fig. 1) are analyzed; this data subset is henceforth called the MOE data set.

The MOE database contains 212 data fields per well. These fields can be subdivided into 1) header (location), 2) geology, 3) hydrogeology, and 4) construction categories (Table 1). Fields in the header category include location and elevation. The geology category contains material, depth, and description. The hydrogeology and construction categories contain fields relevant to the verification of sediment texture (e.g. flow rate and first screen depth). All fields are available for use with each well but, with the exception of location, many fields are incomplete (e.g. screen intervals are reported for only ~20 % of the water wells).

The water well reports were primarily designed to protect the interests of the well owner, specifically with regard to well construction (Singer et al., 1997). Consequently, geological reporting (material description) has been given less attention. Material descriptions were captured in the database from these reports without alteration (Watt, 1952). A basic list of terms to be used for material description was not introduced until computerization in 1972 (S. Singer, pers. comm., 1998; Table 2). It should also be noted that geological descriptions in the MOE database are generally based on examination of drill chips and sediment flushed to the surface in the drilling process; rather than on continuously cored samples that are more commonly encountered by geologists and hydrogeologists.

The geological attributes consist of colour and material descriptors, the latter chosen from 82 terms (materials and descriptive terms) (Table 2). In the MOE database, material descriptors for each unit are applied to three fields (Table 1). Consequently, the number of possible descriptive permutations theoretically exceeds 500 000; the actual number used in the MOE data set exceeds 1800. Not all units in the MOE data set have descriptors entered in all three material fields: the first field is used for about 99% of the units, the second for 28%, the third for only 2.5%, leaving about 52% of all material fields blank (null). More importantly, the material for about 70% of the units is described in a single field only, whereas multiple fields are used in the geological description of about 30% of the units. Of the 49 materials specified (Table 2), 19 describe bedrock lithology, two are minerals, and those remaining either describe sediment texture (e.g. sand, gravel) or the character of the drilled hole (e.g. previously drilled). Of the 33 'descriptive terms' specified, 27 are of questionable geological value (asterisks, Table 2). A decision regarding geological validity was based on the drilling

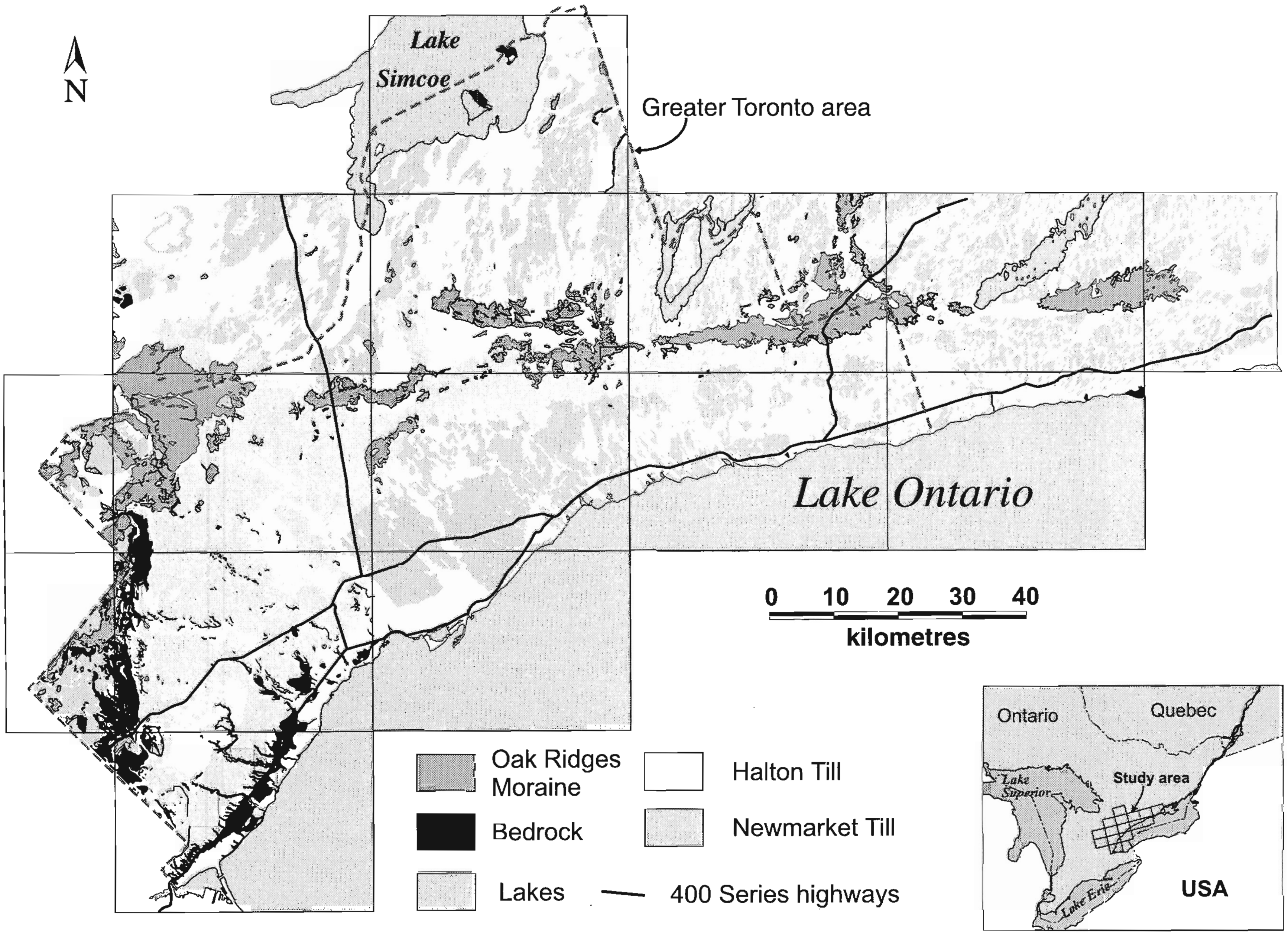

Figure 1. Location map and simplified regional geology of Greater Toronto and Oak Ridges Moraine areas (modified from Sharpe et al., 1997).

technique and the drillers ability to resolve salient details concerning units encountered, e.g. 'thin', and 'cemented'. Other terms such as 'dirty' or 'loose' simply fail to convey information that could be extracted in a meaningful way. The frequency of usage of each material descriptor (materials and descriptive terms, Table 2) varies; only two descriptors are used in more than 10% of the fields, and 13 descriptors in more than 1%. Combined, these 15 descriptors account for about 96% of all descriptor entries (Table 2).

There is a clear need for data standardization in this extensive data set. Material descriptions require standardization when either 1) there is a need for integration and/or

Table 1. Summary of data fields in the MOE water well database, grouped by four principal categories. Numbers in brackets indicate multiple fields in MOE database.

Header	Geology	Hydrogeology	Construction
Well number (2)	Unit - depth to top (24)	Piezometer indicator (1)	Casings (18)
Municipality (2)	Unit - colour (24)	Water - depth found (5)	Screens (8)
Concession – range (4)	Unit - materials (3x24)	Water - kind (5)	Plugs (6)
Lot (2)		Test method (1)	
Owner (1)		Pumping (2)	
Completion date (3)		Levels (2)	
UTM location (4)		Pumping/recovery indicator (1)	
Elevation (2)		Level during pumping (4)	
Basin (5)		Flow rate (1)	
Water use (2)		Clear - cloudy (1)	
Drill method (1)		Recommended setting (1)	
Data source (1)		Recommended rate (1)	
Contractor code (1)		Specific capacity (1)	
Date received (3)		Final status (1)	**total fields = 212**

Table 2. Geological descriptions used in the MOE water well database. Numbers in brackets indicate per cent usage in all three material fields in MOE data set. Asterisk indicates modifiers of questionable lithological value.

Materials					
00	unknown (49.92)	17	shale (0.87)	34	till (0.01)
1	fill (0.17)	18	sandstone (0.02)	35	wood fragments (0.00)
2	topsoil (3.54)	19	slate (0.00)	36	basalt (0.00)
3	muck (0.08)	20	quartzite (0.00)	37	chert (0.00)
4	peat (0.02)	21	granite (0.01)	38	conglomerate (0.00)
5	clay (16.12)	22	greenstone (0.00)	39	feldspar (0.00)
6	silt (1.39)	23	previously bored (0.65)	40	flint (0.00)
7	quicksand (0.29)	24	previously drilled (0.07)	41	gneiss (0.00)
8	fine sand (1.72)	25	overburden (0.01)	42	greywacke (0.00)
9	medium sand (4.74)	26	rock (0.05)	43	gypsum (0.00)
10	coarse sand (1.09)	27	- (0.00)	44	iron formation (0.00)
11	gravel (5.33)	28	sand (4.21)	45	marble (0.00)
12	stones (73.31)	29	fine gravel (0.05)	46	quartz (0.00)
13	boulders (0.79)	30	medium gravel (0.02)	47	schist (0.00)
14	hardpan (0.51)	31	coarse gravel (0.08)	48	soapstone (0.00)
15	limestone (0.75)	32	pea gravel (0.00)		
16	dolomite (0.01)	33	marl (0.00)		
Descriptive terms					
60*	cemented (0.06)	71*	fractured (0.01)	82	shaly (0.03)
61	clayey (0.00)	72	gravelly (0.06)	83*	sharp (0.00)
62*	clean (0.08)	73*	hard (1.01)	84	silty (0.07)
63*	coarse-grained (0.01)	74*	layered (0.25)	85*	soft (0.58)
64*	crystalline (0.00)	75*	light-coloured (0.02)	86*	sticky (0.01)
65*	dark-coloured (0.03)	76*	limy (0.00)	87	stoney (0.08)
66*	dense (0.27)	77*	loose (0.48)	88*	thick (0.00)
67*	dirty (0.04)	78*	medium-grained (0.03)	89*	thin (0.00)
68*	dry (0.10)	79*	packed (0.30)	90*	very (0.03)
69*	fine-grained (0.02)	80*	porous (0.17)	91*	water-bearing (0.09)
70*	fossiliferous (0.01)	81	sandy (0.28)	92*	weathered (0.00)

comparison between disparate data sets; or 2) the number of geological descriptions within a single data set thwarts internal comparisons. The Oak Ridges Moraine NATMAP–Hydrogeology Project faced both of these challenges with the MOE water well data set.

STANDARDIZATION PROCEDURES FOR GEOLOGICAL DESCRIPTIONS

The existing literature contains little information regarding standardization procedures for geological descriptions such as those contained in water well data sets. Several sediment-coding schemes have been proposed (i.e. lithofacies codes, Miall, 1977; Eyles et al., 1983). Whereas these may be appropriate for classifying sediment in vertical exposures or in continuously-cored drillholes, such schemes generally require detailed textural and structural information and are thus inappropriate for standardizing the MOE water well data set. Consequently, the project defined and assessed its own standardization procedures. This paper addresses two phases of data standardization, 1) rationalization and 2) reclassification, and assesses two methods of attaining the latter.

Rationalization

Following an audit of material descriptors in the MOE data set, it became apparent that the first step in standardization should be to rationalize descriptors. Such rationalization is justified when the low frequency of usage of many individual descriptors is reviewed (Table 2); these usage statistics suggest that the data collection process, predominately wash-boring, was unable to attain the level of detailed description implied in Table 2. The rationalization process was achieved by 1) removing selected descriptive terms (asterisks, Table 2); 2) simplifying adjective-noun combinations; and 3) reassigning the remaining descriptors to appropriate groups (Table 3). Only three material terms were found to

Table 3. Rationalized descriptors for MOE water well materials. Numbers in brackets indicate per cent usage in all three material fields in MOE data set.

Rationalized descriptor	MOE dataset descriptor			
1 bedrock (0.1%)	18	sandstone	40	flint
	20	quartzite	41	gneiss
	21	granite	42	greywacke
	22	greenstone	43	gypsum
	26	rock (bedrock)	44	iron fm.
	36	basalt	45	marble
	37	chert	46	quartz
	38	conglomerate	47	schist
	39	feldspar	48	soapstone
1.1 limestone (0.8%)	15	limestone	16	dolostone
1.2 shale (0.9%)	17	shale	82	shaly
	19	slate		
2 gravel (9.7%)	11	gravel	31	coarse gravel
	12	stones	32	pea gravel
	13	boulders	72	gravelly
	29	fine gravel	87	stoney
	30	medium gravel		
3 sand (12.3%)	7	quicksand	10	coarse sand
	8	fine sand	28	sand
	9	medium sand	81	sandy
4 silt (1.5%)	6	silt	84	silty
5 clay (16.1%)	5	clay	61	clayey
6 diamicton (0.5%)	14	hardpan	34	till
7 organic (0.1%)	3	muck	33	marl
	4	peat	35	wood frags.
8 fill (3.7%)	1	fill	25	overburden
	2	topsoil		
9 previously dug (0.7%)	23	previously bored	24	previously drilled
99 null (53.6%)	27	-	00	unknown

have ambiguous meaning: hardpan, marl, and muck. Their assignment to rationalized descriptors (Table 3) was based on conversations with drillers and consultants, and regional mapping experience. Rationalization resulted in a reduction of the 82 descriptors (Table 2) to ten major descriptors and two subcategories (Table 3), and reduced the number of theoretically possible descriptive permutations from more than 500 000 to more than 1400; the actual number used in the MOE data set was 464.

Reclassification

The second phase of standardization is reclassification. This process assigns a single, standardized material description to each water well unit. Two reclassification methods for unit materials are described, the first-attribute method and the rule-based method.

First-attribute method (FAM)

The first-attribute method reclassifies water well materials by considering only the rationalized material descriptions in the first material field (i.e. disregarding the second and third fields). This method reduces the number of possible material descriptions to those in the rationalized categories (Table 3). This is a method often implemented by hydrogeologists (e.g. Beckers and Frind, 1997; Holysh and Kassenaar, 1997; Martin et al., 1997).

Rule-based method (RBM)

The rule-based method assigns a single, material descriptor to each water well unit by applying conditional rules to descriptors and, where necessary, integrating descriptors across multiple fields (~30% of well units). Conditional rules were developed from an understanding of the regional geology. Following extensive regional mapping in the Oak Ridges Moraine area, a regional geological model was developed (e.g. Sharpe et al., 1996). This knowledge resulted in the formulation of an inclusive, yet simple, list of regionally relevant and geologically accurate material descriptions (Table 4). The task of the rule-based method was to apply conditional rules in order to reclassify unit materials to these geologically meaningful categories. For example, diamicton (till) is regionally extensive in southern Ontario, both at the surface and in the subsurface (e.g. Sharpe et al., 1996), yet it is only explicitly described in about 0.05% of units in the data set (diamicton, Table 3); if 'diamicton' is to be better extracted from this data set, then the designation must be applied from conditional rules controlling descriptor integration across multiple fields.

Conditional rules (programming statements) were defined and applied in four steps: I) simplify attribute strings, II) apply global rules, III) apply bedrock rules, and IV) apply sediment texture rules (Table 5). These routines were performed sequentially. Two subroutines were then applied to determine A) diamicton texture and B) bedrock lithology (Table 5). Routines I–III are discussed in more detail below; routines IV, and A and B are self-explanatory.

Table 4. Geological (material) description informed by regional geological knowledge and applied in rule-based method. Percentage usage reported for all three material fields in MOE data set.

	Geological description	Usage %
99	no obvious material code	0.15
11	covered; missing; previously bored	0
10	fill (incl. topsoil, waste)	13.29
9	organic	0.15
8	clay, silty clay	21.21
7	silt, sandy silt, clayey silt	2.52
6	sand, silty sand	28.68
5	gravel, gravelly sand	14.89
4	clay-clayey silt diamicton	0.22
4-1	clay-clayey silt diamicton, stoney	
3	silt-sandy silt diamicton	13.90
3-1	silt-sandy silt diamicton, stoney	
3-3	diamicton, texture unknown	
2	silty sand-sand diamicton	0.41
2-1	silty sand-sand diamicton, stoney	
1	bedrock	4.58
1-1	limestone	
1-2	shale	
1-4	dolomite	
1-5	potential bedrock	
1-7	interbedded limestone/shale	

Routine I was designed to simplify descriptor strings (Table 5, routine I). This routine involved removal of duplicate descriptors (often an artifact of the rationalization process), deletion or modification of descriptors when in geologically unlikely combinations, and removal of leading null fields. The net effect of this routine was to reduce the occurrence of 'clay' which, based on regional mapping (e.g. Sharpe et al., 1997), is over-emphasized in the MOE data set.

Routine II applied six global rules (Table 5, routine II). Most of these rules are self-explanatory. In an attempt to balance the under-representation of regionally relevant, geologically accurate descriptions such as 'diamicton' and 'gravel', conditional rules were applied that emphasized these designations where warranted (Table 5, routines II.2 and II.3).

Routine III applied bedrock rules (Table 5, routine III). This routine was only applied to units that were located at the bottom of wells, or to units whereby all deeper units were classified as bedrock (i.e. it was an iterative routine starting at the lowest unit in every well). The 5 m depth-below-surface condition is based on the assumption that the driller can most probably correctly identify bedrock at shallow depth, and would be more likely to make mistakes at greater depths (Table 5, routine III.2 and III.3). This rule ensures a conservative estimate; it prevents under-estimating the depth to bedrock across the region (e.g. Brennand et al., 1997a).

Table 5. Conditional rules applied by the rule-based method of data standardization to MOE data set.

I. Simplify descriptor strings:
I.1. If organic has an accompanying descriptor, then organic is treated as null (see I.5).
I.2. If clay occurs with sand or gravel, then clay is treated as silt.
I.3. If bedrock descriptor is not for the last unit of the well or not with continuous bedrock beneath, then bedrock is treated as gravel.
I.4. If clay or silt is with shale, then clay and/or silt is treated as null (see I.5).
I.5. Remove duplicate attributes and spaces; eliminate all leading null fields.

II. Apply Global rules
II.1. If a single descriptor, then the description is based directly on that descriptor (see Table 4).
II.2. If till in any field, then treat as diamicton (see Subroutine A below).
II.3. If gravel is in any field with no bedrock and clay is not first descriptor, then treat as gravel.
II.4. If fill and previously dug in any field are without bedrock, then treat as fill; else with bedrock, then treat as potential bedrock.
II.5. If all fields are null, then treat as no obvious material code.
II.6. If previously dug or fill are in any field except with bedrock, then treat as fill.

III. Apply bedrock rules (Apply if last unit in well or if continuous bedrock beneath)
III.1. < 5 m depth, bedrock anywhere then code = bedrock (see Subroutine B below for categories)
III.2. > 5 m depth, bedrock anywhere and gravel anywhere then code = gravel
III.3. > 5 m depth, bedrock anywhere and sand/silt/clay and no gravel then code = diamicton (see Subroutine A below)

IV. Apply sediment texture rules
IV.1 Attribute 1 = sand with attribute 2/3 = silt or clay and no gravel, then treat as sand
IV.2 Attribute 1 = silt with attribute 2/3 = sand or clay and no gravel, then treat as silt
IV.3 Attribute 1 = clay with attribute 2/3 = sand or silt and no gravel, then treat as silt

Subroutine A: determine diamicton texture (Use textural sand-silt-clay attribute in highest attribute position)
1. If sand, then treat as silty sand diamicton
2. If silt, then treat as silt diamciton
3. If clay, then treat as clay silt diamicton
4. If no texture indicated, then treat as silt diamicton

Subroutine B: determine bedrock lithology
1. If bedrock in any field and not with limestone or shale, then treat as bedrock
2. If limestone in any field and not with shale, then reclassify as limestone
3. If shale in any field and not with limestone, then reclassify as shale
4. If limestone and shale in any field, then reclassify as interbedded limestone - shale

Examples of the reclassification of geological units based on the application of conditional rules (Table 5) is presented in Table 6. A complete listing of each rationalized attribute string and its reclassification is presented in Russell et al. (1998a).

ASSESSMENT OF STANDARDIZATION (RECLASSIFICATION) PROCEDURES

Testing is required to assess confidence in the material reclassifications of units achieved by the first-attribute method and the rule-based method. Two tests are presented and discussed, 1) a comparison of the geological reclassification of well units at 1 m depth below the surface with the surficial geology map unit (defined as the material at 1 m depth below the surface, e.g. Sharpe et al., 1997) at each well location, and 2) an assessment of the reclassified material at the first screen depth in the well. The latter test is based on the assumption that the first screen is located in aquifer material (sand or gravel).

Table 6. Examples of geological reclassification based on the application of conditional rules (RBM = rule-based method; Table 5).

Descriptor 1	Descriptor 2	Descriptor 3	RBM reclassification
Bedrock			Bedrock (1)
Clay	Gravel		Silt diamicton (3)
Silt	Shale		Shale (1-2)
Gravel	Sand		Gravel (5)

Comparison to surficial geology

The Oak Ridges Moraine NATMAP–Hydrogeology Project regional surficial geology compilation map was the benchmark for this test (Sharpe et al., 1997; simplified in Fig. 1). The results of the comparison for four of the major map units are presented in Figure 2 (data for all map units are presented in Russell et al., 1998a).

The Oak Ridges Moraine is a regional aquifer (Fig. 1). Its sediments generally range from silty sand to gravel; minor beds of clay (Fig. 3; Gilbert, 1997) and diamicton have been observed (Sharpe et al., 1997). In two boreholes through the Oak Ridges Moraine only about 1% of the total thickness was clay, whereas up to about 80% was silt and sand (Russell et al., 1998c). Using 'sand' and 'gravel' as acceptable materials for this map unit, the rule-based method performs marginally better than the first-attribute method, especially with regard to identifying gravel in the Oak Ridges Moraine. Both methods are able to appropriately describe this map unit and confirm its aquifer status in more than 50% of the wells drilled through it.

Halton Till is a complex fine-grained unit, often forming an aquitard (nonaquifer) in the western part of the region. It is best characterized as a stone-poor (<1%), silt to clay diamicton, interbedded with glaciolacustrine silt and clay; the diamicton component is thicker in the western part of the region and becomes thinner and more sandy in the east where it overlies the Oak Ridges Moraine. In comparison, Newmarket Till is generally an overconsolidated stone-rich (5-10%), silty sand diamicton; relatively thin sand and gravel beds may be observed within it. Newmarket Till is generally characterized as a dissected regional aquitard (e.g. Sharpe et al., 1996). The most accurate geological description for both of these units is 'diamicton' (till). For both map units the rule-based method clearly out-performs the first-attribute method, but in neither case exceeds 30% accuracy (Fig. 2). The better performance of the rule-based method is expected as the conditional rules were, in part, designed to integrate descriptors and generate more meaningful geological descriptions. If the descriptions 'sand' and 'gravel' are also accepted for Newmarket Till, the rule-based method continues to out-perform the first-attribute method, but if the descriptions 'clay' and 'silt' are accepted for Halton Till, then this performance reverses (first-attribute method, 70.5%; rule-based method, 58.4%; Fig. 2). Despite numerous misclassification (Fig. 2), both methods confirm the nonaquifer status of both the Halton Till and Newmarket Till, the rule-based method being more geologically accurate.

When compared with bedrock polygons both methods have a poor correlation (13%, Fig. 2). Despite the application of conservative rules, the rule-based method correlates marginally better than the first-attribute method. The poor correlation of both methods with bedrock polygons may reflect the character of weathered silt and shale of the Queenston and Georgian Bay formations (e.g. White, 1975), both of which may have been understandably misclassified by drillers as 'clay' (Fig. 2). Alternatively, it may suggest that much of the area within bedrock polygons actually has a thin cover (~1 m thick) of surficial sediments. This issue of cartographic resolution was tested independently by comparing well unit reclassification (rule-based method) with known bedrock outcrops within bedrock map polygons. This comparison indicates that within 100 m of an outcrop, about 60% of the water wells intercept bedrock at less than 5 m, but this frequency declines to 39% at 500 m (Russell et al., 1998a). From this comparison it would appear that assessment of the performance of the bedrock reclassification is hindered by cartographic resolution.

The predominance of 'clay' as the description for all map units is overwhelming in the first-attribute method; clay exceeds all other descriptions by more than a 2:1 ratio, except within the Oak Ridges Moraine map unit were sand is dominant (Fig. 2). The first-attribute method truncates descriptions at the first field. For entries in the first field the term 'clay' accounts for 31% of single attribute entries and 70% of multiple attribute entries. Consequently, by ignoring entries in the second and third fields, the first-attribute method is expected to over-emphasize 'clay'. Furthermore, as material descriptions are based on drill chips and sediment flushed to the surface in the drilling process, inaccurate description (e.g. of wet silt or stone-poor diamicton) should be expected throughout the data set.

Assessment at first screen depth

Drillers place screens within water-bearing units to prevent water well resedimentation during pumping. The screen location can thus be used as a proxy for aquifer locations and thus for sand and/or gravel units. An assessment of all reclassified well units coinciding with first screen depth indicates that both the first-attribute method and the rule-based method reclassify more than 85% as sand and/or gravel. However, the rule-based method is more likely to reclassify a unit as gravel rather than sand (Fig. 4).

In summary, the first-attribute method permits a moderately reliable bipartite assignment of sediment to either aquifer or nonaquifer status. This method is generally adequate for about 70% of the units (described by a single field in the MOE data set), but may misclassify about 30% of the units (described by multiple fields in the MOE data set). The rule-based method allowed material standardization (reclassification) to be informed by knowledge of the regional geology. This method again allows moderately reliable aquifer and nonaquifer assignment, but is more geologically accurate.

DISCUSSION

Limitations of the MOE database for geological and hydrogeological investigations

The MOE water well database is a valuable resource for regional geological and hydrogeological investigations. However, standardization procedures and assessments tested by the Oak Ridges Moraine NATMAP–Hydrogeology Project highlight the limitations of integrating this database

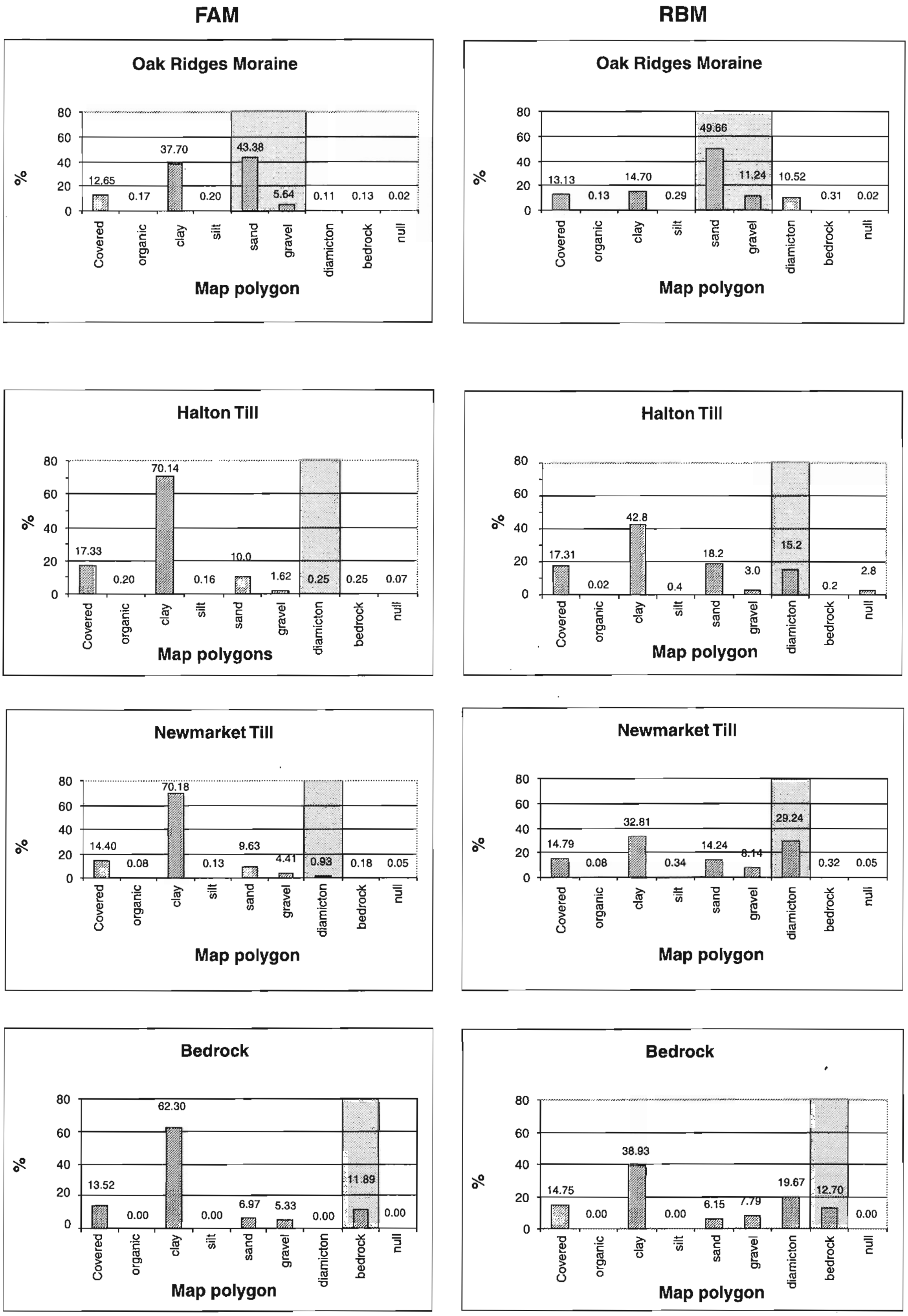

Figure 2.Comparison of surficial geology map units (Sharpe et al., 1997) with MOE unit descriptions (from 1 m depth below surface) reclassified by the first-attribute method (left) and the rule-based method (right). Shaded zones indicate the most appropriate reclassification. FAM — first-attribute method, RBM — rule-based method.

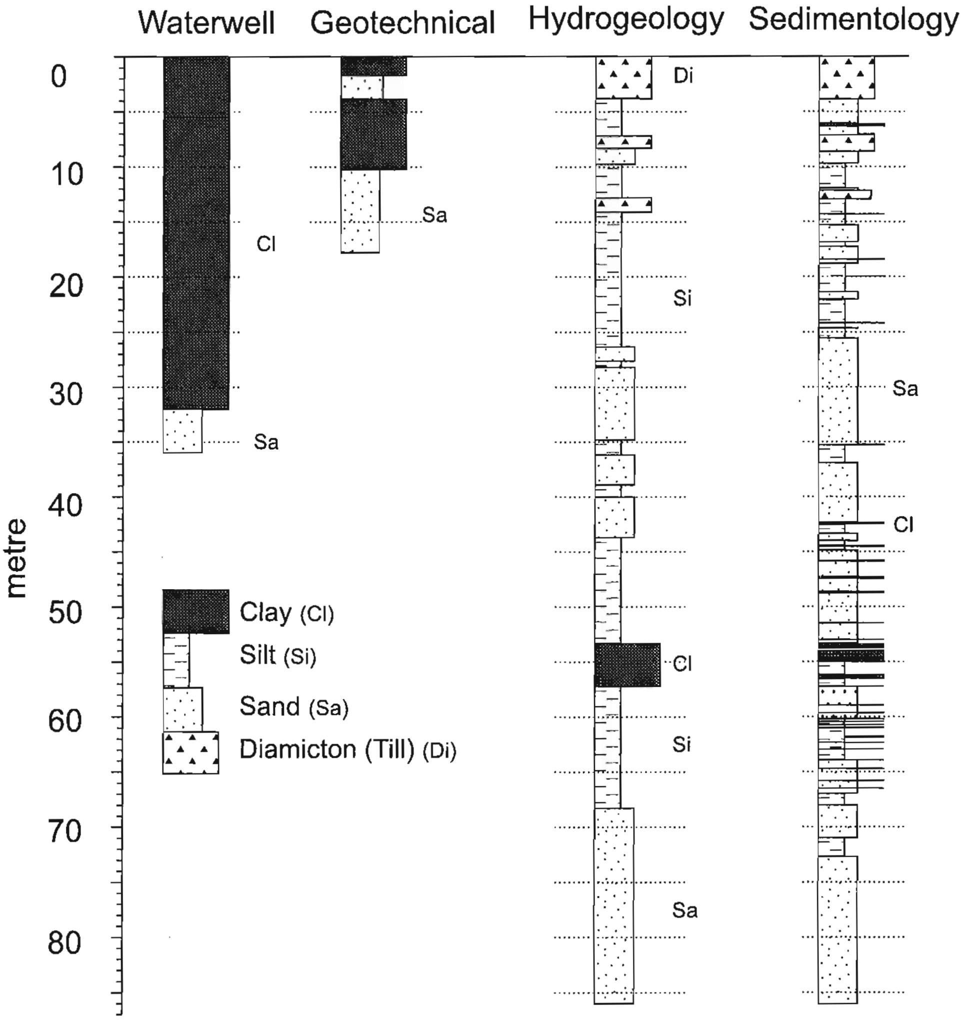

Figure 3. Comparison of the geological resolution available from four types of drilling and logging procedures. Drillholes are from within several kilometres of one another. Note the contrast in unit thickness and variability of sediment textures.

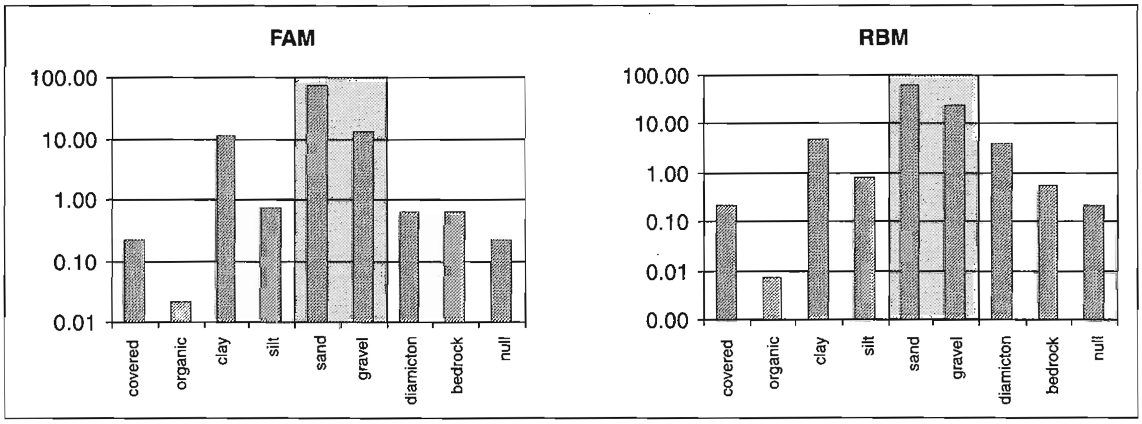

Figure 4. Assessment of reclassified MOE material present at the first screen depth, first-attribute method (FAM, left), rule-based method (RBM, right). Shaded zones indicate the most appropriate reclassification.

Project highlight the limitations of integrating this database into geological or hydrogeological investigations. These limitations include a) location accuracy, b) coverage, and c) geological accuracy and resolution.

Location accuracy

Water well locations are initially reported to the MOE using Lot and Concession designation and a sketch map. This information is then converted to a Universal Transverse Mercator (UTM) co-ordinate, and an elevation is assigned by MOE staff from Ontario Bureau of Mines maps. Spatial comparisons between UTM and Lot and Concession co-ordinates, and between assigned elevation and the Oak Ridges Moraine digital elevation model reported that 27% of well records in the MOE database had planimetric and/or elevation inaccuracies (Kenny et al., 1997).

Coverage

Water well records have a limited vertical coverage as they are drilled to exploit aquifers; in areas of shallow aquifers few wells continue to depth. The Oak Ridges Moraine is a regional aquifer and, as such, less than one third of the total sediment thickness to bedrock is recorded by the water wells intersecting it (Fig. 5; Brennand et al., 1997a; Russell et al., 1998b). Water wells are thus poor data sets to use for assessing potential deeper aquifers and thus for regional groundwater inventory . Whereas water well records can form the most extensive spatial data set in regional geological and hydrogeological investigations, such records may be sparse in metropolitan areas (e.g. Toronto).

Geological accuracy and resolution

The glaciated terrain of southern Ontario is underlain by Paleozoic bedrock, with a terminal grain-size of silt (Dreimanis and Vagners, 1971), and thus silt may be expected to dominate glacial sediments above bedrock. This conclusion is supported by detailed sedimentological reports from continuously-cored drillholes in the Oak Ridges Moraine area. These reports clearly document a very low clay:silt ratio (e.g. Gilbert, 1997; Fig. 3). For two boreholes in the Humber River watershed, clay units formed less than 2% of the total sediment thickness (Russell et al., 1998c). In contrast, disregarding the null fields in the MOE data set, about 40% of all entries in the three material fields are 'clay'. This comparison thus highlights a geologically inaccurate overuse of 'clay' as a descriptor in the MOE data set. Possible reasons for this overuse include 1) likely underestimation of grain size due to the liquified nature of the samples from which drillers make descriptions (a product of the wash-boring drilling technique); and 2) no training requirement in regionally relevant geological descriptions for drillers.

Geological mapping (Sharpe et al., 1997) has shown that diamicton (till) outcrops across about 42% of the region and that these surficial units can attain thicknesses of 30 m, yet in the MOE data set 'till' accounts for only 0.05% of entries in material fields. The rule-based method was able to improve extraction of this regionally relevant, geologically accurate, heterogeneous material from the MOE data set by applying conditional rules and integrating descriptors across multiple fields.

Comparison of geological units from water well records with those from geological and hydrogeological reports highlights a clear disparity in unit resolution (Fig. 3). This disparity likely results from differences in drilling technology, wash-bored and continuously cored drillholes. In the Oak Ridges Moraine area sediment descriptions from continuously cored drillholes (e.g. Gilbert, 1997; Russell et al., 1998c) relate to units with thicknesses generally on the order of decimetres, and for clay units generally less than 1 cm. Material descriptions from water wells relate to units metres to tens of metres thick (Fig. 3). Consequently, the use of water well records for geological purposes should be purely supplemental.

Successful applications of the MOE database

The quantity and spatial distribution of water wells make them an attractive supplemental data source for both geological (e.g. Brennand et al., 1997b) and hydrogeological investigations (e.g. Kreye et al., 1994; Holysh, 1995; Fagan et al., 1997; Singer et al., 1997). However, appropriate integration and application of this data lies in recognizing its limitations and, perhaps, in devising innovative approaches to extracting meaningful information.

The recognition of data limitations and the enhancement of geological accuracy (utilization of the rule-based method) in the MOE database underpin the successful applications of this database in the Oak Ridges Moraine NATMAP–Hydrogeology Project. Successful applications have included 1) structural surface maps (e.g. bedrock topography; Brennand et al., 1997a), 2) isopach maps (e.g. sediment thickness; Russell et al., 1998b), and 3) construction of materials cross-sections to a) delineate aquifers and nonaquifers and thus facilitate the interpretation of stream gauging data (Hinton and Bowen, 1997) and b) interpolate subsurface basin stratigraphy (Russell et al., 1996a).

SUMMARY AND RECOMMENDATIONS

Two procedures for standardizing geological descriptions in the MOE database have been described and assessed. The first-attribute method (FAM) is a simple, effective method for characterizing units described by a single material field, but fails to capitalize on the additional information provided in units described by multiple fields. This procedure is able to broadly delimit aquifers and nonaquifers. The rule-based method (RBM) benefits from regional geological knowledge; the conditional rules applied here should be modified as knowledge is gained and should be regionally specific. The rule-based method is able to broadly delimit aquifers and nonaquifers, and is more geologically accurate. This procedure is recommended where water well data are to be integrated into geological and hydrogeological investigations. In the latter case, this may be important if regional hydrogeological parameters (e.g. hydraulic conductivity) are to be

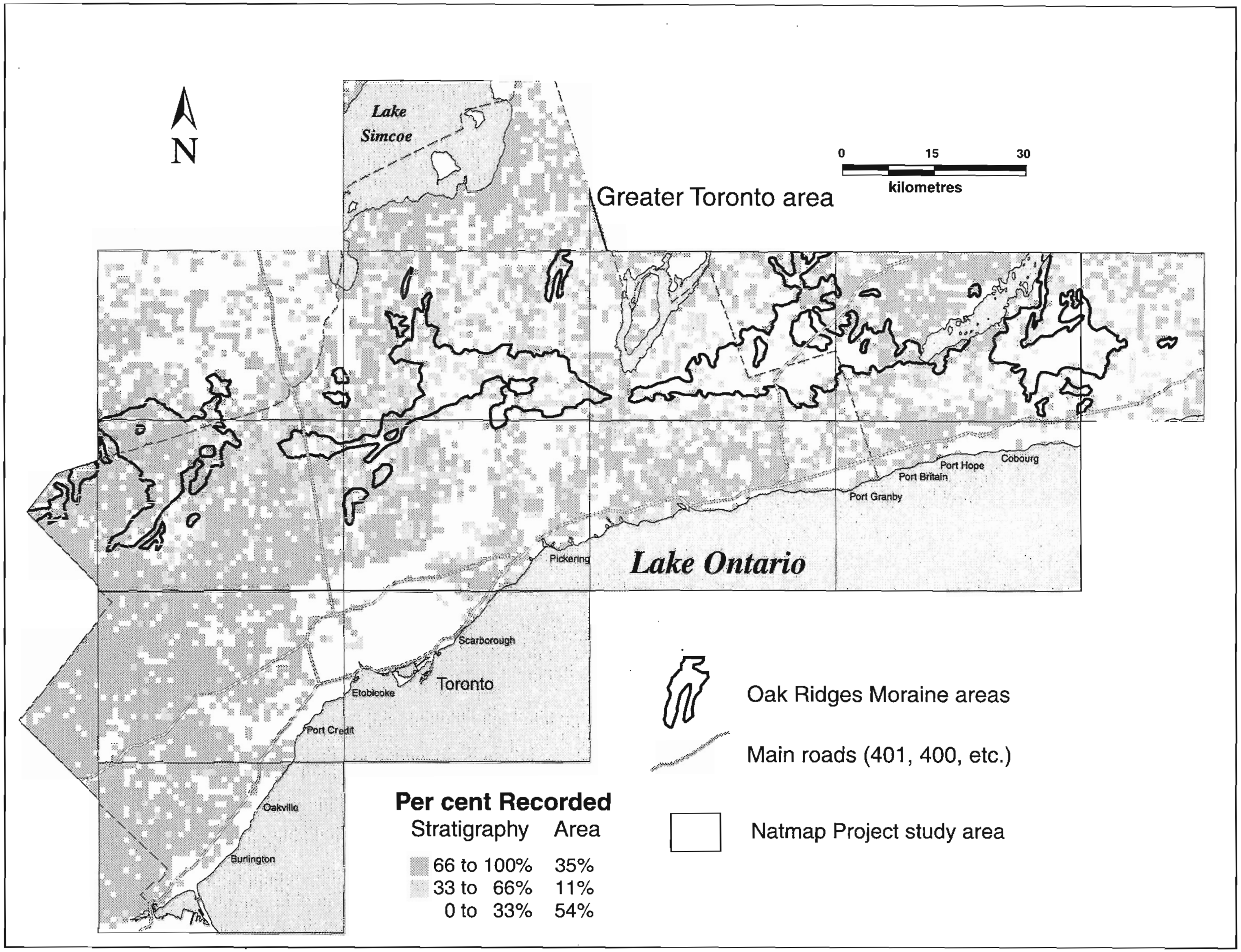

Figure 5*. Sediment thickness intercepted by the deepest MOE water well in a 1 km^2 grid as a percentage of the total sediment thickness as defined by an interpolated bedrock surface and topographic surface DEM (modified from Russell et al. 1998).*

estimated from material descriptions. Limitations to the application of the MOE database in geological and hydrogeological investigations include: 1) location accuracy (Kenny et al., 1997); 2) coverage; and 3) geological accuracy and resolution. As water well descriptions have recognized regional variations, any rationalization and coding process should first carefully screen data sets.

Water well databases are valuable data sets for regional geological and hydrogeological investigations. Despite its limitations, the MOE database has become a cornerstone for the assessment of subsurface conditions by hydrogeologists, and for the creation of municipal groundwater management and extraction plans by Ontario hydrogeologists and planners. Most criticisms of such databases relate to the simple fact that they were never intended for such use. Consequently, in order to enhance water well databases for geological and hydrogeological purposes several recommendations are proposed with regard to standardization of geological descriptions: 1) reduce the attribute fields to two only, 2) reduce the number of material descriptors to about 10-12 (e.g. Tables 3 and 4), 3) implement a standardized description form, and 4) implement a training session on geological descriptions. The value of standardized reporting of water well data has been recognized at the national scale (Gilliland, 1990). Standardization of geological descriptions will reduce confusion, duplication of effort, and cost. All revisions to reporting protocol should be reviewed by user groups, and by provincial or state and national groundwater associations.

ACKNOWLEDGMENTS

The Oak Ridges Moraine Project has been funded by the GSC National Mapping and Hydrogeology programs. External funding has been received from a number of Ontario provincial ministries, notably the Ontario Ministry of Environment. The invaluable assistance of I. Pawlowski and F. Johnson is greatly appreciated. Critical reviews by R.J. Belanger and M. Hinton helped improve the paper. The assistance of P. Stacey and S. Lambert are appreciated.

REFERENCES

Anonymous
1994: Long-term water strategy, GW-1 additional groundwater task; prepared for Regional Municipality of Waterloo by CH2M Hill, 75 p.

Beckers, J. and Frind, E.
1997: The role of geology in the uncertain response of a groundwater system; *in* Geological Association of Canada, Program with Abstracts, Ottawa'97, May, 1997, Ottawa, Ontario, p. A-9.

Belanger, J.R.
1975: UGAIS data record instruction manual; Geological Survey of Canada, Open File 292, 11 p.

Belanger, J.R. and Harrison, J.E.
1980: Regional geoscience information: Ottawa-Hull; Geological Survey of Canada, Paper 77-11, 18 p.

Brennand, T.A.
1998: Urban geology note: Oshawa Ontario; *in* Urban Geology of Canadian Cities, (ed.) P.F. Karrow; Geological Association of Canada, Special Paper 42.

Brennand, T.A., Moore, A., Logan, C., Kenny, F.M., Russell, H.A.J., Sharpe, D.R., and Barnett, P.J.
1997a: Bedrock topography of the Greater Toronto and Oak Ridges Moraine areas, southern Ontario; Geological Survey of Canada, Open File 3419, scale 1: 200 000.

Brennand, T.A., Russell, H.A.J., and Logan, C.
1997b: Development of a regional geoscience database: application to hydrogeologic investigations, Oak Ridges Moraine area, southern Ontario; *in* Geological Association of Canada, Program with Abstracts, Ottawa'97, May, 1997, Ottawa, Ontario, p. A-17.

Dreimanis, A. and Vagners, U.
1971: The bimodal distribution of rock and mineral fragments in basal tills; *in* Till-a symposium, (ed.) R.P. Golthwait; Ohio State University Press, 237-250 p.

Eyles, N., Clark, B.M., Kaye, B.G., Howard, K.W.F., and Eyles, C.H.
1985: The application of basin analysis techniques to glaciated terrains; an example from the Lake Ontario Basin, Canada; Geoscience Canada, v. 12, p. 22-32.

Eyles, N., Eyles, C.H., and Miall, A.D.
1983: Lithofacies types and vertical profile models: an alternative approach to the description and environmental interpretation of glacial diamict and diamictite sequences; Sedimentology, v. 30, p. 393-410.

Fagan, F., Bourque, E., Lefebvre, F., Michaud, Y., Martel, R., Bolduc, A.M., Parent, M., and Boisvert, E.
1997: Hydrogeological mapping applied to land use planning: the Laurentian Piedmont Project; *in* Geological Association of Canada, Program with Abstracts, Ottawa '97, May 19-21, 1997, p. A-48.

Fenco-MacLaren, I.
1994: IWA landfill site search, Metro/York region: Step 6 hydrogeological report sites V3B, V4A, V4D; Interim Waste Authority Report, prepared by M. Gomer, Fenco MacLaren Inc., January 1994, Willowdale, Ontario.

Gilbert, R.
1997: Glaciolacustrine sedimentation in part of the Oak Ridges Moraine; Geographie physique et Quaternaire, v. 7, p. 55-66.

Gilliland, J.
1990: Report on federal/provincial workshop on groundwater data banks; National Hydrology Research Centre, Saskatoon, Saskatchewan, p. 75.

Hinton, M.J. and Bowen, G.S.
1997: Stream baseflow surveys to identify regional groundwater discharge and chemistry in the Oak Ridges Moraine; *in* Geological Association of Canada, Program with Abstracts, Ottawa '97, May 19-21, 1997, Ottawa, Ontario, p. A-68.

Holysh, S.
1995: Halton Aquifer Management Plan, Phase 1 report, background hydrogeology; Regional Municipality of Halton, p. 92.

Holysh, S. and Kassenaar, D.C.
1997: Regional ground water modelling of complex bedrock valley aquifer systems; *in* Geological Association of Canada, Program with Abstracts, Ottawa'97, May, 1997, Ottawa, Ontario, p. A-69.

Kehew, A., Straw, W., Thomas, N., Nicks, L., Kendzierski, S.K., Gardner, R.C., Flint, A.C., Hughes, L.D., and Baker, C.
1998: Glacial terrain mapping with hydrogeological applications in St. Josephs County, Michigan; *in* Abstracts with Program, Northeast Sectional Meeting of the Geological Society of America, Portland, Maine, March, 1998.

Kenny, F.M., Chan, P., and Hunter, G.
1997: Quality control of the positional accuracy of records in Ontario's water well database using automated GIS techniques; *in* Conference Proceedings Geomatics in the Era of RADARSAT GER 97, Ottawa, May 24-30, 1997.

Kreye, R., Ronneseth, K., and Wei, M.
1994: An aquifer classification system for groundwater management in British Columbia; *in* 6th National Drinking Water Conference, Victoria, British Columbia.

LeGrand, H.E. and Rosen, L.
1998: Putting hydrogeology site studies on track; Ground Water, v. 36, p.193.

Mantha, L.
1988: Ministry of the Environment Water Well Information System – selecting, reporting and plotting of wells and their characteristics; Ontario Ministry of Environment and Energy, 29 p.

Martin, P.J., Guiger, N.,and Van Vliet, D.J.
1997: Regional modelling of complex multi-aquifer systems; *in* Geological Association of Canada, Program with Abstracts, Ottawa'97, May, 1997, Ottawa, Ontario, p. A-98.

McCleneghan, M.B. and Dilabio, R.N.W.
1995: Overburden database compilation, Timmins, Ontario (42A/11, 12,13,14); Geological Survey of Canada, Open File 3086, 12 p.

Miall, A.D.
1977: A review of the braided-river depositional environment; Earth-Science Reviews, v. 13, p.1-62.
1984: Principles of Sedimentary Basin Analysis; Springer-Verlag, New York, 490 p.

Russell, H.A.J., Brennand, T.A., Kenny, F.M., Sharpe, D.R., and Barnett, P.J.
1996a: The application of GIS to a Quaternary basin analysis, Oak Ridges Moraine area, southern Ontario; *in* Geomatics 1996, 8th International Conference on Geomatics, May 28-30 (abstract), Ottawa, Ontario.

Russell, H.A.J., Brennand, T.A., Logan, C., and Sharpe, D.R.
1998a: Coding sediment descriptions fom drilling records: documentation of MOE water well coding Greater Toronto and Oak Ridges Moraine areas southern Ontario; Geological Survey of Canada, Open File 3616, 30 p.

Russell, H.A.J., Logan, C., Brennand, T.A., Hinton, M., and Sharpe, D.R.
1996b: A regional geoscience database: an example from the Oak Ridges Moraine NATMAP / Hydrogeology Project; *in* Current Research 1996-E; Geological Survey of Canada, p. 191-198.

Russell, H.A.J., Moore, A., Logan, C., Kenny, F., Brennand, T.A., Sharpe, D.R., and Barnett, P.J.
1998b: Sediment Thickness of the Greater Toronto and Oak Ridges Moraine areas, southern Ontario; Geological Survey of Canada, Open File 2892, scale 1:200 000.

Russell, H.A.J., Sharpe, D.R., and Arnott, W.R.C.
1998c: Sedimentology of the Oak Ridges Moraine, Humber River Watershed, southern Ontario: a preliminary report; *in* Current Research 1998-C; Geological Survey of Canada, p. 155-166.

Sharpe, D.R., Barnett, P.J., Brennand, T.A., Finley, D., Gorrell, G., and Russell, H.A.
1997: Surficial geology of the Greater Toronto and Oak Ridges Moraine areas compilation map sheet; Geological Survey of Canada, Open File 3062, scale 1:200 000.

Sharpe, D.R., Dyke, L.D., Hinton, M.J., Pullan, S.E., Russell, H.A.J., Brennand, T.A., Barnett, P.J., and Pugin, A.
1996: Groundwater prospects in the Oak Ridges Moraine area, southern Ontario: application of regional geological models; *in* Current Research 1996-E; Geological Survey of Canada, 181-190 p.

Sharpe, D.R., Pullan, S., and Warman, T.
1992: A basin analysis of the Wabigoon area of Lake Agassiz, a Quaternary clay basin in northwestern Ontario; Geographie physique et Quaternaire, v. 46, p. 295-309.

Singer, S., Cheng, C.K., and Scafe, M.G.
1997: The hydrogeology of southern Ontario, volume 1; Ontario Ministry of Environment and Energy.

Watt, A.K.
1952: Ground water in Ontario, 1947; Ontario Department of Mines, 116 p.
1961: Ground water Ontario, 1953 and 1954; The Ontario Water Resources Commission, 302 p.

White, O.L.
1975: Quaternary geology of the Bolton area, Southern Ontario; Ontario Division of Mines, Ministry of Natural Resources, Geological Report 117, 119 p.

Geological Survey of Canada Project 930042

EASTERN CANADA AND NATIONAL AND GENERAL PROGRAMS

EST DU CANADA ET PROGRAMMES NATIONAUX ET GÉNÉRAUX

Preliminary results and tectonic setting of the Cap-Rouge earthquake of November 5, 1997, Quebec

L. Nadeau, M. Lamontagne[1], R.J. Wetmiller[1], P. Brouillette,
A. Bent[1], and P. Keating[2]
GSC Quebec, Sainte-Foy

Nadeau, L., Lamontagne, M., Wetmiller, R.J., Brouillette, P., Bent, A., and Keating, P., 1998: Preliminary results and tectonic setting of the Cap-Rouge earthquake of November 5, 1997, Quebec; in *Current Research 1998-E; Geological Survey of Canada, p. 105–115.*

Abstract: The November 5, 1997 magnitude (M) 5.1 (Nuttli scale) Cap-Rouge earthquake was one of the largest event known to have occurred in the Québec City metropolitan area (maximum intensity VII). Forty-five aftershocks of $0.4 \leq M \leq 2.9$ were recorded in the following 35 days.

The location of the main shock rupture, determined from the accurate location of five aftershocks recorded by three or four field stations, is within an (2 x 2 x 2) km^3 volume, centred at about 46.77°N, 71.41°W at a depth of 21.6 km. The focal mechanism calculated from the P-first motions at 38 seismograph stations is consistent with reverse movement on a northeast-striking and steeply dipping fault.

The hypocentres are located in the Grenville Province basement, beneath the St. Lawrence Lowlands platform and overlying Appalachian nappes. Surface geology, oil exploration well, seismic, and magnetic field data are consistent with a seismic source located along the projection to mid-crust of the Neuville Fault, part of the Iapetan paleorift fault system.

Résumé : Le tremblement de terre de magnitude (M) 5.1 (échelle de Nuttli) qui a ébranlé Cap-Rouge le 5 novembre 1997 est l'un des plus grands séismes à se produire dans la région métropolitaine de Québec (intensité maximale VII). Quarante-cinq répliques de magnitude $0.4 \leq M \leq 2.9$ ont été enregistrées au cours des 35 jours qui ont suivis.

L'emplacement de la rupture associée au choc principal, déterminé en situant avec précision les hypocentres de cinq répliques enregistrées à au moins trois des quatre stations du réseau de terrain, se trouve au sein d'un volume de (2 x 2 x 2) km^3 centré à environ 46,77° N, 71,41°W et à une profondeur de 21,6 km. Le mécanisme au foyer calculé à partir des premières arrivées des ondes P à 38 stations séismiques correspond à un mouvement inverse le long d'une faille à pendage abrupt et de direction nord-est.

Les hypocentres se situent dans le socle grenvillien, sous la plate-forme des basses terres du Saint-Laurent et des nappes appalachiennes sus-jacentes. Les données sur la géologie de surface, les données tirées des forages d'exploration pétrolière et les données séismiques et magnétiques attestent d'une source séismique située le long de la projection à mi-profondeur de la croûte de la faille de Neuville, une des failles associées au paléo-rift de Iapetus.

---

[1] Seismology Section, Ottawa
[2] Continental Geoscience Division, Ottawa

INTRODUCTION

The magnitude 5.1 Cap-Rouge earthquake occurred on November 5, 1997 at 21:34. The event was strongly felt in the Québec City metropolitan area (maximum intensity VII) and over a wide region of southern Quebec, eastern Ontario, and the northern New England states. This event is probably the largest historical earthquake centred in the Québec City region and the largest to be felt in the area since the November 25, 1988, magnitude 6.5 Saguenay earthquake (Lamontagne et al., 1988; Du Berger et al., 1991). Coincidentally, the shock occurred immediately following the broadcast on the Discovery Channel of a documentary on earthquakes along the San Andreas Fault. Fortunately, due to the deep focus of the event, damage was limited to the epicentral vicinity. A school in Neuchatel (about 10 km epicentral distance) suffered a few thousand dollars of damage due to fallen concrete blocks and masonry. Otherwise, damage was limited to a few fallen shelves, and cracked plaster and concrete (Cajka and Halchuk, in press).

Following the earthquake, an aftershock team deployed four portable digital seismographs (PRS-4) at five different sites. The main goal of the aftershock survey was to refine the hypocentral location of the main shock by determining the focal depth of the aftershocks. The Québec City region is located near the taper of the St. Lawrence Lowlands platform against the Grenville basement and the overthrusted Appalachian nappes. Given the well constrained geological setting of the region, accurate localization of the hypocentre makes a direct correlation with a known fault system possible. It can provide a key element for a better understanding of neotectonism in the St. Lawrence Valley, which is poorly documented away from the more active Western Québec and Charlevoix seismic zones. This report presents the preliminary results from the study of the Cap-Rouge earthquake, within its regional neo- and paleotectonic framework.

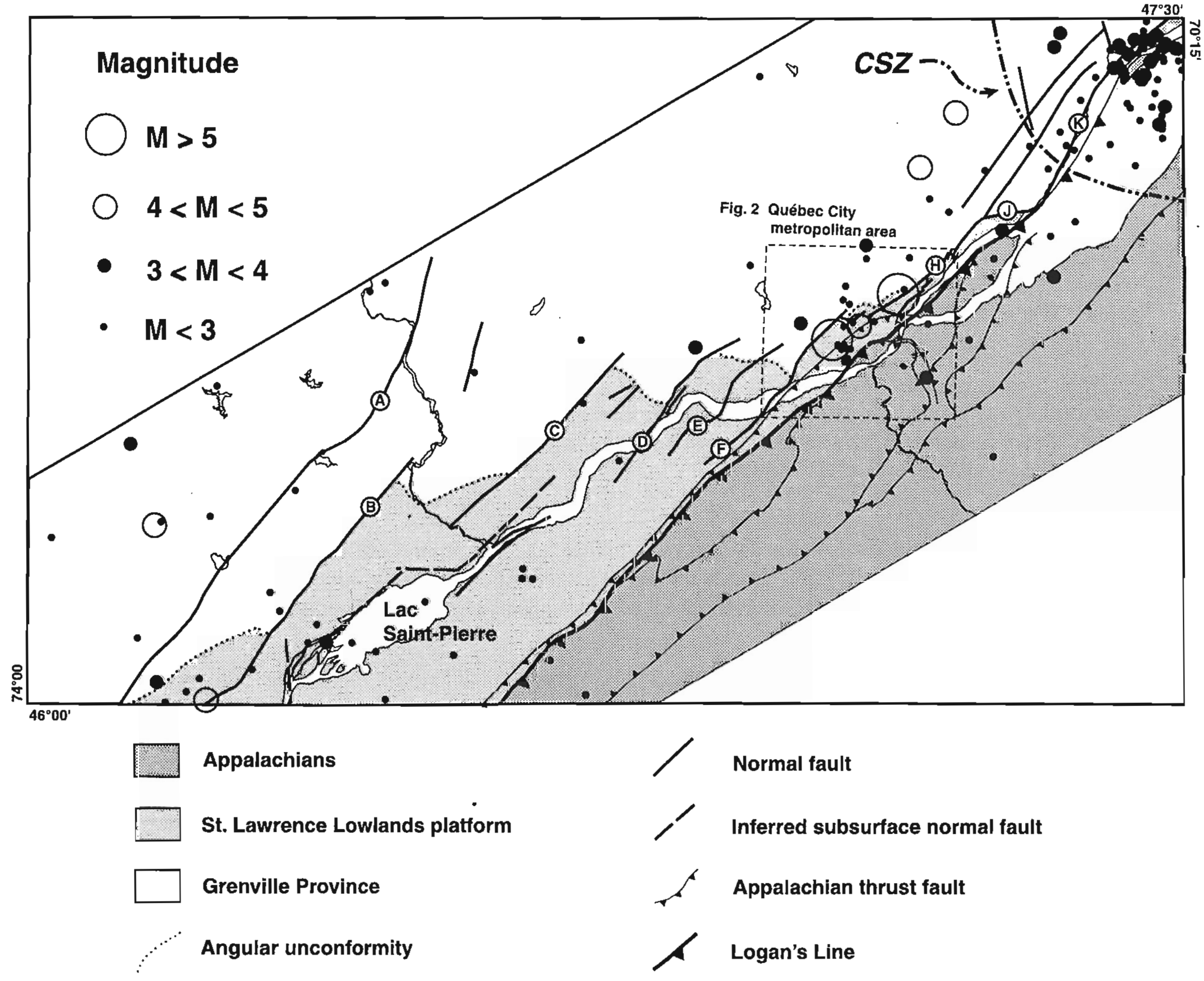

Figure 1. Epicentral map of historical earthquakes in the Québec City–Lac Saint-Pierre region. Includes all earthquakes reported in Table 1. CSZ: Charlevoix seismic zone; normal faults: A: Saint-Maurice, B: Saint-Cuthbert, C: Saint-Prosper, D: Deschambault, E: Jacques-Cartier, F: Neuville, H: Montmorency, J: Cap Tourmente, K: Saint-Laurent

HISTORICAL SEISMIC ACTIVITY

The Québec City region is located in a relatively quiescent area, between the Charlevoix seismic zone to the northeast and the Western Québec seismic zone (Fig. 1; *see* Adams and Basham (1991) and Lamontagne (1987) for comprehensive reviews). The region was the locus of at least seven earthquakes of magnitude (M)≥4.0 since 1608, with the largest event in 1864 at an estimated M~5 (Table 1). Accordingly, the measured M=5.1 Cap-Rouge earthquake stands as the largest historical event to be centred in the Québec City area.

In addition, the Québec City–Lac Saint-Pierre region was also the locus of nine earthquakes of 3.0≤M<4.0 since 1960, and of over 62 earthquakes of 2.0≤M<3.0 between 1980 and April 1998 (Fig. 1, Table 1). Although admittedly modest, the seismic activity of the region stands above regional background of the adjacent shield, St. Lawrence Lowlands, and Appalachian Mountains. A large proportion of the epicentres are located near the shield margin, many along mapped faults or subsurface faults inferred from seismic and oil exploration well data (Fig. 1). Given a thin St. Lawrence platform cover sequence (<2 km, Globensky, 1987), most of the earthquakes originate within Grenville basement structures.

SEQUENCE OF EVENTS

The Cap-Rouge earthquake of November 5, 1997 occurred at 21:34:33 Eastern Standard Time (EST), i.e. November 6 at 02:34:33 Universal Time (UT; during the aftershock survey, Eastern Standard Time (EST) = Universal Time (UT) - five hours). From November 6 to December 24 an aftershock survey was carried out by Geological Survey of Canada personnel R.J. Wetmiller and M. Lamontagne from the Seismology Section (Ottawa) and L. Nadeau and P. Brouillette from the Québec Geoscience Centre (Sainte-Foy). Four Scintrex PRS-4 portable seismographs were deployed at five different sites in the western suburbs of the Québec City metropolitan area (Fig. 2). Field station one was deployed by 21:06 EST November 6, approximately 24 h after the main shock, the third site by 16:20 EST on November 7, and station five by 17:30 EST November 9. The recorder at site 1 was moved to

Table 1. Major earthquakes in the Québec City–Lac Saint-Pierre region since 1608. Events have been selected to insure detection completeness between 1608 and April 1998. Hence, events reported are M≥5.0 after 1608 (two events), M≥4.0 since 1900 (seven events), M≥3.0 since 1965 (16 events), and M≥2.0 since 1980. Events of the same earthquake sequence are marked by asterisks. Data from the GSC – Canadian National Earthquake Database.

Event	Date	Latitude	Longitude	Magnitude
1	**1864/04/20**	**46.90N**	**71.20W**	**5.0**
2	1914/02/14	46.40N	73.60W	4.3
3	1926/11/08	46.01N	73.43W	4.0
4	1927/07/25	47.30N	71.00W	4.0
5	1945/06/18	47.18N	71.12W	4.7
6	1964/01/20	46.83N	71.33W	4.0
7	1967/09/23	46.93N	70.70W	3.4
8	1968/07/24	47.01N	71.30W	3.1
9	1977/10/16	46.58N	73.68W	3.0
10	1980/03/11	46.79N	71.86W	3.7
11	1980/04/01	47.17N	70.90W	2.4
*12	1981/01/01	46.18N	73.08W	2.9
*13	1981/01/01	46.21N	73.20W	2.1
14	1982/02/06	46.25N	73.23W	2.4
15	1982/12/06	46.02N	72.23W	2.6
16	1983/03/21	46.98N	71.30W	2.8
17	1983/07/04	46.74N	72.57W	2.6
18	1983/07/23	46.53N	70.91W	2.9
19	1983/11/01	46.41N	73.57W	2.3
20	1984/01/15	46.54N	72.11W	2.5
*21	1984/02/13	46.89N	71.38W	2.2
*22	1984/02/13	46.88N	71.36W	2.1
23	1984/03/04	47.17N	70.70W	2.2
24	1984/03/19	46.79N	70.98W	2.2
25	1984/05/24	47.02N	70.70W	2.8
26	1984/10/21	46.84N	71.35W	2.3
27	1985/02/06	46.37N	73.93W	2.9
28	1985/05/23	46.81N	72.23W	2.0
29	1985/10/23	47.05N	70.62W	2.1
30	1985/12/26	46.11N	72.64W	2.2
31	1986/02/03	46.84N	71.28W	2.4
32	1986/05/19	46.1N	72.34W	2.1
33	1986/07/01	46.28N	72.39W	2.2
34	1987/01/13	46.91N	71.18W	2.7
35	1988/04/15	46.28N	72.42W	2.5
36	1988/05/12	47.04N	70.82W	3.1
37	1988/10/31	46.48N	73.15W	2.7
38	1988/11/21	46.67N	72.23W	2.1
39	1989/02/22	46.03N	73.49W	2.1
40	1989/09/04	46.30N	72.42W	2.5
41	1990/02/24	46.08N	73.29W	2.1
42	1990/06/21	46.06N	73.45W	2.1
43	1990/10/04	46.42N	73.42W	2.2
44	1990/11/10	47.11N	71.09W	2.0
45	1992/06/28	46.84N	71.52W	3.3
46	1992/07/06	46.15N	73.65W	2.1
47	1992/08/28	46.71N	71.12W	3.5
48	1992/10/28	46.94N	72.86W	2.2
49	1992/11/23	46.98N	71.16W	2.4
50	1992/11/24	46.74N	71.19W	2.8
51	1993/04/18	46.14N	72.97W	2.7
52	1993/04/25	46.14N	73.11W	2.8
53	1993/09/02	46.12N	72.89W	2.0
54	1994/02/28	46.23N	72.73W	2.9
55	1994/03/15	46.97N	71.68W	2.6
56	1994/09/11	46.71N	73.40W	2.6
57	1994/11/17	47.22N	70.75W	2.4
58	1994/11/23	46.92N	72.91W	2.5
59	1995/05/14	46.93N	70.90W	2.4
60	1995/06/26	46.01N	72.86W	2.1
61	1995/08/07	46.83N	71.11W	2.0
62	1995/09/12	47.39N	71.64W	2.1
63	1995/10/05	46.97N	70.89W	2.5
64	1996/03/06	46.75N	71.37W	2.0
65	1996/09/23	46.05N	73.59W	3.0
66	1997/09/28	46.92N	71.37W	2.6
***67**	**1997/11/06**	**46.80N**	**71.42W**	**5.1**
*68	1997/11/06	46.78N	71.39W	2.8
*69	1997/11/06	46.76N	71.37W	2.9
*70	1997/11/06	46.79N	71.38W	2.3
*71	1997/11/06	46.79N	71.40W	2.5
*72	1997/11/06	46.78N	71.39W	2.2
*73	1997/11/06	46.75N	71.38W	2.2
*74	1997/11/07	46.83N	71.38W	2.5
*75	1997/11/08	46.78N	71.37W	2.9
*76	1997/11/08	46.78N	71.36W	2.0
77	1997/12/07	47.08N	71.03W	2.2
78	1998/02/24	46.14N	73.05W	3.0

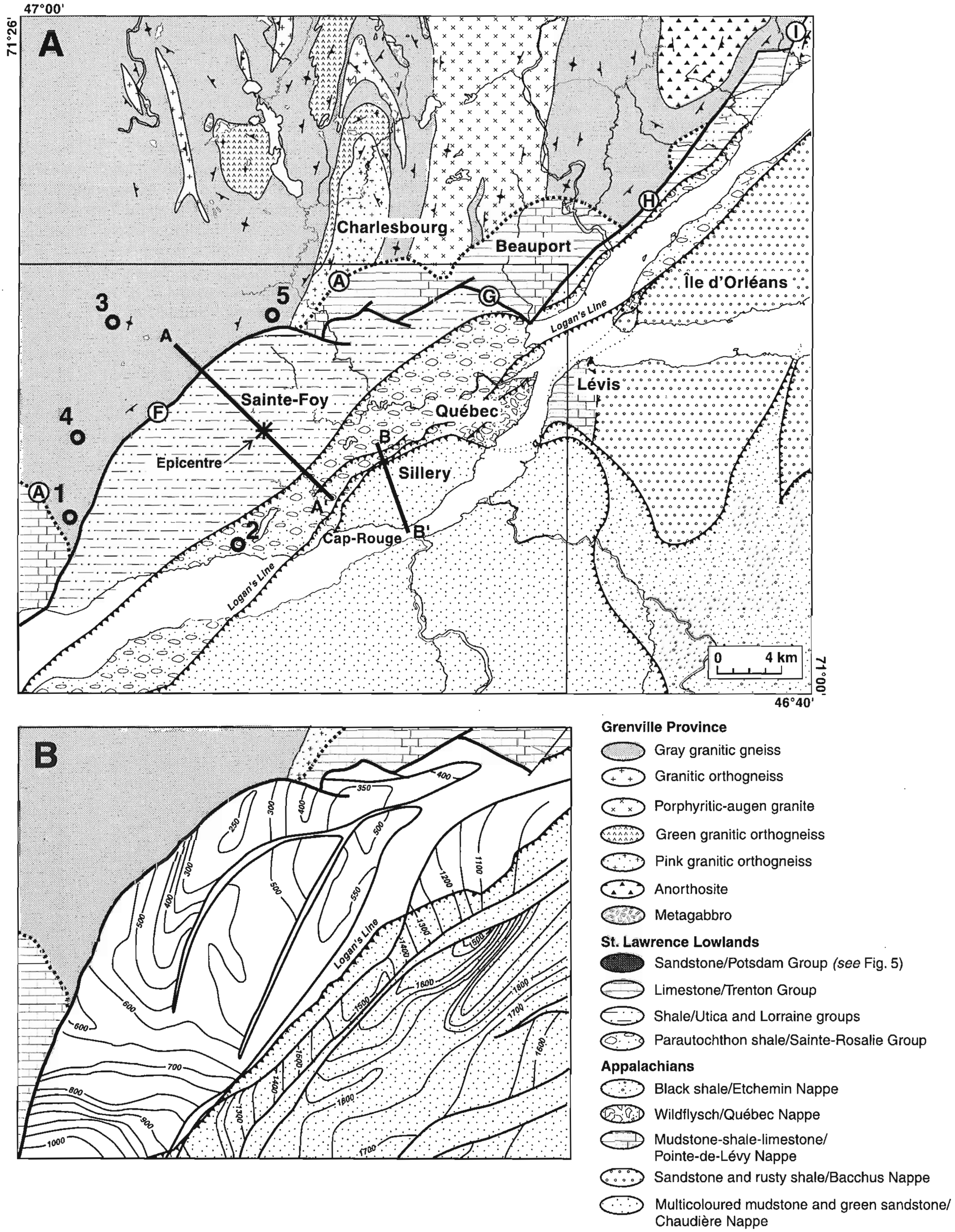
47°00'
71°26'
A
Charlesbourg
Beauport
Île d'Orléans
Sainte-Foy
Québec
Lévis
Sillery
Cap-Rouge
Epicentre
Logan's Line
Logan's Line
A
A'
B
B'
Ⓐ
Ⓕ
Ⓖ
Ⓗ
Ⓘ
1
2
3
4
5
0
4 km
71°00'
46°40'
B
Logan's Line
250
300
350
400
500
550
600
700
800
900
1000
1100
1200
1300
1400
1500
1600
1700
1800
Grenville Province
Gray granitic gneiss
Granitic orthogneiss
Porphyritic-augen granite
Green granitic orthogneiss
Pink granitic orthogneiss
Anorthosite
Metagabbro
St. Lawrence Lowlands
Sandstone/Potsdam Group (see Fig. 5)
Limestone/Trenton Group
Shale/Utica and Lorraine groups
Parautochthon shale/Sainte-Rosalie Group
Appalachians
Black shale/Etchemin Nappe
Wildflysch/Québec Nappe
Mudstone-shale-limestone/ Pointe-de-Lévy Nappe
Sandstone and rusty shale/Bacchus Nappe
Multicoloured mudstone and green sandstone/ Chaudière Nappe

site 4 on November 8 (16:45 EST). While site 2 was installed on bedrock in an unused quarry of parautochthonous shale in the hanging wall of the leading Appalachian thrust, all the other sites were deployed on Grenville basement outcrops on private properties adjacent to or surrounded by occupied residences. The recorders operated in trigger-mode only, using an STA/LTA ratio centred around 40 Hz. Sampling rate was 200 samples/s. Time control was provided by internal clocks in the PRS-4 recorders which were synchronized to a GPS master clock every one to several days. Clock drift was never more than 60 msec for the located aftershocks. The field network, at distances from 4 to 20 km, was able to detect events as small as M=0.1. The permanent seismograph stations closest to the aftershock zone are about 100 km away (stations A54 to the east and DPQ to the west); the detection threshold from the national network was M~1.5.

Earthquake sequence

No foreshock was felt in the area or recorded by the permanent stations of the Canadian National Seismograph Network in the days preceding the event. Eleven aftershocks were recorded by the national network before the first field station was deployed and 34 were identified by the field network (Table 2). Their magnitude and distribution in time is illustrated in Figure 3. The largest aftershocks were the M=2.9 November 8 (14:49 UT) and the M=2.5 November 6 (03:05 UT) events. A total of six aftershocks of magnitude between 2.3 and 2.9 were felt locally within 70 h, and 35 of the 46 reported aftershocks occurred within five days of the main shock. Only three aftershocks M>1.0 events occurred in the following two weeks, the last tremor detected (M=0.7) by the field and the national networks occurred 35 days after the main shock, on December 10. Given the M=5.1 of the main shock, the aftershock sequence shows a very rapid decay both in magnitude and number of events (Fig. 3).

Besides the aftershock activity, the field network recorded numerous other small magnitude seismic events with distinctive waveforms which are assumed to represent quarry or construction blasts in the metropolitan area. In addition, the survey detected artillery exercises which took place at the Canadian Forces Base Valcartier. On December 10 at 14:58 UT, a regional earthquake (M=2.2) occurred in the northeast Québec City metropolitan area. This last earthquake clearly lies outside the area of the aftershock zone and is assumed to represent an independent event.

Table 2. Cap-Rouge earthquake sequence. Aftershocks with accurate hypocental location are shaded. A model depth *(md)* of 18.0 km was used to calculate the epicentres of the firsts 12 aftershocks registered only by the national network, while a *md* of 21.6 km was assumed for other events recorded by a number of field stations and, in some cases, by stations of the national network.

Event	Date	Time (UT)	Latitude	Longitude	Depth	Magnitude
1	**1997/11/06**	**2:34:33**	**46.80N**	**71.41W**	**22.5**	**5.1**
2	1997/11/06	2:55:39	46.78N	71.39W	*md 18*	2.8
3	1997/11/06	3:05:57	46.76N	71.37W	*md 18*	2.9
4	1997/11/06	3:49:10	46.78N	71.38W	*md 18*	1.7
5	1997/11/06	3:53:17	46.79N	71.39W	*md 18*	1.6
6	1997/11/06	5:16:00	46.79N	71.38W	*md 18*	2.3
7	1997/11/06	9:02:46	46.79N	71.40W	*md 18*	2.5
8	1997/11/06	13:22:19	46.79N	71.42W	*md 18*	1.8
9	1997/11/06	14:27:10	46.79N	71.38W	*md 18*	1.7
10	1997/11/06	15:41:41	46.78N	71.39W	*md 18*	2.2
11	1997/11/06	18:52:31	46.75N	71.38W	*md 18*	2.2
12	1997/11/06	20:13:13	46.77N	71.37W	*md 18*	1.8
13	1997/11/07	11:32:48	46.77N	71.41W	*md 21*	2.5
14	1997/11/07	22:59:00	46.77N	71.41W	*md 21*	0.3
15	1997/11/08	1:50:00	46.77N	71.41W	*md 21*	0.4
16	1997/11/08	3:27:50	46.77N	71.41W	*md 21*	1.9
17	1997/11/08	4:21:00	46.77N	71.41W	*md 21*	0.3
18	1997/11/08	7:27:00	46.77N	71.41W	*md 21*	1.0
19	1997/11/08	14:49:26	46.77N	71.41W	*md 21*	2.9
20	1997/11/08	15:32:00	46.77N	71.41W	*md 21*	1.6
21	1997/11/08	15:38:46	46.77N	71.41W	*md 21*	2.0
22	1997/11/08	18:00:00	46.77N	71.41W	*md 21*	0.1
23	1997/11/08	21:01:25	46.77N	71.42W	21.4	0.8
24	1997/11/09	1:14:40	46.77N	71.42W	21.5	1.3
25	1997/11/09	7:11:27	46.76N	71.40W	21.8	0.6
26	1997/11/09	12:23:00	46.77N	71.41W	*md 21*	0.4
27	1997/11/09	20:44:10	46.77N	71.41W	21.4	1.2
28	1997/11/09	23:41:00	46.77N	71.41W	*md 21*	0.6
29	1997/11/10	6:06:00	46.77N	71.41W	*md 21*	0.5
30	1997/11/10	8:50:00	46.77N	71.41W	*md 21*	0.2
31	1997/11/09	13:31:30	46.77N	71.40W	22.1	1.3
32	1997/11/10	23:03:00	46.77N	71.41W	*md 21*	0.9
33	1997/11/11	1:43:00	46.77N	71.41W	*md 21*	1.1
34	1997/11/10	3:58:00	46.77N	71.41W	*md 21*	0.3
35	1997/11/10	5:55:57	46.77N	71.41W	*md 21*	1.2
36	1997/11/10	9:38:00	46.77N	71.41W	*md 21*	0.2
37	1997/11/10	23:42:00	46.77N	71.41W	*md 21*	0.2
38	1997/11/13	9:23:00	46.77N	71.41W	*md 21*	0.4
39	1997/11/14	10:15:41	46.78N	71.42W	21.4	1.2
40	1997/11/17	5:55:00	46.77N	71.41W	*md 21*	1.2
41	1997/11/23	15:24:00	46.77N	71.41W	*md 21*	1.3
42	1997/11/25	10:01:00	46.77N	71.41W	*md 21*	0.5
43	1997/11/30	15:46:00	46.77N	71.41W	*md 21*	0.4
44	1997/11/30	19:29:48	46.77N	71.42W	21.2	0.9
45	1997/12/07	14:04:00	46.77N	71.41W	*md 21*	0.7
46	1997/12/10	9:35:00	46.77N	71.41W	*md 21*	0.7

Figure 2.

A) Geological sketch map of the Québec City region (modified from Feininger and St-Julien, 1995), and B) depth to Grenvillian basement expressed as two-way seismic travel time in milliseconds (adapted from Société québécoise d'initiatives pétrolières, 1984). A – Angular unconformity; Faults include F: Neuville, G: Charlesbourg, H: Montmorency, and I: Château-Richer. Number 1 to 5 – seismograph stations occupied during the field survey; Line A–A′ and B–B′ – location of the cross-section of Figure 5.

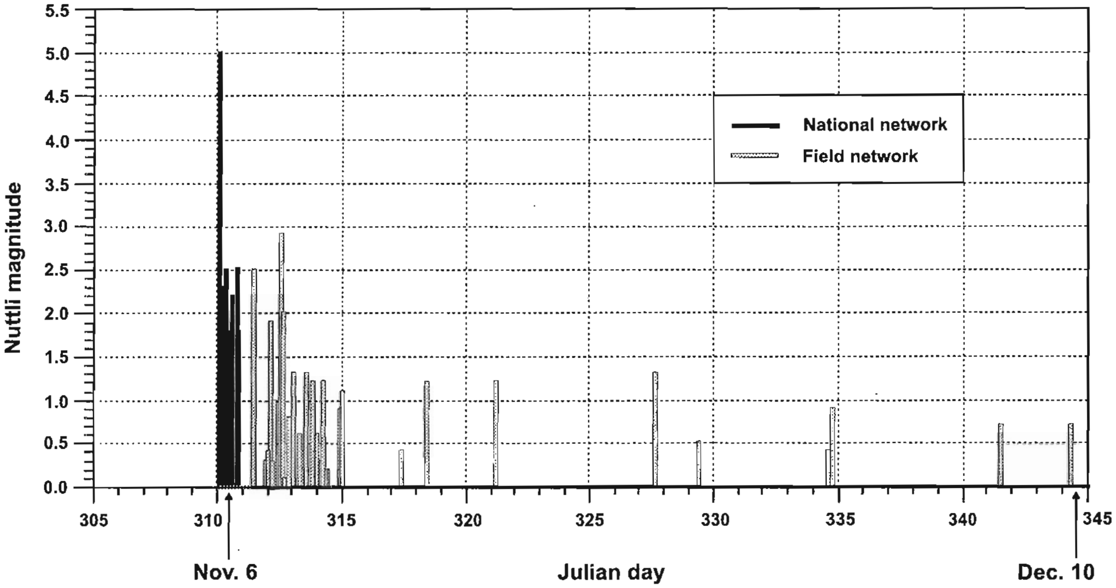

Figure 3. Time-magnitude history of the Cap-Rouge earthquake sequence.

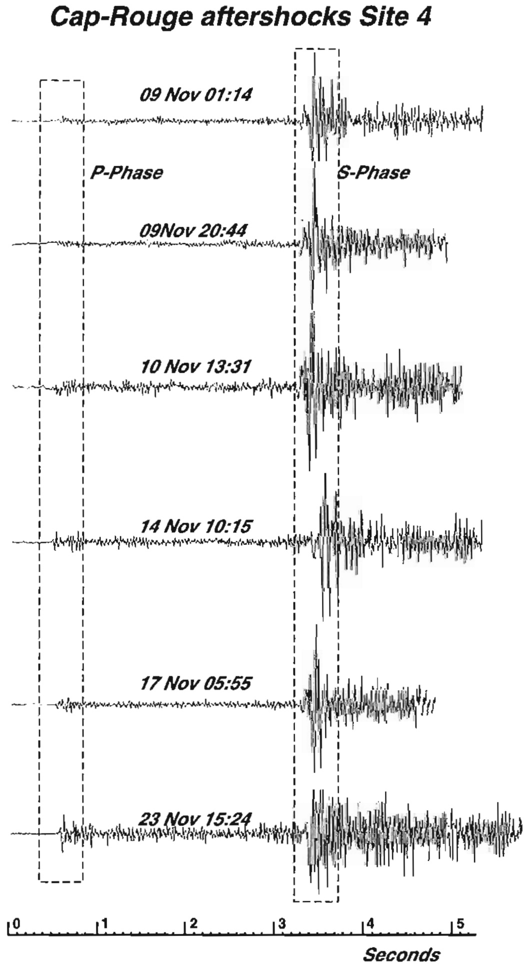

Figure 4. Vertical seismic trace of six coherent events recorded at field station 4. The boxes correspond to the P- and S-arrival times.

Hypocentral localization

Accurate hypocentres were determined for seven aftershocks among which five were recorded by three or four field stations (Table 2). The locations are tightly clustered within an 8 km^3 (2 x 2 x 2) volume, centred around 46.77°N, 71.41°W at 21.60 km depth, which is assumed to mark the location of the main shock rupture. The confined spatial distribution of the hypocentres is consistent with the 'magnitude vs. rupture length' relation of Nuttli (1983) which predicts a fault length rupture of about 1 km for M~5.0 earthquakes. The 21 km focal depth of the main shock rupture makes it deeper than about 90% of all Charlevoix earthquakes (Lamontagne and Ranalli, 1997).

The scatter in the hypocentres field location shows no strong trend and is interpreted to represent random errors. Waveforms of the aftershocks show a marked consistency (Fig. 4) which supports the idea that there is little change in the location of the focus from event to event. Locations of aftershocks epicentres using data from the national network alone, or combined with one or two of the field stations, are biased a few kilometers to the north of the location calculated from the field survey. The epicentre of the main shock, which was determined only by the national network, shows a similar bias and should be refined to the location of the aftershocks.

REGIONAL TECTONIC SETTING

The Québec City region is located at the junction of three geologically and rheologically contrasting crustal blocks (e.g. St-Julien, 1994). The crystalline Laurentides highlands rising to the northwest form the Precambrian basement to the flat-lying, low-relief Ordovician St. Lawrence Lowlands platform, which is overthrusted from the southeast by the Appalachian nappes (Fig. 1, 2, and 5).

Grenville basement

The crystalline basement, part of the Grenville Province, is largely composed of equigranular, fine- to medium-grained, commonly migmatitic, biotite-hornblende granitic to granodioritic gneisses largely derived from plutonic protoliths (Fig. 2). These gneisses host boudinaged amphibolite dykes and exhibit minor structures diagnostic of polyphase ductile deformation under high metamorphic grade pressure and temperature conditions. According to the structural and metamorphic evidences, these gneisses are attributed a pre- or early-Grenvillian age (1300-950 Ma; Davidson, 1995). They comprise a number of structurally concordant sheets of less deformed, somewhat younger, pink to green, porphyritic to augen, granitic to monzonitic orthogneiss, in parts containing igneous orthopyroxene. This assemblage hosts the larger Château-Richer granoblastic anorthosite massif, and a few much smaller kilometre-size metagabbro bodies. Metasedimentary sillimanite-garnet-biotite schist and quartzite are limited to a few outcrops. The tectonic fabric is generally northerly striking and variably dipping, locally defining open, shallowly plunging, kilometric-scale folds (Fig. 2).

It is emphasised that all the basement rocks have been affected by high-grade regional Grenvillian metamorphism and ductile deformation, which culminated prior 1.0 Ga. Potassium-argon and Ar/Ar cooling ages of biotite from various parts of the Grenville Province (Anderson, 1988) clearly indicate that tectonic uplift, denudation, and cooling below about 310°C of the rocks exposed at the present erosional surface was well underway by 850 Ma. This was followed by over 250 million years of continental uplift and erosion, leading to the attainment of a normal continental crustal thickness and to the stabilization of the Grenville Province. Accordingly, the Grenville basement constitutes a thick and rheological stiff body.

Iapetan rifting and the St. Lawrence Lowlands platform

The Precambrian Era ended with the initiation of continental rifting, the breakup of Laurentia, and the opening of the Iapetus ocean leading to the first Appalachian Wilson Cycle (Wilson, 1966; Kumarapeli and Saull, 1966; Dewey, 1969; Dewey and Burke, 1974). The onset of continental rifting in the Ottawa Valley–St. Lawrence Valley region is signalled by the emplacement at 590 Ma (Kamo et al., 1995) of the plume-related diabase Grenville dyke swarm in the fracture system of the Ottawa graben interpreted as a failed arm of the Iapetan paleo-rift system (Kumarapeli and Saull, 1966). This was followed presumably ca. 35 Ma later by the rift-drift transition stage of continental breakup giving birth to the Iapetus Ocean ca. 550 Ma (Kumarapeli, 1993).

The northern limit of the St. Lawrence platform against Grenville basement is marked, in the Québec City region, by a stair-step series of southeast-facing and steeply dipping faults which offset the erosional trace of a shallowly south-westerly dipping angular unconformity (Fig. 1, 2, and 5). This fault system is generally considered to be inherited from block faulting along the main arm of the Iapetan paleorift (Kumarapeli and Saull, 1966). Major faults in the Québec City region with such an heritage include the Neuville, Montmorency, and Château-Richer faults (Fig. 2). These faults have traditionally been described as normal faults (Logan, 1863; Osborne, 1956), an interpretation that has recently been challenged by Shaw (1993) who applied a large-scale synsedimentary senestral strike-slip model to account for facies and stratigraphic relationships across faults dissecting the platform sequence.

The extent of the fracture system and of the associated block faulting across the St. Lawrence platform basement and beneath overthrusted parautochthonous Appalachian nappes is well documented from stratigraphic relationships, exploration wells, and seismic data as well as from the occurrence of basement tectonic slivers telescoped within the Appalachian nappes (St-Julien et al., 1983). Seismic reflection data along line 2001, which extends from the Appalachian front immediately west of Québec City, across the Humber and Dunnage zones, has imaged down-faulted basement blocks as far southeast as the Baie Verte–Brompton line marking the limit of accretionary oceanic terranes. Accordingly, the basement faults limiting the St. Lawrence Lowlands platform on its northwest side are located between 100 and 150 km within the Laurentian shoulder of the Iapetan paleorift.

The Cambro-Ordovician St. Lawrence platform succession progressively thickens towards the southwest from the basal unconformity locally exposed along its northeast limit in the Québec City–Lac Saint Pierre region, to exceed 1500 m in the Montreal region. Following Lavoie's (1994) comprehensive summary, the stratigraphic succession of the St. Lawrence platform comprises an initial Cambrian–Lower Ordovician, subaerial to shallow-marine sequence of siliciclastic sediments (Potsdam Group), followed by Lower to lower Upper Ordovician shallow-water carbonates (Beekmantown, Chazy, Black River, and Trenton groups), Upper Ordovician deep-water siliciclastic and synorogenic flyschoid sediments (Utica, Ste. Rosalie, and Lorraine groups), capped by post-Taconian, uppermost Ordovician molasses (Queenston Group). The regional distribution and

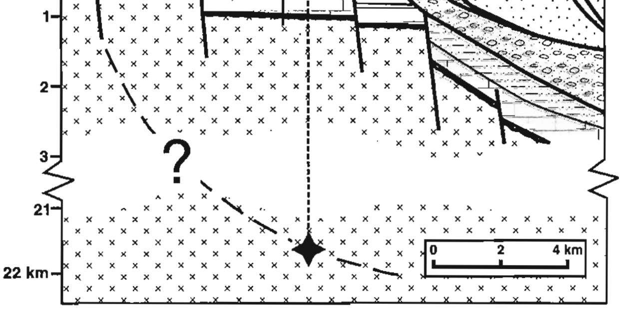

Figure 5. Structural cross-section of the epicentre region. The Cap-Rouge earthquake focus is shown with a star. Legend and shaded rock units as in Figure 2. Number 1 refers to oil exploration well No. 176 - Ancienne-Lorette.

changes in sedimentary facies, the presence of internal unconformities, and important variations in thickness within units and across mapped or inferred subsurface faults indicate that the St. Lawrence Lowlands platform cover sequence was developed on a tectonically active shelf and foreland basin (St-Julien and Hubert, 1975; Shaw, 1993; Lavoie, 1994).

NEUVILLE-MONTMORENCY-ST. LAWRENCE FAULT SYSTEM

In the Québec City region specifically, the St. Lawrence Lowlands platform is discontinuously bounded either by a shallow-dipping unconformity underlying the horizontal Potsdam and Trenton groups, or by the northeast-striking Neuville, Montmorency, Château-Richer, and St. Lawrence faults (Fig. 1 and 2). These four faults are linked via the shorter, easterly striking Charlesbourg and Cap-Tourmente faults, hence defining a stair-step pattern (Fig. 2; Lachapelle, 1993; St-Julien, 1994).

Subsurface extension

The three dimensional pattern of the block faulting dissecting the platform and its basement can be imaged by integrating seismic, magnetic, and gravity data following a method recently applied to map the St. Lawrence paleorift faults of the Charlevoix region (Lamontagne et al., 1998). Likewise, the depth to basement in the Québec City region is well determined by a series of good quality seismic profiles (Société québécoise d'initiatives pétrolières, 1984) and three oil exploration wells (Ministère des Richesses Naturelles du Québec, 1974)). Since the Appalachian nappes and St. Lawrence platform cover sequence are nearly magnetically transparent, the regional and local magnetic field

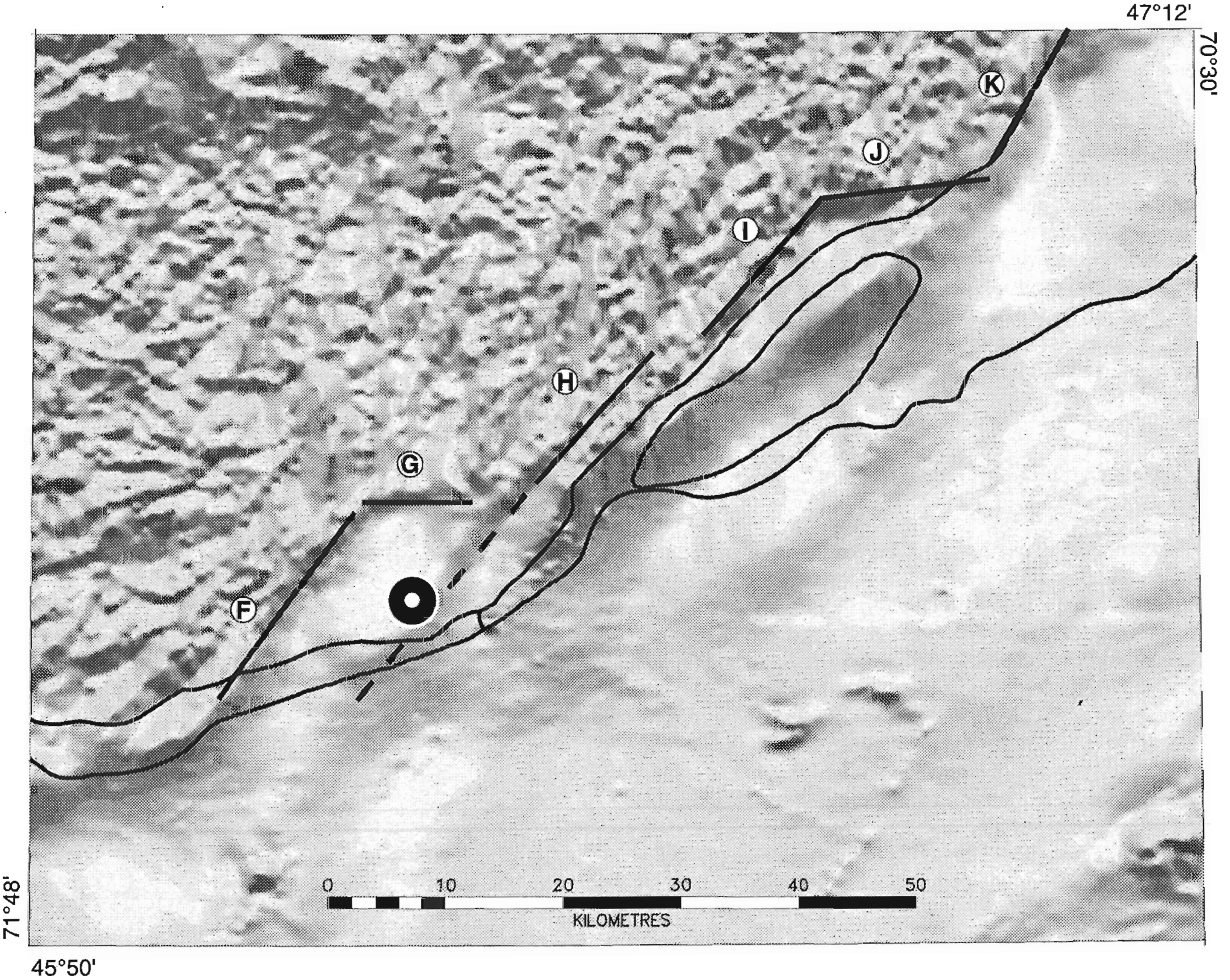

Figure 6. Magnetic field map for the Québec City region. Faults: F: Neuville, G: Charlesbourg, H: Montmorency, I: Château-Richer, J: Cap Tourmente, and K: St. Lauwrence. The Cap-Rouge earthquake epicentre is shown with a star. The epicentre lies on the subsurface extension of the Montmorency Fault.

patterns are strongly dependent on the depth to the crystalline Grenville basement. Where the crystalline basement outcrops, such as on the Laurentides highlands, the magnetic field consists of very high frequency intensity variations. In contrast, where the Grenville basement is deeply buried, such as under the south shore of the St. Lawrence River, the high frequency variations disappear, leaving a smooth field with low frequency variations.

The correspondence between the discontinuities in the magnetic pattern and the map traces of the Neuville, Charlesbourg, Château-Richer, Cap Tourmente, and St. Lawrence faults is striking (Fig. 6). The change in wavelength of the magnetic anomalies is due to an abrupt foundering of the crystalline basement rocks, most likely along steep faults with large vertical downthrows. Cross-correlation with the depth to basement measured in oil exploration wells in the area (Ministère des Richesses Naturelles du Québec, 1974): catalogue no. 160 - Île d'Orléans, no. 175 - Les Saules, and no. 176 - Ancienne-Lorette) shows that these faults which have a vertical downthrow of 1 km or more are easily identified with the magnetic data.

In addition, there is also a strong correlation between magnetic anomalies and subsurface faults inferred from the seismic data. In general, these subsurface faults correspond to elongated magnetic anomalies whose response is slightly higher on the upthrown than on the downthrown side. The southwest extension of the Montmorency Fault below the Ordovician cover is a clear example (Fig. 6). The Cap-Rouge epicentre is located along this structure, and therefore appears to correspond to a major subsurface basement fault along which there is possibly one kilometre or more of vertical downthrow.

It is noteworthy that the above magnetic expression also marks subsurface faults along the platform margin in the Trois-Rivières–Lac Saint-Pierre area (compare regional seismic data (Société québécoise d'initiatives pétrolières, 1984) and residual magnetic potential maps), where a small concentration of earthquakes epicentres is also located (Fig. 1).

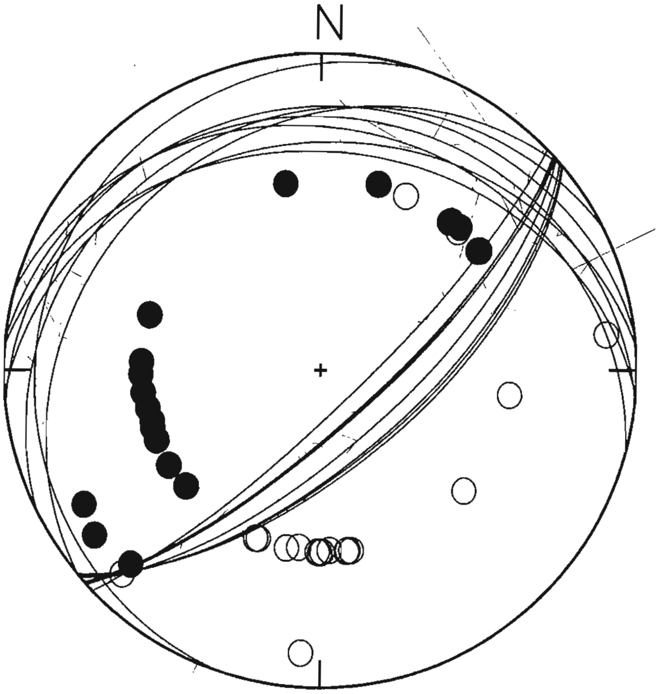

Figure 7. Lower hemisphere focal mechanism solution for the Cap-Rouge earthquake. Solid and open dots denote compressional and dilatational first motion, respectively.

FOCAL MECHANISM SOLUTION

The focal mechanism for the Cap-Rouge earthquake was determined from the P-first motions at 38 seismograph stations located in eastern Canada and the northeastern United States using the grid search algorithm of Snoke et al. (1984). There were no solutions that satisfied all of the data. By searching the focal sphere at 5° intervals, eight solutions were found with two inconsistent polarities (Fig. 7). The same two stations (A64 and MNQ) are always misfit. Station A64 is near the Pg-Pn cross-over distance. If the first arrival is Pg and not Pn, this station would be consistent with the focal mechanism. The preferred solution (strike 49° ± 1, dip 71° ± 5, rake 77° ± 8) is indicative of primarily reverse faulting on a northeast-striking plane that dips steeply to the southeast, or an east-striking plane with a shallow dip toward the north. The former is more consistent with the geology.

DISCUSSION

Comparison with recent Canadian intraplate earthquakes

The Cap-Rouge earthquake 21 km focal depth is shallower than the 29 km depth of the Saguenay 1988 earthquake. The tight spatial clustering of the Cap-Rouge aftershocks focus within a 8 km^3 volume is consistent with a simple fault rupture, in contrast with the much wider 25 x 40 km distribution ellipse of the Saguenay aftershock epicentres. The latter represents more than the actual zone of failure, and indicate a more complex rheological setting (Du Berger et al., 1991). The Cap-Rouge M=5.1 main shock is comparable in magnitude to the M=5.0 Charlevoix 1979 earthquake, the largest event of the Charlevoix seismic zone since the M=6.5 event of 1925. The 21 km focal depth of the Cap-Rouge event makes its source region deeper than that of about 90% of all Charlevoix seismic zone earthquakes (Lamontagne and Ranalli, 1996, 1997) including the 1925 and 1979 events which occurred at about 10 km (Bent, 1992; Hasegawa and Wetmiller, 1980) respectively. Like many of the large Charlevoix seisms, the Cap-Rouge event is located along the Iapetan paleorift fault system. The focal mechanism solution obtained for the Cap-Rouge event is primarily a reverse motion on a northeast-striking and steeply dipping plane. Such thrust motion agrees with that of most eastern Canadian earthquakes including the Charlevoix seismic zone.

Relationships to the Neuville Fault

It is apparent from the cross-sections of Figure 5 that there is no direct link between the midcrustal hypocentral positions of the Cap-Rouge earthquake sequence and the near surface structure of the St. Lawrence platform and thin-skinned Appalachian thrust front. The Cap-Rouge epicentre is located along the upper crustal southwestern extension of the Montmorency Fault beneath the St. Lawrence Lowlands platform (Fig. 6). A direct correlation with the Montmorency Fault only holds if the fault zone extends subvertically down to middle crust.

Such a direct relationship is questionable in view of the fact that block faulting in attenuated rifted margin generally occurs on listric faults (e.g. de Charpel et al., 1978). Indeed, tilted and rotated basement faulted blocks have been imaged along the seismic line 2001, only a few tens of kilometres south of the Logan's Line (St-Julien et al., 1983). The possibility that the earthquake originated along a planar, steeply-dipping normal fault cannot be ruled out *a priori*. Rift-related planar steeply-dipping faults are known to occur at some distance away from the rifted continental edge. The Montmorency Fault may be one of these.

Alternatively, the seismic source may also be located on a less steeply dipping, deeply rooted fault which projects backup to the surface at some distance further north. The Neuville Fault, located 6 km to the northwest of the epicentre, may represent the surface trace of such a fault. This correlation requires an average dip of 75° for the fault plane. This is consistent with the attitude of one of the nodal planes of the focal mechanism. The Neuville Fault is the northwesternmost known paleorift and Paleozoic fault in the area locally marking the limit of the St. Lawrence Lowlands platform. It is well imaged with magnetic and seismics, and has over 1 km of minimum downthrow. Since there is no evidence for a comparable fault in the exposed Grenville Province basement further north, the correlation of the Cap-Rouge earthquake rupture with the Neuville Fault becomes quite compelling.

ACKNOWLEDGMENTS

We thank the Société Québécoise d'Initiatives Pétrolières (SOQUIP) for their information on the faults of the Québec City region. The authors acknowledge Jean Bédard for critically reading and improving the manuscript, and Denis Lavoie who provided helpful comments.

REFERENCES

Adams, J. and Basham, P.
1991: The seismicity and seismotectonics of eastern Canada; *in* Neotectonics of North America; (ed.) D.B. Slemmons, E.R. Engdahl, M.D. Zoback, and D.D. Blackwell; Geological Society of America, Decade Map Volume 1.

Anderson, S.L.
1988: Interpretation of K-Ar mineral dates from the Grenville orogenic belt; American Journal of Sciences, v. 288, p. 701-734.

Bent, A.L.
1992: A re-examination of the 1925 Charlevoix, Québec, earthquake; Bulletin of the Seismological Society of America, v. 82, p. 2097-2113.

Cajka, M.G. and Halchuk, S.
in press: Collecting intensity data via the Internet: the Cap-Rouge, Québec, earthquake; Seismological Research Letters.

de Charpel, O., Guennoc, P., Montadert, L., and Roberts, D.G.
1978: Rifting, crustal attenuation and subsidence in the Bay of Biscay; Nature, v. 275, p. 706-711.

Davidson, A.
1995: A review of the Grenville orogen in its North American type area; Journal of Australian Geology and Geophysics, v. 16, p. 3-24.

Dewey, J.F.
1969: The evolution of the Appalachian / Caledonian orogen; Nature, v. 222, p. 124-129.

Dewey, J.F. and Burke, K.
1974: Hotspots and continental break up: implication for collisional orogeny; Geology, v. 2, p. 57-60.

Du Berger, R., Roy, D.W., Lamontagne, M., Woussen, G., North, R.G., and Wetmiller, R.J.
1991: The Saguenay (Québec) earthquake of November 25, 1988: seismologic data and geologic setting; Tectonophysics, v. 186, p. 59-74.

Feininger, T. and St-Julien P.
1995: Québec popular geology; Québec Geoscience Centre, field guidebook.

Globensky, Y.
1987: Géologie des Basses-Terres du Saint-Laurent; Ministère de l'Énergie et des Ressources du Québec, MM 85-02, 63 p., carte 1999 (échelle 1/250 000).

Hasegawa, H.S. and Wetmiller, R.J.
1980: The Charlevoix earthquake of 19 August 1979 and its seismotectonic environment; Earthquake Notes, v. 51, p. 23-37.

Kamo, S.L., Krogh, T.E., and Kumarapeli, P.S.
1995: Age of the Grenville dyke swarm, Ontario-Québec: implications for the timing of Iapetan rifting; Canadian Journal of Earth Sciences, v. 32, p. 273-280.

Kumarapeli, P.S.
1993: A plume-generated segment of the rifted margin of Laurentia, Southern Canadian Appalachians, seen through a completed Wilson cycle; Tectonophysics, v. 219, p. 47-55.

Kumarapeli, P.S. and Saull, V.A.
1966: The St. Lawrence Valley system: a North American equivalent of the East African rift valley system; Canadian Journal of Earth Sciences, v. 3, p. 639-658.

Lachapelle, R.
1993: La limite sud du Bouclier Canadien dans la région de Québec: un phénomène de fragmentation continentale relié à l'ouverturede l'océan Iapetus; Mémoire de maîtrise, Université du Québec à Montréal, 81 p.

Lamontagne, M.
1987: Seismic activity and structural features in the Charlevoix region, Quebec; Canadian Journal of Earth Sciences, v. 24, p. 2118-2129.

Lamontagne, M. and Ranalli, G.
1996: Thermal and rheological constraints on the earthquake depth distribution in the Charlevoix, Canada, intraplate seismic zone; Tectonophysics, v. 257, p. 55-69
1997: Faults and spatial clustering of earthquakes near La Malbaie, Charlevoix Seismic Zone, Canada; Seismological Research Letters, v. 68, p. 337-352.

Lamontagne, M., Wetmiller, R.J., and Du Berger, R.
1990: Some results from the 25 November, 1988 Saguenay, Québec, earthquake; *in* Current Research, Part B; Geological Survey of Canada, Paper 90-1B, p. 114-121.

Lamontagne, M., Keating, P., Perron, G., and Adam, E.
1998: Offshore faults of the Charlevoix Seismic Zone, as interpreted from seismics, magnetics and gravity; Abstract, Seismological Research Letters, v. 69, p. 80.

Lavoie, D.
1994: Diachronous tectonic collapse of the Ordovician continental margin, eastern Canada: comparison between the Quebec Reentrant and St. Lawrence Promontory; Canadian Journal of Earth Sciences, v. 31, p. 1309-1319.

Logan, W.E.
1863: Geology of Canada; Geological Survey of Canada, Report of Progress to 1863, 983 p.

Ministère des Richesses Naturelles du Québec
1974: Data on wells drilled for petroleum and natural gas in the St. Lawrence Lowlands area, Part II: wells more than 500 feet in depth; Ministère des Richesses Naturelles du Québec, En.G-5, 350 p.

Nuttli, O.W.
1983: Average seismic source parameters relations for mid-plate earthquakes; Bulletin Seismological Society of America, v. 73, p. 519-535.

Osborne, F.F.
1956: Geology near Québec City; Naturaliste Canadien, v. 83, p. 157-223.

St-Julien, P.
1994: Géologie de la région de Québec; Ministère des Ressources Naturelle du Québec, MB 94-40.

St-Julien, P. and Hubert, C.
1975: Evolution of the Taconian orogen in the Quebec Appalachians; American Journal of Sciences, v. 275-A, p. 337-362.

St-Julien, P., Slivitsky, A., and Feininger, T.
1983: A deep structural profile across the Appalachians of southern Quebec; *in* Contributions to the Tectonics and Geophysics of Mountain Chains; (ed.) R.D. Hatcher, Jr., H. Williams, and I. Zietz; Geological Society of America, Memoir 158, p. 103-111.

Shaw, B.R.
1993: Strike-slip interpretation of basin-bounding faults of the St. Lawrence Lowlands basin in the Québec City area, Canada; The American Association of Petroleum Geologists Bulletin, v. 77, p. 743-760.

Snoke, J.A., Munsey, J.W., Teague, A.G., and Bollinger, G.A.
1984: A program for focal mechanism determination by combined use of polarity and SV-P amplitude data; Abstract, Earthquake Notes, v. 3, p. 15.

Société québécoise d'initiatives pétrolières
1980: Carte structurale du socle: 31I, 31H, et 21L; Ministère des Richesses Naturelles du Québec, DP 84-32 (échelle 1/250 000).

Wilson, J.T.
1966: Did the Atlantic close and then reopen?; Nature, v. 211, p. 676-681.

Geological Survey of Canada Project 92002QN

Gestion des données de forage à l'aide d'une approche topologique : application au projet de cartographie hydrogéologique du piémont laurentien, Québec

É. Boisvert et Y. Michaud
CGC–Québec, Sainte-Foy

Boisvert, É. et Michaud, Y., 1998: Gestion des données de forage à l'aide d'une approche topologique : application au projet de cartographie hydrogéologique du piémont laurentien, Québec; dans Recherches en cours 1998-E; Commission géologique du Canada, p. 117–124.

Résumé : Les structures de base de données utilisées pour gérer l'information de forage sont en général mal adaptées à cet usage et réduites à leur plus simple expression. Souvent, elles ne permettent la gestion que d'une partie de l'information disponible dans la description d'un forage, et la structure des données représente inadéquatement l'organisation spatiale du forage. Le présent article propose une nouvelle structure de données faisant appel à la logique des SIG et permettant de mieux gérer la complexité et l'hétérogénéité des données de forage. Cette structure, dite «centrée sur les contacts», résout les principaux problèmes de gestion de ce type de données ponctuelles et linéaires en assurant un meilleur contrôle de l'intégrité de l'information.

Abstract: Database structures used to manage borehole information are generally minimalistic and poorly adapted for this usage. Often, they allow for management of only part of the wealth of data that can be extracted from borehole logs, and the associated data structure does not adequately represent the spatial organization of the information. A new data structure is proposed that uses GIS strategies and allows for better management of the complexity of borehole information. This structure, centered on the concept of "contacts", solves the main problems related to the management of point and line data and provides better control on the integrity of the information.

INTRODUCTION

La principale source d'information dans les projets de cartographie hydrogéologique est la banque de données de forage, colligée à partir de données disponibles auprès de divers ministères et organismes municipaux, provinciaux et fédéraux. La réalisation d'un forage étant coûteuse, les données recueillies à l'aide de cette technique sont précieuses. Il faut cependant noter que la répartition géographique des données est très variable. Dans les zones habitées, par exemple, les forages dans les formations superficielles sont nombreux et permettent une reconstitution assez fidèle de la stratigraphie. Les forages décrits avec minutie sont les plus utiles, car ils comportent de nombreuses observations indispensables à la compréhension de la géologie de sous-surface. La structure de cette information est toutefois complexe et variée, et les données sont réparties dans plusieurs classifications (lithostratigraphique, structurale, texturale, etc.). Le cerveau humain est capable de considérer l'information sous plusieurs formes. Cependant, dans le contexte rigide de la logique informatique, la tâche de rendre cette information cohérente est beaucoup plus difficile. Les structures classiques de base de données utilisées pour gérer l'information de forage ne sont pas très flexibles et souvent réduites à un minimum. Les données qu'il est possible de gérer dans ces structures ne sont qu'un sous-ensemble de l'information de base, souvent reformulée en des termes plus simples. En effet, ces structures de base de données imposent des limitations quant au nombre et à la forme des données qui peuvent être gérées. Certaines données sont ainsi écartées de la base et ne sont pas disponibles pour analyse. Le projet Piémont laurentien intègre, dans une même base de données, des observations de sources diverses et de fiabilité variable. Le défi consiste donc à maintenir dans une même base des données détaillées et générales. Cet article propose une structure de base de données qui fait appel à la logique des SIG, soit la structure «chaîne-noeud» (arc-node) et la segmentation dynamique. Cette approche centrée sur les contacts est implantée dans une structure relationnelle qui permet d'augmenter la cohérence et la fidélité de l'information recueillie lors des forages.

ANALYSE CONCEPTUELLE DES DONNÉES DE FORAGE

Pour bien modéliser l'information de forage, il est important de décortiquer et de comprendre à fond les relations intrinsèques, conceptuelles et spatiales qui permettent de structurer les données en une architecture cohérente pour leur gestion, leur manipulation et leur analyse par ordinateur. Cette étape est fondamentale pour la modélisation, car elle permet de dégager les points communs de l'information recueillie lors du forage et d'analyser les données du point de vue géologique et hydrodynamique. Il faut bien sûr modéliser les attributs fixes d'une description de forage, mais il est aussi important de structurer l'organisation spatiale de l'information car elle est à la base des relations qui existent entre les éléments descripteurs les plus importants du forage.

Représentation spatiale d'un forage

Le forage peut être représenté conceptuellement comme un objet linéaire. Chaque forage montre une série d'observations réparties le long d'une ligne qui traverse un ensemble d'unités dans un espace tridimensionnel, lesquelles unités correspondent aux unités géologiques recoupées. Cette information est représentée autant sous la forme d'éléments ponctuels (points) que d'intervalles linéaires (lignes). Et ce sont là les deux seules formes que prennent les données de forage. Pour construire un plan ou un volume, on doit extrapoler l'information hors du domaine linéaire du forage.

La figure 1 montre un exemple classique d'un journal de forage. L'information est représentée spatialement sous la forme de «limites» ou de «discontinuités» (ponctuelles) le long d'un forage et sous celle d'intervalles (linéaires). Dans la terminologie classique de la géologie, on utilise les termes «contact» et «discontinuité», pour référer aux points le long d'un forage, et les termes «unité», «formation», «séquence», etc., pour référer aux intervalles. En pratique, l'unité, la formation ou la séquence est un intervalle qui est inclus entre deux contacts, tandis que la discontinuité ou le contact correspond à un concept plus général pour représenter un élément ponctuel le long d'un forage. Plusieurs phénomènes peuvent être considérés comme des discontinuités : un front ou un niveau d'oxydation, un niveau graveleux dans une série sableuse, la base ou le sommet d'une déformation synsédimentaire, des plans de failles à l'intérieur d'une même unité et divers niveaux d'eau (pris à des périodes différentes). Le sommet et la base d'un forage sont considérés comme des «contacts» implicites.

On doit souligner que la notion de contact est valide seulement à l'intérieur d'une classification. Pour arriver à établir des «unités» distinctes, il faut les classifier dans un contexte lithologique (sable, argile, granite), lithostratigraphique (Till de Gentilly) ou hydrostratigraphique (aquifère, aquitard). Une discontinuité peut correspondre à un contact dans une classification particulière et ne pas être utilisée dans une autre. Par exemple, le niveau de la nappe phréatique ne sert pas de contact dans une classification lithostratigraphique, mais il est le contact supérieur d'une unité hydrostratigraphique. À l'inverse, la discontinuité entre une unité fossilifère et une autre non fossilifère n'a pas d'importance pour l'hydrogéologue, mais elle est un contact stratigraphique important pour le géologue. Dans les deux cas, les discontinuités sont pertinentes pour qualifier un type particulier de contacts et doivent donc être gérées dans la base de données.

Dans notre modèle de base de données, les contacts servent de limites aux unités, lesquelles ne sont définies dans les forages que si elles sont délimitées spatialement par des contacts. Le long d'un même forage, toutes les classifications utilisent la même série de discontinuités pour former des contacts. Les discontinuités sont donc des entités partagées entres les unités.

Les derniers éléments d'information à considérer dans la description spatiale d'un forage sont ceux indépendants de la description matérielle du forage, soit les segments échantillonnés, les infrastructures de puits ou les commentaires. La position de ces éléments est seulement limitée par la position du forage et non par les autres éléments d'information qui caractérisent le forage, comme les discontinuités. On peut retrouver les segments n'importe où, sans référence aux contacts ni aux intervalles existants. Par exemple, la description des infrastructures de forage (crépine, tubage, etc.) ne concerne pas directement le matériel foré mais constitue quand même une information utile qui est strictement reliée à la présence du forage. Ces intervalles ne sont pas définis par des contacts et ne sont pas des unités. Ils sont nommés ici «segments» et sont typiquement discontinus le long du forage; ils peuvent même se superposer. Les segments sont délimités par un sommet et une base et leur position est exprimée en terme de profondeur le long du forage. Ils se distinguent aussi des unités car ils n'utilisent pas de classification.

STRUCTURES DE BASES DE DONNÉES

Un modèle complet de base de données intégrant tous les éléments de description d'un forage doit pouvoir stocker quatres types d'information (les contacts, les discontinuités, les unités et les segments) et permettre leur représentation spatiale. Il doit aussi tenir compte du fait que les discontinuités sont des éléments qui peuvent être partagées entre les différents types de classifications. Plusieurs structures de bases de données sont utilisées pour représenter l'information recueillie lors d'un forage. Fondamentalement, les descriptions de forage consistent en une série d'attributs fixes concernant le forage dans son ensemble et une série variable d'observations décrivant le contenu du forage. Les attributs fixes sont, par exemple, la position géographique du forage, le nom du propriétaire, le nom du contracteur, ainsi que des éléments d'information divers selon les besoins du compilateur. On rattache à cette information la description d'un nombre variable de caractéristiques, le plus souvent attribuées aux matériaux, dont la position est répartie le long du forage depuis son sommet vers sa base.

La majorité des structures utilisées dans les logiciels servant à gérer des données de forage ont une approche centrée sur les unités, c'est-à-dire que le concept de base est l'unité. Tous les attributs fixes sont rattachés à des unités et le concept

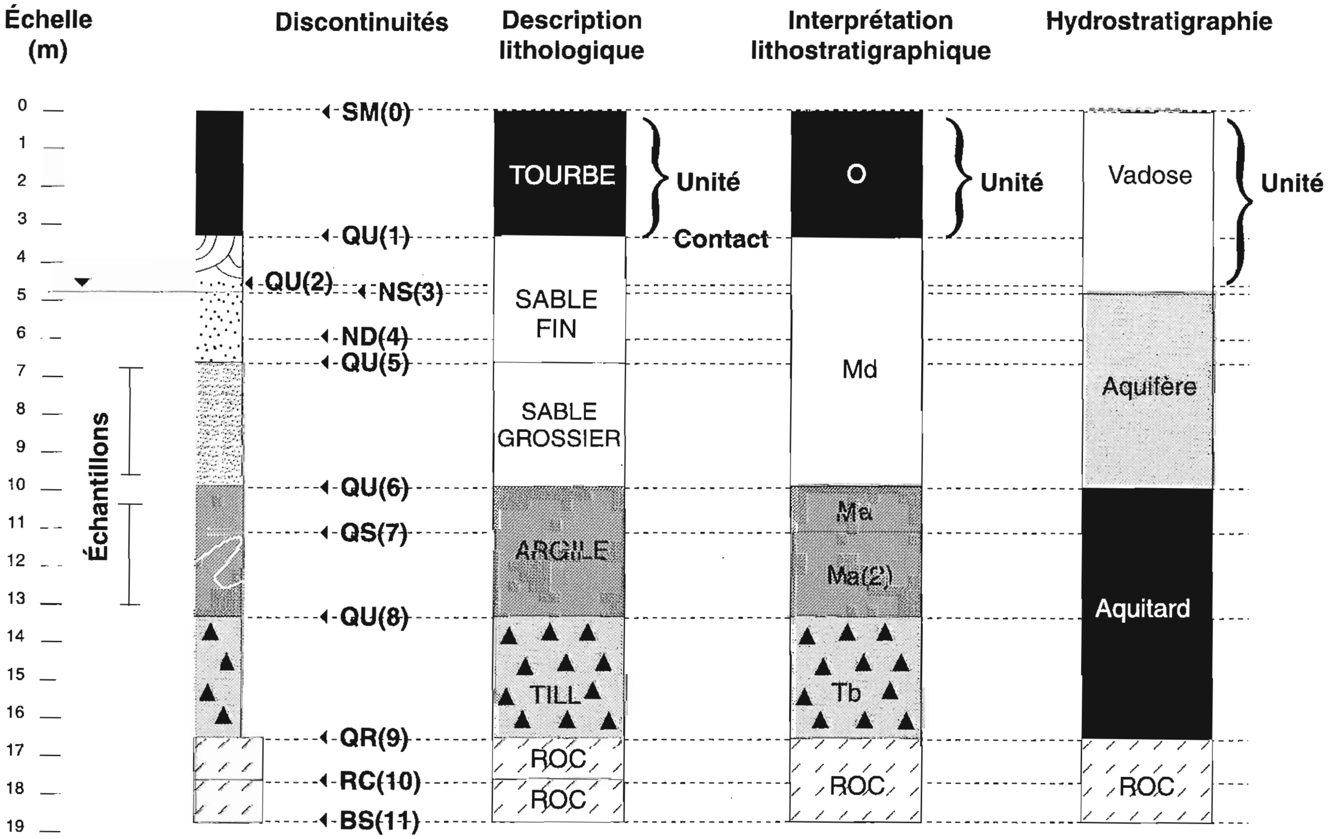

Types de discontinuités				
	SM	Sommet - Quaternaire	QR	Quaternaire - roc
	QU	Quaternaire - Quaternaire	RC	Roc - roc
	NS	Niveau statique	BS	Base
	ND	Niveau dynamique	QS	Structure sédimentaire

Unités litho-stratigraphiques		
	O	Matière organique
	Md	Sable deltaïque
	Ma	Sédiments d'eau profonde
	Tb	Till épais

Figure 1. Exemple : information disponible dans un journal de forage.

de discontinuité est rarement considéré, sinon de façon indirecte. Ainsi, le niveau de la nappe phréatique est géré dans une table distincte et n'est pas intégré sémantiquement à la description du forage. En fait, dans l'approche centrée sur les unités, il est considéré que toutes les discontinuités sont des contacts, ceux-ci étant implicitement gérés dans la base de données par la position de la base et du sommet d'une unité. Les discontinuités qui ne correspondent pas à un contact sont gérées ailleurs dans la base de données.

Il existe essentiellement deux grands types de bases de données, celles à structure bidimensionnelle (*flat files*) et celles à structure relationnelle. Les bases de données orientées-objets (*object-oriented*) sont encore trop marginales pour être utilisées de façon courante.

Structure bidimensionnelle

Dans beaucoup de situations, les données tirées des forages sont colligées dans des chiffriers électroniques. Cette approche est acceptable lorsque le nombre de forages est faible ou que ces données ont peu de chances d'être traitées par une procédure automatique. La structure typique de ce genre de fichier ressemble à celle présentée à la figure 2a. Le forage P1 de cette figure représente la codification du forage fictif de la figure 1. Plusieurs fichiers sont nécessaires pour y représenter les différentes classifications (lithologique, lithostratigraphique, hydrostratigraphique, etc.). On doit alors synchroniser les fichiers entre eux pour éviter les disparités entre les classifications ou utiliser un seul fichier énorme contenant toutes les classifications, mais même cette solution demande une synchronisation manuelle des champs.

Dans ce genre de fichier, la structure organisationnelle de l'information est très simple (une seule matrice), mais elle comporte plusieurs limitations qui rendent inefficaces les procédures automatiques de tri, de remplacement, de reclassification, de calcul, etc. Généralement, les données contenues dans une structure bidimensionnelle sont toutes regroupées dans un seul fichier contenant plusieurs colonnes. Les unités sont souvent représentées par plusieurs colonnes contenant des éléments d'information divers. Les colonnes portent alors un nom avec un suffixe, comme par exemple «Prof1», «Prof2» et «Prof3» qui indiquent la profondeur de la base des unités sus-jacentes dont le suffixe est le même.

De façon générale, les structures bidimensionnelles posent trois problèmes majeurs : 1) elles restreignent la description d'un forage à un nombre fixe d'unités, 2) elles compliquent les opérations de recherche et 3) elles ne permettent que difficilement de donner des attributs aux contacts eux-mêmes (par ex. contact conforme par opposition à contact d'érosion). De plus, le nombre de discontinuités est essentiellement restreint au nombre de contacts.

Le premier problème concerne le nombre d'unités dans un forage qui est très variable et peut facilement atteindre la vingtaine. Le fait d'avoir un nombre fixe de colonnes amène souvent le compilateur à généraliser les forages plus complexes ou à détailler indûment les forages plus simples. Le nombre de colonnes dans la base de données se trouve donc arbitrairement fixé par les forages les plus détaillés qui, somme toute, ne sont pas légion. Ainsi, la majorité de la base de données est constituée de cases vides; mais comme il peut exister de l'information dans tous les champs, elles se doivent d'être considérées en tout temps dans les processus automatiques de mise à jour, de tri, etc.

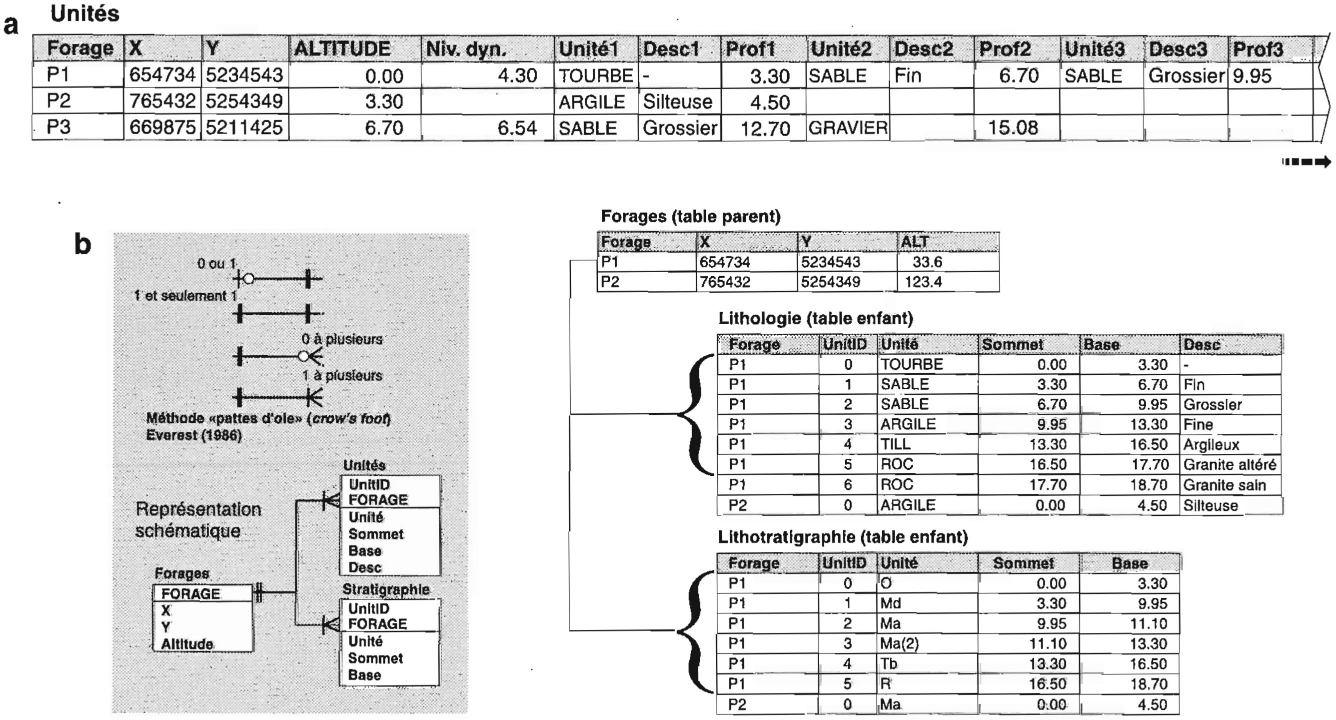

Unités

Forage	X	Y	ALTITUDE	Niv. dyn.	Unité1	Desc1	Prof1	Unité2	Desc2	Prof2	Unité3	Desc3	Prof3
P1	654734	5234543	0.00	4.30	TOURBE	-	3.30	SABLE	Fin	6.70	SABLE	Grossier	9.95
P2	765432	5254349	3.30		ARGILE	Silteuse	4.50						
P3	669875	5211425	6.70	6.54	SABLE	Grossier	12.70	GRAVIER		15.08			

Forages (table parent)

Forage	X	Y	ALT
P1	654734	5234543	33.6
P2	765432	5254349	123.4

Lithologie (table enfant)

Forage	UnitID	Unité	Sommet	Base	Desc
P1	0	TOURBE	0.00	3.30	-
P1	1	SABLE	3.30	6.70	Fin
P1	2	SABLE	6.70	9.95	Grossier
P1	3	ARGILE	9.95	13.30	Fine
P1	4	TILL	13.30	16.50	Argileux
P1	5	ROC	16.50	17.70	Granite altéré
P1	6	ROC	17.70	18.70	Granite sain
P2	0	ARGILE	0.00	4.50	Silteuse

Lithotratigraphie (table enfant)

Forage	UnitID	Unité	Sommet	Base
P1	0	O	0.00	3.30
P1	1	Md	3.30	9.95
P1	2	Ma	9.95	11.10
P1	3	Ma(2)	11.10	13.30
P1	4	Tb	13.30	16.50
P1	5	R	16.50	18.70
P2	0	Ma	0.00	4.50

***Figure 2. a)** Structure bidimensionnelle; **b)** Structure relationnelle centrée sur les unités.*

Le deuxième problème est la complexité des opérations de recherche dans la base de données. Afin de trouver toutes les occurrences d'un type particulier de sédiments, des recherches doivent être effectuées dans tous les champs. Si la base de données contient dix champs, la recherche doit être effectuée dans chacun d'eux (du champ «Unité 1» au champ «Unité 10»).

Quant au troisième problème, il est relié au fait que les éléments d'information relatifs aux contacts étant «implicites», il est impossible de donner des attributs aux contacts eux-mêmes (par ex. contact conforme par opposition à contact d'érosion). Ce genre d'information doit être placé de façon informelle dans un champ de commentaires. Encore là, pour les petites bases de données, les inconvénients sont limités, mais pour les bases de données de plus grande envergure, cette approche est peu utilisable.

Structure relationnelle

La structure relationnelle est beaucoup plus efficace que celle à deux dimensions, car elle élimine la limite du nombre d'unités qu'un forage peut contenir et permet d'effectuer des opérations de recherche beaucoup plus efficacement. Les logiciels de gestion de bases de données qui utilisent la structure relationnelle permettent une modélisation supérieure en faisant appel à une série de tables (relations) reliées entre elles à l'aide de clefs. Les diverses opérations (recherche, mise à jour, tri, etc.) peuvent être exprimées à l'aide d'un langage normalisé de manipulation de données, soit le langage SQL (*Structured Query Language*). La conception d'une structure relationnelle est guidée par des règles de normalisation (*normal forms*; Codd, 1970) qui visent essentiellement à éliminer les redondances et les limitations structurelles d'une base de données.

Structure centrée sur les unités

La structure relationnelle la plus fréquemment utilisée consiste en des listes d'unités reliées par une clef à une table parent de forage (figure 2b). Cette structure est dite «centrée sur les unités» car le concept central de la base de données est l'unité. Dans cette approche, les données sont regroupées en tables d'unités comportant un sommet et une base. Une clef (le champ «Forage» de la figure 2b) permet de lier les deux tables. Cette structure est communément appelée «1 à plusieurs» car elle permet de relier un nombre indéterminé d'enregistrements d'une table enfant à un seul enregistrement d'une table parent (plusieurs unités vers un seul forage). Cette approche élimine donc la limite maximale du nombre d'unités. Ainsi, dans la structure relationnelle classique, les unités recoupées dans un forage sont, à tort, modélisées comme une liste de segments.

Dans la structure relationnelle, chaque classification requiert sa propre table d'unités, tout en réutilisant la même table de forages. On peut ainsi relier à la table de forages des tables d'unités hydrostratigraphiques, lithostratigraphiques, lithologiques ou toute autre classification *ad hoc*. Cette approche est celle utilisée par plusieurs logiciels, dont GMS (Groundwater Modelling System) et Borehole Mapper (Northwood Geoscience Ltd.), et par certains utilitaires, dont DrillPad (Surpac Software). Des structures de bases de données très complexes telles que celle du PPDM (Public Petroleum Database Model) utilisent aussi cette approche. Les données contenues dans le PPDM sont réparties à l'aide d'un concept d'intervalles où sont décrits les matériaux entre un sommet et une base le long d'un forage.

Cette approche est efficace mais elle pose encore le problème de l'intégration de l'information sur les discontinuités. Comme les discontinuités sont toutes des contacts, leur nombre maximal est égal au nombre d'unités plus un dans une classification. Cette structure transgresse l'une des règles de normalisation de Codd (1970), notamment celle concernant la redondance de l'information. En effet, la profondeur de la base d'une unité doit, par définition, correspondre à celle du sommet de l'unité sous-jacente. Dans la structure centrée sur les unités, ce chiffre est répété explicitement dans la base de données (base de l'argile et sommet du till de la figure 2b). Cette profondeur doit se trouver simultanément dans deux enregistrements, ce qui engendre de la redondance. Ainsi, dans les procédures de mise à jour, ce chiffre doit être modifié dans toutes les tables de classification, ce qui amène invariablement des problèmes d'intégrité de l'information et de synchronisation. Par exemple, le fait de changer la position de la base de l'argile dans la table lithologique (figure 2b) implique la modification du sommet du till dans la même table, mais aussi du sommet de l'unité Tb et de la base de l'unité Ma(2) dans la table lithostratigraphique. Il serait toujours possible de forcer la synchronisation des données à l'aide d'un logiciel, mais cela ne réglerait le problème qu'imparfaitement. En effet, l'information sur les discontinuités n'est pas gérée par la base de données, de sorte que l'on ne peut pas inférer si les différences entres les tables de classification sont dues à des erreurs ou à l'utilisation d'une autre discontinuité non documentée. L'absence d'information explicite sur les contacts ne permet pas de s'assurer de l'intégrité des unités d'une classification à l'autre. Par exemple, les procédures automatiques de modification ne peuvent pas faire la différence entre deux discontinuités au même endroit (un contact lithologique et un niveau de nappe au même endroit) et une seule discontinuité partagée par deux classifications. La structure de base de données centrée sur les unités n'indique pas explicitement quels contacts sont censés être synchrones et ceux qui ne le sont pas. Une procédure automatique ne peut donc pas synchroniser adéquatement l'information.

Structure centrée sur les contacts

Le modèle proposé ici pour gérer efficacement des données de forage dans une base de données relationnelle est une version inspirée des structures topologiques conventionnelles fréquemment utilisées dans les SIG vectoriels haut de gamme comme ARC/INFO (ESRI) ou CARIS (Universal Systems). Afin de gérer et de représenter cartographiquement des données à référence spatiale, les SIG modélisent l'information à l'aide d'un modèle topologique. Cette approche de gestion des données mise sur l'interconnectivité spatiale des éléments d'information pour construire un modèle cohérent. Ce modèle permet de normaliser l'information disponible et peut-être de solutionner les problèmes de sous-représentation de certains éléments d'information, de redondance et de synchronisation spécifiques aux données de forage.

En appliquant les principes de base des structures de données connues telles que la structure «chaîne-noeud» et la segmentation dynamique, on peut générer un modèle topologique qui soit flexible et très efficace pour la gestion de données purement tabulaires, sous la forme d'une structure centrée sur les contacts.

La structure «chaîne-noeud» consiste essentiellement en un ensemble de chaînes (*arcs*) interconnectées entre elles par des noeuds (*nodes*). Une chaîne est une polyligne ou une série continue de sommets (*vertices*). Les chaînes partagent entre elles le premier ou le dernier sommet. Ces sommets partagés sont appelés des noeuds (figure 3b). L'ensemble des chaînes interconnectées forme un réseau. Un polygone est composé d'une série de chaînes qui forment une aire fermée. L'avantage de cette approche est que la connectivité entre deux chaînes est déterminée au niveau sémantique (ESRI, 1994), la connexion à ce point n'étant pas l'effet du hasard, mais bien d'une propriété partagée par les deux chaînes.

Une autre structure intéressante utilisée dans le monde des SIG est la segmentation dynamique (*dynamic segmentation*). Cette structure permet d'établir la définition d'un intervalle le long d'une série de chaînes (un réseau) en fonction d'un point de départ et d'un point d'arrivée. Le segment dynamique est donc basé sur une ou des chaînes existantes et défini en terme de distance depuis le début de la chaîne. Les SIG peuvent donc utiliser plusieurs chaînes pour former un segment; le passage d'une chaîne à une autre se fait selon le principe de la connectivité (figure 3b).

La figure 3a présente une analogie entre, d'une part, la structure «chaîne-noeud» et la segmentation dynamique et, d'autre part, la structure centrée sur les contacts. On peut faire un parallèle entre les discontinuités et les sommets d'une chaîne. Une table de classification peut être comparée à un réseau de chaînes (réseau simple) qui forment un réseau linéaire depuis le premier contact (le sommet du forage) jusqu'au dernier (la base). Un réseau simple est créé pour chaque classification. Les segments, naturellement comparés aux segments dynamiques des SIG, peuvent être appliqués à n'importe quel réseau (le résultat sera le même) ou à un réseau virtuel composé d'une chaîne unique allant du sommet à la base du forage. Le tableau 1 résume les équivalences entre la terminologie des deux concepts.

IMPLANTATION DANS UN SGBD RELATIONNEL

L'implantation de cette structure dans un SGBD (système de gestion de base de données) est relativement simple (figure 4). La structure est articulée autour d'une table des discontinuités, chacune d'elles étant indexées par la clef d'identification du forage et une clef d'identification unique (FORAGE et CNTID). Ces discontinuités sont essentiellement des entités spatiotemporelles, c'est-à-dire des positions dans l'espace et le temps. La dimension temporelle est peu utilisée dans le cas de discontinuités géologiques, mais est importante pour les données hydrostratigraphiques qui varient rapidement dans le temps. Le type de positionnement est à la discrétion de la personne qui implante la structure. On peut utiliser des positions absolues (x, y, z, t), relatives (dx, dy, dz,

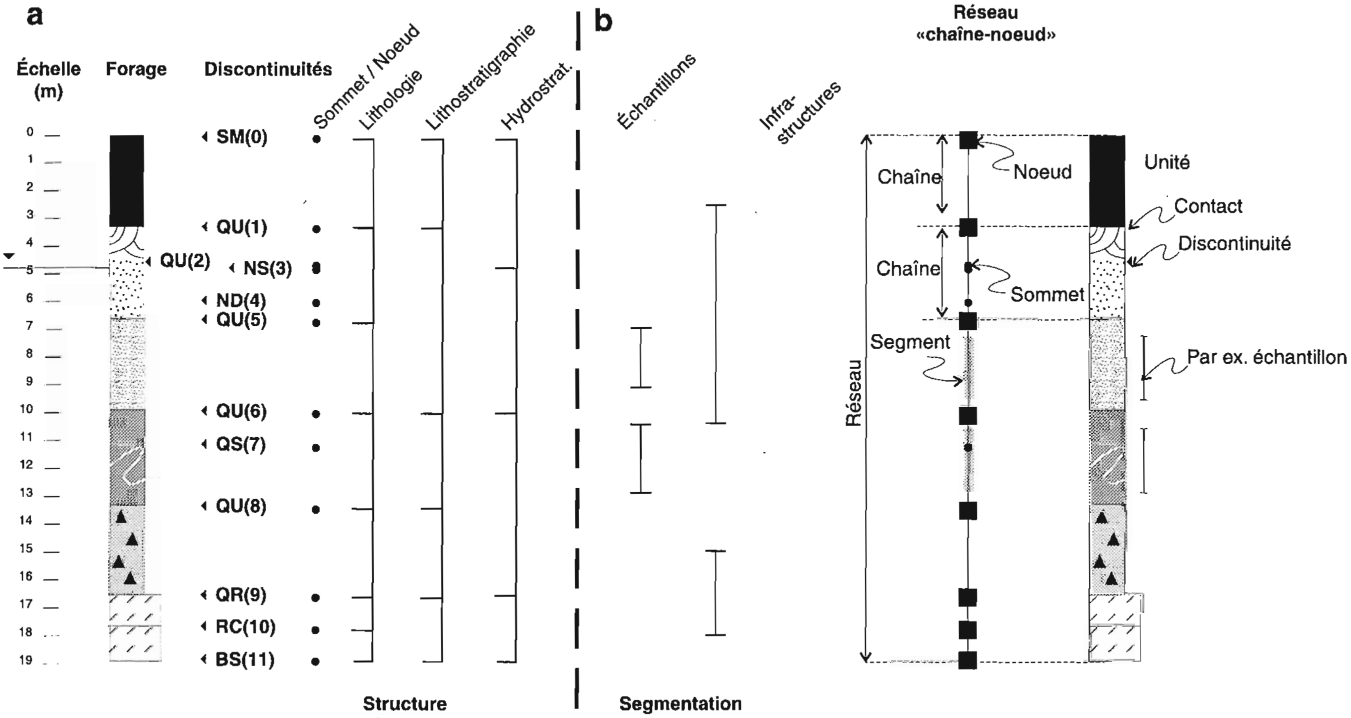

Figure 3. Modélisation de données de forage à l'aide de structures propres aux SIG.

dt) ou relatives linéaires (profondeur, t) qui sont déterminées le long d'un forage. Toutes ces approches ont essentiellement le même rôle : positionner les discontinuités. On peut adjoindre à cette table divers attributs descriptifs ou des clefs supplémentaires pour la relier aux autres tables. Un champ séquentiel (SEQ#) s'assure de la séquence des points dans le bon ordre.

Tableau 1. Équivalences entre la terminologie des SIG et celle de la structure centrée sur les contacts.

SIG	Structure centrée sur les contacts
Sommet (*vertex*)	Discontinuité
Noeud (*node*) = sommet partagé entre des chaînes	Contact
Chaîne (*arc*)	Unité
Réseau	Classification
Segment dynamique	Segment

Les unités sont modélisées dans une série de tables construites selon un gabarit de base (figure 4). Toutes les tables d'unités comportent une clef d'identification du forage, un identifiant unique des unités et deux clefs de référence à des discontinuités, soit une clef de contact sommitale (CNTSUPID) et une clef de contact basal (CNTINFID). Le contenu de ces clefs doit obligatoirement référer à un contact existant, ce qui force l'intégrité référentielle. L'identifiant des discontinuités est indépendant de la séquence le long du forage puisque cette information est maintenue à l'aide d'un champ séquentiel (clef SEQ# de la figure 4b). En théorie, le nombre de tables et le nombre de champs sont illimités. D'autres champs peuvent être ajoutés à loisir pour décrire les unités selon la classification voulue.

Les tables de segments sont les plus simples à réaliser. Elles respectent la même structure de base que les tables d'unités, mais les limites du segment sont exprimées en mètres depuis le début du forage au lieu d'une référence à la table des contacts. Les tables de segments sont identiques aux tables d'unités à structure centrée sur les unités, sauf que les contraintes des unités ne sont pas présentes. Les segments

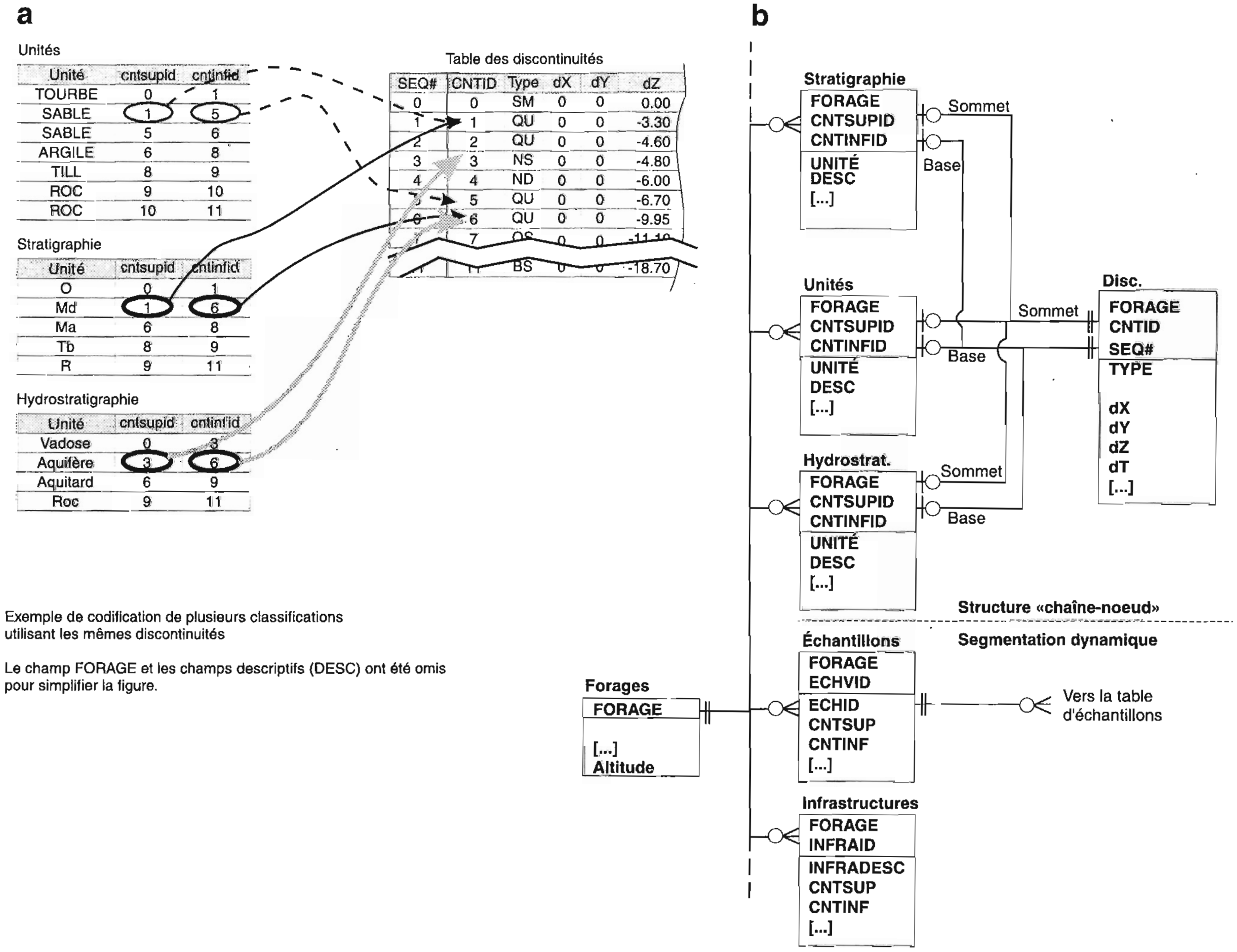

Unités

Unité	cntsupid	cntinfid
TOURBE	0	1
SABLE	1	5
SABLE	5	6
ARGILE	6	8
TILL	8	9
ROC	9	10
ROC	10	11

Stratigraphie

Unité	cntsupid	cntinfid
O	0	1
Md	1	6
Ma	6	8
Tb	8	9
R	9	11

Hydrostratigraphie

Unité	cntsupid	cntinfid
Vadose	0	3
Aquifère	3	6
Aquitard	6	9
Roc	9	11

Table des discontinuités

SEQ#	CNTID	Type	dX	dY	dZ
0	0	SM	0	0	0.00
1	1	QU	0	0	-3.30
2	2	QU	0	0	-4.60
3	3	NS	0	0	-4.80
4	4	ND	0	0	-6.00
5	5	QU	0	0	-6.70
6	6	QU	0	0	-9.95
7	7	OS	0	0	-11.10
	11	BS	0	0	-18.70

Exemple de codification de plusieurs classifications utilisant les mêmes discontinuités

Le champ FORAGE et les champs descriptifs (DESC) ont été omis pour simplifier la figure.

***Figure 4.** Implantation de la structure centrée sur les contacts et exemple de liens entre les tables de données.*

peuvent être discontinus par rapport au tracé total du forage et peuvent se superposer. Il est possible de créer autant de tables de segments que nécessaire en suivant le même gabarit.

AVANTAGES

La structure centrée sur les contacts comporte de nombreux avantages pour la gestion des données de forage :

- *Description des discontinuités le long d'un forage.* On peut indiquer clairement la présence de contacts graduels ou francs, de même que spécifier sans ambiguïté le début et la fin d'une zone de transition.
- *Intégrité référentielle de la base de données.* Dans cette structure, il est impossible de former une unité sans faire appel aux contacts, et le partage des contacts est sans ambiguïté. Les relations entre les unités sont établies de façon explicite. La gestion des contacts se fait à un seul endroit, indépendamment du nombre de classifications. La synchronisation des données est une propriété inhérente de la structure centrée sur les contacts. Les données associées aux discontinuités sont partagées entres les unités au lieu d'être répétées dans toutes les tables de classification.
- *Ajout de discontinuités sans restructurer les tables d'unités.* L'ajout de discontinuités est totalement indépendante de la structure des unités; ainsi, une description très minutieuse (comportant de nombreuses discontinuités) ne surcharge pas les tables d'unités. On peut ajouter des discontinuités sans modifier les clefs uniques de discontinuités déjà présentes, l'ordre étant géré par une clef différente (SEQ#).
- *Ajout d'un nombre infini de classifications.* La structure peut se plier aux classifications les plus diverses sans que la structure générale de la base de données ne soit altérée. Cette souplesse permet de construire des outils de gestion généraux qui s'appliquent à n'importe quelle situation et permettent de créer des interfaces usagers communes à toutes les classifications.
- *Transposition de la structure centrée sur les contacts à d'autres structures topologiques semblables.* Une traverse géologique en serait un exemple.

BASE DE DONNÉES : PROJET PIÉMONT LAURENTIEN

La base de données créée dans le cadre du projet Piémont laurentien contient plus de 8 000 descriptions de forages ou de coupes stratigraphiques. Les données, particulièrement hétérogènes, proviennent principalement de la banque des puisatiers, notamment du ministère de l'Environnement et de la Faune du Québec (MEF), du ministère des Transports du Québec (MTQ), d'Hydro-Québec, de firmes de consultants et de partenaires industriels (comme l'aluminerie Lauralco), mais aussi des membres du projet Piémont laurentien.

La base de données est la partie centrale d'une série d'outils informatiques qui permettent de visualiser et de traiter l'information. Elle sert à la gestion, l'entrée et la restitution des données de forage. Le travail de représentation graphique est effectué à l'aide de logiciels externes. Les données de référence sont conservées dans la base de données sous la forme la plus complète possible et peuvent être restituées sous plusieurs formes à l'aide de requêtes et de modules informatiques. Ainsi, des modules permettent de transférer de l'information de la base de données à divers logiciels, comme GMS, ARC/INFO, MAP/INFO (pour la représentation cartographique) et BoreHole Mapper ou GMS (pour la représentation en coupes transversales et en blocs-diagrammes). Les forages peuvent être visualisés sous la forme de fiches signalétiques par l'intermédiaire de Winlog. La communication avec la base de données peut être directe (par *ODBC, Open Database Connectivity*) ou par l'intermédiaire de fichiers de transfert. La structure centrée sur les contacts étant implantée dans une structure relationnelle, elle est totalement transférable dans Oracle, SyBase, Ingres, etc.

CONCLUSION

La structure centrée sur les contacts est une application intéressante des stratégies utilisées dans les SIG pour assurer la cohérence des données et, donc, en faciliter la gestion. Cette structure permet de gérer une base de données très hétérogène au niveau des types de classification, sans sacrifier les détails importants de la description du forage. La flexibilité de la structure permet également de la reformater dynamiquement pour les applications externes qui utilisent, pour la plupart, une approche centrée sur les unités. L'intégrité référentielle et spatiale est inhérente à la structure de la base de données. De plus, peu de vérifications sont nécessaires à l'entrée des données, puisque la majorité des contraintes sont établies directement par la structure des données.

REMERCIEMENTS

Les auteurs tiennent à remercier Michel Parent, Daniel Lebel (respectivement des bureaux de la CGC à Québec et à Calgary) et Linda Guay (de la Division de l'information géoscientifique) pour leurs commentaires qui ont grandement contribué à améliorer ce texte.

RÉFÉRENCES

Codd, E.
1970: A relational model for large shared data banks; CACM, vol. 13, no. 6, p. 379-387.
ESRI
1994: ARC/INFO data management, concepts, data models, database design, and storage; Redlands, Environmental System Research Institute (ESRI), inc., p. 1-1 - 1-48.
Everest, G.C.
1986: Database management: objectives, system functions, and administration; McGraw-Hill, New York, 816 p.

Projet 960001 HD de la Commission géologique du Canada

Electrical characteristics of nonmineralized rocks from the Bathurst mining camp, New Brunswick[1]

T.J. Katsube, S. Connell, W.D. Goodfellow, and N. Scromeda
Mineral Resources Division, Ottawa

Katsube, T.J., Connell, S., Goodfellow, W.D., and Scromeda N., 1998: Electrical characteristics of nonmineralized rocks from the Bathurst mining camp, New Brunswick; in *Current Research 1998-E; Geological Survey of Canada, p. 125–137.*

Abstract: Laboratory electrical resistivity measurements have been carried out on 20 mainly nonmineralized samples, representing major rock types in the Bathurst mining camp, to assist in the interpretation of airborne and borehole electromagnetic (EM) surveys. Following similar studies on mineralized and nonmineralized rocks from several massive sulphide deposits in this region, this study is based on nonmineralized host rocks.

Results indicate that electrical resistivities (ρ_r) are 0.3–56 000 Ω·m for these samples, the lower end within the detectable limits of EM survey systems and the higher end well above that limit. Iron-formation and carbonaceous sedimentary rocks display resistivity anisotropies of 25:1 to 300:1, with ρ_r values of 12–90 Ω·m, in the conductive direction, values within the EM detectable limit. Data analysis by the three-polarization model suggests that conductive minerals (e.g. magnetite, graphite, carbon) line the pores of the low r_r directions, except for one case where the source is fractures rather than bedding planes.

Résumé : Des mesures de la résistivité électrique ont été faites en laboratoire sur 20 échantillons principalement non minéralisés représentant les principaux lithotypes du camp minier de Bathurst, afin d'appuyer l'interprétation des levés électromagnétiques aériens et en trous de sondage. Cette étude, portant sur les roches encaissantes non minéralisées, fait suite à des études semblables menées sur des roches minéralisées et non minéralisées en provenance de plusieurs gisements de sulfures massifs présents dans cette région.

Les résultats révèlent que la résistivité électrique (ρ_r) de ces échantillons varie de 0,3 à 56 000 Ω·m, les valeurs inférieures étant décelées par les instruments électromagnétiques et les valeurs supérieures ne l'étant pas. Les formations de fer et les roches sédimentaires carbonées montrent des anisotropies de résistivité de 25:1 à 300:1 et des valeurs de résistivité électrique (ρ_r) de 12 à 90 Ω·m, dans la direction de la conductivité, valeurs qui ne sont pas décelables par la méthode électromagnétique. L'analyse des données au moyen du modèle de tri-polarisation laisse supposer que les minéraux conducteurs, tels que la magnétite, le graphite et le carbone, tapissent les pores dans les directions à résistivité électrique faible, à l'exception d'un cas où la source s'avère être des fractures et non des plans de stratification.

---

[1] Contribution to the 1994-1999 Bathurst Mining Camp, Canada-New Brunswick Exploration Science and Technology (EXTECH II) Initative

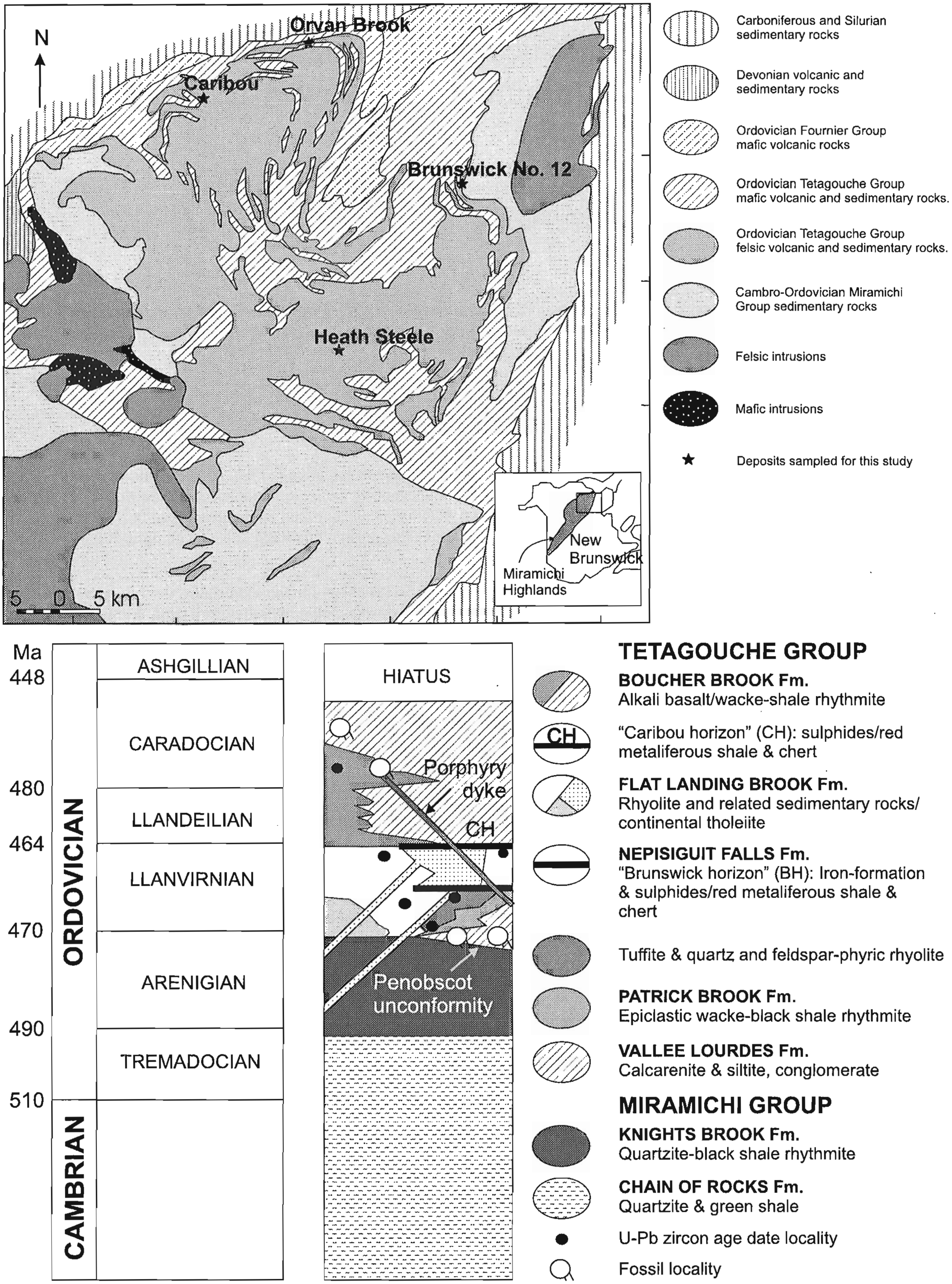
N
Orvan Brook
Caribou
Brunswick No. 12
Heath Steele
New Brunswick
Miramichi Highlands
5 0 5 km
Carboniferous and Silurian sedimentary rocks
Devonian volcanic and sedimentary rocks
Ordovician Fournier Group mafic volcanic rocks
Ordovician Tetagouche Group mafic volcanic and sedimentary rocks.
Ordovician Tetagouche Group felsic volcanic and sedimentary rocks.
Cambro-Ordovician Miramichi Group sedimentary rocks
Felsic intrusions
Mafic intrusions
★ Deposits sampled for this study
Ma
448
480
464
470
490
510
ORDOVICIAN
CAMBRIAN
ASHGILLIAN
CARADOCIAN
LLANDEILIAN
LLANVIRNIAN
ARENIGIAN
TREMADOCIAN
HIATUS
Porphyry dyke
CH
Penobscot unconformity
TETAGOUCHE GROUP
BOUCHER BROOK Fm.
Alkali basalt/wacke-shale rhythmite
CH
"Caribou horizon" (CH): sulphides/red metaliferous shale & chert
FLAT LANDING BROOK Fm.
Rhyolite and related sedimentary rocks/ continental tholeiite
NEPISIGUIT FALLS Fm.
"Brunswick horizon" (BH): Iron-formation & sulphides/red metaliferous shale & chert
Tuffite & quartz and feldspar-phyric rhyolite
PATRICK BROOK Fm.
Epiclastic wacke-black shale rhythmite
VALLEE LOURDES Fm.
Calcarenite & siltite, conglomerate
MIRAMICHI GROUP
KNIGHTS BROOK Fm.
Quartzite-black shale rhythmite
CHAIN OF ROCKS Fm.
Quartzite & green shale
● U-Pb zircon age date locality
Fossil locality

INTRODUCTION

Laboratory electrical resistivity measurements have been carried out on 20 slightly mineralized to nonmineralized core samples from various locations in the Bathurst mining camp (Fig. 1a). These samples represent most of the major rock types in the region. The objective of this study is to provide information to assist in the interpretation of airborne, ground, and borehole EM surveys in this area. Following similar studies on mineralized and nonmineralized rocks from Brunswick No. 12 (Katsube et al., 1997), Caribou (Katsube et al., 1998a), Restigouche (Katsube et al., 1998b), and the Stratmat (Connell et al., 1998) massive sulphide deposits in this mining camp, this study focuses on the nonmineralized rocks. Previous work (Katsube et al., 1996a, b; T.J. Katsube, M. Best, and N. Scromeda, poster presentation at GSC Minerals Colloquium, January 22-24, 1996, Ottawa, Ontario; Jones et al., 1996) has demonstrated the existence of significant electrical anisotropy in rocks. Recent work at this camp has also demonstrated the existence of significant electrical anisotropies (λ), as high as 1000:1, for certain rock types (Katsube et al., 1997). Electrical anisotropy associated with geological features can have a significant effect on the electromagnetic responses, as previously indicated (Connell et al., 1998). This study, therefore, includes laboratory electrical measurements made in three directions where possible, also to determine the electrical anisotropy characteristics.

METHOD OF INVESTIGATION

Samples and sample preparation

Representative regional rock samples were collected from the major rock formations in the Tetagouche and Miramichi groups (Fig. 1b), Bathurst mining camp. Drill cores were sampled to minimize the effects of surface weathering. All samples come from the area around four mineral deposits unaffected by hydrothermal alteration: Brunswick No. 12, Heathe Steele, Caribou, and Orvan Brook (Fig. 1a, b). In the Caribou and Orvan Brook deposit areas, felsic volcanic rocks and underlying carbonaceous shales were sampled from the Spruce Lake Formation of the Tetagouche Group. Around Brunswick No. 12 deposit, mafic volcanic rocks and gabbro were sampled from the Eighteen Mile Formation, rhyolite from the Flat Landing Brook Formation, iron-formation and quartz-feldspar porphyry from the Nepisiguit Falls Formation, and carbonaceous shale and siltstone from the Miramichi Group. Rhyolite and quartz-feldspar porphyry were sampled from the Flat Landing Brook and Nepisiguit Falls formations around Heathe Steele deposit, respectively. Carbonaceous shale in the Heathe Steele area was sampled from the Miramichi Group that underlies the Nepisiguit Falls Formation.

Figure 1.

***a)** Location map of the Bathurst mining camp, New Brunswick (modified from Davies, 1977). Sample origins are indicated by their respective deposit location. **b)** Stratigraphy of part of the Tetagouche and Miramichi groups (modified from van Staal et al., 1990, 1992).*

Information on the twenty core samples (sample numbers MXG-1 to MXG-20), drillhole identification, sample depth, formation, and lithology is presented in Table 1 (*see* Appendix for sample descriptions). Usually, more than one specimen is cut from each sample: at least one for determination of bulk density, δ_B, and electrical resistivity, ρ_r, and one for effective porosity, ϕ_E, determinations whenever possible. In some cases, several rectangular and/or disc-shaped specimens (e.g. a, b, and c) were cut from a single sample for the ρ_r measurements (Fig. 2). Multiple specimens allow for different components of heterogeneity and anisotropy to be characterized. Specimens prepared for ϕ_E measurements are irregular in shape and contain little or no visible sulphides. Samples with a high sulphide content are avoided due to concern over their oxidation at elevated temperatures (100°C) during the ϕ_E determination procedure. The geometric characteristics of the specimens used for ρ_r and δ_B measurements are listed in Table 2. Preparations are in progress for petrographic thin section and scanning electron microscope analyses of selected samples/specimens, to examine the sample texture and fabric, including the connectivity of the sulphide mineral grains.

Bulk density and effective porosity measurements

The caliper method (American Petroleum Institute, 1960) has been used to determine the bulk density (δ_B) of the samples, by measuring the dimensions and weight of the room-dry (23°C) rectangular or disc-shaped specimens. These measurements are also used in porosity determination. Effective porosity (ϕ_E), in principle, represents the pore volume of all

Table 1. Sample identification for samples collected for the regional sample suite from the Bathurst mining camp.

Sample number	Drill hole	Depth (ft)	Fm.	Lithology
MXG-1	H55	6.014840e+67	SL	Felsic volcanic
MXG-2	H55		SL	Felsic volcanic
MXG-3	H55		BB	Carbonaceous argillite
MXG-4	H55		SL	Sulphide stringer zone
MXG-5	HA248		EM	Gabbro (feeder to BB basalts)
MXG-6	HA248		EM	Mafic volcanic flow
MXG-7	HA248		BB	Basaltic flow
MXG-8	HA248		BB	Maroon sediment
MXG-9	HA248		NF	Footwall chloritic sediment
MXG-10	H12-1398		NF	Quartz-feldspar porphyry
MXG-11	H12-1398		NF	Quartz-feldspar porphyry
MXG-12	A243		NF	Quartz-feldspar porphyry
MXG-13	B357		NF	Iron-formation
MXG-14	217.8		FLB	Lapilli tuff
MXG-15	12.415		NF	Quartz-feldspar porphyry
MXG-16	289A-B4		KB	Carbonaceous sediment
MXG-17	S1363		FLB	Porphyritic rhyolite
MXG-18	B3804		NF	Quartz-feldspar porphyry
MXG-19	B3804		NF	Quartz-feldspar porphyry
MXG-20	HORB96-12		BB	Shale/schist

SL = Spruce Lake Formation
BB = Boucher Brook Formation
EM = Eighteen Mile Formation
NF = Nepisiguit Falls Formation
FLB = Flat Landing Brook Formation
KB = Knights Brook Formation

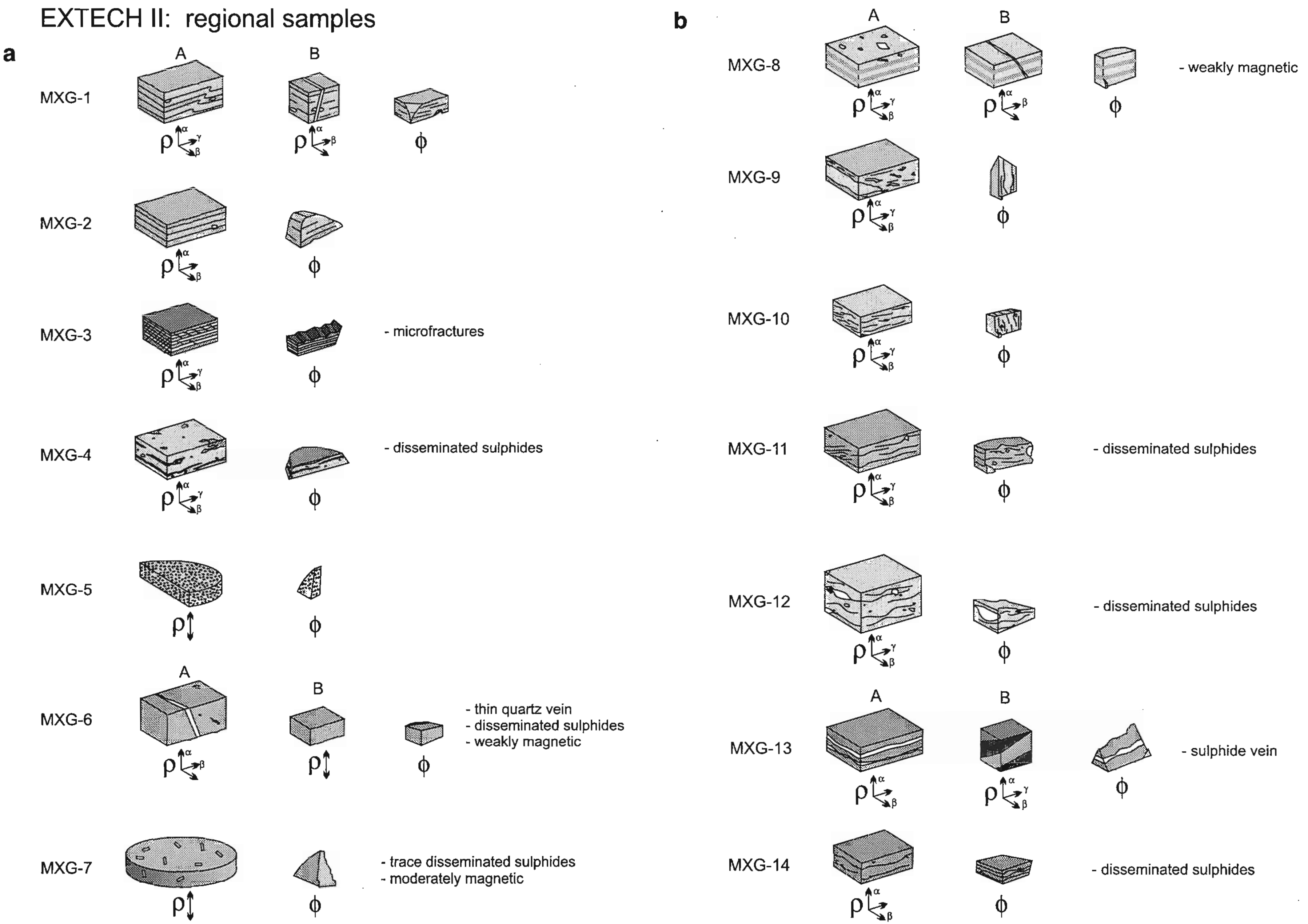
EXTECH II: regional samples
a
A
B
MXG-1
ρ α β γ
ρ α β
ϕ
MXG-2
ρ α β
ϕ
MXG-3
ρ α β γ
ϕ
- microfractures
MXG-4
ρ α β γ
ϕ
- disseminated sulphides
MXG-5
ρ
ϕ
MXG-6
A
B
ρ α β
ρ
ϕ
- thin quartz vein
- disseminated sulphides
- weakly magnetic
MXG-7
ρ
ϕ
- trace disseminated sulphides
- moderately magnetic
b
A
B
MXG-8
ρ α β γ
ρ α β
ϕ
- weakly magnetic
MXG-9
ρ α β γ
ϕ
MXG-10
ρ α β γ
ϕ
MXG-11
ρ α β γ
ϕ
- disseminated sulphides
MXG-12
ρ α β γ
ϕ
- disseminated sulphides
MXG-13
A
B
ρ α β
ρ α β γ
ϕ
- sulphide vein
MXG-14
ρ α β
ϕ
- disseminated sulphides

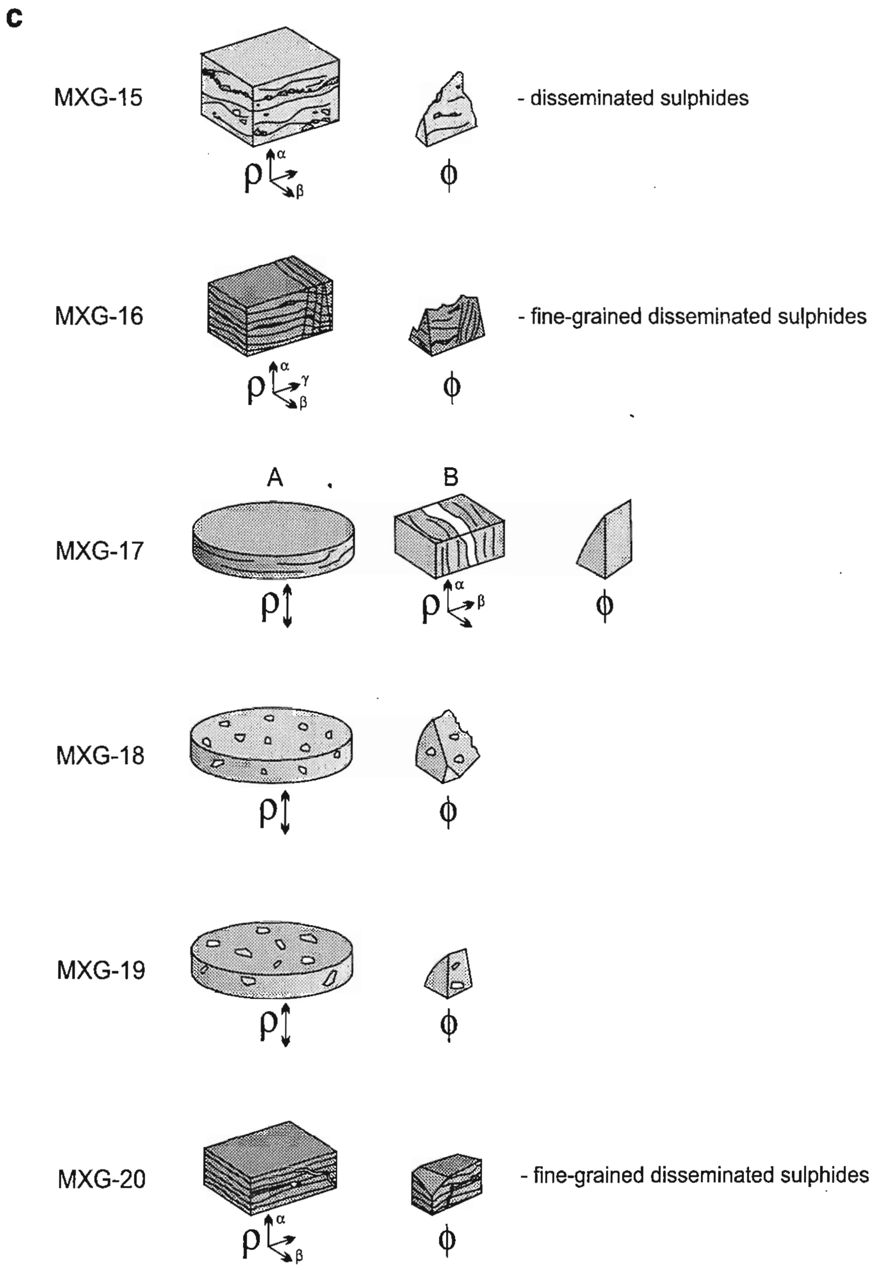

Figure 2.

*Block diagrams of specimens from the 20 samples used for electrical resistivity and porosity measurements in this study **a)** samples MXG-1 to MXG-7, **b)** samples MXG-8 to MXG-14, **c)** samples MXG-15 to MXG-20.*

Table 2a. Dimensions of the rectangular specimens cut out from the core samples for electrical measurements.

Sample	a_1 (cm)	a_2 (cm)	ℓ (cm)	W (g)	V (cm^3)	K_G (10^{-2}m)	δ_B (g/mL)
MXG-1Aα	1.743	1.266	1.243	7.8245	2.74	1.78	2.85
MXG-1Aβ	1.743	1.243	1.266	7.8245	2.74	1.71	2.85
MXG-1Aγ	1.266	1.243	1.743	7.8245	2.74	0.903	2.85
MXG-1Bα	1.188	0.961	0.856	2.8846	0.98	1.33	2.95
MXG-1Bβ	0.961	0.856	1.188	2.8846	0.98	0.692	2.95
MXG-2α	2.233	2.000	0.935	11.8934	4.18	4.78	2.85
MXG-2β	2.233	0.935	2.000	11.8934	4.18	1.04	2.85
MXG-3α	1.678	1.320	0.945	6.3879	2.09	2.34	3.05
MXG-3β	1.678	0.945	1.320	6.3879	2.09	1.20	3.05
MXG-3γ	1.320	0.945	1.678	6.3879	2.09	0.743	3.05
MXG-4α	1.768	1.400	0.673	5.7068	1.67	3.68	3.43
MXG-4β	1.768	0.673	1.400	5.7068	1.67	0.850	3.43
MXG-4γ	1.400	0.673	1.768	5.7068	1.67	0.533	3.43
MXG-6Aα	2.151	1.717	1.228	13.7201	4.54	3.01	3.03
MXG-6Aβ	1.228	1.717	2.151	13.7201	4.54	1.54	3.03
MXG-6B	1.694	1.331	0.788	5.6368	1.78	2.86	3.17
MXG-8Aα	1.800	1.459	1.390	11.0479	3.65	1.89	3.03
MXG-8Aβ	1.800	1.390	1.459	11.0479	3.65	1.71	3.03
MXG-8Aγ	1.459	1.390	1.800	11.0479	3.65	1.13	3.03
MXG-8Bα	1.389	1.366	0.866	5.1264	1.64	2.19	3.12
MXG-8Bβ	1.366	0.866	1.389	5.1264	1.64	0.852	3.12
MXG-9α	1.996	1.743	1.591	16.4902	5.54	2.19	2.98
MXG-9β	1.996	1.591	1.743	16.4902	5.54	1.82	2.98
MXG-9γ	1.743	1.591	1.996	16.4902	5.54	1.39	2.98
MXG-10α	2.005	1.338	1.270	9.9022	3.41	2.11	2.91
MXG-10β	2.005	1.270	1.338	9.9022	3.41	1.90	2.91
MXG-10γ	1.338	1.270	2.005	9.9022	3.41	0.848	2.91
MXG-11α	2.063	1.613	1.129	10.8964	3.76	2.95	2.90
MXG-11β	2.063	1.129	1.613	10.8964	3.76	1.44	2.90
MXG-11γ	1.613	1.129	2.063	10.8964	3.76	0.883	2.90

a_1, a_2 = Length of the two sides of the rectangular specimen
ℓ = Thickness of specimen
W = Weight of specimen under room dry conditions
K_G = Geometric factor
δ_B = Bulk density

Table 2b. Dimensions of the rectangular specimens cut out from the core samples for electrical measurements.

Sample	a_1 (cm)	a_2 (cm)	ℓ (cm)	W (g)	V (cm^3)	K_G (10^{-2}m)	δ_B (g/mL)
MXG-12α	2.256	2.033	1.688	22.1991	7.74	2.72	2.87
MXG-12β	2.256	1.688	2.033	22.1991	7.74	1.87	2.87
MXG-12γ	2.033	1.688	2.256	22.1991	7.74	1.52	2.87
MXG-13Aα	2.080	1.494	0.800	10.1835	2.49	3.88	4.10
MXG-13Aβ	2.080	0.800	1.494	10.1835	2.49	1.11	4.10
MXG-13Bα	1.123	1.035	0.949	4.2966	1.10	1.22	3.90
MXG-13Bβ	1.123	0.949	1.035	4.2966	1.10	1.03	3.90
MXG-13Bγ	1.035	0.949	1.123	4.2966	1.10	0.875	3.90
MXG-14α	2.035	1.986	1.174	13.7993	4.74	3.44	2.91
MXG-14β	1.986	1.174	2.035	13.7993	4.74	1.15	2.91
MXG-15α	2.150	1.789	1.349	15.7613	5.19	2.85	3.04
MXG-15β	2.150	1.349	1.789	15.7613	5.19	1.62	3.04
MXG-16α	1.979	1.334	1.239	9.6138	3.27	2.13	2.94
MXG-16β	1.979	1.239	1.334	9.6138	3.27	1.84	2.94
MXG-16γ	1.334	1.239	1.979	9.6138	3.27	0.835	2.94
MXG-17Bα	2.169	1.743	1.473	15.8029	5.57	2.57	2.84
MXG-17Bβ	1.743	1.473	2.169	15.8029	5.57	1.18	2.84
MXG-20α	1.694	1.105	1.089	6.0766	2.04	1.72	2.98
MXG-20β	1.694	1.089	1.105	6.0766	2.04	1.67	2.98

a_1, a_2 = Length of the two sides of the rectangular specimen
ℓ = Thickness of specimen
W = Weight of specimen under room dry conditions
K_G = Geometric factor
δ_B = Bulk density

Table 2c. Dimensions of disc-shaped specimens cut out from the core samples.

Samples	r_D (cm)	ℓ (cm)	W (g)	V (cm^3)	K_G (10^{-2}m)	δ_B (g/mL)
MXG-5	4.720	0.675	17.9258	5.70	12.4	3.17
MXG-7	4.722	0.745	39.5757	13.05	23.5	3.03
MXG-17A	4.738	0.821	40.4686	14.48	21.5	2.80
MXG-18	4.750	0.870	42.4809	15.42	20.4	2.76
MXG-19	4.737	0.789	38.1807	13.91	22.3	2.75

r_D = Diameter
ℓ = Thickness
W = Weight
K_G = Geometric factor
δ_B = Bulk density

porosity (ϕ_E), in principle, represents the pore volume of all interconnected pores. In this study, it is determined from the difference in weight between the oven-dried (116°C) and water-saturated (23°C) rock specimen. Another parameter derived on a routine basis is the irreducible water saturation, S_{ir}, which represents the pore space occupied by the water bound or adsorbed on the pore surfaces. These measurements are taken at room temperature (23°C) and atmospheric pressure (Scromeda and Katsube, 1994; Katsube and Scromeda, 1995). The American Petroleum Institute *Recommended practices for core-analysis procedure* (American Petroleum Institute, 1960) has generally been followed in these measurements. Details of the standard procedures routinely used in our measurements are described in the literature (Katsube and Salisbury, 1991; Katsube et al., 1992; Scromeda and Katsube, 1994; Katsube and Scromeda, 1995).

Bulk electrical resistivity measurements

Bulk electrical resistivity (ρ_r) is determined from measurements of complex electrical resistivity, ρ^*, procedures for which are described in recent publications (e.g. Katsube, et al., 1991, 1992, 1996a, b; Katsube and Salisbury, 1991; Katsube and Scromeda, 1994). Complex electrical resistivity (ρ^*) consists of two components: real resistivity, ρ_R, and imaginary resistivity, ρ_I (e.g. Katsube, 1975; Katsube and Walsh, 1987: Katsube and Salisbury, 1991). These measurements were made on specimens saturated in distilled water for 24 to 48 h (Katsube and Salisbury, 1991). The parameters, ρ^*, ρ_R, and ρ_I are measured over a frequency range of 1–10^6 Hz, and ρ_r usually represents bulk electrical resistivity at about 10^2–10^3 Hz. Bulk electrical resistivity, ρ_r is a function of the pore structure and pore fluid resistivity, and is understood to exclude any other effects, such as pore surface dielectric and any other polarizations (Katsube, 1975; Katsube and Walsh, 1987). The geometric factor, K_G (with the units 10^{-2} m), required for derivation of ρ^* from the actual electrical measurements, is defined as

$$K_G = A/\ell,$$

where A (cm^2) is the cross-section area and ℓ (cm) is the thickness of the specimen. This parameter was determined for all specimens prior to the electrical measurements, using the specimen dimensional data in Tables 2a, b, and c.

EXPERIMENTAL RESULTS

The results of the bulk density (δ_B) determinations are listed in Table 2. The δ_B values are in the range of 2.75 to 4.10 g/mL. The results of the effective porosity (ϕ_E) determinations are listed in Table 3, for specimens with little or no visible sulphide mineralization, and display values in the range of 0.45 to 2.91%. The δ_B values used in the ϕ_E determination are those calculated from the specimens prepared for resistivity measurements and, therefore, are not specific to those used for the ϕ_E measurements. The calliper method used for the δ_B determination cannot be used on the ϕ_E specimens, because of their irregular shapes. Although considerable effort is made to obtain homogeneity between specimens (e.g. selecting specimens from adjacent areas), the ϕ_E values may contain some errors, for this reason.

The results of the electrical resistivity (ρ_r) measurements are listed in Table 4. The mean ρ_r values are in the range of 0.3 to 55 700 Ω·m. These values are from measurements that have been made at 24 and 48 h after water saturation, in order to ensure the stability of the ρ_r values with time. Under these conditions, it is expected that the distilled water has chemically equilibrated with the rock and that the ρ_r values represent those of the in situ conditions (Katsube et al., 1997). Normally, differences up to ±20% of the mean are considered to be within measurement error and represent stable conditions. In the present study, many of the low resistivity values exceed that difference (MXG-3, MXG-12, MXG-13B, MXG-16, MXG-17A), probably because they were below the measurement resolution. Fifty-four measurements

Table 3. Results of the effective porosity measurements.

Sample	δ_B (g/mL)	W_W (g)	W_D (g)	S_{ir} (%)	ϕ_E (%)
MXG-1	2.85	3.2158	3.1986	15.7	1.53
MXG-2	2.85	4.3605	4.3321	21.5	1.87
MXG-3	3.05	6.4551	6.3942	23.8	2.91
MXG-4	3.43	3.8795	3.8670	31.2	1.11
MXG-5	3.17	1.5071	1.5031	27.5	0.84
MXG-6	3.03	2.8295	2.8227	16.2	0.73
MXG-7	3.03	3.0823	3.0765	15.5	0.57
MXG-8	3.03	3.9272	3.9244	17.9	0.22
MXG-9	2.98	6.4068	6.3516	54.7	2.59
MXG-10	2.91	5.5954	5.5839	11.3	0.60
MXG-11	2.90	6.4158	6.3942	12.5	0.98
MXG-12	2.87	4.8875	4.8784	18.7	0.54
MXG-14	2.91	4.4751	4.4634	12.0	0.76
MXG-15	3.04	6.9215	6.8938	15.2	1.22
MXG-16	2.94	2.6660	2.6528	13.6	1.46
MXG-17	2.80	2.4700	2.4641	10.2	0.67
MXG-18	2.76	4.8151	4.7708	4.3	2.56
MXG-19	2.75	4.2621	4.2552	18.8	0.45
MXG-20	2.98	4.0137	3.9855	35.5	2.11

W_w = Wet weight
W_D = Dry weight
S_{ir} = Irreducible water saturation
δ_B = Bulk density
ϕ_E = Effective porosity

Table 4a. Results of electrical resistivity measurements.

Sample	ρ_r, (10^3 Ω·m) Mes. #1	Mes. #2	Mean**
MXG-1Aα	16.79	15.48	16.14 ± 0.66
MXG-1Aβ	0.66	0.77	0.72 ± 0.06
MXG-1Aγ	1.40	1.57	1.49 ± 0.09
MXG-1Bα	11.71	11.71	11.71
MXG-1Bβ	0.72	0.78	0.75 ± 0.03
MXG-2α	43.53	41.96	42.75 ± 0.79
MXG-2β	1.22	0.87	1.05 ± 0.18
MXG-3α	3.08	3.66	3.37 ± 0.29
MXG-3β	0.19	0.11	0.15 ± 0.04
MXG-3γ	0.060	0.12	0.09 ± 0.03
MXG-4α	0.66	0.80	0.73 ± 0.07
MXG-4β	0.036	0.036	0.036
MXG-4γ	0.11	0.12	0.12 ± 0.01
MXG-5	56.01	55.39	55.70 ± 0.31
MXG-6Aα	5.05	4.35	4.70 ± 0.35
MXG-6Aβ	11.28	9.49	10.39 ± 0.90
MXG-6B	3.35	4.04	3.70 ± 0.35
MXG-7	4.80	5.03	4.92 ± 0.12
MXG-8Aα	12.11	15.35	13.73 ± 1.62
MXG-8Aβ	9.78	13.73	11.76 ± 1.98
MXG-8Aγ	5.90	7.42	6.66 ± 0.76
MXG-8Bα	22.08	20.99	21.54 ± 0.55
MXG-8Bβ	7.99	7.32	7.66 ± 0.34
MXG-9α	14.29	11.22	12.76 ± 1.54
MXG-9β	1.08	0.83	0.96 ± 0.13
MXG-9γ	1.36	1.10	1.23 ± 0.13
MXG-10α	7.66	8.02	7.84 ± 0.08
MXG-10β	1.69	1.56	1.63 ± 0.07
MXG-10γ	1.37	1.37	1.37
MXG-11α	6.68	7.58	7.13 ± 0.45
MXG-11β	1.28	1.49	1.39 ± 0.11
MXG-11γ	0.84	1.01	0.93 ± 0.09

ρ_r = Bulk electrical resistivity
Mes. (#1) = Measurement after 24 h of saturation
Mes. (#2) = Measurement after 48 h of saturation
** = The value after the "±" is the maximum difference between the individually measured values.

Table 4b. Results of electrical resistivity measurements.

Sample	ρ_r, (10^3 Ω·m) Mes. #1	Mes. #2	Mean**
MXG-12α	21.31	14.94	18.13 ± 3.19
MXG-12β	6.78	2.35	4.57 ± 2.22
MXG-12γ	5.52	1.98	3.75 ± 1.77
MXG-13Aα	18.25	24.27	21.26 ± 3.01
MXG-13Aβ	0.069	0.074	0.072 ± 0.003
MXG-13Bα	0.0009	0.0032	0.0021 ± 0.0012
MXG-13Bβ	0.0003	0.0002	0.0003 ± 0.0001
MXG-13Bγ	0.0005	0.0002	0.0004 ± 0.0002
MXG-14α	21.44	27.94	24.69 ± 3.23
MXG-14β	1.43	2.29	1.86 ± 0.43
MXG-15α	3.89	4.62	4.26 ± 0.37
MXG-15β	0.53	0.64	0.59 ± 0.06
MXG-16α	0.035	0.038	0.037 ± 0.002
MXG-16β	0.016	0.0070	0.012 ± 0.0113
MXG-16γ	0.29	0.34	0.32 ± 0.03
MXG-17A	33.27	20.04	26.66 ± 6.62
MXG-17Bα	6.76	6.02	6.39 ± 0.37
MXG-17Bβ	10.93	11.49	11.21 ± 0.28
MXG-18	2.12	2.70	2.41 ± 0.29
MXG-19	5.45	7.03	6.24 ± 0.79
MXG-20α	1.36	1.93	1.65 ± 0.29
MXG-20β	0.042	0.050	0.046 ± 0.004

ρ_r = Bulk electrical resistivity
Mes. (#1) = Measurement after 24 h of saturation
Mes. (#2) = Measurement after 48 h of saturation
** = The value after the "±" is the maximum difference between the individually measured values

(including 3-D measurements) were completed on twenty-five specimens representing twenty samples. The electrical resistivity anisotropies (λ) are in the range of 295:1 (sample MXG-13A) to 1.7:1 (sample MXG-17B), as shown in Table 5. The parameter λ is determined by dividing the largest ρ_r value by the smallest one.

Some examples of the complex resistivity plots used to determine the low to high values of r_r are shown in Figures 3, 4, 5, 6, and 7. Figure 3 displays two complex resistivity plots for an iron-formation specimen (MXG-13A) measured in two different directions (α and β). These are for specimens with intermediate resistivity values, which display two arcs (the second arc is more clearly defined in Fig. 3b). The polarization effects resulting in the second arc are likely caused by the electrodes and the magnetite in the sample. Figure 4 displays a complex resistivity plot for sample MXG-2. A normal arc is shown here and is an example of a complex resistivity plot where little difficulties were experienced when determining ρ_r. The error range in these cases is considerably less than ±20%. Figure 5 displays the resistivity plot of sample MXG-7 with two arcs. The second arc probably resulted from polarization effects caused by the magnetite or other material lining the pores. Figure 6 shows the complex resistivity plots of a maroon sediment (MXG-8B). It shows a considerably distorted arc (Fig. 6b: MXG-8Bb) when measured in the direction parallel to bedding (Fig. 2b) and perpendicular to a small vein. Distortion sometimes occurs in highly resistive rocks, making r_r determination difficult. Figure 7 shows the complex resistivity curves for a carbonaceous sediment (MXG-16) which was measured in three directions. The suppressed arc on the right-hand side is not normal and requires further investigation to determine the cause.

DISCUSSION AND CONCLUSIONS

The electrical resistivities (ρ_r) are in the range of 0.3 to 56 000 Ω·m for these samples, the lower end being well within the detectable limits of the electromagnetic (EM) survey systems (Katsube et al., 1996a, Connell et al., 1998), and the higher end being well above that limit. There are some electrical resistivity anisotropy (λ) values larger than 20:1, which are in the range of 25:1 to 300:1. The largest (λ=300:1) is for an iron-formation sample (MXG-13A), with the minimum and maximum ρ_r values being 72 Ω·m in the direction of the bedding and 20 000 Ω·m in the direction perpendicular to the bedding, respectively. There are three samples (MXG-3, MXG-16, MXG-20) which have λ values within the range of 25:1 to 40:1, with the minimum and maximum ρ_r values being 12–90 Ω·m in the direction of the bedding and 300–3400 Ω·m in the direction perpendicular to the bedding, respectively. These rock types are carbonaceous argillite (MXG-3), carbonaceous sediment (MXG-16), and

Table 5. Results of electrical resistivity measurements.

Sample	Rock type	δ_B (g/mL)	Mean ρ_r (10^3 Ω·m)			Anisotropy λ
			α	β	γ	
MXG-1A	FV	2.85	16.14	0.72	1.49	22:1
MXG-1B		2.95	11.71	0.75		15.6:1
MXG-2	FV	2.85	42.75	1.05		40.7:1
MXG-3	CA	3.05	3.37	0.15	0.09	37:1
MXG-4	S	3.43	0.73	0.036	0.12	20:1
MXG-5	Gab.	3.17	55.70			
MXG-6A	MV	3.03	4.70	10.39		2:1
MXG-6B		3.17	3.70			
MXG-7	Bas.	3.03	4.92			
MXG-8A	Sed.	3.03	13.73	11.76	6.66	2:1
MXG-8B		3.12	21.54	7.66		2.8:1
MXG-9	Sed.	2.98	12.76	0.96	1.23	13:1
MXG-10	QFP	2.91	7.84	1.63	1.37	5.7:1
MXG-11	QFP	2.90	7.13	1.39	0.93	7.7:1
MXG-12	QFP	2.87	18.13	4.57	3.75	4.8:1
MXG-13A	IF	4.10	21.26	0.072		295:1
MXG-13B		3.90	0.0021*	0.0003*	0.0004*	
MXG-14	LT	2.91	24.69	1.86		13:1
MXG-15	QFP	3.04	4.26	0.59		7:1
MXG-16	Sed.	2.94	0.037	0.012	0.32	26.6:1
MXG-17A	PRhy.	2.80	26.66			
MXG-17B		2.84	6.39	11.21		1.7:1
MXG-18	QFP	2.76	2.41			
MXG-19	QFP	2.75	6.24			
MXG-20	Sh.	2.98	1.65	0.046		35.8:1

ρ_r = Bulk electrical resistivity
δ_B = Bulk density (g/mL)
* = Possible reduction in measurement accuracy due to distortion of the complex resistivity plots (arcs); ρ_r is too high for an accurate measurement
FV, MV = Felsic volcanic, mafic volcanic
CA = Carbonaceous argillite
S = Sulphide stringer zone
Gab. = Gabbro
Bas. = Basaltic flow
Sed. = Sediment
QFP = Quartz-feldspar porphyry
IF = Iron-formation
LT = Lapilli tuff
PRhy. = Porphyritic rhyolite
Sh. = Shale/schist

shale/schist (MXG-20). The lower ρ_r values for these four samples (MXG-13A, MXG-3, MXG-16, MXG-20) can be considered to be within the detectable limits of the electromagnetic (EM) survey systems (Katsube et al., 1996a, Connell et al., 1998), and the higher ρ_r values above the detectable limits. There is another felsic volcanic sample (MXG-2) that also displays a λ value (λ=41:1) similar to the last three samples. However, the lower ρ_r value (1000 Ω·m) is above the detectable limit of EM survey systems.

Although, the basic complex resistivity pattern is the three-polarization model (3-PM) (Katsube, 1975, 1977; Katsube and Walsh, 1987) which displays three arcs, only one or two arcs are generally seen for this set of samples. Figure 3b (specimen MXG-13Aβ: iron-formation) is a representative case of the two-arc system for this set of samples. The left-most arc is due to the dielectric polarization effect of the rock and the right-most arc is due to the electrode polarization effect of the sample-holder electrodes or of the sulphide minerals in the sample, or both. This figure is for the ρ_r measurement made in the direction parallel to the bedding (β-direction). Figure 3a shows the disappearance of the right-most arc as the left-most arc becomes dominant with the increased ρ_r. This figure is for the ρ_r measurement made in the direction perpendicular to bedding (α-direction). This trend is in accordance with the electrical theory (Katsube, 1975, 1977; Katsube and Walsh, 1987). Figure 4 (specimen MXG-2) displays cases similar to Figure 3a, where the left-most arc is dominant due to the high ρ_r values.

Figure 5 (specimen MXG-7: basalt flow) displays a two-arc pattern. According to theory (Katsube, 1975, 1977; Katsube and Walsh, 1987), the right end of the right-hand-side arc should not be seen, as is the typical case seen in Figure 3b. The fact that it is seen suggests that this arc may be the middle arc of the three-polarization model, with the right-most arc pushed to the right, outside the range of this figure. That is, the effect of the middle arc is significant in this case. The question is why the effect of this middle arc, normally associated with pore-surface polarizations (Katsube, 1975, 1977), is significant. One explanation is the presence of

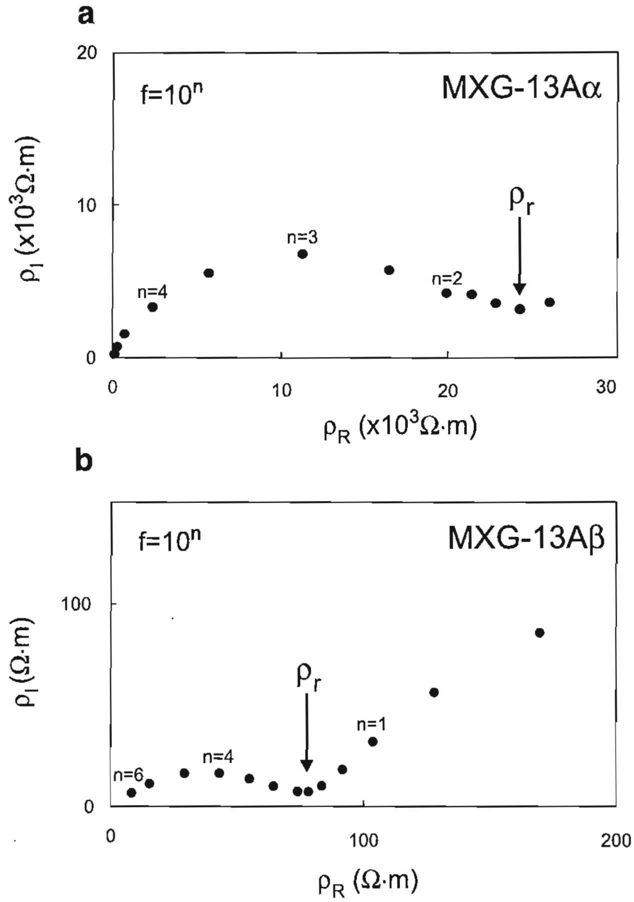

*Figure 3. Complex resistivity plots for an iron-formation (MXG-13A) measured in two different directions (α and β); **a)** ρ_I as a function of ρ_R measured perpendicular to bedding. **b)** ρ_I as a function of ρ_R measured parallel to bedding. f = Frequency.*

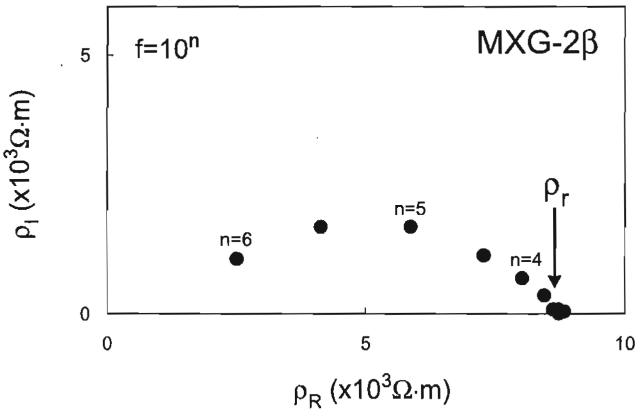

Figure 4. Typical example of complex resistivity (ρ) plot used to determine bulk electrical resistivity (ρ_r), for sample MXG-2, where ρ_R and ρ_I are the real and imaginary resistivities. No difficulty was encountered while determining ρ_r for this specimen. f = Frequency.*

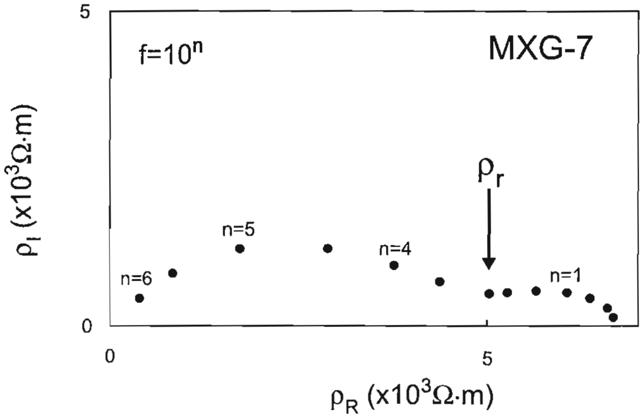

Figure 5. Complex resistivity plot of magnetic basaltic flow (MXG-7) which displays two arcs. The second arc likely resulted from polarization effects caused by the magnetite. f = Frequency.

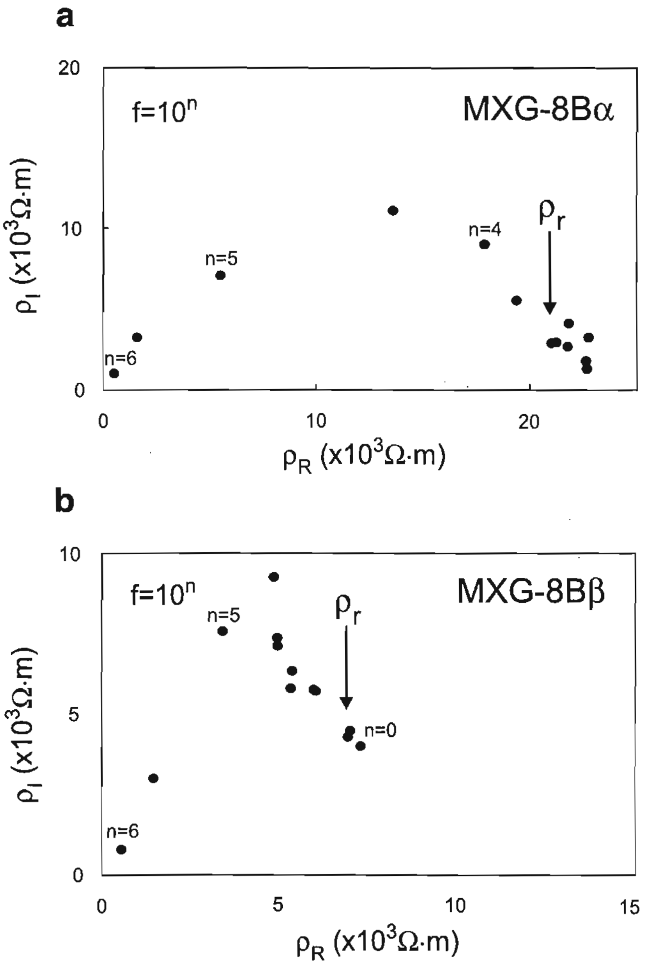

*Figure 6. Typical examples of complex resistivity plots of intermediate to high resistivity rocks. **a)** The maroon sediment (MXG-8B) displays a normal arc (slightly distorted) when measured parallel to a vein. **b)** A distorted arc results, when complex resistivity is measured perpendicular to the vein and parallel to bedding. The determination of ρ_r is difficult in cases such as this. f = Frequency.*

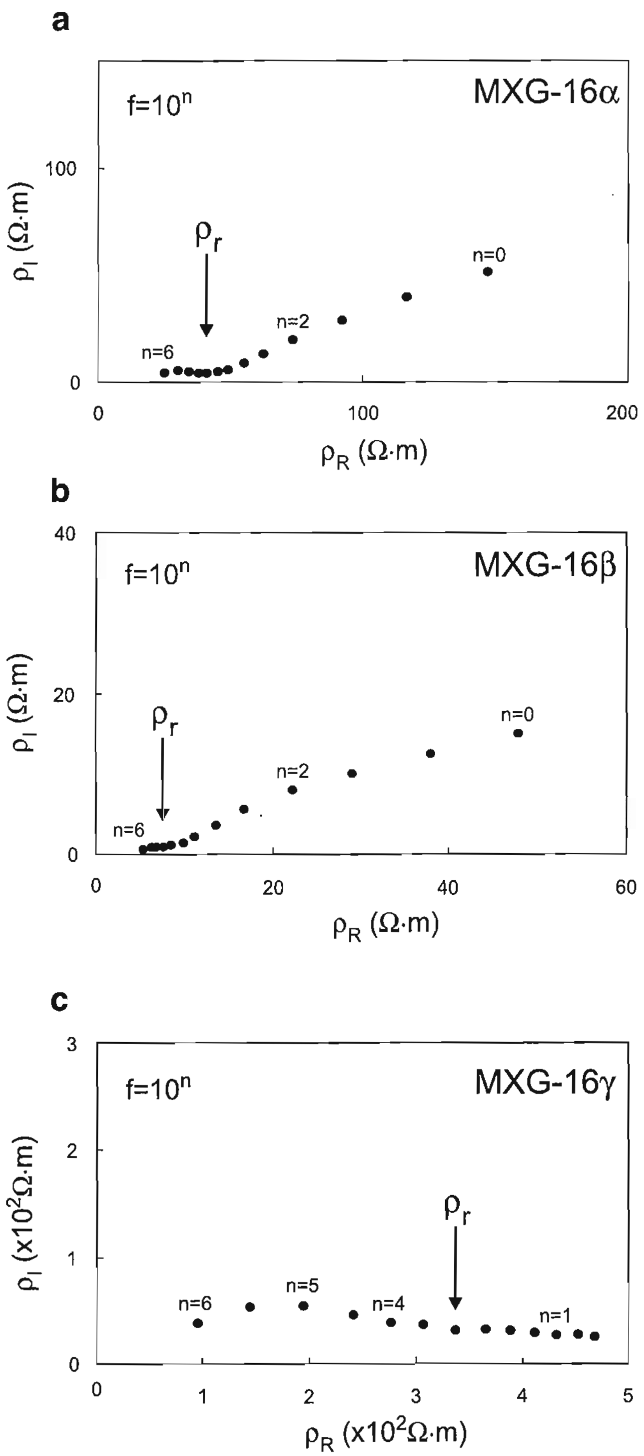

Figure 7. *Complex resistivity plots for a carbonaceous sediment (MXG-16) which was measured in three directions. Imaginary resistivity (ρ_I) as a function of real resistivity (ρ_R) when **a)** measured perpendicular to bedding and parallel to fractures, **b)** measured parallel to bedding and parallel to fractures, **c)** measured parallel to bedding and perpendicular to fractures. f = Frequency.*

magnetite. Although there is an apparent absence of sulphides in the specimen measured, the sample is moderately magnetic. It is possible that magnetite is lining part of the pore surfaces. Although this basaltic flow core/hand sample has fine sulphide stringers, none were visible in the specimen used for this measurement.

Figure 6a (specimen MXG-8: maroon sediment) displays a single and only slightly distorted arc, typical for specimens with rather high ρ_r values (Katsube et al., 1992). This figure is for the ρ_r (22 000 Ω·m) measurement made in the direction perpendicular to the bedding (α-direction) and parallel to a vein (Fig. 2b). However, it is interesting that, when measured in the direction parallel to the bedding (β-direction: Fig. 6b) and perpendicular to the vein (Fig. 2b) the arc becomes extremely distorted, regardless of the lower r_r value (7700 Ω·m). Although, considerable distortion of the arcs can be seen for extremely high ρ_r values (Katsube et al., 1992), the extent of this distortion is not common and requires further investigation. It should be noted that weak magnetism was detected in this sample.

Figure 7 (specimen MXG-16: carbonaceous sediment) shows typical examples of sample/specimens with very low r_r values (12–37 Ω·m, Fig. 7a, b), displaying a very small arc on the left-hand side and a larger one on the right-hand side. However, the right-hand arc is too small and suppressed to be due to the electrode polarization effect of the sample holder electrodes or of the sulphide minerals in the sample. It may be the middle arc of the three-polarization model due to conductive minerals lining the pores, similar to the case of Figure 5 (basalt flow). Figure 7c shows a larger arc on the left-hand side, due to a slightly higher ρ_r value (320 Ω·m). The very suppressed right-hand arc may also be the middle arc of the three-polarization model and due to conductive minerals lining the pores. Since this is a carbonaceous sediment sample, graphite or carbon mineral grains may be lining the pores, resulting in the enhanced middle arc. A pattern similar to that in Figure 7a is produced for a shale/schist sample (MXG-20) when measured in a direction parallel to bedding (β-direction). This sample is also likely to contain carbonaceous material.

Specimen MXG-16 is a darkish carbonaceous sediment with some fine elongated sulphide grains distributed along the bedding. There is a set of fractures, containing blackish material, cutting across the bedding (Fig. 2c). Since the ρ_r measurements in the two directions parallel to the fractures display similar patterns (Fig. 7a, b), these patterns and the low ρ_r values (12–37 Ω·m) are likely due to the fractures. The small left-most arc represents the low ρ_r value of the rock and the right-hand arc, which is probably the middle arc of the three-polarization model, is likely due to the polarization of conductive material lining the pores of the fractures. This conductive material may be graphite or carbon. The slightly higher ρ_r value (320 Ω·m) and larger left-most arc seen in the direction perpendicular to the fractures (Fig. 7c) are probably representing the true characteristic of the rock in the direction parallel to the bedding. The right-hand arc, which is probably the middle arc of the three-polarization model, is relatively smaller than the left-most arc but is actually similar in magnitude to those in Figure 7. The medium ρ_r values and existence of this enhanced middle arc suggests that the pores along the bedding may also have a carbonaceous lining. The sulphides along the bedding may also have some contribution to these patterns. Although a number of mineral distribution models have been offered to explain the complex resistivity patterns seen in these data, further investigation is required for confirmation.

ACKNOWLEDGMENTS

The authors are grateful for the critical review of this paper and for the very useful suggestions by C.J. Mwenifumbo (GSC). This work was supported by the EXTECH II (EXploration and TECHnology) Project which was initiated in 1994 in the Bathurst mining camp.

REFERENCES

American Petroleum Institute (API)
1960: Recommended practices for core-analysis procedure; API Recommended Practice 40 (RP 40) First Edition, American Petroleum Institute, Washington, D.C., p. 55.

Connell, S., Katsube, T.J., Best, M.E., Goodfellow, W.D., and Mwenifumbo, J.
1998: Electrical characteristics of mineralized and nonmineralized rocks at the Stratmat deposit, Bathurst mining camp, New Brunswick; *in* Current Research 1998-E; Geological Survey of Canada.

Davies, J.L. (comp.)
1977: Geological Map of Northern New Brunswick; New Brunswick Department of Natural Resources, Map NR-3, scale 1:250 000.

Jones, A.G., Katsube, T.J., and Ferguson, I.
1996: Paleoproterozoic tectonic processes revealed through electromagnetic studies of the North American Central Plains (NACP) conductivity anomaly; from continental to hand sample scale: in Society of Exploration Geophysicists Expanded Abstracts with Authors' Biographies, Technical Program, 66th Annual Meeting and International Exhibition (Denver, November 10-15, 1996), Volume I, p. 269-272.

Katsube, T.J.
1975: The electrical polarization mechanism model for moist rocks; *in* Report of Activities, Part C; Geological Survey of Canada, Paper 75-1C, p. 353-360.
1977: Electrical properties of rocks; *in* Induced Polarization for Exploration Geologists and Geophysicists, Short Course Presented by the University of Arizona, Tucson, March 14-16, p. 15-44.

Salisbury, M.
1991: Petrophysical characteristics of surface core samples from the Sudbury structure; *in* Current Research, Part E; Geological Survey of Canada, Paper 91-1E, p. 265-271.

Katsube, T.J. and Scromeda, N.
1994: Physical properties of Canadian kimberlites; Somerset Island, Northwest Territories and Saskatchewan; *in* Current Research 1994-B; Geological Survey of Canada, p. 35-42.

Katsube, T.J. and Scromeda, N. (cont.)
1995: Accuracy of Low Porosity Measurements in Granite; *in* Current Research 1995-C; Geological Survey of Canada, p. 265-270.

Katsube, T.J. and Walsh, J.B.
1987: Effective aperture for fluid flow in microcracks; International Journal of Rock Mechanics and Mining Sciences and Geomechanics Abstracts, v. 24, p. 175-183.

Katsube, T.J., Best, M., And Jones, A.G.
1996b: Electrical anisotropy of mineralized and non mineralized rocks; *in* Society of Exploration Geophysicists Expanded Abstracts with Authors; biographies, Technical Program, 66th Annual Meeting and International Exhibition, Denver, November 10-15, 1996, Volume II, p. 179-1281.

Katsube, T.J., Best, M.E., and Mudford, B.S.
1991: Petrophysical characteristics of shales from the Scotian shelf; Geophysics, v. 56, p. 1681-1689.

Katsube, T.J., Connell, S., Scromeda, N., Goodfellow, W.D., and Best, M.E.
1998a: Electrical characteristics of mineralized and nonmineralized rocks at the Caribou deposit, Bathurst mining camp, New Brunswick; *in* Current Research 1998-D, Geological Survey of Canada, p. 25-35.
1998b: Electrical characteristics of mineralized and nonmineralized rocks at the Restigouche deposit, Bathurst mining camp, New Brunswick; *in* Current Research 1998-E; Geological Survey of Canada.

Katsube, T.J., Palacky, G.J., Sangster, D.F., Galley, A.G., and Scromeda, N.
1996a: Electrical properties of disseminated sulphide ore samples from Snow Lake; *in* EXTECH I: A Multidisciplinary Approach to Massive Sulphide Research in Rusty Lake-Snow Lake Greenstone Belts, Manitoba, (ed.) G.F. Bonham-Carter, A.G. Galley, and G.E.M. Hall; Geological Survey of Canada, Bulletin 426, p. 319-329.

Katsube, T.J., Scromeda, N., Best, M.E., and Goodfellow, W.D.
1997: Electrical characteristics of mineralized and nonmineralized rocks at the Brunswick No. 12 deposit, Bathurst mining camp, New Brunswick; *in* Current Research 1997-E; Geological Survey of Canada, p. 97-107.

Katsube, T.J., Scromeda, N., Mareschal, M., and Bailey, R.C.
1992: Electrical resistivity and porosity of crystalline rock samples from the Kapuskasing Structural Zone, Ontario: *in* Current Research, Part E; Geological Survey of Canada, Paper 92-1E, p. 225-236.

Scromeda, N. and Katsube, T.J.
1994: Effect of temperature on drying procedures used in porosity measurements of tight rocks; *in* Current Research 1994-E; Geological Survey of Canada, p. 283-289.

van Staal, C.R. and Langton, J.P.
1990: Geology of Ordovician massive sulphide deposits and their host rocks in northern New Brunswick; *in* Field Guide to Massive Sulphide Deposits in Northern New Brunswick, (ed.) L.R. Fyffe; Fredericton, Minerals and Energy Division, Department of Natural Resource and Energy, New Brunswick, p. 15-41.

van Staal, C.R., Fyffe, L.R., Langton, J.P., and McCutcheon, S.R.
1992: The Ordovician Tetagouche Group, Bathurst camp, northern New Brunswick, Canada: history, tectonic setting, and distribution of massive-sulphide deposits; Exploration Mining Geology, v. 1, no. 2, p. 93-103.

Geological Survey of Canada Project 870057

APPENDIX

Geological descriptions

MXG-1: metamorphosed felsic volcanic
[I.D.: WDG-CAR97-PP-01]
Schistose, pale green with stretched quartz phenocrysts. Hardness approximately 2.

MXG-2: felsic volcanic
[I.D.: WDG-CAR97-PP-02]
Highly deformed, fine- to medium-grained, grey-green volcanic with K-feldspar phenocrysts. Hardness approximately 2.

MXG-3: carbonaceous argillite
[I.D. WDG-CAR97-PP-03]
Very fine-grained, delicately laminated, dark grey argillite containing later quartz veins. Hardness approximately 2.5.

MXG-4: sulphide stringer zone
[I.D.: WDG-CAR97-PP-04]
Pyrite veins transported into cleavage. Fine- to medium-grained disseminated sulphides (approximately 15–20%) predominantly concentrated in carbonaceous layers. Hardness approximately 2.

MXG-5: gabbro
[I.D.: WDG-CAR97-PP-05]
Medium- to course-grained, medium greenish-grey gabbro with fine-grained disseminated sulphides (<1%).

MXG-6: mafic volcanic flow
[I.D.: WDG-CAR97-PP-06]
Pale green, fine-grained mafic volcanic with disseminated sulphides (1–2%), faint foliation, and a thin carbonate vein. Hardness approximately 4.5-5. Weakly magnetic.

MXG-7: basaltic flow
[I.D.: WDG-CAR97-PP-07]
Porphyritic, medium-green, fine-grained basaltic flow with feldspar phenocrysts. Fine-grained disseminated sulphides in thin stringers and blebs (2–3%). Some alteration visible around larger blebs (possibly epidote). Euhedral to subhedral phenocrysts. Weak to moderately magnetic.

MXG-8: maroon sediment
[I.D.: WDG-CAR97-PP-08]
Delicately laminated maroon sediment interbedded with mafic basaltic flows. Weakly magnetic. Very fine vein crosscutting bedding.

MXG-9: footwall chloritic sediment
[I.D.: WDG-CAR97-PP-09]
Calcite infilling vugs in chloritic sediment with fine-grained disseminated sulphides (trace) and a moderate foliation. Hardness approximately 3–4.

MXG-10: quartz-feldspar porphyry
[I.D.: WDG-CAR97-PP-10]
Pale grey porphyry partly altered to chlorite with fine-grained disseminated sulphides (about 2%) and a moderate foliation. Overall hardness approximately 4–5.

MXG-11: quartz-feldspar porphyry
[I.D.: WDG-CAR97-PP-11]
Pale grey-green weakly altered quartz-feldspar porphyry. Overall hardness 4.5–5. Altered areas are yellowish.

MXG-12: quartz-feldspar porphyry
[I.D.: WDG-CAR97-PP-12]
Unaltered quartz-feldspar porphyry. Large, rounded porphyroblasts (up to 1 cm in length), in a softer, greenish groundmass. Hardness approximately 4.5.

MXG-13: bedded magnetite iron-formation
[I.D.: WDG-CAR97-PP-13]
Bedding crosscut by a sulphide vein with drusy textured black mineral. Very fine-grained with a few rounded granules (?). Moderate to strongly magnetic.

MXG-14: lapilli tuff
[I.D.: WDG-CAR97-PP-14]
Highly deformed, greenish grey, rhyolitic lapilli tuff. Fine-grained disseminated pyrite cubes (3%).

MXG-15: quartz-feldspar porphyry
[I.D.: WDG-CAR97-PP-15]
Quartz-feldspar porphyry cut by sulphide veins, highly altered to chlorite and sericite. Part of the sulphide feeder zone. Fine- to coarse-grained disseminated sulphides (10–20%). Greenish grey with a strong cleavage and overall hardness of 4.5–5.

MXG-16: carbonaceous sediment
[I.D.: WDG-CAR97-PP-16]
Black, well bedded, and deformed highly carbonaceous sediment. Disseminated and stringer sulphides (5%) predominantly concentrated along bedding planes. Hardness approximately 2.

MXG-17: porphyritic rhyolite
[I.D.: WDG-CAR97-PP-17]
Pale green moderately altered porphyritic rhyolite. Disseminated sulphides 1–2%, few chloritic patches. Overall hardness about 5.

MXG-18: quartz-feldspar porphyry
[I.D.: WDG-CAR97-PP-18]
Moderately altered quartz feldspar porphyry. Minor quartz veining. Hardness 4.5–5.

MXG-19: quartz-feldspar porphyry
[I.D.: WDG-CAR97-PP-19]
Unaltered quartz-feldspar porphyry. Euhedral potassium feldspar phenocrysts and quartz eyes. Overall hardness 4.5–5.

MXG-20: shale/schist
[I.D.: WDG-CAR97-PP-20]
Black laminated, carbonaceous shale/schist, highly deformed. Patchy disseminated sulphides (1-2%) concentrated along bedding planes. Secondary quartz/carbonate veining which crosscuts bedding. Hardness ranges from 2–4.5.

Electrical characteristics of mineralized and nonmineralized rocks at the Restigouche deposit, Bathurst mining camp, New Brunswick[1]

T.J. Katsube, S. Connell, N. Scromeda, W.D. Goodfellow, and M.E. Best[2]
Mineral Resources Division, Ottawa

Katsube, T.J., Connell, S., Scromeda, N., Goodfellow, W.D., and Best, M.E., 1988: Electrical characteristics of mineralized and nonmineralized rocks at the Restigouche deposit, Bathurst mining camp, New Brunswick; in *Current Research 1998-E; Geological Survey of Canada, p. 139–148.*

Abstract: Electrical properties of mineralized and nonmineralized rock samples from the Restigouche massive sulphide deposit (Bathurst mining camp, New Brunswick) have been measured to provide information for assisting the interpretation of airborne, ground, and borehole EM surveys.

Results show that the electrical resistivities (ρ_r) of massive sulphides and volcanic tuffs are 0.3–3.0 and 490–2300 Ω·m, respectively. The volcanic tuffs are weakly foliated resulting in insignificant electrical anisotropy values (λ<2:1). This is in contrast to previous studies, where values of λ>20:1 have been observed for these tuffs. Heterogeneities in the tuffs are a significant source of ρ_r variation (490–1600 Ω·m) related to the degree of silicification. Minor heterogeneities, such as thin quartz/carbonate veins, have little effect on either ρ_r or λ for massive sulphide samples. One massive sulphide sample, however, containing a chloritic vein displayed ρ_r values of 7.1 and 470 Ω·m in the directions parallel and perpendicular to the vein, resulting in a λ value of 66:1.

Résumé : Les propriétés électriques d'échantillons de roches minéralisées et non minéralisées provenant du gisement de sulfures massifs de Restigouche, dans le camp minier de Bathurst (Nouveau-Brunswick), ont été mesurées afin d'obtenir des données destinées à appuyer l'interprétation des levés électromagnétiques aériens, terrestres et en trous de sondage.

Les résultats montrent que la résistivité électrique (ρ_r) des sulfures massifs et des tufs volcaniques est respectivement de 0,3 à 3,0 et de 490 à 2 300 Ω·m. Les tufs volcaniques sont faiblement feuilletés et, de ce fait, les valeurs de l'anisotropie électrique sont négligeables (λ<2:1), contrairement à celles obtenues lors d'études antérieures menées également dans ces tufs, soit λ>20:1. L'hétérogénéité observée dans les tufs, liée au degré de silicification, est une source importante de variation de la résistivité électrique (490–1 600 Ω·m). Les hétérogénéités moins marquées, comme de minces filons de quartz/carbonates, influent très peu sur la résistivité électrique ou l'anisotropie électrique des échantillons de sulfures massifs. Toutefois, un de ces échantillons renferme un filon de chlorite qui montre des valeurs ρ_r de 7,1 et 470 Ω·m dans les directions parallèles et perpendiculaires au filon, d'où une valeur λ de 66:1.

---

[1] Contribution to the 1994-1999 Bathurst Mining Camp, Canada-New Brunswick Exploration Science and Technology (EXTECH II) Initative

[2] Bemex Consulting International, 5288 Cordova Bay Road, Victoria, British Columbia V8Y 2L4

INTRODUCTION

Electrical characteristics of mineralized and nonmineralized rock samples from the Restigouche massive sulphide deposit (Fig. 1) have been studied in order to determine the electrical connectivity of the sulphide mineralization and its relationship to sulphide facies and tectonic fabrics. The objective of this study is to provide information to assist in the interpretation of airborne, ground, and borehole EM surveys. Following the study on Brunswick No. 12 (Katsube et al., 1997) and Caribou (Katsube et al., 1998) massive sulphide deposits, the Restigouche deposit is the third of five chosen for this type of study in the Bathurst mining camp. These deposits were chosen because of variations in their electromagnetic (EM) responses, sulphide mineral grain sizes, and deformational features.

The EM responses from massive sulphide ore bodies in the Bathurst mining camp are quite variable. Factors such as textures, grain size (connectivity), mineralogy, fractures, and crosscutting veins all affect the EM response of massive sulphides. Previous work (Katsube et al., 1996a, b, 1997; T.J. Katsube, M.E. Best, and N. Scromeda, poster presentation at GSC Minerals Colloquium 1996, January 22-24, 1996, Ottawa, Ontario; Jones et al., 1996) suggests that electrical anisotropy may also affect the magnitude of the EM responses. This study includes laboratory electrical measurements made in three directions where possible. The purpose of this paper is to document the geological information on the samples, the research methodology, and to present the results obtained.

METHOD OF INVESTIGATION

Samples and sample preparation

Twelve core samples (sample numbers MXD-1 to MXD-12) were obtained from the Restigouche massive sulphide deposit in Bathurst, New Brunswick. Information on sample depth and lithology is listed in Table 1. Usually, more than one specimen was cut from each sample, at least one for determination of bulk density (δ_B) and electrical resistivity (ρ_r) and one for effective porosity (ϕ_E) determinations where possible. Several rectangular and/or disc-shaped specimens (e.g. a, b, c, and d) were cut from some samples, to be used for ρ_r measurements (Fig. 2a, b), so that different components of the heterogeneities and anisotropy could be characterized. Tuff specimens prepared for ϕ_E measurements were either

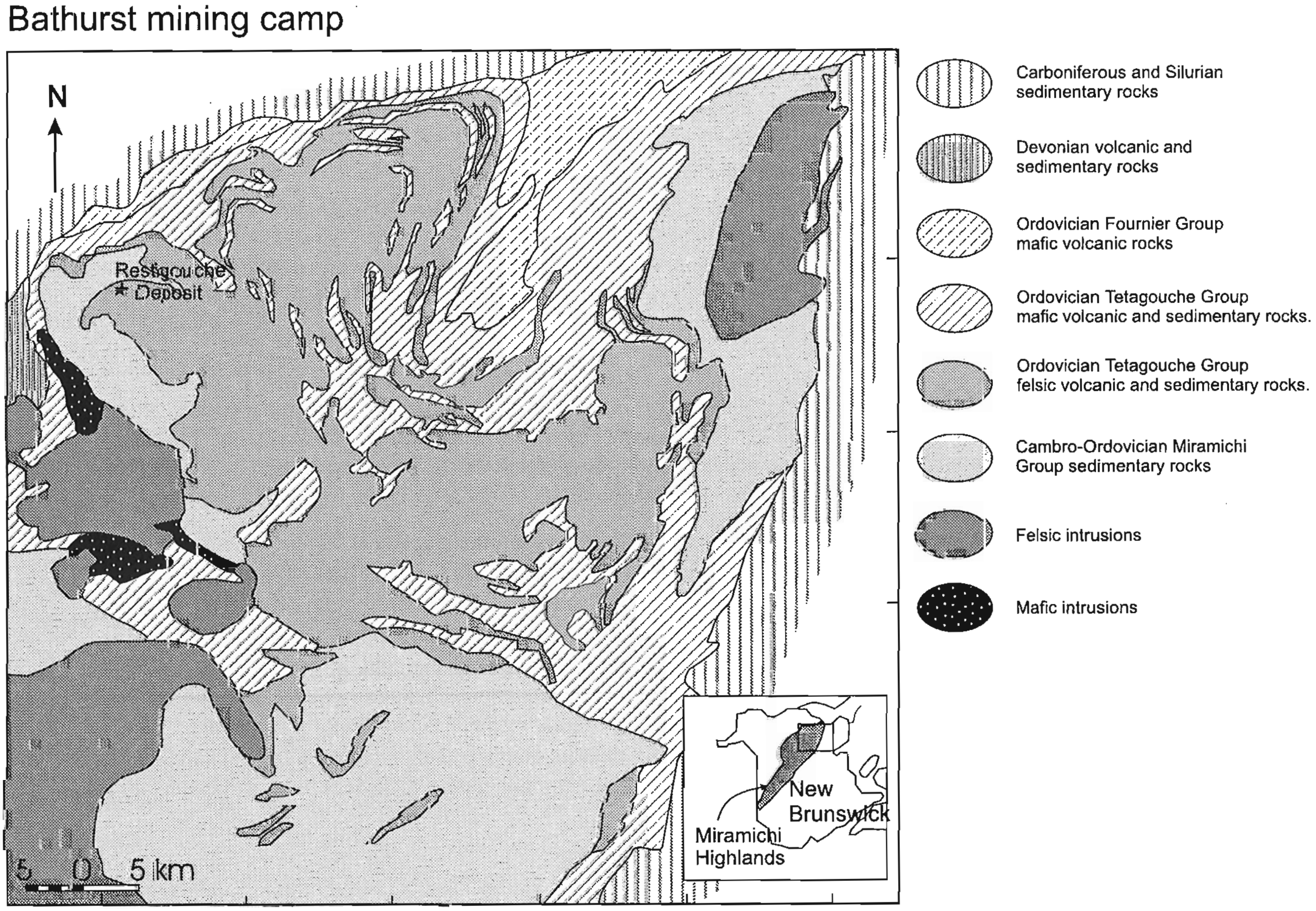

Figure 1. Location map of the Restigouche deposit located within the Bathurst mining camp, New Brunswick (modified from Davies, 1977).

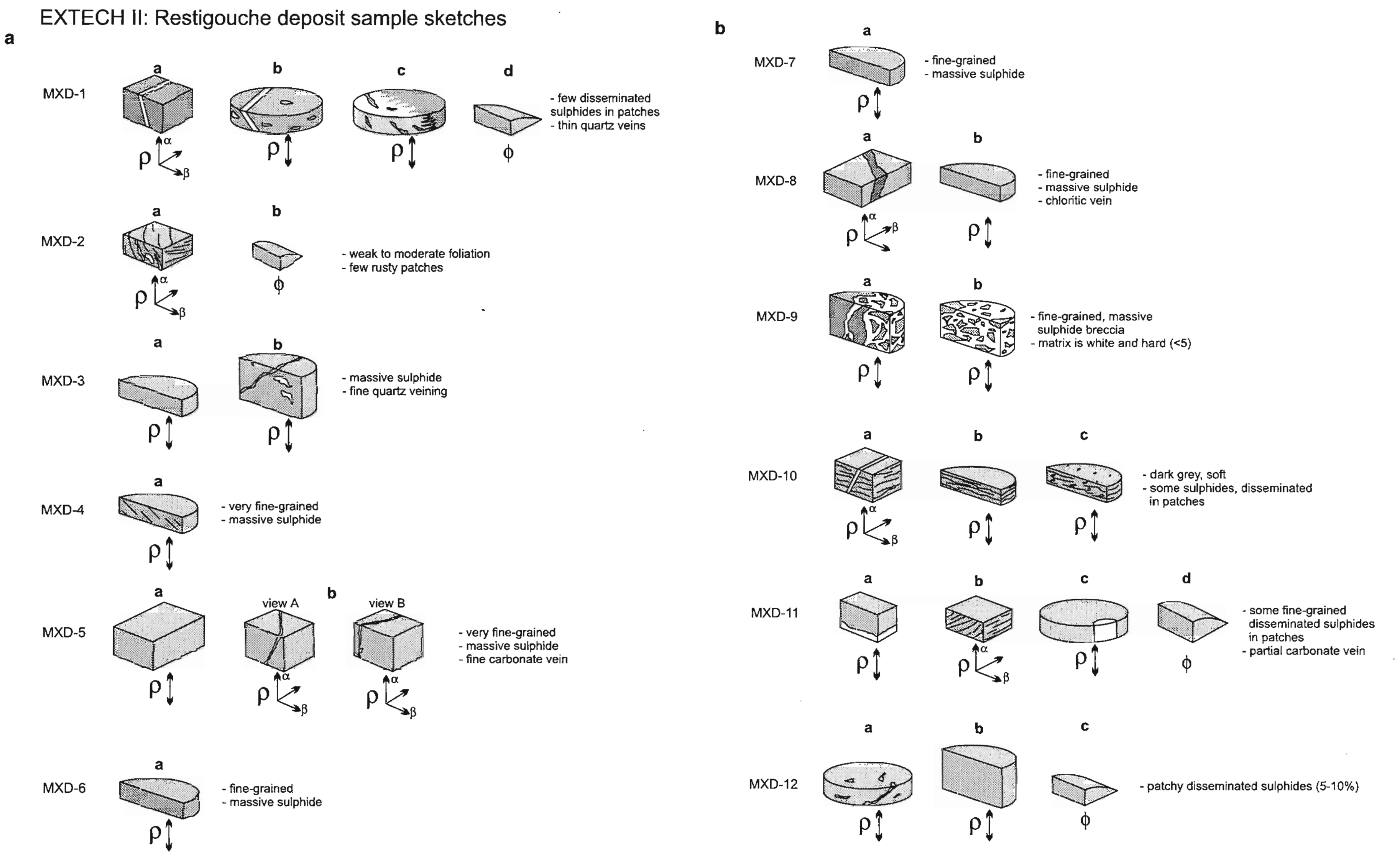

***Figure 2.** Block diagrams of specimens from the 12 samples used for electrical resistivity and porosity measurements in this study a) for samples MXD-1 to MXD-6, b) for samples MXD-7 to MXD-12.*

Table 1. Field descriptions and depths for samples collected from the Restigouche deposit, drillhole no. R-95-2.

Sample number	Depth (m)	Lithology	Directional features measured
MXD-1	23.9	Volcanic tuff	fine quartz veining
MXD-2	16.4	Volcanic tuff	foliation
MXD-3	39.45	Massive sulphide	fine quartz veining
MXD-4	46.7	Massive sulphide	foliation
MXD-5	54.4	Massive sulphide	fine carbonate vein
MXD-6	60.3	Massive sulphide	none
MXD-7	66.2	Massive sulphide	carbonate vein
MXD-8	73.1	Massive sulphide	chlorite vein
MXD-9	63.2	Breccia	none
MXD-10	79.6	Semimassive sulphide	foliation, fine vein
MXD-11	90.8	Volcanic tuff	weak foliation, vein
MXD-12	99.5	Volcanic tuff	none

partial-disc or irregular in shape, containing little or no visible sulphides. Samples with a high sulphide content were avoided due to concern over their oxidation at elevated temperatures (100°C) under moist conditions during the ϕ_E determination procedure. The geometric characteristics of the specimens used for ρ_r and δ_B measurements are listed in Table 2. Preparations are in progress for petrographic thin section and scanning electron microscope analyses of selected samples/specimens, to examine the sample texture and fabric, including the connectivity of the sulphide mineral grains.

Bulk density and effective porosity measurements

The caliper method (American Petroleum Institute, 1960) has been used to determine the bulk density (δ_B) of the samples, by measuring the dimensions and weight of the room dry

Table 2a. Dimensions of rectangular specimens cut from the core samples for electrical measurements, and the results of the bulk density (δ_E) determinations.

Sample	a_1 (cm)	a_2 (cm)	ℓ (cm)	W (g)	V (cm^3)	K_G (10^{-2}m)	δ_B (g/mL)
MXD-1a	2.274	2.523	2.090	34.1185	12.0	2.75	2.86
MXD-2a	1.255	1.348	0.719	3.5138	1.2	2.35	2.89
MXD-5a	1.298	1.676	1.158	11.8082	2.5	1.88	4.69
MXD-5b	1.068	1.665	0.944	7.8276	1.7	1.88	4.66
MXD-8a	0.944	2.425	0.696	6.1460	1.6	3.29	3.86
MXD-10a	1.120	1.130	0.638	3.3226	0.8	1.99	4.12
MXD-11a	0.532	1.531	0.893	2.2058	0.7	0.91	3.03
MXD-11b	1.511	1.766	0.548	4.1597	1.5	4.87	2.84

a_1, a_2 = Length of the two sides of the rectangular specimen
ℓ = Thickness of specimen
W = Weight of specimen under room dry conditions
K_G = Geometric factor
δ_B = Bulk density

Table 2b. Dimensions of disc-shaped specimens cut from the core samples for electrical measurements, and the results of the bulk density (δ_E) determinations.

Samples	r_D (cm)	ℓ (cm)	W (g)	V (cm^3)	K_G (m)	δ_B (g/cm^3)
MXD-1b	4.706	0.935	46.5931	16.3	18.6	2.86
MXD-1c	4.736	0.728	35.8634	12.8	24.2	2.80
MXD-3a	4.730	0.809	31.3200	6.6	10.0	4.77
MXD-3b	4.730	2.299	83.5386	18.2	3.44	4.60
MXD-4	4.730	0.882	31.4576	6.9	8.86	4.56
MXD-6	4.720	1.029	37.5750	8.0	7.56	4.70
MXD-7	4.700	0.947	37.7626	7.9	8.86	4.75
MXD-8b	4.690	0.937	36.1612	7.8	8.90	4.63
MXD-9a	4.710	1.486	47.4411	12.3	5.57	3.86
MXD-9b	4.690	1.223	26.4428	7.4	4.92	3.60
MXD-10b	4.720	1.357	38.7852	10.2	5.56	3.79
MXD-10c	4.700	1.042	33.2930	8.3	7.66	4.00
MXD-11c	4.710	0.678	33.5392	11.8	25.7	2.84
MXD-12a	4.733	1.104	56.1774	19.4	15.9	2.89
MXD-12b	4.710	1.484	25.4194	9.1	4.15	2.78

r_D = Diameter
ℓ = Thickness
W = Weight
K_G = Geometric factor
δ_B = Bulk density

rectangular specimens. These measurements are also used in the procedure to determine porosity. Effective porosity (ϕ_E), in principle, represents the pore volume of all interconnected pores. In this study, it is determined from the difference in weight between the oven-dried and water-saturated rock specimen. Another parameter derived on a routine basis is the irreducible water saturation, S_{ir}, which represents the pore space occupied by the water, bound or adsorbed on the pore surfaces. Measurements are taken at room temperature (23°C) and atmospheric pressure (Scromeda and Katsube, 1994; Katsube and Scromeda, 1995). The American Petroleum Institute *Recommended practices for core-analysis procedure* (American Petroleum Institute, 1960) has generally been followed in these measurements. Details of the standard procedures routinely used in our measurements are described in the literature (Katsube and Salisbury, 1991; Katsube et al., 1992; Scromeda and Katsube, 1994; Katsube and Scromeda, 1995).

Bulk electrical resistivity measurements

Bulk electrical resistivity (ρ_r) is determined from measurements of complex electrical resistivity, ρ^*, procedures for which are described in recent publications (e.g. Katsube et al., 1991, 1992, 1996a, b; Katsube and Salisbury, 1991; Katsube and Scromeda, 1994). Complex electrical resistivity (ρ^*) consists of two components: real resistivity (ρ_R) and imaginary resistivity (ρ_I) (e.g. Katsube, 1975; Katsube and Walsh, 1987; Katsube and Salisbury, 1991). These measurements were made on specimens saturated in distilled water for 24 to 48 h (Katsube and Salisbury, 1991). The parameters, ρ^*, ρ_R, and ρ_I are measured over a frequency range of $1–10^6$ Hz, and ρ_r usually represents a bulk electrical resistivity at about $10^2–10^3$ Hz. It (ρ_r) is a function of the pore structure and pore fluid resistivity, and is understood to exclude any other effects, such as pore surface dielectric and any other polarizations (Katsube, 1975; Katsube and Walsh, 1987). The geometric factor, K_G (with the units 10^{-2} m), required for derivation of ρ^* from the actual electrical measurements, is defined as

$$K_G = A/\ell,$$

where A (cm^2) is the cross-section area and ℓ (cm) is the thickness of the specimen. This parameter was determined for all specimens prior to the electrical measurements, using the specimen dimensional data in Table 2.

EXPERIMENTAL RESULTS

The results of the bulk density (δ_B) determinations are listed in Table 2. The δ_B values are in the range of 2.78 to 4.77 g/mL, a range similar to that of a previous study conducted on rock samples from the same mining camp (Katsube et al., 1997). The varying degree of mineralization in these samples is the most likely cause of this wide range of values. The results of the effective porosity (ϕ_E) determinations are listed in Table 3, for specimens with little or no visible sulphide mineralization, and display values in the range of 0.95–3.96%. The δ_B values used in the ϕ_E determination are those measured on the specimens prepared for resistivity measurements and, therefore, are not specific to those used for the ϕ_E, as previously indicated (Katsube et al., 1997). Since mineralization can vary between the two specimens, these δ_B values do not necessarily represent the true values that should be used in the ϕ_E determinations. Although considerable effort is made to obtain homogeneity between specimens (e.g. selecting specimens from adjacent areas), the ϕ_E values could contain some errors, for this reason.

Table 3. Results of the effective porosity (ϕ_E) measurements.

Sample	δ_B (g/mL)	W_W (g)	W_D (g)	S_{ir} (%)	ϕ_E (%)
MXD-1d	2.86	7.0401	6.9752	12.2	2.66
MXD-2b	2.89	8.9351	8.8142	19.5	3.96
MXD-11d	2.84	6.5282	6.5064	19.7	0.95
MXD-12c	2.78	7.4199	7.3647	12.7	2.08

W_w = Wet weight
W_D = Dry weight
S_{ir} = Irreducible water saturation
δ_B = Bulk density
ϕ_E = Effective porosity

Table 4. Results of electrical resistivity measurements.

Sample	ρ_r, (10^3 Ω·m) Meas. #1	Meas. #2	Mean**
MXD-1aα	0.486	0.504	0.49 ± 0.01
MXD-1aβ	0.791	0.800	0.80 ± 0.01
MXD-1b	0.72	0.75	0.74 ± 0.02
MXD-1c	1.47	1.67	1.57 ± 0.10
MXD-2aα	1.661	1.720	1.69 ± 0.03
MXD-2aβ	1.310	1.388	1.35 ± 0.04
MXD-3a	0.0039	0.0022	0.0031*
MXD-3b	0.0004	0.0004	0.0004*
MXD-4	0.0019	0.0025	0.0022*
MXD-5a	0.0004	0.0005	0.0005*
MXD-5bα	0.0005	0.0006	0.0006*
MXD-5bβ	0.0006	0.0004	0.0005*
MXD-6	0.0018	0.0015	0.0017*
MXD-7	0.0012	0.0022	0.0017*
MXD-8aα	0.0096	0.0046	0.0071*
MXD-8aβ	0.454	0.481	0.47 ± 0.02
MXD-8b	0.0018	0.0025	0.0022*
MXD-9a	0.0044	0.0042	0.0043*
MXD-9b	0.020	0.018	0.019*
MXD-10aα	0.0023	0.0045	0.0034*
MXD-10aβ	0.0018	0.0015	0.0017*
MXD-10b	0.0028	0.0028	0.0028*
MXD-10c	0.0042	0.0025	0.0034*
MXD-11a	1.695	1.395	1.55 ± 0.16
MXD-11bα	1.02	1.23	1.13 ± 0.11
MXD-11bβ	2.19	2.19	2.19 ± 0.00
MXD-11c	2.26	2.37	2.32 ± 0.06
MXD-12a	0.57	0.60	0.59 ± 0.02
MXD-12b	0.62	0.61	0.62 ± 0.01

ρ_r = Bulk electrical resistivity
Meas. (#1) = Measurement after 24 h of saturation
Meas. (#2) = Measurement after 48 h of saturation
* = Possible error ≥ ±100%
** = The value after the "±" is the maximum difference between the mean and the individually measured values

The results of the electrical resistivity (ρ_r) measurements are listed in Table 4. The ρ_r values are in the range of 0.4–2300 Ω·m, a range that falls within that of a previous study (Katsube et al., 1997) on samples from the same mining camp. These values are the result of measurements that have been made at 24 and 48 h after water saturation, in order to ensure the stability of the ρ_r values with time. Under these conditions, it is expected that the distilled water has chemically equilibrated with the rock and that the ρ_r values represent those of the in situ condition (Katsube et al., 1997). Normally, differences up to ±20% of the mean are considered to be within measurement error and represent stable conditions. Twenty-nine measurements (including 3-D measurements) were completed on 23 specimens representing 12 samples.

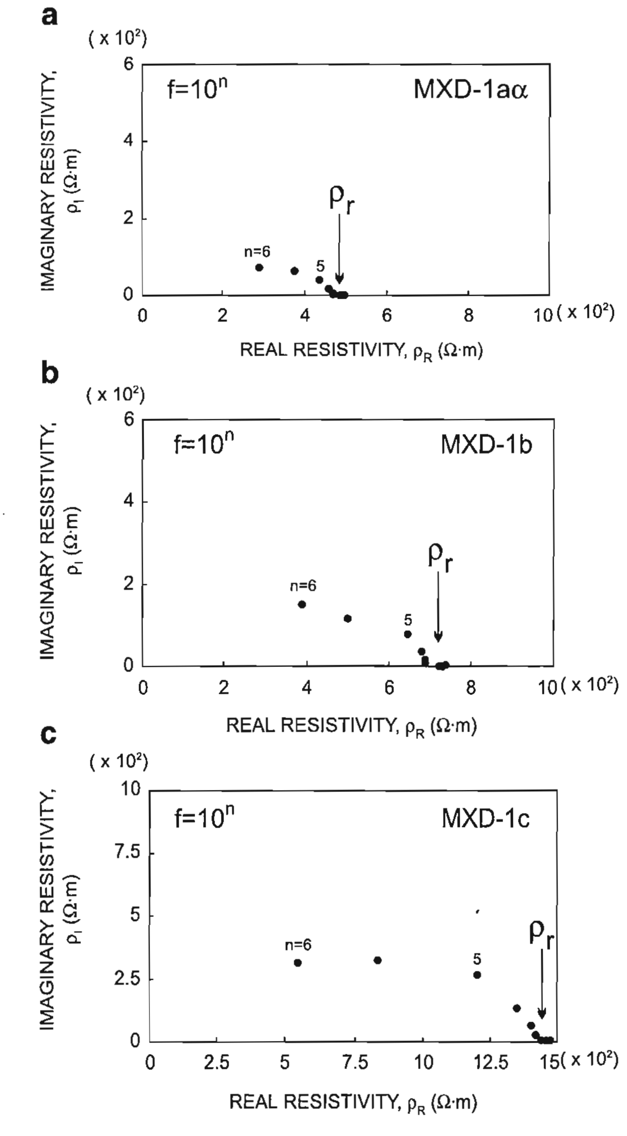

Figure 3. *R-95-2. Typical examples of complex resistivity (ρ^*) plots used to determine bulk electrical resistivity (ρ_R), where ρ_R and ρ_I are the real and imaginary resistivities (Katsube, 1975; Katsube and Walsh, 1987; Katsube and Salisbury, 1991). Imaginary resistivity (ρ_I) as a function of real resistivity (ρ_R),* ***a)*** *for sample/specimen MXD-1a (24 h saturation) displaying a normal arc representing the electrical characteristics of the rock sample, a pattern usually seen in rocks with intermediate resistivity;* ***b)*** *for sample/specimen MXD-1b (24 h saturation) displaying a slightly distorted arc;* ***c)*** *for sample/specimen MXD-1c (24 h saturation) displaying a slightly distorted arc and increased resistivity from an altered section of the sample. f = Frequency.*

Some examples of the complex resistivity plots used to determine the ρ_r values are shown in Figures 3 to 6. Details of the analytical procedure are described elsewhere (e.g. Katsube and Scromeda, 1994; Katsube et al., 1996b). Examples of the complex resistivity plots used to determine ρ_r values in the intermediate resistivity range are displayed in Figure 3, for samples\specimens MXD-1a, MXD-1b, and MXD-1c.

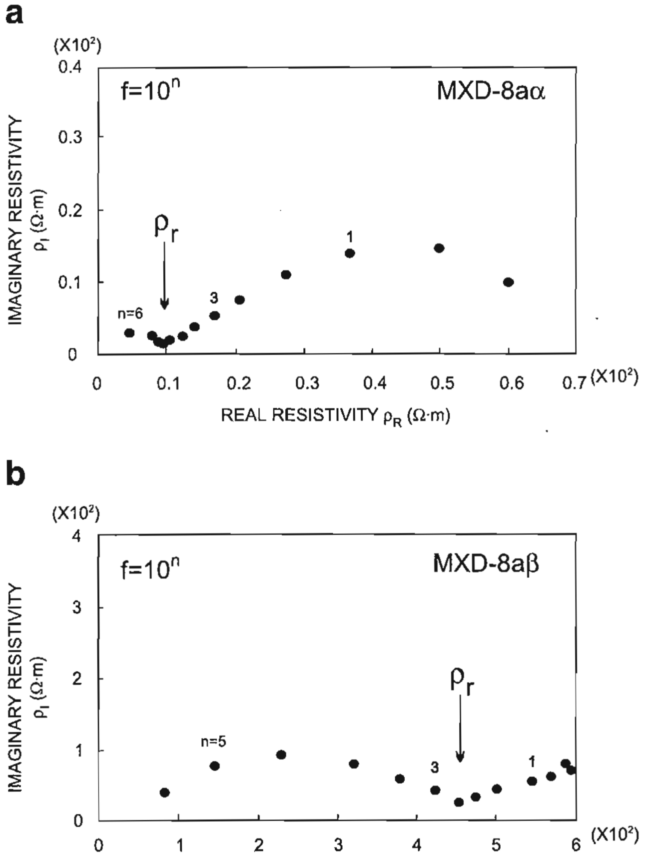

Figure 4. ***a)*** *Imaginary resistivity (ρ_I) as a function of real resistivity (ρ_R), for sample/specimen MXD-8aa (24 h saturation) displaying two arcs, commonly seen in low resistivity rocks with a high sulphide content. The left side represents the electrical characteristics of the rock sample, and the other (right side) represents electrode polarization. Electrode polarization likely resulted from the combined effect of the current electrode (of the measuring system) and the sulphide minerals. The chlorite vein likely had an effect on the results as well.* ***b)*** *Complex resistivity plot of the host rock from specimen MXD-8ab. f = Frequency.*

The ρ_r values clearly show an increase from, 490–800 Ω·m to 1600 Ω·m, as the degree of alteration increases. The measured specimens include one containing a single quartz vein (sample/specimen MXD-1a), one with a quartz vein and early stage of silicification (sample/specimen MXD-1b), to one with an advanced stage of silicification (sample/specimen MXD-1c). The shape of the complex resistivity arc remains relatively constant throughout these transitions. Examples of complex resistivity plots used to determine ρ_r for a sample/specimen (sample/specimen MXD-8aα and MXD-8aβ) that shows considerably different ρ_r values for the two directions α and β, is displayed in Figure 4. This sample/specimen is conductive (ρ_r=7.1 Ω·m) in the α-direction, but considerably more resistive (ρ_r=470 Ω·m) in the β-direction, a direction that is perpendicular to a chloritic vein (*see* Fig. 2b). A set of complex resistivity plots of normally shaped arcs, typical of intermediate to high ρ_r (980–2300 Ω·m) samples, is displayed in Figure 5 for sample/specimens MXD-11a, b, and c. The carbonate vein of MXD-11a appears to have little effect on the electrical characteristics of this sample. Figure 6 displays examples (sample/specimens MXD-10a, MXD-10b, and MXD-10c) of complex resistivity plots which caused considerable difficulty in the determination of the ρ_r values. While the arc for specimen MXD-10aβ was relatively normal, the other three measurements (MXD-10aα, b, and c) presented distorted arcs. These results caused difficulties in deciding whether the data represented one distorted arc or a combination of several arcs. Such cases were, however, treated as one distorted arc, and the ρ_r values determined as indicated in Figure 6.

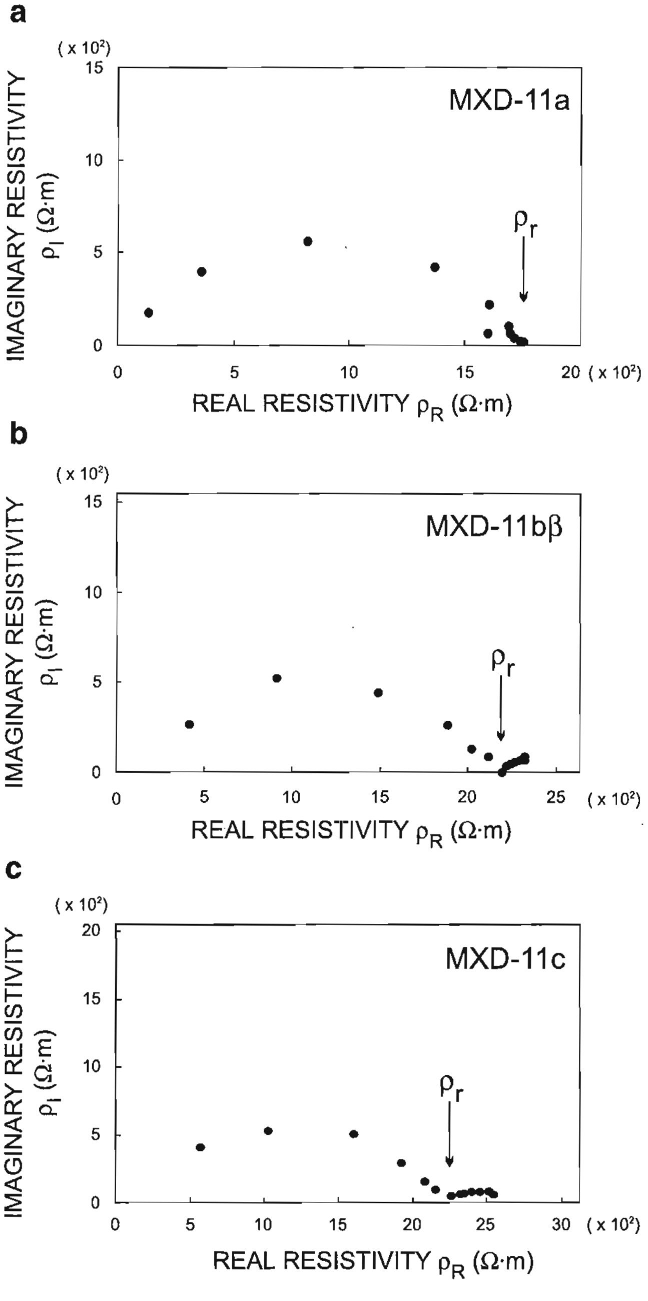

***Figure 5.** These normally-shaped arcs are typical of intermediate to high ρ_r samples. **a)** Imaginary resistivity (ρ_I) as a function of real resistivity (ρ_R), for sample/specimen MXD-11a (24 h saturation); **b)** for sample/specimen MXD-11b (24 h saturation) and **c)** for sample/specimen MXD-11c (24 h saturation).*

DISCUSSION

The suite of 12 samples used in this study consist of eight semimassive to massive sulphides and four volcanic tuff samples. The four tuff samples (MXD-1, MXD-2, MXD-11, MXD-12) display bulk densities (δ_B) in the range of 2.86 to 3.03 g/mL, and the eight semimassive/massive sulphide samples (MXD-3, MXD-4, MXD-5, MXD-6, MXD-7, MXD-8, MXD-9, and MXD-10) display δ_B values of 3.60 to 4.75 g/mL. Most of these 12 samples are heterogeneous, containing veins (quartz, carbonate, and chloride) and altered zones (e.g. silicification), which result in variable and anisotropic electrical resistivity (ρ_r). The four volcanic tuff samples have very minor patchy mineralization with ρ_r values in the range of 490–2320 Ω·m. The eight semimassive/massive sulphides display ρ_r values in the range of 0.3–20 Ω·m, with an exception of sample/specimen MXD-8a which has a ρ_r value of 470 Ω·m in a direction perpendicular to a chloritic vein.

These four volcanic tuff samples display weak foliation (if any), with relatively insignificant electrical anisotropy values of λ=1.3 to 2 (Table 5). Their ρ_r values (490 to 2320 Ω·m) are in the low to intermediate range for rocks. The heterogeneities appear to be a more significant factor in influencing the ρ_r values (490–2320 Ω·m), for these samples. For example, sample MXD-1 displays ρ_r values of 490 to 1600 Ω·m which are closely related to the degree of veining and alteration, which varies from a specimen with one thin quartz vein to a specimen with major silicification (Fig. 2a). The ρ_r values increase with increased degrees of silicification and veining. The electrical anisotropy resulting from the single thin vein is 1.6:1 (Table 5). Sample MXD-11, which is a weakly foliated volcanic tuff, displays ρ_r values of 1100 to 2300 Ω·m and an λ value of 2:1 (Table 5) which both parameters appear to be somewhat related to the foliation and a carbonate vein.

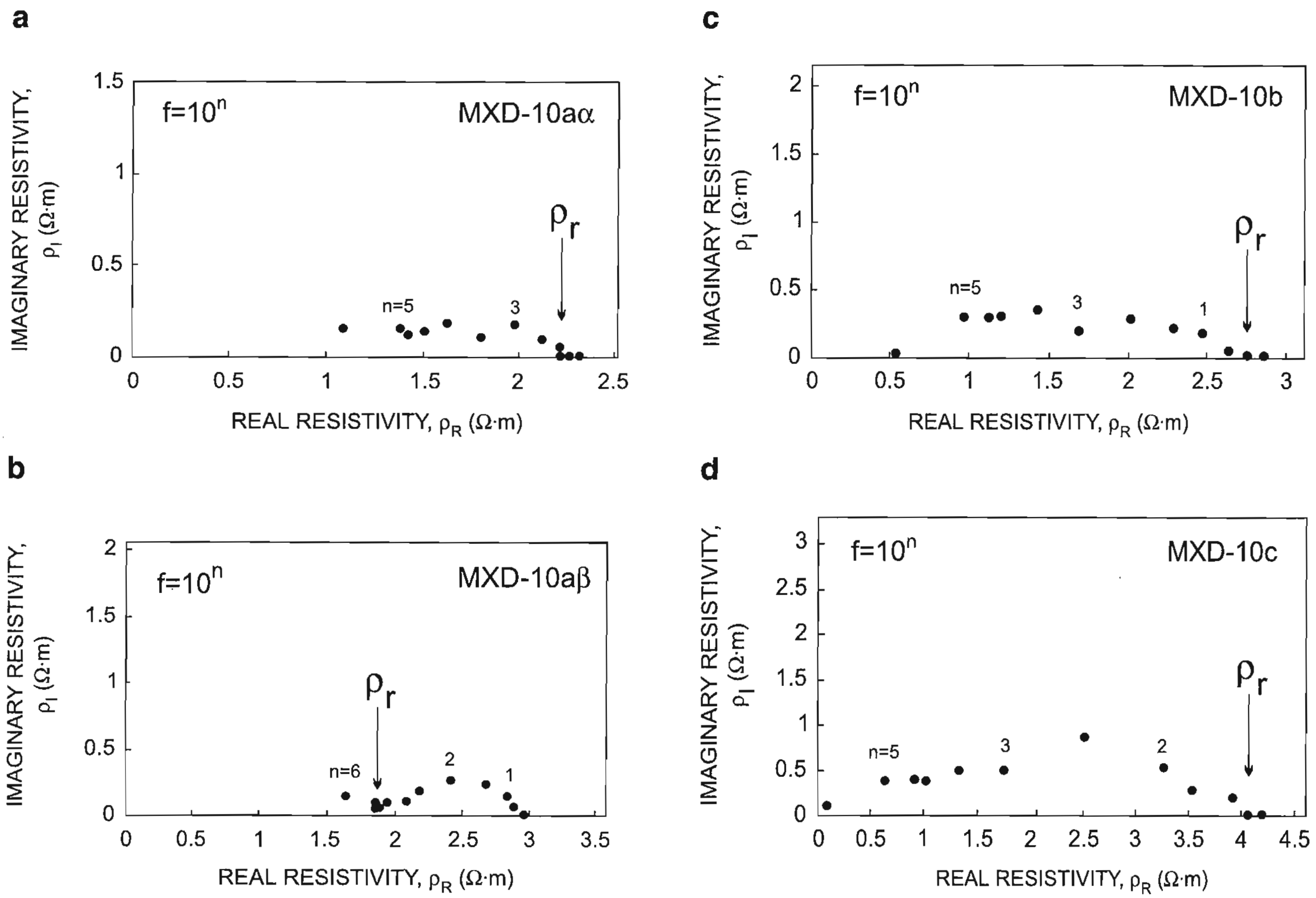

Figure 6. *These normally shaped arcs are typical of intermediate to high ρ_r samples. Imaginary resistivity (ρ_I) as a function of real resistivity (ρ_R);* ***a)*** *for sample/specimen MXD-10aa (24 h saturation);* ***b)*** *for sample/specimen MXD-10ab (24 h saturation);* ***c)*** *for sample/specimen MXD-10b (24 h saturation) and* ***d)*** *for sample/specimen MXD-10c (24 h saturation). f = Frequency.*

Six of the eight semimassive to massive sulphide samples (MXD-3, MXD-4, MXD-5, MXD-6, MXD-7, and MXD-10) display ρ_r values in the range of 0.3–3 Ω·m, which is a normal range of values for such a lithology. Although some of these samples (MXD-3, MXD-5, and MXD-10) contain fine quartz/carbonate veins, these veins appear to have little effect on either the ρ_r or λ values. The remaining two of the eight massive sulphide samples (MXD-8 and MXD-9), however, display ρ_r values in the range of 1-470 Ω·m, which are considerably larger. For example, sample/specimen MXD-8a is a massive sulphide containing a chloritic vein. The ρ_r values in the directions parallel and perpendicular to the vein are 7.1 and 470 Ω·m, respectively, resulting in a λ value of 66:1. Sample MXD-9 is a massive sulphide breccia which contains sections where massive sulphide clasts float in a matrix of white quartz/carbonate. Two sections of the sample, represented by specimens MXD-9a and MXD-9b, which are dominated by either massive sulphides or quartz/carbonates (Fig. 2b), display ρ_r values of 4.2 Ω·m or 19 Ω·m, respectively. That is, the matrix material displays ρ_r values four to five times larger than that of the massive sulphides.

Table 5. Electrical anisotropy (λ) characteristics of samples from the Restigouche deposit.

Sample No.	Specimen No.	ρ_{rH}(Ω·m) minimum	ρ_{rV}(Ω·m) maximum	λ
MXD-1	a	490	800	1.6:1
MXD-2	a	1350	1690	1.25:1
MXD-8	a	7.09	470	66:1
MXD-11	b	1.13	2.19	2:1

ρ_{rH} = Bulk electrical resistivity values taken in the direction parallel to the foliation or bedding
ρ_{rV} = Bulk electrical resistivity values taken perpendicular to the foliation or bedding
λ = Electrical resistivity anisotropy

CONCLUSIONS

The suite of 12 samples used in this study consist of eight semimassive to massive sulphides and four volcanic tuff samples. Most of these samples contain heterogeneities, such as veins (quartz, carbonate, and chloride) and altered zones (e.g. silicification), which cause variations and anisotropies in the electrical resistivity (ρ_r) values. The four volcanic tuff samples display ρ_r values in the range of 490–2300 Ω·m. They are characterized by a weak foliation, if present, resulting in insignificant electrical anisotropy values of $\lambda=1.3$ to 2. The heterogeneities have a more significant effect on the ρ_r values, for these samples. For example, one sample displays ρ_r values of 490–1600 Ω·m which are closely related to the degree of alteration (silicification). They vary from a specimen (490 Ω·m) with one thin quartz vein to a specimen (1600 Ω·m) with major silicification.

The ρ_r of the semimassive to massive sulphide samples is represented by a range of 0.3–3 Ω·m, which is a normal range of values for such rocks. The minor heterogeneities, such as fine quartz/carbonate veins contained in some of these samples have little effect on either the ρ_r or λ values. However, one massive sulphide sample containing a chloritic vein displays ρ_r values of 7.1 Ω·m and 470 Ω·m in the directions parallel and perpendicular to the vein, respectively, resulting in a λ value of 66:1. A massive sulphide breccia sample, containing sections where massive sulphide clasts float in a matrix of quartz/carbonate, displays ρ_r values of 4.3–19 Ω·m, for the massive sulphide and matrix dominated sections, respectively. The matrix material displays a ρ_r value four to five times larger than that of the massive sulphides.

ACKNOWLEDGMENTS

The authors are grateful for the critical review of this paper and for the very useful suggestions by K.A. Richardson (GSC). This work was supported by the EXTECH II (EXploration and TECHnology) Project which was initiated in 1994 in the Bathurst mining camp.

REFERENCES

American Petroleum Institute (API)

1960: Recommended practices for core-analysis procedure; API Recommended Practice 40 (RP 40) First Edition, American Petroleum Institute, Washington, D.C., p. 55.

Davies, J.L. (comp.)

1977: Geological Map of Northern New Brunswick; New Brunswick Department of Natural Resources, Map NR-3, scale 1:250 000.

Jones, A.G., Katsube, T.J., and Ferguson, I.

1996: Paleoproterozoic tectonic processes revealed through electromagnetic studies of the North American Central Plains (NACP) conductivity anomaly; from continental to hand sample scale: in Society of Exploration Geophysicists Expanded Abstracts with Authors' Biographies, Technical Program, 66th Annual Meeting and International Exhibition, Denver, November 10-15, 1996, Volume I, p. 269-272.

Katsube, T.J.

1975: The electrical polarization mechanism model for moist rocks; *in* Report of Activities, Part C: Geological Survey of Canada, Paper 75-1C, p. 353-360.

Katsube, T.J. and Salisbury, M.

1991: Petrophysical characteristics of surface core samples from the Sudbury structure; *in* Current Research, Part E; Geological Survey of Canada, Paper 91-1E, p. 265-271.

Katsube, T.J. and Scromeda, N.

1994: Physical properties of Canadian kimberlites, Somerset Island, Northwest Territories and Saskatchewan; *in* Current Research 1994-B; Geological Survey of Canada, p. 35-42.

1995: Accuracy of low porosity measurements in granite; *in* Current Research 1995-C; Geological Survey of Canada, p. 265-270.

Katsube, T.J. and Walsh, J.B.

1987: Effective aperture for fluid flow in microcracks; International Journal of Rock Mechanics and Mining Sciences and Geomechanics Abstracts, v. 24, p. 175-183.

Katsube, T.J., Best, M., and Jones, A.G.

1996a: Electrical anisotropy of mineralized and non mineralized rocks; *in* Society of Exploration Geophysicists Expanded Abstracts with Authors" Biographies, Technical Program, 66rd Annual Meeting and International Exhibition (Denver, November 10-15, 1996), Volume II, p. 1279-1281.

Katsube, T.J., Best, M.E., and Mudford, B.S.

1991: Petrophysical characteristics of shales from the Scotian shelf; Geophysics, v. 56, p. 1681-1689.

Katsube, T.J., Connell, S., Scromeda, N., Goodfellow, W.D., and Best, M.E.

1998: Electrical characteristics of mineralized and nonmineralized rocks at the Caribou deposit, Bathurst mining camp, New Brunswick; *in* Current Research 1998-D; Geological Survey of Canada, p. 25-35.

Katsube, T.J., Palacky, G.J., Sangster, D.F., Galley, A.G., and Scromeda, N.

1996b: Electrical properties of disseminated sulphide ore samples from Snow Lake; *in* EXTECH I: A Multidisciplinary Approach to Massive Sulphide Research in the Rusty Lake-Snow Lake Greenstone Belts, Manitoba, (ed.) G.F. Bonham-Carter, A.G. Galley, and G.E.M. Hall; Geological Survey of Canada, Bulletin 426, p. 319-329.

Katsube, T.J., Scromeda, N., Best, M.E., and Goodfellow, W.D.

1997: Electrical characteristics of mineralized and nonmineralized rocks at the Brunswick No. 12 deposit, Bathurst mining camp, New Brunswick; *in* Current Research 1997-E; Geological Survey of Canada, p. 97-107.

Katsube, T.J., Scromeda, N., Mareschal, M., and Bailey, R.C.

1992: Electrical resistivity and porosity of crystalline rock samples from the Kapuskasing Structural Zone, Ontario; *in* Current Research, Part E; Geological Survey of Canada, Paper 92-1E, p. 225-236.

Scromeda, N. and Katsube, T.J.

1994: Effect of temperature on drying procedures used in porosity measurements of tight rocks; *in* Current Research 1994-E; Geological Survey of Canada, p. 283-289.

Geological Survey of Canada Project 870057

APPENDIX

Geological descriptions

MXD-1: Volcanic tuff which is very soft, grey, porphyritic (quartz eyes), and contains a thin vein. The base of the core appears to be slightly silicified with some disseminated sulphides/rusty vugs.

MXD-2: Volcanic tuff which is very soft and crumbly, and characterized by rusty spots and foliation.

MXD-3: Dark coloured, massive sulphide which is foliated, and contains a thin quartz vein.

MXD-4: Very fine grained, dark grey massive sulphide. Moderately foliated with some quartz-rich sections (partial vein) seen at the base of the core.

MXD-5: Very fine-grained, dark grey massive sulphide, with some small fractures infilled with soft carbonate material.

MXD-6: Fine-grained, dark coloured massive sulphide.

MXD-7: Fine-grained massive sulphide containing part of a carbonate vein.

MXD-8: Fine-grained, dark coloured massive sulphide containing a chloritic vein.

MXD-9: Breccia with dark coloured fine-grained clasts (centimetre scale) of massive sulphides suspended in a matrix of fine-grained quartz/carbonate.

MXD-10: Dark grey, mafic (soft), foliated volcanic tuff with some soft, white veins. Sulphides are primarily concentrated at the base of the sample.

MXD-11: Moderately foliated volcanic tuff with a minor content of sulphides, containing a partial carbonate vein.

MXD-12: Mafic volcanic tuff containing patchy, disseminated sulphides. A dominant cleavage is present.

Electrical characteristics of mineralized and nonmineralized rocks at the Stratmat deposit, Bathurst mining camp, New Brunswick[1]

S. Connell, T.J. Katsube, M.E. Best[2], W.D. Goodfellow,
and J. Mwenifumbo
Mineral Resources Division, Ottawa

Connell, S., Katsube, T.J., Best, M.E., Goodfellow, W.D., and Mwenifumbo, J., 1988: Electrical characteristics of mineralized and nonmineralized rocks at the Stratmat deposit, Bathurst mining camp, New Brunswick; in *Current Research 1998-E; Geological Survey of Canada, p. 149–162.*

Abstract: Laboratory measurements have been carried out on 27 mineralized and nonmineralized rock samples from the Stratmat massive sulphide deposit, in order to determine the electrical characteristics of the sulphides and their host rocks. The purpose is to provide information to assist in the interpretation of airborne, ground, and borehole electromagnetic surveys in the Bathurst mining camp.

Results indicate that the bulk electrical resistivity (ρ_r) values are in the range of <1.0 to 3.5×10^4 Ω·m. Electrical resistivity anisotropies (λ) observed are relatively small, with the maximum λ value being 10:1 for a moderately foliated massive sulphide sample. This is in contrast with previous findings (e.g. λ>1000:1). The host rock samples (e.g. tuff, argillite) displayed λ values of 2:1 to 10:1. One such sample (λ=8:1) contained some fine-grained disseminated sulphides concentrated along the foliation and yielded ρ_r values of 1.72×10^3 and 14.60×10^3 Ω·m in the directions parallel and perpendicular to the foliation, respectively.

Résumé : Des mesures ont été faites en laboratoire sur 27 échantillons de roches minéralisées et non minéralisées prélevés dans le gisement de sulfures massifs de Stratmat afin de déterminer les caractéristiques électriques des sulfures et de leurs roches encaissantes. Le but de cette détermination est de fournir des données destinées à appuyer l'interprétation des levés électromagnétiques aériens, terrestres et en trous de sondage dans le camp minier de Bathurst.

Les résultats indiquent que les valeurs de la résistivité électrique (ρ_r) apparente s'échelonnent de moins de 1,0 à 3,5 x 10^4 Ω·m. Les anisotropies de résistivité électrique (λ) observées sont relativement faibles, la valeur maximale λ étant de 10:1 dans un échantillon de sulfures massifs modérément feuilletés. Ces résultats ne confirment pas ceux obtenus antérieurement, soit λ>1 000:1. Les échantillons de roche encaissante (p. ex. tufs et argilites) affichent des valeurs λ de 2:1 à 10:1. Un de ces échantillons (λ=8:1) contient des sulfures disséminés à grain fin concentrés parallèlement à la foliation. Il montre des valeurs ρ_r de 1,72 x 10^3 et de 14,60 x 10^3 Ω·m dans des directions respectivement parallèles et perpendiculaires à la foliation.

---

[1] Contribution to the 1994-1999 Bathurst Mining Camp, Canada-New Brunswick Exploration Science and Technology (EXTECH II) Initative

[2] Bemex Consulting International, 5288 Cordova Bay Road, Victoria, British Columbia V8Y 2L4

INTRODUCTION

Laboratory electrical measurements have been carried out on 27 mineralized and nonmineralized rock samples from the Stratmat massive sulphide deposit (Fig. 1), in order to determine the electrical characteristics of the sulphide mineralization and its host rocks. The objective of this study is to provide information to assist in the interpretation of airborne, ground, and borehole electromagnetic (EM) surveys in the Bathurst mining camp. Following the studies on Brunswick No. 12 (Katsube et al., 1997), Caribou (Katsube et al., 1998a), and Restigouche (Katsube et al., 1998b) massive sulphide deposits, the Stratmat deposit is the fourth chosen for this type of study in this area. Previous work (Katsube et al., 1996a, b; T.J. Katsube, M. Best, and N. Scromeda, poster presentation, GSC Minerals Colloquium 1996, January 22-24, 1996, Ottawa, Ontario; Jones et al., 1996) has demonstrated the existence of significant electrical anisotropy in rocks, and has suggested that it may affect the magnitude of the EM responses. This study includes laboratory electrical measurements made in three directions where possible, to determine the electrical anisotropy characteristics.

Recent work on deposits in this camp has also revealed the existence of significant electrical anisotropies. For example, electrical anisotropies (λ) as high as 1000:1 for chloritized iron-formation (Katsube et al., 1997) and 70:1 for volcanic tuff units (Katsube et al., 1998a) have been reported. Electrical anisotropies due to different types of mineralogical and microstructural interferences in massive sulphides, such as quartz veins (Katsube et al., 1997), calcitic veins (λ=6:1 to 390:1, Katsube et al., 1998b), and chloritic veins (λ=66:1, Katsube et al., 1998b) have also been reported. Variation in electrical resistivity (ρ_r, 490 to 1600 $\Omega \cdot m$) due to varied degrees of silicification in different samples, have also been reported (Katsube et al., 1998b). The purposes of this paper are to document information on the electrical characteristics of the rocks in the area of the Stratmat deposit, and to enhance the database for electrical properties of rocks, which will benefit the interpretation of EM surveys in the Bathurst mining camp.

Knowledge of the electrical characteristics of mineralized and nonmineralized rocks within a mining camp can improve the design of EM surveys and provide important information for interpreting EM data. In this report, this utility is illustrated with two examples. Electrical anisotropy associated

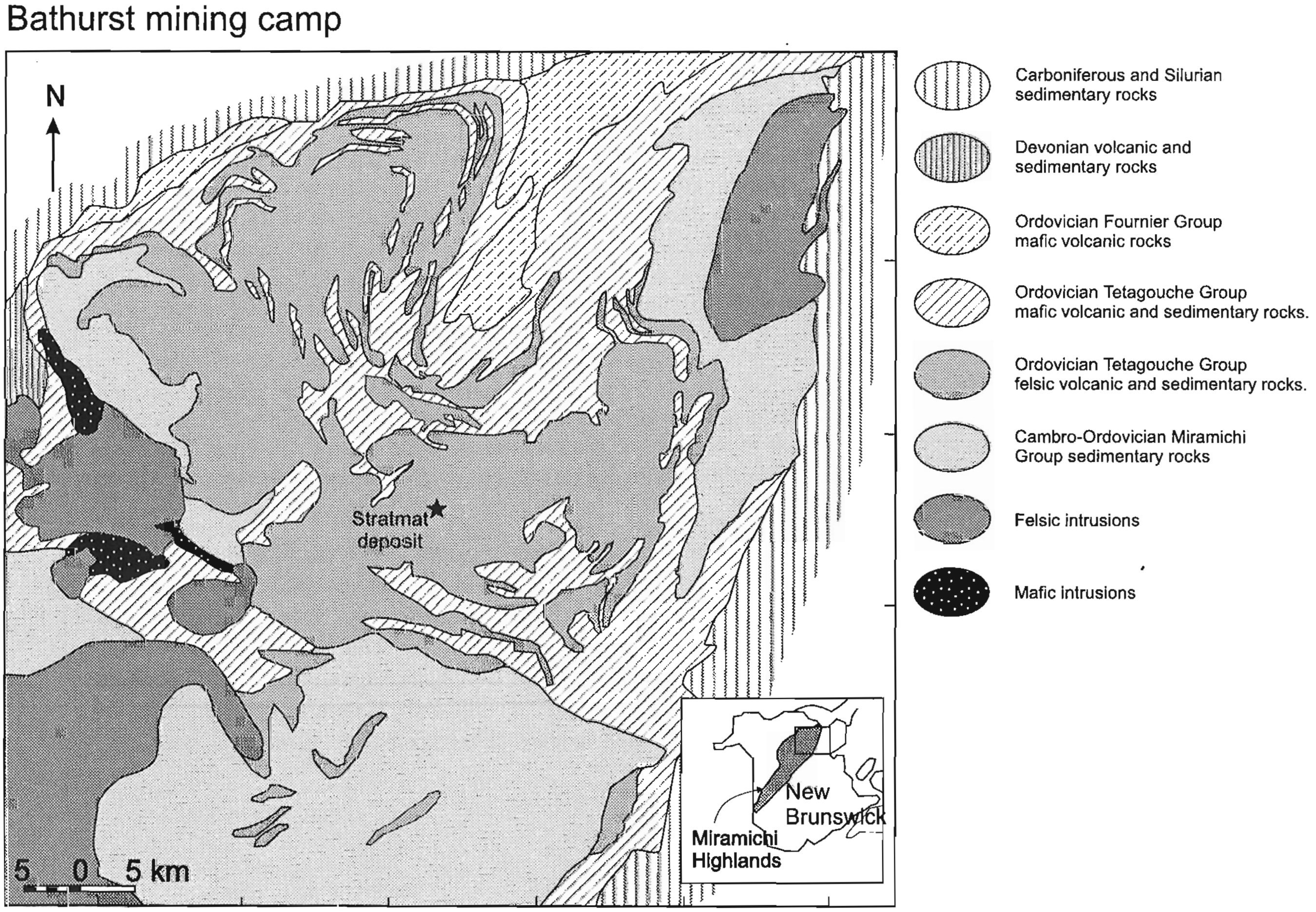

***Figure 1.** Location map for the Stramat Main Zone deposit situated within the Bathurst mining camp, New Brunswick (modified from J.L. Davies, 1977).*

with geological bodies can have a significant effect on their electromagnetic responses. For example, orientation of the transmitter and receiver coils relative to the axes of anisotropy determines the amount of coupling between a geological body and an EM system. Survey orientation should be chosen to maximize the coupling which, depending on the axes of anisotropy, may or may not be perpendicular to geological strike. Poor electrical connectivity within a mineralized body produces a weak conductor. Such conductors generate small EM responses at low frequencies. If the possibility of poor connectivity can be established prior to an EM survey (by appropriate laboratory measurements) then higher operating frequencies, or shorter measurement times for time-domain EM systems, can be used to obtain a measurable EM response. The higher frequencies also provide more detailed depth and scale information to better interpret the conductive nature of the body.

METHOD OF INVESTIGATION

Samples and sample preparation

Twenty-seven core samples (sample numbers MXF-1 to MXF-27) were obtained from the Stratmat Main Zone deposit (Fig. 1). Information on drillhole identification (I.D.), core sample depth, and geological units are presented in Table 1 and shown in Figure 2. Detailed geological descriptions of the samples are listed in the Appendix.

Table 1. Identification of samples from Stratmat drillholes ST218, ST219, ST220, and ST221.

Sample no.	Depth (m)	Geological unit
ST 218		
MXF-1	37.8	Lapilli tuff
MXF-2	97.6	Crystal tuff
MXF-3	110.5	Sulphide
MXF-4	117	Sulphide
MXF-5	123.5	Sulphide
MXF-6	129	Argillite
MXF-7	143.5	Crystal tuff
MXF-8	150.4	Felsic tuff
ST 219		
MXF-9	72.3	Crystal tuff
MXF-10	113.8	Gabbro
MXF-11	117.8	Argillite
MXF-12	130.7	Crystal tuff
ST 220		
MXF-13	76	Crystal tuff
MXF-14	90.2	Argillite
MXF-15	100.3	Sulphide
MXF-16	102	Sulphide
MXF-17	105	Sulphide
MXF-18	110.6	Argillite
MXF-19	113.3	Crystal tuff
MXF-20	120	Felsic tuff
ST 221		
MXF-21	86.5	Crystal tuff
MXF-22	107	Sulphide
MXF-23	116	Sulphide
MXF-24	126.1	Argillite
MXF-25	127.5	Greywacke
MXF-26	142.3	Diabase dyke
MXF-27	172.2	Lapilli tuff

At least two specimens were cut from each sample, one being used to determine bulk density, δ_B, and electrical resistivity, ρ_r, and one for the determination of effective porosity, ϕ_E. Some samples were cut into several rectangular specimens (e.g. specimen numbers: a, b, c, and d) so that different components of the heterogeneities and anisotropy of the sample could be characterized by the ρ_r measurements, as illustrated in Figure 3. Specimens prepared for anisotropic studies were of rectangular shape (Tables 2a, b, c) to allow three directional electrical resistivity measurements. The three directions are identified by α, β, and γ. Those prepared for ϕ_E measurements were either partial discs or irregular in shape. The δ_B and ρ_r measurements were performed on 33 specimens prepared from the 27 samples. The measurement of ϕ_E was made on specimens representing 19 of these samples which contained little or no visible sulphides. The geometric characteristics of the specimens used for ρ_r and δ_B measurements

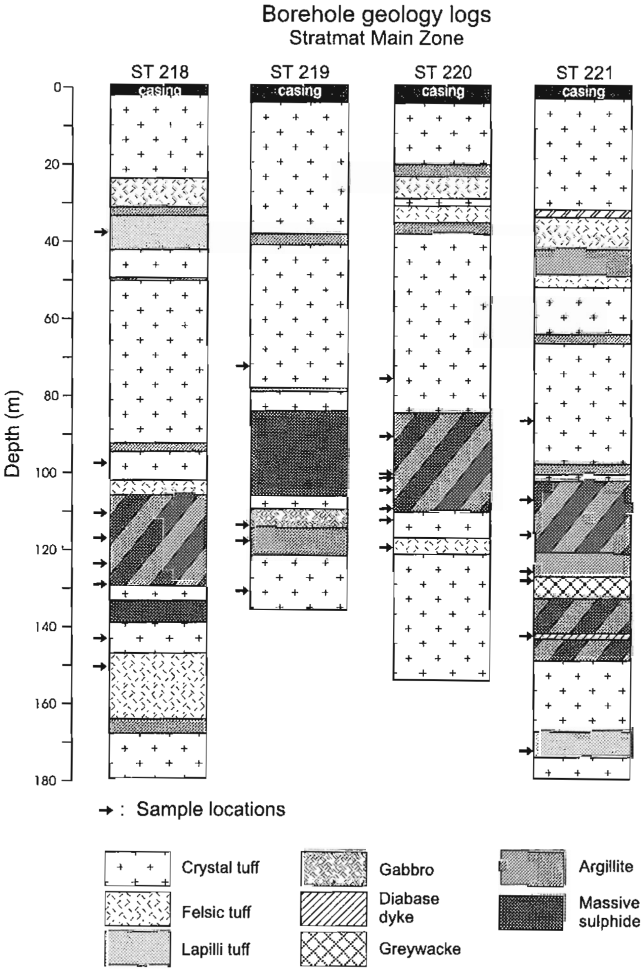

Figure 2. Geological logs of Stratmat Main Zone drill cores (Noranda Mining and Exploration Inc., Bathurst) ST218, ST219, ST220, and ST221. The arrows in the figure indicate the positions of the samples that were used in this study.

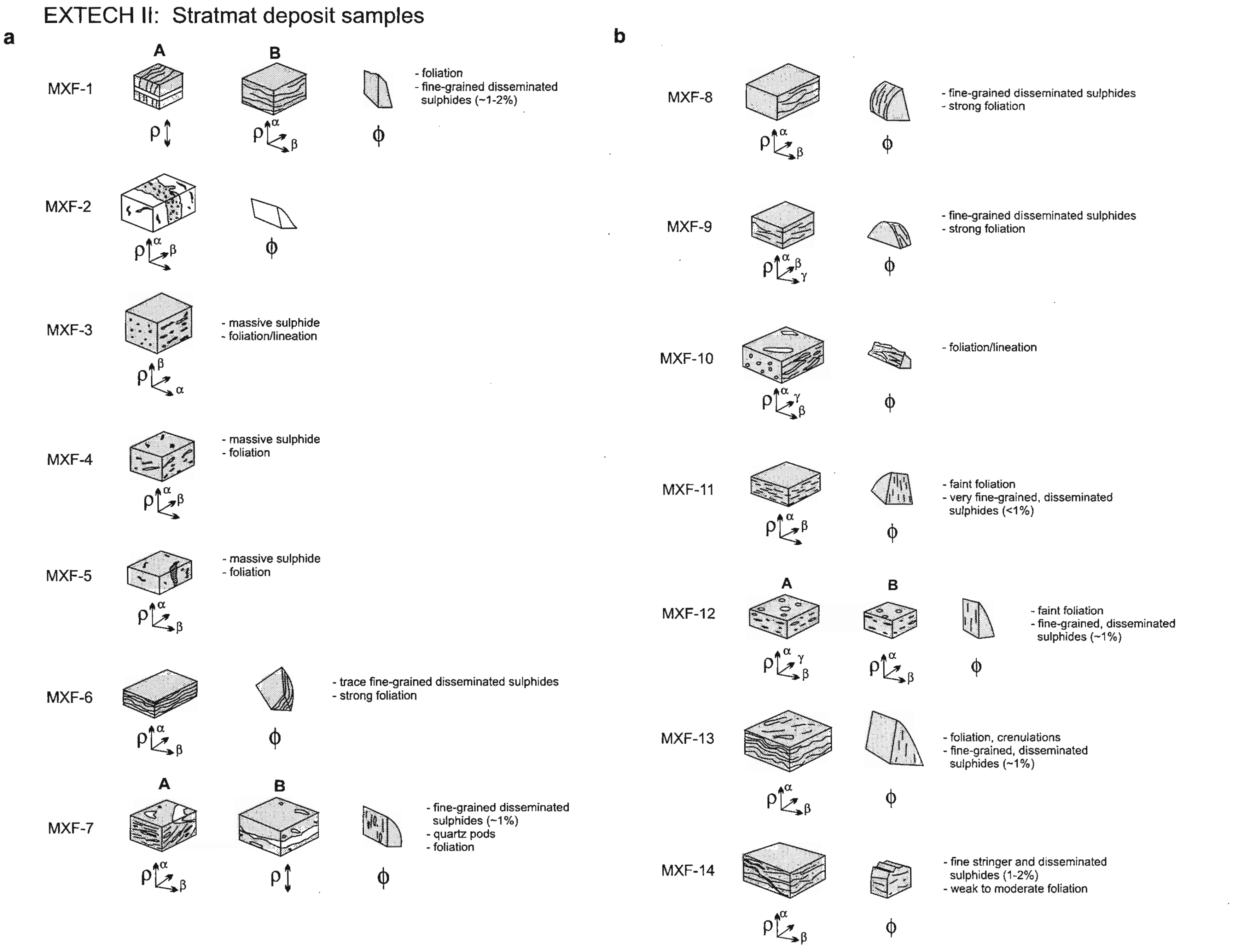
a
EXTECH II: Stratmat deposit samples
A
B
MXF-1
ρ
α
β
ϕ
- foliation
- fine-grained disseminated sulphides (~1-2%)
MXF-2
ρ α β
ϕ
MXF-3
ρ β α
- massive sulphide
- foliation/lineation
MXF-4
ρ α β
- massive sulphide
- foliation
MXF-5
ρ α β
- massive sulphide
- foliation
MXF-6
ρ α β
ϕ
- trace fine-grained disseminated sulphides
- strong foliation
MXF-7
A
B
ρ α β
ρ
ϕ
- fine-grained disseminated sulphides (~1%)
- quartz pods
- foliation
b
MXF-8
ρ α β
ϕ
- fine-grained disseminated sulphides
- strong foliation
MXF-9
ρ α β γ
ϕ
- fine-grained disseminated sulphides
- strong foliation
MXF-10
ρ α γ β
ϕ
- foliation/lineation
MXF-11
ρ α β
ϕ
- faint foliation
- very fine-grained, disseminated sulphides (<1%)
MXF-12
A
B
ρ α γ β
ρ α β
ϕ
- faint foliation
- fine-grained, disseminated sulphides (~1%)
MXF-13
ρ α β
ϕ
- foliation, crenulations
- fine-grained, disseminated sulphides (~1%)
MXF-14
ρ α β
ϕ
- fine stringer and disseminated sulphides (1-2%)
- weak to moderate foliation

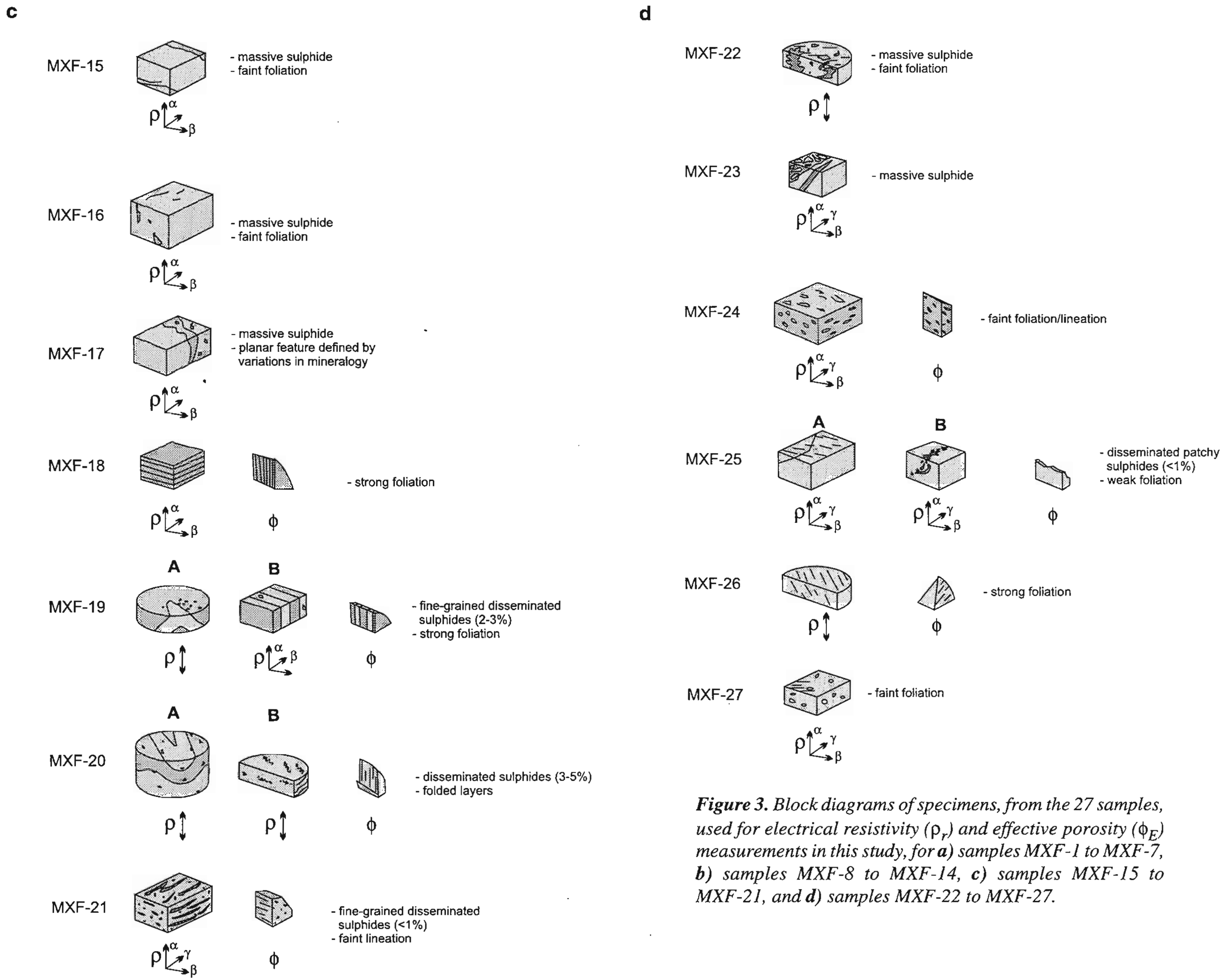

Figure 3. *Block diagrams of specimens, from the 27 samples, used for electrical resistivity (ρ_r) and effective porosity (ϕ_E) measurements in this study, for* ***a)*** *samples MXF-1 to MXF-7,* ***b)*** *samples MXF-8 to MXF-14,* ***c)*** *samples MXF-15 to MXF-21, and* ***d)*** *samples MXF-22 to MXF-27.*

Table 2a. Dimensions of the rectangular specimens cut out from the core samples for electrical measurements.

Sample	a_1 (cm)	a_2 (cm)	ℓ (cm)	W (g)	V (cm^3)	K_G (10^{-2}m)	δ_B (g/mL)
MXF-1A	1.150	1.183	1.389	5.8617	1.89	0.979	3.10
MXF-1Bα	1.186	1.214	0.858	3.8964	1.24	1.68	3.15
MXF-1Bβ	0.858	1.214	1.186	3.8964	1.24	0.878	3.15
MXF-2α	0.804	1.273	0.705	2.3902	0.72	1.45	3.31
MXF-2β	0.705	0.804	1.273	2.3902	0.72	0.445	3.31
MXF-3α	1.090	1.304	1.000	6.2695	1.42	1.42	4.41
MXF-3β	1.000	1.304	1.090	6.2695	1.42	1.20	4.41
MXF-4α	1.013	1.099	0.924	5.2953	1.03	1.20	5.15
MXF-4β	0.924	1.013	1.099	5.2953	1.03	0.852	5.15
MXF-5α	0.971	1.468	0.836	6.1266	1.19	1.71	5.14
MXF-5β	0.836	1.468	0.971	6.1266	1.19	1.25	5.14
MXF-6α	0.609	0.963	0.428	0.9265	0.25	1.37	3.69
MXF-6β	0.428	0.963	0.609	0.9265	0.25	0.677	3.69
MXF-7Aα	1.178	1.315	1.050	5.1302	1.63	1.48	3.15
MXF-7Aβ	1.050	1.315	0.178	5.1302	1.63	1.17	3.15
MXF-7B	1.143	1.385	0.939	4.7133	1.49	1.69	3.17
MXF-8α	1.308	2.041	1.155	9.4468	3.08	2.31	3.06
MXF-8β	1.155	2.041	1.308	9.4468	3.08	1.80	3.06
MXF-9α	1.040	1.340	0.910	3.9406	1.27	1.53	3.11
MXF-9β	0.910	1.340	1.040	3.9406	1.27	1.17	3.11
MXF-9γ	0.910	1.040	1.340	3.9406	1.27	0.706	3.11
MXF-10α	1.310	1.410	0.890	5.4057	1.64	2.08	3.29
MXF-10β	0.890	1.410	1.310	5.4057	1.64	0.958	3.29
MXF-10γ	0.890	1.310	1.410	5.4057	1.64	0.827	3.29

a_1, a_2 = Length of the two sides of the rectangular specimen
ℓ = Thickness of specimen
W = Weight of specimen under room dry conditions
K_G = Geometric factor
δ_B = Bulk density
V = Volume

Table 2b. Dimensions of the rectangular specimens cut out from the core samples for electrical measurements.

Sample	a_1 (cm)	a_2 (cm)	ℓ (cm)	W (g)	V (cm^3)	K_G (10^{-2}m)	δ_B (g/mL)
MXF-11α	1.380	1.350	0.980	5.7238	1.83	1.90	3.14
MXF-11β	0.980	1.350	1.380	5.7238	1.83	0.959	3.14
MXF-12Aα	1.370	1.490	0.900	5.7185	1.84	2.27	3.11
MXF-12Aβ	0.900	1.490	1.370	5.7185	1.84	0.979	3.11
MXF-12Aγ	0.900	1.370	1.490	5.7185	1.84	0.828	3.11
MXF-12Bα	0.890	0.905	0.870	2.3352	0.70	0.931	3.31
MXF-12Bβ	0.870	0.890	0.905	2.3352	0.70	0.856	3.33
MXF-13α	1.183	1.351	0.890	4.5000	1.42	1.80	3.16
MXF-13β	0.890	1.351	1.183	4.5000	1.42	1.02	3.16
MXF-14α	1.134	1.233	1.009	4.6589	1.41	1.39	3.30
MXF-14β	1.009	1.233	1.134	4.6589	1.41	1.10	3.30
MXF-15α	0.966	1.078	0.830	4.4945	0.86	1.25	5.20
MXF-15β	0.830	1.078	0.966	4.4945	0.86	0.926	5.20
MXF-16α	1.446	1.689	1.263	16.0191	3.08	1.93	5.19
MXF-16β	1.263	1.689	1.446	16.0191	3.08	1.48	5.19
MXF-17α	1.325	1.620	1.084	11.2957	2.33	1.98	4.85
MXF-17β	1.084	1.325	1.620	11.2957	2.33	0.88	4.85
MXF-18α	0.934	1.019	0.609	2.0000	0.58	1.56	3.45
MXF-18β	0.609	1.019	0.934	2.0000	0.58	0.664	3.45
MXF-19Bα	1.156	1.248	1.058	4.7637	1.53	1.36	3.12
MXF-19Bβ	1.058	1.156	1.248	4.7637	1.53	0.980	3.12

a_1, a_2 = Length of the two sides of the rectangular specimen
ℓ = Thickness of specimen
W = Weight of specimen under room dry conditions
K_G = Geometric factor
δ_B = Bulk density
V = Volume

Table 2c. Dimensions of the rectangular specimens cut out from the core samples for electrical measurements.

Sample	a_1 (cm)	a_2 (cm)	ℓ (cm)	W (g)	V (cm^3)	K_G (10^{-2}m)	δ_B (g/mL)
MXF-21α	0.900	1.300	0.760	2.8835	0.89	1.54	3.24
MXF-21β	0.760	1.300	0.900	2.8835	0.89	1.10	3.24
MXF-21γ	0.760	0.900	1.300	2.8835	0.89	0.526	3.24
MXF-23α	0.980	1.050	0.810	3.9042	0.83	1.27	4.68
MXF-23β	0.810	1.050	0.980	3.9042	0.83	0.868	4.68
MXF-23γ	0.810	0.980	1.050	3.9042	0.83	0.756	4.68
MXF-24α	1.030	1.240	1.010	4.2028	1.29	1.26	3.26
MXF-24β	1.010	1.240	1.030	4.2028	1.29	1.22	3.26
MXF-24γ	1.010	1.030	1.240	4.2028	1.29	0.839	3.26
MXF-25Aα	1.130	1.460	1.080	5.5484	1.78	1.53	3.11
MXF-25Aβ	1.080	1.460	1.130	5.5484	1.78	1.40	3.11
MXF-25Aγ	1.080	1.130	1.460	5.5484	1.78	0.836	3.11
MXF-25Bα	1.080	1.050	0.700	2.6916	0.79	1.62	3.39
MXF-25Bβ	0.700	1.050	1.080	2.6916	0.79	0.681	3.39
MXF-25Bγ	0.700	1.080	1.050	2.6916	0.79	0.720	3.39
MXF-27α	1.180	1.320	0.650	3.2271	1.01	2.40	3.19
MXF-27β	0.650	1.320	1.181	3.2271	1.01	0.727	3.19
MXF-27γ	0.650	1.181	1.320	3.2271	1.01	0.582	3.19

a_1, a_2 = Length of the two sides of the rectangular specimen
ℓ = Thickness of specimen
W = Weight of specimen under room dry conditions
K_G = Geometric factor
δ_B = Bulk density
V = Volume

Table 2d. Dimensions of the disc-shaped specimens cut out from the core samples.

Samples	r_D (cm)	ℓ (cm)	W (g)	V (cm^3)	K_G (10^{-2} m)	δ_B (g/mL)
MXF-19A	4.70	0.509	26.9960	8.8	34.1	3.06
MXF-20A	4.70	1.101	57.8494	19.1	15.8	3.03
MXF-20B	4.70	0.650	24.4566	7.9	18.77	3.08
MXF-22	4.70	0.590	24.7054	4.9	14.18	5.01
MXF-26	4.68	0.670	15.8548	5.2	11.62	3.04

r_D = Diameter
ℓ = Thickness
W = Weight
K_G = Geometric factor
δ_B = Bulk density
V = Volume

are listed in Table 2. Preparations are in progress for petrographic thin section analysis and scanning electron microscope analysis of selected samples/specimens.

Bulk density and effective porosity measurements

The caliper method (American Petroleum Institute, 1960) has been used to determine the bulk density (δ_B) of the samples, by measuring the dimensions and weight of their rectangular or disc specimens. This measurement also forms part of the procedure to determine effective porosity (ϕ_E). Effective porosity (ϕ_E), in principle, represents the pore volume of all interconnected pores. In this study, it is determined from the difference in weight between the oven-dried and water-saturated rock specimen. Another parameter derived on a routine basis is the static irreducible water saturation, S_{ir}, which represents the pore space occupied by the bound or adsorbed water on the pore surfaces. Measurements are taken at room temperature (23°C) and atmospheric pressure. The American Petroleum Institute *Recommended practices for core-analysis procedure* (American Petroleum Institute, 1960) has generally been followed in these measurements. Details of the standard procedures routinely used in this study are described in the literature (Katsube and Salisbury, 1991; Katsube et al., 1992; Scromeda and Katsube, 1994; Katsube and Scromeda, 1995).

Bulk electrical resistivity measurements

The bulk electrical resistivity (ρ_r) is determined from measurements of complex electrical resistivity, ρ^*, procedures for which are described in recent publications (e.g. Katsube et al., 1991, 1992, 1996a, b; Katsube and Salisbury, 1991; Katsube and Scromeda, 1994). Complex electrical resistivity (ρ^*) consists of two components: real resistivity, ρ_R and imaginary resistivity, ρ_I (e.g. Katsube, 1975; Katsube and Walsh, 1987: Katsube and Salisbury, 1991). These measurements were made on specimens saturated with distilled water for 24 to 48 h (Katsube and Salisbury, 1991). The parameters, ρ^*, ρ_R, and ρ_I are measured over a frequency range of 1–10^6 Hz, and ρ_r usually represents a bulk electrical resistivity at frequencies of about 10^2–10^3 Hz. The ρ_r is a function of the pore structure and pore fluid resistivity, and is understood to exclude any other effects, such as pore surface, dielectric, or any other polarizations (Katsube, 1975; Katsube and Walsh,

Table 3. Results of the effective porosity measurements.

Sample	δ_B (g/mL)	W_W (g)	W_D (g)	S_{ir} (%)	ϕ_E (%)
MXF-1	3.15	1.4578	1.4469	16.51	2.37
MXF-2	3.31	1.8382	1.8273	17.43	1.97
MXF-6	3.69	1.7794	1.7668	17.46	2.63
MXF-7	3.15	2.2750	2.2667	14.46	1.15
MXF-8	3.06	5.2353	5.2158	14.87	1.14
MXF-9	3.11	14.7972	14.7662	24.84	0.65
MXF-10	3.29	1.2672	1.2640	15.62	0.83
MXF-11	3.14	7.1721	7.1575	26.03	0.64
MXF-12	3.11	1.2865	1.2820	33.33	1.09
MXF-13	3.16	1.9514	1.9453	19.67	0.99
MXF-14	3.30	2.8570	2.8400	22.94	1.98
MXF-18	3.45	1.9956	1.9875	16.05	1.41
MXF-19	3.12	2.6569	2.6477	30.43	1.08
MXF-20	3.08	2.1981	2.1887	26.60	1.32
MXF-21	3.24	2.6421	2.6286	21.48	1.66
MXF-24	3.26	3.5380	3.5229	18.54	1.40
MXF-25	3.11	3.5272	3.5137	17.78	1.19
MXF-26	3.04	2.8759	2.8689	31.43	0.74
MXF-27	3.18	3.1618	3.1529	13.48	0.90

W_W = Wet weight
W_D = Dry weight
S_{ir} = Irreducible water saturation
δ_B = Bulk density
ϕ_E = Effective porosity

1987). The geometric factor, K_G (with the units 10^{-2} m), required for derivation of ρ^* from the actual electrical measurements is defined as

$$K_G = A/\ell,$$

where A (cm^2) is the cross-section area and ℓ (cm) is the thickness of the specimen. This parameter was determined for all specimens prior to the electrical measurements, using the specimen dimensional data in Table 2.

EXPERIMENTAL RESULTS

The results of the bulk density (δ_B) determinations are listed in Table 2. They range from 3.03 to 5.19 g/mL. These values are relatively high, probably due to their disseminated sulphide content. The effective porosity (ϕ_E) values are listed in Table 3 for specimens visibly barren of sulphide minerals, and are in the range of 0.64 to 2.63%. The δ_B values used in the ϕ_E determination are from the specimens used in the electrical measurements, and are not specific to the specimens used in the porosity determination. The caliper method used for the δ_B determination cannot be used on the ϕ_E specimens, because of their irregular shapes. Although considerable

Table 4a. Results of electrical resistivity measurements.

Sample	ρ_r, (10^3 Ω·m) Mes. #1	Mes. #2	Mean**
MXF-1A	1.35	1.29	1.32 ± 0.03
MXF-1Bα	1.97	2.34	2.16 ± 0.19
MXF-1Bβ	0.91	1.04	0.98 ± 0.06
MXF-2α	2.38	2.58	2.48 ± 0.10
MXF-2β	5.72*	5.73*	5.73* ± 0.01
MXF-3α	0.0022 ←	0.0019 ←	0.00205*
MXF-3β	0.02030 ←	0.02034 ←	0.02032*
MXF-4α	0.00027 ←	0.00030 ←	0.00029*
MXF-4β	0.00016 ←	0.000147 ←	0.00016*
MXF-5α	0.00065 ←	0.00062 ←	0.00064*
MXF-5β	0.00030 ←	0.00039 ←	0.00035*
MXF-6α	1.55	1.65	1.60 ± 0.05
MXF-6β	0.45	0.42	0.44 ± 0.02
MXF-7Aα	8.91	7.24	8.08 ± 0.84
MXF-7Ab	3.26	2.84	3.05 ± 0.21
MXF-7B	8.37	8.66	8.52 ± 0.15
MXF-8α	9.62	9.51	9.57 ± 0.06
MXF-8β	2.48	2.54	2.51 ± 0.03
MXF-9α	12.56*	18.79	15.68 ± 3.12
MXF-9β	5.33	5.86	5.60 ± 0.27
MXF-9γ	2.98	3.12	3.05 ± 0.07
MXF-10α	13.58	13.42	13.50 ± 0.08
MXF-10β	6.94	7.18	7.06 ± 0.12
MXF-10γ	3.18	2.87	3.03 ± 0.16

ρ_r = Bulk electrical resistivity
Mes. (#1) = Measurement after 24 h of saturation
Mes. (#2) = Measurement after 48 h of saturation
* = ρ_r is too low for an accurate measurement, possible error > ±100%
← = ρ_r value taken at 10^5 Hz as the resistivity is very low
** = The value after the "±" is the maximum difference between the mean and the individually measured values

Table 4b. Results of electrical resistivity measurements.

Sample	ρ_r, (10^3 Ω·m) Mes. #1	Mes. #2	Mean**
MXF-11α	12.69	15.08	13.89 ± 1.20
MXF-11β	1.54	1.67	1.60 ± 0.06
MXF-12Aα	9.32	8.90	9.1 ± 0.20
MXF-12Aβ	2.79	2.73	2.76 ± 0.03
MXF-12Aγ	1.17	1.15	1.17 ± 0.02
MXF-12Bα	6.44	6.51	6.48 ± 0.04
MXF-12Bβ	1.17	1.34	1.26 ± 0.09
MXF-13α	5.50	6.53	6.02 ± 0.52
MXF-13β	0.90	0.95	0.95 ± 0.05
MXF-14α	2.53	2.56	2.55 ± 0.02
MXF-14β	0.92	0.89	0.91 ± 0.02
MXF-15α	0.00010 ←	0.00010 ←	0.00010*
MXF-15β	0.000053 ←	0.000064 ←	0.00006*
MXF-16α	0.00018 ←	0.00023 ←	0.00021*
MXF-16β	0.00014 ←	0.00014 ←	0.00014*
MXF-17α	0.00045 ←	0.00072 ←	0.00059*
MXF-17β	0.00035 ←	0.00039 ←	0.00037*
MXF-18α	6.89	7.13	7.01 ± 0.12
MXF-18β	0.88	0.97	0.93 ± 0.04
MXF-19A	14.85	13.54	14.20 ± 0.66
MXF-19Bα	2.56	2.91	2.74 ± 0.18
MXF-19Bβ	7.02	9.24	8.13 ± 1.11
MXF-20A	5.40	7.72	6.56 ± 1.16
MXF-20B	6.79	9.28	8.04 ± 1.25

ρ_r = Bulk electrical resistivity
Mes. (#1) = Measurement after 24 h of saturation
Mes. (#2) = Measurement after 48 h of saturation
* = ρ_r is too low for an accurate measurement, possible error > ±100%
← = ρ_r value taken at 10^5 Hz as the resistivity is very low
** = The value after the "±" is the maximum difference between the mean and the individually measured values

effort is made to obtain homogeneity between specimens (e.g. selecting specimens from adjacent areas), the ϕ_E values could contain some errors for this reason.

The results of the electrical resistivity (ρ_r) measurements are listed in Table 4. Determinations have been made at 24 and 48 h after water saturation to check the stability of the ρ_r values with time. Under these conditions, it is expected that the distilled water that was used to saturate the specimen has chemically equilibrated with the rock, and represents the pore water of the in situ condition. Normally, differences of up to ±20% of their mean ρ_r value are considered to be within measurement error and represent a stable condition. In the present study, some of the specimens with a low ρ_r display differences that exceed that value (e.g. MXF-9a and MXF-26), likely due to their ρ_r values being below measurement resolution. Sixty-eight determinations, including multidirectional measurements, were made for 33 specimens prepared from the 27 samples.

Some examples of the complex resistivity plots used to determine the high, low, and intermediate values of ρ_r are shown in Figures 4, 5, 6 , 7, and 8. Detailed explanations for the complex resistivity plots have been previously published (Katsube et al., 1998a). Figure 4 (sample MXF-11) displays complex resistivity plots of normal curves, typical of high ρ_r specimens. This sample is a strongly foliated argillite with an increase in ρ_r perpendicular to the foliation. Figure 5 (sample MXF-17) displays very distorted complex resistivity plots, which are typical for specimens with very low ρ_r, and which make it difficult to determine ρ_r. Such plots are generally characteristic of samples rich in sulphides, which is also the case for this sample. Figure 6 (sample MXF-23) displays complex resistivity plots for low (Fig. 6a and 6c) and intermediate (Fig. 6b) ρ_r values. The two arcs in Figure 6b represent the electrical characteristics of the rock sample (left-hand arc) and the electrode polarization (right-hand arc) due to the sulphide minerals, respectively. This is a massive sulphide sample with a slight foliation (Fig. 3d). Distinct electrical anisotropies are present in this sample/specimen, with an increased ρ_r in the direction (β-direction, Fig. 6b) perpendicular to the foliation. The ρ_r values were taken at frequencies higher than usual (10^5 Hz) for the α- and γ-directions (Fig. 6a and 6c), due to difficulties in their determination with the distorted arcs.

Table 4c. Results of electrical resistivity measurements.

Sample	ρ_r, (10^3 Ω·m) Mes. #1	 Mes. #2	Mean**
MXF-21α	3.68	4.29	3.98 ± 0.13
MXF-21β	1.13	1.23	1.17 ± 0.04
MXF-21γ	0.38	0.43	0.41 ± 0.03
MXF-22	0.000318 ←	0.0008223 ←	0.00057*
MXF-23α	0.001321 ←	0.00198 ←	0.00165*
MXF-23β	0.03154 ←	0.006169 ←	0.01886*
MXF-23γ	0.002199 ←	0.0005863 ←	0.00139*
MXF-24α	4.27	4.37	4.32 ± 0.05
MXF-24β	3.77	3.32	3.55 ± 0.23
MXF-24γ	0.92	0.92	0.92 ± 0.00
MXF-25Aα	9.11	8.70	8.91 ± 021
MXF-25Aβ	5.38	4.91	5.15 ± 0.24
MXF-25Aγ	9.57*	11.53	10.55 ± 0.98
MXF-25Bα	7.65	7.74	7.70 ± 0.05
MXF-25Bβ	8.73*	7.01*	7.87 ± 0.86
MXF-25Bγ	4.19	4.05	4.12 ± 0.07
MXF-26	42.13	26.59	34.36 ± 7.77
MXF-27α	14.62	15.85	15.24 ± 0.62
MXF-27β	4.09	3.99	4.04 ± 0.05
MXF-27γ	3.89	4.07	3.98±0.09

ρ_r = Bulk electrical resistivity
Mes. (#1) = Measurement after 24 h of saturation
Mes. (#2) = Measurement after 48 h of saturation
* = ρ_r is too low for an accurate measurement, possible error > ±100%
← = ρ_r value taken at 10^5 Hz as the resistivity is very low
** = The value after the "±" is the maximum difference between the mean and the individually measured values

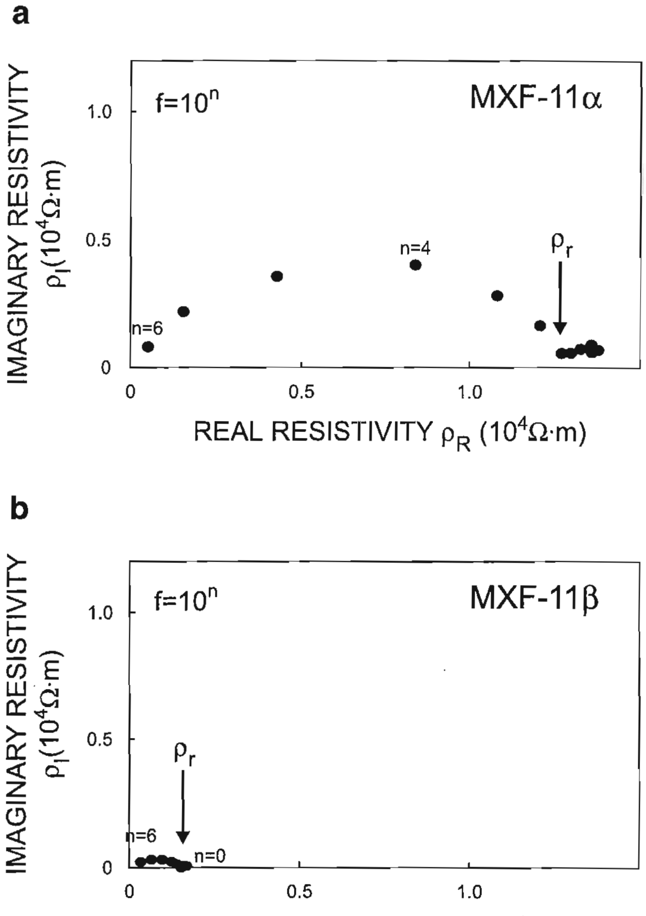

Figure 4. Typical examples of complex resistivity (ρ) plots used to determine bulk electrical resistivity (ρ_r), where ρ_R and ρ_I are the real and imaginary resistivities. Imaginary resistivity (ρ_I) as a function of ρ_R, for **a)** specimen MXF-11 (α-direction) displaying a normal arc usually seen in highly resistive rocks, and **b)** for the same specimen (β-direction) displaying a considerable decrease in ρ_r when measured parallel to the foliation. f = Frequency.*

Two more examples of complex resistivity plots are shown in Figures 7 and 8. Figure 7 (sample MXF-9) compares complex resistivity plots obtained for ρ_r values determined in the three directions (α-, β-, and γ-directions). Figure 7a (α-direction) shows a distorted arc, typical for high ρ_r values. Figures 7b (β-direction) and 7c (γ-direction) show normal arcs typical for intermediate ρ_r values. Figure 8 (Sample MXF-26) shows a complex resistivity plot obtained for a very high ρ_r value, displaying a very normally-shaped arc.

DISCUSSION AND CONCLUSIONS

The lower end of the range of bulk density (δ_B) values (3.03-5.19 g/mL), obtained in this study, is higher than the range of values previously obtained (Katsube et al., 1997,

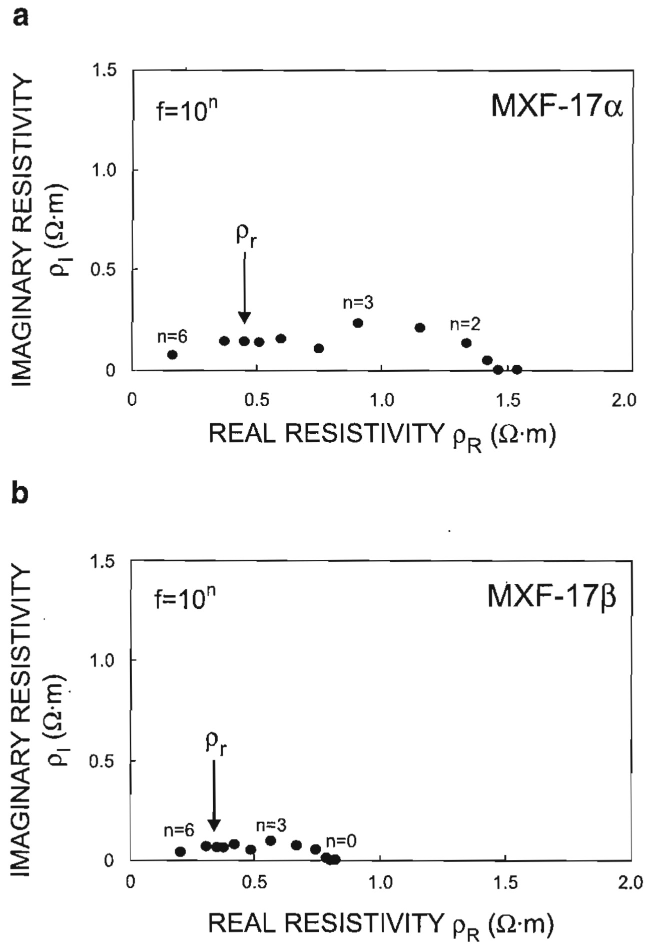

Figure 5. *Typical examples of complex resistivity (ρ^*) plots, for cases where difficulty is experienced in determining ρ_r due to slightly distorted arcs, a pattern commonly seen in very low resistivity rocks. Imaginary resistivity (ρ_I) as a function of ρ_R for* ***a)*** *specimen MXF-17 measured in the α-direction, and* ***b)*** *for the same specimen measured in the β-direction, showing a slight decrease in ρ_r when measured perpendicular to a planar feature (β-direction) defined by a variation in mineralogy. f = Frequency.*

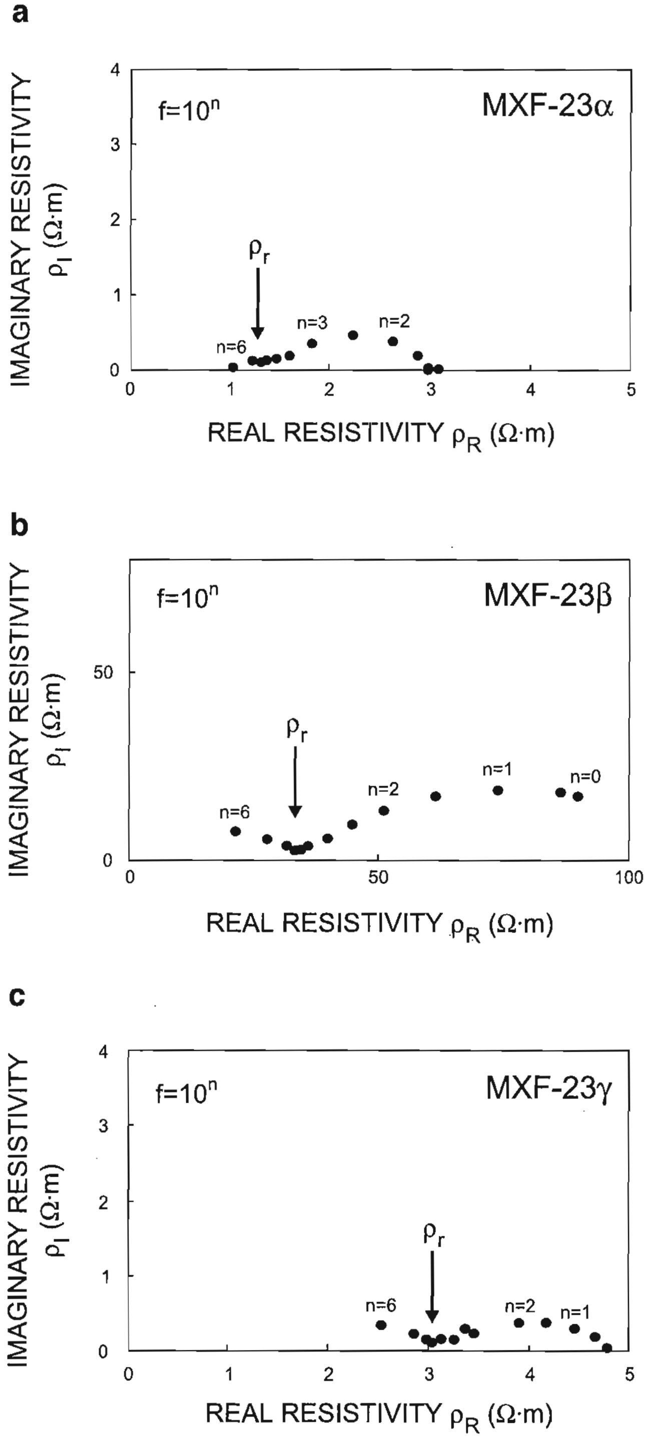

Figure 6. *Imaginary resistivity (ρ_I) as a function of ρ_R for specimen MXF-23 measured in all three directions:* ***a)*** *the α-direction (24 h saturation),* ***b)*** *the β-direction (24 h saturation), and* ***c)*** *the γ-direction (24 h saturation). f = Frequency.*

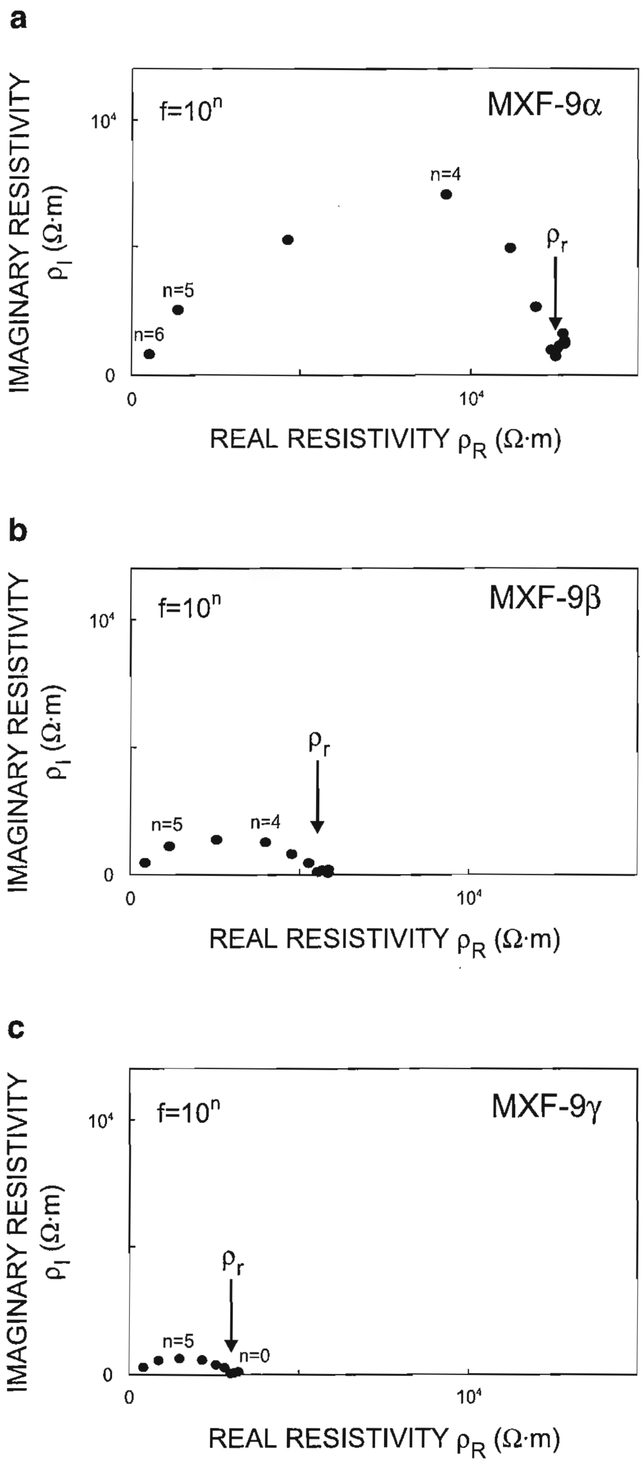

Figure 7. *Imaginary resistivity (ρ_I) as a function of ρ_R for specimen MXF-9, comparing complex resistivity plots obtained for all three directions (α-, β-, and γ-directions):* ***a)*** *for the α-direction, showing a distorted arc,* ***b)*** *for the β-direction, and* ***c)*** *for the γ-direction, both showing normal arcs. f = Frequency.*

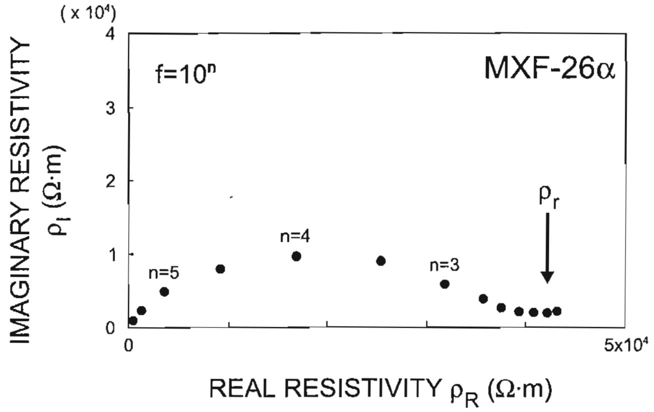

Figure 8. *Imaginary resistivity (ρ_I) as a function of ρ_R for specimen MXF-26, displaying a very high ρ_r value, with a very normally-shaped arc. f = Frequency.*

1998a) for rocks from the Bathurst mining camp. These high values may be due to rather high mafic mineral or sulphide mineral contents. The upper end of the range of δ_B values, is associated with the sulphide-rich samples. This is a normal trend for such rocks (Katsube et al., 1997, 1998a). The effective porosity (ϕ_E) values, from this study (0.64–2.63%) are within the range previously reported for rock samples from this camp (Katsube et al., 1997, 1998a). The bulk electrical resistivity (ρ_r) values, are in the range of <1.0 to $3.4\text{x}10^4$ Ω·m, again within the previously reported range of values for rock samples from this camp (Katsube et al., 1997, 1998a).

Although weak to moderate foliations do exist, the electrical resistivity anisotropies (λ) observed in the sample suite used in this study are not very large. The maximum λ value is 10:1, for a massive sulphide sample (MXF-3). This electrical anisotropy is likely a result of the foliation and faint lineation visible in the sample. There appears to be a secondary sulphide mineral growth along the foliation, which is not mechanically deformed. This implies that, although there is evidence of enhanced electrical conductivity (ρ_r=2 Ω·m) in the direction parallel to the foliation (α-direction) of this sample, the interconnectivity between the individual sulphide mineral grains may be poor. Good interconnectivity should result in ρ_r<0.1 Ω·m, and larger λ values similar to previously reported cases (e.g. λ>1000:1, Katsube et al., 1997). Petrographic thin section and scanning electron microscopic analysis are required to resolve this question.

The nonmassive sulphide samples (e.g. tuff, argillite, Table 5), of this suite, display λ values of 2:1 to 10:1. The anisotropic effect of a sample (crystal tuff: MXF-21) that displays one of the maximum λ values (10:1), is likely a result of the foliation and faint lineation. Fine-grained disseminated sulphides are concentrated along the foliation to a certain extent. This could have some effect on the ρ_r value being considerably lower in the direction parallel to the foliation ($0.41\text{x}10^3$ Ω·m), compared to that in the direction perpendicular to the foliation ($3.98\text{x}10^3$ Ω·m).

Table 5. Summary of electrical resistivity measurements (refer to Figure 3 for sketches of the measured specimens showing directional features where present).

Sample	Rock type	δ_B (g/mL)	Mean ρ_r, (10^3 Ω·m)			Anisotropy
			α	β	γ	λ
MXF-1A	LT	3.10	1.32			
MXF-1B		3.15	2.16	0.98		2:1
MXF-2	CT	3.31	2.48*	5.73*		2:1
MXF-3	S	4.41	0.0020 ←	0.02032 ←		10:1
MXF-4	S	5.15	0.00029 ←	0.00015 ←		
MXF-5	S	5.14	0.00063 ←	0.00034 ←		
MXF-6	A	3.69	1.60	0.44		4:1
MXF-7A	CT	3.15	8.08	3.05		3:1
MXF-7B		3.17	8.52			
MXF-8	FT	3.06	9.57	2.51		4:1
MXF-9	CT	3.11	15.95*	6.00	3.19	5:1
MXF-10	G	3.29	13.50	7.35	3.13	4:1
MXF-11	A	3.14	14.60	1.72		8:1
MXF-12A	CT	3.11	9.1	2.76	1.17	8:1
MXF-12B		3.31	6.48	1.26		5:1
MXF-13	CT	3.16	6.06	0.95		6:1
MXF-14	A	3.30	2.55	0.91		3:1
MXF-15	S	5.20	0.00010 ←	0.000059 ←		
MXF-16	S	5.19	0.00021 ←	0.00014 ←		
MXF-17	S	4.85	0.00058 ←	0.00037 ←		
MXF-18	A	3.45	7.01	0.93		7.5:1
MXF-19A	CT	3.06	14.20			
MXF-19B		3.12	2.74	8.13		3:1
MXF-20A	FT	3.03	6.56			
MXF-20B		3.08	8.04			
MXF-21	CT	3.24	3.98	1.17	0.41	10:1
MXF-22	S	5.01	0.0005701 ←			
MXF-23	S	4.68	0.0016505 ←	0.0188545 ←	0.0013926 ←	
MXF-24	A	3.26	4.32	3.55	0.92	4:1
MXF-25A	G	3.11	8.91*	5.15	10.55	2:1
MXF-25B		3.39	7.70*	7.87	4.12*	2:1
MXF-26	DD	3.04	34.36			
MXF-27	LT	3.19	15.24	4.04	3.98	4:1

ρ_r = Bulk electrical resistivity
α, β, γ = Three directions of the electrical measurements
δ_B = Bulk density (g/mL)
* = Possible reduction in measurement accuracy due to distortion of the complex resistivity plots (arcs); ρ_r is too low for an accurate measurement
← = ρ_r value determined at 10^5 Hz due to very low resistivity levels
LT, CT, FT = Lapilli tuff, crystal tuff, felsic tuff
S = Sulphide
A = Argillite
G = Gabbro
DD = Diabase dyke

The mineralized and nonmineralized rocks discussed in the previous two paragraphs have a maximum anisotropy ratio of 10:1, even though their absolute resistivity values differ by approximately 200 times: 2 to 20 Ω·m for the mineralized example (MXF-3) and 400 to 4000 Ω·m for the nonmineralized example (MXF-21). Large anisotropy ratios do not necessarily imply large differences in the EM responses measured along different axes of anisotropy. There are two other factors that must be considered when determining the effects of anisotropy on EM responses. The first is the absolute value of the resistivity. Electromagnetic responses due to differences in low absolute resistivities (e.g. 2 and 20 Ω·m) are more likely to be seen in comparison to those for high absolute resistivities (e.g. 400 and 4000 Ω·m). The second factor is related to the dimension of the body which determines the response parameter. Even large anisotropic effects may be missed when the response parameter is small. In summary, the effect of electrical anisotropy on EM responses depends on the relative size of the electrical anisotropy and the response parameter of the body.

There is a tendency for foliated massive sulphide samples to display very distorted complex resistivity arcs, such as shown in Figure 6 for sample MXF-17. While these arcs for low ρ_r samples are usually rather suppressed (e.g. Katsube et al., 1997), the high degree of distortion with the suggestion of a multi-arc system (Fig. 6) seems to be unique to these foliated massive sulphide samples. Such an example is also seen in a previous publication (Fig. 4 *in* Katsube et al., 1998a). Further study is required to understand the reason for this distortion.

ACKNOWLEDGMENTS

The authors are grateful for the critical review of this paper and for the very useful suggestions by M.D. Thomas (GSC). The authors also thank Noranda Mining and Exploration Inc., Bathurst, for providing the geological log data in Figure 2. This work has been supported by the EXTECH II (Exploration and TECHnology) Project which was initiated in 1994 in the Bathurst mining camp.

REFERENCES

American Petroleum Institute (API)
1960: Recommended practices for core-analysis procedure; API Recommended Practice 40 (RP 40) First Edition, American Petroleum Institute, Washington, D.C., p. 55.

Davies, J.L. (comp.)
1977: Geological Map of Northern New Brunswick; New Brunswick Department of Natural Resources, Map NR-3, scale 1:250 000.

Jones, A.G., Katsube, T.J., and Ferguson, I.
1996: Paleoproterozoic tectonic processes revealed through electromagnetic studies of the North American Central Plains (NACP) conductivity anomaly; from continental to hand sample scale; *in* Society of Exploration Geophysicists Expanded Abstracts with Authors' Biographies, Technical Program, 66th Annual Meeting and International Exhibition, Denver, November 10-15, 1996, Volume I, p. 269-272.

Katsube, T.J.
1975: The electrical polarization mechanism model for moist rocks; *in* Report of Activities, Part C; Geological Survey of Canada, Paper 75-1C, p. 353-360.

Katsube, T.J. and Salisbury, M.
1991: Petrophysical characteristics of surface core samples from the Sudbury structure; *in* Geological Survey of Canada, Paper 91-1E, 265-271.

Katsube, T.J. and Scromeda, N.
1994: Physical properties of Canadian kimberlites, Somerset Island, Northwest Territories and Saskatchewan; *in* Current Research 1994-B; Geological Survey of Canada, p. 35-42.

Katsube, T.J. and Scromeda, N. (cont.)
1995: Accuracy of low porosity measurements in granite; *in* Current Research 1995-C; Geological Survey of Canada, 265-270.

Katsube, T.J. and Walsh, J.B.
1987: Effective aperture for fluid flow in microcracks; International Journal of Rock Mechanics and Mining Sciences and Geomechanics Abstracts, v. 24, p. 175-183.

Katsube, T.J., Best, M., and Jones, A.G.,
1996a: Electrical anisotropy of mineralized and non mineralized rocks: In Society of Exploration Geophysicists Expanded Abstracts with Authors Biographies, Technical Program, 66rd Annual Meeting and International Exhibition (Denver, November 10-15, 1996), Volume II, 1279-1281.

Katsube, T.J., Best, M.E., and Mudford, B.S.
1991: Petrophysical characteristics of shales from the Scotian shelf; Geophysics, v. 56, p. 1681-1689.

Katsube, T.J., Connell, S., Scromeda, N., Goodfellow, W.D., and Best, M.E.
1998a: Electrical characteristics of mineralized and nonmineralized rocks at the Caribou deposit, Bathurst mining camp, New Brunswick; *in* Current Research 1998-D; Geological Survey of Canada, p. 25-35.
1998b: Electrical characteristics of mineralized and nonmineralized rocks at the Restigouche deposit, Bathurst mining camp, New Brunswick; *in* Current Research 1998-E; Geological Survey of Canada.

Katsube, T.J., Palacky, G.J., Sangster, D.F., Galley, A.G., and Scromeda, N.,
1996b: Electrical properties of disseminated sulphide ore samples from Snow Lake; *in* EXTECH I: A Multidisciplinary Approach to Massive Sulphide Research in the Rusty Lake-Snow Lake Greenstone Belts, Manitoba, (ed.) G.F. Bonham-Carter, A.G. Galley, and G.E.M. Hall; Geological Survey of Canada, Bulletin 426, p. 319-329.

Katsube, T.J., Scromeda, N., Best, M.E., and Goodfellow, W.D.
1997: Electrical characteristics of mineralized and nonmineralized rocks at the Brunswick No. 12 deposit, Bathurst mining camp, New Brunswick; *in* Current Research 1997-E; Geological Survey of Canada, p. 97-107.

Katsube, T.J., Scromeda, N., Mareschal, M., and Bailey, R.C.
1992: Electrical resistivity and porosity of crystalline rock samples from the Kapuskasing Structural Zone, Ontario; *in* Current Research, Part E; Geological Survey of Canada, Paper 92-1E, p. 225-236.

Scromeda, N. and Katsube, T.J.
1994: Effect of temperature on drying procedures used in porosity measurements of tight rocks; *in* Current Research 1994-E; Geological Survey of Canada, p. 283-289.

Geological Survey of Canada Project 870057

APPENDIX

Geological descriptions

DRILLHOLE ST 218

MXF-1: Fine-grained lapilli tuff, hardness of 3–4, trace to minor disseminated sulphides visible with a thin quartz vein running parallel to one of the cleavage directions.

MXF-2: Crystal tuff consisting of patches of very soft, dark, fine-grained matrix (chloritic) with a few stretched, siliceous patches/bands, overall hardness is 3–4.

MXF-3: Massive sulphide with a dominant planar feature (layering) and a few siliceous pods. The layering is defined by variations in mineralogy (sulphides and silica).

MXF-4: Massive sulphide with a faint layering visible in the form of discontinuous silica-rich bands.

MXF-5: Massive sulphide with a moderate to weak planar feature. A hard metallic black mineral infills extensional fractures and appears to be a relatively discontinuous feature.

MXF-6: Sheared chloritic argillite, hardness 2–3, medium grey, with trace fine-grained disseminated sulphides.

MXF-7: Poorly foliated crystal tuff with siliceous pods, few rusty patches, stretched lapilli in a dark grey-green siliceous matrix. Trace pyrite is visible along the dominant foliation. The overall hardness is about 4.

MXF-8: Felsic tuff very similar to sample MXF-7 although not as many fragments. The sample is fairly soft (hardness 3–5), has a few siliceous nodules and a moderate foliation.

DRILLHOLE ST219

MXF-9: Crystal tuff with two cleavage/shear directions. Millimetre-scale subrounded fragments (lapilli) are visible in a very fine-grained, chloritic matrix, overall hardness 4.

MXF-10: Fine-grained gabbro with a strong cleavage, greasy feel, green (almost black) and overall hardness of 2–3. On a fresh cut surface stretched grains are visible, showing a strong lineation.

MXF-11: Sheared, dark grey argillite with a faint foliation. There appears to be some slightly coarser laminae, otherwise very fine-grained with a few siliceous fragments. Very fine-grained disseminated sulphides (<1%) concentrated along the foliation.

MXF-12: Sheared, fine-grained crystal tuff, slightly granular with trace fine-grained disseminated sulphides. The groundmass is soft with an overall hardness of 4.

DRILLHOLE ST220

MXF-13: Crystal tuff with a strong planar feature, crenulated in places, hardness of 4 with laminations clearly visible in places. Medium-light grey matrix hosting very fine-grained disseminated sulphides (~1%).

MXF-14: Argillite with a few siliceous pods, and minor disseminated, fine-grained sulphides. Hardness is about 4. Medium grey chloritic matrix with fine sulphide stringers crosscutting the dominant foliation.

MXF-15: Massive, fine-grained sulphide with a few rusty patches and porous areas (pods).

MXF-16: Massive sulphide, fine- to medium-grained with a black mineral infilling thin fractures parallel to the core axis.

MXF-17: Massive sulphide with a weak to moderate foliation and a few open pods/pits. Siliceous in places.

MXF-18: Argillite with a moderate cleavage, hardness 3, green, and hosts trace disseminated sulphides. Faint banding is visible which appears to be a result of variations in grain size.

MXF-19: Crystal tuff with two cleavage directions, hardness of 4–5, buff-grey with small white feldspar crystals (slightly rounded). Fine-grained disseminated sulphides are visible in patches (2–3%).

MXF-20: Folded felsic tuff with disseminated sulphides, hardness 3, greenish/black in places with a high chlorite/sericite content. Bedding is defined by variations in grain size.

DRILLHOLE: ST221

MXF-21: Moderately to well foliated crystal tuff with trace to minor disseminated sulphides, faint lineation, hardness 4, pale greenish grey with a few pods/pores. Abundant small white and bluish grey siliceous lapilli.

MXF-22: Fine-grained massive sulphide.

MXF-23: Massive sulphide with a planar feature (small extensional fractures).

MXF-24: Grey-green argillite with a well defined cleavage and a few larger rounded grains <1 mm. Hardness is about 3.

MXF-25: Medium to light grey, granular, greywacke with some minor disseminated sulphides infilling small extensional fractures. The hardness is 3.

MXF-26: Dark green/grey diabase dyke with a moderate foliation, disseminated sulphides, elongate white calcite crystals throughout fine-grained chloritic matrix. Hardness is 3–4.

MXF-27: Lappilli tuff hosting minor disseminated sulphides, faint foliation and fairly large, siliceous lapilli. Hardness is about 3.

Mapping the response of permafrost in Canada to climate warming

Sharon L. Smith[1] and Margo M. Burgess
Terrain Sciences Division, Ottawa

Smith, S.L. and Burgess, M.M., 1998: Mapping the response of permafrost in Canada to climate warming; in *Current Research 1998-E; Geological Survey of Canada, p. 163–171.*

Abstract: The sensitivity of permafrost to climate warming is being examined as a contribution to a Geological Survey of Canada set of national syntheses on the impacts of climate change on active geological processes in Canada. Factors that influence the response of permafrost to climate warming have been compiled to produce preliminary maps showing the relative response of the ground thermal regime and the relative magnitude of the impact of thaw. About 50% of the present permafrost region contains permafrost warmer than -2°C. The potential for thaw and complete degradation of this warm permafrost is the greatest given current General Circulation Model predictions of air temperature warming of up to 4 and 5°C. The maps indicate that while the thermal response to an increase in air temperature would be relatively low for this warm permafrost (due to the buffering effects of surface vegetation, snow, and organic covers), the impact of associated permafrost thaw would be relatively high.

Résumé : La sensibilité du pergélisol au réchauffement du climat a été étudiée dans le cadre de synthèses effectuées à l'échelle nationale par la Commission géologique du Canada, portant sur les conséquences du changement climatique sur les phénomènes géologiques actuels au Canada. Les facteurs qui influent sur la réponse du pergélisol au réchauffement du climat ont fait l'objet d'une compilation dans le but de dresser des cartes provisoires mettant en évidence la réponse relative du régime thermique du sol et l'importance relative de l'incidence du dégel. Dans environ 50 p. cent de la région de pergélisol actuelle, la température est supérieure à -2 °C. Le dégel et la régression complète de ce pergélisol chaud sont l'éventualité la plus possible, basée sur le modèle de la circulation générale, qui prévoit un réchauffement de la température de l'air atteignant jusqu'à 4 et 5 °C. Les cartes révèlent que même si la réponse thermique du pergélisol chaud à un réchauffement de l'air serait plutôt faible (due à l'effet tampon des couvertures végétale, neigeuse et organique), l'incidence du dégel du pergélisol associé serait relativement importante.

---

[1] 2-775 Trojan Ave., Ottawa, Ontario K1K 2P6

INTRODUCTION

A major issue of concern in climate change studies is the effect that climate warming may have on permafrost in Canada. The Canadian Climate Centre General Circulation Model predicts an increase in mean annual air temperature in response to a doubling of atmospheric carbon dioxide ranging from 4°C in the southern portion of the permafrost region to 7°C in the high arctic (Berry, 1991; Maxwell, 1997). At the present time, about 50% of the Canadian landmass is underlain by permafrost of which a significant portion is warmer than -2°C (Fig. 1). Most of this warmer permafrost, with a thickness of generally less than 75 m, may ultimately disappear in response to climate warming. In areas of thicker and colder permafrost, warming would likely result in some thickening of the active layer and thinning of permafrost (Dyke et al., 1997).

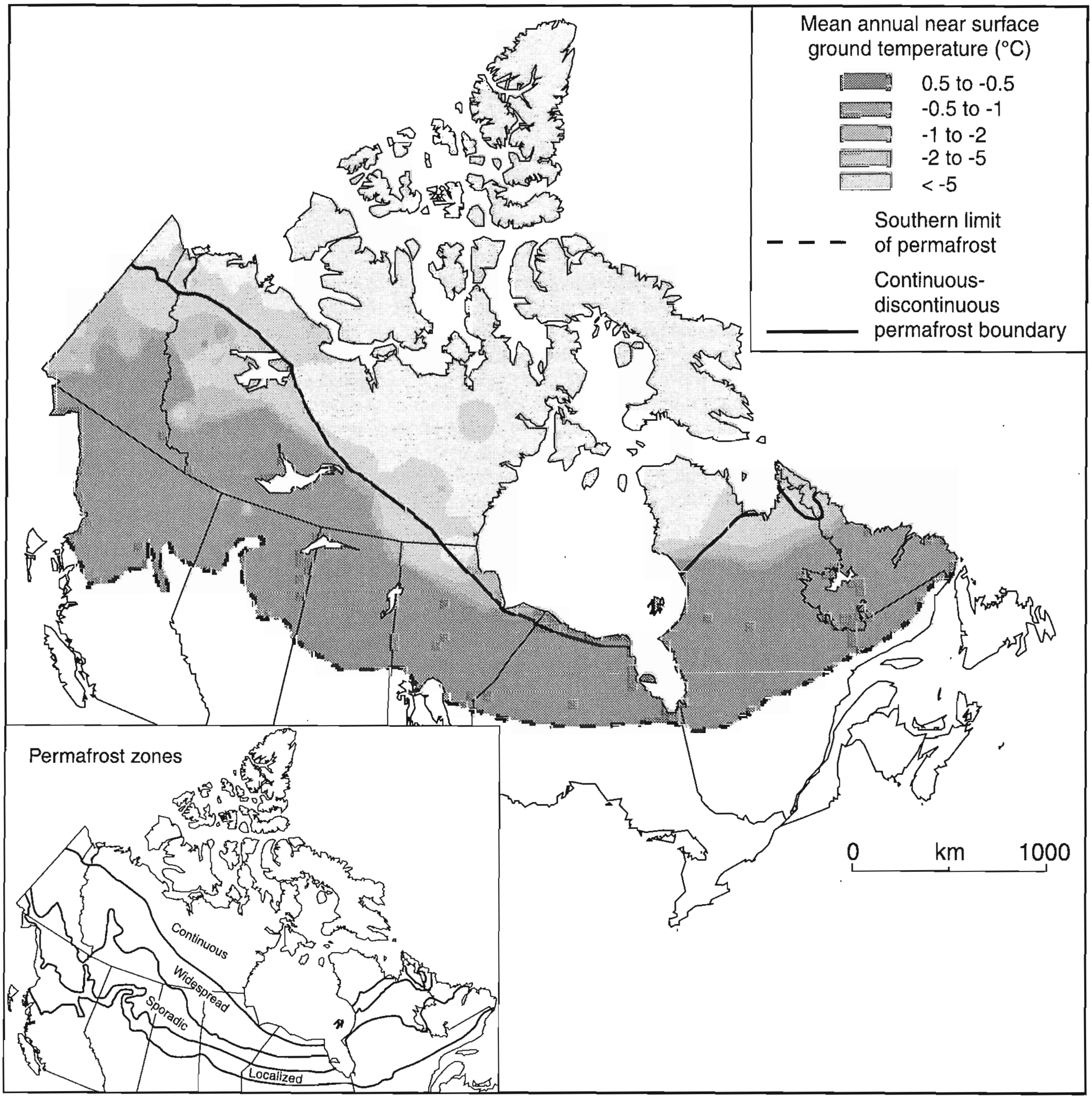

__Figure 1.__ Regional variation in mean annual near-surface ground temperature for the Canadian permafrost region. The southern limit of permafrost and the boundaries for permafrost zones in the inset map have been extracted from the map of Kettles et al. (1997). The discontinuous permafrost zone includes the area shown to have a ground temperature warmer than -2°C. Within this zone there will be areas where the ground temperature is above 0°C.

The impacts of the warming and thaw of permafrost will be most important in regions of ice-rich permafrost. Warming or thawing of ground ice can result in loss of strength and ground instability, creating engineering implications for infrastructures such as buildings, roads, pipelines, utilities, mines, and tailings disposal and impacts on the natural landscape including an increase in landslide activity and thermokarst terrain, and alteration of the hydrological regime.

The Geological Survey of Canada is currently preparing a series of national syntheses of geological responses to climate change. The sensitivity of permafrost to climate warming is one component of this series. Previous studies (e.g. Woo et al., 1992; Kettles et al., 1997) have considered how the boundaries of the permafrost region may change in response to increases in air temperature predicted under specific climate warming scenarios. These studies have produced maps of the equilibrium permafrost boundaries under $2xCO_2$ conditions and have assumed a spatially uniform increase in ground surface temperature of the same magnitude as air temperature. However, the more immediate concern of the transient response of warming from the present climate to $2xCO_2$ conditions was not considered. The present study does not attempt to predict the ultimate change in permafrost distribution that may occur following climate warming. Instead, it examines the sensitivity of permafrost to warming by considering the main factors which determine the response of the permafrost thermal regime to warming and the magnitude of the impact of any permafrost thaw that occurs. Using Geographic Information System (GIS) techniques, preliminary maps have been produced that classify areas according to 1) the thermal response to warming: the relative rate and magnitude of ground temperature change, and 2) the physical response: the relative magnitude of the impact of permafrost thaw. To our knowledge, this is the first time this type of approach has been used to examine the response of permafrost to climate change on a national scale.

APPROACH FOR CHARACTERIZING PERMAFROST RESPONSE TO CLIMATE WARMING

Several factors determine the thermal and physical response of permafrost to changes in air temperature. For each factor considered, a rating scale was applied that assigns a high ranking to the condition for which the response will be greatest. Relevant factors were combined using an added factor analysis approach (Environmental Conservation Service Task Force, 1981) in which there is a progressive adding of the ranks for each factor. The highest totals correspond to the greatest response. The two maps produced represent the summation of the factors influencing either the thermal or physical response of permafrost to climate warming. The maps are considered preliminary in that the rating scales and the rankings have not been finalized.

Data layers representing each factor have been combined using a raster-based GIS. The resolution used is 10 km (each pixel covers 100 km^2). This resolution is considered appropriate since the quality of data used is variable and, for some regions, sparsely available.

Thermal response: rate and magnitude of ground temperature change

Although the atmospheric climate is the main factor determining the distribution of permafrost, the existence of permafrost depends on the ground temperature. The relationship between air and ground temperature is complex, and is influenced by many local factors. At a given site, the rate and magnitude of response of the ground temperature to changes in air temperature depends on the local characteristics.

Luthin and Guymon (1974) have summarized the boundary layer interactions affecting the ground thermal regime in a buffer layer model which links the atmospheric climate to the subsurface climate. The model consists of three components, the buffer zone, the mineral soil, and the thermal regime. A modified version of this model (Fig. 2) is used to classify the thermal response to warming. The buffer zone component considers the factors that act as thermal buffers between the atmosphere and the ground. These factors determine how direct the link is between climate and ground temperature and therefore influence the rate and magnitude of heat transfer from the atmosphere to the ground. The mineral soil component considers the rate of heat transfer through the underlying soil or rock. The buffer zone and the mineral soil components determine the rate and magnitude of the response of the thermal regime to warming.

Buffer zone

The vegetation canopy, snow cover, and the surface organic layer act as thermal buffers between the atmosphere and the ground. Before changes in the atmospheric climate can affect the ground thermal regime, they must be transmitted through the buffer layer. The effects of warming should be greater in areas where the link between climate and ground temperature is more direct (Smith, 1988) which would be the case where there is little vegetation, snow cover, or organic material. Information on snow cover, vegetation cover, and the distribution of organic material has been assembled and rating scales developed as described below and qualitatively outlined in Figure 2.

Snow cover

The low thermal conductivity of snow makes it a good insulator (Nicholson and Granberg, 1973). A thick snow cover reduces the energy exchanges between the air and the ground surface and insulates the ground from changes in air temperature.

Annual mean maximum snow depths for 300 Canadian sites were extracted from Environment Canada's "snow climate normal database" (Braaten, 1996). The point data were interpolated using a weighted moving average technique to produce a data layer representing general regional patterns and trends in snow cover. The rating scale used for snow cover reflects the decrease in heat transfer between the atmosphere and ground surface that accompanies an increase in snow depth.

Several studies examining the relationship between the ground thermal regime and snow depth were reviewed to determine the class limits to be used for the rating scale. Nicholson and Granberg (1973) suggest that ground temperatures in Shefferville, Quebec are insulated from changes in air temperature when the snow cover is 75 cm thick while Annersten (1966) suggests 40 cm is sufficient. Harris (1981) gives a critical snow depth of 50 cm for western Canada. Studies done by Stuart et al. (1991) in the Mackenzie Valley indicate that while the insulating effect of snow depends on its density,

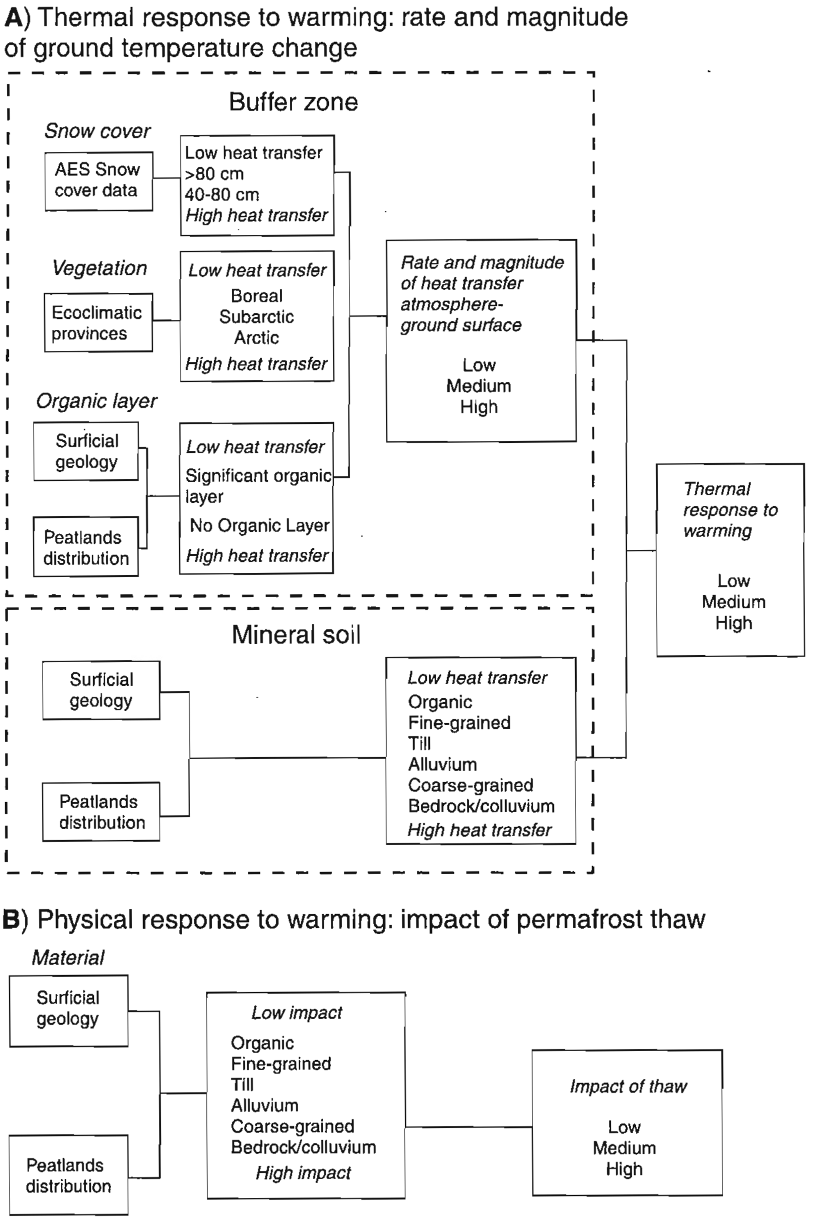

A) Thermal response to warming: rate and magnitude of ground temperature change

B) Physical response to warming: impact of permafrost thaw

Figure 2. ***A)*** *Approach used to classify the thermal response of permafrost to climate warming, based on the buffer layer model of Luthin and Guymon (1974).* ***B)*** *Approach used to classify the physical response of permafrost to warming. AES: Atmospheric Environment Service (of Environment Canada).*

the threshold thickness which they refer to as the thermal damping depth is generally between 40 and 50 cm. Taking these results into account, class limits of 40 and 80 cm were chosen for this study.

Vegetation canopy

The vegetation canopy affects the amount of net radiation by providing shade in summer and modifies the advective heat available for transfer to the soil (Luthin and Guymon, 1974). The link between the atmosphere and the ground is less direct in areas having a vegetation canopy and therefore a reduced response of the ground thermal regime would be expected in these areas compared to those with little vegetation cover.

For this study, the permafrost region was divided into three ecoclimatic provinces (Ecoregions Working Group, 1989), the treeless Arctic province, the Subarctic province consisting of open-canopied conifer woodlands with tundra patches, and the Boreal province consisting of close-canopied forests of conifer or mixed conifer-hardwood. The rate and magnitude of heat transfer between the atmosphere and the ground are thus lower in the Boreal province and higher in the Arctic province.

Organic layer

The presence and nature of organic material or peat are important factors controlling permafrost occurrence in the southern margins of the permafrost zone where mean annual ground temperatures are close to 0°C (Zoltai, 1971; Thie, 1974; Zoltai and Tarnocai, 1975; Vitt et al., 1994). The insulation offered by peat, especially when dry in summer, acts to thermally buffer the ground from the effects of climate warming (Smith, 1988; Woo et al., 1992; Halsey et al., 1995).

The peatlands map of Tarnocai et al. (1995) and the surficial geology map of Fulton (1995) were used to delineate areas having a significant organic cover. For this study, a region was considered to have a significant organic cover if the areal coverage of bogs or fens was greater than 50%. Areas which have a significant organic layer were given a low rating (Fig. 2) because the ground thermal regime is buffered from the thermal effects of climate warming.

Mineral soil

This component considers the transfer of heat through the underlying soil or rock. The rate of heat transfer depends on the thermal conductivity of the underlying material. Sand and bedrock generally have higher thermal conductivity and the thermal regime should respond more rapidly to climate warming where these materials are present compared to areas where organic or fine-grained silt and clay are present. Therefore, organic and fine-grained material were given low ratings (Fig. 2) compared to coarser grained material and bedrock. Information for this layer was extracted from the surficial geology map of Fulton (1995). The grain size of material was considered to be of greater importance than the environment of deposition and therefore units on the surficial geology map were combined to produce those shown in Figure 2.

Map of thermal response to warming

The data layers comprising the buffer layer and mineral soil components were combined to produce a map (Fig. 3) which categorizes areas according to their relative thermal response to climate warming. Areas having a high response are those that have a minimal buffer layer and have surficial materials consisting of coarser grained sediments or bedrock. Areas having a low response are those that have a significant buffer layer and are underlain by organic or fine-grained soils. Both the magnitude and rate of response of the ground temperature to warming will be lower in these latter areas.

Existing ground thermal regime

The likelihood of permafrost thaw also depends on the present ground thermal regime. Permafrost that is currently at temperatures close to 0°C would have a greater potential for thaw than permafrost that is at a much lower temperature, for example, colder than -5°C.

Mean annual near-surface ground temperature for over 400 sites was extracted from a GSC database. An interpolation of the point data was performed to produce the map shown in Figure 1. Ground temperatures can exhibit significant local variation, and the map presented only shows regional trends in near-surface ground temperature within the present permafrost region. The southern boundary of the permafrost region was extracted from the permafrost zone map of Kettles et al. (1997). Within the zone shown to have temperatures greater than -2°C, permafrost is discontinuous and there are significant areas where the ground temperature is above 0°C. This is especially true towards the southern margins of the discontinuous zone, where permafrost is localized, associated mainly with peatlands, and may only underlie about 10% of the land surface. Towards the northern limit of the discontinuous permafrost zone (widespread discontinuous zone), permafrost may underlie up to 90% of the land surface.

Physical response: impact of permafrost thaw

Although the consequences of climate warming in the permafrost region are many and varied, only the effect of thawing on ground stability is considered in this study. Thawing of permafrost which contains little or no ice will have little effect on ground stability and the consequences of warming may be negligible. Melting of ice-rich permafrost however, can lead to a loss of strength and ground instability resulting in thaw settlement, thermokarst development, increased soil creep, and active layer detachment slides (Bennett and French, 1990; Lewkowicz, 1990; Burn and Smith, 1993; Aylsworth and Duk-Rodkin, 1997; Dyke et al., 1997). This can have important implications for infrastructure and landscape stability.

The main factor determining the impact of permafrost thaw is the ice content of the frozen material. The structural ice component consists of pore ice and segregated ice lenses (Heginbottom et al., 1995) and is generally highest in organic and fine-grained material and lowest in coarse-grained sediments and bedrock. In addition to structural ice, ground ice may be in the form of ice wedges or other massive bodies of nearly pure ice.

The approach used to classify the impact of permafrost thaw is outlined in Figure 2. Information obtained from the surficial geology map (Fulton, 1995) and the peatlands map of Tarnocai et al. (1995) was used to produce a map that ranks materials according to their susceptibility to thaw instability. Organic and fine-grained materials which generally have high ice contents are given a higher rank than coarser grained materials or bedrock which generally have low ice contents. The map produced (Fig. 4), classifies areas according to their relative physical response (high, medium, or low), that is, the impact of permafrost thaw. If massive ice is present (Fig. 4 inset), the impact of permafrost thaw will be high even though the surficial materials, and thus the structural ice content, may suggest less impact.

RESPONSE OF PERMAFROST TO WARMING

The maps produced (Fig. 3, 4) show the spatial variation in the thermal response (i.e. rate and magnitude of ground temperature change) and the physical response (i.e. impact of permafrost thaw) to climate warming. Ground temperature

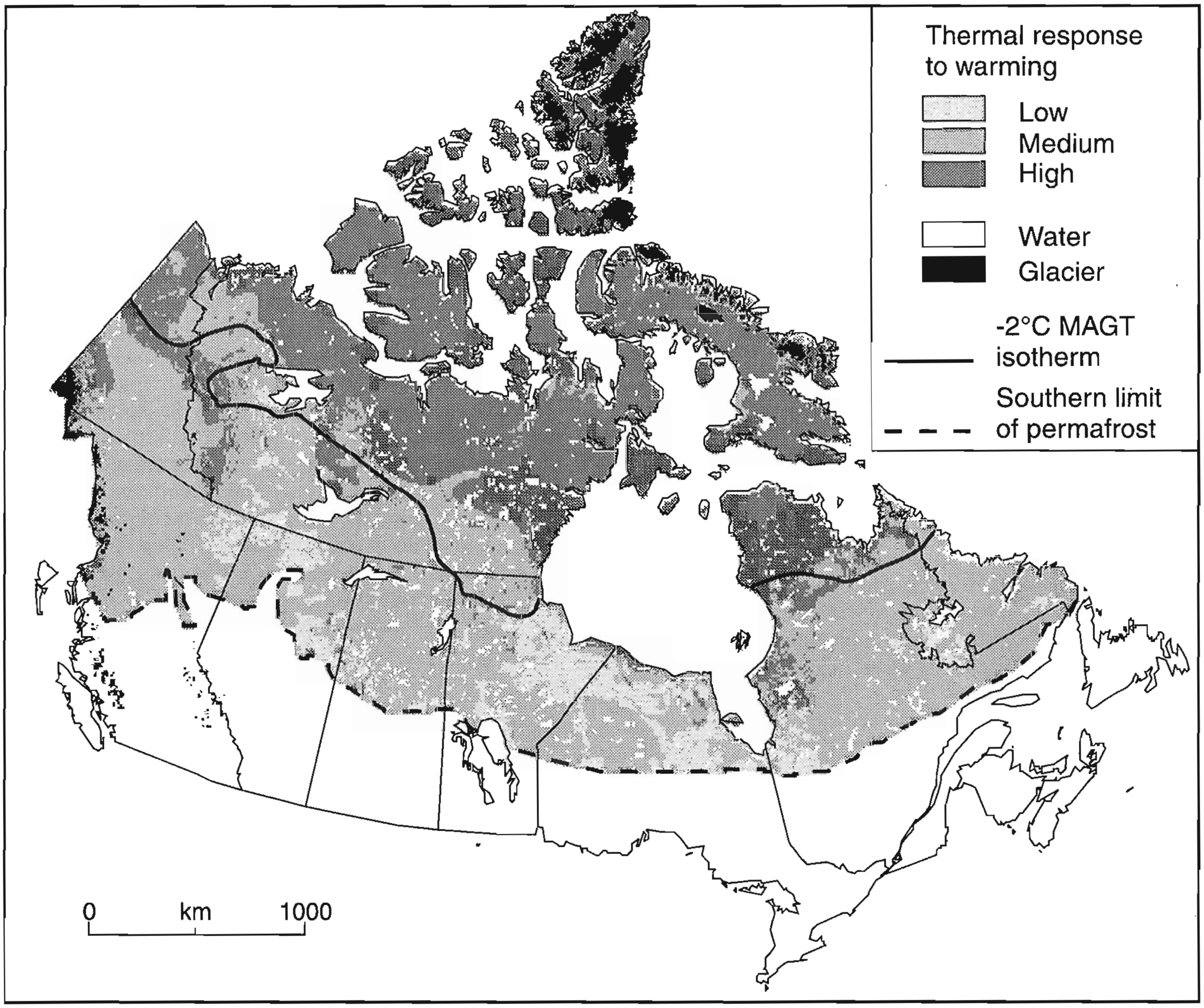

Figure 3. The relative thermal response of permafrost to climate warming. The -2°C mean annual near-surface ground temperature (MAGT) isotherm has been added to indicate areas in which permafrost would likely thaw first. Note: white areas along some coastlines resulted from the transfer of the original digital map to the smaller scale version presented here.

information (Fig. 1) can be used to determine where the permafrost temperature is close to 0°C and therefore delineate areas where the potential for permafrost thaw is the greatest and where the impact of warming may be realized first.

The proportion of the present permafrost region assigned to each of the three categories, shown in Figure 3, representing the thermal response to warming is given in Table 1. More than 90% of the present permafrost region would have a medium to high thermal response to increases in air temperature. Most of this area is located in the northern portion of the permafrost region where there is a limited buffer layer. In the southern portion of the permafrost region where the buffer layer is substantial, the thermal response to warming would generally be low to medium.

The region presently having a mean annual near surface ground temperature greater than -2°C is superimposed on the map in Figure 3. A substantial portion (about 53%) of the present permafrost zone has permafrost at a temperature of

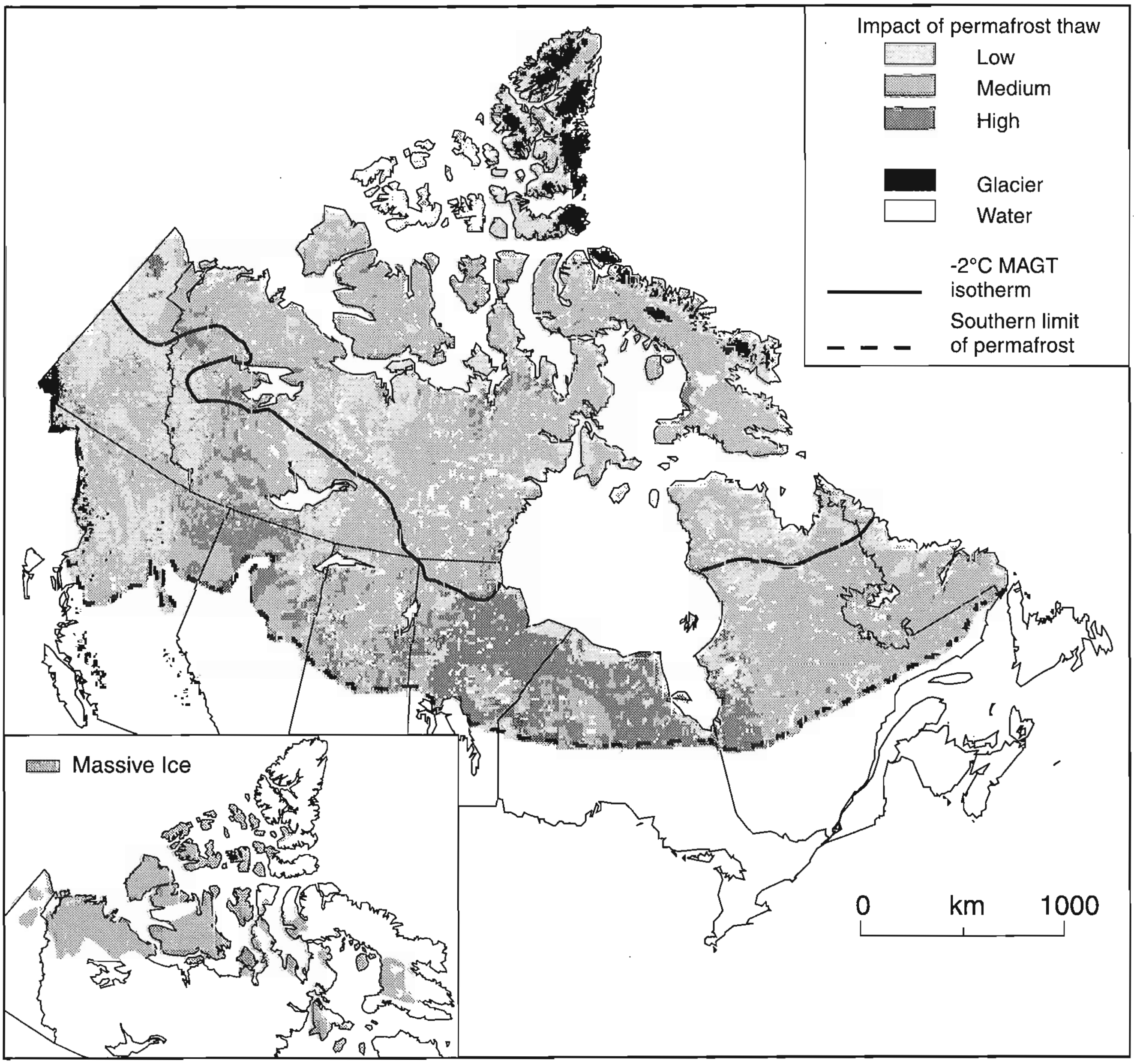

Figure 4. Relative physical response of permafrost (i.e. the impact of thaw) to climate warming. Areas where massive ice is abundant (see inset) were extracted from the permafrost map of Heginbottom et al. (1995). In areas where massive ice is present the impact of thaw will be greater than that indicated on the main map which reflects structural ice content of the surficial materials. Note: white areas along some coastlines resulted from the transfer of the original digital map to the smaller scale version presented here; MAGT: mean annual near-surface ground temperature.

Table 1. Proportion of present permafrost region that would be expected to show a low, medium, or high thermal response to warming. The area calculations consider the entire land mass within the permafrost region (*see* Fig. 1) rather than the actual area underlain by permafrost.

Thermal response to warming	Per cent present permafrost region
Low	8.1
Medium	53
High	38.9

Table 2. Proportion of present permafrost region where low, medium, or high impact of permafrost thaw is expected. The area calculations consider the entire land mass within the permafrost region (*see* Fig. 1) rather than the actual area underlain by permafrost.

Impact of permafrost thaw	Per cent present permafrost region
Low	33.6
Medium	54.2
High	12.2

-2°C or warmer and most of this region would have a medium response to climate warming. The potential for permafrost thaw is greater within this region than areas to the north where, although the permafrost would exhibit a higher thermal response to climate warming, the ground temperatures are much lower.

The impact of any permafrost thaw occurring in response to warming would be high in about 12% (Table 2) of the present permafrost region. Although this area seems small, it is located in the southern portion of the permafrost zone where ground temperatures are warmer than -2°C (Fig. 4). Throughout the region where permafrost is warmer than -2°C the impact of thaw is medium to high. Throughout the rest of the permafrost region where ground temperatures are lower, the impact of permafrost thaw is generally low to medium. However, there are extensive areas where massive ice is present (Fig. 4), and the impact of permafrost thaw in these areas would be more severe.

SUMMARY

Warming and thawing of permafrost due to climate change will result in instabilities in the landscape and changes to engineering behaviour of soils, with direct impacts on northern ecosystems, communities, lifestyles, and infrastructures. An ability to characterize the sensitivity of permafrost to climate warming is important to ensure the integrity of existing northern infrastructures, to adequately design future developments, and to assess and adapt to climate change impacts on the natural environment.

The results presented here represent a first attempt to map the characteristics of the response of permafrost in Canada to climate warming. The major factors influencing the thermal response of permafrost were considered, and a map showing the spatial distribution of the relative thermal response was produced. Ground temperature information was superimposed on this map to highlight areas where permafrost is near the melting point and has the highest potential for thaw. The results suggest that the potential for permafrost thaw is high in a significant portion of the present permafrost region. Combining the thermal response to warming and the present ground thermal regime into one index is the next logical step in mapping the potential for permafrost thaw.

This study also considered the impact of permafrost thaw in response to climate warming. In the zone where permafrost is likely to thaw first, the impact of permafrost thaw on ground stability is expected to be high over a significant area.

The sensitivity of permafrost to climate warming consists of two components, the potential for permafrost thaw and the impact of thaw. Once the final versions of these two components are refined, the study will move to its next stage: a map combining these two components into a single sensitivity index.

ACKNOWLEDGMENTS

Digital snow cover data were provided by Ross Brown of the Atmospheric Environment Service. J.A. Heginbottom and I. Kettles allowed access to their digital permafrost and peatlands maps. Andrew Moore provided digital data layers in a compatible format. The many helpful discussions with Stephen Wolfe are greatly appreciated.

REFERENCES

Annersten, L.J.
1966: Interaction between surface cover and permafrost; Biuletyn periglacjalny, v. 15, p. 27-33.

Aylsworth, J.M. and Duk-Rodkin, A.
1997: Landslides and permafrost in the Mackenzie Valley; *in* Mackenzie Basin Impact Study (MBIS), Final Report, Environmental Adaptation Research Group, Atmospheric Environment Service, Environment Canada, p. 118-122.

Bennett, L.P. and French, H.M.
1990: In situ permafrost creep, Melville Island, and implications for global change; *in* Proceedings of the Fifth Canadian Permafrost Conference, Université Laval, Quebec, p. 119-123.

Berry, M.O.
1991: Recent temperature trends in Canada; The Operational Geographer, v. 9, p. 9-13.

Braaten, R.
1996: An updated Canadian snow depth database; Internal Report, Climate Processes and Earth Observation Division, Atmospheric Environment Service, Environment Canada, 25 p.

Burn, C.R. and Smith, M.W.
1993: Issues in Canadian permafrost research; Progress in Physical Geography, v. 17, p. 156-172.

Dyke, L.D., Aylsworth, J.M., Burgess, M.M., Nixon, F.M. and Wright, F.
1997: Permafrost in the Mackenzie Basin, its influences on land-altering processes, and its relationship to climate change; *in* Mackenzie Basin Impact Study (MBIS), Final Report, Environmental Adaptation Research Group, Atmospheric Environment Service, Environment Canada, p. 112-117.

Ecoregions Working Group
1989: Ecoclimatic regions of Canada; Environment Canada, Ecological Land Classifications Series, No. 23, 118 p.

Environmental Conservation Service Task Force
1981: Ecological land survey guidelines for environmental impact analysis; Environment Canada, Ecological Land Classification Series, No. 13, 42 p,

Fulton, R.J.
1995: Surficial materials of Canada; Geological Survey of Canada, Map 1880A, scale 1:5 000 000.

Halsey, L.A., Vitt, D.H., and Zoltai, S.C.
1995: Disequilibrium response of permafrost in boreal continental western Canada to climate change; Climate Change, v. 30, p. 57-73.

Harris, S.A.
1981: Climatic relationships of permafrost zones in areas of low winter snow-cover; Arctic, v. 34, p.64-70.

Heginbottom, J.A., Dubreuil, M-A., and Harker, P.A.
1995: Canada - Permafrost; National Atlas of Canada, Natural Resources of Canada, Ottawa (MCR 4177).

Kettles, I.M., Tarnocai, C., and Bauke, S.D.
1997: Predicted permafrost distribution in Canada under a climate warming scenario; *in* Current Research 1997-E; Geological Survey of Canada, p. 109-115.

Lewkowicz, A.G.
1990: Morphology, frequency and magnitude of active-layer detachment slides, Fosheim Peninsula, Ellesmere Island, N.W.T.; *in* Proceedings of the Fifth Canadian Permafrost Conference, Université Laval, Quebec, p. 111-118.

Luthin, J.N. and Guymon, G.L.
1974: Soil moisture-vegetation-temperature relationships in central Alaska; Journal of Hydrology, v. 23, p. 233-246.

Maxwell, B.
1997: Responding to global climate change in Canada's Arctic; Volume II of the Canada Country Study: Climate Impacts and Adaptation, Environmental Adaptation Research Group, Atmospheric Environment Service, Environment Canada, 82 p.

Nicholson, F.H. and Granberg, H.B.
1973: Permafrost and snow cover relationships near Schefferville; *in* Proceedings of the Second International Conference on Permafrost, North American Contribution, p. 151-158.

Smith, M.W.
1988: The significance of climatic change for the permafrost environment; *in* Proceedings of the Fifth International Conference on Permafrost, Trondheim Norway, v. 3, p. 18-23.

Stuart, R.A., Etkin, D.A., and Judge, A.S.
1991: Recent observations of air temperature and snow depth in the Mackenzie Valley area and their implications on the stability of permafrost layers; Canadian Climate Centre Report No. 91-2, Atmospheric Environment Service, Environment Canada, 178 p.

Tarnocai, C., Kettles, I.M., and Ballard, M.
1995: Peatlands of Canada; Geological Survey of Canada, Open File 3152, scale 1:6 000 000.

Thie, J.
1974: Distribution and thawing of permafrost in the southern part of the discontinuous permafrost zone in Manitoba; Arctic, v. 27, p. 189-200.

Vitt, D.H., Halsey, L.A., and Zoltai, S.C.
1994: The bog landforms of continental western Canada in relation to climate and permafrost patterns; Arctic and Alpine Research, v. 26, p. 1-13.

Woo, M., Lewkowicz, A.G., and Rouse, W.R.
1992: Response of the Canadian permafrost environment to climate change; Physical Geography, v. 13, p. 287-317.

Zoltai, S.C.
1971: Southern limit of permafrost features in peat landforms, Manitoba and Saskatchewan; Geological Association of Canada, Special Paper #9, p. 305-310.

Zoltai, S.C. and Tarnocai, C.
1975: Perennially frozen peatlands in the western arctic and subarctic of Canada; Canadian Journal Earth Sciences, v. 12, p. 28-43.

Geological Survey of Canada projects 940009, 950035, and 980003

Investigation of automated particle size analysis techniques

P.J. Lindsay, J.B. Percival[1], A.C. Tsai[1], and M.H.M. Wygergangs
Terrain Sciences Division, Ottawa

Lindsay, P.J., Percival, J.B., Tsai, A.C., and Wygergangs, M.H.M., 1998: Investigation of automated particle size analysis techniques; in *Current Research 1998-E; Geological Survey of Canada, p. 173–182.*

Abstract: The behaviour and properties of particles is dependent upon their morphology, size, and size distribution. Particle morphology such as shape and texture can influence bulk physical properties. The traditional method to determine particle size distribution of sediments and soils at the GSC (Sedimentology Laboratory) has been sieve and pipette analysis. Pipette analysis is a time-consuming method with a low turnover of samples. In 1990, a laser particle-size analyzer was purchased to increase productivity. This study compares the laser particle-size analyzer to the classical pipette as an effective routine method for particle size analysis. Other instrumental methods employed in the GSC and at another federal government department are also compared. The methods focus primarily on the composite analysis of fine-grained, amorphous Si materials (fly ash) from thermal electrical generating plants. The instrumental techniques offer comparable grain size information to pipette analysis for the silt- and clay-size ranges. Thus, any one of these instrumental techniques can be recommended for grain size analysis of fine (silt and clay) particles.

Résumé : Le comportement et les propriétés des particules varient selon leur morphologie, leur dimension et leur répartition granulométrique. La morphologie des particules, telle que la forme et la texture, peuvent avoir une incidence sur les propriétés physiques en général. La méthode classique utilisée au Laboratoire de sédimentologie de la Commission géologique du Canada pour déterminer la répartition granulométrique des sédiments et des sols est l'analyse par tamisage et à la pipette. La méthode à la pipette prend beaucoup de temps et porte sur un volume restreint d'échantillons. En 1990, le Laboratoire a fait l'acquisition d'un analyseur granulométrique à laser afin d'accroître sa productivité. La présente étude fait une comparaison entre cet analyseur et la méthode classique à la pipette comme méthode efficace utilisée sur une base régulière pour l'exécution d'analyses granulométriques. La comparaison porte aussi sur d'autres méthodes instrumentales utilisées à la Commission et dans d'autres ministères du gouvernement fédéral. Ces méthodes mettent prioritairement l'accent sur l'analyse combinée de matériaux siliceux amorphes à grain fin (cendres volantes) prélevés dans des centrales thermiques. En ce qui à trait à l'étude granulométrique des particules de la taille du silt et de l'argile, les données fournies par les techniques instrumentales sont comparables à celles de la méthode à la pipette. Par conséquent, nous recommandons l'une ou l'autre de ces techniques pour effectuer l'analyse granulométrique de particules à grain fin (silt et argile).

---

[1] Mineral Resources Division, Ottawa

INTRODUCTION

The behaviour and properties of particles is dependent upon their morphology, size, and size distribution. Particle morphology such as shape and texture influence bulk physical properties including bulk density, porosity, permeability, and cohesion (Allen, 1997a). Particle size distribution can reflect mineralogical partitioning and thus is an indicator of variation in the physical and chemical properties of sediments (DiLabio, 1995; Shilts, 1995). Spatial and temporal variability of trace element concentrations in sediments may be attributed, in part, to particle size (Jones and Bowser, 1978; Jenne et al., 1980; Förstner and Wittmann, 1981; de Groot et al., 1982; Howoritz and Elrick, 1987; Howoritz et al., 1989; Barbanti and Bothner, 1993). For example, Shilts (1995) noted that the clay-size fraction (<2 µm) not only preferentially adsorbs contaminants due to its high cation exchange capacity, but is the first to yield anthropogenically derived or naturally occurring trace elements as a result of sediment disturbance. Thus, quantitative analysis of the size distribution of particles is not only important in sediment transport studies, stratigraphic correlations, mapping, assessing modern and past geological environments, geotechnical studies, and surface (kinetic) reactions (Lewis, 1984; McCave and Syvitski, 1991), but also in geochemical studies.

Traditionally, the sedimentology laboratory of the GSC has employed classical methods to determine the particle size distribution of materials. In 1990, a Galai®(formally distributed as a Brinkman PSA) laser particle-size analyzer was purchased. The introduction of this instrument allowed for an increase in the productivity of particle size determinations. This paper will demonstrate that the laser method of analysis is effective as a **routine** method for particle size analysis. In addition, the classical pipette method and laser method are compared to other instrumental methods used in various labs in the GSC and another federal government department.

PARTICLE SIZE ANALYSIS

Particle size distribution is the percentage, by mass, volume, or number, of particles in a range of specific sizes. The methods used to determine particle size distribution are classified as 'classical' (i.e. sieve and pipette), and 'instrumental' (i.e. electrical sensing zone, X-ray sedimentation, laser, and image analysis). The instrumental methods are generally faster and considered as reproducible as the classical methods, but may also require extensive sample preparation (Percival and Lindsay, 1997).

McCave and Syvitski (1991) suggested that the accuracy of particle size analysis is dependent upon the definition of the size being determined. These include the following: 1) projected area size by image analysis, 2) intermediate diameter size by sieve, 3) volume size by electronic sensor counter, or 4) quartz equivalent spherical sedimentation diameter by pipette method. The selection of a particular technique is not as critical as standardization of procedures and that all samples to be compared should be analyzed in precisely the same manner (Lewis, 1984). The use of standard reference material for particle size analysis also requires confirmation of a given methodology as being close to true accuracy (McCave and Syvitski, 1991). Thus, precision, not accuracy, becomes an important consideration when choosing a method that will reflect the nature of an investigation.

An important consideration when doing particle size analysis is the total error. Allen (1997a) indicated that total error may arise from 1) incorrect sampling, 2) instrumental limitations, 3) improper procedure, and 4) operator error. To elaborate, the quality of the data is highly dependent upon how **representative** the sample is of the original bulk material. Instrumental limitations can include applicable size range, ease of operation, and assumptions of the definition of size. Most analyzers require that particles be in suspension during measurement. If particles are inadequately dispersed, errors will occur. Instruments also require proper set-up and good calibration before measurements are made.

METHODS OF ANALYSIS

Sample selection and preparation

Three fly ash samples (GEN-1-FA, KPHTR-1-FA, WATR-1-FA) from thermal power generating plants in western Canada were selected. These samples have small grain size (nominally less than 20 µm) and are composed of amorphous spherical Si grains with minor to trace amounts of Fe-, Ca-, and Na-rich spheres (K.A.B. Hendry, J.B. Percival, and A.C. Tsai, unpub. internal report, Mineralogy and Chemistry Subdivision, Mineral Resources Division, 1994). They may contain trace amounts of base metals. A homogenous split was suspended in a 0.1% sodium meta-phosphate solution (for dispersion) at a ratio of 2 g sample per 100 mL solution. The suspensions were placed in an ultrasonic bath (Branson EMLX 30-12, 25 kHz) for 10 min to disperse the particles. No sieving was performed to remove any coarse particles at this stage.

Each of the three samples was submitted to various laboratories using a variety of instrumental methods of analyses (Table 1). Particle size analysis by pipette and laser (i.e. Galai®) methods were carried out in the GSC Sedimentology Laboratory (Terrain Sciences Division), and by image analysis in the GSC Microbeam Laboratory (Mineral Resources Division). Other laboratories remain anonymous. Each laboratory was instructed to hand shake the suspension before extraction of a suitable aliquot for determination. If required, the suspension could be diluted with distilled water. Five aliquots from each sample were analyzed to test reproducibility. Each laboratory was also instructed to calibrate their instruments prior to analyses. Theory and methods of analyses are described below.

Table 1. Types of instruments used in determining particle size distribution of fly ash samples.

Method no.	Instrument/technique	Theory of operation	Type of results Volume	Area	Number
I	Pipette analysis	Settling velocity	x		
II	Galai	Laser - time of transition	x	x	x
III	Coulter Counter	Electrical sensing zone	x		
IV	Fritsch - Analyzette 22	Laser diffraction	x		
V	Granulometre HR 850	Laser diffraction	x		
VI	Scanning Electron Microscope	Image analysis	x	x	x

CLASSICAL METHOD

Pipette method

Theory

The pipette method (method I) of analysis is a sedimentation procedure using pipette sampling of a dispersed sample in solution, at controlled depths and times, based on Stoke's Law (Day, 1965). It is assumed that particles are spherical with a density of quartz and settle independently with no hindered settling effects at a constant temperature (McCave and Syvitski, 1991).

Procedure

In this analysis, 50 g of presieved (<0.063 mm) sample was dispersed in a 5% $(NaPO_3)_6$ solution and brought to a constant volume in a 1 L graduated cylinder. The suspension was agitated to ensure complete mixing. A pipette was then carefully inserted to a 10 cm depth and 25 mL aliquots of suspension were withdrawn at predetermined times (Day, 1965; Jackson, 1979; Lewis, 1984). The aliquots were placed in a preweighed container and set in an oven to dry at 105°C for 24 h. The weight of the dried material was determined and corrected for weight of the dissolved salts (i.e. $(NaPO_3)_6$).

Results were tabulated as wt% for specified size ranges, listed as either millimetre or phi units. From these results, combined with sieve analysis of particles larger than 0.063 mm and smaller than 2 mm, the per cent sand, silt, and clay can be calculated. Relevant statistics include mean, standard deviation, skewness, and kurtosis in phi (ϕ) values. Mean values have been converted into micrometres (μm).

INSTRUMENTAL METHODS

Laser – time of transition theory (Galai PSA 2010®)

Theory

The Galai Particle Size Analyzer® (formerly distributed by Brinkmann Instruments; method II) measures the diameter of a particle directly, using the "time of transition theory" (Brinkman Instruments Manual). This direct measurement avoids sources of error inherent in many techniques that are dependant on secondary correlations, the index of refraction, or Brownian motion, etc. A laser scans the sample measurement field (e.g. sample cell) at a fixed velocity. The time of transit of the laser beam, across a particle, multiplied by the laser velocity, gives a displacement which is equal to the diameter of the particle:

$$d = T \times V \qquad (1)$$

where d = particle diameter (mm), T = time of transit across a particle (s), and V = velocity of laser beam (mm/s). Particles are introduced into the sample cell and are scanned by the laser beam producing a voltage pulse in a photodiode mounted behind the measurement area. The width of the pulse represents the time of interaction with a particle and is related to its size; the rise time is related to the degree of focus such that it is shortest for particles in the laser's focal plane (Walker and Reynolds, 1991). Particles out of focus, or those with long pulses, are disregarded.

A separate feature of this instrument is a video camera mounted in the measurement area at 90 degrees to the laser beam. It captures visual images of the particles and takes 'still' pictures every three seconds, while they are in dynamic flow. This visual representation gives direct information on particle shapes and aggregates, and may be helpful in identifying particulate matter that have 'signature' shapes (i.e. certain diatoms or phyllosilicate minerals).

Procedure

As standard procedure, all samples are wet-sieved through a 0.063 mm sieve to determine if any appreciable amount of coarse material exists and if these data must be incorporated into the calculations. Samples were suspended in a dilute solution and pumped by peristaltic action from a reservoir through the sample (flow-through) cell and back to the reservoir. Data accumulation continued until the confidence level (established before the analysis) was reached in each grain size range. Relevant statistics include mean, standard deviation, and median.

Electrical sensing zone (Coulter Counter®)

Theory

The Coulter (method III) technique is based on the electrical sensing zone principle. It is dependent on particles being suspended in an electrolyte and passing through a small orifice between electrodes. The volume of electrolyte displaced by the particles is proportional to the volume of the particles, and corresponds to the change in electrical resistivity measured by the electrodes (Haley and Joyce, 1984; McCave and Syvitski, 1991). The change in resistivity due to a particle of a given diameter is:

$$\Delta R=[(8r_f d)/(3\ D^4)][1+4/5(d/D)^2 + 24/35(d/D)4^4 \ldots] \quad (2)$$

where r_f = resistivity of the fluid (Ω), D = aperture diameter (mm), and d = particle diameter (mm). The technique is generally valid for particle sizes in a 20:1 ratio corresponding to between 2% and 40% of the effective aperture diameter. Particles finer than 2% of the aperture diameter are not detected and must be analyzed using a smaller aperture whereas those larger than 40% of the aperture size must be removed to prevent blockage of the aperture. Multiple apertures are required if the sediment samples have a broad size distribution and the data can be blended.

Procedure

The sample was suspended in an electrolyte solution of NaCl. A 100 μL aliquot was drawn through a 50 μm aperture under vacuum with a current of 3200 μA. Measurement of the height of the voltage pulse was used to calculate the volume of the particles and the number of pulses were used to calculate the number of particles and their size range. Results are reported as cumulative number and volume per millilitre of electrolyte. Relevant statistics include mean, standard deviation, and median.

Laser diffraction spectroscopy

Theory

Laser diffraction analysis (methods IV and V) is based on the Fraunhofer theory, which states that the intensity of light scattered by a particle is directly proportional to the particle size, assuming particles are spherical (McCave et al., 1986). Large particles scatter light at high intensities through low angles, and small particles scatter light at low intensities through high angles (Walker and Reynolds, 1991). Below 0.007 mm, particles do not diffract light in the manner required for the application of the Fraunhofer theory because their diameter approaches that of the wavelength of light (McCave et al., 1986; de Boer et al., 1987). For particles in this size range, the mode of scattering is termed Mie scattering and depends upon particle size and differences in the refractive indices (Hayley and Joyce, 1984). Combining these two scattering modes permits a particle size range from clay through the sand size. Instrument scattering inversion software compensates for 'other' than Fraunhofer scattering.

Procedure

For the Fritsch-Analyzette 22® (method IV) and the Granulometre HR 850® (method V) the procedure is generalized as follows. Particles were circulated through a cell and illuminated by a beam of monochromatic light focused onto a multi-element detector which senses the distribution of the scattered light intensity. A series of lenses and proprietary filters, focuses the undiffracted light at the centre of the detector leaving only the surrounding diffraction pattern (McCave et al., 1986). This angular distribution of light intensity is used to calculate size distributions. Relevant statistics provided include mean, standard deviation, median, skewness, and kurtosis for method IV, and median for method V.

Image analysis

Theory

Image analysis is used to characterize, classify, compare, and calculate morphological measurements of features in images (Petruk, 1989; Walker and LeCheminant, 1989). Scanning electron microscope- (SEM) based image analysis entails digital capture of specimen images (or 'fields') by a standalone image analyzer (e.g. PC-based with image analysis software), or an integrated energy dispersive spectroscopy (EDS) and image analysis system such as the Oxford/Link eXL II. The SEM contrast and brightness are set for sufficient grey level separation between the background and the features of interest. The analyzer's grey level discriminators are set such that feature edges can be detected.

With each found feature, morphological data can be acquired. Feature area can be calculated by multiplying the number of pixels representing a feature and the area of each pixel. A 'Feret diameter' (also called 'projected diameter' or 'caliper diameter') can also be measured. A Feret diameter is the right angle distance between two parallel tangents taken on opposite sides of a feature (Allen, 1997b). Typically, multiple Feret diameters are collected at regularly spaced angles to obtain an adequate description of feature shape. From these measurements, mean Feret diameter, orientation, aspect ratio, and other measurements can be derived. Features can be classified according to any of these parameters. If chemical data are collected using the EDS analyzer, features can also be chemically or mineralogically classified.

Procedure

Coal fly ash stored in water was hand agitated and ultrasonically agitated to produce a homogeneous suspension. Approximately 3 mL of this was extracted and ultrasonically mixed with 500 mL of distilled water. A small quantity of Spray Nine® was added to mitigate agglomeration. To achieve a particle spacing of 15 μm, approximately 100 mL of suspension was wet-sieved through a 0.4 μm polycarbonate membrane.

Prepared fly ash samples were loaded into a Leica Cambridge S360 Stereoscan SEM fitted with an Oxford/Link eXL II analyzer. While in the backscattered electron imaging mode, brightness and contrast were set to produce adequate contrast between the fly ash and the membranes. A random field was selected but if agglomerates, touching particles, or very few particles, were observed, another field was selected. The analyzer digitally captured the field. A brightness detection threshold was set, 32 Feret projections were selected and a feature scan was conducted. A new field was then selected, captured, and scanned and repeated until a statistically adequate number of particles were collected. The Feret diameter was recalculated as micrometres (µm^3) using the formula for a sphere to enable comparison with other data sets.

RESULTS AND DISCUSSION

Summary statistics of particle size analyses for each sample, GEN-1-FA, KPHTR-1-FA and WATR-1-FA, from each of the six methods (Table 1) are presented in Tables 2 to 4. Each of the methods produced data in a different format which required separate manipulations to compare data sets. For example, data from methods I (pipette analysis) and IV (laser diffraction) were provided in phi units and only average values were recast into equivalent micrometres; the Feret diameters measured using method VI (image analysis) were converted into volume measurements. In addition, the data sets did not necessarily encompass the same grain size range. For example, methods III (electrical sensing) and IV did not include grains greater than coarse silt (>44 µm and 31 µm, respectively). Precision

Table 2. Summary of particle size distribution (in µm, volume-based) statistics for sample GEN-1-FA. Data in brackets are in phi (ϕ) units or based on phi units.

Method no.	Mean	Std. dev.	Median	Skewness	Kurtosis
I (Φ)	4.74 (7.72)	(1.73)		(0.67)	(3.51)
II	10.19	11.14	6.18		
	9.01	9.63	6.09		
	12.05	12.54	6.73		
	8.46	7.41	5.71		
	12.65	14.40	6.42		
Avg.	**10.47**	**11.02**	**6.23**		
III	1.97	0.99	1.84		
	2.00	1.04	1.85		
	1.92	0.96	1.78		
	1.98	1.05	1.03		
	1.98	1.10	1.79		
	4.05	5.90	3.47		
Avg.	**2.39**	**2.01**	**1.98**		
IV (Φ)	(8.01)	(1.44)	(8.14)	(0.15)	(0.83)
	(7.73)	(1.51)	(7.91)	(0.19)	(0.85)
	(7.91)	(1.45)	(8.05)	(0.15)	(0.83)
	(7.83)	(1.50)	(7.97)	(0.15)	(0.84)
	(7.88)	(1.45)	(8.03)	(0.17)	(0.83)
Avg.	**4.28 (7.87)**	**(1.47)**	**(8.02)**	**(0.16)**	**(0.84)**
V			4.34		
			4.36		
			4.33		
			4.38		
			4.34		
Avg.			**4.35**		
VI [1]	4.49	8.72	1.32	3.55	14.15

[1] Data based on excluding all sand grains > 0.063 mm (63 µm).
I = Pipette; II = Galai; III = Coulter Counter; IV = Fritsch;
V = Granulometre ; VI = SEM.

Table 3. Summary of particle size distribution (in µm, volume-based) statistics for sample KPHTR-1-FA. Data in brackets are in phi (ϕ) units or based in phi units.

Method no.	Mean	Std. dev.	Median	Skewness	Kurtosis
I (Φ)	8.49 (6.88)	(2.18)		(0.53)	(3.04)
II	2.35	1.64	8.60		
	2.46	1.75	10.86		
	2.46	1.74	10.37		
	2.48	1.75	10.49		
	2.42	1.71	11.59		
Avg.	**2.43**	**1.72**	**10.38**		
III	1.76	0.82	1.62		
	1.73	0.78	1.58		
	1.73	0.8	1.58		
	1.76	0.84	1.60		
	1.76	0.88	1.58		
Avg.	**1.75**	**0.82**	**1.59**		
IV (Φ)	(7.32)	(1.65)	(6.80)	(0.44)	(0.83)
	(7.13)	(1.80)	(6.63)	(0.40)	(0.78)
	(7.18)	(1.78)	(6.72)	(0.37)	(0.77)
	(7.32)	(1.75)	(6.91)	(0.34)	(0.77)
	(7.13)	(1.79)	(6.66)	(0.38)	(0.77)
	(7.25)	(1.76)	(6.81)	(0.36)	(0.77)
Avg.	**6.71 (7.22)**	**(1.75)**	**9.29 (6.75)**	**(0.38)**	**(0.78)**
V			6.07		
			6.06		
			6.02		
			6.11		
			6.13		
Avg.			**6.08**		
VI [1]	1.97	5.20	0.28	4.96	31.45

[1] Data based on excluding all sand grains > 0.063 mm (63 µm).
I = Pipette; II = Galai; III = Coulter Counter; IV = Fritsch;
V = Granulometre ; VI = SEM.

Table 4. Summary of particle size distribution (in µm, volume-based) statistics for sample WATR-1-FA. Data in brackets are in phi (ϕ) units or based in phi units.

Method no.	Mean	Std. dev.	Median	Skewness	Kurtosis
I (Φ)	2.61 (8.58)	(1.86)		(0.33)	(2.51)
II	1.53	0.91	4.43		
	1.52	0.90	4.27		
	1.54	0.92	4.33		
	1.56?	0.95	4.43		
	1.53	0.91	4.38		
Avg.	**1.54**	**0.92**	**4.37**		
III	1.64	0.64	1.51		
	1.70	0.67	1.52		
	1.66	0.67	1.53		
	1.67	0.70	1.54		
	1.67	0.68	1.53		
Avg.	**1.67**	**0.67**	**1.53**		
IV (Φ)	(9.16)	(1.06)	(9.18)	(-0.001)	(0.93)
	(9.16)	(1.09)	(9.18)	(-0.005)	(0.93)
	(9.21)	(1.03)	(9.21)	(0.02)	(0.93)
	(9.24)	(0.99)	(9.23)	(0.04)	(0.93)
	(9.23)	(0.99)	(9.21)	(0.04)	(0.93)
Avg.	**1.72 (9.18)**	**(1.03)**	**1.7 (9.20)**	**(0.02)**	**(0.93)**
V			2.05		
			2.05		
			2.06		
			2.06		
			2.04		
Avg.			**2.05**		
VI [1]	2.49	6.41	0.49	5.03	29.31

[1] Data based on excluding all sand grains > 0.063 mm (63 µm).
I = Pipette; II = Galai; III = Coulter Counter; IV = Fritsch; V = Granulometre ; VI = SEM.

and accuracy of the replicate analyses has not been assessed in this report. More detailed work will be required to fully analyze the data sets produced by the various instruments.

Sample GEN-1-FA contains 1.5% sand-, 87.1% silt-, and 10.4% clay-size material based on sieve and pipette analysis (method I). The mean grain size has been estimated at 4.7 µm (7.72 phi; Table 2). The small amount of sand-sized material probably does not affect the overall mean grain size to any great extent. This grain size is comparable to that obtained by methods IV and VI, greater than data from methods II and III. No mean grain size is available for method V. If the median grain size of method V is compared to other methods it is greater than methods III and VI, but less than method II. The skewness and kurtosis data indicate a tendency towards very fine-grained size, in the clay-size range. This is especially valid for method VI (SEM) which shows that the median grain size is only 1.3 µm. Typical features measured by method VI are shown in Figure 1a. The grains are extremely spherical and clay-size (<2 µm). One of the larger, irregularly-shaped grains observed is shown in Figure 1b. If these larger grains are included in the calculation, then the mean grain size for GEN-1-FA becomes 17 µm with a extremely high degree of skewness and kurtosis (Table 5).

Sample KPHTR-1-FA data are given in Table 3. It contains 8.4% sand-, 80.9% silt-, and 10.7% clay-size material based on combined sieve and pipette analysis (method I). The mean grain size has been estimated at 8.5 µm (6.88 phi). The larger proportion of sand-sized material probably does affect the overall mean grain size, however, for method V it was difficult to obtain a representative sample due to fast settling of the heavier particles. The mean grain size obtained from method I is comparable to that obtained by methods IV, and is greater than data from methods II, III, and VI. If the median grain size of method V is compared to other methods it is again greater than methods III and VI but less than II and IV. The skewness and kurtosis data also indicate a tendency towards very fine-grained size, in the clay-size range, especially for method VI which shows a median grain size of only 0.3 µm. Typical features measured by method VI are shown in Figures 1c and 1d. The grains are spherical and fine-grained, however, a few grains can be irregularly shaped. Note the sphere in Figure 1d containing a group of smaller spheres. It is unlikely that this feature was measured during the collection of the data as it is touching another grain. If all grains measured are included in the statistical calculations, then the mean grain size for KPHTR-1-FA becomes 112 µm with a very high degree of skewness and kurtosis (Table 5). Note that the maximum grain size measured (based on one grain) is an order of magnitude larger than for the other two samples.

Sample WATR-1-FA contains 1.1% sand-, 75.1% silt-, and 23.8% clay-size material from sieve and pipette analysis (method I). The mean grain size has been estimated at 2.6 µm (8.58 phi). The small amount of sand-sized material probably does not affect the overall mean grain size. This mean grain size is comparable to that obtained by method VI and is greater than data from the other methods (except method V). If the median grain size of method V is compared to other methods it is only slightly greater than methods III and VI, greater than method VI, but less than method II. The skewness and kurtosis data indicate a tendency towards very fine-grained size, in the clay-size range. This is especially true for method VI which shows that the median grain size is only 0.5 µm. Typical features measured by method VI are shown in Figure 1e. The grains are extremely spherical and fine grained; irregularly shaped grains have been observed as well (Fig. 1f). If all grains measured are included in the calculation, then the mean grain size for WATR-1-FA becomes 15 µm with a high degree of skewness and kurtosis (Table 5).

Cumulative per cent size distributions for each of the three samples are shown in Figures 2 to 4. In general, methods I through V show a similar, slightly flattened S-shaped distribution. The flatness suggests poor sorting of the clay- and silt-sized material. In contrast, method VI shows a flatter distribution with a higher percentage of clay-sized (<2 μm) grains.

The grain size distribution is more uniform for methods I through V for sample GEN-1-FA (Fig. 2) relative to the other two samples. In all cases, method II shows the lowest cumulative per cent clay-sized material. Methods I and III show similar distributions for samples GEN-1-FA and WATR-1-FA but not for sample KPHTR-1-FA. Methods IV and V tend to show a finer grained distribution relative to methods I through III.

Method I (pipette) has drawbacks because of inherent sources of error in the methodology and its turnaround time, but it is still used in many laboratories where the cost of the instrumental methods is prohibitive. In addition to the capital

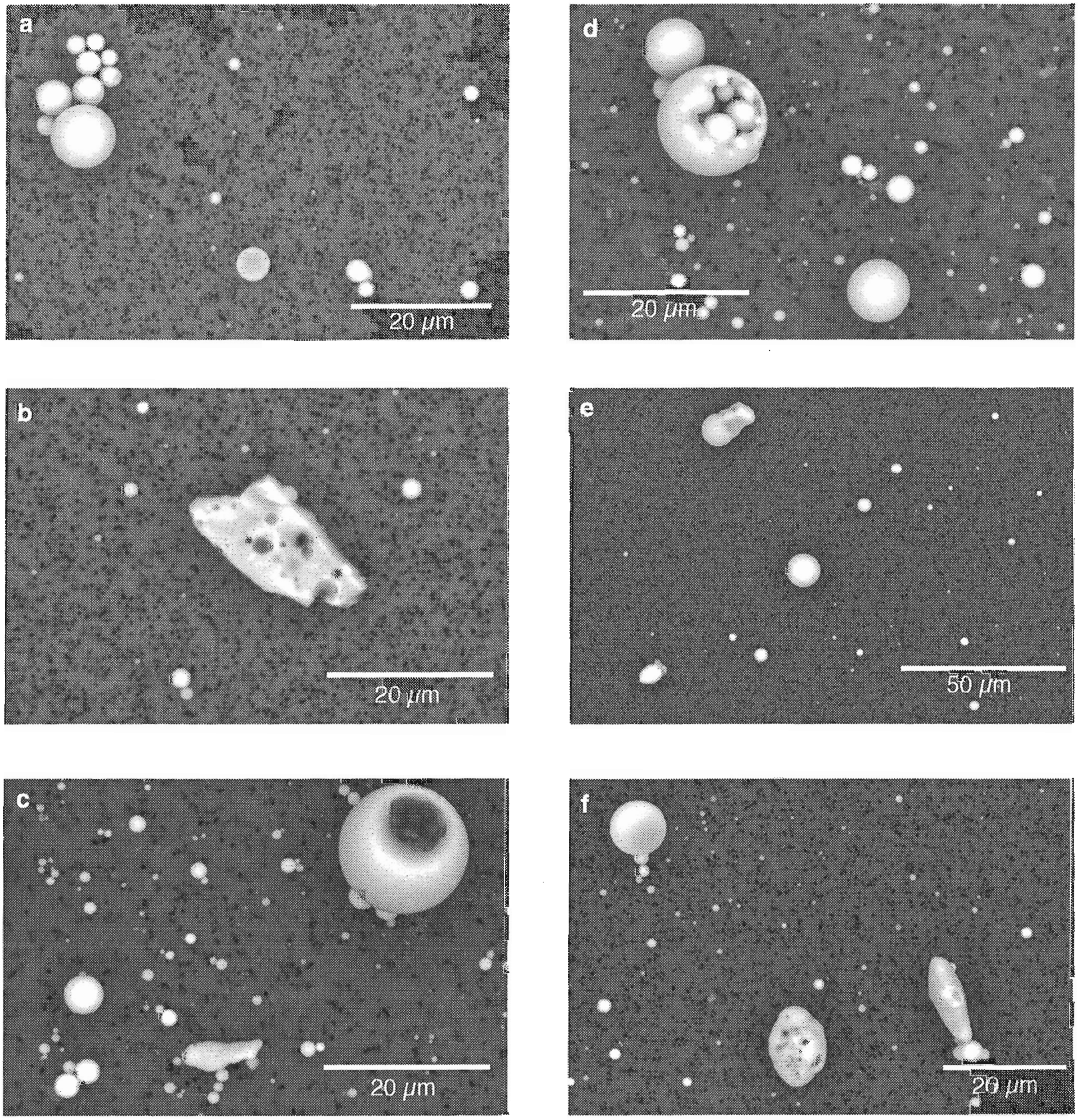

Figure 1. *Representative SEM photomicrographs of amorphous Si spheres in samples **a)** GEN-1-FA, **b)** GEN-1-FA, **c)** KPHTR-1-FA, **d)** KPHTR-1-FA, **e)** WATR-1-FA, and **f)** WATR-1-FA.*

Table 5. Summary statistics for SEM-based image analysis data in cubic micrometres (μm^3).

Sample no.	Mean	Std. dev.	Median	Minimum	Maximum	Skewness	Kurtosis
Excluding grains > 0.063 mm							
GEN-1FA	4.49	8.72	1.32	0.009	62.83	3.55	14.15
KPHTR-1-FA	1.97	5.20	0.28	0.006	52.70	4.96	31.45
WATR-1-FA	2.49	6.41	0.49	0.012	74060	5.03	29.31
Including all grains							
GEN-1FA	16.97	248.71	1.36	0.009	7662.36	29.25	895.0
KPHTR-1-FA	112.19	2397.53	0.28	0.006	59402.38	24.50	606.15
WATR-1-FA	14.81	119.42	0.51	0.012	1994.69	13.04	184.78

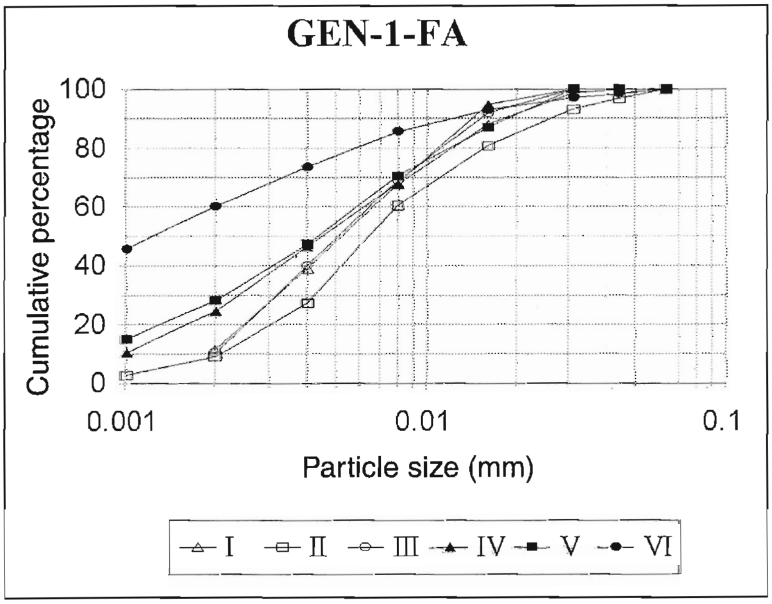

Figure 2.

Particle size distribution for sample GEN-1-FA. Data shown for grains less than 0.063 mm (63 µm).

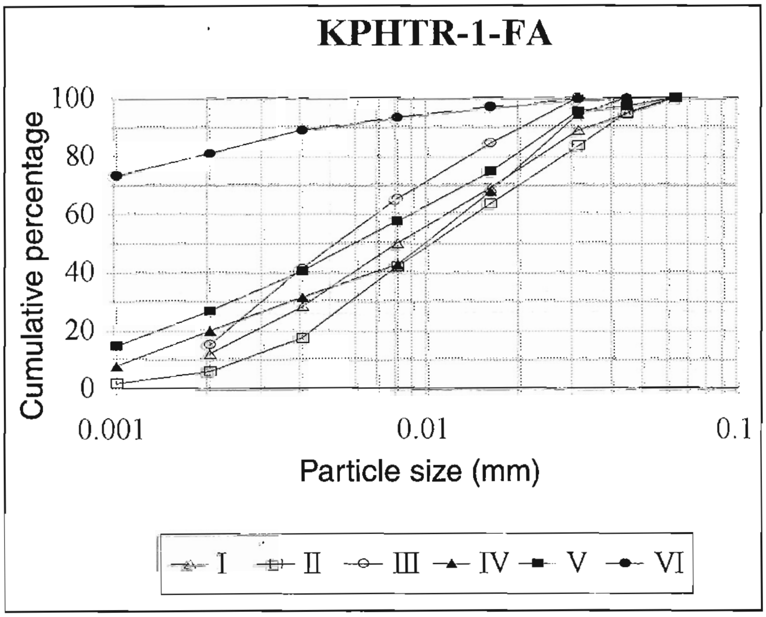

Figure 3.

Particle size distribution for sample KPHTR-1-FA. Data shown for grains less than 0.063 mm (63 µm).

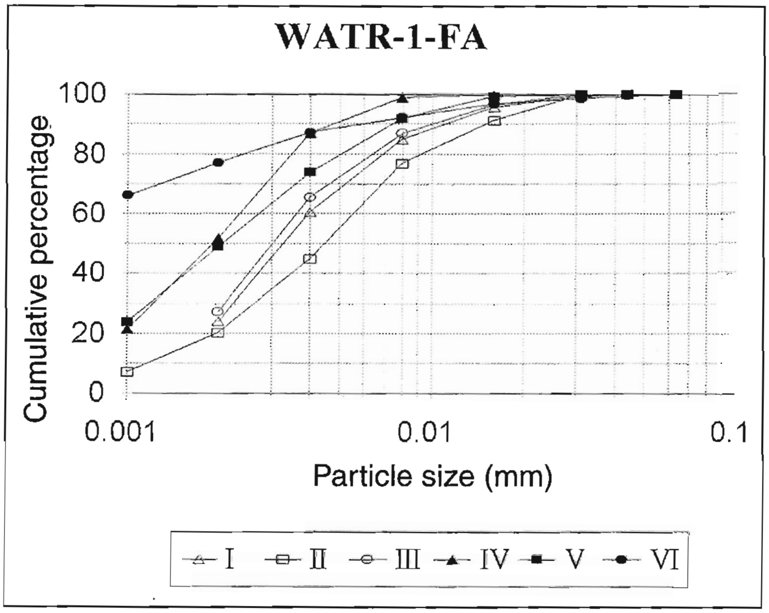

Figure 4.

Particle size distribution for sample WATR-1-FA. Data shown for grains less than 0.063 mm (63 µm).

expenditures required to purchase these instruments, some of them require extensive training for their operation (e.g. SEM-based image analysis). The data produced by the instrumental methods, however, is comparable to that of method I, with the exception of method VI. Method III (Coulter Counter®) provides the closest match to the particle size distribution of the pipette method (I).

Method II (Galai®) appears to be less sensitive for the clay-size fraction but is reasonably well correlated for the silt fraction relative to the classical pipette and other instrumental methods. It is possible that operational parameters such as pump speed need to be optimized in order to ensure that all very fine-grained particles pass through the laser's focal plane. Laser diffraction methods IV (Fritsch®) and V (Granulometre®) show very similar grain size distribution patterns (Fig. 2 to 4) and appear to be more sensitive for the fine-grained particles than methods I, II, and III graphs. This sensitivity may be related to Mie scattering where the physical properties of the particles (<7 µm) begin to influence the refractive patterns.

Method VI (SEM-image analysis) shows comparable mean grain size data to the other methods, especially when the few (<14) larger (sand-sized) grains are omitted from the data set, however, it shows a very different grain size distribution pattern. This reflects the fundamental difference in sample size. In method VI, up to 1000 grains were individually measured. The instrumental techniques, however, measure hundreds of thousands of grains in a very short time span to ensure a representative distribution of grains within pre-set size classes. This method is invaluable for examining the morphology of the material and is recommended only for specialized studies of fine-grained sediments.

CONCLUSIONS

Particle size analysis is an extremely complicated procedure in that most sediments are composed of a complex mixture of particles of varying sizes, shapes, densities, and matrices. All of the procedures described above make some assumption about particle sphericity, density, or light scattering ability (Percival and Lindsay, 1997). No two procedures yielded identical results for the same sample. This comparison of instrumental methods to classical pipette analysis has focused primarily on the analysis of fine-grained, amorphous Si materials (fly ash). The instrumental techniques offer comparable grain size information to pipette analysis for the silt- and clay-size ranges.

Overall, any of these instrumental techniques, with the exception of image analysis by SEM, can be recommended for grain size analysis of fine (silt and clay) particles. The image analysis method requires specialized training, high capital expenditures, and is limited by the number of particles that can be analyzed in a reasonable time-frame. This method, however, is extremely useful in detailed studies of particles. In addition, most instruments have integrated software applications that provide automated, statistical handling of large data sets simultaneously with the analysis making it efficient and less prone to calculation errors. Standardization of sample preparation and calibration of instrument are essential. Follow-up analyses will address the precision and accuracy of the data.

The Galai® instrument currently used in the Sedimentology Laboratory also has its limitations and probably needs to be optimized for the clay-size particles. It is effective for routine analyses of fine-grained materials replacing the older, time-consuming pipette analysis. However, all these methods do require sieve analysis of material coarser than 0.063 mm to obtain representative and complete grain size information.

ACKNOWLEDGMENTS

The authors are grateful to the following laboratories for their time and energy in analyzing the samples: Glaciology (TSD), GSC Quebec, and an anonymous laboratory. Special thanks to F. Goodarzi of GSC Calgary for supplying the fly ash samples and to R. Lacroix (GID) for preparation of SEM images. This paper benefited from reviews by B. McClenaghan (TSD) and G. LeCheminant.

REFERENCES

Allen, T.
1997a: Particle Size Measurement, v. 1, Particle Sampling and Particle Size Measurement, 5th ed.; Chapman & Hall, London, 517 p.
1997b: Particle Size Measurement, v. 2, Surface Area and Pore Size Determination, 5th ed.; Chapman & Hall, London, 251 p.
Barbanti, A. and Bothner, M.H.
1993: A procedure for partitioning bulk sediments into distinct grain-size fractions for geochemical analysis; Environmental Geology, v. 21, p. 3-13.
Day, P.A.
1965: Particle fractionation and particle size analysis; *in* Methods of Soil Analysis, Part 1, Physical and Mineralogical Properties, Including Statistics of Measurement and Sampling, (ed.) C.A. Black; Agronomy Monograph 9, American Society of Agronomy, Madison, Wisconsin, p. 545-567.
de Boer, G.B.J., de Weerd, C., Thoenes, D., and Goossens, H.W.J.
1987: Laser diffraction spectrometry: Fraunhofer diffraction versus Mie scattering; Particle Characterization, v. 4, p. 14-19.
de Groot, A.J., Zschuppe, K.H., and Salomons, W.
1982: Standardization of methods of analysis for heavy metals in sediments; *in* Sediment/Freshwater Interaction, (ed.) P.G. Sly; Hydrobiologia, v. 92, p. 689-695.
DiLabio, R.N.W.
1995: Residence sites of trace elements in oxidized till; *in* Drift Exploration in the Canadian Cordillera; British Columbia Ministry of Energy, Mines and Petroleum Resources, Paper 1995-2, p. 139-148.
Förstner, U. and Wittmann, G.
1981: Metal Pollution in the Aquatic Environment (2nd ed.), Springer-Verlag, New York, 197 p.
Haley, M.P. and Joyce, I.H.
1984: Modern instrumental techniques for particle size evaluation; Journal of Canadian Ceramic Society, v. 53, p. 15-20.
Horowitz, A.J. and Elrick, K.A.
1987: The relation of stream sediment surface area, grain size and composition to trace element chemistry; Applied Geochemistry, v. 2, p. 437-451.
Horowitz, A.J., Elrick, K.A., and Hooper, R.P.
1989: The prediction of aquatic sediment-associated trace element concentrations using selected geochemical factors; Hydrological Processes, v. 3, p. 347-364.
Jackson, M.L.
1979: Soil Chemical Analysis-Advanced Course, 2nd edition, 11th printing; published by the author, Madison, Wisconsin, 895 p.
Jenne, E., Kennedy, V., Burchard, J., and Ball, J.
1980: Sediment collection and processing for selective extraction and for total metal analysis; *in* Contaminants and Sediments, (ed.) R. Baker; Ann Arbor Science Publishers Inc., Ann Arbor, Michigan, p. 169-190.
Jones, B.F. and Bowser, C.J.
1978: The mineralogy and related chemistry of lake sediments; *in* Lakes-Chemistry, Geology, Physics, (ed.) A. Lerner; Springer-Verlag, New York Inc., p. 179-235.
Lewis, D.W.
1984: Practical Sedimentology; Hutchinson Ross Publishing Co., Stroudsburg, P.A., 229 p.
McCave, I.N. and Syvitski, J.P.M.
1991: Principles and methods of geological particle size analysis; *in* Principles, Methods, and Applications of Particle Size Analysis, (ed.) J.P.M. Syvitski; Cambridge University Press, New York, p. 3-24.
McCave, I.N., Bryant, R.J., Cook, H.F., and Coughanowr, C.A.
1986: Evaluation of a laser-diffraction-size analyzer for use with natural sediments; Journal Sedimentary Petrology, v. 56, p. 561-563.
Percival, J.B. and Lindsay, P.J.
1997: Measurement of physical properties of sediments; *in* Manual of Physico-Chemical Analysis of Aquatic Sediments, (ed.) A. Mudroch, J.M. Azcue, and P. Mudroch; Lewis Publishers (CRC Press, Inc.), Boca Raton, p. 7-45.
Petruk, W.
1989: Image analysis of minerals; *in* Image Analysis Applied to Mineral and Earth Sciences, (ed.) W. Petruk; Mineralogical Association Canada, Short Course, p. 6-18.
Shilts, W.W.
1995: Geochemical partitioning in till; *in* Drift Exploration in the Canadian Cordillera; British Columbia Ministry of Energy, Mines and Petroleum Resources, Paper 1995-2, p. 149-166.
Walker, D.A. and LeCheminant, G.M.
1989: An integrated image and x-ray analysis system: description and techniques in a multiple use laboratory; *in* Image Analysis Applied to Mineral and Earth Sciences, (ed.) W. Petruk; Mineralogical Association Canada, Short Course, p. 43-55.
Walker, L.K. and Reynolds, V.G.
1991: Particle size analyzer comparison; Mineral Sciences Laboratories Division Report MSL 91-61 (TR), CANMET, Energy, Mines and Resources Canada, 38 p.

Geological Survey of Canada projects 950032 and 680023

Shale permeability characteristics

T.J. Katsube and S. Connell
Mineral Resources Division, Ottawa

Katsube, T.J. and Connell, S., 1998: Shale permeability characteristics; in *Current Research 1998-E; Geological Survey of Canada, p. 183–192.*

Abstract: Permeability versus pressure data for 27 tight shale and compacted seafloor mud samples (28 measurements), obtained from several sedimentary basins in North America by the Geological Survey of Canada, have been analyzed in order to determine the shale permeability-pressure characteristics. Tight shales are known to have some of the lowest permeabilities (10^{-23}–10^{-19} m^2) for rocks.

Results indicate that these samples can be divided into three groups, AA, BB, and CC, on the basis of their permeability (k) versus effective pressure (P_e) characteristics. Group AA is characterized by relatively large k values ($1.0\text{x}10^{-20}$–$1.6\text{x}10^{-18}$ m^2) that decrease at moderate to rapid rates with increasing P_e to 20–30 MPa where they level out. The group BB characteristics are similar, except that the k values are considerably smaller ($1.0\text{x}10^{-22}$–$1.0\text{x}10^{-19}$ m^2). Group CC is characterized by large k values ($3\text{x}10^{-19}$–$1.6\text{x}10^{-18}$ m^2) that decrease rapidly to very small k values ($3\text{x}10^{-22}$–$1.6\text{x}10^{-21}$ m^2) at P_e=60 MPa. Group CC may represent a texture with a weakened pore framework.

Résumé : Des données portant sur la perméabilité en fonction de la pression de 27 échantillons de shale compact et de boue compactée de fond marin (représentant 28 mesures), prélevées par la Commission géologique du Canada dans plusieurs bassins sédimentaires de l'Amérique du Nord, ont été étudiées afin de déterminer les caractéristiques de perméabilité et de pression des shales. Les shales compacts sont reconnus comme les roches ayant les taux de perméabilité parmi les plus faibles, soit de 10^{-23} à 10^{-19} m^2.

Les résultats révèlent que ces échantillons se répartissent en trois groupes, soit AA, BB et CC, en fonction des caractéristiques de la perméabilité (k) et de la pression effective (P_e). Le groupe AA se caractérise par des valeurs de perméabilité relativement élevées, soit $1 \text{ x } 10^{-20}$–$1{,}6 \text{ x } 10^{-18}$ m^2. Ces valeurs décroissent modérément à rapidement avec l'augmentation de la pression effective qui s'échelonne de 20 à 30 MPa avant de plafonner. Les caractéristiques du groupe BB sont similaires à celle du groupe précédent, à l'exception d'une valeur de perméabilité qui est considérablement plus faible, soit 10^{-22} à 10^{-19} m^2. Le groupe CC se distingue par des valeurs de perméabilité élevées, soit $3 \text{ x } 10^{-19}$–$1{,}6 \text{ x } 10^{-18}$ m^2. Celles-ci chutent rapidement pour atteindre des valeurs extrêmement faibles de $3 \text{ x } 10^{-22}$–$1{,}6 \text{ x } 10^{-21}$ m^2 avec une pression effective de 60 MPa. Le groupe CC représente vraisemblablement une texture dont la structure des pores est plus perméable.

INTRODUCTION

Permeability versus pressure data for 27 tight shale and compacted seafloor mud samples (28 measurements), obtained from several sedimentary basins in North America by the Geological Survey of Canada, have been analyzed to determine the shale permeability-pressure characteristics. Tight shales are known to have some of the lowest permeabilities (10^{-23}–10^{-19} m^2: Brace, 1980; Katsube and Williamson, 1994; Neuzil, 1994) for rocks. While tight shale or compacted mud permeability data has been obtained by other researchers (e.g. Brace, 1980; Morrow et al., 1984; Neuzil, 1994), the GSC permeability data is unique in that they are always accompanied by other data, so that related petrophysical studies are possible. For example, in most cases, they have corresponding mercury porosimetry data (Katsube, 1992; Katsube and Issler, 1993; Katsube et al., 1998a). They are often accompanied by helium porosimetry (Issler and Katsube, 1994) and shale texture data (Katsube and Williamson, 1994), and sometimes formation resistivity factor data (Katsube et al., 1991, 1992; Katsube and Williamson, 1994; Katsube et al., 1996b). A routine procedure at the GSC specifies that each sample prepared for petrophysical tests be divided into a number of specimens, so that various related tests can be performed, including ones to be archived for subsequent tests when deemed necessary. The purpose of this paper is to publish all shale permeability data obtained by the GSC to date, to identify their sources and to document their permeability-pressure characteristics.

Shale pore-structure is characterized by unimodal pore-size distributions (Katsube and Williamson, 1994), and these distributions can be characterized by the following four parameters: effective porosity (ϕ_E), pore surface area (A), pore-size distribution mode (d_m), and storage porosity ratio (ϕ_r). The definitions of these parameters can be found in the literature (e.g. Katsube et al., 1997). In recent studies, the range of values for these parameters have been used to characterize shale texture (e.g. Katsube and Williamson, 1994, 1995, in press; Katsube et al., 1997, 1998a). A summary of these values and their implications are listed in Table 1. The determination of these ranges, however, is in the preliminary stage and, at present, can be used only as a guide to interpretation of the petrophysical data.

PERMEABILITY DATA

Source of permeability data

The permeability data (Table 2) for the 27 shale samples (28 measurements), were obtained from previous publications (Katsube, 1992; Coyner et al., 1993; Issler and Katsube, 1994; Katsube and Coyner, 1994; Katsube et al., 1996a, b). The samples are from the Beaufort–Mackenzie Basin (Northern Canada), the Western Canada Sedimentary Basin (Western Canada), and the Venture Gas Field (Sable Basin, offshore eastern Canada, Fig. 1). Seven of the measurements are for six samples (Table 2a: B-AR-5 to B-9) from the Beaufort–Mackenzie Basin (Katsube et al., 1996b). Another five samples (Table 2b: ACD-03R to ACD-13R and BEI-01 to CRB-02) are from the Western Canada Sedimentary Basin (Katsube et al., 1998). Still another ten samples (Table 2d: V-1 to V-10) are from the Venture Gas Field (Coyner et al., 1993; Katsube and Coyner, 1994). In addition to these, there are six compacted seafloor samples (Table 2c: k.002.189 to k.017.543a and V-SF-1) from the Venture Gas Field (Katsube et al., 1996a). All these literature data are presented in terms of permeability (k) as a function of effective pressures (P_e), as displayed in Tables 2a–d.

Table 1. Petrophysical parameters used to characterize shale pore-structure, their range of values, and their implications for shale texture. These results are compiled from the literature (e.g. Katsube and Williamson, 1994, 1995, in press; Katsube et al., 1997, 1998a).

Parameters	Range of values	Implications
d_m (nm)	$d_m<10$	- well compacted\fine-grained
	$10< d_m <25$	- compacted but fractured (nano-fractures)
	$25< d_m <1000$	- under-compacted\medium- to coarse-grained
	$1000< d_m$	- very coarse-grained
A (m^2/g)	$A<10$	- diagenetically altered (cemented)\coarse-grained
	$10<A<20$	- diagenetically altered with dissolution pores\unaltered
	$A>10$	- unaltered\fine-grained
ϕ_E (%)	$\phi_E<5$	- diagenetically altered (cemented)
	$5<\phi_E<10$	- diagenetically altered with dissolution pores\unaltered and well compacted
	$10<\phi_E$	- under-compacted\dissolution pores\medium- to coarse-grained
ϕ_r	$\phi_{rr}<0.5$	- diagenetic cement\unaltered and well compacted
	$0.5<\phi_{rr}$	- dissolution pores\under-compacted\ coarse-grained

d_m = Mode of the pore-size distribution
A = Pore surface area
ϕ_E = Effective porosity
ϕ_r = Storage porosity ratio
\ = Implies one or the other and usually not both

Table 2a. Permeability data for shale samples from the Beaufort–Mackenzie Basin.

P_e	k $(10^{-21}m^2)$	P_e	k $(10^{-21}m^2)$	P_e	k $(10^{-21}m^2)$	P_e	k (±10%) $(10^{-21}m^2)$
B-AR-5		**B-TA-1**		**B-5**		**B-9**	
5.0	4.7 ± 0.8	2.5	7.6 ± 1.2	10	46 ± 2	2.5	390
10	1.8 ± 0.0	5.0	2.9 ± 0.9	15	22 ± 2	5.0	409
15	1.2 ± 0.2	7.5	1.7 ± 0.2	20	24 ± 2	7.5	286
20	0.77 ± 0.05	10	0.96 ± 0.38	30	16.2 ± 0.2	10	265
25	0.85 ± 0.05	15	0.54 ± 0.04	35	13.8 ± 0.2	12.5	259
30	0.60 ± 0.10	20	0.39 ± 0.02	40	12.6 ± 0.2	15	238
		25	0.24 ± 0.04	50	8.2 ± 0.8	17.5	221
B-ML-2				60	7.8 ± 0.1	20	203
2.5	0.5 ± 0.12	**B-TG-6**		70	6.8 ± 0.1	22.5	177
5.0	0.32 ± 0.09	5.0	188 ± 8	80	6.4 ± 0.1	25	158
10	0.32 ± 0.05	10	65 ± 5	90	5.9 ± 0.1	30	141
15	0.22 ± 0.02	15	23 ± 4	100	5.0 ± 0.1	35	129
30	0.17 ± 0.02	20	8.7 ± 0.0			40	112
		25	6.3 ± 0.3			50	82
B-ML-2*		30	4.7 ± 0.2			60	74
2.5	2.9 ± 0.3	35	4.5 ± 0.5			70	58
5.0	1.8 ± 0.2	40	3.2 ± 0.8			80	54
10	1.0 ± 0.1	45	2.3 ± 0.1			90	47
20	0.6 ± 0.06	50	1.7 ± 0.4			100	39
30	0.4 ± 0.04						
50	0.3 ± 0.03						

P_e = Effective pressure (MPa)
k = Permeability $(10^{-21}m^2)$
* = Horizontal measurement

Table 2b. Permeability data for shale samples from the Western Canada Sedimentary Basin.

P_e	k $(10^{-21}m^2)$	P_e	k $(10^{-21}m^2)$	P_e	k $(10^{-21}m^2)$
ACD-03R		**BEI-01**		**CRB-02**	
5.0	23.1 ± 0.4	5.0	9.71 ± 0.11	5.0	17.1 ± 0.9
10.0	15.2 ± 0.2	10.0	5.15 ± 0.10	10.0	8.85 ± 1.56
15.0	7.97 ± 0.12	15.0	2.52 ± 0.08	15.0	2.41 ± 0.31
20.0	4.55 ± 0.19	20.0	1.78 ± 0.22	20.0	1.15 ± 0.15
25.0	3.69 ± 0.04	25.0	0.99 ± 0.11	25.0	0.689 ± 0.076
30.0	2.96 ± 0.12	30.0	0.87 ± 0.14	30.0	0.485 ± 0.058
35.0	2.20 ± 0.04	35.0	0.747 ± 0.066	35.0	0.420 ± 0.043
40.0	1.77 ± 0.09	40.0	0.52 ± 0.15	40.0	0.397 ± 0.044
		45.0	0.318 ± 0.020	45.0	0.329 ± 0.027
		50.0	0.236 ± 0.007	50.0	0.261 ± 0.018
ACD-13R	**(error ±10%)**	**BRS-12**			
2.5	15.9	2.5	9.25 ± 0.09		
5.0	11.7	5.0	6.23 ± 0.66		
7.5	7.9	7.5	5.58 ± 0.50		
10.0	6.97	10.0	4.34 ± 0.25		
15.0	3.98	15.0	3.71 ± 0.12		
20.0	2.78	20.0	2.21 ± 0.19		
25.0	2.12	25.0	1.18 ± 0.10		
30.0	1.44	30.0	0.94 ± 0.04		
35.0	1.26	35.0	0.85 ± 0.09		
40.0	0.935	40.0	0.68 ± 0.03		
45.0	0.852	45.0	0.60 ± 0.05		
50.0	0.758				

P_e = Effective pressure (MPa)
k = Permeability $(10^{-21}m^2)$

Table 2c. Permeability data for compacted mud samples from the Venture Gas Field.

P_e	k ($10^{-21}m^2$)	P_e	k ($10^{-21}m^2$)	P_e	k ($10^{-21}m^2$)
k.002.189		**k.017.543a**		**V-SF-1**	443
4.0	920 ± 30	10.2	125 ± 32	1.0	325 ± 5
22	640 ± 80	21.9	62 ± 16	2.0	223 ± 8
40	400 ± 90	40	27 ± 16	3.0	157 ± 224
58	310 ± 70	57.8	14 ± 7.2	4.0	97 ± 8
74	220 ± 80	76.2	11.8 ± 3.1	5.0	60 ± 1
94	180 ± 50	94.1	10.6 ± 1.0	6.0	63
k.002.343		**k.002.630**		7.0	62.5 ± 5
3.4	107 ± 7	3.8	141 ± 20	8.0	61.5 ± 5
22	<10	39.8	13.1 ± 3.5	9.0	57 ± 2
		57.8	<10	10.0	68
				4.4	46
				9.6	29
				14.7	25
k.017.543				19.3	23
4.0	290 ± 30			25.0	19
40	45 ± 8			29.8	23
58	20.9			34.9	14
74	13.3			40.1	
95	10.0				

P_e = Effective pressure (MPa)
k = Permeability ($10^{-21}m^2$)

Table 2d. Permeability data for shale samples from the Venture Gas Field, offshore Nova Scotia.

P_e	k ($10^{-21}m^2$)	P_e	k ($10^{-21}m^2$)	P_e	k ($10^{-21}m^2$)	P_e	k ($10^{-21}m^2$)
V-1		**V-4**		**V-7**		**V-9**	
2.5	8.5 ± 1	5:0	31.0 ± 2	2.5	21 ± 10.0	10	2.0 ± 0.1
5.0	4.7 ± 0.4	10	22.0 ± 2	5.0	14 ± 7.0	20	1.2 ± 0.1
10	1.7 ± 0.1	20	18.0 ± 2	7.5	11 ± 5.0	10	2.4 ± 0.1
40	0.7 ± 0.1	30	5.3 ± 0.6	10	8. ± 4.0	15	1.4 ± 0.1
		40	2.0 ± 0.4	15	4.3 ± 2.1	20	1.3 ± 0.1
				20	3.0 ± 1.5	25	1.0 ± 0.1
				25	1.4 ± 0.7	30	0.6 ± 0.1
				30	1.3 ± 0.2	40	0.4 ± 0.1
V-2		**V-5**		35	0.88 ± 0.44	**V-10**	
10	35.0 ± 6	10	20.0 ± 2	40	0.88 ± 0.44	2.5	16.0 ± 2
20	29.0 ± 3	20	13.0 ± 2	45	0.64 ± 0.32	5.0	9.4 ± 1
30	5.4 ± 0.6	30	8.2 ± 0.9	50	0.43 ± 0.44	10	4.2 ± 0.4
				55	0.41 ± 0.20	40	0.9 ± 0.1
				60	0.33 ± 0.16	60	0.1 ± 0.1
V-3		**V-6**		**V-8**			
2.8	737. ± 4	3.5	2.1 ± 0.1	10	58.0 ± 4		
5.0	437. ± 35	5.0	0.8 ± 0.1	20	26.0 ± 4		
7.5	350. ± 11	10	0.54 ± 0.01	30	19.0 ± 2		
10	296. ± 4	12.5	0.31 ± 0.15	40	17.0 ± 2		
15	148. ± 8.6	15	0.27 ± 0.03	60	11.0 ± 1		
20	34.7 ± 12.5	10	0.29 ± 0.15				
25	14. ± 1.5						
30	6.2 ± 0.7						
35	3.2 ± 0.1						
40	0.9 ± 0.3						
55	1.2 ± 0.4						
50	0.8 ± 0.3						
60	0.3 ± 0.05						

P_e = Effective pressure (MPa)
k = Permeability ($10^{-21}m^2$)

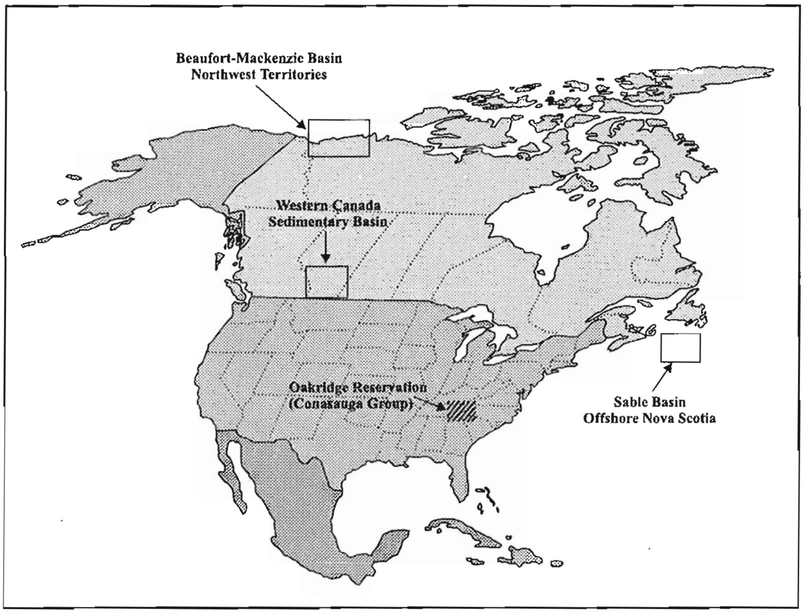

Figure 1.

Location map of significant North American shale samples. Canadian samples are from the Sable Basin (Venture Gas Field), Western Canada Sedimentary Basin, and Beaufort-MacKenzie Basin.

Related petrophysical data

The other petrophysical data, related to those in Table 2, are listed in Table 3. These data are for the petrophysical parameters: grain density (δ_{GD}), helium porosity (ϕ_{He}), dry bulk density (δ_{BD}), skeletal density (δ_{SD}), mercury porosities (ϕ_{Hg1}, ϕ_{Hg2}), pore surface area (A), storage porosity (ϕ_s), storage porosity ratio (ϕ_r), connecting porosity (ϕ_c), and pore-size distribution mode (d_m). The definitions for most of these parameters, including A, ϕ_s, ϕ_r, and ϕ_c, can be found in the literature (e.g. Katsube et al., 1997). Most of the data in Table 3 can be found in the literature related to studies carried out on various basins: Venture Gas Field (Sable Basin, Katsube, 1992), Venture Gas Field seafloor (Katsube et al., 1996a), Beaufort–Mackenzie Basin (Issler and Katsube, 1994; Katsube and Best, 1992), and Western Canada Sedimentary Basin (Katsube et al., 1998a). The data for the parameters A, ϕ_s, ϕ_r, and d_m, that were not available in some of the literature have now been obtained or calculated (Katsube et al., 1997) to complete the table. In principle, the values of ϕ_{He}, ϕ_{Hg1}, and ϕ_{Hg2} represent that of the effective porosity (ϕ_E) and should all be identical. However, as indicated in the literature (Dorsch and Katsube, 1996; Dorsch et al., 1996; Katsube et al., 1997), they often display differences for various reasons.

ANALYTICAL RESULTS

Analytical results of the permeability versus effective pressure (k-P_e) data (Table 2) are displayed in Figures 2–5. Although all of the basic petrophysical data related to the permeability data in Table 3 have previously been documented, some of the derived data (A, ϕ_s, ϕ_r, ϕ_c, and d_m) have been just recently calculated using the following equations (Katsube et al., 1997, 1998a):

$$\phi_s = \phi_r\,\phi_{Hg1},$$

$$\phi_r = \phi_s/\phi_{Hg1},$$

$$\phi_c = \phi_{Hg1}(1-\phi_{rr}).$$

These 27 shale samples can be divided into three distinct groups (Fig. 2, 3, and 4): AA, BB, and CC, on the basis of their k-P_e curve characteristics. Group AA (Fig. 2) consists of most of the compacted seafloor samples (k.002.189, k.002.630, k.017.543, k.017.543a, and V-SF-1), as well as some of the shales from the Beaufort–Mackenzie Basin (B-5 and B-9) and Venture Gas Field (Sable Basin, V-4, V-5, and V-8). The k-P_e curves for these shales are characterized by relatively large k values of $3\text{x}10^{-19}$–$1.6\text{x}10^{-18}$ m², at the effective pressure (P_e) of zero, that decrease with moderate to rapid rates with increasing pressure until about 20–30 MPa, where they level out at k values of 10^{-20}–10^{-18} m². Group BB (Fig. 3) consists of all remaining shale samples from the three basins: Beaufort–Mackenzie Basin, Venture Gas Field, and the Western Canada Sedimentary Basin, except the one compacted and three shale samples that constitute group CC. The k-P_e curve characteristics of this group is very similar to that of group AA, except the k values at the effective pressures (P_e) of zero and 20–30 MPa are considerably smaller: $1.0\text{x}10^{-21}$–$1.0\text{x}10^{-19}$ m² and $1.0\text{x}10^{-22}$–$1.6\text{x}10^{-21}$ m², respectively. Group CC (Fig. 4) consists of one compacted seafloor sample (k.002.343) from the Venture Gas Field and three shale samples: two (V-2, V-3) from the Venture Gas Field and one (B-TG-6) from the Beaufort–Mackenzie Basin. The k-P_e curves for the samples in this group are characterized by relatively large k values of $3\text{x}10^{-19}$–$1.6\text{x}10^{-18}$ m² at P_e=0, similar to group AA, that continue to decrease rapidly to k values of $3\text{x}10^{-22}$–$1.6\text{x}10^{-21}$ m² at P_e=60 MPa, similar to group BB. That is, the k values of this group cover the ranges of both groups AA and BB. A comparison of the k-P_e curve characteristics for the three groups are made in Figure 5.

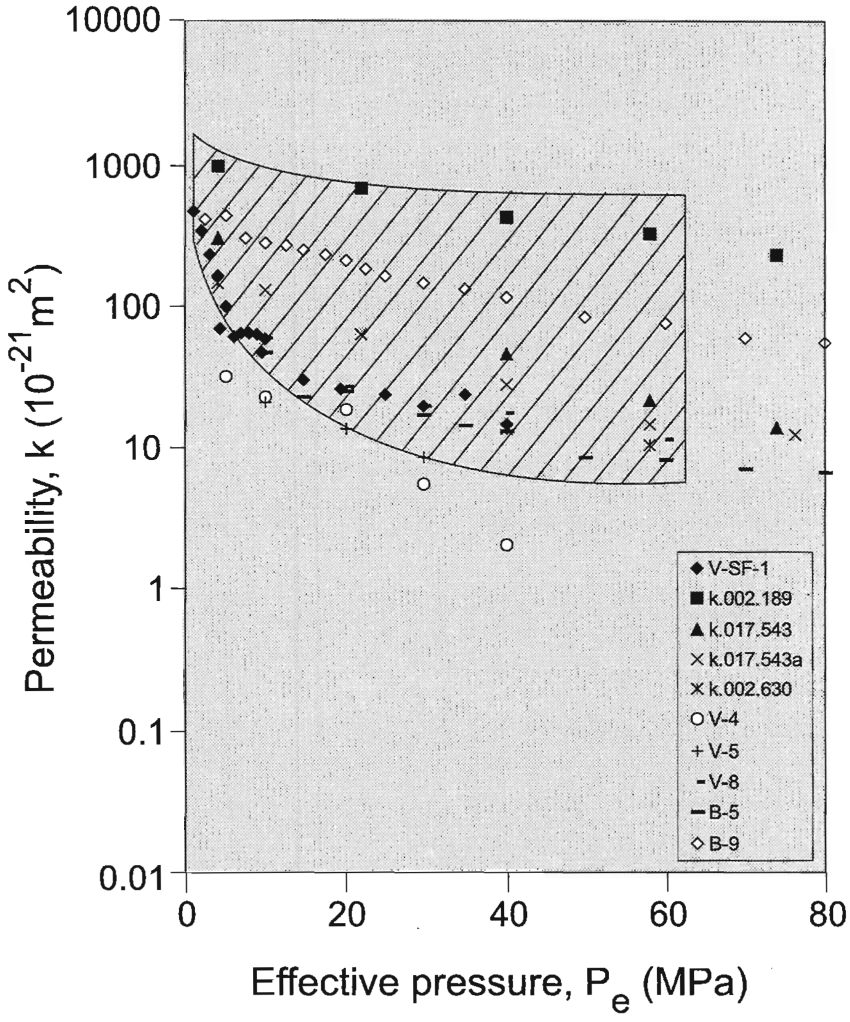

Figure 2. *Permeability (k) versus effective pressure (P_e) plots for group AA, consisting of the compacted seafloor and shale samples used in this study.*

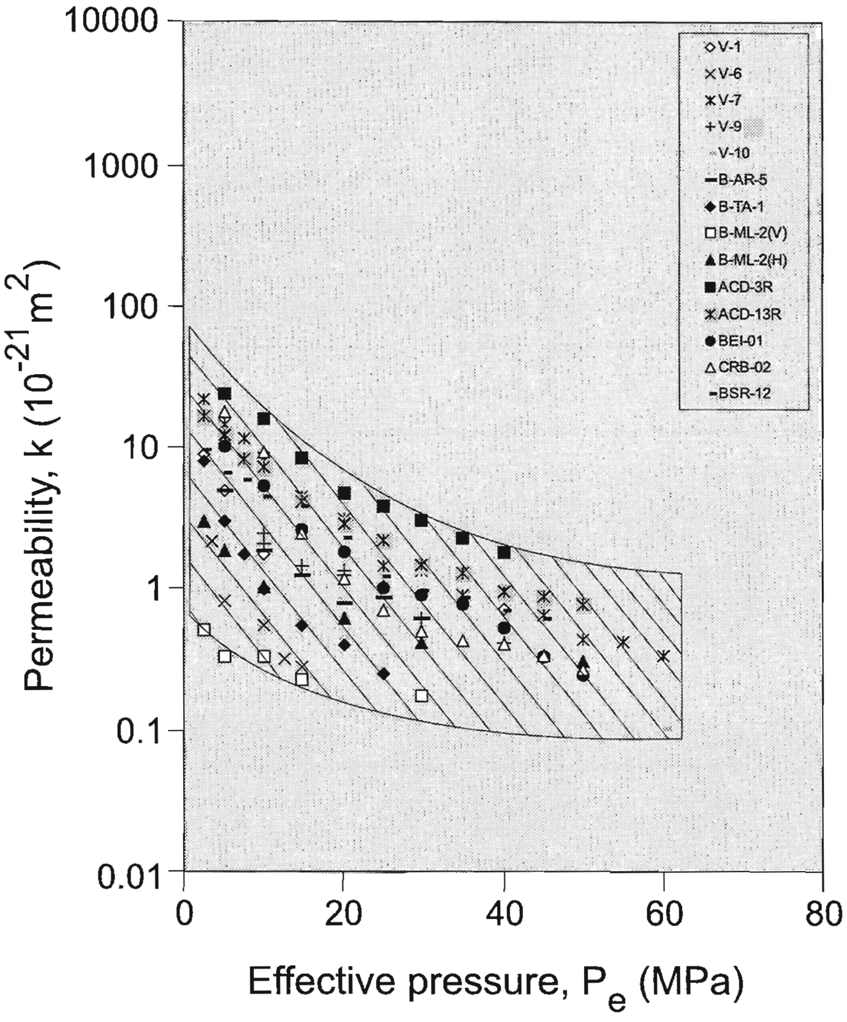

Figure 3. *Permeability (k) versus effective pressure (P_e) plots for group BB, consisting of the shale samples used in this study.*

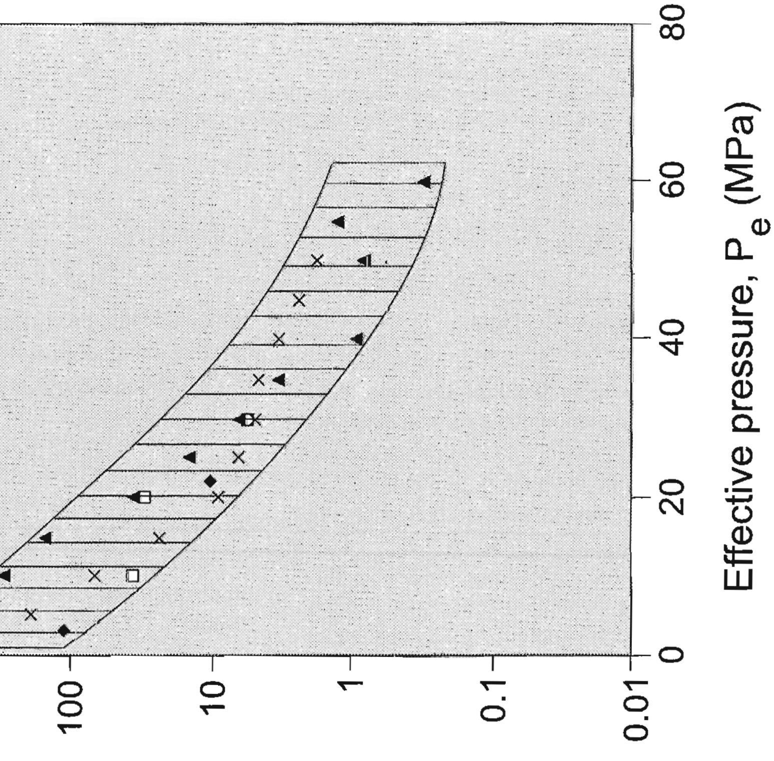

Figure 4. *Permeability (k) versus effective pressure (P_e) plots for group CC, consisting of compacted seafloor and shale samples used in this study.*

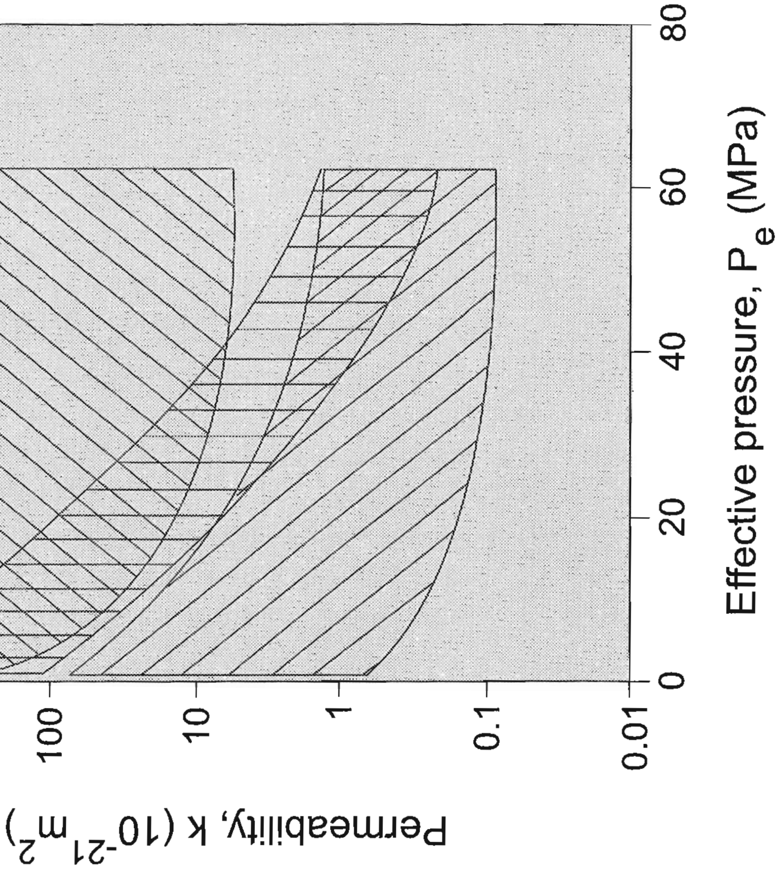

Figure 5. *Comparison of groups AA, BB, and CC (Fig. 2–4).*

Table 3. Petrophysical characteristics of the shale and compacted sea-floor samples used in this study.

Sample Number	Fm	h	δ_{GD}	δ_{BD}	δ_{SD}	ϕ_{He}	ϕ_{Hg1}	ϕ_{Hg1}	A	ϕ_S	ϕ_r	ϕ_c	d_m
Beaufort-Mackenzie Basin													
B-AR-5*	Rch	4 380	2.72	2.47	2.73	-	8.46	9.6	11.9	6.2	0.73	2.28	13
B-TA-1	Tg	2 880	2.39	2.10	2.26	6.8	6.29	7.0	18.5	2.0	0.32	4.28	3.2
B-TG-6	Rch	2 460	2.73	2.55	2.77	10.6	6.92	7.8	11.7	5.3	0.77	1.59	7.9
B-ML-2*	Tg	3 180	2.71	2.61	2.76	7.4	5.09	5.4	5.37	3.24	0.64	1.83	20
B-5		3 760		2.39	2.70		11.1	11.4	8.04	5.88	0.53	5.22	32
B-9		2 590		2.22	2.65		14.5	16.4	9.82	8.00	0.55	6.53	50
Western Canada Sedimentary Basin													
CRB-02	SWS	570	2.59	2.26	2.59	19.4	12.4	12.7	18.8	7.9	0.64	4.46	13
BEI-01	UC	580	2.73	2.49	2.64	8.4	5.6	5.9	13.1	3.2	0.58	2.35	5.0
ACD-03R	SWS	560	2.73	2.46	2.68	8.1	7.8	8.3	13.3	4.6	0.59	3.20	7.9
ACD013R	BF	610	2.65	2.38	2.65	9.6	9.6	10.3	13.4	6.0	0.63	3.55	5/130
BSR-12	WG	1 260	2.74	2.48	2.66	6.9	6.5	6.9	9.7	3.8	0.58	2.73	7.9
Venture Gas Field													
k.002.189		1.9											
k.002.343		3.5		1.86	2.73		30.9	31.7	13.3	18.3	0.59	12.67	79
k.002.630		6.3											
k.017.543		5.4		1.88	2.73		30.7	31.2	18.2	10.8	0.35	19.96	50
k.017.543a		5.5											
V-SF-1		7.6											
V-1		4 690		2.77	2.92		4.43	4.94	8.43	2.2	0.50	2.22	5.0
V-2		4 690		2.58	2.79		7.04	7.65	8.87	2.7	0.39	4.29	20
V-3		4 910		2.62	2.80		5.60	6.32	9.50	3.5	0.62	2.13	7.9
V-4		4 960		2.80	3.03		6.70	7.60	12.2	3.6	0.54	3.08	5.0
V-5		5 120		2.64	2.74		2.98	3.67	6.06	0.9	0.31	2.06	3.2
V-6		5 130		2.73	2.78		1.50	1.61	3.04	0.01	0.068	1.40	7.9
V-7		5 270		2.65	2.81		5.18	5.85	10.1	3.2	0.62	1.97	7.9
V-8		5 270		2.57	2.83		8.37	9.06	14.9	3.9	0.47	4.44	5.0
V-9		5 550		2.69	2.76		2.13	2.31	3.86	0.4	0.18	1.75	7.9
V-10		5 560		2.74	2.91		5.08	5.84	9.07	2.8	0.56	2.24	5.0

* = Overpressured
h = True vertical depth (TVD) in metres
δ_{GD} = Grain density (g/mL)
δ_{BD} = Bulk density (g/mL)
δ_{SD} = Skeletal density (g/mL)
ϕ_{He} = Total porosity measured by helium porosimetry (%)
ϕ_{Hg1} = Total porosity measured by mercury porosimetry for pore sizes up to 10 μm (%)
ϕ_{Hg2} = Total porosity measured by mercury porosimetry for pore sizes up to 250 μm (%)
A = Surface area (m²/g)
ϕ_S = Storage porosity (%)
ϕ_r = Storage porosity ratio: ϕ_S/ϕ_{Hg1}
ϕ_c = Connecting porosity: $\phi_{Hg1}(1-\phi_{rr})$
d_m = Mode of pore-size distribution (nm)

DISCUSSION AND CONCLUSIONS

The petrophysical characteristics of the three groups, AA, BB, and CC, were determined by calculating the mean values and ranges of the petrophysical parameters (δ_{BD}, δ_{SD}, ϕ_E, A, ϕ_s, ϕ_r, ϕ_c, d_m) for each group, using the data in Table 3. The results are listed in Table 4. The mean of these parameters are represented by δ_{BDD}, δ_{SDD}, ϕ_{EE}, A_a, ϕ_{ss}, ϕ_{rr}, ϕ_{cc}, d_{mm}. Two mean values were determined for each group (Table 4). The first value was calculated using all data of the group, and the second value was determined after eliminating outstanding or abnormal values from the group. In most cases there was little difference between the two results.

Groups AA and BB show distinct differences between the mean values (Table 4) of two of their four characteristic petrophysical parameters: d_{mm} (25–43 versus 7.3–7.4 nm) and ϕ_{EE} (10–12 versus 6.0–6.2%). The other two characteristic petrophysical parameters, A_a and ϕ_{rr}, also show differences, but not as significant as the prior two. According to Table 1, the ranges of these two parameters (d_{mm}, ϕ_{EE}) suggest that group AA represents shales that are generally medium- to coarse-grained and/or under-compacted. In contrast, they suggest that group BB represents shales that are fine grained and well compacted. Group CC (samples: k.002.343, V-2, V-3, B-TG-6) is characterized by large ϕ_{rr} values (0.58) compared to the others (0.38–0.53), suggesting the existence of dissolution pores and/or under-compacted texture (Table 1). Samples V-2 and V-3 of the group are shales that have experienced significant diagenetic cementation, but are currently at an advanced stage of dissolution (Katsube and Williamson, 1994). Sample B-TG-6 is an unaltered shale (Issler and Katsube, 1994; Bloch and Issler, 1996) from a depth of 2.46 km with a very large ϕ_{rr} value (0.77). Sample k.002.343 is compacted seafloor material (Katsube

Table 4. Group (AA, BB, CC) average values and ranges for the characteristic petrophysical parameters.

Group	δ_{BDD} (g/mL)	δ_{SDD} (g/mL)	ϕ_{EE} (%)	A_a (m²/g)	ϕ_{ss} (%)	ϕ_{rr}	ϕ_{cc} (%)	d_{mm} (nm)
AA	*2.42*	*2.78*	*12.39*	*11.4*	*5.51*	*0.38*	*6.88*	*25.1*
	(1.88-2.80)	*(2.65-3.03)*	*(2.98-30.7)*	*(6.06-18.2)*	*(0.9-10.8)*	*(0.31-0.55)*	*(2.06-19.96)*	*(3.2-50)*
	2.45	**2.75**	**10.16**	**11.24**	**5.35**	**0.47**	**4.82**	**43.1**
	(2.22-2.64)	(2.70-2.83)	(6.7-14.5)	(8.04-14.9)	(3.6-8.0)	(0.35-0.54)	(3.08-6.53)	(5-50)
BB	*2.52*	*2.70*	*6.16*	*10.65*	*3.50*	*0.51*	*2.64*	*7.4*
	(2.10-2.77)	*(2.26-2.92)*	*(1.50-12.4)*	*(3.04-18.8)*	*(0.01-7.9)*	*(0.068-0.73)*	*(1.40-4.46)*	*(3.2-20)*
	2.54	**2.72**	**6.01**	**10.61**	**3.42**	**0.53**	**2.58**	**7.3**
	(2.26-2.74)	(2.59-2.91)	(2.13-9.6)	(3.86-18.5)	(0.4-6.2)	(0.18-0.64)	(1.75-4.28)	(5-13)
CC	*2.40*	*2.77*	*14.35*	*10.84*	*7.45*	*0.59*	*5.17*	*17.7*
	(1.86-2.62)	*(2.73-2.8)*	*(5.6-30.9)*	*(8.87-13.3)*	*(2.7-18.3)*	*(0.39-0.77)*	*(1.59-12.67)*	*(7.9-79)*
	2.56	**2.78**	**6.98**	**10.60**	**4.40**	**0.61**	**3.21**	**10.8**
	(2.55-2.58)	(2.77-2.79)	(6.92-7.04)	(9.5-11.7)	(3.5-5.3)	(0.59-0.62)	(2.13-4.29)	(7.9-20)

Note: The values in italics are those calculated using the data for all samples in the group. The values in bold are those calculated after eliminating outstanding or abnormal values (maximum or minimum or both values) in the group. The maximum and minimum values for each group are in brackets.

δ_{BDD} = Arithmetic mean of the bulk densities (δ_{BD})
δ_{SDD} = Arithmetic mean of the skeletal densities (δ_{SD})
ϕ_{EE} = Arithmetic mean of the effective porosities (ϕ_E); the values of ϕ_{Hg1} from Table 3 is used to represent this value
A_a = Arithmetic mean of the surface areas (A)
ϕ_{SS} = Arithmetic mean of the storage porosities (ϕ_S)
ϕ_{rr} = Arithmetic mean of the storage porosity ratios (ϕ_r)
ϕ_{cc} = Arithmetic mean of the connecting porosities (ϕ_c)
d_{mm} = Geometric mean of the pore-size distribution modes (d_m)

et al., 1996a) with also a large ϕ_{rr} value (0.59). It also displays large d_{mm} (79 nm) and ϕ_{EE} (31%) values. These characteristics of group CC are similar to that of the "weakened pore framework model" (Katsube and Williamson, 1994) that consists of large storage pores, due to intensive dissolution. This suggests rapid permeability and porosity decrease under increased effective pressures due to collapsing of the weakened pores.

ACKNOWLEDGMENTS

The authors thank L. Dyke (GSC, Ottawa) for critically reviewing this paper and for his interesting comments.

REFERENCES

Bloch, J. and Issler, D.R.
1996: Petrographic and geochemical analyses of Beaufort-Mackenzie Basin shales; Geological Survey of Canada, Open File 3220, 95 p.

Brace, W.F.
1980: Permeability of crystalline and argillaceous rocks; International Journal of Rock Mechanics Mineral Sciences and Geomechanics Abstracts, v. 17, p. 241-251.

Coyner, K., Katsube, T.J., Best, M.E., and Williamson, M.
1993: Gas and water permeability of tight shales from the Venture Gas Field offshore Nova Scotia; *in* Current Research, Part D; Geological Survey of Canada, Paper 93-1D, p. 129-136.

Dorsch, J. and Katsube, T.J.
1996: Effective porosity and pore-throat sizes of mudrock saprolite from the Nolichucky shale within Bear Creek Valley on the Oak Ridge Reservation: Implication for contaminant transport and retardation through matrix diffusion; Oak Ridge National Laboratory (U.S. Department of Energy), ORNL/GWPO-025, p. 72.

Dorsch, J., Katsube, T.J., Sanford, W.E., Dugan, B.E., and Tourkow, L.M.
1996: Effective porosity and pore-throat sizes of Conasauga group mudrock: application, test and evaluation of petrophysical techniques; Oak Ridge National Laboratory (U.S. Department of Energy), ORNL/GWPO-021, p. 113.

Issler, D.R. and Katsube, T.J.
1994: Effective porosity of shale samples from thw Beaufort-MacKenzie Basin, northern Canada; *in* Current Research 1994-B; Geological Survey of Canada, p. 19-26.

Katsube, T.J.
1992: Statistical analysis of pore-size distribution data of tight shales from the Scotian Shelf; *in* Current Research, Part E; Geological Survey of Canada, Paper 92-1E, p. 365-372.

Katsube, T.J. and Best, M.E.
1992: Pore structure of shales from the Beaufort-Mackenzie Basin, Northwest Territories; *in* Current Research, Part E; Geological Survey of Canada, Paper 92-1E, p. 157-162.

Katsube, T.J. and Coyner, K.
1994: Determination of permeability-compaction relationship from interpretation of permeability-stress data for shales from eastern and northern Canada; *in* Current Research 1994-D; Geological Survey of Canada, p. 169-177.

Katsube, T.J. and Issler, D.R.
1993: Pore-size distributions of shales from the Beaufort-Mackenzie Basin, northern Canada; *in* Current Research, Part E; Geological Survey of Canada, Paper 93-1E, p. 123-132.

Katsube, T.J. and Williamson, M.A.
1994: Effects of diagenesis on shale nano-pore structure and implications for sealing capacity; Clay Minerals, v. 29, p. 451-461.
1995: Critical depth of burial of subsiding shales and its effect on abnormal pressure development: Proceedings of the Oil and Gas Forum' 95 (Energy from Sediments), Geological Survey of Canada, Open File 3058, p. 283-286.
in press: Shale petrophysical characteristics: permeability history of subsiding shales; *in* Proceedings on Shale Research, GSA Annual Meeting - New Orleans, Louisiana, November 6-9, 1995, p. 363-385.

Katsube, T.J., Best, M.E., and Mudford, B.S.
1991: Petrophysical characteristics of shales from the Scotian shelf; Geophysics, v. 56, p. 1681-1688.

Katsube, T.J., Boitnott, G.N., Lindsay, P.J., and Williamson, M.
1996a: Pore structure evolution of compacting muds from the seafloor offshore Nova Scotia; *in* Current Research 1996-D; Geological Survey of Canada, p. 17-26.

Katsube, T.J., Cox, W.C., and Issler, D.R.
1998a: Porosity characteristics of shale formations from the Western Canada Sedimentary Basin; *in* Current Research 1998-E; Geological Survey of Canada.

Katsube, T.J., Dorsch, J., and Connell, S.
1997: Pore surface area characteristics of the Nolichucky shale within the Oak Ridge Reservation (Tennessee, U.S.A.): implication for fluid expulsion efficiency; *in* Current Research 1997-E; Geological Survey of Canada, p. 117-124.

Katsube, T.J., Issler, D.R., and Cox, W.C.
1998b: Shale permeability and its relation to pore-size distribution; *in* Current Research 1998-D; Geological Survey of Canada, p. 51-57.

Katsube, T.J., Issler, D.R., and Coyner, K.
1996b: Petrophysical characteristics of shales from the Beaufort-Mackenzie Basin, northern Canada; permeability, formation factor, and porosity versus pressure; *in* Current Research 1996-B; Geological Survey of Canada, p. 45-50.

Katsube, T.J., Williamson, M., and Best, M.E.
1992: Shale pore structure evolution and its effect on permeability; *in* Symposium Volume III of the Thirty-Third Annual Symposium of the Society of Professional Well Log Analysts (SPWLA), The Society of Core Analysts Preprints, Oklahoma City, Oklahoma, June 15-17, 1992, Paper SCA-9214, p. 1-22.

Morrow, C., Shi, L., and Byerlee, J.
1984: Permeability of fault gauge under confining pressure and shear stress; Journal of Geophysical Research, v. 89, p. 3193-3200.

Neuzil, C.E.
1994: How permeable are clays and shales?; Water Resources Research, v. 30, p. 145-150.

Geological Survey of Canada Project 870057

Metamorphism of hydrothermally altered rocks

Edgar Froese
Continental Geoscience Division, Ottawa

Froese, E., 1998: Metamorphism of hydrothermally altered rocks; in *Current Research 1998-E; Geological Survey of Canada, p. 193–196.*

Abstract: In some metamorphosed volcanic belts, evidence of premetamorphic hydrothermal activity is preserved in the form of distinct metamorphic mineral assemblages. By considering the effect of metamorphism on rocks of various compositions, it is possible to deduce premetamorphic mineral assemblages, some of which could be products of hydrothermal alteration. In some rocks, precursor minerals kaolinite, muscovite, and chlorite would indicate aluminous, potassic, and ferromagnesian alteration, respectively. The stabilities of alteration minerals can be related to $\log f_{O_2}$-pH conditions of the hydrothermal fluid.

Résumé : Dans certaines zones volcaniques métamorphisées, les manifestations de l'activité hydrothermale prémétamorphique sont conservées sous la forme de paragenèses métamorphiques distinctes. L'étude des effets du métamorphisme sur les roches de composition variée permet de déduire des paragenèses prémétamorphiques dont certaines pourraient résulter de l'altération hydrothermale. Dans certaines roches, des minéraux précurseurs tels que la kaolinite, la muscovite et la chlorite semblent avoir subi respectivement une altération alumineuse, potassique et ferromagnésienne. Les stabilités des minéraux d'altération peuvent être reliées dans le but de consigner les conditions de f_{O_2}-pH du fluide hydrothermal.

INTRODUCTION

Hydrothermal alteration changes the composition of rocks by tending to produce a preponderance of one mineral. Thus the formation of kaolinite, muscovite, and chlorite reflect, respectively, aluminous, potassic, and ferromagnesian alteration.

At a later stage of the geological history, hydrothermally altered rocks may be subjected to metamorphism. Allard and Carpenter (1988) referred to metamorphosed products of hydrothermal alteration as mineralogical anomalies and discussed their significance in exploration. The anomalous character of the alteration minerals and their metamorphosed equivalents stems from their occurrence in rocks whose unaltered composition would preclude their formation. Thus, aluminous assemblages (e.g. kyanite-staurolite) and ferromagnesian assemblages (e.g. cordierite-orthoamphibole) would not be expected in volcanic rocks. Although dealing with common minerals, their unexpected occurrence in some rock types and their unusual modal proportions attest to a premetamorphic change in rock composition.

Alteration types are indicators of different conditions of formation. Therefore, in metamorphosed hydrothermally altered rocks, it is of interest to deduce the premetamorphic alteration type from the metamorphic mineral assemblages. For this purpose, it is advantageous to examine the effects of premetamorphic composition and imposed metamorphism in producing the present mineralogical constitution of metamorphosed hydrothermally altered rocks.

In order to relate the formation of alteration minerals to environmental conditions, their stabilities may be shown on a $\log f_{O_2}$ - pH diagram saturated with iron oxides and sulphides (Hannington et al., 1998). In the presence of oxides and sulphides, chlorite incorporates appreciable amounts of Fe and should not be represented merely by its Mg end member. Accordingly, in this note, the stability field of Fe-Mg chlorite is shown, with contours of X_{Mg} of chlorite. Mineral assemblages resulting from the metamorphism of altered rocks are discussed by plotting the alteration minerals on an AKF diagram familiar from metamorphic petrology, where A = Al_2O_3-K_2O, K = K_2O, and F = (Fe,Mg)O. This system is then examined at different grades of metamorphism but with the modification of treating FeO and MgO as separate components. This procedure avoids the problem of crossing tie lines.

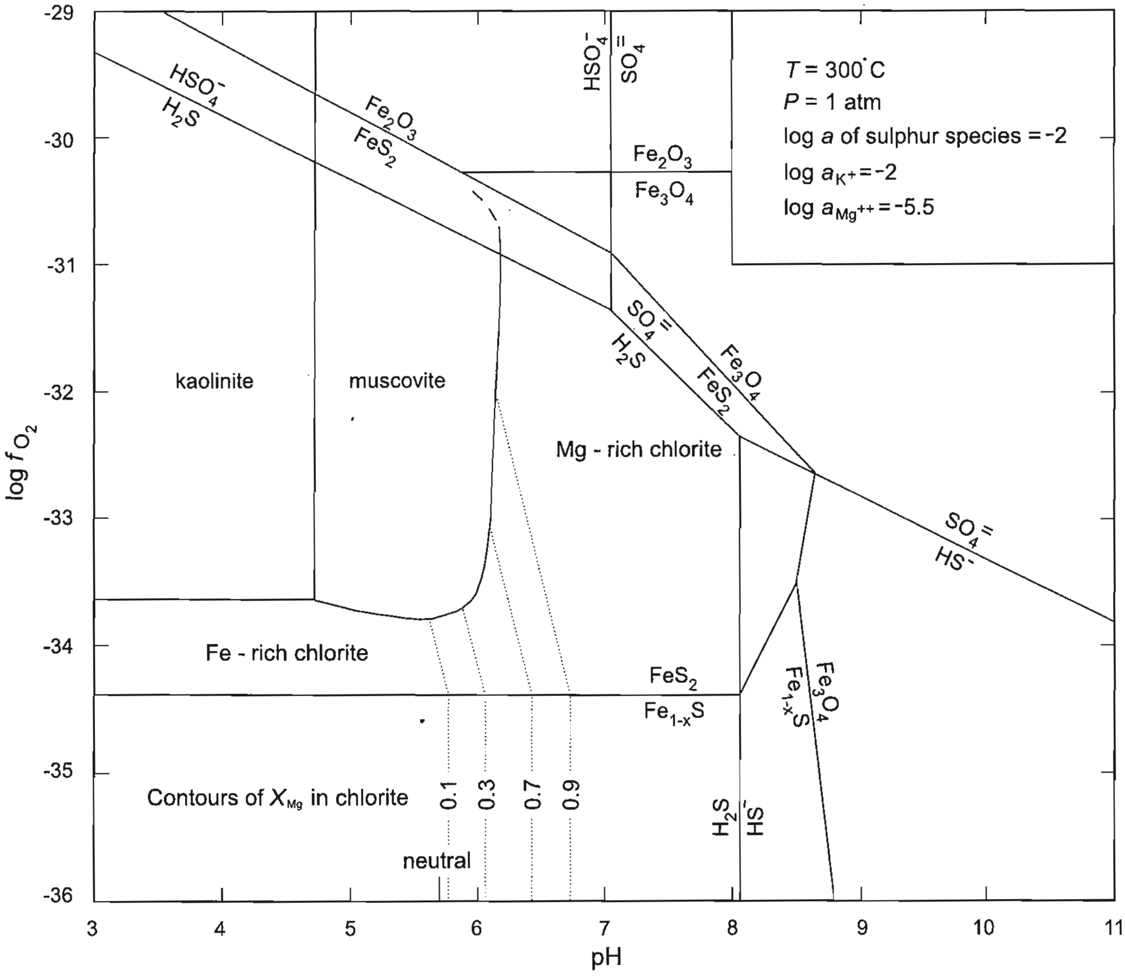

Figure 1. The hydrothermal stability of kaolinite, muscovite, and chlorite.

The more magnesian minerals are represented in the system A = Al_2O_3-K_2O, K = K_2O, and M = MgO. The component FeO can lead to the appearance of an additional Fe-rich mineral, either staurolite or almandine.

STABILITY OF HYDROTHERMAL MINERALS

Important variables governing mineral stabilities in a hydrothermal environment are f_{O_2}, f_{S_2}, and pH. Various diagrams, incorporating these variables, have been used to represent the stabilities of oxides, sulphides, and silicates (Meyer and Hemley, 1967). On the log f_{O_2}-pH diagram shown in Figure 1, the predominance fields of the sulphur species and the stability fields of the iron oxides and sulphides have been taken from Froese (1981). Each sulphur species, within its predominance field, is assumed to have a constant activity. Equilibrium constants of reactions involving silicates have been taken from Helgeson (1969).

In Figure 1, the kaolinite-muscovite boundary, for log $a_{K^+} = -2$, is given according to the reaction:

$$2KAl_2Si_3AlO_{10}(OH)_2 + 2H^+ + 3H_2O$$
$$= 3Al_2Si_2O_5(OH)_4 + 2K^+$$
$$\log K = 5.44$$

Contours of X_{Mg} in chlorite can be drawn on the basis of reaction equations involving the two end members of chlorite, one of the iron minerals and a sulphur species. For example, in the stability field of pyrite and in the predominance field of H_2S, the following equation applies:

$$0.2Fe_5AlSi_3AlO_{10}(OH)_8 + Mg^{++} + 2H_2S + 0.5O_2$$
$$= 0.2Mg_5AlSi_3AlO_{10}(OH)_8 + FeS_2 + 2H^+ + H_2O$$

The slope, for a given composition and $a_{Mg^{++}}$, follows from the reaction equation and the location can be shown by assuming one point, e.g. log fO_2 = 33.5 and pH = 6.5 for $X_{Mg} = 0.9$. This assumption places the change from Fe-rich to Mg-rich chlorite near neutral pH. For the same log f_{O_2}, the pH of a different contour can be calculated by assuming an ideal solution model for chlorite. Some chlorite composition contours are terminated by the reaction with muscovite:

$$3Mg_5AlSi_3AlO_{10}(OH)_8 + 28H^+ + 2K^+$$
$$= 2KAl_2Si_3AlO_{10}(OH)_2 + 15Mg^{++} + 3SiO_2 + 24H_2O$$
$$\log K = 94.16$$

In order to obtain a pH value at the chlorite-muscovite boundary, it is necessary to know a_{K^+} and a_{Mg+}. Using log $a_{K^+} = -2$, as for the kaolinite-muscovite boundary, and an assumed value of log $a_{Mg+} = -5.5$, gives a muscovite field extending to near-neutral conditions. Other contours for Fe-rich chlorite (not shown on the diagram) are terminated by the reaction:

$$Mg_5AlSi_3AlO_{10}(OH)_8 + 10H^+$$
$$= Al_2Si_2O_5(OH)_4 + 5Mg^{++} + SiO_2 + 7H_2O$$
$$\log K = 33.20$$

It is apparent that, in contrast to kaolinite and muscovite, Mg chlorite is favoured by an alkaline environment. On the other hand, at low logf_{O_2}, the stability of Fe chlorite extends to acidic conditions.

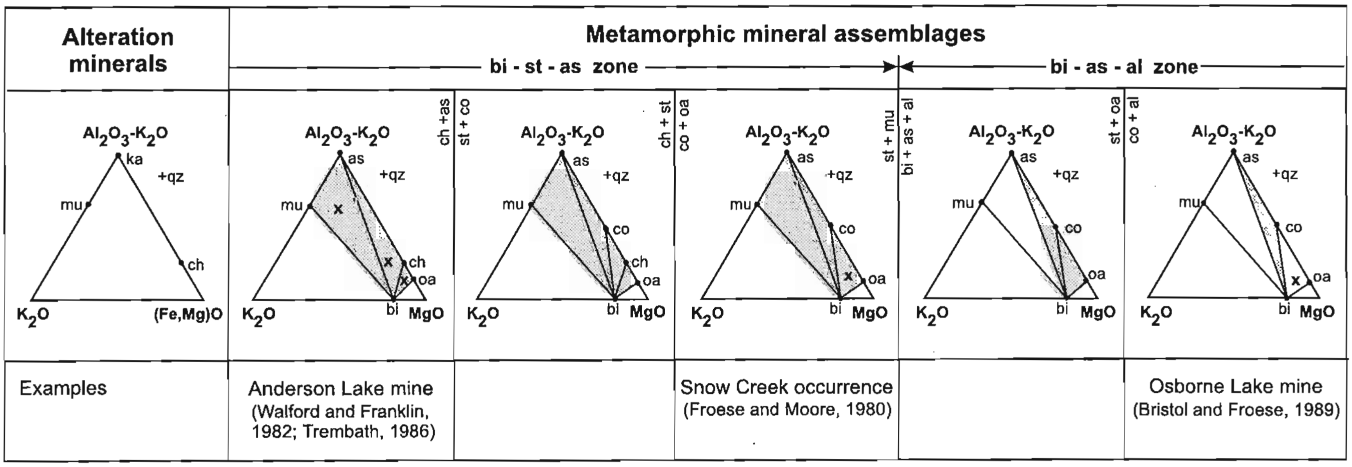

Mineral abbreviations:

qz	quartz	**as**	aluminium silicate
mu	muscovite	**bi**	biotite
ka	kaolinite	**oa**	orthoamphibole
ch	chlorite	**co**	cordierite

shaded area **+ staurolite**
unshade area **+ almandine**

Observed mineral assemblages **x**

Figure 2. Metamorphic mineral assemblages in hydrothermally altered rocks.

METAMORPHISM

The compositional relationship among alteration minerals may be shown conveniently on the AKF diagram of metamorphic petrology (Meyer and Hemley, 1967), where A = Al_2O_3-K_2O, K = K_2O, and F = (Fe,Mg)O. In Figure 2, kaolinite, muscovite, and chlorite are plotted on such a diagram. Also shown are metamorphosed equivalents at different grades of metamorphism. Because FeO and MgO act as two components, the metamorphic minerals are shown in the four-component system (Al_2O_3-K_2O)-K_2O-FeO-MgO. This is accomplished by representing the Mg-rich minerals in the system (Al_2O_3-K_2O)-K_2O-MgO and indicating the presence of one additional Fe-rich mineral, either staurolite or almandine, introduced by regarding FeO as a fourth component. A maximum number of four minerals is stable. This procedure avoids crossing tie lines, which is a problematic feature in showing mineral assemblages on an AKF diagram which treats FeO and MgO as one component; also, it retains a compositional representation very similar to the AKF diagram which is used to provide a succinct overview of alteration types. In this manner, metamorphic mineral assemblages may be used as indicators of premetamorphic alteration. As examples, metamorphic mineral assemblages in metamorphosed alteration zones are given from the Snow Lake area, Manitoba, which displays a prominent metamorphic zonation (Froese and Moore, 1980; Kraus and Menard, 1997).

ACKNOWLEDGMENTS

The diagrams were drafted by D. Lemkow. The manuscript benefitted from critical reading by K.L. Currie and R.G. Berman.

REFERENCES

Allard, G.O. and Carpenter, R.H.
1988: Mineralogical anomalies in metamorphosed terrains: a neglected but promising exploration tool; International Conference – Geochemical Evolution of the Continental Crust, Pocos de Caldas, Brazil, Abstracts Volume, p. 229-236.

Bristol, C.C. and Froese, E.
1989: Highly metamorphosed altered rocks associated with the Osborne Lake volcanogenic massive sulfide deposit; Canadian Mineralogist, v. 27, p. 593-600.

Froese, E.
1981: Applications of thermodynamics in the study of mineral deposits; Geological Survey of Canada, Paper 80-28, 38 p.

Froese, E. and Moore, J.M.
1980: Metamorphism in the Snow Lake area, Manitoba; Geological Survey of Canada, Paper 78-27, 16 p.

Hannington, M.D., Poulsen, K.H., Thompson, J.F.H., and Sillitoe, R.H.
1998: Volcanogenic gold and epithermal-style mineralization in the VMS environment; Reviews in Economic Geology, v. 8, p. 183-214.

Helgeson, H.C.
1969: Thermodynamics of hydrothermal systems at elevated temperatures and pressures; American Journal of Science, v. 267, p. 729-804.

Kraus, J. and Menard, T.
1997: A thermal gradient at constant pressure: implications for low- to medium-pressure metamorphism in a compressional tectonic setting, Flin Flon and Kisseynew domains, Trans-Hudson orogen, central Canada; Canadian Mineralogist, v. 35, p. 1117-1136.

Meyer, C. and Hemley, J.J.
1967: Wall rock alteration; *in* Geochemistry of Hydrothermal Ore Deposits; Holt, Rinehart and Winston, New York, p. 166-235.

Trembath, G.D.
1986: The compositional variation of staurolite in the area of Anderson Lake mine, Snow Lake, Manitoba; M.Sc. thesis, University of Manitoba, Winnipeg, Manitoba, 187 p.

Walford, P.C. and Franklin, J.M.
1982: The Anderson Lake mine, Snow Lake, Manitoba; Geological Association of Canada, Special Paper 25, p. 481-523.

Geological Survey of Canada Project 800007

AUTHOR INDEX

NOTE TO CONTRIBUTORS

Submissions to the Discussion section of Current Research are welcome from both the staff of the Geological Survey of Canada and from the public. Discussions are limited to six double-spaced typewritten pages (about 1500 words) and are subject to review by the Managing Editor. Discussions are restricted to the scientific content of Geological Survey reports. General discussions concerning sector or government policy will not be accepted. All manuscripts must be computer word-processed on an IBM compatible system and must be submitted with a diskette using WordPerfect. Illustrations will be accepted only if, in the opinion of the editor, they are considered essential. In any case no redrafting will be undertaken and reproducible copy must accompany the original submissions. Discussion is limited to recent reports (not more than two years old) and may be in either English or French. Every effort is made to include both Discussion and Reply in the same issue. Current Research is published in January and July. Submissions should be sent to the Managing Editor, Geological Survey of Canada, 601 Booth Street, Ottawa K1A 0E8.

AVIS AUX AUTEURS D'ARTICLES

Nous encourageons tant le personnel de la Commission géologique que le grand public à nous faire parvenir des articles destinés à la section discussion de la publication Recherches en cours. Le texte doit comprendre au plus six pages dactylographiées à double interligne (environ 1500 mots), texte qui peut faire l'objet d'un réexamen par la rédactrice en chef administrative. Les discussions doivent se limiter au contenu scientifique des rapports de la Commission géologique. Les discussions générales sur le Secteur ou les politiques gouvernementales ne seront pas acceptées. Le texte doit être soumis à un traitement de texte informatisé par un système IBM compatible et enregistré sur disquette WordPerfect. Les illustrations ne seront acceptées que dans la mesure où, selon l'opinion du rédacteur, elles seront considérées comme essentielles. Aucune retouche ne sera faite aux illustrations et dans tous les cas, une copie qui puisse être reproduite doit accompagner le texte original. Les discussions en français ou en anglais doivent se limiter aux rapports récents (au plus de deux ans). On s'efforcera de faire coïncider les articles destinés aux rubriques discussions et réponses dans le même numéro. La publication Recherches en cours paraît en janvier et en juillet. Les articles doivent être envoyés à la rédactrice en chef administrative, Commission géologique du Canada, 601, rue Booth, Ottawa K1A 0E8.

Geological Survey of Canada Current Research is released twice a year, in January and July. The four parts published in January 1998 (Current Research 1998-A to D) are listed below and can be purchased separately.

Recherches en cours, une publication de la Commission géologique du Canada, est publiée deux fois par année, en janvier et en juillet. Les quatre parties publiées en janvier 1998 (Recherches en cours 1998-A à D) sont énumérées ci-dessous et sont vendues séparément.

Part A: Cordillera and Pacific Margin
Partie A : Cordillère et marge du Pacifique
Part B: Interior Plains and Arctic Canada
Partie B : Plaines intérieures et région arctique du Canada

Part C: Canadian Shield
Partie C : Bouclier canadien

Part D: Eastern Canada and national and general programs
Partie D : Est du Canada et programmes nationaux et généraux

Part E: this volume
Partie E : ce volume